FINAL REPORT

Scientific Understanding of Non-Chromated Corrosion Inhibitors Function

SERDP Project WP-1620

Gerald S. Frankel
Rudolph G. Buchheit
The Ohio State University

Mark Jaworowski
United Technologies Research Center

Greg Swain
Michigan State University

SERDP
DOD • EPA • DOE

REPORT DOCUMENTATION PAGE

Public reporting burden for this collection of information is estimated to average 1 hour per response, including the time for reviewing instructions, searching existing data sources, gathering and maintaining the data needed, and completing and reviewing this collection of information. Send comments regarding this burden estimate or any other aspect of this collection of information, including suggestions for reducing this burden to Department of Defense, Washington Headquarters Services, Directorate for Information Operations and Reports (0704-0188), 1215 Jefferson Davis Highway, Suite 1204, Arlington, VA 22202-4302. Respondents should be aware that notwithstanding any other provision of law, no person shall be subject to any penalty for failing to comply with a collection of information if it does not display a currently valid OMB control number. **PLEASE DO NOT RETURN YOUR FORM TO THE ABOVE ADDRESS.**

1. REPORT DATE (DD-MM-YYYY) 01-25-2013	2. REPORT TYPE FINAL	3. DATES COVERED (From - To) March 2008 – August 2012

4. TITLE AND SUBTITLE
"Scientific Understanding of Non-Chromated Corrosion Inhibitors Function"

5a. CONTRACT NUMBER
W912HQ-08-C-0011

5b. GRANT NUMBER

5c. PROGRAM ELEMENT NUMBER

6. AUTHOR(S)
Frankel, Gerald S.; Buchheit, Rudolph G.; Jaworowski, Mark; Swain, Greg.

5d. PROJECT NUMBER
WP-1620

5e. TASK NUMBER

5f. WORK UNIT NUMBER

7. PERFORMING ORGANIZATION NAME(S) AND ADDRESS(ES)

The Ohio State University, Columbus, OH 43210
United Technologies Research Center, East Hartford, CT

Michigan State University, Ann Arbor, MI

8. PERFORMING ORGANIZATION REPORT NUMBER

9. SPONSORING / MONITORING AGENCY NAME(S) AND ADDRESS(ES)
Strategic Environmental Research and Development Program
4800 Mark Center Drive, Suite 17D08
Alexandria, VA 22350-3605

10. SPONSOR/MONITOR'S ACRONYM(S)
SERDP

11. SPONSOR/MONITOR'S REPORT NUMBER(S)

12. DISTRIBUTION / AVAILABILITY STATEMENT

13. SUPPLEMENTARY NOTES

14. ABSTRACT
This project generated understanding of the mechanisms of non-chromate corrosion inhibiting coating systems by studying cross-cutting issues and leading chromate-free chemicals and systems. In Task 1, Trivalent Chromium Process coatings were found to release chromium into solution, which can then form a film on nearby uncoated alloy surface. Transient formation of Cr(VI) was observed, and postulated to form by oxidation of Cr(III) oxide by locally produced H_2O_2, which is a product of oxygen reduction. Inhibition in solution by common species found in commercial chromate-free primers was studied: molybdate, silicate, and praseodymium in Task 2, and Ce^{3+}, Pr^{3+}, La^{3+} and Zn^{2+} cations in Task 3. A mechanism for inhibition by each species was postulated. In Task 4, effects of surface treatments and roughness on adhesion of coatings were studied using the Blister Test. In Task 5, solubility of modern chromate-free pigments was found to depend on reactions with their environment and with their internal co-pigments, and their transport properties were influenced by ionic current and the fine structure of the primer matrix. Interactions between the various components of Cr-free coating systems were studied in Task 6. In Task 7, Direct Optical Interrogation was used for in-situ monitoring of metallic thin film corrosion underneath organic coating systems.

15. SUBJECT TERMS Al alloys, Non-chromate corrosion-protective coating systems, Non-chromate corrosion inhibitors, Non-chromate surface treatments, Trivalent Chromium Process, Transient formation of Cr(VI), Molybdate, Silicate, Lanthanides, Zinc cations, Coating adhesion, Blister Test, Inhibitor solubility, Inhibitor transport in coatings, Coating component interactions, Under-coating corrosion.

16. SECURITY CLASSIFICATION OF:			17. LIMITATION OF ABSTRACT	18. NUMBER OF PAGES	19a. NAME OF RESPONSIBLE PERSON Gerald S. Frankel
a. REPORT	**b. ABSTRACT**	**c. THIS PAGE**		370	19b. TELEPHONE NUMBER (include area code) 614-688-4128

Table of Contents

List of Acronyms

AES	Atomic Emission Spectroscopy (p. 234)
AES	Auger Electron Spectroscopy (p. 236)
AFM	Atomic Force Microscopy
AFOSR	Air Force Office of Scientific Research
ANN	Artificial Neural Network
ASTM	American Society for Testing and Materials
BFM	Breakpoint frequency method
BT	Blister test
CCC	Chromate conversion coating
CE	Counter electrode
CEC	Cation Exchange Capacity
CI	Constant Infusion
CP	Constant Pressure
CPE	Constant Phase Element
DBES	Doppler broadening of energy spectra
DD	Degreased and deoxidized
DDTCP	Degreased and deoxidized + TCP
DOI	Direct optical interrogation
EC	Equivalent circuit
EDAX/EDXS	Energy Dispersive Analysis by X-rays/Energy Dispersive X-ray Spectroscopy
EDS	Energy Dispersive Spectroscopy
EIS	Electrochemical Impedance Spectroscopy
FIB	Focused ion beam
FTIR	Fourier transform infrared spectroscopy
GBT	Galvanic Blister Test
GC/MS	Gas chromatography / mass spectroscopy
ICP	Inductively coupled plasma
IMC	Intermetallic Compound
MSDS	Materials Safety Data Sheet
NAVAIR	Naval Air Systems Command (of the U. S. Navy)
NCP	Non-Chromium Process
NMR	Nuclear Magnetic Resonance
OCP	Open circuit potential
OES	Optical emission spectroscopy
OLI	short for OLI Systems, Inc.
OP	Optical Profilometer
ORR	Oxygen reduction reaction
OSU	Ohio State University
PALS	Positron Annihilation Lifetime Spectroscopy
PVA	Polyvinyl alcohol
PVB	Polyvinyl buterol

RC	Resistor - capacitor
REM	Rare earth metal
RDE	Rotating disk electrode
rms	root mean squared
RT	Room Temperature
RTU	ready to use
SCE	Saturated calomel electrode
SEM	Scanning Electron Microscopy
SERDP	Strategic Environmental Research and Development Program
SHE	Standard Hydrogen Electrode
SKP	Scanning Kelvin probe
SKPFM	Scanning Kelvin probe force microscopy
SP	Set-point (p. 103)
SP	Scribe Protection (p. 186)
TCP	Trivalent Chrome Process
TEM	Transmission Electron Microscopy
TGA	Thermogravimetric analysis
TTF	Time to failure
UTRC	United Technologies Research Center
UV-vis	Ultraviolet - visible
VOC	Voaltile Organic Compound
XPS	X-ray photoelectron spectroscopy
XRD	X-ray diffraction

List of Figures

corrected spectral intensity between 780-940 cm^{-1}.

List of Tables

Keywords

1. Al alloys
2. Non-chromate corrosion-protective coating systems
3. Non-chromate corrosion inhibitors
4. Non-chromate surface treatments
5. Trivalent Chromium Process
6. Transient formation of Cr(VI)
7. Molybdate
8. Silicate
9. Lanthanides
10. Zinc cations
11. Coating adhesion
12. Blister Test
13. Inhibitor solubility
14. Inhibitor transport in coatings
15. Coating component interactions
16. Under-coating corrosion

Acknowledgements

1. Executive Summary

This report summarizes the findings and accomplishments achieved during a 4-year project aimed at generating understanding of the mechanisms of non-chromate corrosion inhibiting coating systems. It is divided into a number of tasks that ran concurrently. The approach was to study cross-cutting issues and a few leading chromate-free chemicals and systems.

Task 1: Trivalent chromium process (TCP) coatings were studied on several Al alloys. The TCP coating is approximately 50-100 nm thick and is primarily hydrated zirconia with co-precipitation of $Cr(OH)_3$. The layer formation is driven by an increase in the interfacial pH caused by dissolution of the oxide layer and localized oxygen reduction at Cu-rich intermetallic sites. TCP coating provides both anodic and cathodic protection by physically blocking Al-rich sites (oxidation) and Cu-rich intermetallics (reduction), resulting in 10x greater polarization resistance and suppressed anodic and cathodic currents around the open circuit potential. TCP coating can release chromium into solution, which can then form a film on the surface of an uncoated alloy surface exposed in close proximity. The polarization resistance of the uncoated surface near a TCP-coated surface is higher than uncoated controls, which indicates the TCP coating can provide active corrosion inhibition. There is evidence for transient formation of Cr(VI) species in the coating after some period of drying and or electrolyte solution exposure. Cr(VI) likely forms due to the oxidation of Cr(III) oxide by locally produced H_2O_2, which is a product of oxygen reduction. This transient Cr(VI) might be the source of the active corrosion inhibition.

Task 2: The inhibition performance of molybdate, silicate, and praseodymium was studied and a mechanism for each inhibitor was postulated. These are common inhibitors found in commercial chromate-free primers. Molybdate, inhibition is optimal at near-neutral pH. MoO_3 imparts anodic inhibition by ennobling the pitting potential. The inhibition mechanism involves an oxidation-reduction process whereby MoO_2 is formed and subsequently re-oxidized in two steps to form MoO_3 over the intermetallic particles. At low pH, molybdate is ineffective because of polymerization. Silicate is a strong anodic inhibitor in highly alkaline conditions, increasing the pitting potential by as much as 1 V. At high pH the dissolution of the aluminum oxide film on the surface promotes the formation of an aluminosilicate thin-film that is physically adsorbed to the negatively charged surface by Na^+ ions. At near-neutral pH, silicate blocks the activation of intermetallic particles on the surface by the formation of silicate- and silica-based particulates. Praseodymium imparts cathodic inhibition at near-neutral pH, lowering the oxygen reduction kinetics by a factor of 10. Pr carbonate hydroxide forms over the ORR supporting IMC particles as the local pH increases. As the cathodes on the surface become blocked by a thick-oxide, new sites are activated resulting in the formation of a thick-film across the whole surface. In low and high solution pH, praseodymium renders poor inhibition. *In situ* AFM scratching experiments reveal that at their respective optimum inhibition concentrations, all three inhibitors reduce the removal rate of the S-phase particles in comparison to the inhibitor-free case.

Task 3: Studies of inhibition of Al alloy corrosion by Ce^{3+}, Pr^{3+}, La^{3+} and Zn^{2+} cations in solution have been undertaken. A comparative study on the corrosion inhibition caused by rare earth metal cations, Ce^{3+}, Pr^{3+}, La^{3+} and Zn^{2+} cations on AA 2024-T3 alloy was done. Cathodic

polarization showed that these inhibitor ions suppress the oxygen reduction reaction (ORR) to varying extents with Zn^{2+} providing the best inhibition. It was observed that Pr^{3+} exhibits windows of concentration (100-300 ppm) in which the corrosion rate is minimum; similar to the Ce^{3+} cation. Scanning Electron Microscopy (SEM) studies showed that the mechanism of inhibition of the Pr^{3+} ion is also similar to that of the Ce^{3+} ion. Lanthanum is not an effective inhibitor of the alloy as inferred from both electrochemical experiments and microscopic analysis on 2024-T3. Results show that Zn^{2+} is an effective inhibitor with inhibition arising from the precipitation of mixed Zn hydroxide/Zn hydroxycarbonate surface film. The presence of the film on the surface slows both anodic and cathodic reaction kinetics, but film formation is gradual and Zn^{2+} is best characterized as a "slow inhibitor". To explore inhibitor delivery in corrosion resistant coatings, inhibitor cations were exchanged into insoluble ion-exchanging sodium bentonites and incorporated as pigments in organic coatings applied to AA 2024-T3 substrates. Electrochemical impedance measurements were carried out on coated samples during exposure in 0.5 M NaCl solutions. Salt spray exposure tests on scribed panels were preformed and results were compared to those from $SrCrO_4$ pigmented coatings. Zn-exchanged bentonite pigmented coatings showed better performance compared to lanthanide cation-exchanged bentonites when incorporated into epoxy coatings with total impedance magnitude in the same order as the $SrCrO_4$ comparator.

Task 4: The blister test was used to study the effect of surface treatments on adhesion of coatings. Roughness degree and surface topography are very important factors for adhesion strength of PVB to AA2024-T3. Adhesion strength increases with roughness and surface area due to a larger interaction in the primer/substrate interface. Randomly abraded samples have higher adhesion strength than randomly abraded samples. Numerous approaches were tested to sample adhesion strength using the BT after adhesion degradation of the interface, but no adhesion strength degradation was found. Galvanic coupling of SS316 fasteners to AA2024-T3 activates the underlying metal due to the high cathodic current on the fastener. The minimum potential along the scribe tends to decrease with increased galvanic coupling owing to activation of the aluminum alloy. This contradicts the typical assumptions of galvanic coupling. The galvanic interaction and coating degradation varies with different fastener materials according to SS316 > Ti 6-4 > AA2024-T3 ≈ No fastener. Conversion coating treatment improves adhesion strength of acetoacetate and epoxy coated samples to AA2024-T3. Cleaning and deoxidizing improves adhesion of acetoacetate samples for all conversion coatings except for chromate conversion coating. For epoxy coatings the addition of the cleaning/deoxidizing step improves the adhesion strength of the chromate conversion coated samples, but no effect is noticeable for titania-based surface treatment and for Trivalent Chrome Process treatment.

Task 5: The solubility of modern chromate-free pigments was found to depend beneficially on reactions both with their environment and with their internal co-pigments, with their transport properties influenced both by ionic current and the fine structure of the primer matrix. All inhibitors studied exhibited significant solubility enhancement with exposure to strong electrolytes such as salt water, with the magnitude of the solubility enhancement governed by the ionic charge of the soluble inhibitor complex. Silicate based corrosion inhibitors were found to increase in solubility on exposure to air due to reactions with dissolved carbon dioxide. Praseodymium based corrosion inhibitors were found to undergo a beneficial reaction with a supporting pigment compound to generate an enhanced solubility corrosion inhibitor complex. Measurement of inhibitor enrichment on primer surfaces exposed to electric fields indicate both

the role of electrophoresis in inhibitor transport and the differential ionic direction of charged inhibitor species to active surface sites. The water and inhibitor transport properties of aerospace primers were found to be regulated by a fine structure characterized by dense polymer layers at the substrate and air interfaces that encapsulate a nanoporous inner layer. This beneficial barrier aspects of this structure are somewhat offset by its tendency to promote water transport within the plane of the primer film.

Task 6: A range of emergent Cr-free coating systems were characterized to understand the levels of corrosion protection provided to high-strength Al alloy substrates (2024-T3 and 7075-T6) in standardized and laboratory testing and to illuminate the interactions between the various components of the coating system—topcoat, primer, pretreatment that lead to the levels of corrosion protection observed. Specifically, electrochemical impedance spectroscopy and ASTM B117 exposure testing were carried out on coating systems comprising DoD-qualified primers and pretreatment products. The results showed that all Cr-free coating system combinations were inferior to chromate coating system incumbents. The results also allowed a rank ordering of performance. A central finding was that the nature of the pretreatment was critical in overall corrosion protection. The nature of the results enabled development of an empirical model to relate results from short-term Electrochemical Impedance Spectroscopy (EIS) measurements to long-term exposure measurements. Destructive forensic measurements of coating systems after ASTM B117 exposure reinforce the essential role of surface pretreatment to overall protectiveness. These results suggest that Cr-free pretreatments do not regularly form the foundations for Cr-free corrosion-resistant coating systems. The idea that low-chrome system is far superior to a no-chrome coating systems is supported in the results. With respect to primer coating formulations, the data suggest that inhibitor pigments used are not releasing sufficient amounts of inhibitor ions and that the active inhibitor species may not be sufficiently protective to have a meaningful inhibiting effect on aluminum alloy corrosion. The extent to which inhibiting pigment particle dissolution or resin permeance restricts inhibitor ion availability remains to be clarified.

Task 7: An approach referred to as Direct Optical Interrogation (DOI) was used for in-situ monitoring the corrosion of metallic thin films underneath the organic coating systems. Al and Al-Cu (4.9%) thin films were deposited on glass substrates. Different coating systems including various primers and topcoat combinations were applied on top of the metallic thin films. The corrosion damage accumulation under coatings during free corrosion exposures not only depends on the particular aggressive electrolytes but also on the metallization of thin films as well as the local environments. In HCl solutions, uniform corrosion with copious hydrogen gas evolution can be observed. In contrast, in near-neutral sodium chloride solutions where oxygen reduction is expected to drive the corrosion cell process, localized corrosion occurs with pit morphologies ranging from smooth to irregularly shaped. Furthermore, a rigorous estimation of undercoating corrosion site growth kinetics can be made using video capture of the pit perimeter and pit bottom area. Results show that localized corrosion growth is episodic with short bursts of growth occurring between long periods of passivity. Site growth rates during active dissolution range from mA/cm^2 to A/cm^2 depending on the metallization of the thin films and the coating systems. By integrating the electrochemical experiments (Electrochemical Impedance Spectroscopy-EIS) with the optical image analyzer, the undercoating corrosion damage can be evaluated in novel ways.

2. Project Background

This project was focused on developing understanding of the mechanisms of corrosion inhibition by chromate-free chemicals and systems. It started on March 24, 2008, and concluded on August 30, 2012. This final report describes detailed findings of the work.

Over the past 15 years, scientific studies on the mechanism of chromate inhibition have led to a new understanding of chromates and also resulted in the development of new techniques and approaches to study corrosion inhibition. The ultimate goal of that work, to assist in the development of non-chromate inhibitors was not realized, partly because the same type of activity has not been focused on the non-chromate inhibitors. Non-chromate conversion coatings and inhibiting pigments had been developed with some success by Edisonian approaches, but the fundamental understanding of their functionality was still lacking, thereby inhibiting further advances and creating risk associated with their use.

This background section will review the lessons learned from previous work on chromates and provide details of the understanding of some non-chromate components at the time that this project began.

2.1. Chromate inhibition mechanism

Since the replacement inhibiting systems have to duplicate the performance of chromates, it is of considerable value to consider what is known about chromate inhibition. Chromates are extraordinarily effective corrosion inhibitors for many metals [1], and most of the work has focused on inhibition of high-strength Al alloys used in aerospace applications, which are extremely difficult to protect completely. Chromates (Cr(VI)) present at low concentration (mM range) in otherwise aggressive chloride-containing solutions will reduce to Cr(III) on Al alloy surfaces, inhibiting the rate of the primary cathodic reaction, oxygen reduction. Under some conditions, only a monolayer of Cr(III) species forms because it inhibits further chromate reduction as well as oxygen reduction [2]. Since the oxidative corrosion reaction requires a cathodic reaction to consume the electrons generated, inhibition of the reduction reaction can be extremely effective at reducing the rate of corrosion. The Cr(III) layer also provides a modest anodic inhibition as evidenced by protection of susceptible intermetallic particles (e.g. Al_2CuMg or S phase) [3] and an increase in the breakdown potential required to form pits [4]. This anodic protection in turn affects the cathodic reaction by reducing the enrichment and redistribution of Cu that occurs by attack of Cu-rich particles and Cu-containing matrix [4]. The enrichment of Cu by these processes enhances the cathodic reaction because the Cu provides a catalytic surface [5]. So the combination of cathodic and anodic inhibition makes chromate ions extremely effective at reducing the rate of corrosion.

Chromates also protect Al surfaces by way of conversion coatings and anodizing sealant baths. Chromate conversion coatings (CCCs) protect the Al alloy surface by acting as a barrier and providing a reservoir of soluble chromate ions that results in so-called active inhibition. CCCs form by a sol-gel process involving reduction, hydrolysis, polymerization, and condensation of the Cr(III) species, which forms a barrier coating about 100 nm in thickness [6-8]. This Cr(III) backbone also acts as a host for chromate ions, which adsorb onto it and can later be released. The release of chromate from a CCC analog was shown to be pH dependent, with uptake

occurring at low pHs and release at high pHs following a Langmuir adsorption law [9]. This reservoir of adsorbed and releasable chromate provides the active corrosion inhibiting characteristic of CCCs. A non-coated region in close proximity to a CCC-coated area is protected from corrosion by the release and reduction of the soluble chromate [10]. CCCs also promote good adhesion to a paint coating applied on top. These characteristics explain why scribed samples coated with a CCC and paint overcoat (even one with no chromate pigment) exhibits no scribe corrosion and minimizes scribe creep (undercutting of the scribed polymer edge) during exposure to aggressive environments such as a salt spray cabinet.

Further protection is provided by chromate pigments added to primer coatings. Strontium chromate ($SrCrO_4$) is typically the compound added owing to its limited solubility. Soluble inhibitors provided by paint pigments must generate sufficient concentration of ionic species to inhibit the corrosion reactions but less than that necessary to cause blister formation.[11] Solubilization is promoted by water uptake in the polymer, so pigmented primer resins such as epoxies are typically rather water permeable. Topcoats are commonly polyurethanes and are usually less water permeable than epoxy primers.

Replicating the key aspects of chromates, i.e. inhibition of oxygen reduction, anodic inhibition via a protective film, self-healing, and adhesion promotion, resulting in scribe protection and limited scribe creep for corrosion-susceptible alloys, is a requirement for a Cr-free coating system. However, the mechanisms need not be the same as for chromates, and likely will not be the same.

2.2. Non-chromate Conversion Coatings

The current understanding of Cr-free pretreatments based on cerium, trivalent chromium, and zirconium and titanium is reviewed in this section.

Ceria based conversion coatings or cerate treatment: Rare earth metal (REM) salts have been shown to inhibit corrosion for a variety of metals and alloys including high strength aluminum alloys. REMs have received significant attention because they impart good corrosion protection and are relatively environment-friendly [12-15]. Of all the non-chromate inhibitors, the REMs have been the most studied and are the best understood. A number of studies investigated the corrosion inhibition efficacy of La, Y, and Ce salts [12, 16, 17]. Ce salts showed the greatest potential for increasing corrosion resistance of aluminum alloys [14, 15, 18]. Early studies conducted by Hinton et al. showed that additions of cerium chloride ($CeCl_3$) to NaCl solutions suppressed corrosion of 7075-T6 [12, 16]. Corrosion protection was imparted by the precipitation of a hydrated cerium oxide/hydroxide on local cathodes due to the increase of pH associated with the oxygen reduction reaction (ORR) [12-19]. As a consequence of the blockage of local cathodes, Ce and REMs are considered to be cathodic inhibitors. Davenport et al. showed that the film developed by immersing Al in $CeCl_3$ had a mixed Ce(III)/Ce(IV) oxidation state [15, 18].

The degree of protection of Ce films strongly depends on immersion time. In this regard, the main disadvantage of the early Ce surface treatments was the long time required to achieve high corrosion protection [19-21]. Optimum protection was shown to require approximately 20 h, but some authors have pretreated Al samples for about a week. Hinton and co-workers discovered

that the precipitation of Ce hydroxide could be dramatically accelerated by adding hydrogen peroxide to the coating baths to obtain a mixed Ce(III)/Ce(IV) solution [22]. In accelerated cerium-based solutions, Hughes et al. showed that the reduction of H_2O_2 is responsible for a pH increase, which accelerates Ce hydroxide deposition [23].

More recent accelerated ceria based conversion coating formulas are acidic, with a pH in the range from 3 to 1.9, with $CeCl_3$ and approximately 3 vol% H_2O_2 [19, 21, 23]. Typical coating procedures include an initial desmutting for 10 min at 35°C, followed by immersion in the conversion coating for about 6-10 min [21, 23]. Additional steps after coating formation include sealing, rinsing, and drying. The seal is generally silicate based. It is applied at 80°C, and can have a thickness of about 200 nm.

Surface conversion coatings prepared by accelerated Ce formulas have been shown by some to improve adhesion and impart corrosion protection to an extent similar to Cr. The corrosion rate of Ce coated AA7075-T6 panels after 40 days immersion in NaCl solutions was similar to that of chromate conversion coated samples [22]. Furthermore, due to the mixed oxidation state of the film, active corrosion protection has been reported [19, 21, 22, 24]. However, other authors have found that corrosion rate and pitting potentials were not significantly affected by Ce treatment [25]. Based on long term OCP measurements and cathodic polarization curves, Kolics et al. suggested that the cerium-rich film formed on the surface does not provide a sufficient barrier layer to block electrochemical processes [25]. The OCP of untreated and Ce-coated samples was identical and the rate of the ORR was not affected to a large extent [25]. In addition, Ce-conversion coatings developed by Wang et al. have only shown modest reduction in the corrosion current and virtually no change in the pitting potential [20].

Hybrid Cerium Processes: There are a number of hybrid processes that involve a large number of steps, most of which are carried out at high temperatures (90-95°C). The steps include an alkaline clean, rinse, desmut, rinse, coat, rinse, seal, rinse, and then swab with adhesion promoter [21]. (Surface preparation steps can be critical for all surface treatment processes.) Some of these conversion coatings are alkaline and can contain potassium permanganate and strontium chloride.[21] A Ce-Mo process has also been reported, in which Ce and Mo play synergistic roles [26, 27]. The Ce-Mo conversion treatment involves a very complicated sequence of steps that includes immersion in 10 mM $Ce(NO_3)_3$ at 100°C, a subsequent immersion in 10 mM $CeCl_3$ also at 100°C, and finally a potentiostatic polarization at 0.5 V SCE in deaerated 0.1 M sodium molybdate (Na_2MoO_4) [26]. Surface analysis showed that Ce was present as Ce(III) and Ce(IV), while Mo was detected only in its hexavalent form. Most of these hybrid processes have shown excellent corrosion resistance. However, the complexity of the steps involved in the treatments and the elevated temperatures make these alternatives commercially unattractive [21, 26].

Trivalent chromium coatings: Agarwala and coworkers found that conversion coatings containing exclusively Cr(III) can be developed on aluminum from an alkaline bath containing $Cr_2(SO_4)_3$ and Na_2SiF_6 or NaF [28]. The pH of the bath was increased until precipitation of basic compounds was observed. Thin tan-colored films were obtained after 10 min of immersion, violet films after 20 min, and blue films after 40 min immersion. The mechanism of formation is not well understood but may involve a sol-gel process similar to Cr(VI) coatings. The film is mostly composed of a hydrated chromium hydroxide. Trivalent chromium conversion coatings passed 200 h salt fog tests, showing no signs of corrosion. The most corrosion resistant films

were obtained by a post treatment with an oxidizer such as peroxide or permanganate. However, post-treatment in an oxidizing bath likely results in the formation of Cr(VI) species, which will violate regulations.

New trivalent chrome baths, generically referred to as Trivalent Chrome Process (TCP), were developed at NAVAIR and have been shown to impart excellent corrosion protection [29]. They are currently the only non-chromate products that have been qualified according to Class 1A of MIL SPEC MIL-DTL-5541F, Chemical Conversion Materials for Coating Aluminum and Aluminum Alloys. TCP baths are similar to fluorozirconate/fluorotitanate baths described below, except that they contain Cr(III) species, which improve the properties. The film is similar to the Zr coating but it is enriched in $Cr(OH)_3$ and Cr_2O_3 [29]. TCP has been shown to impart excellent corrosion protection to AA7075-T6 panels but only poor protection to A2024-T3, possibly due to Cu enrichment at the surface [29]. It has been proposed that removal of the Cu rich layer by desmutting could enhance coating performance. Modified TCP formulations have been reported to provide better protection [30].

TCP was a major focus of the proposed program. As will be discussed below, trivalent chromium coatings should not be able to impart active corrosion protection, and evidence for this phenomenon must be investigated and understood.

Zirconium and titanium pretreatments: Conversion coatings based on fluorozirconates and fluorotitanates are currently being used in some aerospace applications [21, 26]. The main advantages of the process are its simplicity and the improved adhesion with organic primers. The conversion coating solutions generally contain an acidic hexafluoro metal complex (H_2ZrF_6, or H_2TiF_6), sequestering agents to prevent precipitation of aluminum dissolved during the pretreatment process, and commonly a polymer (e.g. polyacrylic acid, carboxyl vinyl polymer, ammonium polyacrylate) [31]. Polymers improve adhesion and corrosion resistance [21]. In addition, small amounts of HF are added to aid in the removal of the aluminum oxide passive film. Coatings can be applied by conventional techniques such as rinse, immersion or spray, or they can be formed by a non-rinse process.

These coatings have replaced chromates in some applications but given their composition, active corrosion protection is unlikely with these coatings, which could limit the use of Zr-Ti conversion processes in the most demanding aeronautical applications.

2.3. Non-chromate Paint Pigments

Paints for metals can be divided into primers and topcoats. Primers act as adhesion promoters and reservoirs of corrosion inhibitors. A typical corrosion protective primer is a bisphenol epoxy resin containing approximately 30 wt% of $SrCrO_4$ as inhibiting pigment [11]. These coatings are not barriers to water; they rapidly take up water until they become water saturated [32]. The water present in the coating will dissolve the pigment up to its solubility limit [33]. If the solubility of the pigment is large, blistering of the primer can occur [11]. To date several inorganic non-chromate compounds have been tested as pigments but none have performed as well [11, 34-36]. In the following, promising alternatives are discussed.

Hydrotalcite pigments: Buchheit and coworkers have investigated the use of crystalline

hydrotalcite as surface pretreatments and paint pigments [19, 33, 37]. Hydrotalcites are anionic clays composed of alternating layers of a compound like Al-Zn hydroxide and exchangeable anions. When such hydrotalcites are exposed to an aggressive electrolyte containing Cl$^-$, anion exchange occurs, releasing the anions from the hydrotalcite interlayers, which could act as a corrosion inhibitor. The exchange is chemical in nature and is controlled by an equilibrium constant and exchange isotherm. It was shown that hydrotalcites produced with Zn and vanadates imparted good corrosion protection to AA2024-T3 [33]. Most vanadate salts are extremely soluble, which limits their use as a pigment. However, hosting vanadates within hydrotalcite seems to reduce the effective solubility and modulate the release. The simplicity of the process and the potential control of releasable anions make hydrotalcites commercially very attractive. Moreover, since replacement of the vanadate anion with Cl$^-$ is followed by a change in the crystalline structure of the hydrotalcite, x-ray diffraction of the coatings could be used to monitor the early stages of corrosion [33].

Organic pigments: Organic pigments based on the chemistry of alkanethiols $C_nH_{2n+1}SH$ (such as perfluoroalkyl amideethanethiols) are promising. Alkanethiols can be strongly chemisorbed on metallic surfaces and tend to form dense structures by self-assembly [38, 39]. Several other organic compounds such as diphosphone-alkanes and dimercapto thiodiazole also can form self-assembled films on different metallic substrates and they have been the subject of investigations [40]. Self-assembly of alkanethiols occurs spontaneously on Cu and Au surfaces [38, 41]. Alkanethiol molecules consist of two functional groups; one is responsible for the chemisorption and the other determines the hydrophobicity of the chemisorbed molecule [40]. This process is attractive because of the possibility of tailor-making films in short time by spray or simple immersion [38, 40, 42, 43]. However, this technology is still in its earliest stages and the investigations reported so far mainly cover theoretical aspects of the film formation mechanisms on Cu, Au and Ag thin films rather than more applied work on real commercial substrates.

Rare Earth Metal (REM)-based pigments: Following successful lines of research in the area of soluble rare earth metal (REM) inhibitors and conversion coatings, such as those based on Ce ions, new REM pigments for organic coatings have become commercially available in the past several years [44]. A distinctive aspect of this coating formulation is pigmentation with nanoencapsulated REM inhibitors. These coatings have performed well in standard testing and are receiving a great deal of attention from the military user community. However, at the present time, the mechanistic understanding underlying important aspects of inhibitor function and applicability appears to lag the understanding of its performance profile in accelerated testing. REM inhibitors have also been incorporated in cation-exchanging clay particles [45]. These particles have been dispersed in organic resins as corrosion inhibiting pigments, and the resulting corrosion resistance has been demonstrated. This line of research has been fundamental in nature and has revealed some important attributes and limitations of REM inhibition [46]. Taken together, these two inhibitor development activities show the need to increase the understanding of REM inhibition in coatings so that corrosion protection technologies are selected and deployed with a proper recognition of their advantages and limitations.

2.4 References

1. M. W Kendig, A. J. Davenport, and H. S. Isaacs, Corros. Sci., 34, 41 (1993).
2. W. Clark and R.L. McCreery, J. Electrochem. Soc., 149 B379 (2002).
3. P. Schmutz and G.S. Frankel, J. Electrochem. Soc., 146, 4461 (1999).

4. G.O. Ilevbare, J.R. Scully, J. Yuan, and R.G. Kelly, Corrosion, 56, 227 (2000).
5. R.G. Buchheit, R.P. Grant, P.F. Hlava, B. Mckenzie, and G.L. Zender, J. Electrochem. Soc., 144, 2621 (1997).
6. L. Xia and R.L. McCreery, J. Electrochem. Soc., 146, 3696 (1999).
7. L. Xia and R.L. McCreery, J. Electrochem. Soc., 145, 3083 (1998).
8. G.S. Frankel and R.L. McCreery, Interface, 10, 34 (2001).
9. L. Xia, E. Akiyama, G.S. Frankel, and R.L. McCreery, J. Electrochem. Soc., 147, 2556 (2000).
10. J. Zhao, G.S. Frankel, and R.L. McCreery, J. Electrochem. Soc., 2258 (1998).
11. J. Sinko, Prog. Org. Coat., 42, 267 (2001).
12. B.R.W. Hinton, D.R. Arnott, and N.E. Ryan, Met. Forum, 7, 211 (1984).
13. D.R. Arnott, M.P. Ryan, B.R.W. Hinton, and B.A. Sexton, Appl. Surf. Sci., 22-23, 236 (1985).
14. A.J. Aldekiewicz, H.S. Isaacs, and A.J. Davenport, J. Electrochem. Soc., 142, 3342 (1995).
15. A.J. Aldekiewicz, H.S. Issacs, and A.J. Davenport, J. Electrochem. Soc., 143, 147 (1996).
16. B.R.W. Hinton, M.P. Ryan, D.R. Arnott, and P.N. Trathan, Corros. Australas., 10, 12 (1985).
17. D.R. Arnott, B.R.W. Hinton, and M.P. Ryan, Mater. Performance,, 26, 211 (1987).
18. A.J. Davenport, H.S. Isaacs, and M.W. Kendig, Corr. Sci., 32, 653 (1991).
19. R.G. Buchheit, S.B. Mamidipally, P. Schmutz, and H. Guan, Corrosion, 58, 3 (2002).
20. C. Wang, F. Jiang, and F. Wang, Corrosion, 60, 237 (2004).
21. R.G. Buchheit and A.E. Hughes, "Chromate and Chromate-Free Conversion Coatings," in ASM Handbook Corrosion: Fundamentals, Testing, and Protection, ASM International, (2003).
22. B.R.W. Hinton, Met. Fin., 89, 55 (1991).
23. A.E. Hughes, J.D. Gorman, P.J.K. Patterson, and R. Carter, Surf. Interface Anal., 36, 290 (2004).
24. A. Aballe, M. Bethencourt, F.J. Botana, M.J. Cano, and M. Marcos, Mat. Corr., 53, 176 (2002).
25. A. Kolics, A.S. Besing, P. Baradlai, and A. Wieckowski, J. Electrochem. Soc., 150, B512 (2003).
26. A.E. Hughes, J.D. Gorman, and P.J.K. Patterson., Corr. Sci., 38, 1957 (1996).
27. M.W. Kendig and C. Thomas, J. Electrochem. Soc., 139, L103 (1992).
28. V.S. Agarwala and F. Pearlstein, Plat. Surf. Finish., 50 (1994).
29. W.C. Nickerson and E. Lipnickas, TriService Corrosion Conference Proceedings, (2003).
30. C.A. Matsdorf, W.C. Nickerson, and E. Lipnickas. "NACE paper 2005-54," NACE International, (2005).
31. J.H. Nordlien, J.C. Walmsley, H. Osterberg, and K. Nisancioglu, Surf. Coat. Technol., 153, 72 (2003).
32. J. Sinko, Prog. Org. Coat., 42, 267 (2001).
33. R.G. Buchheit, H. Guan, S. Mahajanam, and F. Wong, Prog. Org. Coat., 47, 174 (2003).
34. R.L. Cook and S.R. Taylor, Corrosion, 56, 321 (2000).
35. A. Nazarov, D. Thierry, T. Prosek, and N.L. Bozec, J. Electrochem. Soc., 152, B220 (2005).
36. C.J.E. Smith, ATB Metalurgie, 37, 266 (1997).
37. W. Zhang and R.G. Buchheit, Corrosion, 58, 591 (2002).
38. G.M. Bommarito and A.V. Pocius, Thin Solid Films, 327-329, 481 (1998).

39. M. Itoh, H. Nishihara, and K. Aramaki, J. Electrochem. Soc., 141, 2018 (1994).
40. P. Póczik and I. Felhosi, European Federation of Corrosion Publications, 28, 3 (1999).
41. T.D. Burleigh, C. Shi, S. Kilic, S. Kovacik, T. Thompson, and R.M. Enick, Corrosion, 58, 49 (2002).
42. I. Doudevski and D. Schwartz, J. Am. Chem. Soc., 123, 6867 (2001).
43. A. Shida, H. Sugimura, M. Futsuhara, and O. Takai, Surf. Coat. Technol., 169-170, 686 (2003).
44. J. Stoffer, T. O'Keefe, E. Morris, P. Yu, and S.A. Hayes, "Corrosion Resistant Coating," U.S. Patent, US2004/0249043A1, (2004).
45. G. Williams and H.N. McMurray, Electrochem. Sol. St. Lett., (2003).
46. G. Williams, H.N. McMurray, and D.A. Worsley, J. Electrochem. Soc., 149, B154 (2002).

3. Objective

The primary objective of this work was to develop fundamental understanding of the existing chromate-free inhibitors and inhibitory coating systems with the ultimate goal of providing scientists and engineers developing such coatings with information that will help them improve their products. The problem of finding suitable replacements for chromates has been a focus of the corrosion inhibition and protection community for decades. The early efforts were largely unsuccessful, prompting the funding of research by SERDP and AFOSR to take a step back and look closely at the mechanisms of corrosion inhibition provided by chromates. Two of the PIs of this project (Frankel and Buchheit) led those large projects. The research on chromates during the late 1990's and early 2000's provided considerable new insight to mechanisms of chromates. Since those projects ended, isolated projects have made use of the understanding of chromates to address the inhibition mechanisms of some nonchromate inhibitors. This project represented the first large-scale research effort addressing non-chromate inhibitors. It was possible to make extensive use of the techniques and understanding developed in the earlier work, enabling considerable progress to be made toward understanding non-chromate systems and providing feedback to the developers of those systems

4. Technical Approach

The approach used in this project was to address, concurrently, a number of critical, cross-cutting, and underlying issues. These issues formed the basis for individual projects or tasks which were run simultaneously. They included studies of some leading technologies. Brief explanations of each task are given here, and the details of the accomplishments are given in the next section:

<u>Fundamental Studies of the Trivalent Chrome Process (TCP).</u> TCP is a leading non-chromate conversion coating, but there is no understanding of its structure and how it provides active corrosion inhibition.

<u>Mechanisms of selected inhibitors.</u> Experience has shown that application of the techniques used to study chromates can advance the understanding of the inhibition mechanism of non-chromate inhibitors.

<u>Active inhibition, barrier properties and adhesion.</u> The design of coating systems relies on some combination of these three coating functionalities, and the tradeoffs must be understood.

<u>Paint adhesion strength and mechanism.</u> One major function of surface treatments is the improved adhesion of the primer layer, but there is little understanding of the adhesion and de-adhesion mechanisms.

<u>Inhibitor activation and transport in the primer layer.</u> Inhibitive pigments in a polymeric paint matrix must be activated and transported to corroding sites, but again little fundamental understanding exists.

<u>Interactions between polymer matrix, pigment, surface treatment, and alloy.</u> Coating components largely have been developed independently but function as a system. The interactions and synergies are critical.

<u>Characterization of local environments in coating systems.</u> It is the coating/metal interfacial environment that controls the behavior of inhibiting species. The pH, oxidizing power, chemical aggressiveness (Cl$^-$ content) and temperature are the critical local environmental parameters that must be understood.

5. Results and Accomplishments

In this section, the accomplishments and progress in the project are given, broken out by task.

5.1 Task 1: Fundamental Studies of the Trivalent Chrome Process (TCP)

5.1.1 Objectives

This task focused on trivalent chrome process (TCP) conversion coatings. A number of important issues related to TCP were addressed:

1. What is the formation mechanism, composition and structure of the TCP coating on AA2024?
2. How does the TCP coating inhibit the anodic and or cathodic kinetics of reactions occurring on the Al matrix and the Cu-rich intermetallics?
3. Does TCP provide active corrosion protection or is it simply a barrier?
4. Is there any evidence for transient formation of Cr(VI) species in the coating during formation and drying, or during immersion in electrolyte solutions?
5. What level of short-term chemical stability does the coating exhibit and is any benefit gained by aging (prolonged air drying)?
6. What are the structure and inhibitory properties of the TCP coating on AA6061 and 7075 alloys?

5.1.2 Background

Chromate conversion coatings (CCCs) have long been employed in the surface finishing process for AA2024-T3 and other metal alloys for their excellent ability to resist localized corrosion and to promote paint adhesion. "Self-healing" is the predominant feature of CCCs, in which substrate metal exposed at a scratch or defect in the CCC is protected by the Cr(VI) species leached from the coating. However, due to the toxic and carcinogenic effects of hexavalent chromium compounds on the environment and human health, there have been increasingly stringent legislations regarding their use and waste disposal. Consequently, significant efforts have focused on chromate-free corrosion inhibitor systems that can provide comparable performance.

The trivalent chrome process (TCP) developed at NAVAIR is currently one of the leading non-chromate conversion coatings on the market and has been shown to provide excellent corrosion protection and paint adhesion in standardized tests. The TCP process is a drop-in replacement for hexavalent chromate treatments and it contains no Cr(VI) in the coating bath and resulting film. The TCP coating baths are similar to commercial fluorozirconate/fluorotitanate-based conversion coating systems, but they also contain Cr(III) species, which improve the coating to provide better protection. There are currently several Cr(VI)-free products that meets the requirements according to Class 1A of MIL SPEC MIL-DTL-5541F, Chemical Conversion Materials for Coating Aluminum and Aluminum Alloys. These different products are all based on Cr(III). However, before this program there was a lack of fundamental understanding of how TCP worked to provide corrosion protection. A number of questions addressed in this work are shown in the objectives section above.

5.1.3 Materials and Methods

5.1.3.1 Electrode Preparation and TCP Coating Procedure (Immersion). New AA2024-T3, AA6061 and AA7075 samples were used (1 cm^2 plates). Some of the testing was performed on unpolished plates, but most were initially polished to smooth and clean the surface. The polishing involved wet sanding with 1500 grit silicon carbide paper followed by a 20 min ultrasonic cleaning in ultrapure water. The sample was then polished using 0.05 µm alumina

powder, slurried with ultrapure water, on a felt polishing pad. This was followed by another 20 min ultrasonic cleaning in ultrapure water. Polishing was performed until the surface exhibited a mirror-like finish with no visible polishing striations.

A polished or unpolished plate was then degreased for 10 min. in Turco 6849^{TM} (Henkel Corp., 20 % v/v) at 55 ^{o}C. This was followed by rinsing with tap water for 2 min. The sample was then deoxidized for 2 min. in Turco Liquid Smut-Go NC^{TM} (Henkel Corp., 20% v/v) at room temperature (19-23 ^{o}C). This was again followed by rinsing with tap water for 2 min. Finally, the cleaned and deoxidized sample was coated with TCP for 10 min. (Alodine^{TM} T5900, Henkel Corp., 100% RTU) at room temperature (immersion coating). While the actual Alodine^{TM} T5900 composition is proprietary, it contains potassium hexafluorozirconate (K_2ZrF_6), sulfate (SO_3^{-2}), fluoroboric acid (HBF_4), and a chrome (III) salt. The pH of this solution was 3.85. The coated sample was again rinsed with tap water for 2 min., then with ultrapure water for 30 s, and allowed to air dry. For reasons that remain unclear, the tap water rinses are critical for proper and reproducible TCP film formation on this alloy. It could be that the more basic pH of the tap water (~6.8), as compared to the ultrapure water (~5.8), aids in the formation of the hydrated zirconia coating (see below). In most cases, the coated samples were dried overnight at room temperature in a covered storage dish prior to any electrochemical or structural characterization. Alodine^{TM} 5200 (Henkel Corp.) was also coated (immersion) on some polished AA2024 samples, for comparison. This is a hexafluorozirconate coating similar to the T5900, but it contains no added chromium salt. Samples receiving this coating were prepared by degreasing and deoxidation, as described above. The 5200 solution was diluted with ultrapure water to yield a 3% (v/v) solution. The pH of this solution was 2.74. The alloy sample was then immersed for 2 min. at room temperature (21-25 ^{o}C) to form the coating. The coated sample was then removed, rinsed with tap water for 30 s and dried overnight at room temperature in a covered dish before use.

In other experiments, AA2024-T3 samples were coated using two procedures. Process I consisted of: (i) etching for 15 min at 55°C in 15% (v/v) Turco 6849^{TM}, (ii) desmutting for 5 min at room temperature in 20% (v/v) Liquid Turco Smut-go NC^{TM}, (iii) coating with TCP in Alodine^{TM} 5900S bath for 5 min at room temperature. These solutions are products of Henkel Corp., Madison Heights, MI. Turco 6849 contains nonylphenoxypoly ethanol, sodium xylene sulfonate, ethanolamine and sodium tripolyphosphate and has a pH of 11.7~12.2. Smut-go NC solution contains ferric sulfate, nitric acid and sodium bifluoride and has a pH ~ 0. Alodine^{TM} 5900S is a fluorozirconate based bath. Deionized water rinsing was performed between each step. Samples were given a final rinse and blown dry with compressed air at room temperature (RT) at least 1 h prior to use if not mentioned otherwise. As a comparison, other samples were treated using the second treatment procedure, Process II, consisting of: (i) etching at 65°C for 2 min in a solution of 32.4 g/l Na_2SiO_3 + 48 g/l Na_2CO_3 with pH 13.4, (ii) desmutting at 55°C for 3 min in a solution of 72 ml/l HNO_3 + 30 g/l Sanchem 1000 (sodium bromate based, Sanchem Inc., Chicago, IL) with pH 0.25 and (iii) conversion coating at RT for 5 min in Alodine ^{TM} 5900S bath. Samples were rinsed with deionized (DI) water after each step and blown dry with compressed air at RT at the end. The control samples in polarization experiments were prepared by ultrasonic cleaning in ethyl alcohol to eliminate organic contamination. This condition is termed "as received" hereafter.

In some cases, the TCP-coated samples were aged prior to testing. This involved placing (drying) the coated samples in a covered dish at room temperature for periods of time from 1-14 days. At different time points, the samples were immersed in an electrolyte solution (typically air-saturated 0.5 M Na_2SO_4) and electrochemical characterization was performed.

5.1.3.2 Chemicals. All chemicals were reagent grade quality, or better, and used without any additional purification. The sodium sulfate (Na_2SO_4) was 99.9% pure (Sigma-Aldrich) and the sodium chloride (NaCl) was reagent grade (Fisher Scientific). The hydrogen peroxide (H_2O_2) was a 30% solution (Fisher). All glassware was cleaned in an Alconox bath, rinsed thoroughly with ultrapure water, and then dried prior to use. All solutions were prepared and rinsing was done with ultrapure water that was prepared by passing distilled water over anion and cation exchange resins and over activated carbon (Barnstead Ultrapure, >17 Mohm-cm).

5.1.3.3 Electrochemical Measurements. All electrochemical measurements were conducted in a single compartment glass cell. The coated sample was mounted at the bottom of the cell with an o-ring defining the exposed geometric area (0.2 cm^2). The counter electrode was a Pt wire sealed in glass that was housed in a separate glass tube with a porous glass frit. The reference was an Ag/AgCl electrode (4 M KCl, E^o = 0.197 V vs. SHE) that was housed in a Luggin capillary with a cracked glass tip. The counter electrode was positioned normal to the planar working electrode at a distance of *ca.* 1 cm while the reference electrode was placed near the surface of the working electrode at a 45° angle. Measurements were made in air-saturated 0.5 M Na_2SO_4 or dilute Harrison's solution, 0.05 wt% NaCl + 0.35 wt% $(NH_4)_2SO_4$, at room temperature. The typical electrochemical testing proceeded as follows: (i) measuring the open circuit potential (OCP) for 30 min, (ii) performing impedance analysis from 0.01 to 10^6 Hz at the OCP, (iii) recording slow scan potentiodynamic cathodic and anodic curves, $\pm$ 30 mV relative to the OCP, to determine the polarization resistance, R_p, and (iv) performing slow scan cathodic and then anodic potentiodynamic scans from the OCP to a cathodic limit of -1.1 V and an anodic limit of 0.6 V. The potentiodynamic scans were recorded at 2 mV/s. The EIS measurements were made using a 10 mV rms AC sine wave at the OCP.

5.1.3.4 Characterization. Optical microscopy was performed using an Olympus BX60M light microscope. Scanning electron micrographs were obtained using a field-emission scanning electron microscope equipped with energy dispersive x-ray microanalysis (EDS). The microstructure of the TCP coating was evaluated by Raman spectroscopy, which provided information about the presence of Cr(III)-oxide and Cr(VI)-oxide vibrational modes. Spectra were acquired at room temperature using a Raman 2000 spectrograph (formerly Chromex, now Bruker Optics) equipped with a Nd:YAG laser (500 mW at 532 nm). Spectra were recorded using a *ca.* 3-μm spot size with a typical integration time of 20 s. Wavenumber calibration was accomplished with a naphthalene standard.

X-ray photoelectron spectra (XPS) of the uncoated and TCP-coated samples were recorded using a Physical Electronics PHI 5400 spectrometer with a magnesium X-ray source. A take-off angle of 45° was used for all measurements at a base pressure less than 5×10^{-9} Torr. Inert gas sputtering (PHI-06-350) was used to remove surface contaminants and coating material from a small area for depth profiling. The ion gun was operated with argon gas at *ca.* 1 keV. Other XPS measurements were used to investigate the presence of Si on surfaces of AA2024-T3 coupons after etching and desmutting and to examine the oxidation states of the chromium species on

TCP-coated AA2024-T3. A Kratos AXIS Ultra instrument controlled by a VISION data system was used with a mono-chromatic Al Kα X-ray source operated at 1486.6 eV and 150 W. Typical operating pressures were around $2x10^{-8}$ Torr. All spectra were calibrated by the carbon 1s peak at 284.6 eV.

TCP coated AA2024-T3 samples with dimensions of $10 \times 10 \times 2$ mm were examined using a Phillips Electronics model XL-30F Environmental Scanning Electron Microscope (ESEM) with a field emission gun at 15 kV accelerating voltage. A gold coating was sputtered onto the TCP coating surfaces to make them conductive during the imaging process. A secondary electron detector was used to image the coating. The formation and evolution of shrinkage crack morphology due to dehydration was studied by ESEM to allow examination in a high humidity environment. Samples with a diameter of 6 mm and thickness of 2 mm were conversion coated for 10 min and rinsed. These samples were not dried at all or coated with Au, but rather were kept wet during transfer into the ESEM chamber. The temperature in the chamber was cooled to 0.5°C and the water partial pressure was maintained at 5 Torr to keep water in the liquid phase. By raising the temperature slowly with a Peltier stage, the samples were then gradually dehydrated, during which time the formation of shrinkage cracks was monitored by SEM imaging. Formation of shrinkage crack morphology after atmospheric aging was also examined by ESEM. Samples were conversion coated for 5 min, rinsed, and then kept in a sealed container with relative humidity controlled at about 34% by saturated magnesium chloride solution. Separate samples were removed from the container after 6 h, 12 h, 24 h and 48 h aging, and transferred into the ESEM chamber, without an Au overlayer. The temperature in the chamber was maintained at 24°C and the water partial pressure was at 7.8 Torr to keep the relative humidity at 35%, which was similar to the exposure condition.

An FEI Nova 600 Dual Beam Focused Ion Beam (FIB) instrument was used to prepare cross-sectional transmission electron microscopy (TEM) samples from TCP treated specimens. A layer of Pt with a thickness of ~1.5 μm was sputter deposited on the area of interest to protect the TCP coating from milling. For some samples, a layer of Au with thickness of around 50 nm was first vapor deposited by sputtering for added protection. Electron transparent TCP foils with dimensions of 15 μm × 5 μm were produced by FIB with a 30 keV Ga ion beam and finally thinned to a thickness of ~100 nm. The extraction of TCP foils was performed by a micromanipulator with a Pyrex needle (~1 μm in diameter) under an optical microscope. Then the thin foils were placed on a 200-mesh Ni grid with a carbon support film for TEM examination. An FEI Tecnai F20 electron microscope was used to characterize the cross-sectional TCP foils at high magnification. Energy Dispersive Spectroscopy (EDS) line profiles were acquired at 200 kV and FEI/Emispec TIA software was used to analyze the data. Cross-sectional foils of TCP-coated substrates were prepared by FIB and coating thickness was then examined directly in the TEM.

5.1.3.5 Artificial Scratch Test Experiments. The samples for the artificial scratch test were treated by (i) degreasing for 15 min at 55ºC in an alkaline solution (15% v/v Turco 6849[TM]), (ii) deoxidation for 5 min at room temperature in an acid solution (20% v/v Liquid Turco Smut-go NC[TM]) (iii) conversion coating for 5 min at room temperature in a commercial bath (Alodine[TM] 5900S). The recommended contact time for immersion is 5 ~ 9 min. These solutions are all products of Henkel Corp. The samples were rinsed with deionized water after each step. After the last rinse they were blown dried with compressed air at room temperature and exposed to lab

air for at least 1 h prior to use if not mentioned otherwise. Samples that were treated with only steps (i) and (ii), termed "non-TCP," were used as controls.

The artificial scratch technique was used to assess active corrosion inhibition. The standard configuration of the artificial scratch cell used a non-TCP sample situated above a TCP-coated sample separated by an o-ring 5 mm in thickness and 40 mm in diameter. The non-TCP sample was always placed above the TCP-coated sample to eliminate the condition of inhibitor transport by gravity alone. A Pt wire attached to a Pt mesh counter electrode (CE) was inserted through a hole in the o-ring. The CE was stiff enough that it stayed suspended in the cell without making contact to either Al alloy electrode. The samples were fastened together with bolts through holes drilled at the edges. Another hole 6.2 mm in diameter was drilled through the top non-TCP sample to facilitate insertion of a saturated calomel reference electrode (SCE) for electrochemical measurements. The edge of this hole was sealed with red lacquer to prevent crevice corrosion. Some cells used two non-TCP plates as a control.

The cell interior volume defined by the o-ring and the two Al alloy plates was filled with corrosive solution. The solutions used in the artificial scratch cell were 0.5 M NaCl and dilute Harrison's solution (0.05 wt% NaCl + 0.35 wt% $(NH_4)_2SO_4$), which is much less aggressive and has been used many times in corrosion studies of Al alloys. The solutions were prepared with reagent grade chemicals and deionized water with a resistivity of 18.2 MΩ•cm.

The cells were kept in sealed containers with high relative humidity to avoid the evaporation of electrolyte from the hole in the top panel. It should be noted that the cells were left open to air, but access to air was limited to the 6.2 mm diameter hole used for the reference electrode. They were periodically removed from the container and a reference electrode was inserted in the top hole for each electrochemical measurement. Separate Electrochemical Impedance Spectroscopy (EIS) measurements were made periodically using each side of the artificial scratch cell as the working electrode. Measurements performed on the non-TCP and TCP coated surfaces of the artificial scratch cells evaluated the corrosion resistance of the TCP coating and its active corrosion protection properties, respectively. A 10 mV signal was applied around the open circuit potential at frequencies ranging from 10^5 to 10^{-2} Hz.

In some experiments, the two surfaces were electrically shorted by copper tape during exposure, which is the condition of a real scratch through a coating. For shorted artificial scratch cells, the electrical connection of two surfaces by copper tape was removed during EIS tests and reconnected after the tests were finished. In some other cells, the area of the top non-TCP panel was reduced by application of corrosion-protective tape leaving a hole with diameter of 3 mm, making the area ratio of TCP to non-TCP surfaces equal to 177. Otherwise, for the regular artificial scratch cell, the area ratio of TCP to non-TCP surfaces is 1.03.

Optical Emission Spectrometry (ICP-OES) was used to detect the presence of chromium and other dissolved species that might leach out from a TCP coating. TCP coated samples were exposed to 20 ml dilute Harrison's solution for various times in a cell with an exposed area of 7.35 cm^2. The exposed solution was acidified with nitric acid prior to ICP-OES testing. The content was determined with parts-per-billion sensitivity.

X-ray Photoelectron Spectroscopy (XPS) measurements were performed on 1×1 cm cut from the non-TCP surfaces of artificial scratch cells to examine the presence of chromium species and their oxidation states. Before the signal was collected, the sample surfaces were etched by Ar gas for 120 s to remove contaminants from handling. A mono-chromatic Al Kα X-ray source was used at 1486.6 eV and 150 W. Typical operating pressures were around 2x10-8 Torr. All spectra were calibrated by the carbon 1s peak at 284.6 eV.

5.1.4   Results

Figure 1.1 shows an optical micrograph of an AA2024 plate that was half coated with TCP. The image was taken after a 5-day full immersion in 0.5 M NaCl (air saturated) at room temperature. Clearly, the uncoated side of the plate (right) has a greater level of pitting and surface roughening than does the TCP-coated side (left). This image provides qualitative evidence that the TCP coating is stable on the alloy surface, at least in the short term, and provides some corrosion protection even in an aggressive electrolyte like NaCl. Similar observations have been made for AA2024 samples after a 30-day beach exposure (*i.e.*, significantly more pitting seen on the uncoated versus the coated samples). The fact that some pitting is seen on the coated side suggests that either the immersion coating is not completely covering the alloy surface (*i.e.*, blocking sites) and or it covers the surface but does not provide full barrier protection. The latter could be due to channels and imperfections that might exist in the coating.
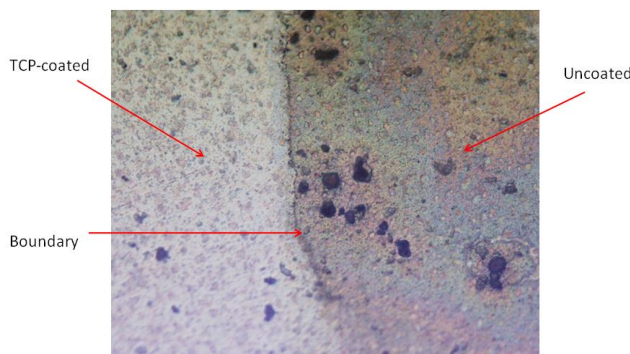
Figure 1.1. Optical micrograph of an AA2024 plate half coated with TCP (left side of image) after a 5-day immersion in 0.5 M NaCl (air saturated) at room temperature.

5.1.4.1 Formation of the TCP Coating. Figure 1.2 shows the OCP-time profile recorded during the formation of the TCP on a degreased and deoxidized (unpolished) AA2024. The immersion lasted 10 min. Curves for two coating solutions are presented: (i) the "ready to use (RTU)" 100% full-strength Alodine[TM] T5900 solution and (ii) the RTU solution diluted by 50% (v/v) with ultrapure water. The OCP transients are similar in shape and magnitude for both solutions. The TCP solution is very aggressive toward AA2024 as evidenced by the cathodic shift in the OCP to *ca.* -0.95 V vs. Ag/AgCl within the first 50-75 s. The fluoride in the solution facilitates the dissolution of the oxide layer on these surfaces. Oxide film dissolution to expose bare aluminum appears to be an essential first step in the formation of the TCP coating, as has been proposed previously [1,2]. The OCP goes through a minimum before a slight positive increase to -0.90 V vs Ag/AgCl within the first 100-200 s. Afterward, the potential stabilizes at this value for the duration of the immersion period.
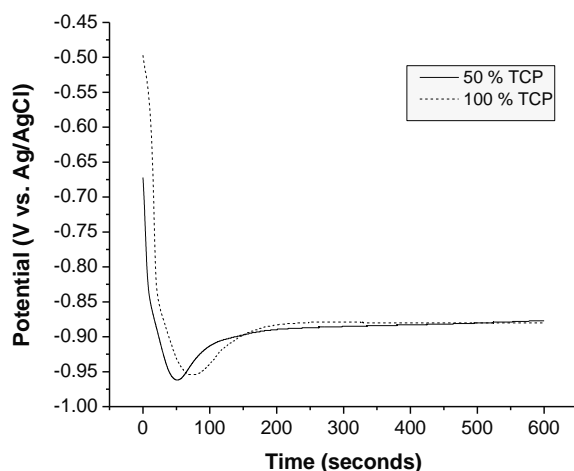
Figure 1.2. Open circuit potential (OCP)-time profiles recorded during the formation of the TCP coating on AA2024. Two different strengths of the Alodine 5900 RTU solution were used: full strength (100%) and diluted (50%). Coatings were formed at room temperature (20-25 $^{\circ}$C).

The importance of the initial oxide layer dissolution during the coating formation process is illustrated in Figure 1.3. In this figure, OCP-time transients are shown for high oxide AA2024 samples in 50 and 100% (v/v) Alodine T5900. The samples (unpolished) were prepared by degreasing and deoxidation, followed by immersion in boiling water for 1 min. For the thicker oxide, there is a slower cathodic shift in the OCP as compared to the low oxide metal presented in Figure 1.2. This reflects the extra time needed to dissolve the thicker oxide and expose bare Al. The cathodic limit of *ca.* -0.9 V vs Ag/AgCl is reached after about 500 s on the high oxide samples as compared to the 100 s seen for the low oxide surfaces. Once the oxide is dissolved, then the TCP formation proceeds in an identical manner on all of the surfaces, based on the similarity in the OCP values. The increase in pH due to hydrogen discharge accompanying the oxidation and dissolution of the Al matrix drives the hydrolysis of the hexafluorozirconate to form hydrated zirconia that precipitates on the surface according to the following reaction:

$$ZrF_6^{-2} + 4OH^- \rightarrow ZrO_2 \bullet 2H_2O + 6F^-$$
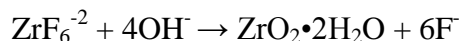
We have not yet attempted any measurement near the interface to confirm the pH increase.
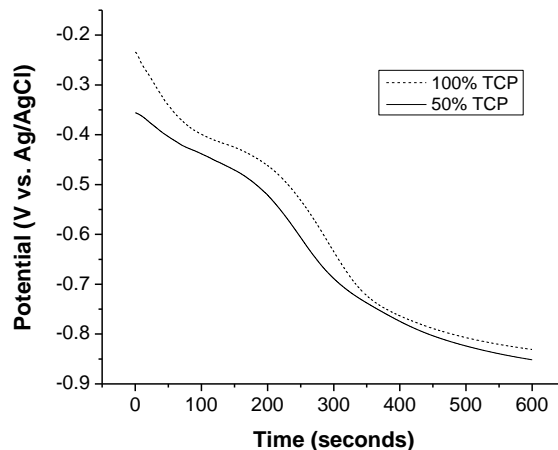
Figure 1.3. Open circuit potential (OCP)-time profiles recorded during the formation of the TCP coating on AA2024. The two metal samples were boiled in water for 1 min to produce a relatively thick hydroxide/ oxyhydroxide layer. Two different strengths of the Alodine 5900 solution were used: full strength (100%) and diluted (50%). Coatings were formed at room temperature (20-25 ^{o}C).

5.1.4.2 Structure of the TCP Coating. Figure 1.4 shows *ex situ* tapping-mode AFM images of a polished, degreased and deoxidized AA2024 surface after TCP coating. Height mode images are shown over a 10 × 10 μm^2 area. The uncoated surface was relatively smooth with no intermetallics or defects in the imaged area. The roughness is 20.9 nm (root-mean-square, rms) over the 100 μm^2 area. The image of the coated surface (Fig. 1.4) reveals a nodular morphology. The film conforms to the underlying surface topography as a similar nominal roughness of 21.3 nm (rms) is found over the same geometric area. On these length scales, the coating conforms to the underlying metal topography and appears devoid of large-scale cracks and imperfections.
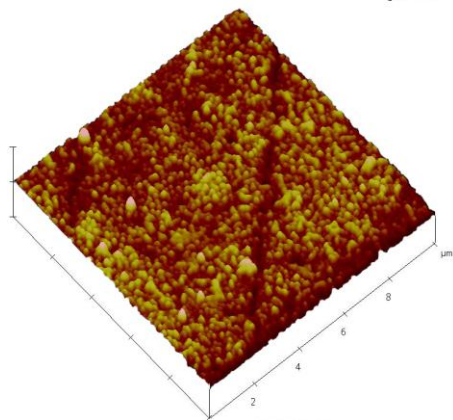
Figure 1.4. *Ex situ*, tapping-mode AFM images of uncoated and TCP-coated AA2024. Images (10 × 10 μm^2) are presented in the height mode.

Figure 1.5 presents elemental depth profiling data for TCP-coated AA2024 samples obtained by scanning auger microprobe analysis. Figure 1.5A and B show the same data with the signal intensities plotted on an expanded scale in Figure 1.5B. Tracking the Al signal with depth

indicates the film is on the order of 50 nm thick (*in vacuo*). Further evidence that the immersion coating is about 50 nm thick comes from tracking the Cu signal with depth. This Cu signal arises from intermetallic particles at the alloy surface and should not be affected by the aggressive TCP coating solution. As can be seen, the Cu signal intensity (Fig. 1.5B) starts to increase at about 50 nm into the coating. Recently reported ellipsometric data of a hydrated coating, formed in a manner similar to our coatings, revealed a nominal film thickness of 90 nm for a 10-min. immersion coating[1].
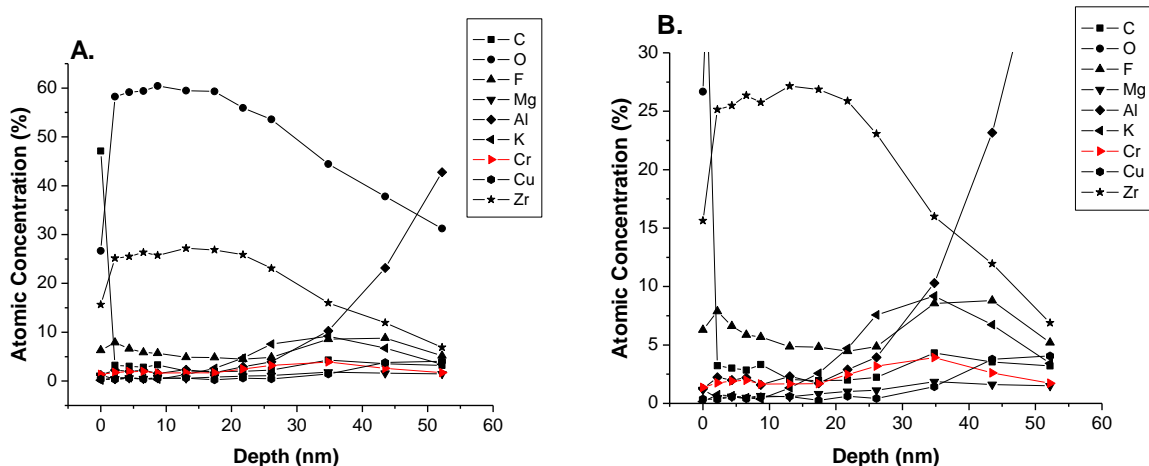
Figure 1.5. Scanning auger electron spectroscopy depth profiling analysis of TCP-coated AA2024. Depth profiling levels are shown for several important elements including Al, Zr, O, Cr, Cu, K and F. Arrows in (A) identify traces for Zr and O. Arrow in (B) identifies the F signal.

A noteworthy observation in Figure 1.5A is that the Zr atomic concentration tracks the O rather than the F concentration. The Zr and O levels are relatively constant with depth into the coating with the atomic concentration ratio (O/Zr) of is about 2:1. This is consistent with the empirical formula of dehydrated zirconia, ZrO_2. The zirconia layer is on the order of 30 nm thick and it interfaces with a 20 nm, or so, thick AlF_x-rich layer at the alloy surface. The conclusion is based on the fact that the K and F atomic concentrations are elevated in the interfacial region making up this AlF_x-rich zone. We suppose that this AlF_x-rich region consists of K_xAlF_{3+x} (fluoroaluminate). When the Al-rich matrix undergoes oxidation during the coating process, corrosion products form in the F^--rich solution that get precipitated as an K_xAlF_{3+x}-rich layer (fluoroaluminate) on the metal surface. Therefore, the initial increase in the Al atomic concentration with depth likely originates from this precipitated interfacial layer. Figure 1.5B reveals that the increased Al concentration actually begins to increase about 20-30 nm into the coating. Another explanation for the elevated K level in the interfacial region is that the cation is there to charge compensate the excess F^- from the coating arising from the hydrolysis of the hexafluorozirconate. Finally, the all-important Cr concentration is elevated near the alloy surface but the element does not appear to be distributed uniformly throughout the coating thickness. The Cr level is comparatively low at about 4-5 wt.% but comparable to the solution concentration, < 5 wt.%.

Additional evidence for the presence of Cr species in the coating comes from XPS data. Figure 1.6 shows the Cr 2p region of the survey scan for TCP-coated AA2024. XPS is useful for

assessing the oxidation state of the Cr in the coating. There are two peaks in the spectrum at *ca.* 576 and 586 eV. They represent Cr $2p_{3/2}$ and $2p_{1/2}$ photoelectrons, respectively. The $2p_{3/2}$ peak is sensitive to the Cr oxidation state and can be fit with two peaks when both Cr(III) and Cr(VI) are present in a mixed oxide: 576.7 eV for Cr(III) and 579.3 eV for Cr(VI). A narrow Cr $2p_{3/2}$ peak is seen for the TCP coating with no higher binding energy tail. Therefore, the coating as formed appears to consist of mainly Cr(III) species ($Cr(OH)_3$, Cr_2O_3 and or CrOOH). In other words, the freshly prepared coating contains chromium in a trivalent rather than a hexavalent oxidation state. It should be noted that the samples used for XPS measurements were coated and dried for 1-2 h before placement in the vacuum chamber for elemental analysis.
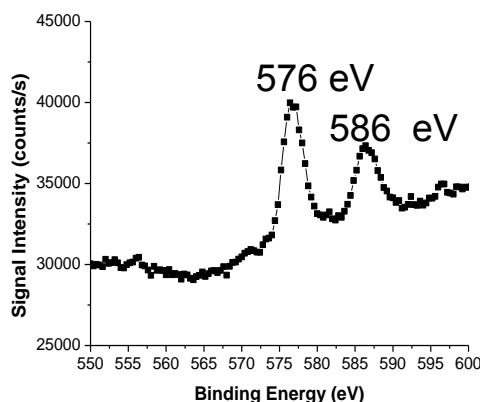
Figure 1.6. XPS survey scan in the Cr 2p region for a TCP-coated AA2024 sample.

Figure 1.7A presents an SEM image of a pitted region of a TCP-coated AA2024 sample, along with an x-ray line profile across several Cu-rich intermetallic particles and pits. A 40 μm line profile is demarked in the image. The pit diameters range from 1 to about 5 μm and likely form during the coating process. Figure 1.7B-E shows energy-dispersive X-ray analysis (EDS) line profiles for Cu, Zr, O and Cr recorded across the pitted areas. In Figure 1.7B, the profile for Cu (Kα) shows elevated metal levels in two of the pits at the 15 and 35 μm points of the profile. The Cr (Kα), Zr (Lα) and O (Kα) signal intensities shown in Figure 1.7C-E are reflective of the presence of TCP. It can be seen that the signal intensities for all three elements are higher near the pit edges than on the terraces surrounding the pits. This is a common observation from probing numerous pit areas on TCP-coated AA2024. The Zr and O signals arise from the hydrated zirconia, $ZrO_2 \cdot 2H_2O$, that precipitates during the immersion process. The Cr signal arises from Cr(III) localized within the coating, likely as Cr_2O_3 based on the XPS result in Figure 1.6. Based on the x-ray signal intensities, the levels of Cr regionally in the coating are less than the Zr or O levels, as expected. Another important observation is that TCP appears to coat some but not all the Cu-rich intermetallics. For example, at the 15 μm position across the line profile, the Zr, O and Cr x-ray signals all increase with the increase in Cu signal. In contrast, the larger Cu-rich intermetallic at the 35 μm position does not appear to have much of the coating present.

A
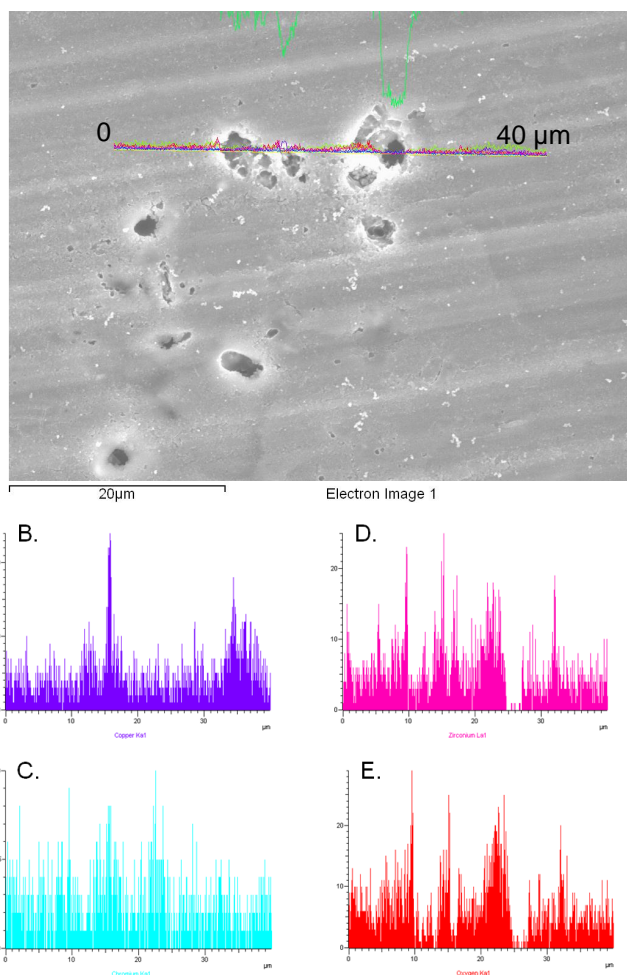
Figure 1.7. (A) SEM micrograph of a TCP-coated AA2024 sample. (B-E) EDAX x-ray line profiles for Cu, Cr, Zr and O, respectively, across the 40 µm line profile shown in (A). X-axes dimensions are all 0-40 µm.

5.1.4.3 Pretreatment effects. The surfaces of the AA2024-T3 were examined following each pretreatment step prior to immersion in the TCP bath because it is critical to understand their effects on the subsequent treatment step. In particular, it was of interest to see if silicate residue negatively impacted the formation of the TCP film. Alkaline etching by both Process I and Process II resulted in dissolution of the surface with a largely reduced amount of contaminant particles on the surface but did not completely dissolve the characteristic rolling lines and pits on the as received surface.

XPS was performed on AA2024-T3 samples after the two etching methods. Less Si was clearly observed after Process I than after Process II. The spectra were fitted and quantitative analysis was performed using sensitivity factors. The Si/Al atomic concentration ratio of total Si to total

Al (including both Al^0 and Al^{3+} components) was found to be 0.43 and 1.98 for the surfaces after etching by Process I and II, respectively.

The second step in the coating preparation, acidic desmutting, has been proven to be critical because it alters the morphology and chemistry of the AA2024-T3 alloy surface and can have a significant effect on the formation of the conversion coating. After 5 min of acid desmutting using Process I, the surface exhibited pits hundreds of nanometers in diameter or larger over the entire surface. A similar morphology was observed after 3 min of the Process II desmutting step. XPS analysis performed after desmutting shows that a small amount of Si was still on the surface. The Si/Al atomic concentration ratio was 2×10^{-4} and 3×10^{-4} for the surfaces after desmutting by Process I and II, respectively.

5.1.4.4 Surface Morphology of TCP Coating. Figure 1.8 shows an SEM image of TCP coating formed on the substrate of AA2024-T3 after 10 min exposure to the TCP bath following Process I. The sample surface was entirely covered with round particles of 500 nm diameter, which merged together to form a compact film. Some larger agglomerations of the small particles were observed on the surface. This surface morphology is similar to what has been found for CCCs. Furthermore, the TCP coating exhibited cracking similar to the mud-cracking that has been observed in SEM images of CCC. The TCP coating peeled off the substrate at certain locations due to the cracks. It has been shown that exposure to the vacuum during SEM promotes dehydration of the CCCs rather rapidly. Similar cracking was observed with the Process II pretreatment.
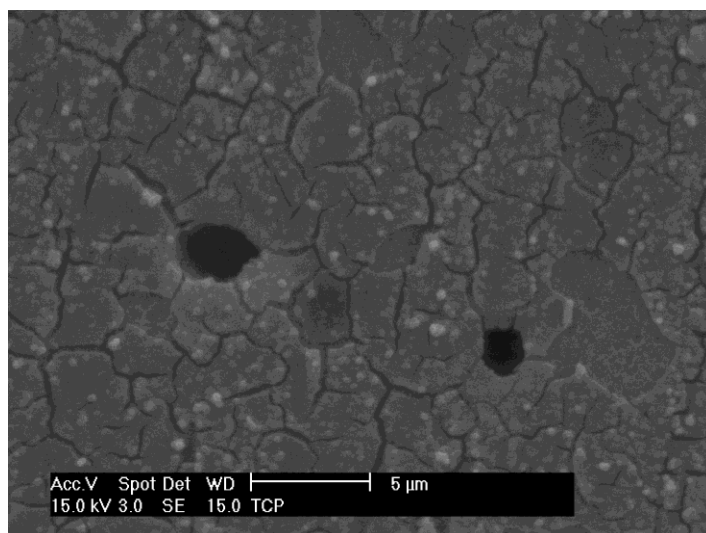
Figure 1.8. SEM micrograph of 10 min TCP on AA2024-T3 after Process I pretreatment.

The drying of a 10 min TCP coating formed on AA2024-T3 after 10 min immersion was studied in the ESEM. ESEM imaging was started on a freshly coated and still wet sample surface so that the initiation and evolution of mud-crack morphology could be monitored in-situ. Two major parameters in the ESEM chamber, pressure and temperature, were well controlled to maintain water in the liquid phase before imaging. Then they were adjusted in a manner that water evaporated gradually and the TCP dried slowly for imaging of film crack initiation. Under the

initial condition of 3 ^{o}C and 5 Torr (Figure 1.9a), the TCP coating appeared to be un-cracked and consisted of layers of merged spherical particles. When the temperature was raised to 10°C (Figures 1.9b and c), the particle margins became sharper and were more easily identified in the ESEM. Upon heating to 22°C and maintaining the relative humidity at 10%, cracks started to form and new cracking occurred as the aging continued. The coating appeared to flake off the substrate at different regions on the surface, as shown in Figures 1.9d, e and f.
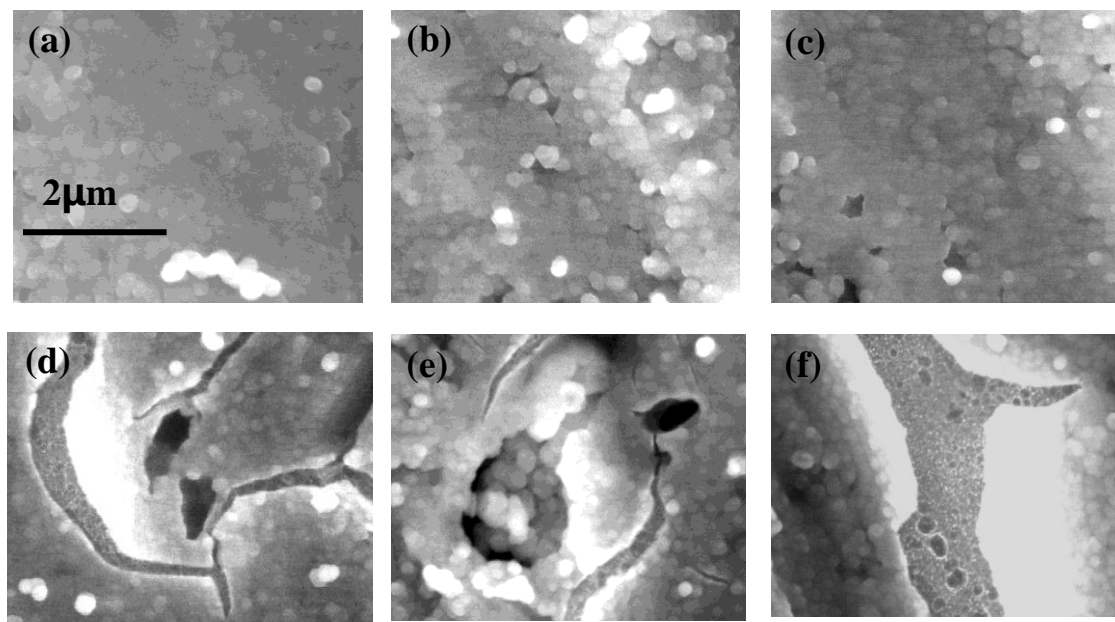
Figure 1.9. Crack formation during dehydration as observed by ESEM (sequence of cumulative exposure time). Imaging conditions are (a) 3°C, 5 Torr; (b) and (c) 10 ^{o}C, 5 Torr; (d), (e) and (f) 22 ^{o}C, 2 Torr.

Crack formation during natural aging was also investigated. Freshly prepared TCP coated samples were kept in a sealed container with RH of about 34%. After various aging times, the coating surfaces were examined by ESEM under the condition of 24 ^{o}C, 7.8 Torr and 35 %RH. After 12 h, the surface was characterized by the presence of a compact film consisting of spherical particles, and no cracking was observed. After 24 h atmospheric aging, the coating still showed macroscopic uniformity. However, very small cracks could be discerned. The cracking density and size were considerably increased after 48 h aging, Figure 1.10. Some cracks were over 5 μm in length.

5.1.4.5 Compositional Analysis of TCP on AA2024. Figure 1.11a is a TEM image of the cross-section of a TCP coating on an AA2024-T3 substrate formed after Process I. Many TEM analyses were performed and variation in the thickness of the conversion layer in the range of 60-100 nm was observed. The coating appeared to be delaminated from the substrate surface in many regions that were observed in the TEM. For instance, Figure 1.11a shows a large crack between the coating and the alloy. It is likely that this separation is an artifact that occurred in the

TEM or during sample preparation, such as in the high vacuum of the FIB tool, by a process related to the cracking during dehydration described above.
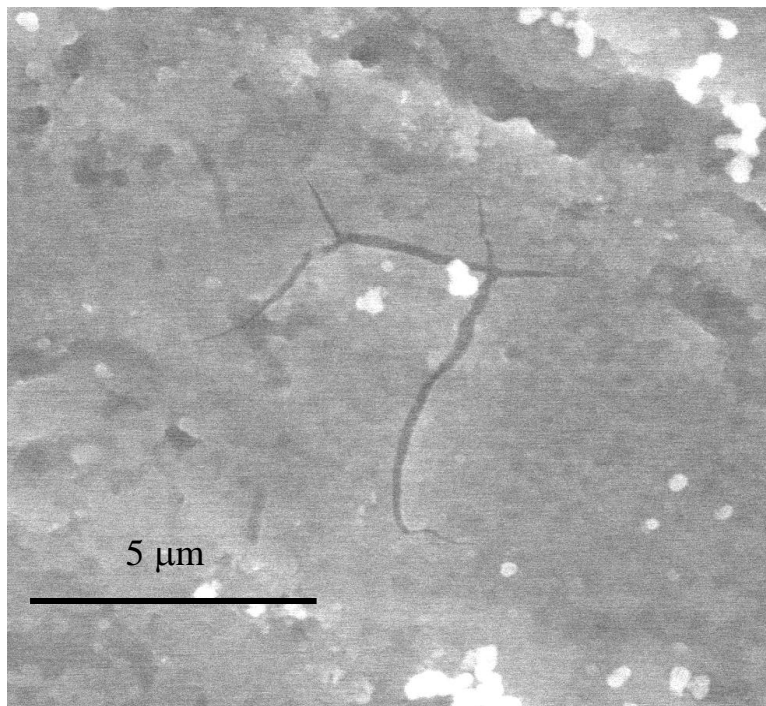
Figure 1.10.Crack formation after atmospheric aging for 48 h, as observed by ESEM under the condition 24°C, 7.7 Torr, 35% RH.

Figure 1.11b shows compositional line profiles of the TCP coating along the red line in Figure 1.11a, as measured by EDS. Based on the position where the Al signal intensifies, this film is on the order of 70 nm in thickness. The coating is mainly composed of Zr, Cr, O, Al and F, with Zr comprising 40 wt% in the TCP region. The Cr content is only one fourth the Zr content. It is therefore reasonable to consider TCP to be a zirconate film that contains Cr. The O signal extends beyond where the Zr and Cr signals decrease and overlaps with decay of the Al signal. However, accurate quantification of the O signal in EDS measurements is not possible. Thus the oxygen content from the EDS line profiling is not conclusive. Furthermore, EDS cannot sense hydrogen but the EDS measurements show that the film is at least partially hydrated so the coating is referred to as oxyhydroxide. The F level appears to be enriched at the metal-film interface. This indicates that the coating is bilayered with a layer of aluminum oxyhydroxide between the metal matrix and the Zr-Cr oxide.

Figures 1.11c and d show the analysis of another sample, this one formed after Process II, the coating thickness appears to be comparable to the sample after Process I, as shown in Figure 1.11c. The Cr and Zr signals were largest in the outer layer of TCP film, Figure 1.11d, which is similar to the film formed after Process I. However, only a trace amount of F was observed at the

interface of TCP and metal matrix indicating that the small amount of Si at the surface might affect the role of F in the TCP film formation process. EIS spectra from the two pretreatment processes (not shown) were found to be essentially identical.

a)

b)

c)

d)
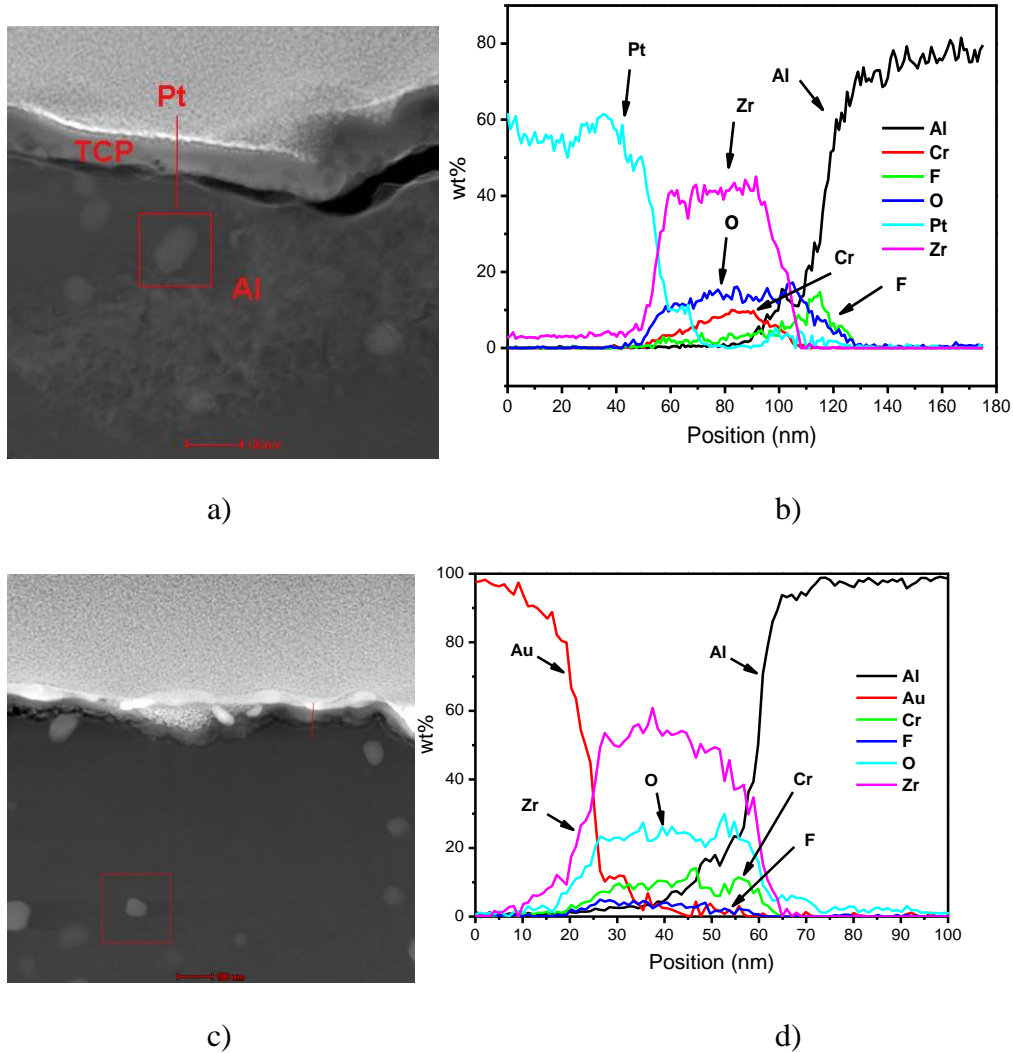
Figure 1.11. Analytical TEM of 10 min TCP on matrix of AA2024-T3 after Process I, (a,b) and after Process II (c,d); transmission electron micrographs (a,c}; nano-EDS line profiles (b,d).

5.1.4.6 Basic Electrochemical Properties of the TCP Coating. The basic electrochemical properties of the TCP-coated AA2024 samples were evaluated in air-saturated 0.5 M Na_2SO_4[3]. Figures 1.12a and b show (a) open circuit potential (OCP)-time transients and (b) bar graphs of the polarization resistance for TCP-coated and uncoated samples. To investigate the effect Cr(III) in the TCP coating has on the passivation of AA2024, comparison measurements were made using AA2024 samples coated with Alodine[TM] 5200. OCP-time transient and polarization resistance, R_p, data for these samples are also presented in Figure 1.12a and b. The OCP for the TCP-coated sample starts off 100 to 150 mV more noble than the value for the uncoated sample. However, over the 30 min. period, the potentials begin to merge and stabilize. The overall finding from many measurements is that there is not a major difference in the OCP for the coated

and uncoated AA2024 surfaces in this medium. The OCP values, which tend to quickly stabilize after solution exposure, are generally more noble for the TCP-coated samples by only 50-100 mV. The OCP for the Alodine[TM] 5200-coated samples was also slightly more noble than that for the uncoated alloy. The OCP measurement was validated using ASTM G69-97. Measurements of polished and uncoated AA2024 yielded values of -612 mV ($\pm$ 4) and -619 mV ($\pm$ 5) at the 95% confidence interval. These values are within the expected range of -600 to -620 mV vs Ag/AgCl.

Figure 1.12b shows that R_p for the TCP-coated samples is generally a factor of 8-10$\times$ greater than the uncoated samples. The nominal values were 5.42×10^4 ohm-cm^2 ($\pm 0.31 \times 10^4$) for the uncoated samples and 4.03×10^5 ohm-cm^2 ($\pm 1.15 \times 10^5$) for the coated samples (n$\geq$3). These values are in good agreement with those obtained from EIS data. While the TCP coating provides some level of protection to AA2024, the 10^5 -10^6 ohm-cm^2 R_p indicates the coating is not providing full barrier protection. Such barrier coatings would be expected to yield R_p values on the order of 10^9 ohm-cm^2. The polarization resistance of the 5200-coated samples was nominally 1.77×10^5 ohm-cm^2 ($\pm 0.65 \times 10^5$) (n=3). This value is 3-4$\times$ higher than the nominal value for the uncoated alloys but 3-4$\times$ lower than the nominal value for the TCP-coated samples. Therefore, assuming the general structure of the coatings is similar (*i.e.*, hydrated ZrO$_2$), these results suggest that the Cr(III) in the TCP coating contributes to the passivation of AA2024.
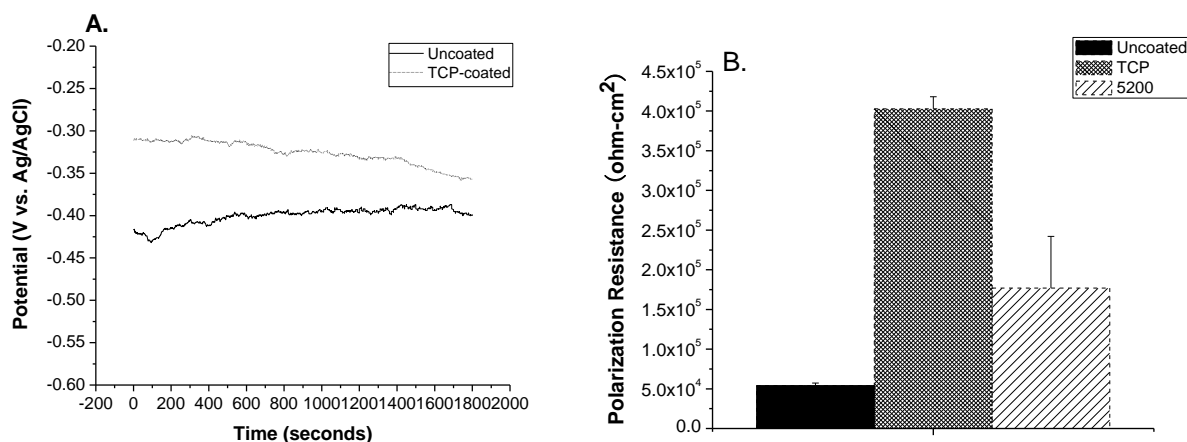
Figure 1.12. (A) Plots of the open circuit potential (OCP) versus time for bare, Alodine 5200-coated (Cr free) and TCP-coated AA 2024 samples in air-saturated 0.5 M Na$_2$SO$_4$. (B) Graphs of the polarization resistance, obtained from slow scan potentiodynamic polarization scans $\pm$30 mV vs. OCP, for bare, Alodine[TM] 5200-coated and TCP-coated AA2024 samples in the same medium.

Figure 1.13 shows typical slow-scan potentiodynamic polarization curves for bare, Alodine[TM] 5200-coated and TCP-coated AA2024 samples. The measurements were made in air-saturated 0.5 M Na$_2$SO$_4$. Similar to the data in Figure 1.12, the presence of either coating does not cause a significant shift in the OCP value. Both coatings do, however, produce attenuated anodic and cathodic currents around the OCP. For example, the anodic current from the OCP to about 0.4 V vs Ag/AgCl is about a factor of 10$\times$ lower for the TCP-coated sample. Attenuated current is also seen during the cathodic sweep from the OCP to about -0.8 V vs Ag/AgCl. The cathodic current

in this potential region arises from oxygen reduction and the inhibition by the TCP may result from the blockade of at least some of the Cu-rich intermetallics. The anodic and cathodic currents around the OCP are suppressed by both the TCP and Alodine[TM] 5200 coatings with the suppression being slightly greater for TCP.
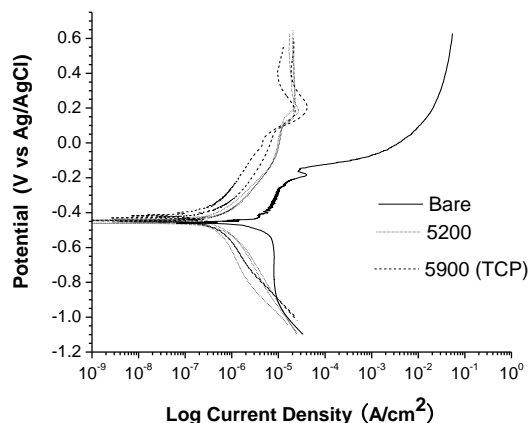
Figure 1.13. Slow-scan potentiodynamic polarization curves recorded for bare, Alodine 5200-coated (Cr free), and TCP-coated AA2024 samples in air-saturated 0.5 M Na_2SO_4.

5.1.4.7 Electrochemical Stability of the TCP Coating. The short-term stability of the TCP coating on AA2024 was assessed by measuring the OCP and total impedance-frequency and profile at the OCP during continuous immersion in air-saturated 0.5 M Na_2SO_4. Measurements were made at 50 ^{o}C over a 4-h period. The coated sample used in these measurements was aged overnight prior to use. Figure 1.14A and B show 4-h data for a TCP-coated AA2024 sample. The coating appears to possess good structural and chemical stability, at least under these conditions, based on the consistency of (i) the OCP, *ca.* -0.250 V vs Ag/AgCl, and (ii) the impedance-frequency profiles, particularly the low frequency polarization resistance, *ca.* 10^5-10^6 ohm·cm^2, with time. Other experiments in more aggressive environments (0.5 M NaCl) also were consistent with good structural and chemical stability during 4-h immersion tests.
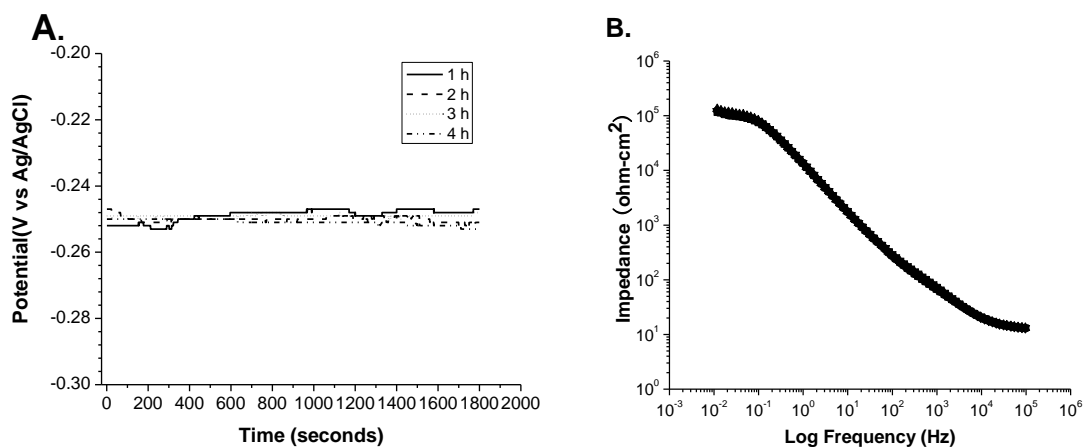
Figure 1.14. (A) OCP-time curves and (B) impedance-frequency plots for a TCP-coated AA2024 sample over a 4-h period during exposure to air-saturated 0.5 M Na_2SO_4 at 50 ^{o}C. The impedance data for all four time points overlap.

5.1.4.8 Effects of Aging on the Film Properties. Chromate conversion coatings (CCCs) can be viewed as having a biphasic structure of an interpenetrating solid Cr(III) matrix and aqueous channels [4-8]. The aqueous channels are likely the pathways for Cr(VI) transport [4-8]. We hypothesized that like the CCCs, the TCP coating may also consist of imperfections and hydrated channels, and that aging or dehydration might improve the barrier properties by condensing the film and collapsing these channels. This hypothesis was tested by aging TCP-coated samples in air from 24-96 h (1-4 days). Daily electrochemical testing was performed to assess the passivation properties. For some, but not all samples, aging produced a significant improvement in the coating's barrier properties. Figure 1.15A and B show plots of the total impedance and phase shift as a function of the frequency for TCP-coated AA2024 samples. This particular sample was aged in air for 3 days at room temperature, while the other was aged only overnight. Impedance analysis was performed at the OCP in 0.5 M Na_2SO_4 (air saturated). It can be seen that the low frequency impedance, R_p, increased to 10^9 ohm-cm^2 for the 3-day aged sample (Fig. 1.15A). This is three orders of magnitude greater than the low frequency impedance of 10^5-10^6 ohm-cm^2 seen for typical samples. The phase shift-frequency plot shows the capacitive-like behavior of the 3-day aged coating, especially at high frequencies (Fig. 1.15B). Clearly, at least in this case, aging can have a beneficial effect by producing significantly improved barrier properties. *At present, only some 30%, but not all, of the TCP-coated samples tested have exhibited improved barrier properties after 1-4 day aging.* We are presently carrying out a systematic study of aging effects and will report on this in a future publication.
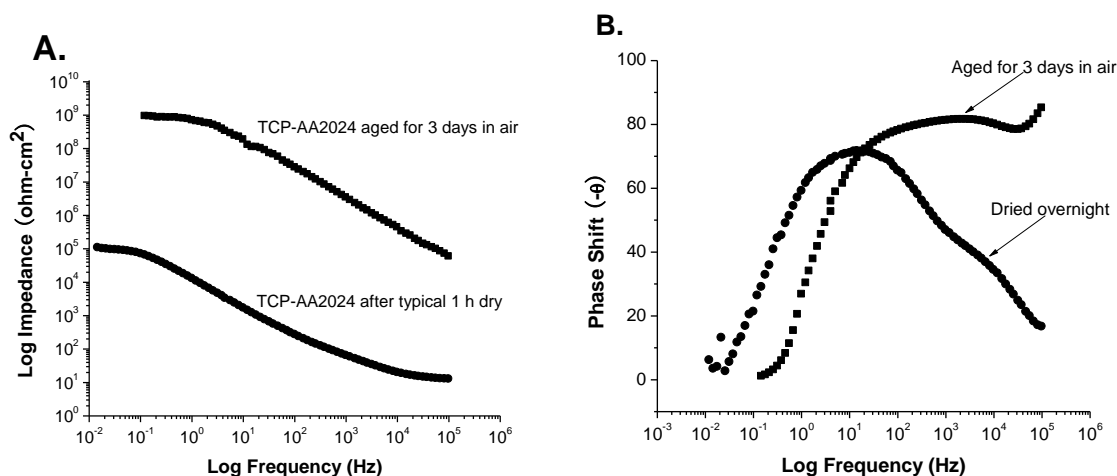
Figure 1.15. (A) Total impedance-frequency and (B) phase shift-frequency plots for a TCP-coated AA2024 sample aged for 3 days in air. The electrochemical measurements were made at the OCP in 0.5 M Na_2SO_4 (air saturated).

5.1.4.9 Artificial Scratch Tests. Artificial scratch cells were opened after various exposure times (7, 14 and 21 days) and examined for evidence of corrosion. Figure 1.16 shows the two sides of a cell exposed to 0.5 M NaCl for 21 days. The TCP-treated AA2024-T3 sheet still exhibited the pale tan color characteristic of TCP, Figure 1.16a. The non-TCP side of the cell, Figure 1.16b, exhibited attack, but considerably less than the two sides of the control cell comprising two non-TCP samples, Figures 1.16c and 1.16d. The crevice corrosion evident on both sides of the control cell is absent on both sides of the TCP/non-TCP cell.

ICP-OES analysis was performed to determine the concentrations of dissolved species released from TCP-treated samples into dilute Harrison's solution. Figure 1.17a shows that the concentrations of Cr, Cu and Zr ions were low and constant for the first 3 days. After 5 days the Cu and Cr ion contents increased. The chromium concentration was about 0.3 µM during the first days and then increased, reaching 2.7 µM after 10 days. It stayed around 3 µM until a sharp increase to 7.5 µM was observed for the 60-day-exposure sample. For the whole exposure time, the zirconium content in the exposed solution stayed just above the detection limit of the equipment, ~0.05 µM, which suggests that the zirconium was insoluble and remained in the coating. The concentration of released copper increased to 0.7 µM upon exposure, and then increased again after around 5 days to around 3 µM, where it stayed with some fluctuation for the duration of the exposure. The Al ion concentration is shown in Figure 1.17b. A spike in the Al ion concentration was observed during the first days of exposure reaching a maximum concentration of 5 µM. During the following 15 days of exposure, the concentration of Al remained at about 2 µM. An increase to 5 µM was found for the 30 days exposure sample, after which the Al ion concentration increased steeply to 175 µM at 50 and 60 days.

| (a) | (b) | (c) | (d) |
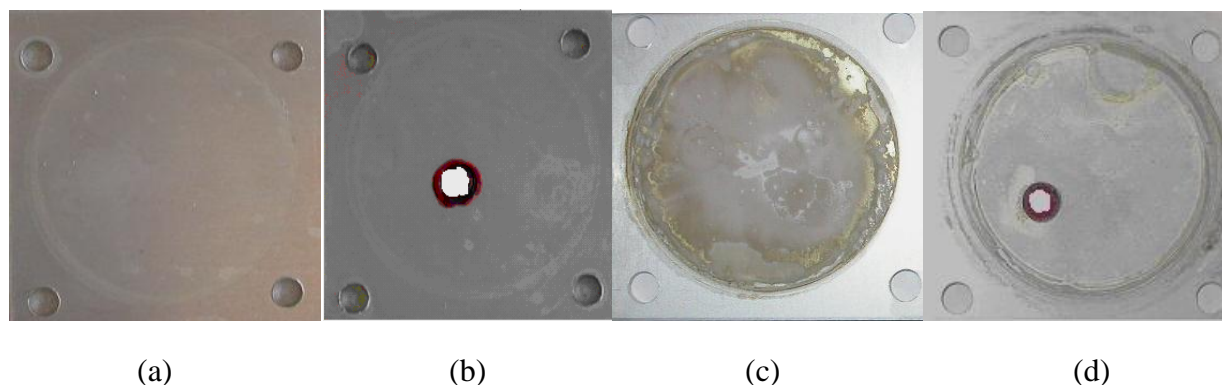
Figure 1.16. Photographs of artificial scratch cell sheets exposed to 0.5 M NaCl. (a) TCP-treated surface exposed for 21 days, (b) non-TCP surface exposed near TCP-treated surface for 21 days, (c) bottom non-TCP surface exposed in control cell for 14 days, (d) top non-TCP surface exposed in control cell for 14 days.

The surfaces of non-TCP samples from artificial scratch cells were studied by XPS to investigate the presence and oxidation states of chromium species. After exposure in 0.5 M NaCl, XPS measurements indicated a trace amount of chromium species on the non-TCP surface, Figure 1.18a. This might explain the remarkable corrosion inhibition exhibited by the non-TCP panel from visual inspection test, as shown in Figure 1.16b. After exposure in dilute Harrison's solution, which is much less aggressive, XPS analysis also confirmed the presence of chromium species on the surface of the non-TCP AA2024-T3 surface, Figure 1.18b. A fresh sample showed no evidence of Cr on the surface. The Cr peak height on the non-TCP surface increased and the Cr 2p peak position shifted toward higher binding energy with exposure time. The binding energy shift indicates that the composition of the chromium species on the non-TCP surface changed during exposure in the artificial scratch cell. Fitting of the XPS spectra indicated that these species are mainly Cr(III), but that a small portion of Cr(VI) could be present, Figure 1.18c.
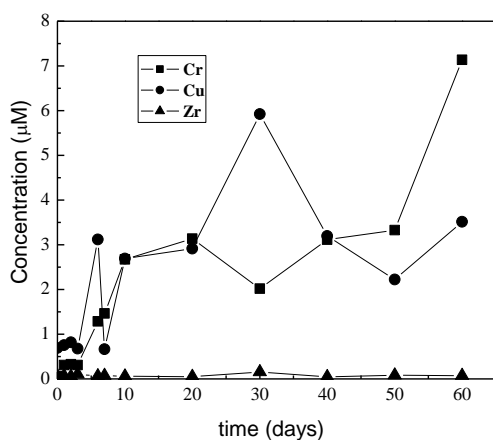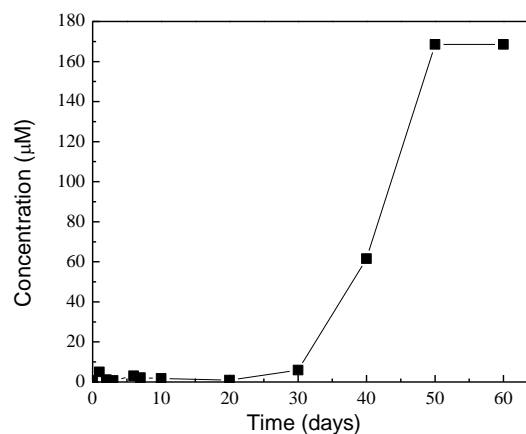
(a)   (b)

Figure 1.17. ICP OES analysis of dilute Harrison's solution after static exposure of TCP-treated AA2024-T3. (a) Cr, Cu, and Zr concentration (b) Al concentration
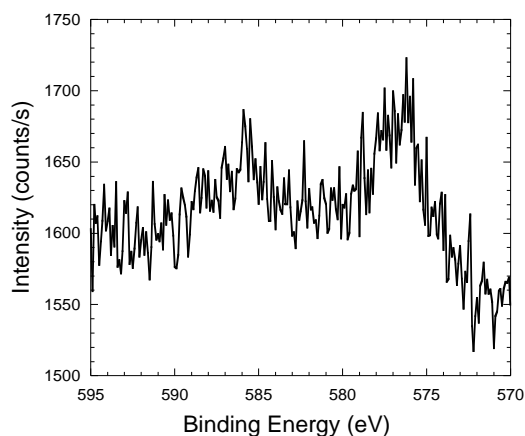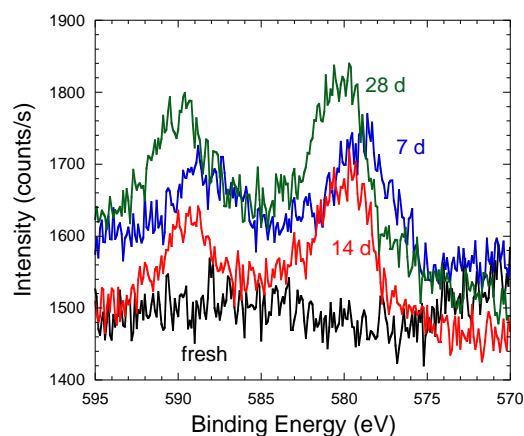
(a)   (b)
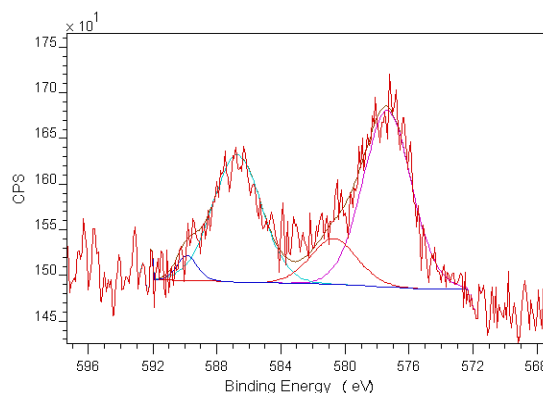
(c)

Figure 1.18. Cr 2p XPS spectra measured on non-TCP surfaces exposed to the artificial scratch cell. a) exposure to 0.5 M NaCl after 14 d b) after 0, 7, 14 and 28 days in dilute Harrison's solution. (c) Fitting of the Cr 2p spectrum of the non-TCP surface of an artificial scratch cell with dilute Harrison's solution after 14 days exposure

33

Al 2p XPS spectra were also collected from the non-TCP samples, Figure 1.19. For the 0 day sample, which was not exposed to the electrolyte, Al 2p peaks were observed at 75.91eV and 72.8 eV, representing Al(III) and Al metal, respectively. The oxide on the sample surface was thin enough that the underlying metal could be sensed by XPS. The spectrum of the sample exposed for 7 days exhibited an increase in the intensity of the Al(III) peak and a decrease in the Al metal peak. After 14 days exposure, the Al metal peak was only a slight bump and after 28 days this peak was not observed. The binding energy of the Al(III) peak showed a similar trend as the Cr peak in that the binding energy shifted with time to higher values. This shift suggests the formation of AlOOH and then Al(OH)$_3$ with time.
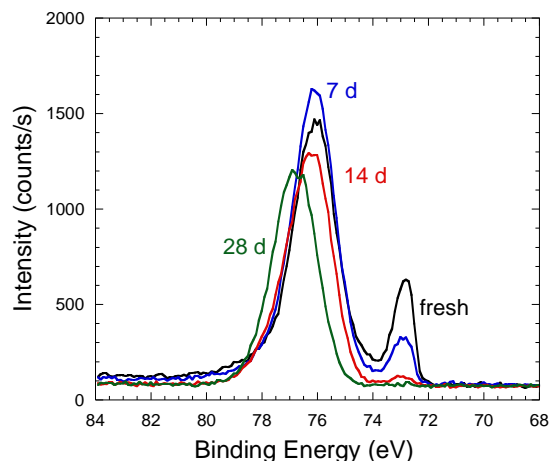
Figure 1.19. Al 2p spectra of non-TCP surfaces exposed for different times in the artificial scratch cell containing dilute Harrison's solution

Impedance data were acquired periodically from both sides of the artificial scratch cells containing the dilute Harrison's solution. The first electrolyte used in the artificial scratch cell was 0.5 M NaCl. The TCP-treated side started out with a low frequency impedance (which should be close in magnitude to the polarization resistance) that was almost two orders of magnitude higher than the non-TCP side. With time, the polarization resistance of the TCP side decreased, but it remained about 10 times greater than the non-TCP side even after 20 days exposure. The polarization resistance of the non-TCP sample was similar to a control surface where both sides of the cell were non-TCP samples. This implies that there was no significant corrosion inhibition provided by the nearby TCP surface to the non-TCP surface. Note that these results are not in agreement with those from visual inspection as shown in Figure 1.16, which indicated inhibition in 0.5 M NaCl. Dilute Harrison's solution, which is much less aggressive than the 0.5 M NaCl solution, was used for the following experiments.

EIS measurements were made as a function of time on the TCP coated side of the artificial scratch cell exposed to dilute Harrison's solution and, as a control experiment, also on the top side of an artificial scratch cell in which both sides were non-TCP samples. The impedance magnitudes at 0.01 Hz for surfaces in the artificial scratch cells and control cells as a function of exposure time are compiled in Figure 1.20. The symbols are the average values as a function of exposure time for six replicate experiments at each condition and the error bars are the standard deviations. The sample notation in the figure shows the two samples exposed in the cell with the tested sample underlined. For example, the notation for the non-TCP sample in a standard

artificial scratch cell is <u>non-TCP</u>/TCP. The initial values of the low frequency impedance for the TCP and non-TCP surfaces as well as the non-TCP sample in the control cell were all similar, in the range of $0.5 - 1.2 \times 10^5$ ohm-cm^2, and all increased with time. Within the first 24 hours of exposure (Fig. 1.20a), the average low frequency impedance of the non-TCP surface in the artificial scratch cell increased to 3.5×10^5 ohm-cm^2, which was only slightly lower than the TCP surface and almost twice that of the non-TCP control surface. After 24 hours (Fig. 1.20b), the average low frequency impedance of the TCP surface increased, reaching 1.2×10^6 ohm-cm^2 at 168 hours. It remained stable at about 10^6 ohm-cm^2 through the whole 700 hours of testing. The low frequency impedance of the non-TCP surface remained at about 4×10^5 ohm-cm^2 after the first 24 h. The low frequency impedance of the non-TCP control remained at about 2×10^5 ohm-cm^2, half the value of that for the non-TCP sample. As will be discussed below, this is evidence of active corrosion inhibition by TCP treatments.

(a)   (b)
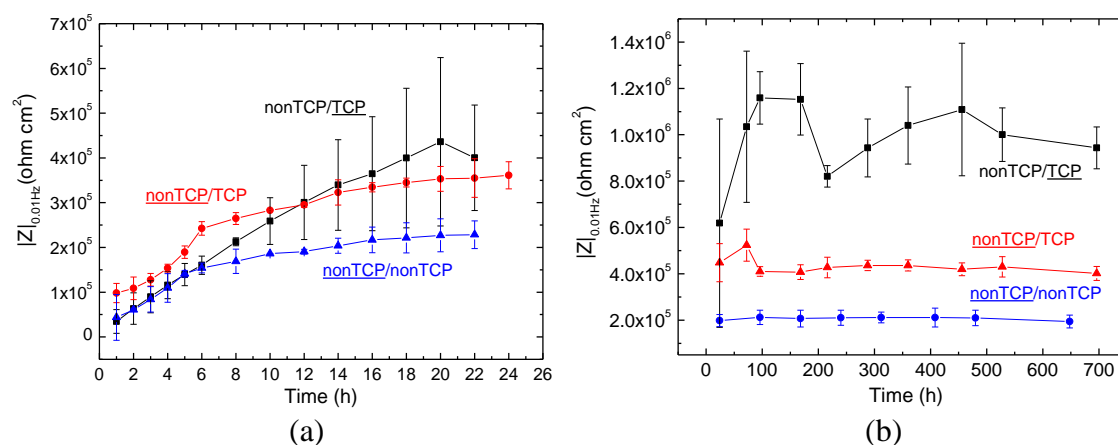
Figure 1.20. Impedance magnitude at 0.01 Hz for TCP and non-TCP surfaces in artificial scratch cells and for control cells containing dilute Harrison's solution. a) exposure times less than 24 h, b) exposure times after 24 h. The sample notation in the figure indicates the two samples exposed in the cell with the tested sample underlined.

To better simulate real scratches, in which defects are electrically shorted to the TCP coating, the two panels in the artificial scratch cells were connected by copper tape during exposure. This type of artificial scratch cell is termed "shorted" in the following figures. The non-shorted cell is termed "open". Furthermore, the non-TCP treated surfaces in some of the artificial scratch cells were partly covered by corrosion protective tape to increase the TCP to non-TCP surface area ratio (AR) as described in the experimental section.

Figure 1.21a shows the open circuit potentials collected for different surfaces in artificial scratch cells under various conditions. For shorted cells, the potentials were measured after unshorting them but before EIS measurements. In the open artificial scratch cells, the corrosion potential for TCP coated surface (non-TCP/<u>TCP</u>, open, AR=1.03) was about -520 mV SCE for 4 days and then decreased to -600 mV vs. SCE. The OCP for non-TCP surfaces (<u>non-TCP</u>/TCP open, AR=1.03) was lower, decreasing during the first day to -710 mV vs. SCE and then increasing after 100 h to about -650 mV vs. SCE. The non-TCP sample in the control cell exhibited similar behavior to the <u>non-TCP</u>/TCP sample. The OCP of the non-TCP surface in a shorted cell (<u>non-TCP</u>/TCP, shorted, AR=1.03) was higher than in the open cell as expected. It was about -570

35

mV vs. SCE during the first week of exposure and then increased. The OCP was about the same for the higher AR (non-TCP/TCP, shorted, AR=177), except that the increase at long times was not observed. The OCP of the TCP surface in shorted cells (non-TCP/TCP, shorted, AR=1.03 or 177) was similar to the value for TCP in the open cells. Overall, the TCP surfaces in all types of artificial scratch cells exhibited OCP values of about -550 mV vs. SCE in the first 300 h of exposure; while the electrical shorting and higher area ratio both raised the corrosion potential values of the non-TCP surface by 100 mV.

EIS was performed on the cells with shorting and different area ratios. The impedance values at 0.01 Hz for TCP and non-TCP surfaces in different types of artificial scratch cells are shown in Figure 1.21b. Little effect of shorting was observed for non-TCP/TCP samples with AR = 1.03. However, the TCP surface (non-TCP/TCP, AR = 1.03) had a significantly lower impedance value when shorted. Results for the shorted cell with AR = 177 appear to be spurious as the impedance for the non-TCP sample was even lower than the non-TCP surface in the control cell.
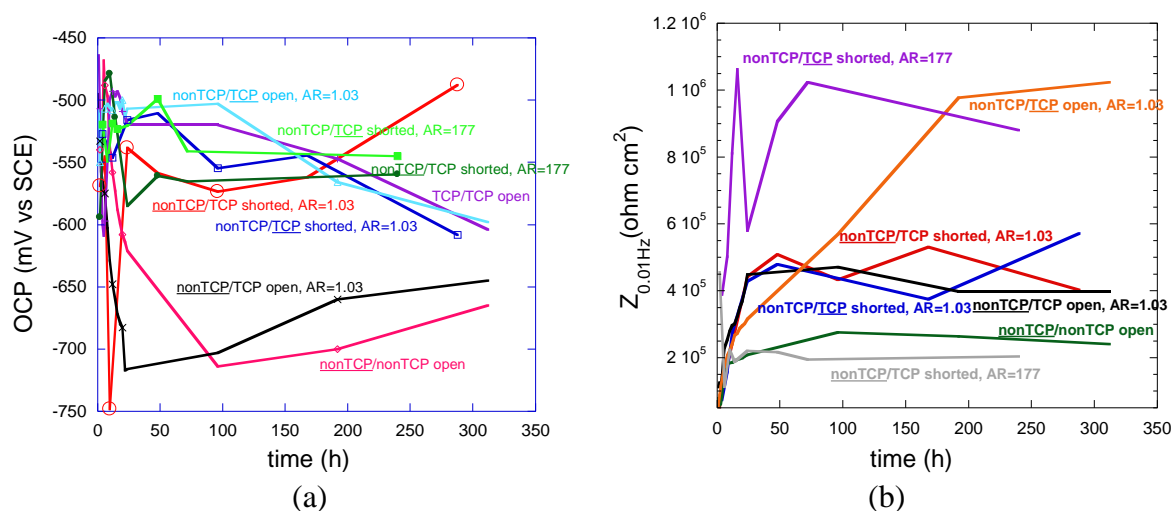
Figure 1.21. Results for TCP coated and non-TCP surfaces in artificial scratch cells containing dilute Harrison's solution under different conditions of shorting and area ratio. "AR" is TCP/non-TCP surface area ratio. "Open" is for non-shorted cell. The surfaces on which the OCP values were measured are underlined, whereas the other surface in the cell is given after the slash. (s) Open circuit potential (b) impedance magnitude at 0.01Hz.

5.1.4.10 Active Inhibition by TCP. In this work several approaches were used to assess the active corrosion inhibition properties of TCP. The ICP-OES characterization of the electrolyte exposed to the TCP coating for different exposure times, Figure 1.17, proved that chromium species in the TCP coating were released into the aqueous environment while zirconium was barely detected. The fact that chromium can be released from the TCP coating provides evidence for one of the requirements of self-healing, i.e. release of active species. Evidence for a second requirement of self-healing, transport to a nearby bare surface, was provided by the XPS analysis, Figure 1.18, which showed the presence of chromium on the surface of the non-TCP sample. Visual observation shows that the non-TCP surface was well protected by the nearby TCP coating in the artificial scratch cell, as shown in Figure 1.16b. In contrast, severe corrosion was observed on the control non-TCP surfaces.

The artificial scratch cell was also used to investigate TCP. The uniqueness of this approach is that it can provide clear evidence of the self-healing property of a coating system. A lower corrosion rate of the non-TCP surface in the cell relative to a control cell can only be attributed to the inhibitor released from the coating nearby. Chromate was previously found to be released from the chromate conversion coating and migrate to a nearby uncoated surface resulting in the enhancement of the corrosion resistance of the uncoated surface by two orders of magnitude relative to the control case with no chromate conversion coating.

In accordance with the clear evidence of Cr release, transport and protection, the EIS data from the artificial scratch cells with non-TCP surfaces exposed close to TCP surfaces provided evidence of active corrosion inhibition of the non-TCP surface. However, the extent of the protection was much less than that found for chromate conversion coatings. For instance, the low frequency impedance for the non-TCP surface was only about twice that found for control experiments with two non-TCP surfaces. Since the low frequency impedance is considered to be proportional to the polarization resistance, the higher value for the non-TCP surface indicates a somewhat lower corrosion rate, probably resulting from the chromium released from the nearby TCP coating. A rapid increase in the impedance value for the non-TCP surface was observed during the first 24 h of exposure, suggesting a rapid response of the TCP coating associated with chromium release, transport, and deposition during this time.

The values of coating capacitance for artificial scratch cells also suggested mild active corrosion protection. The increase in the capacitance of the control surface is likely associated with attack. However, for the non-TCP/TCP surface, the capacitance value decreased slightly with time, which could be associated with active corrosion inhibition provided by the TCP coated surface across the electrolyte.

The standard artificial scratch cell approach used in this work did not include electrical shorting of the two sides of the cell. Experiments performed on shorted cells at the standard area ratio of 1.03 found essentially no influence of the shorting. Interestingly, when the TCP/non-TCP area ratio was increased from 1.03 to 177, the low frequency impedance decreased to a lower value than the control sample. It was expected that the smaller exposed non-TCP area would benefit from having relatively more chromium for protection. It is possible that the tape used to mask the non-TCP area adversely affected its performance, perhaps because of crevice corrosion.

Based on the evidence presented above, it is clear that TCP can provide some amount of active corrosion inhibition. However, the mechanism for active corrosion protection by TCP should be different than the mechanism for chromate conversion coating mechanism because the Cr^{3+} ion is generally not regarded to be soluble whereas chromate ions are extremely soluble. The active protection provided by TCP is much more subtle than that provided by CCC. It was shown above that Cr species are released into solution contacting TCPs and can deposit on a nearby bare Al surface. It will be shown in the next section that transient formation of Cr(VI) can occur on TCP surfaces during oxygen reduction. Another possibility is that Cr(III) is released non-faradaically into the solution, i.e. by a chemical dissolution process. Once in solution, the Cr(III) species could diffuse to the bare or non-TCP area and deposit. For instance, the ICP-OES results showed the existence of chromium species in the electrolyte exposed to the TCP coating but no Zr species. It is possible that certain amount of organometallic Cr(III) species in the TCP bath is incorporated into the mixed Zr-Cr oxide during coating formation and can desorb from the

coating into the electrolyte. It is also possible that Cr(III) hydroxide disintegrates from the mixed Zr-Cr oxide film due to the exposure to aggressive ions in the electrolyte such as chloride. The dilute Harrison's solution contains ammonia at a pH of about 5.8, which might promote the release of Cr(III) from the TCP into solution in the form of $[Cr(NH_3)_6]^{3+}$ which is soluble and mobile. However, given the solubility differences and the evidence presented by others for the local generation of Cr(VI), it is more likely that Cr(VI) species are involved in the active inhibition mechanism.

5.1.4.11 Raman Spectroscopy. Raman spectroscopy is a useful technique for detecting the presence of Cr(III) and or Cr(VI) oxides. The spectra serve as molecular fingerprints that can be used to distinguish specific chemical species on a surface or in a coating [5-8]. The technique is quite useful in corrosion systems for monitoring samples in air or in solution; for investigating dynamic systems from the second to multiple day time domain; and for probing small micrometer-sized areas for sufficiently strong scatterers. McCreery and coworkers used Raman spectroscopy extensively (*in situ* and *ex situ*) to spatially and temporally detect Cr(III) and Cr(VI) oxide species in CCCs [4-8]. In Figure 1.22, background-corrected spectra from 400-1200 cm^{-1} are presented for uncoated (degreased and deoxidized) AA2024, and alloy samples coated with Alodine 5200 and TCP, respectively. The region in and around a pit was probed for the TCP-coated sample. The spectra for the uncoated and 5200-coated samples are featureless. Featureless spectra were obtained at all regions of both surfaces. In contrast, two peaks are seen for the TCP-coated sample at 547 and 880 cm^{-1}. These two peaks are assigned to scattering by Cr(III) and Cr(VI) oxide species, respectively [4-8]. Even though it is a weak scatterer, Cr(III) oxide was detected in the TCP-coating after as little as 1 h of aging in air. These peaks are not detected in coatings immediately after formation though, therefore, some level of air drying is necessary. The Cr(VI) oxide is a stronger scatterer than Cr(III) oxide so lower levels of the former are more readily detectable by this technique. The presence of the two peaks is consistent with a mixed oxide composition. As noted in the work by McCreery and coworkers, the peak at 880 cm^{-1} is associated with a mixed Cr(III)-Cr(VI) oxide [5-8]. We have also observed that the Cr(VI) oxide peak increases in intensity during 1-4 day solution immersion in air-saturated 0.5 M Na_2SO_4. The peak is considerably more prominent after similar exposure to 0.5 M NaCl, Finally, the peak is most prominent after similar exposure to a 0.5 M Na_2SO_4 solution containing added H_2O_2.

The Cr(III) and Cr(VI) oxide peaks are not observed uniformly over the entire TCP-coated surface but rather appear to be localized in and around pits. This was evident from recording a series of Raman spectra (line scans) between 400-1200 cm^{-1} spatially across a precipitate formed in a pit. No scattering intensity for either of the Cr oxides was detected on the terraces outside the pit. However, there was intense scattering in and around the pit. The bands at 547 and 880 cm^{-1} were quite prominent and their intensities correlated with one another, consistent with both species being part of a mixed oxide. Importantly, these data indicate that transient formation of Cr(VI) species can form in the coating.

38
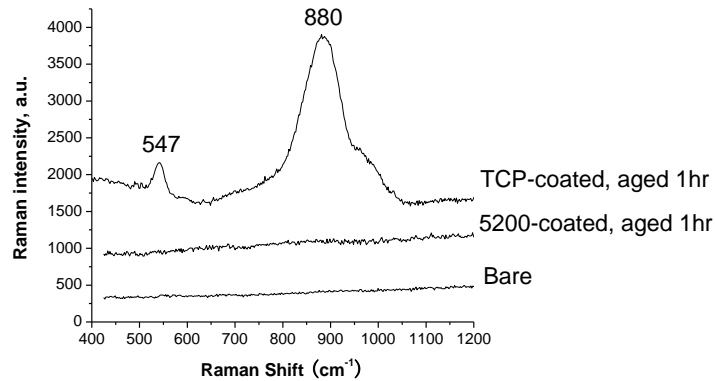
Figure 1.22. *Ex situ* Raman spectra recorded for uncoated (degreased and deoxidized), Alodine 5200-coated and TCP-coated AA2024 plates.

5.1.4.12 Raman Spectroscopy of Transiently Formed Cr(VI) Oxide. Given the interesting finding of transiently formed Cr(VI) oxide shown in Figure 1.22, we carried out more detailed studies to determine [9]:

(1)   What is the mechanism by which the Cr(VI) oxide species transiently forms in the TCP coating on AA2024?

(2)   When does it form and what is the chemical environment around the Cr(VI) oxide species?

(3)   Does the Cr(VI) oxide species provide any active corrosion protection on AA2024?

Our hypothesis was that dissolved oxygen is reduced at the Cu-rich intermetallic sites to hydrogen peroxide, H_2O_2, and that H_2O_2 diffuses to nearby Cr-rich sites in the coating and oxidizes native Cr(III) to Cr(VI). H_2O_2 may be produced from the two-electron reduction of dissolved oxygen, as shown below. We suppose the conversion of $Cr(OH)_3$ transiently to chromate (CrO_4^{2-}) involves the following two steps:

$$O_2 + 2H^+ + 2e^- \leftrightarrow H_2O_2 \quad \text{(locally produced)} \tag{1}$$

$$2Cr(OH)_3 + 3H_2O_2 + 4OH^- \rightarrow 2CrO_4^{2-} + 8H_2O \tag{2}$$
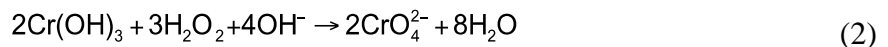
An important question to answer is by what chemical reaction can the Cr(VI)-O species form from the Cr(III) oxide in the coating. We hypothesize that Cr(III) is oxidized to Cr(VI) by H_2O_2 that is produced by the two-electron reduction of dissolved oxygen at nearby Cu-rich intermetallic sites. The O_2 reduction reaction on Cu is complex and we have no direct proof for the formation of H_2O_2 on this TCP-coated alloy. Nevertheless, this product is possible so we performed several tests to determine if O_2 is linked to Cr(VI) generation. In one, we coated two AA2024 samples with TCP. One was aged one overnight under a vacuum while the other aged in the laboratory air for the same period of time. Both samples were aged at room temperature. Our hypothesis was that if O_2 availability was limited (*in vacuo*) then the corresponding level of H_2O_2 would be limited in the coating and there would be little oxidation of Cr(III) to Cr(VI)-O.

39

In other words, no Cr(VI)-O peak was expected in the Raman spectrum for the sample aged *in vacuo*.

Multiple spectra were acquired across the TCP-coated surfaces and two representative curves are shown in Figure 1.23. The Cr(VI)-O peak, centered at 853 cm^{-1} was often detected in and around the pits on the sample aged in air while no such peak was found in the coating aged *in vacuo*. For the latter, only the Cr(III)-O peak at 538 cm^{-1} was observed. The 438 and 680 cm^{-1} peaks are associated with Cu-O bonds of the Cu-rich intermetallic compound. No evidence of any Cr(VI)-O species was found when probing the coated sample aged in vacuum. This strongly implies the involvement of dissolved O_2 in the transient formation of Cr(VI), possibly through the production of H_2O_2. Recall that the scattering cross section for Cr(VI)-O is considerably larger than the value for Cr(III)-O so the technique is sensitive to the presence of the former.
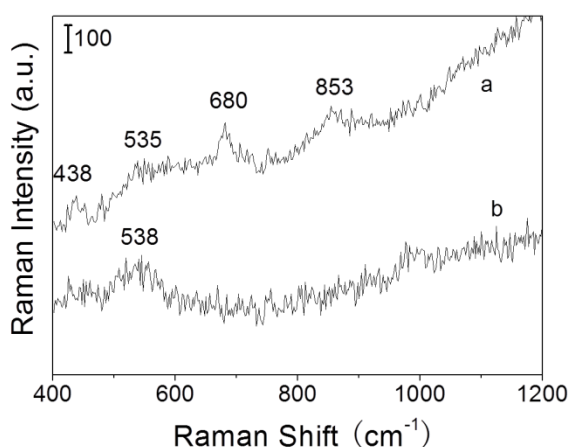
Figure 1.23. Raman spectra for the TCP-coated samples aged (a) in air and (b) in vacuum at room temperature overnight. Spectra were acquired within the pitted areas.

To further confirm the importance of dissolved O_2 in the conversion of Cr(III)-O to Cr(VI)-O, we coated another two samples and immersed them for 3 days in 0.5 M NaCl, with and without dissolved O_2. After immersion and prior to Raman analysis, the samples were rinsed for 10 s in ultrapure water. The sample immersed in the air-saturated solution was then dried in the laboratory air (room temperature) for 30 min. The sample immersed in the O_2-free solution was dried for the same period of time *in vacuo* at room temperature. Figure 1.24a shows that the 860 cm^{-1} Cr(VI)-O band forms during immersion in the air-saturated solution but does not in the deaerated solution. Deaeration was accomplished under vacuum. For the sample immersed in the air-saturated electrolyte, both the Cr(VI)-O peak and the Cr(III)-O peak (520 cm^{-1}) are present, consistent with the formation of a mixed oxide. In contrast, the spectrum for the sample immersed in the deaerated electrolyte shows only the Cr(III)-O peak at 520 cm^{-1}. These results further confirm the necessary role of dissolved oxygen in the transient formation of Cr(VI) in the TCP coating.
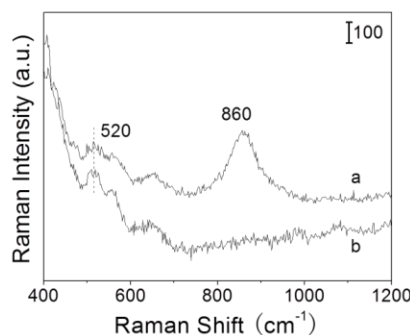
Figure 1.24. Raman spectra for the TCP-coated samples immersed in 0.5M NaCl (a) with and (b) without oxygen for three days. Spectra were acquired on the terrace near the pits.

To test how effective (kinetically) H_2O_2 is at oxidizing Cr(III) to Cr(VI), we coated three alloy samples with TCP and immersed each in an air-saturated 0.5 M Na_2SO_4 containing different concentrations of H_2O_2 (0.01, 0.1 and 1% v/v). Our hypothesis was that the Cr(VI)-O peak intensity would increase proportionally with the H_2O_2 solution concentration if this oxidant acts to rapidly to oxidize Cr(III)-O. The immersion period was 1 h in each solution. A TCP-coated sample immersed in H_2O_2-free 0.5M Na_2SO_4 for the same period of time was used as the control. Before acquiring Raman spectra, the samples were removed from the immersion solution, rinsed in tap water for 30 s and aged in air for 30 min. Spectra were acquired on the terrace sites near pits about 10 μm in diameter. Figure 1.25 shows that the Cr(VI)-O peak at 860 cm^{-1} increases proportionally with the H_2O_2 concentration. The sample immersed in H_2O_2-free Na_2O_4 solution has no significant Cr(VI)-O peak intensity. These results confirm the ability of H_2O_2 to rapidly oxidize Cr(III) to Cr(VI) in the coating.
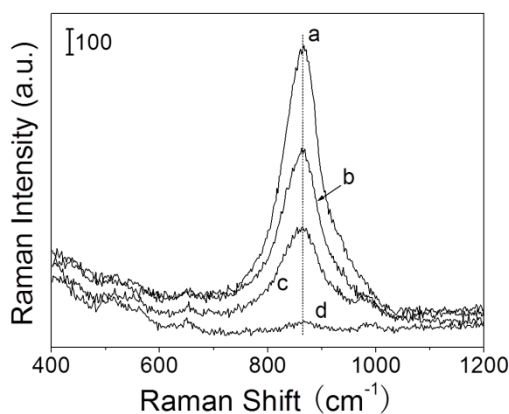
Figure 1.25. Raman spectra of the TCP-coated samples immersed in 0.5M Na_2SO_4 added with H_2O_2 by (a) 1%, (b) 0.1% and (c) 0.011% (v/v). Spectra were recorded on the terrace near the pits. (d) A spectrum recorded on the terrace of a coated sample immersed in 0.5M non-H_2O_2 Na_2SO_4.

5.1.4.13 TCP-coated AA2024 samples before immersion testing. After coating with TCP, samples were aged overnight in air at room temperature. It is supposed that the coating retains

41

some level of hydration during the aging period, like chromate conversion coatings, and that water facilitates O_2 dissolution into the coating. This is followed by reduction of at least some of the O_2 to H_2O_2 at the Cu intermetallic sites. This product then locally oxidizes Cr(III) in the coating to Cr(VI). Figure 1.26A shows a SEM micrograph of a coated AA2024 sample after overnight aging. The surface, typical of all coated samples investigated (n>10), is characterized by three distinct features: (a) a large pit (~10 μm diam.), (b) relatively smooth terrace sites with no damage and (c) several elongated precipitates (~1 μm) distributed over the undamaged terrace sites. Raman spectra were recorded from each of these three sites and representatives are shown in Figure 1.26B. The TCP-coated AA2024 sample contains two types of pits. One type contains Cu-rich intermetallic compounds and the other is devoid of Cu. There is a characteristic spectrum for each. Figure 1.26B-a1 shows the spectrum acquired at a Cu-rich pit. The two sharp peaks at 434 and 680 cm^{-1} are attributed to Cu-O vibrations. The broad peak at 552 cm^{-1} is attributed to a Cr(III)-O bond from either $Cr(OH)_3$ or α-Cr_2O_3[5-8]. This is evidence that the TCP coating forms on at least some of the Cu-rich intermetallic sites, consistent with our previously reported EDX results. The 854 cm^{-1} peak arises from a Cr(VI)-O bond presumably produced from the oxidation of Cr(III) in the coating by H_2O_2. Figure 1.26B-a2 is the spectrum acquired from a pit devoid of Cu. Consequently, there are no 434 or 680 cm^{-1} peak seen. The weak 556 cm^{-1} peak is attributed to Cr(III)-O. A spectrum recorded from a terrace site is shown in Figure 1.26B-b and contains only the Cr(III)-O peak at 520 cm^{-1}. Figure 1.26B-c shows a typical spectrum acquired at one of the elongated precipitate particles. The broad peak at 536 cm^{-1} is due to the hydrated Cr(III) oxide in the TCP coating. Both $Cr(OH)_3$ and Cr_2O_3 likely have an amorphous structure. The Cr(III)-O peak position depends on the level of hydration (i.e., bond length, $Cr(OH)_3$, Cr_2O_3 and even CrOOH). Spectra for a bare AA2024 samples and one coated with the non-chrome containing Alodine^{TM} 5200 are presented in Figs. 1.26B-d and 1.26B-e, for comparison. Both are featureless within the spectral window, as expected. The important conclusion is that Cr(VI) oxide species can transiently form in the TCP coating even during overnight aging, with the Cr(VI) species being localized near Cu-rich intermetallic sites.

Spectra for the TCP-coated samples aged in the laboratory air for 15 days were also studied (data not shown here). Spectral features similar to those shown in Figure 1.26 were found. The Cr(VI)-O peak in the 840-904 cm^{-1} range always accompanied the Cu-O peaks at 434 and 680 cm^{-1}. Spectra from the coating in pits devoid of Cu and on the Al terrace sites contain only the $Cr(OH)_3$ or α-CrOOH peak in the 520-580 cm^{-1} range.

5.1.4.14 Transient formation of Cr(VI) during immersion testing. After the typical overnight aging in air at room temperature, the TCP-coated samples were then immersed in air-saturated 0.5M NaCl solution for 30 days. Spectra were recorded at different times during the immersion period. At the time of measurement, each sample was removed from the solution, rinsed with tap water for 10 s and dried in air for 30 min. Figure 1.27 shows representative spectra acquired at a pit and on the terrace sites after 3 days. The spectrum in Figure 1.27-a has multiple peaks reflective of the formation of both $Cr(OH)_3$ or α-CrOOH (556 cm^{-1}) and Cr(VI)-O (847 cm^{-1}) near a Cu-rich intermetallic site (434 and 680 cm^{-1}). In contrast, in pits devoid of Cu, the spectrum has only the Cr(VI)-O peak at 860 cm^{-1}, as shown in Figure 1.17-b. Contrary to the samples aged in air, the Cr(VI)-O peak is found in most pits regardless of the presence of Cu during full solution immersion. Spectra in Figure 1.27-c and d were acquired at a terrace site and from an elongated precipitate particle (Fig. 1.26A), respectively. Both exhibit both a Cr(III)-O

peak at 520 cm^{-1} and an intense Cr(VI)-O peak at 860 cm^{-1}, which is indicative of a mixed oxide. Recall the difference in scattering cross section for the two species. Figure 1.27-e shows the spectrum from an elongated precipitate that is characteristic of a mixed Cr(III)/Cr(VI) oxide. As a control, an uncoated AA2024 sample was immersed in the air-saturated 0.5M NaCl for 3 days, removed and rinsed with tap water for 10 s, and then dried under flow N$_2$ at room temperature. Figure 1.27-f is a spectrum for this sample. No peaks are present, as expected. These results indicate that under full immersion, Cr(VI)-O and mixed Cr(III)/Cr(VI) oxides can form in areas outside of the immediate Cu-rich intermetallic region. The bulk solution allows H$_2$O$_2$, presumably produced locally at the Cu-rich intermetallic sites, to diffuse away from these sites and oxidize Cr(III) in the coating at remote locations.
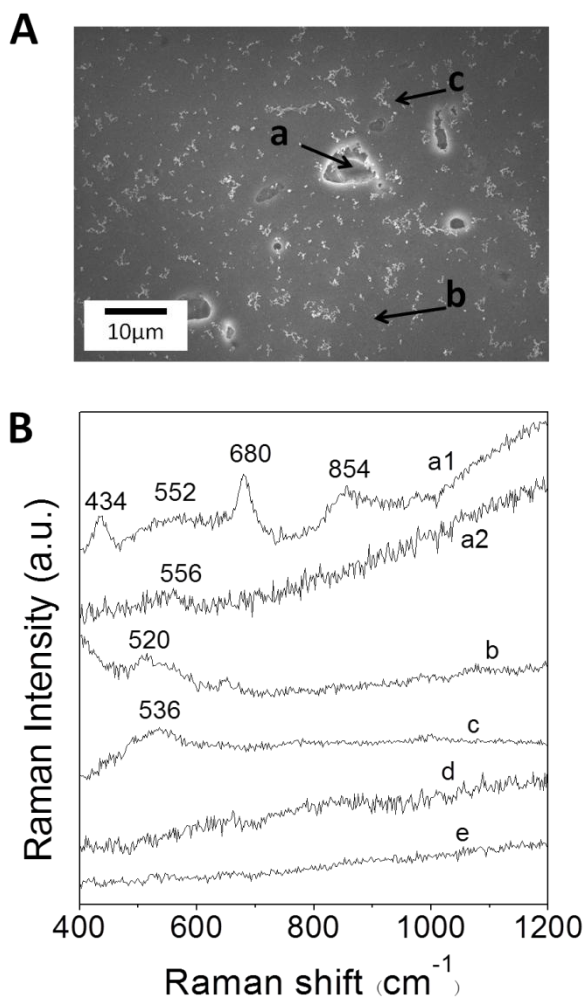
Figure 1.26. (A) SEM micrograph of the surface of a TCP-coated AA2024 sample. Three regions are identified as (a) a large pit (~10 μm diam.), (b) relatively smooth terrace sites with no damage and (c) several elongated precipitates (~1 μm) distributed over the undamaged terrace sites. (B) Raman spectra for (a1) in a pit with a spectrum that is featured with multiple peaks at 434, 552, 680 and 854 cm^{-1}, (a2) in a pit that exhibits only one peak at 556 cm^{-1}, (b) on the terrace devoid of any pits, (c) on the elongated precipitates. The spectra for (d) a non-chrome 5200-coated sample and (e) a bare sample are also shown as control.
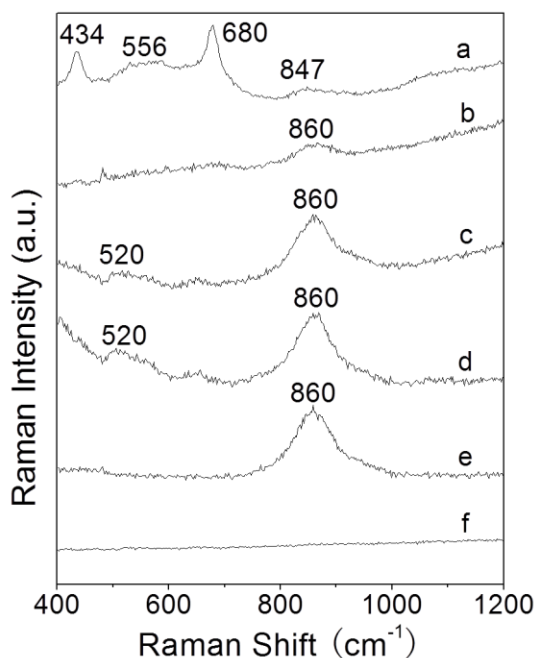
Figure 1.27. Raman spectra for the TCP-coated AA2024 immersed in air-saturated 0.5M NaCl for 3 days. They were acquired (a) in a pit that contains a Cu-rich intermetallic particle, (b) in a pit devoid of Cu and (c) at a terrace site, and (d) on an elongated precipitate. Relevant reference spectra of (e) a Cr(III)/Cr(VI) mixed oxide and (f) a bare sample are shown as control.

Figure 1.28 shows the Cr(VI)-O 860 cm^{-1} peak area for TCP-coated AA2024 as a function of the immersion time in (a) air-saturated 0.5 M Na_2SO_4, (b) the same 0.5 M NaCl and (c) air-saturated 0.5 M NaCl solution that was replaced daily. Prior to recording the spectra, a sample was removed from the immersion solution, rinsed with tap water for 10 s and then aged in air for 30 min. Each datum represents the average and standard deviation of spectral recordings from 5 different locations on a sample. The spectra were recorded at terrace sites near to but outside of pits. Two trends are seen for all the samples: (i) the Cr(VI)-O peak area increases rapidly within the first five days of immersion before reaching a relatively constant level for the remainder period, and (ii) the peak intensity is larger for the sample immersed in 0.5 M NaCl than the sample in 0.5M Na_2SO_4. Additionally, the sample immersed in a 0.5 M NaCl solution that was refreshed with dissolved O_2 daily exhibits the largest Cr(VI) peak area (*i.e.*, greatest coating content) over the immersion period. The stability of the peak area after the first five days suggests that the transiently formed Cr(VI) content in the coating is stable at least under these immersion test conditions.
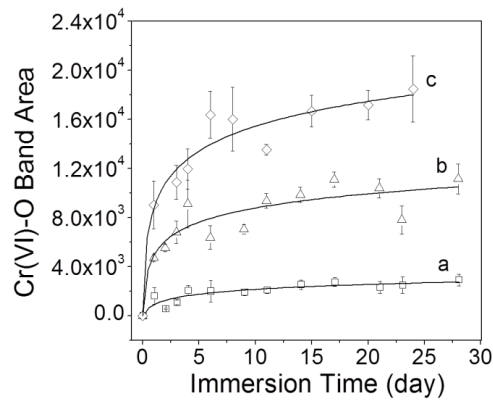
Figure 1.28. Plots of the intensity of the Cr(VI) peak as a function of immersion time in air-saturated (a) 0.5 M Na_2SO_4, (b) 0.5 M NaCl and (c) daily-refreshed 0.5 M NaCl. Spectra were recorded on the terrace near the pits. The trend lines are drawn in solid. Each datum represents the average and standard deviation from a 5-spot quadrant on each sample. The peak areas were determined by integrating the background-corrected spectral intensity between 780-940 cm^{-1}.

5.1.4.15 Corrosion protection linked with the transient formation of Cr(VI). Figure 1.29 shows how the Cr(VI)-O peak area (860 cm^{-1}) in the TCP-coated samples correlates with the pitting of samples immersed in the air-saturated 0.5 M NaCl for 15 days. The sample was immersed in the same solution for the period but it was re-equilibrated with the air daily. Raman spectra were recorded at terrace sites between pits. The pit density for the uncoated samples increased in a near linear fashion with immersion time from $\sim 1 \times 10^5$ to 2.5×10^5 pits/cm^2. The polished and cleaned (degreased and deoxidized) sample has some surface damage and pitting to begin with. The Smut-Go (deoxidizing solution) is rich in F^- and, therefore, is aggressive to the alloy surface. In contrast, the pit density on the coated samples remained relatively constant at $\sim 1 \times 10^5$ pits/cm^2. The Cr(VI)-O peak area (860 cm^{-1}) increased with time but the pit density remained relatively constant. The results suggest there is a correlation between the formation of Cr(VI)-O species and pitting resistance.
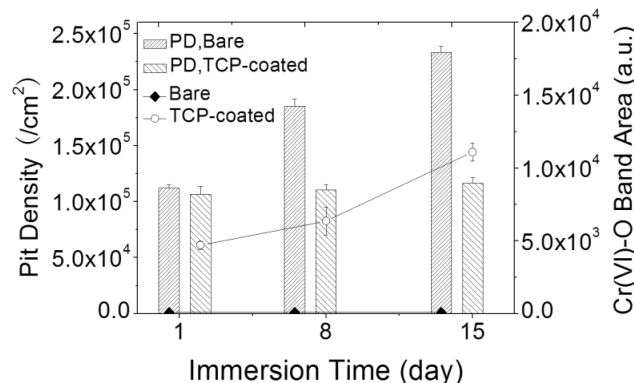
Figure 1.29. Profiles of pit density and band areas of Cr(VI)-O vs. immersion time on the TCP-coated AA2024 samples immersed in the air-saturated 0.5M NaCl for 15 days.

A question to consider though is, does the transiently formed Cr(VI) species actively protect the surface? This was probed by scratch testing a TCP-coated sample. Figure 1.30A shows an optical micrograph of a TCP-coated region of the AA2024 surface adjacent to an uncoated area. The uncoated region was produced by scratch removal of the TCP coating with a sharp blade. As seen in Fig. 1.30B, the spectrum from the scratched area prior to full immersion is featureless with no Cr(III)-O or Cr(VI)-O peaks. The sample was then immersed in air-saturated 0.5M NaCl + 0.01% (v/v) H_2O_2 for 24 h. Due to absence of the coating, the uncoated area corroded during immersion and a resulting circular pit (region b) with a $\sim$ 20 µm diameter is seen (Fig. 1.30A-b). Spectra from the three different spots were recorded and are presented in Fig. 1.30B. In the coated area (region a), a strong 861 cm^{-1} peak is evident and attributed to the formation of Cr(VI) by H_2O_2 (Fig. 1.30B-a). In or near the circular pit (region b), the spectrum features a broad Cr(III)-O peak at 587 cm^{-1} and a Cr(VI)-O peak at 856 cm^{-1} (Fig. 1.30B-b), consistent with the formation of a mixed Cr(III)/Cr(VI) oxide. The origin of the 976 cm^{-1} peak is unknown but the literature shows this mode is present in the Raman spectrum for a CrO_3 reference compound [5-8]. The Cr(III) and Cr(VI) species detected on the scratched surface is consistent with active transport of Cr(VI). Figure 1.30B-c shows the spectrum obtained at a terrace site in the scratched area between the circular pit and the coated area. It shows weak intensity for both Cr(III)- and Cr(VI)-O. In summary, it seems that the Cr(III) in the coating is transiently oxidized to Cr(VI) (*e.g.*, CrO_4^{2-}), possibly by locally produced H_2O_2. The Cr(VI) species has some mobility and can be released into the solution. Solution CrO_4^{2-} species in the nearby solution phase can then react at corroding sites on the aluminum alloy to produce $Cr(OH)_3$ or α-CrOOH that is reflected as a broad peak at 587 cm^{-1} [5-8]. The following reaction is proposed with the $Cr(OH)_3$ serving as a passivation layer:

$$2Al + CrO_4^{2-} + 5H^+ \rightarrow Cr(OH)_3 + H_2O + 2Al^{3+} \tag{3}$$
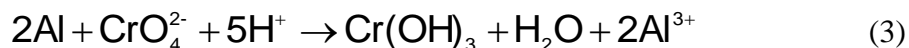
5.1.4.16 Structure and Properties of TCP-Coated AA6061 and 7075. The open circuit potentials (OCP) of AA6061 and 7075 alloy samples were recorded during the formation of the TCP coating, as Figure 1.31 presents. This profile essentially represents the formation potential. The profiles for these two alloys are similar to the profile for AA2024. The potential for both alloys shift cathodically to between -1.2 and -1.3 V vs Ag/AgCl quickly after immersion. Both profiles pass through minimum before stabilizing at a slightly more positive potential. The initial cathodic potential shift results from attack of the metal surface by H^+ and F^- in the TCP bath. These ions dissolve the passivating oxidation layer exposing bare aluminum. Then with the surface unprotected, corrosion of the aluminum occurs along with the reduction of dissolved oxygen and water, with both of the latter two reactions leading to an increase in the interfacial pH. The increase in interfacial pH leads to the precipitation of hydrated zirconia, which stabilizes the potential at a less negative value. The potentials for AA6061 remained at the minimum value for 200 s as compared to 100 s for AA7075. The longer period for AA6061 is probably due to a more homogeneous and thicker passivating oxide layer than exists on AA7075.
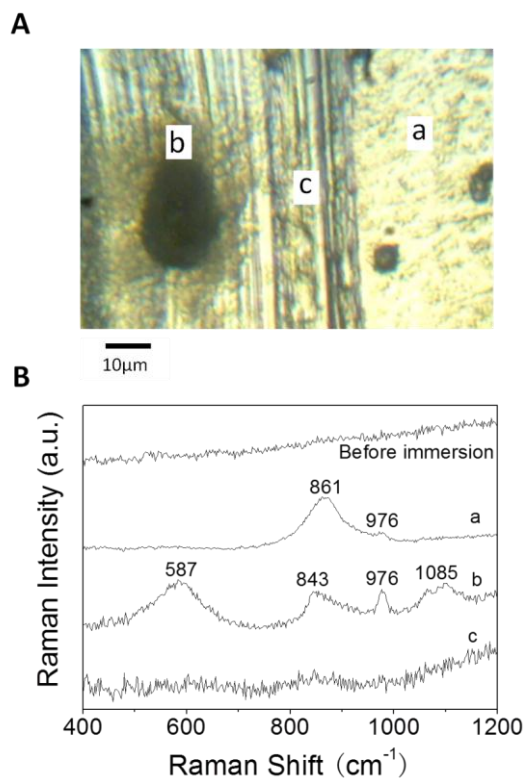
Figure 1.30. (A) Video micrograph of a scratched TCP-coated AA2024 sample after 1-day immersion in 0.5M NaCl + 0.01% (v/v) H_2O_2 solution. Afterwards, the scratched sample was rinsed in tap water for 10 s and dried in air at room temperature for 30 min before spectra recording. (B) Raman spectrum of the scratched sample before immersion and spectra after immersion (a) on the coated area, (b) in or near the pitted area in the scratched area and (c) at the terrace site in the scratched area.
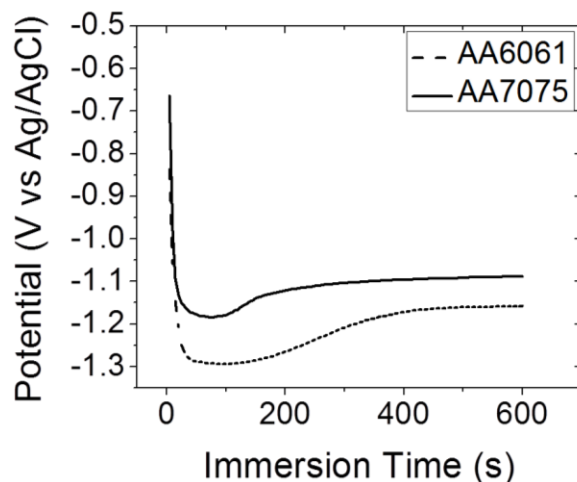
Figure 1.31. Potential vs. time profiles recorded during the formation of the TCP coating on AA6061 and 7075 at room temperature (20-25°C). Full strength (100%) Alodine 5900 RTU solution was used with the sample under full immersion.

47

5.1.4.17 Structure of the TCP coatings. Figure 1.32A and B presents the Auger depth profiles of the elemental composition in the TCP coating on each alloy. For both coated alloys, the characteristic coating elements, *e.g.* Zr, Cr, O, K and F, are seen. As is the case for AA2024, the TCP coating on these two alloys has an apparent biphasic structure. For the first *ca.* 30 nm into the coating, Zr tracks the O signal with an atomic concentration ratio (O/Zr) of about 2:1. This is consistent with the empirical formula of dehydrated zirconia, ZrO_2. Then in the interfacial region between the hydrated zirconia and the alloy surface, the K, Al and F signals increase and constitute the K_xAlF_{3+x} layer. This interfacial region appears to be between 25-75 nm. The overall coating thickness is greater for AA061 than AA7075. The Cr content appears to be uniformly distributed throughout the coating thickness. Since the Cr signal comes from the TCP coating, the decreased Cr signal intensity at ca. 100 nm into the TCP-coated AA6061 can be used as an indication of the coating thickness on AA6061 (*in vacuo*). Similarly, the coating on AA7075 appears to be about 80 nm thick. Additional evidence for the thickness of the coating comes from tracking the Ca signals. The Ca signal results from the tap water rinse of the coating post formation. We suppose that the TCP coatings on AA6061 and 7075, similar to the coating on AA2024, contain hydrated channels that allow Ca^{2+} diffuse through the coating to the metal surface. The overall thickness of the TCP coating also appears to be about 100 nm for AA6061 and 80 nm for AA7075. It should be noted that these measurements were made *in vacuo* and this causes coating shrinkage. The true (hydrated) thicknesses of the TCP coatings on AA6061 and 7075 are expected to be several tens of nanometers larger than the values estimated from these measurements.
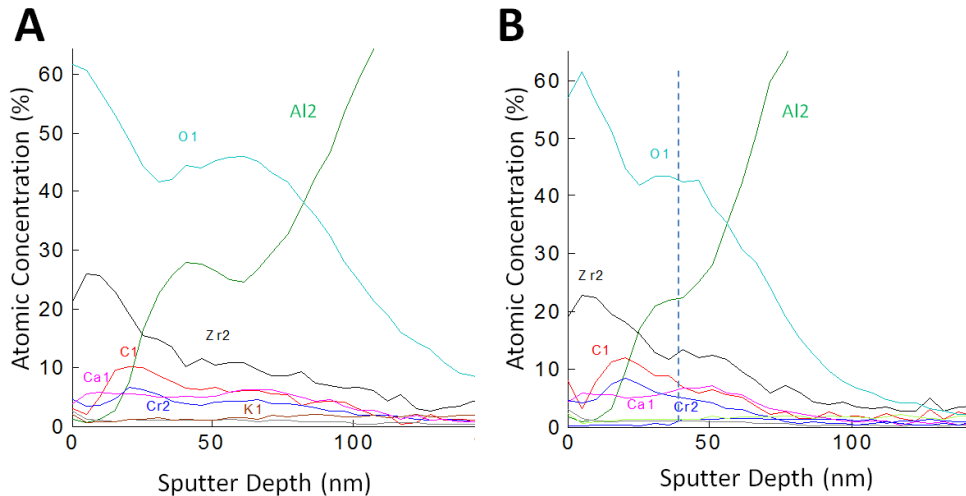
Figure 1.32. Auger depth profiles for the TCP coatings on (A) AA6061 and (B) AA7075.

Figure 1.33 presents an SEM micrograph of a TCP-coated AA6061 sample, along with the energy dispersive X-ray (EDX) line profiles for several elements across an intermetallic compound and the elongated precipitate particles of TCP. The coated surface features some smoothness along with several cracks and elongated precipitate particles. The cracks may result from dehydration in vacuum [1]. The intermetallic compound in AA6061 contains mainly Fe and Si, as evidenced by elevated elemental intensities at *ca.* 3 µm (Fig. 1.33B). This intermetallic compound is about 3 µm in diameter. The signals for the characteristic elements of the TCP coating, *e.g.* Zr, O, Cr and F, are present. Their intensity tracks the Fe and Si intensities suggesting the intermetallic as well as the aluminum is coated during the TCP formation process.

The Zr and O signals arise from the zirconia and the Cr signal comes from Cr(III) oxide. The F signal is attributed to FeF_x or SiF_x that forms from the attack of F^- on the Fe-Si intermetallic during the immersion in the F^--rich TCP bath.

Figure 1.34A presents a SEM micrograph of TCP-coated AA7075 along with the energy dispersive X-ray (EDX) line profiles for several elements across an intermetallic compound and the elongated precipitate particles of TCP. The coating on AA7075 consists of smooth features with fewer of the elongated precipitates. Two types of intermetallic compounds are seen based on their morphologies. One type features a corroded Al matrix adjacent to a Cu-containing intermetallic particle. The EDX line profiling shows the enrichment of Cu in this compound at 10 μm (Fig. 1.34B). The signal intensities for Zr, O and Cr are significantly elevated at this intermetallic site relative to those of the surrounding Al matrix. The other type of compound exhibits a smooth morphology at 28 μm. It is rich in Fe (Fig. 1.34B). The signal intensities for Zr, O and Cr are increased at the Fe-rich site relative to those at the terrace sites but to a smaller extent than at the Cu-rich site. The F signal intensity is elevated on the Fe-rich compound (28 μm) but not on the Cu-rich site (10 μm). This is attributed to Fe being vulnerable to the attack by F^- during the immersion in the TCP baths.
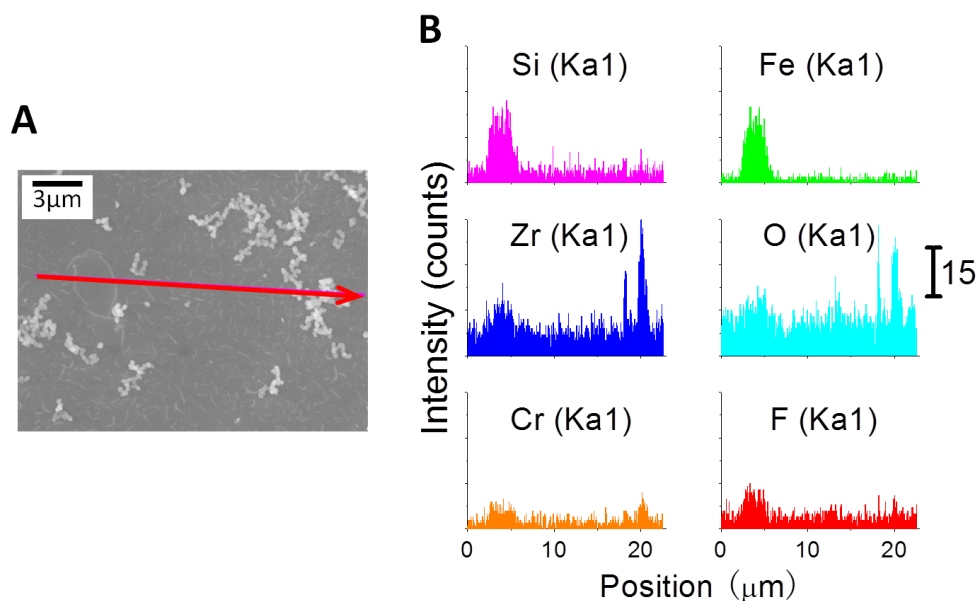
Figure 1.33. An (A) SEM image and (B) elemental line profiles across an Fe and Si-rich intermetallic particle on TCP-coated AA6061. Profiles were recorded after overnight aging in air. White features in the image are elongated precipitates of the TCP coating.
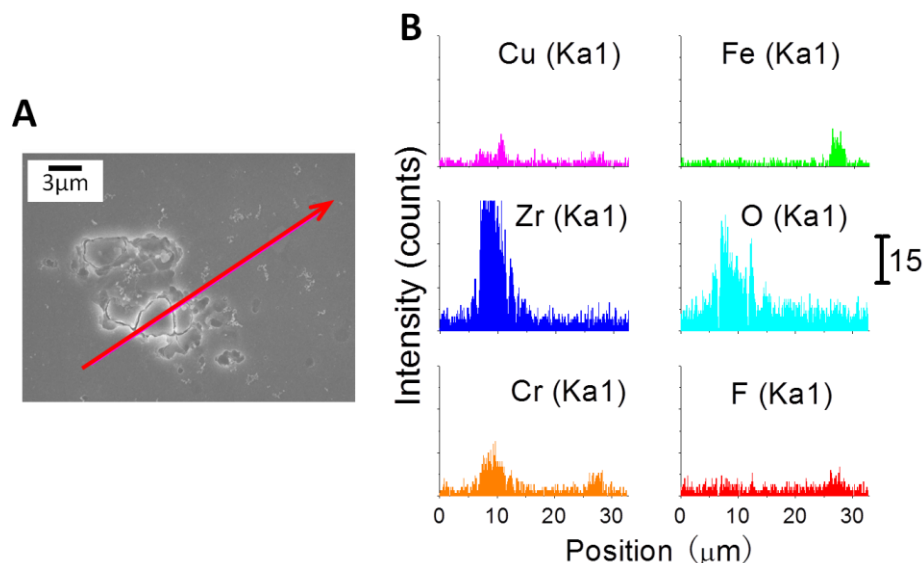
Figure 1.34. (A) SEM images and (B) the elemental line profiling across an intermetallic and pits on the TCP-coated AA7075. Profiles were recorded on a film after overnight aging in air.

5.1.4.18 Basic electrochemical properties of the TCP-coated alloys. The basic electrochemical properties of the TCP-coated AA6061 and 7075 samples were evaluated in air-saturated 0.5 M Na_2SO_4. The bare samples were tested right after deoxidation, while the coated samples were aged overnight before any measurement. Figure 1.35A presents bar graphs for E_{corr} for the bare and TCP-coated alloy samples. The data for AA2024 are from our previous report.[3] The coated AA2024 and 7075 samples have E_{corr} values that are not significantly different from the bare samples (Fig. 1.35A). In contrast, the TCP-coated AA6061 samples exhibit an E_{corr} that is about 500 mV negative of the value for the bare samples. This negative shift of E_{corr} is to balance the reduced cathodic current.

Figure 1.35B presents R_p values measured at E_{corr} for the bare and coated alloys. The TCP coating provides a 100× increase in R_p on AA6061 (2.44×10^6 vs. 2.85×10^4 ohm-cm^2). In contrast, R_p for the coated AA2024 and AA7075 samples is only 10× greater than the bare samples. These results for AA2024 are in agreement with the previous 8-10× increase in R_p after coating. The TCP coating provides good corrosion protection around E_{corr} on all three alloys, with a greater level of protection on AA6061. It should be noted that the coating is not providing a full barrier protection on any of the alloys, since R_p is only 10^6 ohm-cm^2 and not $\geq 10^9$ ohm-cm^2 that would be expected for a full barrier layer. Therefore, the coating likely consists of hydrated channels and defects.
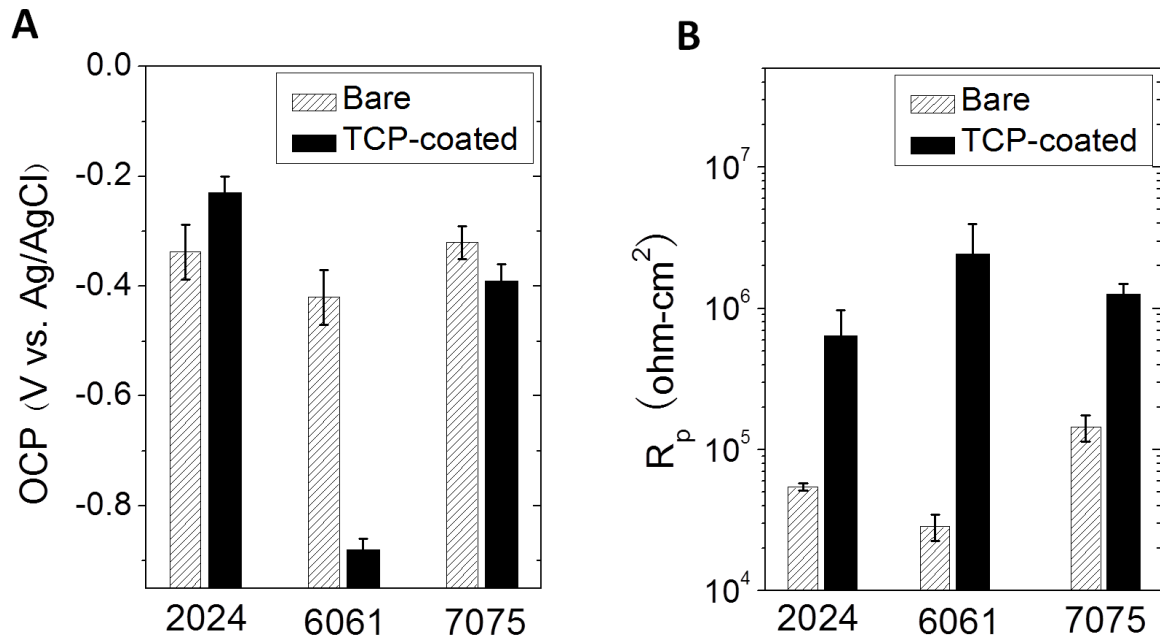
Figure 1.35. (A) Corrosion potentials (E_{corr}) and (B) polarization resistances (R_p) for TCP-coated AA2024, 6061 and 7075 in air-saturated 0.5 M Na_2SO_4. E_{corr} and R_p values were also recorded for the bare alloys (degreased and deoxidized) as controls. Each datum is an average value of no less than 4 samples. Data shown are for the 90% confidence interval.

Figure 1.36A presents slow-scan potentiodynamic polarization curves for bare and TCP-coated AA6061 in air-saturated 0.5 M Na_2SO_4. The presence of the coating causes a 500 mV negative shift of E_{corr}, consistent with the data in Fig. 1.36A. The coating results in significantly attenuated cathodic currents around E_{corr} (-0.9 V vs Ag/AgCl). Moreover, the anodic current was also suppressed by 10x, for example, at +200 mV vs. E_{corr} (-0.7 V for the coated sample and -0.3 V vs Ag/AgCl for the bare sample). Attenuated anodic and cathodic currents are also seen for the TCP-coated AA7075 sample relative to the bare sample (Fig. 1.36B). The anodic current is reduced by about 10x for the coated sample and the Cu-stripping peak at 0.2 V vs. Ag/AgCl is suppressed by nearly 10×. The cathodic current for the coated AA7075 sample is about 100× smaller than the current for the bare sample. The cathodic current in this potential region arises from oxygen reduction and the inhibition by the TCP may result from the blockade of the Fe-rich (AA6061 and 7075) and Cu-rich (AA7075) intermetallic sites. The reduced anodic current may come from passivation of the Al matrix by the TCP coating in the vicinity of the intermetallic compounds.
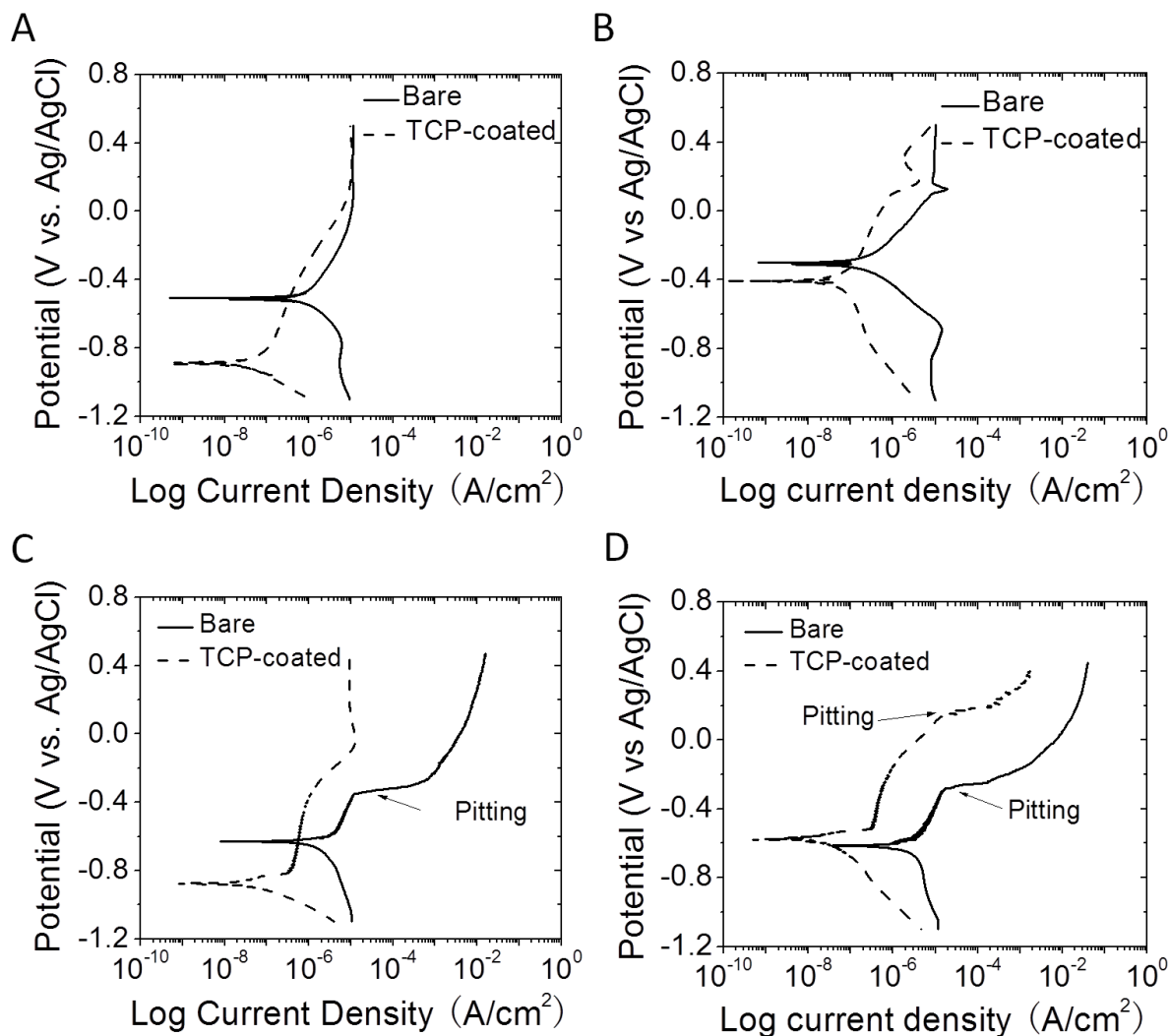
Figure 1.36. Potentiodynamic scans for bare and TCP-coated AA6061 and 7075 recorded in two air-saturated electrolyte solutions: (A) AA6061 and (B) AA7075 in 0.5 M Na_2SO_4, and (C) AA6061 and (D) AA7075 in 0.5 M Na_2SO_4 + 0.05 M NaCl. Scan rate = 2 mV/s.

Polarization curves for the two alloys were also recorded in air-saturated 0.5 M Na_2SO_4 + 0.05 M NaCl, as shown in Figure 1.36C for AA6061 and Figure 1.36D for AA7075. Similar to the Na_2SO_4 solution, the cathodic and anodic currents of the coated alloys are suppressed around E_{corr} by about 10×. In addition, due to the presence of Cl⁻, alloys are vulnerable to pitting at E_{pit}. The bare alloy samples are pitted at *ca.* -0.343 V vs Ag/AgCl for AA6061 and *ca.* -0.269 V vs Ag/AgCl for AA7075. After pitting, the current densities for both bare alloys at these potentials increase dramatically by 3 orders of magnitude. However, the TCP coating inhibits the pitting to some extent. For example, the coated AA7075 exhibits a positively shifted E_{pit} of ca. 0.171 V vs Ag/AgCl. Additionally,, the coated AA6061 is not pitted at all within the potential window from -1.1 to 0.5 V vs Ag/AgCl.

Table 1.1. Corrosion current (i_{corr}) and corrosion rate (m) data for the TCP-coated and bare AA2024, 6061 and 7075 alloys during immersion in air-saturated 0.5 M Na_2SO_4. All data are expected at a 90% confidence level. Each datum is an average measurement for 4 samples.

Alloy		AA2024		AA6061		AA7075	
Treatment		Bare	TCP	Bare	TCP	Bare	TCP
0.5 M Na_2SO_4	E_{corr} (V vs Ag/AgCl)	-0.338±0.050	-0.230±0.030	-0.420±0.050	-0.880±0.020	-0.320±0.030	-0.390±0.030
	R_p (x10^5 ohm-cm^2)	0.542±0.032	6.430±0.329	0.285±0.060	24.436±15.256	1.440±0.307	12.600±2.270
	i_{corr} (µA)	0.113±0.031	0.015±0.005	0.185±0.034	0.007±0.002	0.070±0.014	0.008±0.001
0.5 M Na_2SO_4 + 0.05 M NaCl	E_{corr} (V vs Ag/AgCl)	-0.495±0.007	-0.473±0.012	-0.616±0.007	-0.809±0.031	-0.613±0.006	-0.519±0.027
	E_{pit} (V vs Ag/AgCl)	-0.336±0.052	-0.123±0.046	-0.273±0.111	No pitting	-0.355±0.083	0.074±0.058
	ΔE (V vs Ag/AgCl)	0.159	0.350	0.343	>1.309	0.258	0.593
	R_p (x10^5 ohm-cm^2)	0.291±0.012	3.796±0.433	0.187±0.007	19.964±3.230	0.187±0.0143	13.123±2.043
	i_{corr} (µA)	0.276±0.023	0.014±0.002	0.367±0.012	0.005±0.002	-0.299±0.011	0.006±0.001

Table 1.1 summarizes and compares the basic electrochemical properties of the bare and TCP-coated alloys in air-saturated 0.5 M Na_2SO_4 and 0.5M Na_2SO_4 + 0.05 M NaCl. The more aggressive Cl^-, as compared to SO_4^{2-}, leads to a more severe attack to the uncoated alloys. For example, E_{corr} is more negative in the NaCl-containing electrolyte than that in Na_2SO_4, R_p is at least 2× smaller and i_{corr} is larger by 2×. Moreover, the uncoated alloys undergo pitting at at E_{pit}. In contrast, the TCP-coated alloys are resistant to pitting with a larger difference between E_{corr} and E_{pit} (so called ΔE). The TCP-coated AA2024 exhibits a 200 mV larger ΔE than the bare sample, ΔE for the coated AA7075 is increased by about 300 mV, and the coated AA6061 was not even pitted in the potential window from -1.0 V to 0.5 V vs Ag/AgCl. Similar to results in Na_2SO_4, R_p is increased by about 10× for AA2024 and by about 100× for both AA6061 and 7075 in the NaCl-containing electrolyte. Correspondingly, a smaller i_{corr} is seen for all three coated alloys by 10× for AA2024, and 100× for both AA6061 and 7075. All these results suggest that the TCP coating provides some corrosion protection to all the aluminum alloys in the aggressive NaCl-containing solution, especially for AA6061 that showed the most improved corrosion resistance. Our observation that TCP provides improved corrosion resistance to AA7075, as compared to 2024, is consistent with the conclusion from salt-spray tests by Nickerson et al. [10].

Table 1.2. Best fit parameters from experimental EIS results of the TCP-coated AA2024, 6061 and 7075 in air-saturated 0.5 M Na_2SO_4 at room temperature.

Alloys	R_{el} ($\Omega \cdot cm^2$)	CPE_1 (s^n/Ω-cm^2)	n_1	R_{po} (s^n/Ω-cm^2)	CPE_2 (µF/cm^2)	n_2	R_p ($\Omega \cdot cm^2$)
AA2024	115.9	4.52	0.79	3159	1.89	0.88	1.71x10^6
AA6061	109.0	1.46	0.94	63930	0.02	1	7.36x10^6
AA7075	115.5	2.01	0.85	56745	0.14	1	4.61x10^6

Figure 1.37 presents Bode plots for the three TCP-coated alloys in air-saturated 0.5M Na_2SO_4. In Fig. 1.37A, the TCP-coated AA6061 shows the highest low-frequency impedance (7.36 × 10^6

ohm-cm^2), followed by the coated AA7075 (4.61×10^6 ohm-cm^2). The coated AA2024 has the lowest low-frequency impedance (1.71×10^6 ohm-cm^2). This is consistent with R_p data obtained by polarization curves shown in Fig. 1.35. Fig. 1.37B presents the phase-frequency profiles of the three coated alloys. Two distinct time constants are observed for the coated AA2024 and 7075 but not for AA6061. This might be related to the composition and structure of the coating on and around the intermetallic particles, especially for AA2024 and 7075. The Cu-rich intermetallic particles are more noble than the Fe-rich particles relative to the surrounding Al matrix. The Al surrounding the Cu-rich site is more vulnerable to corrosion than is the Al around the Fe-rich site. The coating on AA2024 is rougher and more defective than is the coating on AA6061. The TCP-coated AA2024 sample presents two distinctive time constants, while the two time constants for the coated AA6061 sample overlap. AA7075 contains both types of intermetallic particles and behaves in between the AA2024 and 6061 samples. The roughnesses of the coated samples are seen from the constant phase element (CPE) exponents, n, in Table 1.2. The coated AA2024 sample has smaller n_1 and n_2 values, which indicate rougher electrolyte/coating and coating/metal interfaces relative to the coated AA6061 and 7075 samples, The CPE magnitude of the coating (CPE$_1$) and the double layer capacitance (CPE$_2$) on the AA2024 sample are larger than those for the other two alloy samples, due to the greater roughness, which leads to a larger specific surface area.
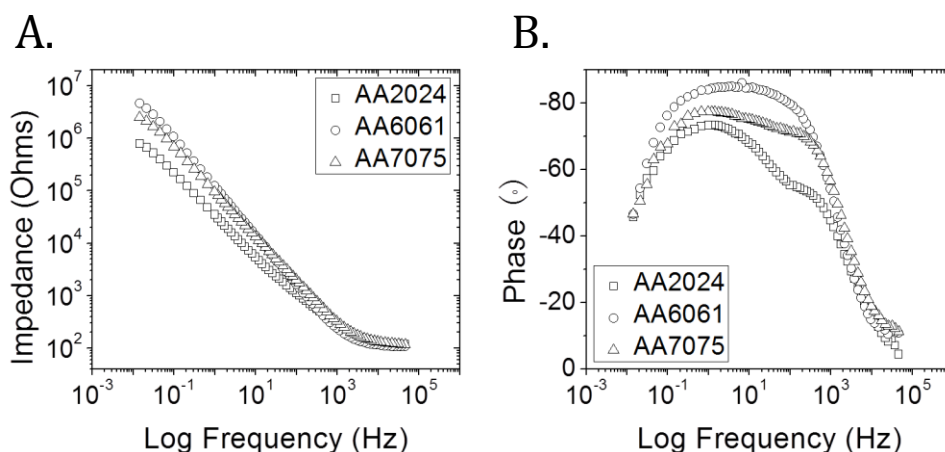
Figure 1.37. Bode plots for the TCP-coated alloys, AA2024, 6061 and 7075 at E$_{corr}$. Measurements were made in air-saturated 0.5M Na$_2$SO$_4$ after the samples were aged in air overnight at room temperature.

5.1.4.19 Electrochemical stability of the TCP-coated alloys. The stability of the TCP coatings on AA6061 and 7075 was assessed by measuring R_p and pit density values over a 14-day immersion in the air-saturated 0.5M Na$_2$SO$_4$. The coated samples were aged overnight before starting an immersion test. Three samples of each alloy type were immersed and removed for characterization at 1, 7 and 14 days. The data are presented in Figure 1.38. The coated AA6061 samples exhibited the largest R_p throughout the immersion period, followed by the coated AA7075 samples and finally the coated AA2024 samples. The R_p values were relatively stable over the 14-day period. Constant pit densities were also seen for all three alloys indicating good TCP coating stability. The pit density of these samples originate during the deoxidation step, which is very aggressive to the alloy surface. Immersion in the mild Na$_2$SO$_4$ introduces no

additional pitting. The TCP coating protects the samples from corrosion. The R_p values are inversely proportional to the pit density, as expected.
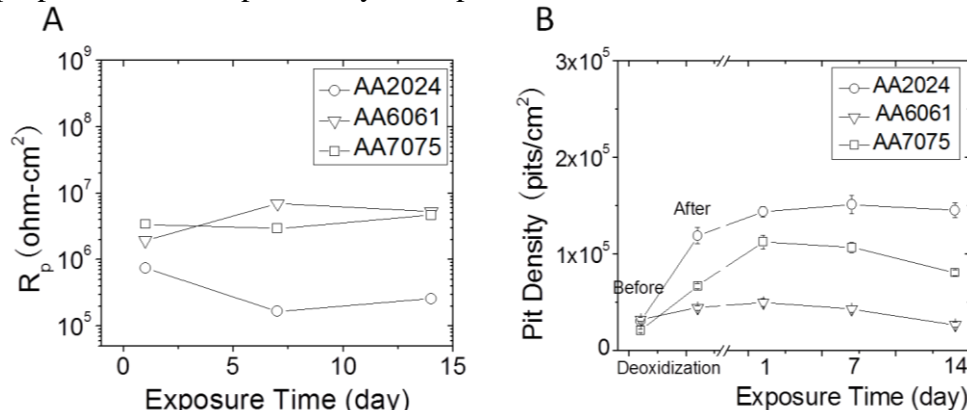
Figure 1.38. (A) Polarization resistance (R_p) and (B) pit density vs. time profiles recorded during the full immersion of TCP-coated AA2024, 6061 and 7075 in air-saturated 0.5M Na_2SO_4 at room temperature.

The TCP-coated and bare alloys were also fully immersed in the more aggressive air-saturated 0.5 M NaCl electrolyte solution for 14 days. The pit density as a function of immersion time is shown in Figure 1.39. The pit density, particularly for the uncoated AA2024 and 6061 progressively increase with immersion time. In contrast, all the coated samples exhibit relatively constant pit density throughout the immersion period. No significant pitting or cracking were observed on the coated samples.

5.1.4.20 Transient formation of Cr(VI) during immersion. Previously, we demonstrated that Cr(III) can transiently form on TCP-coated AA2024 during immersion. The same holds true for TCP-coated AA6061 and 7075. Three samples of each alloy were immersed in the air-saturated 0.5M NaCl for 30 days. Spectra were collected at five spots on each sample. Figure 1.40 presents typical spectra acquired at the intermetallic sites and on the terrace outside pits of coated AA6061 and 7075 after a 15-day immersion. The spectra acquired near an intermetallic and on the terrace away from any intermetallic on AA6061 exhibits a symmetric 860 cm^{-1} peak (Fig. 1.40-a, b), which indicates the presence of the Cr(III)/Cr(VI) mixed oxide (Fig. 1.40-e). The same applies for the spectrum acquired at a terrace site on AA7075 (Fig. 1.40-d). In contrast, a spectrum acquired at the intermetallic site on AA7075 contains an asymmetric peak centered at 850 cm^{-1} (Fig. 1.40-c). The 437 and 678 cm^{-1} peaks that are attributed to Cu-O bonds associated with the Cu-rich intermetallic compound. The variation of the Cr(VI)-O peak position is due to the interaction of the Cr(VI)-O species with Al oxides.[1] The 850 cm^{-1} Cr(VI) peak in Fig. 1.40-c is identified as the Al(III)/Cr(VI) mixed oxide at pH 7.40 (Fig. 1.40-f).
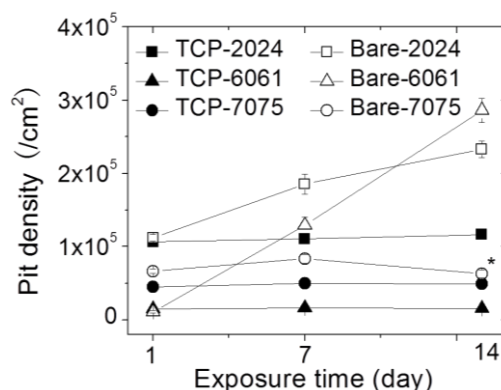
Figure 1.39. Pit density vs. time profiles recorded during the full immersion of TCP-coated and bare AA2024, 6061 and 7075 in air-saturated 0.5M NaCl at room temperature.
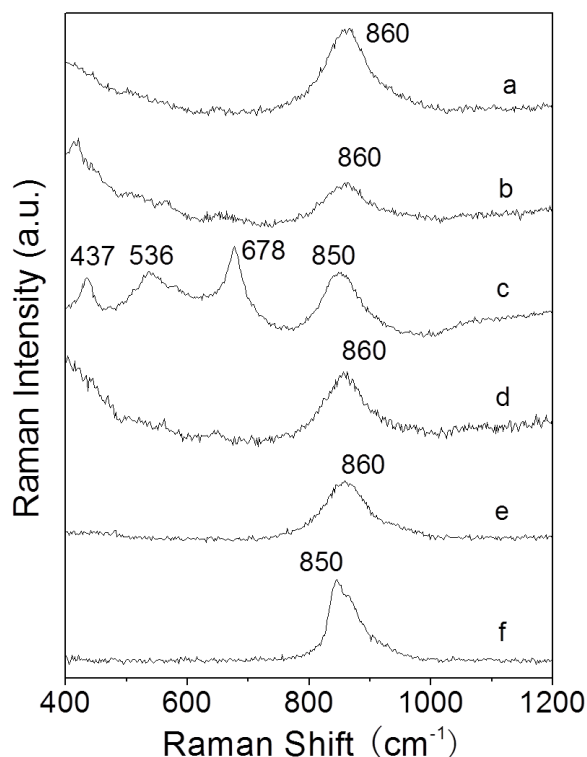
Figure 1.40. Raman spectra recorded at (a) an Fe-rich intermetallic site and (b) the terrace near but outside the pit on the TCP-coated AA6061, (c) a Cu-rich intermetallic site and (d) the terrace outside the pit on the coated AA7075, after full immersion in air-saturated 0.5M NaCl for 15 days. Spectra for (e) the Cr(III)/Cr(VI) mixed oxide and (f) the Al(III)/Cr(VI) mixed oxide (pH 7.40) are also shown for identification

Figure 1.41 presents the 860 cm^{-1} peak areas as a function of immersion time. Each datum represents the average of spectral recordings from 5 different locations on each sample. The Cr(VI)-O peak area increases rapidly within the first 5 days of immersion before reaching a relatively constant level for the remainder period. The coated AA7075 sample exhibits larger Cr(VI)-O peak areas than AA6061 during the immersion period. The stability of the peak area after the first five days indicates chemical stability of the transiently formed Cr(VI) species on the surface.
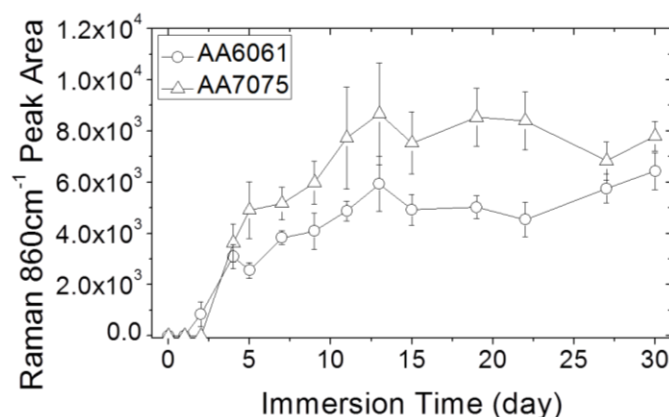
Figure 1.41. Cr(VI) peak intensity vs. time for the three TCP-coated alloys that were immersed in the air-saturated 0.5M NaCl for about 30 days. Spectra were recorded on the terrace near the pits.

5.1.5 Discussion

The research addressed several key questions: what is the formation mechanism, composition and structure of the TCP immersion coating on AA2024; how does the TCP coating inhibit the anodic and or cathodic kinetics of reactions occurring on the Al matrix and the Cu-rich intermetallics; what level of short-term stability does the coating exhibit and is any benefit gained by aging; and is there any evidence for transient formation of Cr(VI) in the coating?

5.1.5.1 Formation mechanism, composition and structure of TCP immersion coating on AA2024. The formation of TCP immersion coatings occurs by multiple chemical steps, but appears driven by an increase in the interfacial pH. The initial chemical step involves dissolution of the native oxide layer, as evidenced by the negative shift in the OCP (Fig. 1.2). This is in agreement with recent observations made by Dong et al. [2], and Dardona and Jaworowski [1.] The oxygen reduction reaction, and possibly hydrogen discharge, that accompanies the oxidation and dissolution of the Al alloy consumes protons and causes an interfacial pH increase. Oxygen reduction is also a counterbalancing cathodic reaction that occurs at the Cu-rich intermetallics and likely contributes to the interfacial pH increase.

X-ray analysis data revealed that TCP coating consists of Zr and O, consistent with the formation of zirconia, and that the coating is present over most regions of the alloy surface. X-ray data were also consistent with a biphasic coating consisting of an outer $ZrO_2 \cdot 2H_2O$ layer and an interfacial K_xAlF_{3+x}-rich layer (fluoroaluminate). This is based on the elevated levels of Al, F and K detected (Fig. 1.5). The apparent thickness of the coating is on the order of 50 nm. We refer to this as an apparent thickness because the TEM and x-ray data used to estimate the thickness were all taken *in vacuo*. Coating shrinkage is expected so the true thickness is on the order of 100 nm [1]. Once the oxide layer is dissolved, the exposed aluminum undergoes oxidation in the fluoride-rich coating solution (pH 3.3) forming AlF_6^{-3} ions. The fluoride at the metal surface originates from the hydrolysis of hexafluorozirconate and the HBF_4 in the coating solution. Al^{3+} formation is promoted by the presence of F^-. We suppose that this leads to the formation of a fluoroaluminate interfacial layer.

Cr is incorporated but its distribution does not appear uniform throughout the coating. Cr levels are elevated in and around pits based on X-ray analysis (Fig. 1.7, 1.33 and 1.34) and Raman spectroscopic studies (Fig. 1.26). A steeper pH gradient likely exists near these sites during the coating formation and this may be a driver for the formation of Cr(III) oxide. The $Cr(OH)_3$, CrOOH and or Cr_2O_3 appear to co-precipitate along with the hydrated ZrO_2. It should be noted that we have not yet confirmed by a pH measurement during the coating process that an interfacial pH increase.

Line profiling X-ray analysis revealed the coating forms on most areas of the aluminum alloy but not over all the Cu-rich intermetallics. Furthermore, the immersion coating does not form an impermeable barrier on the alloy surface. This conclusion is based on the fact that the polarization resistance is 10^5-10^6 ohm-cm^2 in air-saturated 0.5 M Na_2SO_4 rather than $>10^6$ ohm-cm^2, as expected for more impermeable barrier coatings on aluminum alloys (Fig. 1.12). We suppose the biphasic coating is hydrated and contains channels and pathways through which dissolved O_2 and ions can diffuse to reach the underlying metal surface. This leads to localized corrosion on the coated surface.

5.1.5.2 Inhibition of the anodic and or cathodic kinetics of reactions occurring on the Al matrix and the Cu-rich intermetallics by TCP coating. TCP provides some anodic protection by coating the Al–rich sites and inhibiting the metal oxidation reaction. This appears to occur mainly by physical blockade of these "active" sites from contact with the electrolyte solution. Anodic protection is evidenced by the slightly more noble OCPs generally recorded for the TCP-coated alloys in 0.5 M Na_2SO_4 (air-saturated), as compared to the uncoated alloys. The potentiodynamic polarization scans revealed suppression of the anodic current around the OCP, consistent with some anodic protection. The coating also provides some cathodic protection by blocking or partially blocking sites on the Cu-rich intermetallics (Fig. 1.7). The potentiodynamic polarization scans also revealed suppression of the cathodic current near the OCP. The fact that polarization resistance of TCP-coated AA2024 is about 10× larger than that the value for uncoated alloy is also indicative of some level of corrosion protection. More experiments are needed to determine if Cr(III)/Cr(VI) in the coating provides any active corrosion protection. However, suggestive of some active protection is the fact that the polarization resistance of the Cr(III)-containing TCP coating is 2-4× greater than for the non-Cr(III) Alodine 5200 hexafluorozirconate coating.

5.1.5.3 Short-term structural and chemical stability of the coating exhibit and effects of aging. At least in the short-term (multiple hours) of continuous immersion, the TCP coating is structurally and chemically stable during exposure to mild (air saturated 0.5 M Na_2SO_4) or aggressive (air saturated 0.5 M NaCl) electrolyte solutions at room temperature or 50 $^{\circ}$C. The unchanging OCP and total-impedance frequency data (Fig. 1.14) reveal that at least over a 4-h period, no major structural or chemical changes developed in the coating. Some interesting aging effects have also been seen. We hypothesized that if the coating is slowly dehydrated then channels and imperfections that exist might collapse, thus improving the coating's barrier properties. Preliminary impedance analysis revealed that the barrier properties can be significantly improved as the low frequency polarization resistance increased to 10^9 ohm-cm^2 (see Fig. 1.15). Unfortunately, these improvements have only been seen in approximately 30% of the coated samples. It is unclear at this point why the aging effects are not more reproducible.

Work is ongoing to understand how to reproducibly control the barrier properties of the TCP coatings through post-formation aging.

5.1.5.4 Evidence for transient formation of Cr(VI) in the coating. Perhaps the most controversial finding of the work is the observation by Raman spectroscopy that some Cr(VI)-oxide species, 850-880 cm^{-1}, form transiently in the coating. No Cr(VI) species were detected immediately after coating formation or in the TCP solution. However, the mixed Cr(VI) oxide band was observed in some coatings after as little as 1 h of air drying and in all coatings after immersion in air-saturated Na_2SO_4 or NaCl. In many cases, Cr(III) oxide scattering at 550 cm^{-1} is detected along with the Cr(VI) oxide scattering between 850-880 cm^{-1}. This is consistent with a mixed oxide composition [5-8]. However, we have coated samples for which only the Cr(VI) oxide peak is detected at 850 cm^{-1}. It is unclear at this point if the Cr(VI) species is mobile and provides any active corrosion protection [5-8]. The question is, by what mechanism does the Cr(VI) species form? One possibility is that at some of the Cu-rich intermetallic sites, dissolved oxygen is reduced via a 2e$^-$/2H$^+$ pathway to H_2O_2. Colley et al. have shown that the apparent number of electrodes involved in the oxygen reduction reaction on Cu decreases from 4 toward 2 as the rate of mass transport increases [11]. Based on this work, there would appear to be conditions under which H_2O_2 (2e$^-$) rather than H_2O (4e$^-$) would be produced and available to oxidize nearby Cr(III) to Cr(VI). Indeed, we have found that H_2O_2 added to Cr(III) solutions can oxidize the metal ion to Cr(VI). Additionally, we have found that the Raman peak (850-890 cm^{-1}) intensity for the Cr(VI) oxide species in TCP coating increases proportionally with the H_2O_2 concentration in 0.5 M Na_2SO_4 during hour-long and multiple day immersion tests.

The Cr(VI) formation occurs when the coated alloy is immersed in air-saturated electrolyte solutions or even after exposure to humid air (aging). Evidence was found that supports a two-step process. Oxygen diffuses within hydrated pockets of water to the Cu-rich intermetallic sites where it may be reduced to H_2O_2. The H_2O_2, a strong oxidant, then diffuses to nearby sites to oxidize native Cr(III) in the coating to Cr(VI). In samples aged in the laboratory air, the Cr(VI) formation is localized to intermetallic areas where the H_2O_2 is formed. When fully immersed, the locally produced H_2O_2 can diffuse to sites more remote from the pits and oxidize the Cr(III). The Cr(VI) exists mainly in the form of chromate (CrO_4^{2-}) and appears to exist as a mixed Cr(III)/Cr(VI) oxide or Cr(VI)/Al oxide. The covalent, polymeric Cr(III)/Cr(VI) mixed oxide accounts for the chemical stability of the TCP coating. Preliminary data suggest that the CrO_4^{2-} is mobile and diffuses to corroding sites where it gets reduced to form a passivating mixed oxide of Cr(OH)$_3$. It appears that the protection mechanism is similar to that of the chromate conversion coatings.

5.1.5.5 Structure and inhibitory properties of the TCP coating on AA6061 and 7075 alloys. The trivalent chrome process (TCP) coatings were formed on both AA6061 and 7075 through immersion in the TCP bath for 10 min and aged in air at room temperature overnight. The TCP coating on AA6061 in vacuum is about 100 nm thick that is more than both on AA2024 (*ca.* 50 nm) and 7075 (*ca.* 50 nm). The formation of the TCP coatings on AA6061 and 7075 is similar to AA2024: the formation of hydrated zirconia layer (ZrO$_2$·2H$_2$O) is driven by an increase in the interfacial pH caused by the dissolution of Al oxide layer and localized oxygen reduction reaction at the intermetallic sites. The coating exhibits a biphasic structure that contains a hydrated zirconia overlayer and potassium fluoroaluminate interfacial layer. The TCP coating provides both anodic and cathodic protection to AA6061 and 7075 by physically blocking Al

matrix and intermetallic sites, but better on AA6061 samples. This is evidenced by a larger increased extent of the polarization resistance from the bare to the coated AA6061 (*ca.* 100×) than the coated AA7075 samples (*ca.* 10×). The more suppressed anodic and cathodic currents are seen on the coated AA6061 than AA7075 around the OCP's in the potentiodynamic scans. In the 14-day immersion in mild electrolyte the structure and chemical composition of the coating are stable as evidenced by unchanging electrochemical and structural properties.

5.1.6. Conclusions

Trichrome process coatings were formed on AA2024, 6061 and 7075 alloys that were first degreased and deoxidized. The TCP coating on all three alloys is approximately 50-100 nm thick and coats most of the alloy surface. The formation of the hydrated zirconia ($ZrO_2 \bullet 2H_2O$) coating is driven by an increase in the interfacial pH caused by (i) dissolution of the oxide layer and (ii) localized oxygen reduction at Cu-rich intermetallic sites. The coating composition is biphasic consisting of a hydrated zirconia overlayer and a K- and F-rich fluoroaluminate interfacial layer (K_xAlF_{3+x}). At least initially, $Cr(OH)_3$ is coprecipitated with the hydrated zirconia. The Cr-rich regions of the coating are in and around pits. The TCP coating provides both anodic and cathodic protection by physically blocking Al-rich sites (oxidation) and Cu-rich intermetallics (reduction). This is evidenced by the 10x greater polarization resistance for the TCP-coated alloys and the suppressed anodic and cathodic currents around the OCP in the potentiodynamic scans. At least in the short-term (4-h in mild and aggressive electrolytes) the structure and chemical composition of the coating are stable as evidenced by unchanging electrochemical properties. Preliminary, evidence indicates that ageing (3-7 day air dry) can have some beneficial effects by increasing the barrier properties of the coating. Finally, Raman spectroscopy revealed evidence for transient formation of Cr(VI) species in the coating after some period of drying and or electrolyte solution exposure. We suppose that Cr(VI) forms due to the oxidation of Cr(III) oxide by locally produced H_2O_2. The H_2O_2 is a product of oxygen reduction at the Cu-rich IMCs.

5.1.7 References

1.   S. Dardona and M. Jaworowski, *Appl. Phys. Lett.* **97**, 181908 (2010).

2.   X. Dong, P. Wang, S. Argekar and D. W. Schaefer, *Langmuir* **26** (13), 10833 (2010).

3.   L. Li, G. P. Swain, A. Howell, D. Woodbury, and G. M. Swain, *J. Electrochem. Soc.*, **158**, C274-C283 (2011).

4.   W. J. Clark and R. L. McCreery, *J. Electrochem. Soc.* **149** (9), B379 (2002).

5.   J. Zhao, L. Xia, A. Sehgal, D. Lu, R. L. McCreery and G. S. Frankel, *Surf. Coat. Technol.* **140**, 51 (2001).

6.   L. Xia, E. Akiyama, G. Frankel and R. McCreery, *J. Electrochem. Soc.* **147** (7), 2556 (2000).

7.   J. D. Ramsey and R. L. McCreery, *J. Electrochem. Soc.* **146** (11), 4076 (1999).

8.   J. Zhao, G. Frankel and R. L. McCreery, *J. Electrochem. Soc.* **145** (7), 2258 (1998).

9.   L. Li, D-Y. Kim and G. M. Swain, *J. Electrochem. Soc.* **159** (7), C1 (2012).

10.   A. Iyer, W. Willis, S. Frueh, W. Nickerson, A. Fowler, J. Barnes, L. Hagos, J. Escarsega, J. La Scala and S. L. Suib, *Plating and Surface Finishing*, **5** (May), 32 (2010).

11.   A. L. Colley, J. V. Macpherson, and P. R. Unwin, *Electrochem. Commun.*, **10**, 1334 (2008).

5.2 Task 2: Mechanisms of selected inhibitors

5.2.1 Objective

The objective of this study was to fundamentally understand the inhibition mechanism of selected soluble non-chromate inhibitors, thereby developing the kind of understanding that was accomplished for cerium and vanadate inhibitors. Inhibitors found to be present in commercial pigments by our team members at UTRC (see Task 5) were selected as candidate inhibitors. These included molybdate, silicate, and praseodymium. All of the work was performed on Al alloy 2024-T3.

5.2.2 Background

Since most inhibiting conversion coatings and pigments act by releasing soluble species into local aqueous environments, it is of interest to understand the fundamental mechanism of inhibition provided by various species dissolved in aqueous solution. Over the past 10 years, scientific studies on the mechanism of chromate inhibition has led to a new understanding and resulted in the development of new techniques and approaches to study corrosion inhibition. Other non-chromate inhibitors have been studied in detail including cerium and vanadates, but fundamental understanding of the functionality of chromate-free inhibition is still lacking. The objective of this study was to fundamentally understand the inhibition provided by selected soluble non-chromate inhibitors, with the goal of developing the kind of understanding that was accomplished for cerium and vanadates.

5.2.3 Materials and Methods

Samples of solution heat treated, naturally aged AA2024-T3 (3.9-4.9% Cu, 1.2-1.8% Mg, 0.3-0.9% Mn, 0.5% Fe, 0.5% Si) were mechanically polished up to 1200 grit SiC in nonaqueous slurry to minimize the onset of corrosion. Samples analyzed by AFM and SEM were polished up to 1 μm diamond paste. All samples were cleaned with ethyl-alcohol in an ultrasonic bath, air dried, and stored overnight in a desiccator. Sample size for *in situ* AFM scratching were restricted to 1x1x0.3 cm by the sample-holder head; otherwise sample dimensions of 2.5x2.5x0.3 cm were employed.

All chemicals were of reagent-grade. Solutions were prepared using 18.2 Ω cm^2 deionized water containing 0.1 M NaCl. Solution pH was adjusted with diluted solutions of concentrated H_2SO_4 and NaOH. Solution pH was measured with a standard pH meter before and after each experiment.

A flat-cell setup was utilized to conduct electrochemical experiments using a Pt mesh counter electrode and a saturated calomel reference electrode (SCE). Polarization curve scans were run at a rate of 0.167 mV/sec starting at OCP. Stabilization of OCP was reached prior to the start of each experiment and tests were replicated at least three times. EIS was conducted at frequencies ranging from 10 mHz to 0.1 MHz, at 10 mV applied AC voltage. Aerated chronoamperometry experiments have been performed to study the effects of inhibitor injection into solution by measuring the time evolution of the cathodic current at fixed applied potentials. Furthermore, OCP exposure experiments were performed on AA2024-T3 coupons immersed in aerated 0.1 M NaCl solutions with and without inhibitor. After 48 hours, the samples were removed and

carefully rinsed with DI water, air dried and stored overnight in a desiccator before been viewed under the SEM. Furthermore, XPS spectra were acquired using a Kratos Ultra with a monochromated Al X-ray source at 130 W.

In situ AFM scratching experiments were performed with a *Veeco* Multimode AFM coupled with a Nanoscope IIIa controller. Naturally aerated electrolyte (10 ml) was introduced into a special glass cell at a rate of 10 ml/h using a peristaltic pump. Scratching was performed in contact mode with a Si cantilever tip. In contact mode, the tip deflection is kept constant at a force that is set by a user-controlled parameter, the set-point voltage (SP). The SP is representative of the photodiode potential and ranged between -0.5 to 10 V, correlating to about 100 and 500 nN [1]. The interactional force between the tip and the surface is proportional to the SP; increasing the SP from low to high potential increases the force applied on the surface by the tip. Tips were replaced after each experiment due to wear from hydrogen gas evolution and other corrosion products that form during scratching. Furthermore, scan rates were held constant at 2 Hz, translating to a capture time of 4 to 5 minutes per scan. Prior to each experiment, scanning Kelvin probe force microscopy (SKPFM) was conducted in air, allowing for the simultaneous measurement of the surface topography and Volta-potential distribution.

5.2.4 Results

5.2.4.1 Molybdate

Figure 2.1 shows naturally aerated polarization curves in 0.1 M NaCl solution with varying sodium molybdate concentrations. A two order of magnitude decrease in anodic kinetics and a 250 mV increase in the pitting potential were found at an optimum molybdate concentration of 125 mM. The solution pH at this concentration was 8.1. Electrochemical impedance testing (Figure 2.2) was conducted over a period of 2 months on samples exposed in chloride solution with and without 125 mM molybdate concentration. The polarization resistance (Figure 2.2a) in solution containing molybdate was an order of magnitude higher than the control but gradually decreased with time. In contrast, the polarization resistance of the control remained unchanged with time. Figure 2.2b shows a gradual increase in the capacitance of samples exposed to 0.1M NaCl with and without 125 mM molybdate, from 14.1 to 112 $\mu F/cm^2$, and 80.7 to 231 $\mu F/cm^2$, respectively. The lower capacitance and higher polarization resistance for the sample in the solution containing molybdate indicates a more protective surface film.

SEM/EDS analysis of a sample exposed to 0.1 M NaCl solution containing 125 mM molybdate showed attack in the form of trenching around the intermetallic particles (Figure 2.3). However, EDS showed Mg and Al were still present in the S-phase particles. Furthermore, SEM micrographs reveal the presence of a film over both S-phase and FeMn(Si) intermetallic particles that is rich in Mo, Na, and Cl.

XPS was performed on a sample exposed to 0.1 M NaCl solution with 125 mM molybdate at OCP to detect the presence of molybdate on the surface and its oxidation state. After exposure to molybdate containing solution for 5 hours XPS revealed a significant presence of molybdate on the surface. Fitting was performed by constraining the two spin-orbit-split components with an energy separation of 3.2 eV [2]. The spectrum reveals three peaks at 231.2 eV, 232.3 eV, and 232.8 eV, identified as $MoCl_5$, $Al_2(MoO_4)_3$, and MoO_3, with relative concentrations of about 10,

20, and 70%, respectively (Figure 2.4). The results show that Mo is present on the surface predominantly in Mo^{+6} state with some reduced species in the Mo^{5+} state.
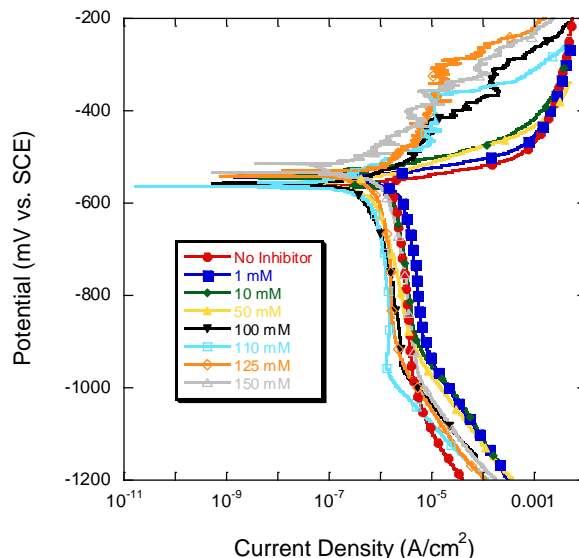
Figure 2.1. Naturally aerated polarization curves for AA2024-T3 in 0.1 M NaCl solution at varying Na_2MoO_4 concentrations.

(a)   (b)
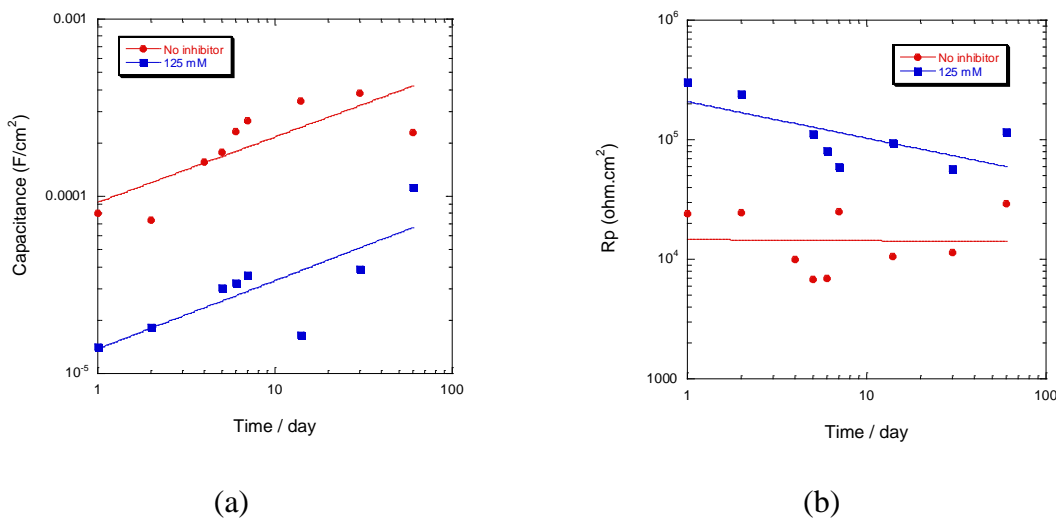
Figure 2.2. Evolution of (a) polarization resistance and (b) capacitance with time for AA2024-T3 in chloride solution with and without 125 mM Na_2MoO_4.

Figure 2.5 shows cathodic chronoamperometric measurements at -900 mV SCE in 0.1 M NaCl before and after injection of 0.1M NaCl solution or concentrated molybdate solution to make 125 mM total molybdate after mixing. The control experiment, injection of aerated 0.1 M NaCl, produced no increase in cathodic current as expected. Injection of concentrated molybdate solution resulted in a cathodic current peak that reached -130 µA/cm^2 followed by a rapid

decrease to a net anodic current in just a few seconds. Afterwards, the current gradually decreased to a steady state value of +830 nA/cm^2, which indicates cathodic inhibition. The polarization curves in Figure 2.1 do not predict that the current should go positive with injection of 125 mM molybdate. XPS analysis of the sample surface revealed two Mo peaks at 231.3 eV and 232.5 eV, identified as MoCl$_5$, and MoO$_3$, respectively (Figure 2.6). Other implications of these results are discussed below.
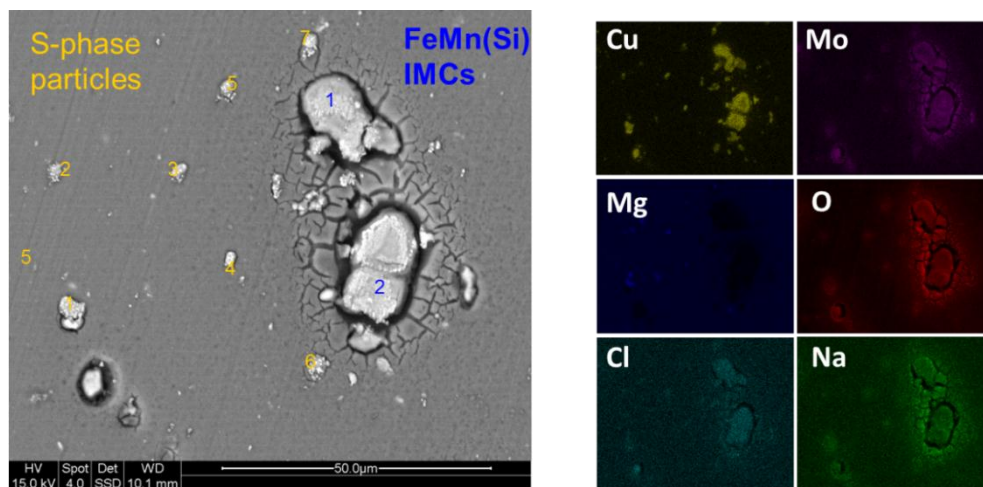
Figure 2.3. SEM/EDS after 2-day exposure in 0.1 M NaCl solution containing 125 mM MoO$_4^{-2}$.
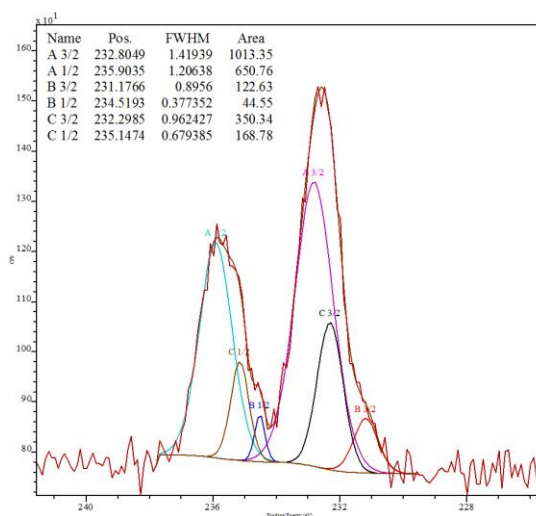
Figure 2.4. The Mo 3d spectra for a sample exposed to 0.1 M NaCl solution containing 125 mM Na$_2$MoO$_4$.

Experiments also were performed in deaerated electrolytes to analyze the effect of oxygen on the inhibition mechanisms and performance. Figure 2.7 compared the effect of oxygen in solution with and without 125 mM MoO$_4^{-2}$. In deaerated inhibitor-free solution, AA2024-T3 exhibits two

breakdown potentials [3,4]. E_{b1} is associated with the transient dissolution of the S-phase particles, while E_{b2} is associated with intergranular corrosion. A number of differences are observed in deaerated solution containing molybdate. Molybdate still imparts strong anodic inhibition, raising the breakdown potential by 250 mV at 125 mM concentration. However, the passive current density and the cathodic current density are both higher in deaerated solution containing molybdate. The passive current density is about 10x lower in deaerated solution containing molybdate compared to the same aerated solution.
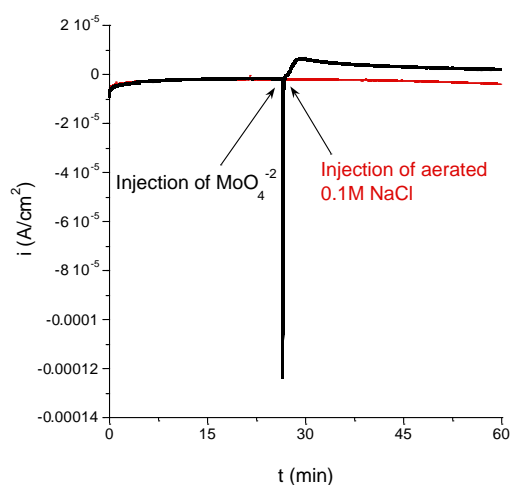
Figure 2.5. Chronoamperometry in aerated 0.1 M NaCl at E_{app} = -900 mV SCE.
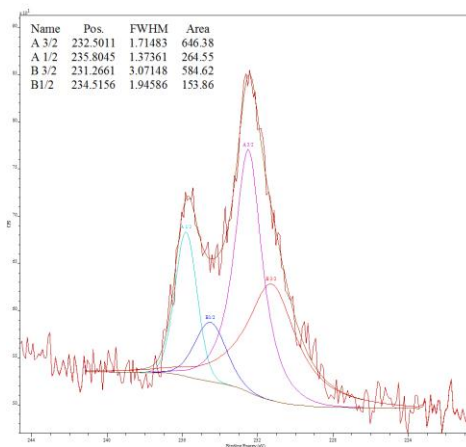
Figure 2.6. Mo 3d spectra after MoO_4^{2-} injection at fixed potential of -900 mV SCE.

Figure 2.8 shows the effect of molybdate in solution at pH 5. In the absence of oxygen, the addition of molybdate increases the cathodic limiting current density relative to the molybdate free solution indicating non self-inhibiting reduction. The poor inhibition provided by molybdate at low pH is attributed to a polymerization of the species in acidic media as discussed below.

66
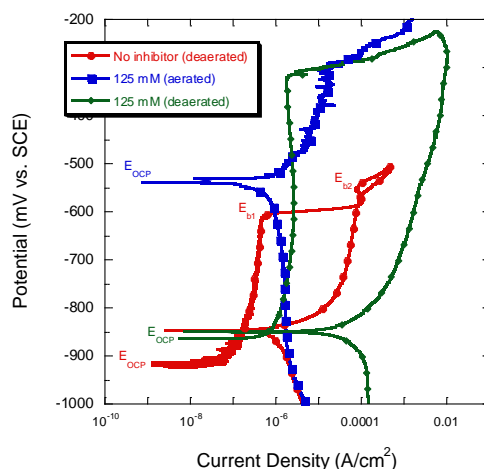
Figure 2.7. Polarization curves showing the effect of oxygen on inhibition performance.
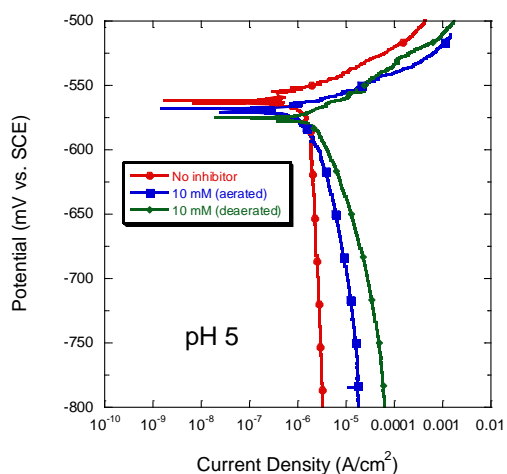
Figure 2.8. Polarization curves in 0.1 M NaCl solution with and without Na_2MoO_4 at pH 5.

5.2.4.2 Silicate

Figure 2.9a shows naturally aerated polarization curves in 0.1 M NaCl solution with varying sodium silicate concentrations. Higher silicate concentrations significantly improve corrosion resistance by decreasing the passivation current density by 10x and increasing the pitting potential by 1 V. A summary of the critical potentials is given in figure 2.9b. Optimum inhibition was observed at a concentration of 25 mM, which was also supported by impedance measurements. The natural pH of the solution at 25 mM was measured at 12.3. Impedance measurements revealed a 10x increase in the polarization resistance with respect to the control. At concentrations higher than 25 mM, inhibition decreased, perhaps owing to an even greater increase in solution pH.

(a)   (b)
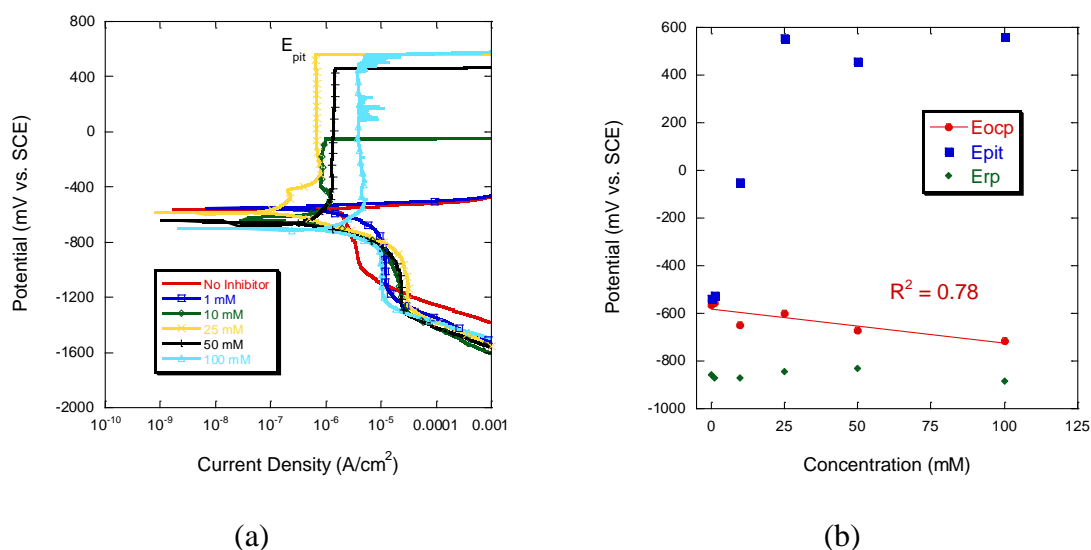
Figure 2.9. (a) Polarization curves in naturally aerated conditions at varying Na_2SiO_3
concentrations (b) Changes in E_{ocp}, E_{pit}, and E_{rp} with concentration.

Impedance testing over a period of 1 week in 0.1 M NaCl + 25 mM silicate solution revealed a
two order of magnitude increase in polarization resistance from 73 $k\Omega \cdot cm^2$ to 7.1 $M\Omega \cdot cm^2$, and a
decrease in capacitance from 11.2 uF/cm^2 to 5.7 uF/cm^2 (Figure 2.10).

(a)   (b)
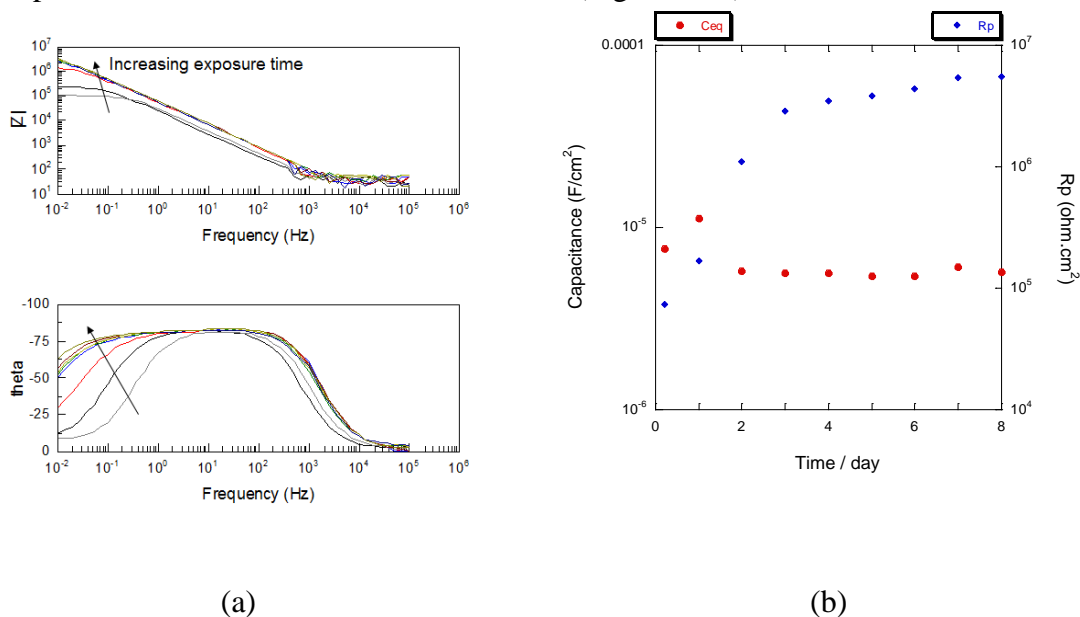
Figure 2.10. Impedance data showing time-dependent evolution of SiO_3^{-2} inhibition. (a)
Spectra data (b) Change in capacitance and polarization resistance with time.

Figure 2.11 shows chronoamperometric data at -900 mV SCE before and after injecting 0.1 M
NaCl solution or concentrated silicate solution to make 25 mM total silicate after mixing.

Immediately after silicate injection at -900 mV SCE the current jumped to high anodic current resulting in a peak followed by a rapid decrease to cathodic current, which was lower than the initial steady state value. The current after injection was about 69% of the value before injection. The jump to high anodic current immediately after silicate injection is related to the dissolution of the aluminum oxide film in response to the high pH increase upon injection of the silicate. The subsequent decrease in current suggests rapid adsorption of silicate on the surface of AA2024-T3.

A sample immersed in 0.1M NaCl solution containing 25 mM silicate resulted in the formation of a thin, translucent film visible with the naked eye over the surface. SEM/EDS analysis revealed minor trenching around intermetallic particles (Figure 2.12). However, preferential dissolution of Mg and Al over the S-phase particles was suppressed. A significant amount of Si was also detected over the S-phase particles using EDS.
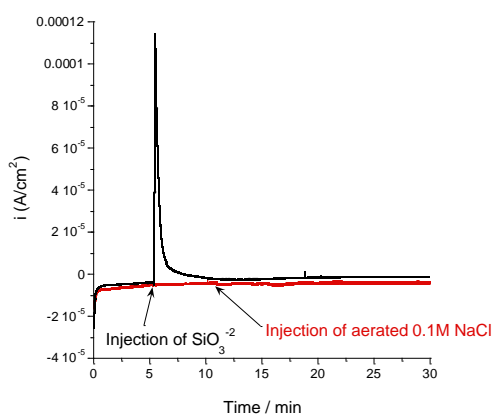
Figure 2.11. Aerated chronoamperometry in 0.1 M NaCl at E_{app} = -900 mV SCE.
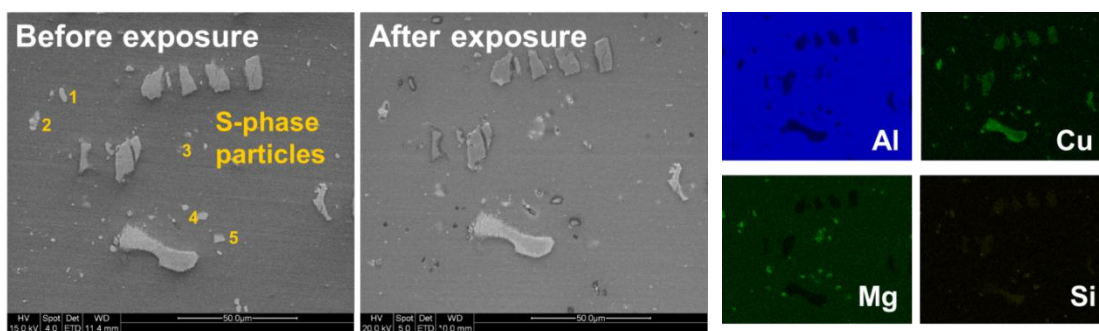
Figure 2.12. SEM/EDS before and after 3d exposure in 0.1 M NaCl solution containing 25 mM SiO_3^{-2}.

XPS studies on a sample exposed to 0.1 M NaCl + 25 mM silicate solution for 24 h (Figure 2.13) revealed a significant presence of Si on the surface, identified as silicate, and a significant amount of Na. Virtually no amount of Si or Na was detected on the surface of the control sample exposed to 0.1 M NaCl only. Figure 2.14 shows the sputter depth profile after 2 day exposure to

25 mM Na_2SiO_3 in 0.1M NaCl. The results show that Si, Na, Al, and O are present throughout the whole film. Towards the Al_2O_3/Al interface, the profiles of both sodium and silicon gradually decrease in concentration. Furthermore, no significant amounts of Cu or Mg were detected within the film.
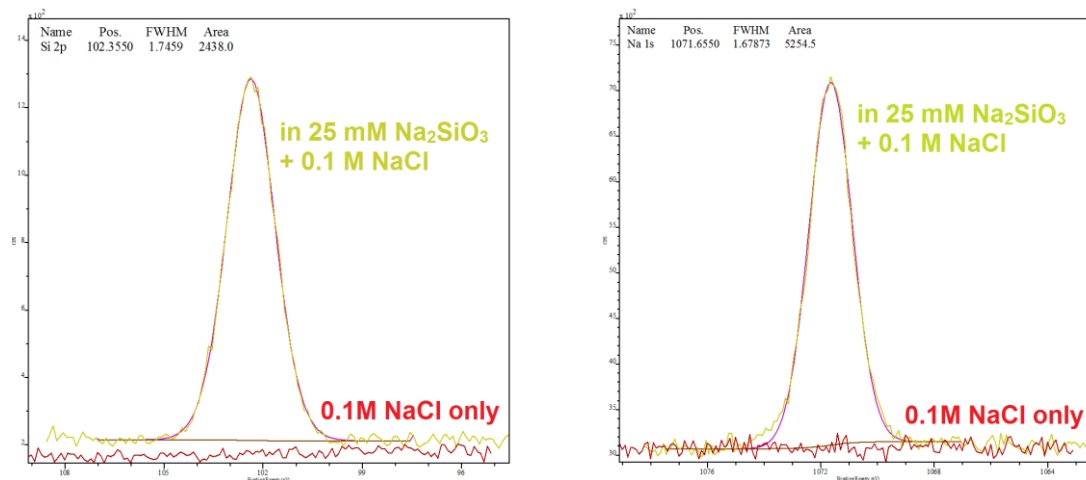
Figure 2.13. The Si 2p and Na 1s spectra for a sample exposed to 0.1 M NaCl solution with and without 25 mM $Na_2SiO_3^{-2}$ for 24 hours.
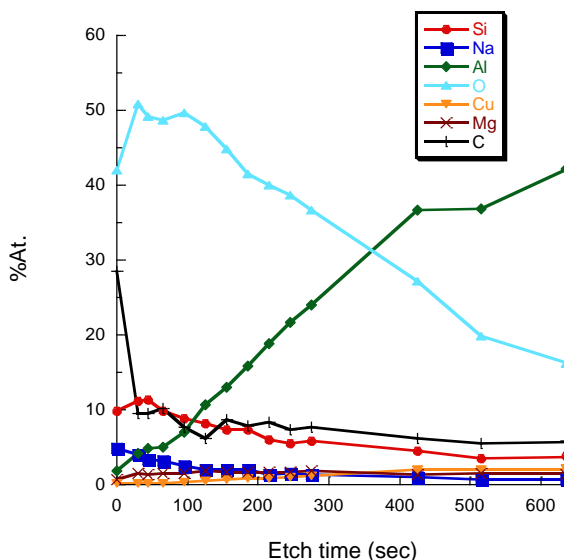
Figure 2.14. XPS sputter depth profile after immersion in 0.1 M NaCl with 25 mM Na_sSiO_3.

In near-neutral pH solution, electrochemical experiments show very slight anodic inhibition (Figure 2.15a). SEM/EDS analysis of a sample exposed to 25 mM silicate in 0.1 M NaCl solution at pH 7.3 showed Si-containing particulates over both S-phase and larger FeMn(Si) intermetallic particles (Figure 2.16). At pH 4, polarization curves reveal a slight increase in oxygen reduction kinetics in the presence of 25 mM silicate and no effect on the anodic kinetics

(Figure 2.15b). Free-corrosion experiments at pH 4 resulted in the formation of a thick-white film over the surface that is rich in Si as characterized by EDS (Figure 2.17). Characterization using XRD revealed that the film is amorphous in nature.

(a)　　　　　　　　　　　　　　　　　(b)
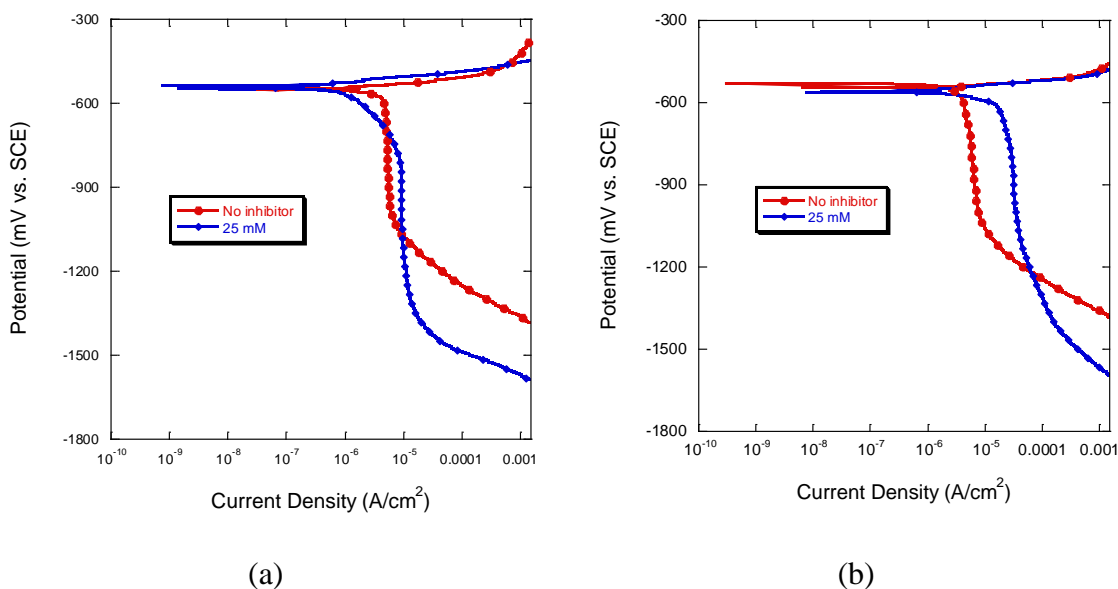
Figure 2.15. Aerated polarization curves with and without 25 mM Na$_2$SiO$_3$ at pH (a) 7.3 and (b) 4.
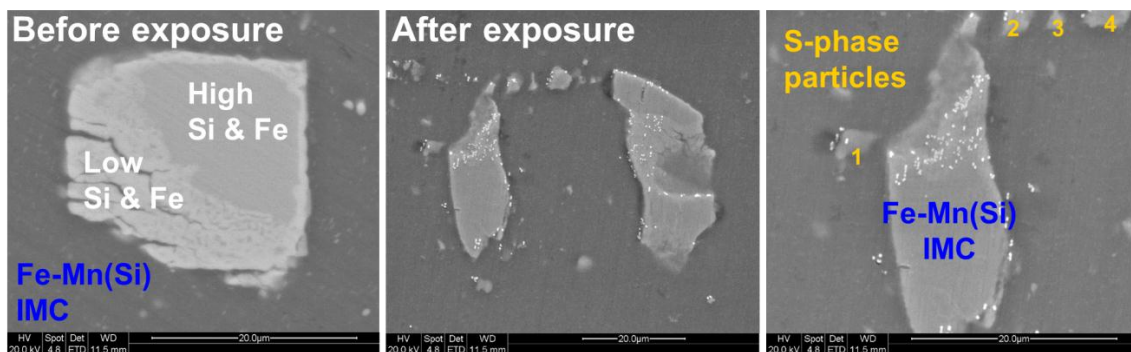
Figure 2.16. SEM micrographs before and after exposure to 25 mM Na$_2$SiO$_3$ at pH 7.30.

Figure 2.18a shows the Si 2p spectra of a sample exposed to 0.1 M sodium chloride solution containing 25 mM silicate at pH 7.3 for 48 hours. The spectrum reveals two peaks at 102.6 eV and 103.1 eV, identified as silicate and silica, respectively. Furthermore, silica is present on the surface at about 87% of the Si concentration. Similarly, at pH 4 XPS reveals the presence of two peaks at 101.9 eV and 102.8 eV, identified as silicate and silica, respectively (Figure 2.14b). However, in this case silicate is present on the surface at about 93% of the Si concentration. Impedance measurements (Figure 2.19) show a 3x increase in polarization resistance compared to the control, and an increase in capacitance for both cases suggesting that the formed film provides minor passive inhibition compared to the no inhibitor case at pH 4.

5.2.4.3 Praseodymium

Naturally aerated polarization curves in 0.1 M NaCl solution were conducted at varying praseodymium concentrations (Figure 2.20). The results revealed no change in the OCP but a significant reduction in oxygen reduction kinetics. The maximum effect was observed at a concentration of 0.2 mM where the ORR was reduced by an order of a magnitude. Free-corrosion experiments of AA2024-T3 coupons immersed in praseodymium containing 0.1 M sodium chloride solution for 2 weeks showed no signs of corrosion. SEM/EDS analysis (Figure 2.21) before and after a 2-day exposure revealed the presence of a thick-oxide precipitate over the S-phase particles. Interestingly, no significant amounts of Pr were detected over the Fe-Mn IMCs by EDS but was detected using SKPFM (Figure 2.22).
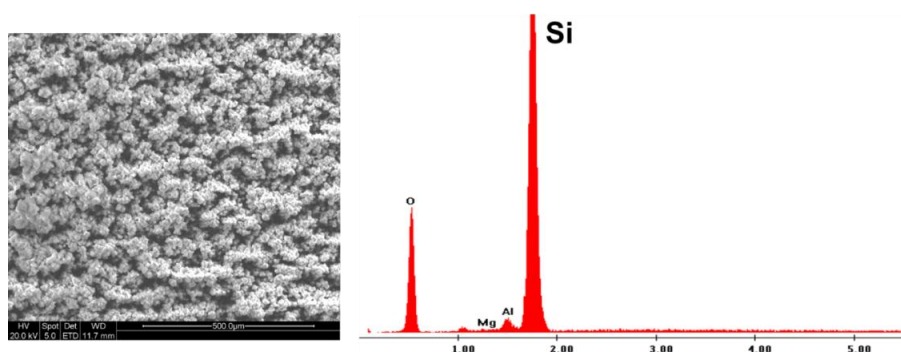
Figure 2.17. SEM/EDS images after exposure to 25 mM Na_2SiO_3 in 0.1 M NaCl at pH 4.

(a)   (b)
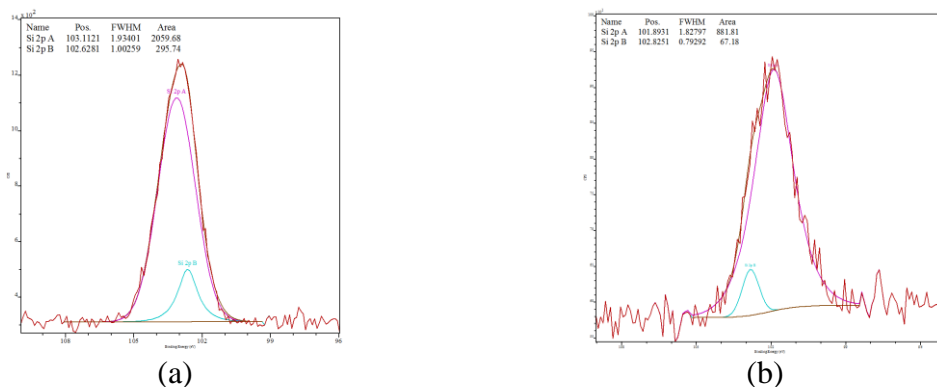
Figure 2.18. The Si 2p spectra for a sample exposed to 0.1 M NaCl solution with and without 25 mM $Na_2SiO_3^{-2}$ for 24 hours at pH (a) 7.3 and (b) 4.
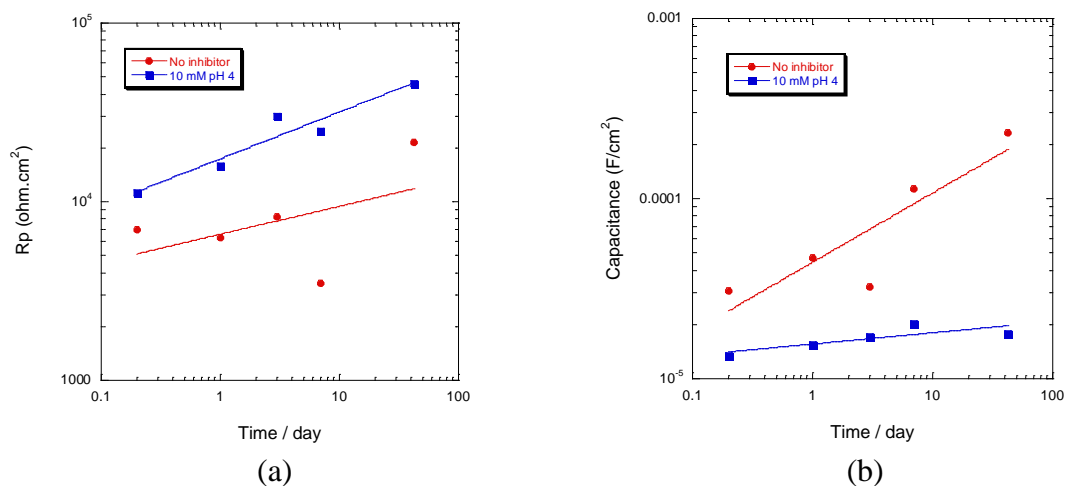
Figure 2.19. EIS summary of (a) capacitance and (b) polarization resistance at pH 4.
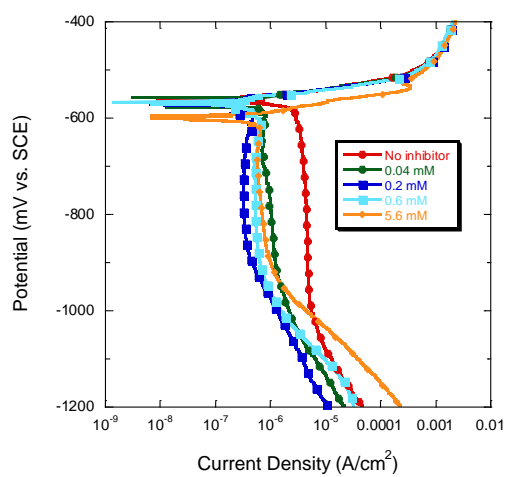
Figure 2.20. Naturally aerated polarization curves in 0.1 M NaCl at varying Pr^{3+} concentrations.
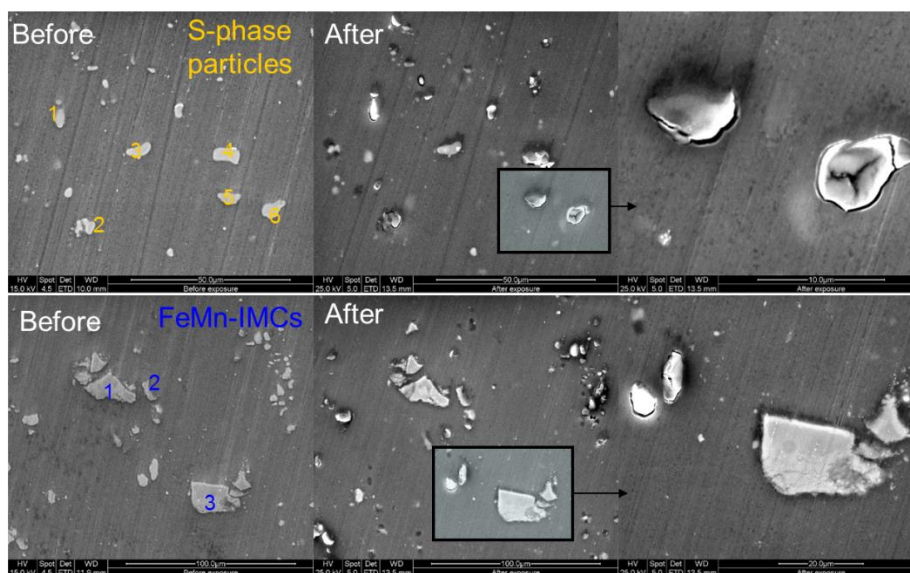
Figure 2.21. SEM micrographs after 2 days immersion in 0.1 M NaCl solution with 0.2 mM Pr^{3+}.
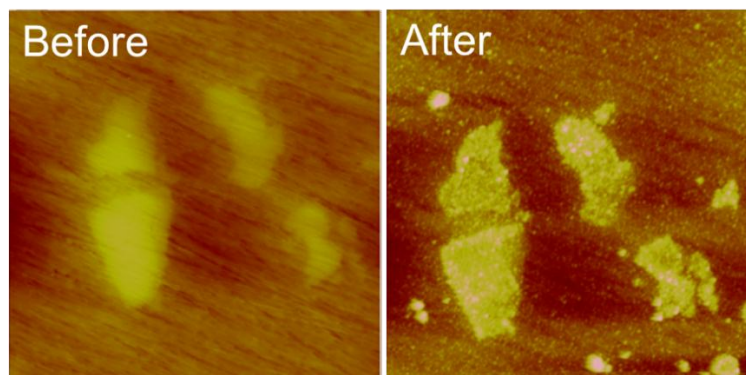
Figure 2.22. SKPFM images of FeMn(Si) IMCs before and after exposure to 0.2 mM Pr^{3+} containing solution.

SEM analysis of a sample immersed for 30 days in 0.1 M NaCl solution containing 0.2 mM Pr^{3+} revealed the presence of nodules 5 μm in diameter. Furthermore, mud-cracking across the surface in the SEM vacuum suggests the formation of a thick film which was characterized as $Pr_2(CO_3)_2(OH)_2.H_2O$ using XRD (Figure 2.23).

Naturally aerated polarization curves in 0.1 M NaCl solution containing 0.2 mM Pr^{3+} at pH 3 (Figure 2.24a) show a 100 mV decrease in OCP relative to the Pr-free solution.   Impedance testing over a period of one week shows that the polarization resistance remains constant and equal to the control case (Figure 2.25). Furthermore, the capacitance increased from 147 to 677 $\mu F/cm^2$. SEM/EDS analysis after 3 day exposure at OCP revealed the presence of a film over

74

the whole surface with significant amount of sulfur detected over the intermetallic particles (Figure 2.26). SEM analysis also revealed that the S-phase particles were still intact underneath the formed film. XPS characterization showed significant amounts of sulfur in the film with no trace of Pr. The only source of sulfur in the solution is from H_2SO_4, which was added to adjust the pH. These observations suggest that the film formed over the surface is not owed to praseodymium inhibition but to the presence of this incidental sulfur concentration.
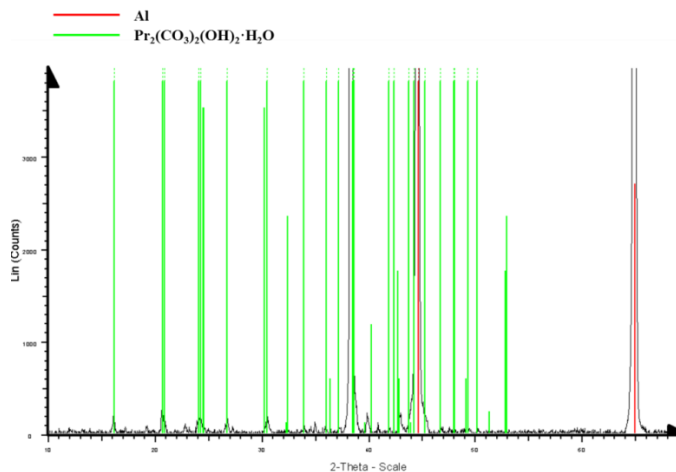
Figure 2.23. XRD pattern after 30 days immersion 0.1 M NaCl solution with 0.2 mM Pr^{3+}.

In high pH solution (pH 10), SEM analysis revealed the deposition of corrosion product across the surface rich in Pr (Figure 2.27). Furthermore, thick-oxide precipitates rich in Pr were present over both S-phase and FeMn(Si) intermetallic particles. Interestingly, virtually no inhibition was observed electrochemically to correlate with the oxide precipitation (Figure 2.24b).

(a)   (b)
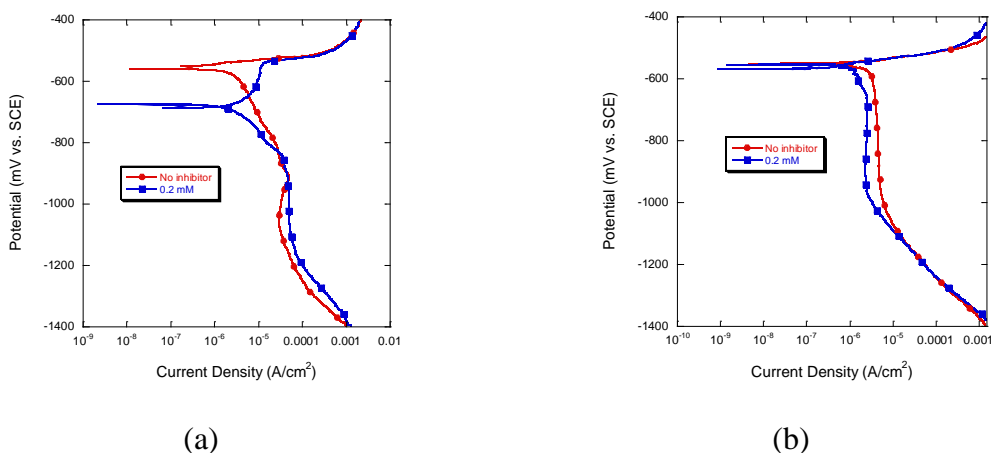
Figure 2.24. Naturally aerated polarization curves in 0.2 mM Pr^{3+} containing solution at pH (a) 4 and (b) 10.
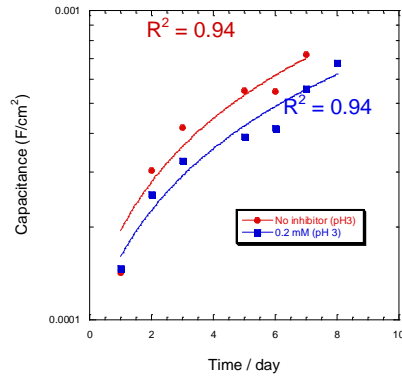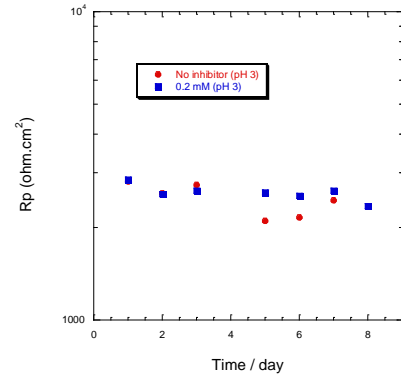
(a)   (b)

Figure 2.25. EIS summary of (a) effective capacitance and (b) polarization resistance at pH 3.
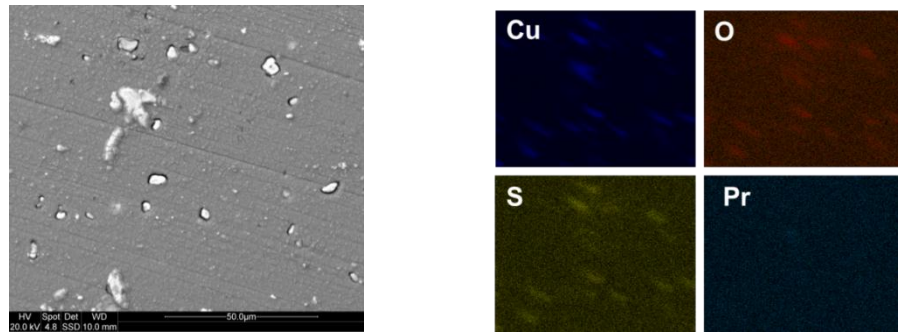
Figure 2.26. SEM micrograph and EDS maps of after 3 day immersion in 0.2 mM Pr^{3+} containing solution at pH 3.
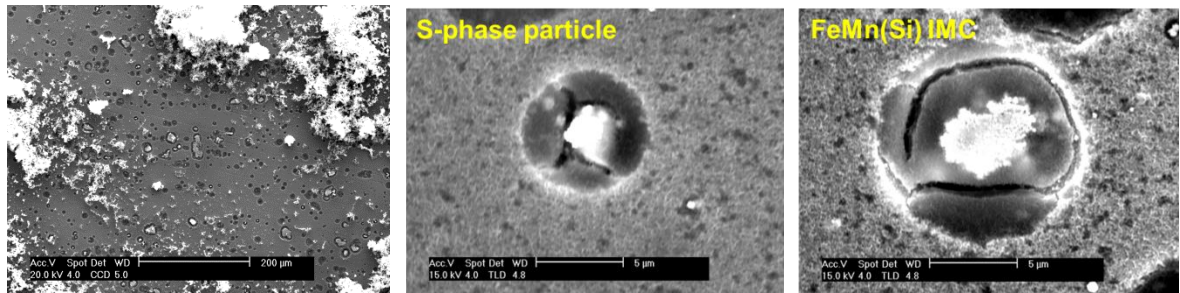
Figure 2.27. SEM micrographs after 4-day immersion in 0.2 mM Pr^{3+} containing solution at pH 10.

2.4.4 *In situ* AFM Scratching Results

In situ AFM scratching involves rastering a region in contact-mode with a Si cantilever at sufficiently high forces (as measured by photodiode setpoint voltage, SP) to destabilize passivity. This technique provides real time information of the early stages of localized corrosion with sub-microscopic resolution. When analyzing the evolution and kinetics of attack, three things have to be considered: the force that initiates attack, the time for attack to nucleate, and the corrosion morphology. Higher forces and longer nucleation times imply greater inhibition performance. AFM scratching was used to investigate the influence of the various inhibitors in 0.1 M NaCl.

Figure 2.28 shows the chronological sequence of scratching in aerated 0.1 M NaCl solution with 125 mM MoO_4^{2-}. No attack was observed within or around any IMC, or on the matrix after scratching for over 10 hours and gradually increasing the scratching force to 525 nN. As the experiment progressed it is apparent that the IMCs all protrude higher from the surface as illustrated in the topography images by the increasing brightness of the IMCs. This would suggest the formation of a protective film over the IMC particles. SEM/EDS analysis after *in situ* scratching confirms that no attack occurred within the rastered area (Figure 2.29).
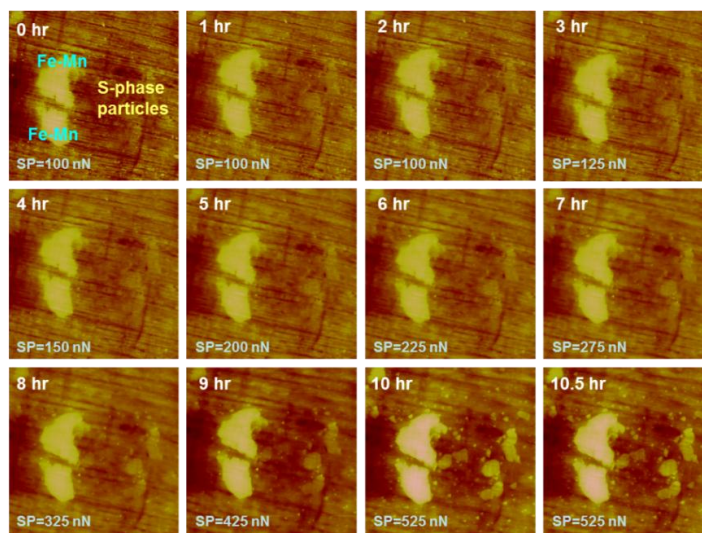
Figure 2.28. *In situ* AFM scratching in 0.1 M NaCl with 125 mM MoO_4^{2-}. Scan size=80µm. Z range=350nm.
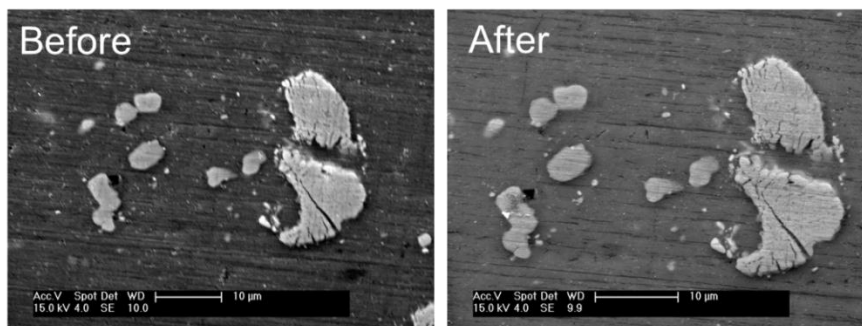
Figure 2.29. SEM micrographs before and after *in situ* AFM scratching in 125 mM MoO_4^{2-}.

Figure 2.30 shows the chronological sequence of attack in solution containing low concentration of silicate. Increasing the scratching force to 175 nN after 3.5 hours of scratching in 0.1 M NaCl solution with 1 mM SiO_3^{2-} resulted in the complete removal of an S-phase particle. No further attack was observed until the scratching force was increased to 400 nN, at which point attack in the form of a pit initiated on the aluminum matrix. Scratching in a solution containing 25 mM silicate resulted in a dramatic improvement in the dissolution rate of AA2024-T3 (Figure 2.31). Increasing the scratching force to 200 nN resulted in minor dissolution of the S-phase particle. Dissolution continued until the end of the experiment when scratching was stopped. SEM/EDS analysis revealed that the S-phase particle was still intact and Mg and Al were still detectable within the particle. No other form of attack was observed (Figure 2.32).
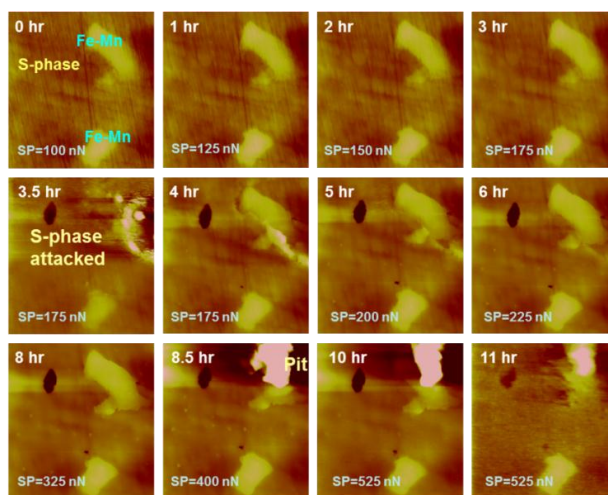
Figure 2.30. *In situ* AFM scratching in 0.1 M NaCl with 1 mM SiO_2^{2-}. Scan size=55µm. Z range=400nm.

Figure 2.33 shows the sequence of attack in solution containing 0.2 mM Pr^{3+}. Attack in the form of a pit on the Al matrix at the periphery of the S-phase particle occurred after 4 hours of scratching at relatively low forces. After gradually increasing the scratching force, trenching was observed around the periphery of both S-phase and FeMn(Si) intermetallic particles. It should be noted that AFM scratching can remove the protective films, but those films can reform because of the continued exposure to inhibitor-containing solution. The Pr-rich film was probably removed during scratching. Nevertheless, as discussed below, the attack in solution containing praseodymium was less than in the case of solution with no inhibitor. SEM/EDS analysis after scratching shows the IMCs still are intact even after scratching at high forces for over 11 hours (Figure 2.34).
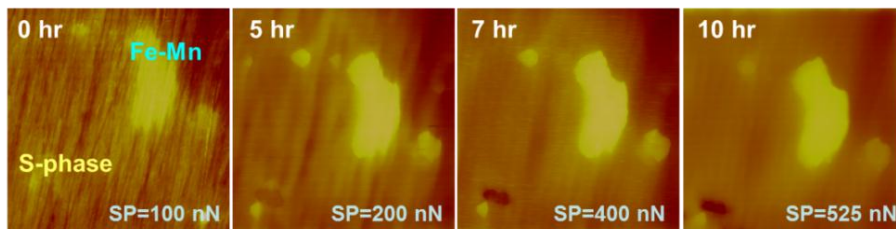
Figure 2.31. *In situ* AFM scratching in 0.1 M NaCl + 25 mM SiO_3^{2-}. Scan size=45µm. Z range=400nm.
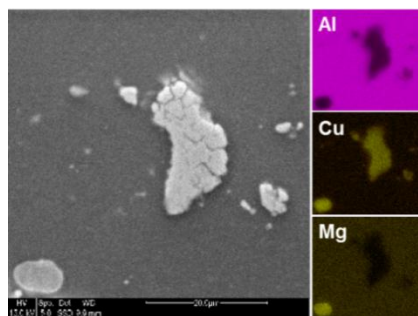
Figure 2.32. *Ex situ* SEM/EDS analysis after AFM scratching in 25 mM SiO_3^{2-}.
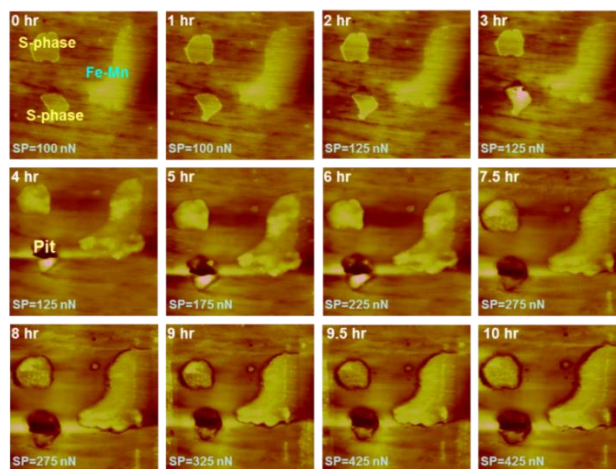
Figure 2.33. *In situ* AFM scratching in 0.1 M NaCl with 0.2 mM Pr^{3+}. Scan size=50µm. Z range=500nm.
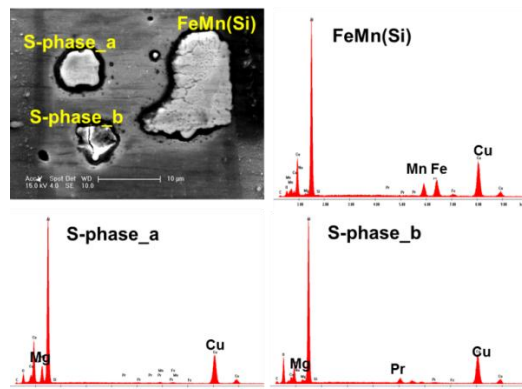
Figure 2.34. SEM/EDS after *in situ* AFM scratching in 0.2 mM Pr^{3+}.

5.2.5 Discussion of Inhibition Mechanism by Selected Inhibitors

5.2.5.1 Molybdate

Equilibria in aqueous solutions of molybdate have been studied in detail [5-7]. It has been found that at concentrations above 10^{-3} M the dominant species in solution at pH 7-12 is MoO_4^{2-}. In acidic solution, polymerization condensation occurs as the ion becomes protonated resulting in the formation of heptamolybdate ion $Mo_7O_{24}^{6-}$ at pH 3-5, and the octamolybdate ion $Mo_8O_{26}^{4-}$ at pH less than 2:

$$7MoO_4^{2-} + 8H^+ \rightarrow Mo_7O_{24}^{6-} + 4H_2O \qquad (2.1)$$

$$8MoO_4^{2-} + 12H^+ \rightarrow Mo_8O_{26}^{4-} + 6H_2O \qquad (2.2)$$
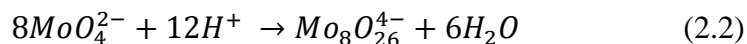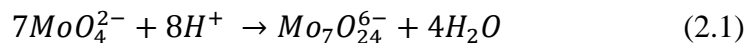
At lower molybdenum concentrations, the presence of significant amounts of $HMoO_4^-$ and H_2MoO_4 has also been reported [8]. Figure 2.35 shows the specie diagram for MoO_4^- in 0.1 M NaCl aqueous solution generated using *MEDUSA*. The plot shows that the solubility of MoO_4^- significantly decreases below pH 6 as the molybdate polymerizes to form protonated species of the $Mo_7O_{24}^{6-}$ ion which were shown to reduce in a fashion that is not self-inhibiting (Figure 2.8).

The mechanism by which molybdate imparts inhibition is not well understood and different mechanistic proposals have been put forward over the years [2,9-10]. According to Moshier *et al.* molybdate forms an adsorbed layer on the surface that is concentration dependent [2]. At molybdate concentrations less than 100 ppm, a thick film forms consisting mostly of MoO_2. In contrast, at higher concentration, the ratio of Mo^{4+} to Mo^{6+} concentration decreases and the molybdate anion MoO_4^{2-} is preferentially adsorbed on the surface thereby impeding the ingress of chloride ions. An alternative mechanism proposed by Breslin *et al.* involves an oxidation-reduction process whereby aluminum is oxidized and molybdate is reduced [9]. It is suggested that there is competitive adsorption between molybdate and chloride ions at flawed regions in the passive film. At sufficiently high molybdate concentrations, reduction of Mo^{6+} to Mo^{4+} is favored resulting in the formation of a protective MoO_2 film:

$$3MoO_4{}^{2-} + 6H^+ + 2Al \rightarrow 3MoO_2 + Al_2O_3 \cdot 3H_2O \,(2.3)$$
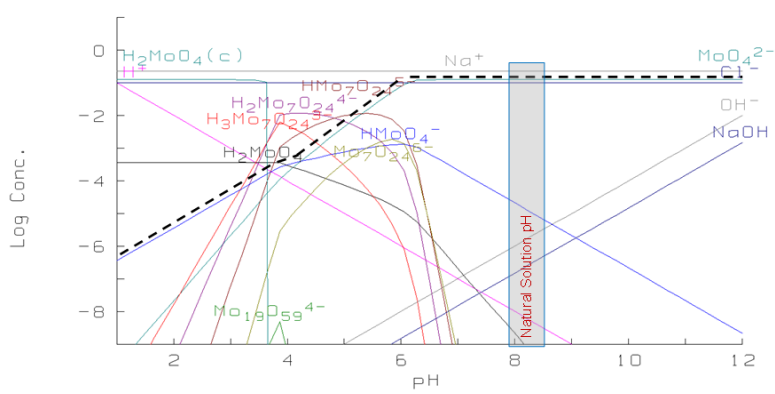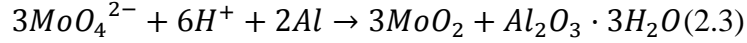
Figure 2.35. Specie diagram for $MoO_4{}^{2-}$ in 0.1 M NaCl aqueous solution. Generated using MEDUSA software. Dashed line signifies maximum solubility.

From the aforementioned results, it is clear that molybdate imparts anodic inhibition by increasing the pitting potential of AA2024-T3 (Figure 2.1). A mechanism is proposed that takes into account the oxidation-reduction process inferred by Breslin. SEM/EDS characterization of a surface exposed to chloride solutions containing 125 mM $MoO_4{}^{2-}$ showed molybdate to be present only over the IMCs (Figure 2.36), which have been shown to be the most electrochemically active spots over the surface of AA2024-T3 [3,4]. Hence these sites can be viewed as flawed regions on the surface where there is competing adsorption between the chloride ions and the molybdate species. Moreover, EDS maps illustrated in Figure 2.3 show that an oxide forms over these IMCs that is rich in Mo, Na, and Cl. Given the partial oxidizing nature of the molybdate anion (Figure 2.37), it is postulated that the first step in the inhibition mechanism by molybdate involves the oxidation-reduction process described by eqn. 2.3. This is supported by a jump in the cathodic current after injecting molybdate in 0.1M NaCl at an applied potential of -900 mV SCE (Figure 2.5). During this step the oxidation state changes from +6 in the $MoO_4{}^{2-}$ ion to +4 in MoO_2. However, after the abrupt increase in cathodic current, there is an immediate decrease in current to anodic values, which suggests subsequent oxidation of the Mo^{+4} state to the Mo^{+5} state. This is supported by the XPS data in Figure 2.6. It is surmised that the next step in the inhibition process by molybdate involves the oxidation of MoO_2 and to form $MoCl_5$ by:

$$2MoO_2 + 10NaCl + H_2O \rightarrow 2MoCl_5 + 5Na_2O + 2H^+ + 2e^- \qquad (2.4)$$
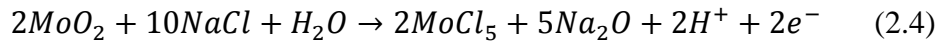
This may explain the presence of Mo, Na, and Cl detected over the IMCs via EDS. Furthermore, $MoCl_5$ was characterized by XPS both in the samples exposed to solution at OCP, and in the samples held at a fixed cathodic potential. However, XPS also revealed the presence of MoO_3 which accounts for almost 80% of the Mo concentration on the surface which suggest that $MoCl_5$ is further re-oxidized to Mo^{+6}. This is illustrated by the following electrochemical reaction:

$$MoCl_5 + 3H_2O \rightarrow MoO_3 + 6H^+ + 5Cl^- + e^- \qquad (2.5)$$

81
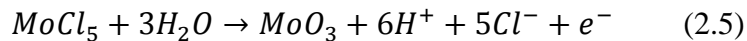
It should be noted that eqns. 2.4 and 2.5 are not found anywhere in the literature. The generation of H^+ in Eq. 2.5 is supported by a measured decrease in the solution pH from 8.1 to 7.35 after exposure for 2 days at OCP. The increase in acidity may also explain the attack observed around the periphery of the IMCs. An increase in acidity will also result in the formation of polymerized species, which were found to be poor inhibitors of corrosion as discussed above. Furthermore, it has been reported that the solubility of MoO_3 decreases with increasing acidity, which may explain the stability of the oxide after its formation [11]. Thus, it is postulated that MoO_3 is the species responsible for the ennoblement of the pitting potential of the alloy surface and lowering of the corrosion rate of AA2024-T3.
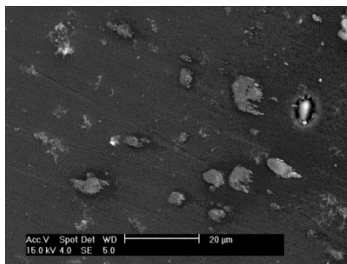
Figure 2.36. SEM micrograph after immersion in 0.1 M NaCl with 125 mM MoO_4^{2-}.
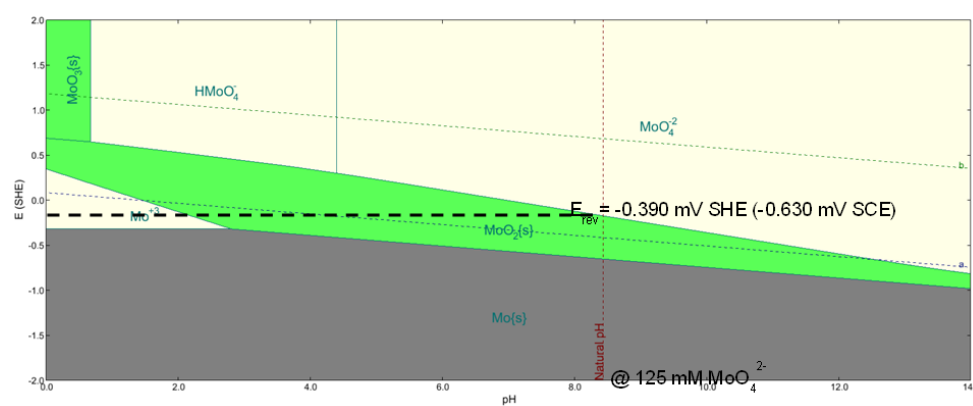
Figure 2.37. Pourbaix diagram of molybdate in aqueous solution at 25°C. Generated using OLI Analyzer.

It should be noted that no evidence has been generated to support the first step in the mechanism described above, the reduction of Mo^{6+} in MoO_4^{2-} to Mo^{4+} in MoO_2. This step was postulated based on suggestions in the literature. However, it is possible that Mo^{6+} reduces directly to Mo^{5+} in $MoCl_5$, which was observed in the XPS data.

5.2.5.2 Silicate

Many efforts have been reported in literature to describe the chemistry of soluble silicates [12-16]. It has been shown that the anionic complexity of silicate in solution is related to

82

concentration and the silicon to cation ratio (i.e. SiO_2/Na_2O). In this study, SiO_2/Na_2O was equal to 1. The solution pH was measured after progressive addition of Na_2SiO_3 to 0.1 M NaCl solution. As illustrated in Figure 2.38, increasing the silicate concentration linearly increases the solution pH. At SiO_2/Na_2O =1 the solution can be described as an aqueous solution of silicic acid and hydroxyl ions as illustrated in the following chemical equation:

$$SiO_3^{-2} + 3H_2O \rightarrow Si(OH)_4 + 2OH^- \text{ (2.6)}$$
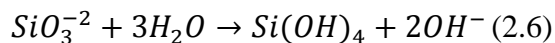
^{29}Si-NMR has been recognized as the most valuable method to study the anionic speciation in silicate solutions [12-13, 15-16]. However, performing these measurements is notoriously difficult. Attempts to conduct [29]NMR in this particularly study failed due to intense background resonance. Nevertheless, Gaggiano *et al.* used solid-state [29]NMR to study anionic species in silicate solution at 0.1 M concentration. It was found that, at SiO_2/Na_2O =1, the predominant species in solution is the anionic monomer of the type $(HO)_{4-x}SiO_x^{x-}$.

Based on the above results on silicate and on the speciation information gathered through literature, inhibition mechanisms are proposed for alkaline and acidic solutions. At high pH, the aluminum-oxide film is chemically unstable and dissolves to form $Al(OH)_4^-$ ions in solution:

$$Al_2O_3 + 3H_2O + 2OH^- \rightarrow 2Al(OH)_4^- \qquad \text{(2.7)}$$
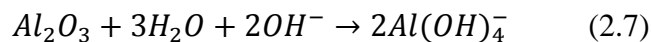
The silicate ions in solution will then react with the $Al(OH)_4^-$ species through the following chemical reaction as proposed by Swaddle [14]:

$$(OH)_{4-x}SiO_x^{x-} + Al(OH)_4^- \rightarrow (OH)_3AlOSiO_x(OH)_{3-x}^{(x+1)-} + H_2O \text{ (2.8)}$$
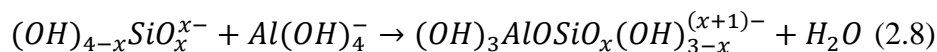
It has been reported that the isoelectric point of oxide-covered aluminum is 9-9.5 [17]. Therefore, in alkaline silicate solution both the oxide surface and aluminosilicate anions are negatively charged. Sodium detected in the film by XPS suggests that Na^+ ions in the solution adsorb on the negatively charged oxide surface behaving as a coagulating agent [18]. The Na^+ ions on the surface coordinate with the oxygen atoms of the aluminosilicate anions acting as a bridge between the anions and the surface. Furthermore, Na^+ is observed to behave this way all throughout the film as indicated by XPS depth profiling (Figure 2.14). The chemisorbed layer provides a protective film over the aluminum alloy surface as supported by the electrochemical polarization curves (Figure 2.9) and the impedance data (Figure 2.10). To summarize, at high pH the dissolution of the oxide film on the surface promotes the formation of a protective aluminosilicate film that is physically adsorbed via a coupling mechanism with Na^+ ions. This mechanism has been proposed recently in the literature by Gaggiano *et al.* [16].
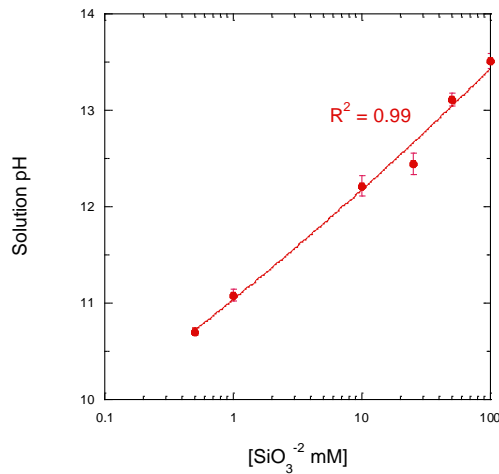
Figure 2.38. Effect of silicate concentration on solution pH.

In more acidic media, silicate provides poor inhibition as shown in the electrochemical and impedance tests at low solution pH (Figure 2.15 and 2.19). Nevertheless, a mechanism is proposed to account for the effect of silicate at near-neutral and low solution pH.

At near-neutral pH, the aluminum surface is passivated except at IMCs. SEM/EDS analysis of a sample exposed to silicate solution at pH 7.3 revealed modest corrosion inhibition and the presence of deposits over the IMCs (Figure 2.16), which are likely silicate- and silica- based derivatives according to XPS results (Figure 2.18a). Thus, a mechanism is proposed whereby the first step involves the selective dissolution of Al and Mg over the S-phase particles during exposure to aggressive solution:

$$Al \rightarrow Al^{3+} + 3e^{-} \qquad (2.9)$$

$$Mg \rightarrow Al^{3+} + 2e^{-} \qquad (2.10)$$
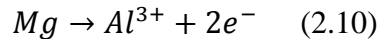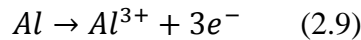
The metallic ions generated by eqns. 2.9 and 2.10 then chemically react with the monomeric silicate anions present locally over the IMCs to form deposits of aluminosilicate and silica-magnesium particles. The following chemical equations illustrate these processes in the case where the form of species present in solution is of the type $(HO)_2SiO_2^{2-}$:

$$2Al^{3+} + 3(OH)_2SiO_2^{2-} \rightarrow Al_2(SiO_3)_3 \cdot (OH)_2 \qquad (2.11)$$

$$Mg^{2+} + (OH)_2SiO_2^{2-} \rightarrow MgSiO_2 \cdot (OH)_2 \qquad (2.12)$$
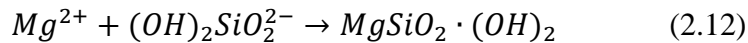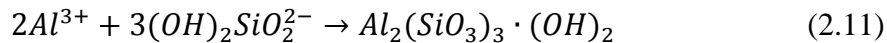
The resulting species deposit over the IMCs and perhaps block further attack. Furthermore, based on the XPS results, 87% of the Si concentration on the surface was identified as silica, which signifies that the majority of the particulates over the S-phase particles are of the silica-magnesium type. A similar effect is proposed over the larger FeMn(Si) IMCs where SEM

analysis coupled with XPS revealed the presence of Si-based particulates over regions that are intrinsically free of Si.

In the acidic regime, silicate species are present as silicic acid, or H_4SiO_4. Free-corrosion experiments revealed the presence of a thick white-film over the surface visible with the naked eye. XPS analysis showed that silicate was the phase present (Figure 2.18b). At low solution pH, the aluminum surface becomes activated and in the process the interfacial electrolyte pH increases:

$$Al_2O_3 + 3H^+ \rightarrow 2Al^{3+} + 3OH^- \qquad (2.13)$$
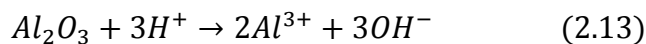
It is proposed that this increase in interfacial pH increases the local monomeric silicate anion concentration as shown in the following chemical equation:

$$H_4SiO_4 + 2OH^- \rightarrow (OH)_2SiO_2^{2-} + 2H_2O \qquad (2.14)$$
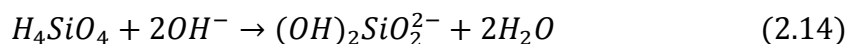
Afterwards, the monomeric silicate anions present near the surface chemically react with the activated aluminum species forming an aluminosilicate film as observed in the SEM micrograph of Figure 2.17. The process is shown in the following chemical equation:

$$2Al^{3+} + 3(OH)_2SiO_2^{2-} \rightarrow Al_2O_3(SiO_3)_3 \cdot (OH)_3 + 3H^+ \qquad (2.15)$$

Eqn. 2.15 is the same reaction as that shown by eqn. 2.11. The difference in mechanism at pH 7.3 and pH 4 lies in the fact that in the more acidic regime the whole aluminum surface becomes activated leading to the formation of a thick aluminosilicate film that provides little protection as observed in the impedance data (Figure 2.19). Moreover, the mechanism at low pH is further supported by the fact that 93% of the Si concentration on the surface was identified as silicate by XPS (Figure 2.18b). It should be noted that no report has been found in literature that discusses the effect of silicate in the acidic regime.

5.2.5.3 Praseodymium

There have been few studies on the corrosion inhibition mechanism of praseodymium chloride in solution. Markley *et al.* found that adding 0.2 mM of praseodymium diphenyl phosphate in 0.1 M NaCl solution reduced the OCP by 70 mV and decreased oxygen reduction kinetics by 10x [19]. Figure 2.39 shows the speciation diagram for $PrCl_3$ in 0.1 M NaCl aqueous solution generated using *MEDUSA*. The plot shows that the solubility of Pr^{3+} decreases at pH values greater than 6 owing to the formation of insoluble praseodymium-carbonate, $Pr_2(CO_3)_3$.

Based on the results of this study, praseodymium imparts cathodic inhibition in a similar fashion as other rare earth metals like cerium [20-24]. In the presence of praseodymium, a film is precipitated over cathodic sites on the alloy surface as the local pH increases due to the oxygen reduction reaction (ORR):

$$O_2 + 2H_2O + 4e^- \rightarrow OH^- \qquad (2.16)$$
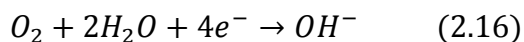
The XRD data shown in Figure 2.23 indicated that the oxide is praseodymium-carbonate-hydroxide-hydrate, or $Pr_2(CO_3)_2(OH)_2 \cdot H_2O$,. The increase in local pH drives the formation of

Pr$_2$(CO$_3$)$_3$ species above the IMC particles, which then react with the generated hydroxyl ions to form a thick oxide film as shown in the following chemical equation:

$$Pr_2(CO)_3 + 2H_2O \rightarrow Pr_2(CO_3)_2(OH)_2 \cdot H_2O + H_2CO_3 \quad (2.17)$$
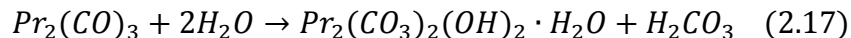
Interestingly, no significant amount of Pr was detected over the FeMn(Si) IMCs in contrast to the S-phase particles using EDS. However, the fact that particles were observed with SKPFM (Figure 2.22) suggests that the same mechanism occurs over them. The absence of a thick oxide film in conjunction with no observation of local attack suggests that a very small amount of Pr is effective in blocking oxygen reduction over the FeMn(Si) IMCs. Furthermore, with time the surface of the alloy becomes completely covered by the praseodymium-carbonate film as old cathodic sites become blocked by the deposits and new sites become activated.
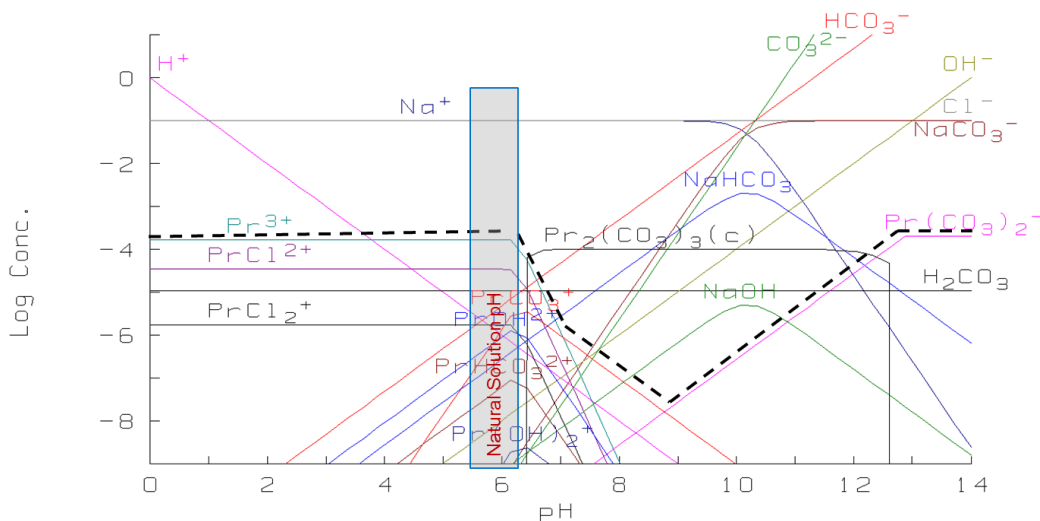
Figure 2.39. Speciation diagram for Pr^{3+} in 0.1 M NaCl aqueous solution. Generated using MEDUSA software. Dashed line signifies maximum solubility.

SEM/EDS analysis of a sample immersed in pH 3 solution containing Pr^{3+} (Figure 2.26) suggests that a thick sulfur-based oxide forms over the IMC particles with little to no praseodymium detected. These observations indicate that the film formed over the surface is owed to the presence of sulfur in solution when adjusting the pH with sulfuric acid. However, this sulfur-based film provides virtually no inhibition as no improvement in the polarization resistance is observed with time in relation to the inhibitor-free case (Figure 2.25b).

At higher solution pH, the aluminum surface becomes activated and dissolution of the oxide layer occurs. SEM observations (Figure 2.27) indicate that a thick oxide film still forms preferentially over the IMCs as a result of ORR. However, due to the dissolution of the oxide film at high pH the Al matrix undergoes uniform corrosion, which may not be effectively controlled by the inhibitor. This may explain why electrochemically no inhibition was observed by praseodymium at a high pH (Figure 2.24b).

5.2.4.4 *In Situ* **AFM Scratching**

Before discussing the AFM scratching results, it is of interest to look at the scratching behavior of AA2024-T3 in inhibitor-free solution and in the presence of chromate [25,26]. Figure 2.28 shows the evolution of attack during scratching in inhibitor-free solution at a constant scratching force of 100 nN [25]. Attack was observed after 22 minutes of scratching at the periphery of a large S-phase particle as indicated by the arrow in Figure 2.40. After 30 minutes of scratching the larger FeMn(Si) particle began to show signs of trenching as well. After 1 hour, the large S-phase particle and part of the larger IMC was no longer present in the topography image. Compared to the inhibitor-free case, all the inhibitors tested in this study significantly reduce the dissolution rate of S-phase particles in 0.1 M NaCl.
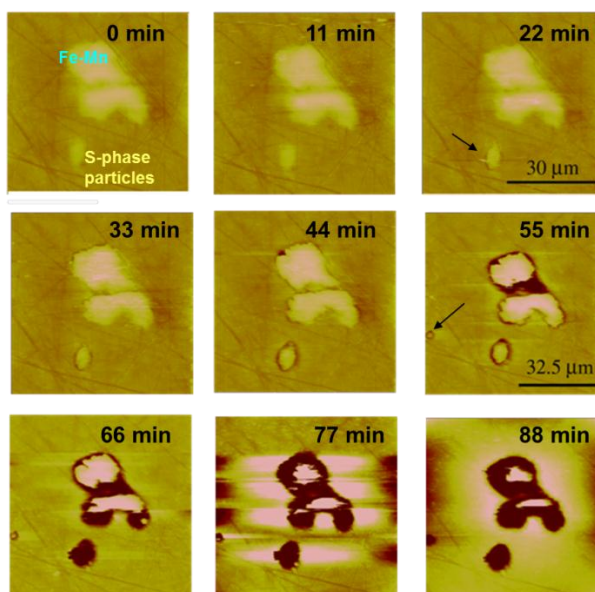
Figure 2.40. Sequence of attack in inhibitor-free solution. Z range =1.5µm. The scratching force was held constant at 100 nN [25].

In the presence of 0.1 mM dichromate, scratching in 0.5 M NaCl resulted in the protection of S-phase particles but pitting in the matrix (Figure 2.41a) [26]. At higher dichromate concentrations of 50 mM, a scratching force of 200 nN was needed to cause breakdown which occurred at the S-phase particles (Figure 2.41b). In studies involving vanadates, forces in the 300 to 400 nN range were required to trigger corrosion attack in 0.5M NaCl solution containing 1 mM monovanadate [25]. In that study, attack nucleated in the Al matrix and most S-phase particles remained free of attack.

Compared to the corrosion morphology of chromate and vanadates, only molybdate and silicate at their corresponding optimum inhibition concentrations provided better inhibition efficacy based on their respective corrosion morphologies. In the presence of 125 mM molybdate, no attack was observed on the rastered area as observed in Figure 2.28. In the case of 25 mM silicate, little attack was observed over the S-phase particle (Figure 2.31). *Ex situ* SEM analysis revealed that the attacked S-phase particle was still largely intact (Figure 2.32). In contrast, at

much lower silicate concentration the S-phase particle was rapidly attacked and pitting manifested on the Al matrix. Praseodymium did not perform better than chromate with respect to the corrosion morphology, but that may be related to the removal of the thick-oxides formed over the IMCs during scratching which might have hindered the inhibition strength of praseodymium. Figure 2.33 shows trenching at the periphery of the IMC particles as the main form of attack. Nonetheless, SEM/EDS analysis after scratching revealed that the larger IMCs within the scratched region were still intact even after scratching at high forces (Figure 2.34). This suggests that an oxide film, undetectable by EDS, may still form over the IMC particles.

It should be noted that, to do a more comprehensive comparison with dichromate, it is necessary to perform AFM scratching studies with dichromate at a chloride concentration of 0.1 M as was done for molybdate, silicate, and praseodymium.

<center>(a)   (b)</center>
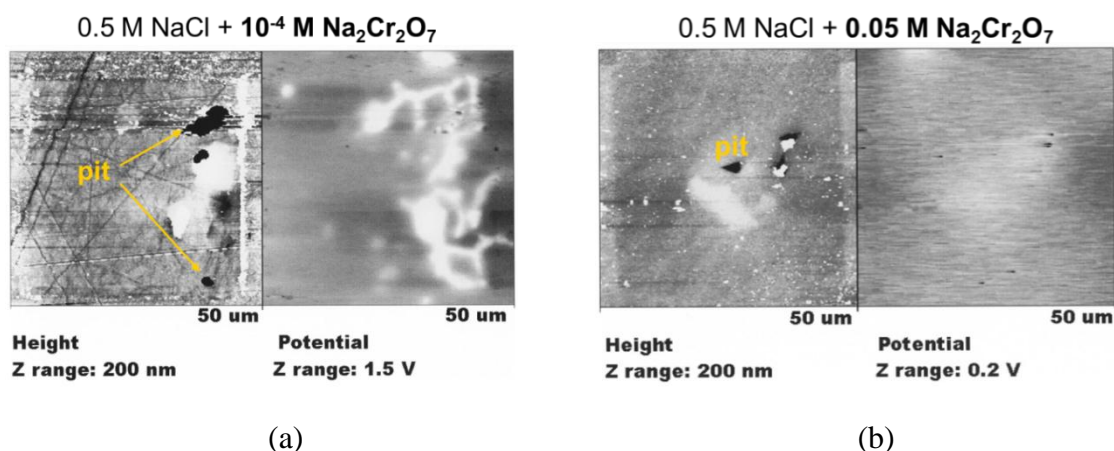
Figure 2.41. *In situ* AFM scratching in 0.1 M NaCl solution with different $[Cr_2O_7^{2-}]$ [26].

5.2.6 Conclusions and Implications for Future Work

The inhibition performance of molybdate, silicate, and praseodymium was discussed and a mechanism for each inhibitor was postulated. In the case of molybdate, optimum inhibition was observed at near-neutral pH at a concentration of 125 mM in 0.1 M NaCl solution. It was inferred that MoO_3 is the species responsible for the ennoblement of the pitting potential of the alloy surface thereby imparting anodic inhibition on AA2024-T3. The first step in the mechanism involved an oxidation-reduction process whereby MoO_2 was formed and subsequently re-oxidized in two steps to form MoO_3 over the IMC particles. At low pH, molybdate undergoes polymerization with the resulting species shown to have rendered poor corrosion inhibition.

Silicate is a strong anodic inhibitor in high alkaline conditions. At an optimum concentration of 25 mM the pitting potential increased over 1 V. It was postulated that at high pH the dissolution of the aluminum oxide film on the surface promotes the formation of an aluminosilicate thin-film that is physically adsorbed to the negatively charged surface by Na^+ ions. At near-neutral pH, silicate blocks the activation of IMC particles on the surface by a precipitation mechanism that

results in the formation of silicate- and silica-based particulates. At even lower pH, the main form of species in solution is silicic acid. However, it was shown that activation of the aluminum surface promotes the formation of monomeric silicate ions and the deposition of aluminosilicate film across the whole surface, which was shown to provide some corrosion inhibition in comparison to the inhibitor-free case.

Praseodymium imparted cathodic inhibition at near-neutral pH, lowering the oxygen reduction kinetics by a factor of 10 at an optimum concentration of 0.2 mM. It is proposed that an oxide characterized as $Pr_2(CO_3)_2(OH)_2 \cdot H_2O$ forms over the ORR supporting IMC particles as the local pH increases. As the cathodes on the surface become blocked by a thick-oxide, new sites are activated resulting in the formation of a thick-film across the whole surface. In low and high solution pH, praseodymium renders poor inhibition. In the latter case, it was shown that praseodymium still forms a thick-oxide film over the IMCs as a result of ORR but is unable to stop the uniform dissolution of the Al-oxide film.

Lastly, *in situ* AFM scratching experiments reveal that at their respective optimum inhibition concentrations, all three inhibitors reduced the removal rate of the S-phase particles in comparison to the inhibitor-free case. In the case of molybdate, no form of attack was observed even after scratching at high forces. Similarly, almost no attack was observed in the scratched region in the presence of silicate ions in solution. In the case of praseodymium, attack in the form of trenching was observed around all IMC particles, however *ex situ* SEM analysis showed the larger particles to be still intact and Mg and Al were still detected over the S-phase particles by EDS.

This work sheds light on the inhibition mechanisms of selected chromate-free inhibitors in hopes of helping to facilitate improvements in chromate-free protection schemes. More specifically, this work can be useful in studies involving inhibitor combinations that incorporate the inhibitors looked at in this study. However, one must consider the effect of these inhibitors beyond the realm of bulk solution inhibition. For instance, implications based on the AFM scratching results coupled with electrochemical experiments would suggest that molybdate may be a suitable replacement for chromate. However, the large ratio of molybdate-to-chloride ion concentration may not be adequate for organic coating applications since the high concentration of inhibitor release necessary for corrosion inhibition may lead to coating degradation via osmotic blistering [27]. Therefore, caution must be exercised when extending the application of these selected inhibitors into the realm of coating systems.

5.2.7 Acknowledgements

5.2.8 References

1.   P. Schmutz and G.S. Frankel, *J. Electrochem. Soc.*, **145**, 2295 (1998).

2.   W.C. Moshier and G.D. Davis, *Corrosion*, **46**, 43 (1990).

3.   W. Zhang and G.S. Frankel, *J. Electrochem. Soc.*, **149**, B510 (2002).

4.   W. Zhang and G.S. Frankel, *Electrochim. Acta.*, **48**, 1193 (2003).

5.   J. Aveston, E.W. Anacker, and J.S. Johnson, *Inorg. Chem.*, **3**, 735 (1964).

6.   R.H. Busey and O.L. Keller, *J. Chem. Phys.*, **41**, 215 (1964).

7.   C.V. Krishnan, M. Garnett, B. Hsiao, and B. Chu, *Int. J. Electrochem. Sci.*, **2**, 29 (2007).

8.   Y. Sasaki and L.G. Sillen, *Acta Chem. Scand.*, **18**, 1014 (1959).

9.   C.B. Breslin, G. Treacy, and W.M. Carroll, *Corrosion Sci.*, **36**, 1143 (1993).

10.   M.A. Stranick, *Corrosion 85*, 380, Nace, Houston, TX (1985).

11.   Z. Szklarska-Smialowska, *Proc. Symp. Critical Factors in Localized Corrosion*, **9**, 311 (1992).

12.   S.D. Kinrade and T.W. Swaddle, *Inorg. Chem.*, **23**, 4253 (1988).

13.   S.D. Kinrade and T.W. Swaddle, *Inorg. Chem.*, **23**, 4259 (1988).

14.   T.W. Swaddle, *Coord. Chem. Rev.*, **219-221**, 665 (2001).

15.   J.L. Provis, P. Duxson, G.C. Lukey, F. Sparovic, W.M. Kriven, and J.S.J. van Deventer, *Ind. Eng. Chem. Res.*, **44**, 8899 (2005).

16.   R. Gaggiano, P. Moriame, M. Biesemans, I. De Graeve, and H. Terryn, *Surf. Coat. Technol.*, **206**, 1269 (2011).

17.   E. McCafferty and J.P. Wightman, *J. Colloid Interface Sci.*, **194**, 344 (1997).

18.   R. Iler, *The Chemistry of Silica*, (Chichester, NY, Brisbane, Toronto, Singapore: J. Whiley & Sons, 1979).

19.   T.A. Markley, A.E. Hughes, T.C. Ang, G.B. Deacon, P. Junk, and M. Forsyth, *Electrochem. Solid-State. Let.*, **10**, C72 (2007).

20.   B.R.W. Hinton, D.R. Arnott, and N.E. Ryan, *Met. For.*, **7**, 12 (1984).

21.   D.R. Arnott, B.R.W. Hinton, and N.E. Ryan, *Corrosion*, **45**, 12 (1989).

22.   B.R.W. Hinton, *J. Alloys Comp.*, **180**, 15 (1992).

23.   A.J. Aldykewics, H.S. Isaacs, and A.J. Davenport, *J. Electrochem. Soc.*, **142**, 3342 (1995).

24.   A.J. Aldykewics, A.J. Davenport, and H.S. Isaacs, *J. Electrochem. Soc.*, **143**, 147 (1996).

25.   M. Iannuzzi and G.S. Frankel, *Corrosion*, **63**, 672 (2007).

26.   P. Schmutz and G.S. Frankel, *J. Electrochem. Soc.*, **146**, 4461 (1999).

27.   J. Sinko, *Prog. in Org. Coatings*, **42**, 267 (2001).

5.3 Task 3: Active inhibition, barrier properties and adhesion

Objectives

The objective of this task was to use a range of experimental and modeling approaches to evaluate the efficacy of active inhibitor species in emergent chromium-free coating systems for the purpose of understanding their role in promoting corrosion protection. A further objective is to study the tradeoffs between active inhibition and other elements of corrosion protection.

5.3.1 Corrosion inhibition of AA 2024-T3 alloy by Lanthanide cations – Ce^{3+}, Pr^{3+}, La^{3+}

5.3.1.1 Introduction

AA 2024-T3 is a solution heat treated, cold worked and naturally aged alloy commonly used in the aerospace industry. Its composition by weight percent is 3.8-4.9 Cu, 1.2-1.8 Mg, 0.3-0.9 Mn, and small quantities of Si, Fe, Zn, Cr and Ti with the balance being aluminum [1]. Elemental alloy additions result in superior mechanical properties and a heterogeneous microstructure. This gives high strength but this leads to a significant decrease in corrosion resistance [1]. As a result of mircostructural heterogeneity, localized attack occurs due to a fluctuating galvanic interaction with the matrix. This manifests in the form of pitting, crevice, intergranular and filiform corrosion [2-8]. It is therefore of considerable importance to understand the corrosion of these Al alloys and develop effective strategies to inhibit corrosion in aggressive environments.

The copper-containing second phase particles are nobler than the surrounding matrix and act as local cathodes causing pitting [3, 7, 8]. The constituent particles include Al_2CuMg, $Al_6(Fe,Mn,Cu)$, $(Al,Cu)_6Mn$, Al_7Fe_2Cu among which the S phase particles are the most abundant. S phase particles are first anodic to the matrix and undergo selective dissolution leading to a rich copper remnant and a non-faradaic redistribution of copper on the surrounding matrix [8]. The redistribution of copper is by its oxidization and reduction on the matrix and this serves to initiate new pits. The intact particle remnant is noble to the matrix and stimulates peripheral pitting [8]. Hence, suppression of localized attack can be achieved by protecting the Al_2CuMg precipitates from dissolution.

Chromates have been historically used to prevent the corrosion of these alloys [9, 10]. The toxicity and carcinogenic nature of the chromate ion has led to the development of alternative pigments that are environmentally acceptable and offer corrosion resistance to the high strength aluminum alloys. Among the candidate inhibitors are rare earth metal (REM) compounds, which have received much of attention over the past two decades. The early work by Hinton et al. by immersion in various concentrations of the rare earth chloride solutions to reduce the corrosion of high strength AA 7075 (Al-Zn-Mg-Cu), demonstrated that they can be good aqueous corrosion inhibitors [11, 12]. It was shown that the maximum inhibition of corrosion of AA 7075 in 0.1M NaCl occurs at a concentration of 100 ppm of the Ce^{3+}, La^{3+}, Y^{3+} chlorides and it remains constant at concentrations above this. These results were obtained from weight loss immersion tests for 21 days. Evidence of a colored film was seen after 21 days without any pitting while the substrate immersed in uninhibited NaCl solution was deeply pitted [11]. Potentiodynamic polarization of AA 7075 in 0.1M NaCl with 1000 ppm of chloride salts of Ce^{3+},

Pr^{3+}, Y^{3+} showed [12] an order of magnitude reduction of the ORR and the pitting process is delayed by shifting the corrosion potential (OCP) to the passive region away from pitting potential (E_{pit}). Among the rare earths, Ce has shown the most effective corrosion inhibition [11, 13, 14].

A 500 ppm addition of the mixed Ce^{3+}, La^{3+} inhibitors in a 1:1 ratio to 3.5 wt% NaCl solution, provided a six fold increase in polarization resistance on AA 5083 alloy and proved to be better synergistically than their individual additions [15]. Potentiodynamic polarization curves for the AA 2024 at different immersion times in 0.05M NaCl solution with and without 0.05% Ce^{3+}/La^{3+} nitrates [16]exhibited two breakdown potentials, one for the S phase at a negative potential to the second one which is for the intergranular corrosion. [16]. The reduction in the cathodic current (oxygen reduction) in the polarization curve with additions of 0.05 % $Ce(NO_3)_3$, increased with the increase in immersion time at OCP from 10 min to two hours before polarization. Polarization curves that were run after two hours of immersion at OCP also showed reductions in anodic currents of about two orders of magnitude until the second breakdown potential and ennoblement of the second breakdown potential increased with increase in immersion time. This suggests that cerium is a "slow inhibitor" as its inhibition efficiency increases with increase in exposure time. Polarization curves that were run with additions of 0.05% lanthanum nitrate also showed reduction in both anodic and cathodic currents but not to the extent of inhibition showed by that of $Ce(NO_3)_3$. However, inhibition by La^{3+} cation was immediate and it was seen at immersion times as small as 10 min. It does not seem to depend on exposure time indicating that lanthanum has faster kinetics of inhibition than Ce^{3+} cation [16].

The mechanism of inhibition by the rare earth cations is a cathodic mechanism where a barrier film on the cathodic sites shuts down the oxygen reduction reaction (ORR). Initial studies on AA 2024 clearly demonstrated the cathodic inhibition by the REM cations, which shifted the cathodic arm of the curve to more negative potentials away from the pitting potential. Hence, a mechanism that described the formation of an REM oxide/hydroxide film on the cathodic intermetallics was proposed. The local increase in the pH at the copper-bearing sites causes the precipitation of the hydroxides, which would form a diffusional barrier to the supply of oxygen. Scanning electron microscopy (SEM) and energy dispersive spectroscopy (EDS) studies proved this hypothesis [14, 17]. Yasakau et al. proposed that the higher efficiency of the Ce^{3+} cation over other REM cations could be because of the lower solubility of the Ce^{3+} hydroxide over others [16].

The presence of dense cerium rich hydroxide films, the difference in the kinetics of formation and the superior inhibition properties of Ce^{3+} are better explained by another mechanism [18]. As discussed earlier, the $2e^-$ oxygen reduction produces hydrogen peroxide, which oxidizes the Ce^{3+} to Ce^{4+}. The Ce^{4+} hydroxide formed is extremely insoluble having a critical pH of 3. Complete suppression of the cathodic corrosion process occurs by further addition of $Ce(OH)_3$ over the cathodic sites. The evidence for the presence of Ce^{4+} species is also reported [18, 19].

The film forming capabilities of the lanthanides led to the formulation of new alternative conversion coatings to the chromate conversion coatings (CCCs) by either immersion or electrochemical activation. Ce sealing of anodized 2024 Al alloy ($Ce(NO_3)_3$, H_2O_2, H_3BO_3) produced two layers of protection. The outer layer is the cerium conversion coating and the inner layer, a sealed anodized coating. This enhanced the protection of the alloy to the extent that no

signs of corrosion were detected after 60 days of immersion in 3.5 wt% sodium chloride solutions. The alloy remains passive until a 500 mV above its open circuit potential (OCP) which was -780 mV$_{SCE}$ (Saturated Calomel Electrode reference) during its anodic polarization with an almost zero current density [20]. The corrosion resistance was comparable to that of chromate sealed anodized coatings [21]. Mansfeld et al. [22] developed a three-step process in which the first and last involve immersion of the alloy in dilute hot Ce acetate and chloride solutions respectively and anodic polarization of 0.1V MSE in 0.1M Na$_2$MoO$_4$. ORR was completely inhibited by the strong oxide film thus formed and exhibited high resistance to localized corrosion.

New commercial pigments (Deft 02GN083, Deft 02GN084, and Deft 44GN098) contain releasable Pr^{3+}. The use of Pr^{3+} cation is comparatively novel and the inherent mechanism of protection by the cation on 2024-T3 alloy is not as widely reported. The objective of this work is to extend lanthanide inhibitor research and understand the mechanism and extent of corrosion inhibition by Pr^{3+} relative to Ce^{3+} and La^{3+} inhibitors. This chapter consists of inhibitor evaluation carried out by electrochemical potentiodynamic polarization experiments on AA 2024-T3 coupons and copper rotating disk electrode experiments. Free corrosion exposure experiments of the 2024-T3 coupons were carried out in inhibited chloride solutions and microscopic analysis was done on these samples to understand the mechanism involved.

5.3.1.2 Experimental Procedures

5.3.1.2.1 Materials and Chemicals AA 2024- T3 was the substrate material and the sheet stock coupons of 2 mm thickness were obtained from a commercial supplier. This alloy was solution heat-treated and cold worked with a nominal chemical composition of 3.8-4.9% Cu, 1.2-1.8% Mg, 0.3-0.9% Mn with the remainder being aluminum. The copper cylindrical rod with 5mm diameter (0.2in) and 99.999% (metals basis) used for rotating disk electrode experiments was purchased from Alfa Aesar. All the chemicals used for the electrochemical experiments (chlorides of cerium, praseodymium, lanthanum and sodium chloride) were of reagent grade and were obtained from commercial sources. Deionized water of 18.2 MΩcm resistivity was used in these experiments.

5.3.1.2.2 Preparation of AA 2024-T3 substrate. AA 2024-T3 coupons were shear cut into 2 cm x 2 cm square samples and the surface was wiped with ethanol to remove any dust. The coupons used for polarization experiments were polished starting from 600 grit until 1200 grit in ethanol to avoid any corrosion prior to potentiodynamic polarization experiments. The samples were then ultrasonically cleaned in acetone to remove any polishing particles that may have adhered to the surface during polishing. These samples were used immediately for polarization to avoid thickening of the aluminum oxide layer. The coupons used for free corrosion exposure experiments were abraded with the SiC grit papers and polished through 1μm diamond paste. These samples were ultrasonically cleaned and the backs of the samples were covered with an insulation tape to avoid any coupling between the two faces of the sample.

5.3.1.2.3 Potentiodynamic polarization. Polarization of AA 2024-T3 coupons was carried out using a Gamry^{TM} Ref 600 potentiostat. This was done in a standard three-electrode set up in a quiescent, aerated flat cell with a saturated calomel reference electrode and a platinum mesh as counter. The working electrode has an exposed area of 1 cm^2. Cathodic polarization was done in

0.1M NaCl solution with varying concentrations of rare-earth metal chloride starting from 50 ppm to 600 ppm to determine the extent of ORR inhibition and the window of maximum inhibition. All the scans were repeated at least twice and OCP was monitored for 30 min to obtain a stable OCP prior to polarization. The cathodic scan was started at 20 mV above OCP and it was stopped after the water reduction has started (about -2.0 V below OCP). The scan rate used was 0.5 mV/s. The polarization curves were analyzed using Gamry's Echem Analyst^{TM} software.

5.3.1.2.4 Free corrosion exposure. AA 2024-T3 coupons were exposed to 40 ml of 0.1M NaCl solutions containing 300 ppm of Ce, Pr and La chlorides for a period of 24 hours. The coupon was immersed with the polished surface facing upward and the surface covered with insulting tape facing downward. A control sample was also immersed in chloride-only solution without any inhibitor addition. At the end of the exposure, these samples were washed with ethyl alcohol and air-dried. They were visually investigated and the microstructural differences were examined using a Quanta 200 Scanning Electron Microscope with an EDS component attached to it that is used for chemical mapping of the surface. A scanning electron microscope with an accelerating voltage of 20 kV was used for all characterizations. An energy dispersive spectrometer is used for chemical mapping of a spot or an area on the surface for elemental analysis.

5.3.1.2.5 Polarization on copper rotating disk electrode. A Cu rotating disk electrode was used to study the effect of dissolved lanthanide cations of concentrations of 100 ppm on the oxygen reduction kinetics in aerated 0.1M NaCl solution. Cu was selected as an electrode material as a model for the Cu-rich intermetallic particles that serve as sites for pitting in Al alloys.

A changeable Cu electrode tip with a diameter of 5 mm and a length between 3mm to 4mm was cut using a Buehler made IsoMet® Low Speed Saw machine. The Cu sample was then ultrasonically cleaned to avoid contamination from the lubricating oil. The Cu disk was then carefully embedded into the Teflon^{TM} change disk tip using the tools purchased from Pine Instruments. A thin layer of red lacquer was coated on the lateral circumference of the copper disk to make sure that no current signal is picked up from this region. The Teflon^{TM} change disk along with embedded copper is then polished through the silicon carbide grit papers in ethanol (Buehler made 600 grit- 2400 grit) and through the diamond pastes (6 μm, 1 μm) and finally polished using colloidal silica (0.05 μm). This was done to make sure that the copper and the outer Teflon^{TM} surface were at the same level. Again, the polishing in ethanol was done to avoid any corrosion prior to the polarization experiments. A specially designed holder made out of Plexiglass^{TM} was used to polish the Teflon change disk tip to avoid bumps and reduce the irregularities on the sample surface that could originate when polishing the small Teflon^{TM} disk tip alone.

Cathodic polarization curves were run on the copper disk while rotating the electrode at 500 rpm, 1000 rpm, 1500 rpm and 2000 rpm using a modulated speed rotator from Pine Research Instrumentation. The scan was started after conditioning the electrode at -620 mV$_{SCE}$ for 10 min and stopped at -1200 mV$_{SCE}$. The scan rate was 0.5 mV/s. The data were analyzed using the Levich equation [23]:

$$i_L = \frac{I_L}{A} = 0.2nFC_B D_O^{\frac{2}{3}} \nu^{-\frac{1}{6}} \omega^{\frac{1}{2}}$$

(eq. 3.1.1)

where i_L is the limiting current density in mA/cm^2, I_L is the limiting diffusion current, A is the area of the electrode, D_o is the diffusion coefficient of O_2 (2.7×10^{-5} cm^{2}s^{-1}) [24], ν is the kinematic viscosity (0.01 cm^{2}s^{-1}) [25], C_B is the bulk concentration of O_2 (7 ppm), ω is the rotation rate in rpm, n and F represent the number of electrons exchanged in the cathodic reaction and Faraday's constant respectively. The bulk concentration of oxygen was determined from visual inspection using a dissolved oxygen test kit, Model 0-12 obtained from CHEMetrics, Inc.

5.3.1.3 Results

5.3.1.3.1 Speciation of the lanthanide ions. The MEDUSA^{TM} (Make Equilibrium Diagrams Using Sophisticated Algorithms) software package is a thermodynamic chemical equilibrium modeling tool capable of a multiple point survey for the trend analysis due to the effect of change in pH of the electrolyte solution. The HYDRA software embedded within the MEDUSA software contains a hydrochemical equilibrium constant database with logK values at 25 ˚C. The database provided with HYDRA was developed at Inorganic Chemistry, Royal Institute of Technology (KTH), Stockholm, Sweden. The HYDRA software enables one to define the aqueous chemical system of interest where the starting concentration of the cationic and anionic species in solution and/or partial pressures of gases known can be entered as inputs by the user. Data can be added or removed or modified if needed after the input file has been opened by MEDUSA to generate the diagram.

AA 2024-T3 has a complex microstructure and significant pH fluctuations on the surface during corrosion due to the oxygen reduction reaction and hydrolyses of the metal cations are possible. Speciation and solubility of rare earth cations is pH-dependent. Therefore, studying the speciation of the lanthanide cations sheds light on operating mechanism of inhibition by these cations. The inputs needed to develop concentration vs pH diagrams are chloride ion concentration (100 mM [Cl$^-$]), 300 ppm of the REM chloride salt and the partial pressure of carbon dioxide gas in air, which is about $10^{-3.5}$ atm. Several authors have studied the speciation diagrams of the lanthanide cations but the effect of carbon dioxide was not taken into consideration [16, 26].

The speciation diagram obtained by adding 300 ppm of Ce^{3+} ions in 0.1M NaCl solutions with and without CO$_3^{2-}$ anions are shown in Figures 3.1a and 3.1b respectively. The concentrations of different ionic species and precipitated compounds were plotted on a logarithmic scale as a function of pH. The natural pH of the solution was at a value little less than 6 and is indicated by a bar in the plots. Figure 3.1a shows the solubility of the Ce^{3+} cation in the presence of OH$^-$ and Cl$^-$ ions. The solubility of the total Ce^{3+} ion concentration remained high in the solution until pH 7.6 predominated by the presence of uncomplexed Ce^{3+} cation. Other complex cations CeCl^{2+} and CeCl$_2^+$ were also present in the acidic and neutral pH conditions, at concentrations of about an order and two orders of magnitude, respectively, lower than that of Ce^{3+} cation. The red dashed line represents the sum of the concentrations of the dissolved species (solubility). The solubility reduced steeply above pH 7.6, by about three orders of magnitude due to the hydrolysis of the cation to form Ce(OH)$_3$ precipitate. The total solubility was minimum from pH

8.7 through pH 12.6 due to the lower solubility of dissolved $Ce(OH)_3$. The solubility slowly rose above pH 12.6 by further hydrolysis to form $Ce(OH)_4^{-1}$. Thus, it can be predicted that the film formation for Ce^{3+} occurs when the pH of the electrolyte falls in the valley between pH 7.6 and pH 12.6 due to hydrolysis of the cation to form $Ce(OH)_3$ deposits.

Figure 3.1b shows the solubility diagram due to additional complexation with carbonates. The black dotted line represents the sum of the concentrations of the dissolved species. The change in the total solubility of Ce^{3+} due to addition of CO_2 is shown in the diagram by superimposing the total solubility of Ce^{3+} in the absence of CO_2 adopted from Figure 3.1a (red dashed line). Soluble Ce^{3+} cations predominated the lower pH regions below pH 6.15 in Figure 3.1b and the total solubility started to reduce drastically above pH 6.15 due to complexation with carbonate anions to form $Ce_2(CO_3)_3$ precipitate. The total solubility was minimum at pH 8.8 due to the sparingly soluble $Ce(CO_3)^+$ and insoluble $Ce_2(CO_3)_3$ precipitate. The solubility increased steadily from pH 8.8 until the precipitate completely dissolved above pH 14 by further complexation with carbonate anions to form soluble $Ce(CO_3)_2^{-1}$ anion. Hence, complexation with carbonates shifted the pH valley for film formation to lower pH values of pH 6.15 from pH 7.6 and deepened the valley by about two orders of magnitude. This means that carbonate anions aid in the precipitation of the Ce^{3+} cations due to small increments in the pH of the electrolyte above 6.15 by forming a much more insoluble carbonate precipitate.

The solubility diagrams for Pr^{3+} and La^{3+} cations in the absence of CO_2 are not shown as they were similar to that of the Ce^{3+} cation. Figures 3.1c and 3.1d show the solubility diagrams for Pr^{3+} and La^{3+} cations respectively in the presence of CO_2. The REM carbonate started to precipitate at a pH of about 6.15 for Ce and Pr and at a pH of 5.85 for La. The solubility rose slowly above pH 8.8 for all the REM cations. Above pH 8.8, the solubility started to increase by further complexation with the carbonate anions.

Half an order of magnitude increase in pH from 5.5 to 6 decreased the solubility of the La^{3+} ions drastically by about three orders of magnitude while the solubility of Ce^{3+} and Pr^{3+} ions still remained higher than that of lanthanum. This was observed directly during the preparation of lanthanum chloride inhibited sodium chloride solutions where lanthanum took longer time to dissolve when compared to the chlorides of cerium and praseodymium.

The speciation diagrams help us understand the local chemistry of the interfacial electrolyte layer on AA 2024, which undergoes variation of pH at different regions due to its heterogeneous microstructure. It can be concluded from these thermodynamic calculations that CO_2-bearing precipitation aids in the film formation by Ce^{3+}, Pr^{3+} and La^{3+} cations on the Cu-rich sites which experience local increases in pH.

5.3.1.3.2 Potentiodynamic polarization in aerated conditions. Cathodic polarization of AA 2024-T3 coupons was carried out in aerated 0.1M NaCl solutions containing rare earth metal chloride salts at their natural pH. The purpose of these experiments was to verify the cathodic inhibition known for Ce^{3+} cation and check whether or not Pr^{3+} and La^{3+} cations provide comparable inhibition. Varying the concentrations of these cations enables identification of the critical concentration that provides maximum inhibition. Polarization in chloride-only solutions

was done to compare the effect of addition of lanthanide cations on the kinetics of the oxygen reduction reaction. Figures 3.2a, 3.2b and 3.2c show the polarization curves of Ce^{3+} Pr^{3+} and La^{3+} cations respectively with concentrations ranging from 50 to 600 ppm. Ce^{3+}, Pr^{3+} and La^{3+} inhibited ORR to varying extents. Ce^{3+} shifted the cathodic arm of the curve near the corrosion potential to the maximum extent while La^{3+} barely caused a change in the cathodic arm of the curve. An increase in cathodic kinetics was observed at potentials below -1.0 V_{SCE} for all the solutions with inhibitor additions compared to the chloride-only solution. The inhibitors shifted the open circuit potential (OCP) to negative potentials away from the pitting potential thus improving the corrosion resistance by decreasing the tendency for pit initiation. This shift in OCP to active potentials for Ce^{3+} and Pr^{3+} was higher at concentrations of 50 ppm – 300 ppm and lower at 600 ppm while the shift in OCP for La^{3+} was same at all concentrations of 50 ppm – 600 ppm.

(a)

(b)

(c)
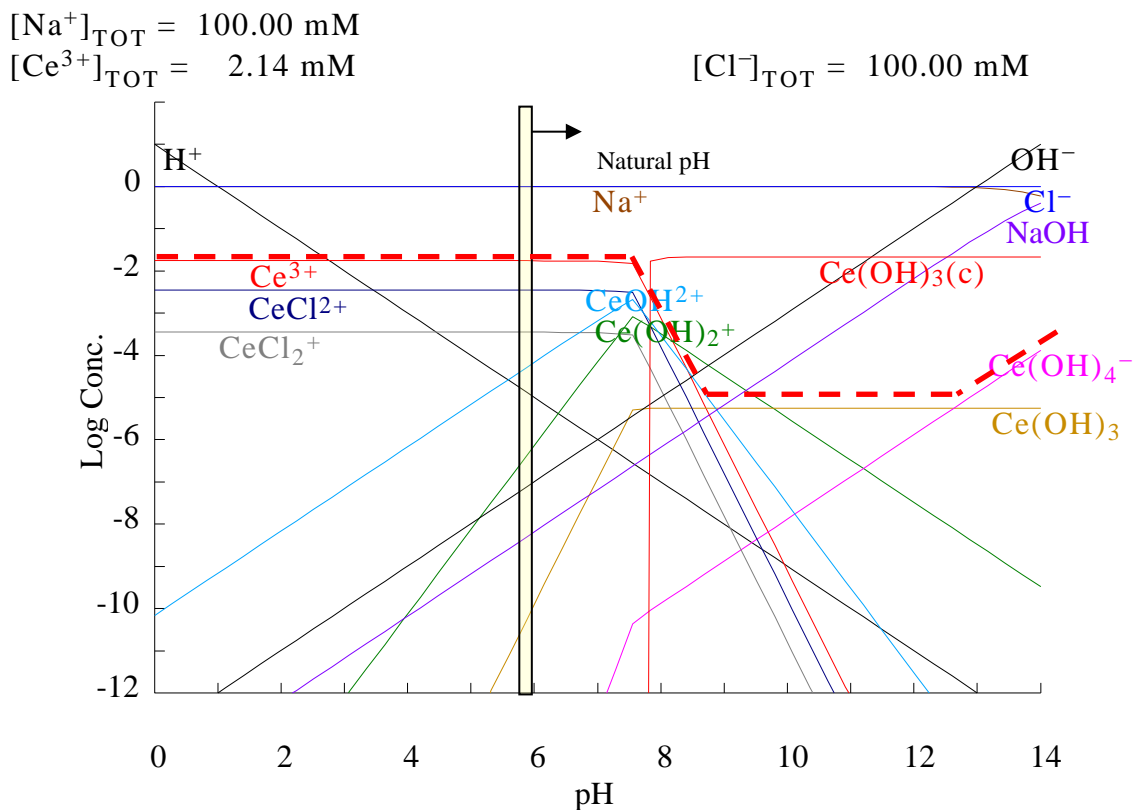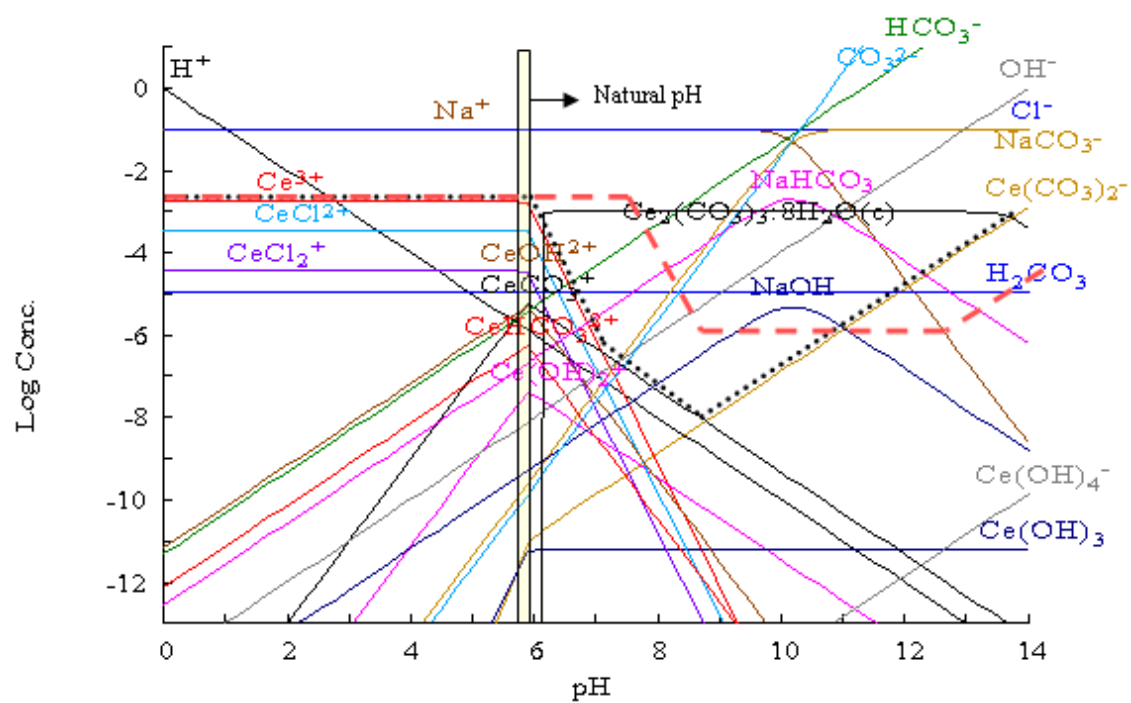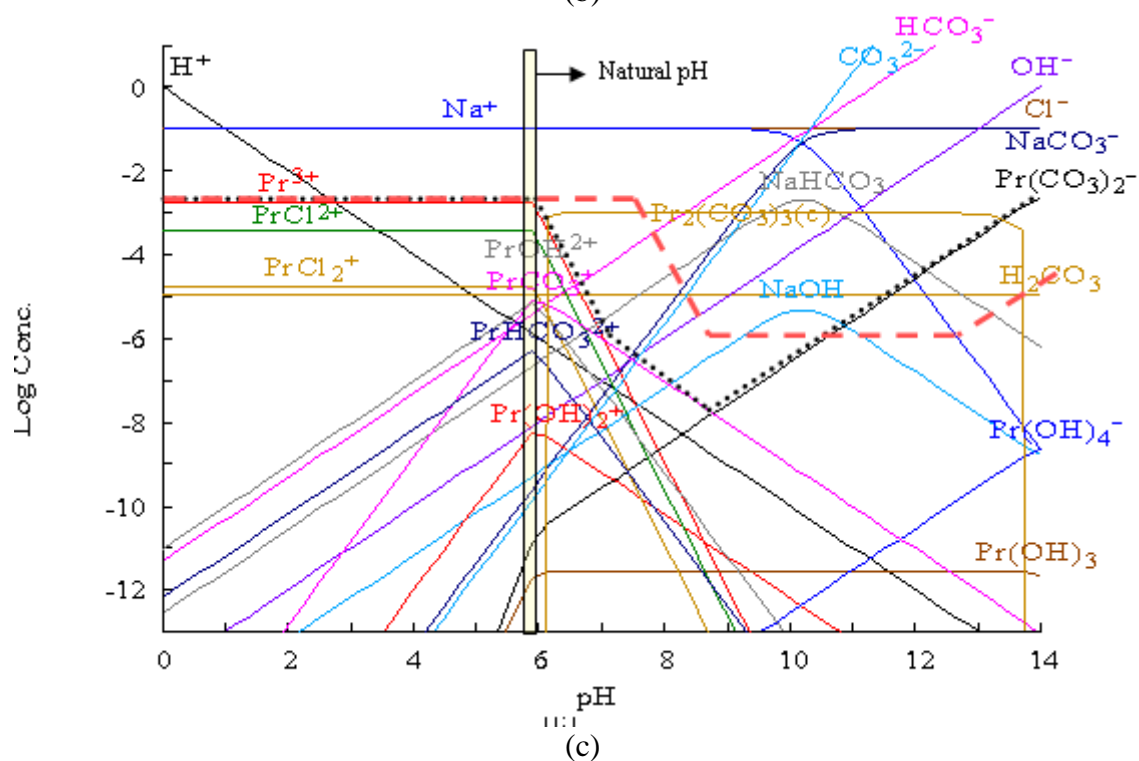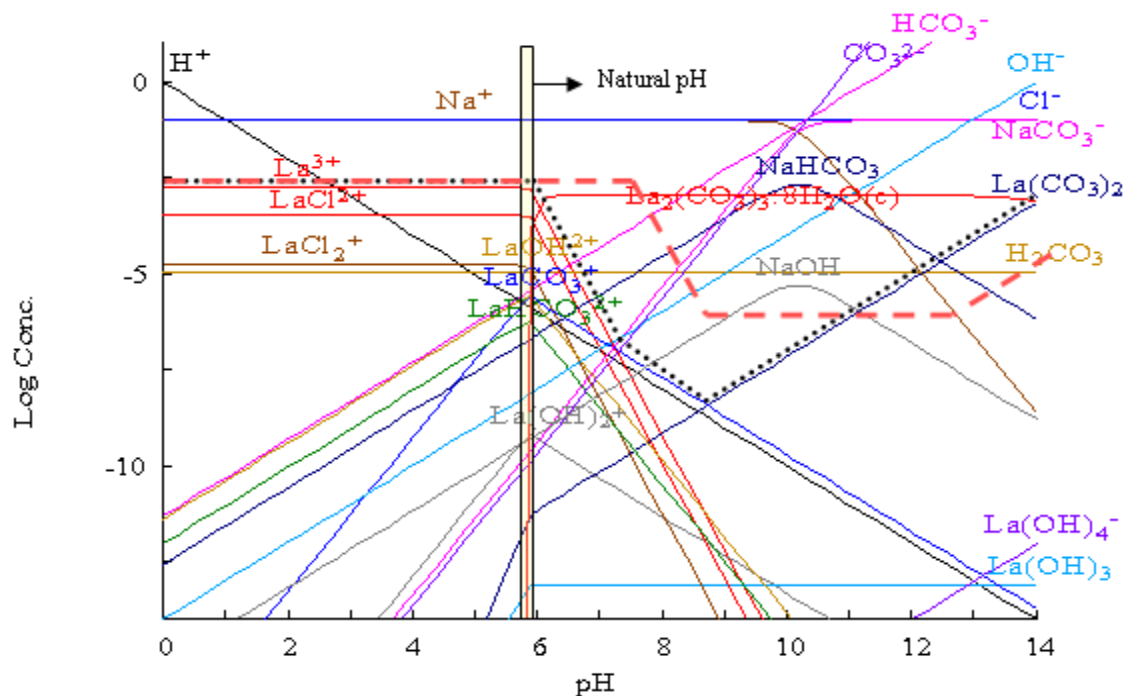
(d)

Figure 3.1. (a) Speciation diagram for Ce species in 0.1M NaCl +300 ppm of Ce^{3+} ion in the absence of carbonates (OH$^-$ and Cl$^-$ anions). Speciation diagram for (b) Ce (c) Pr (d) La species in the presence of carbonates from atmospheric CO_2 (OH$^-$, Cl$^-$ and CO_3^{2-} anions) in 0.1M NaCl +300 ppm of cation
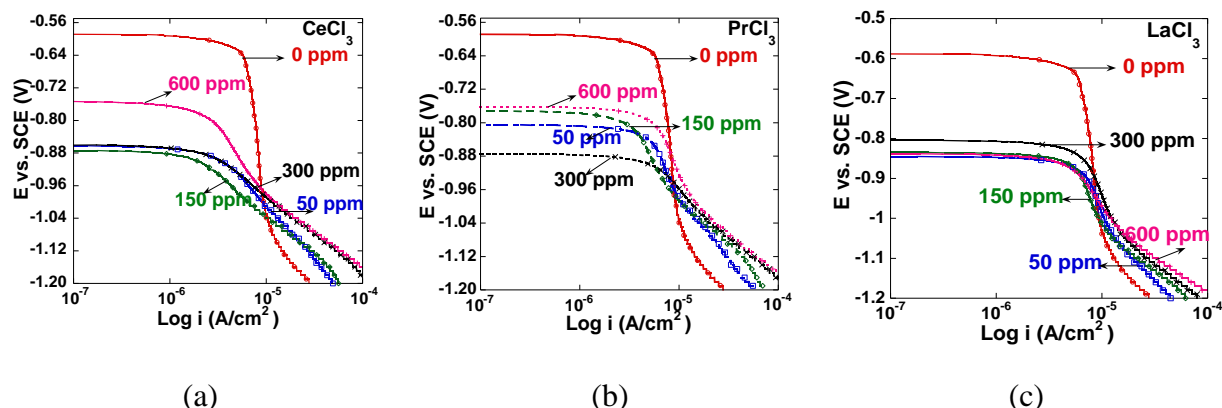
(a)   (b)   (c)

Figure 3.2. (a) Cathodic polarization curves of AA 2024-T3 in aerated 0.1M NaCl solution with different concentrations of (a) CeCl$_3$. (b) PrCl$_3$ (c) LaCl$_3$.

5.3.1.3.3 Free corrosion exposure in lanthanide solutions. AA 2024-T3 coupons were immersed at open circuit in 100 mM NaCl solution containing 300 ppm of the inhibitor chloride at natural pH. Visual inspection shows inhibition by Ce^{3+} and Pr^{3+} was comparable while La^{3+} showed least inhibition relative to the sample immersed in chloride-only solution. The sample

immersed in Ce^{3+} remained bright while that in Pr^{3+} turned grey with no visible pits. The sample in La^{3+} turned light brown with visible pitting across the surface. SEM analysis of the surface, compositional mapping, and spot EDS analysis were done to characterize deposition of Pr^{3+} and La^{3+} cations on alloy surfaces.

Figure 3.3a shows the SEM image of the coupon immersed in the Pr^{3+} inhibited chloride solution. Pitting took place adjacent to the blocky intermetallics and the number of pits was reduced when compared to the control sample exposed in the chloride only solution (not shown). The spot EDS analysis on intermetallic particles showed evidence of the presence of Pr species. Chemical mapping of an area on the sample is shown in Figure 3.3b. The Pr and oxygen maps suggested possible precipitation of an oxide or hydroxide or a carbonate hydroxide of Pr over the intermetallics. There was no evidence of magnesium present in the intermetallics in the chemical maps of the samples immersed in inhibitor-free solutions. The presence of intact Mg in the S phase (Al_2CuMg) as seen in the magnesium mapping of the coupon immersed in Pr^{3+} inhibited solutions indicated that Pr^{3+} ions suppressed the selective dissolution of Mg from the intermetallic particles. Al_2CuMg and AlCuFeMn intermetallics act as local cathodes and support the oxygen reduction causing an increase in the pH at the intermetallic/electrolyte interface. This reduced the solubility of the Pr^{3+} cation in the interfacial electrolyte leading to precipitation on the intermetallic particles thus retarding the oxygen reduction.

As previously reported, spot EDS analysis on the coupon immersed in Ce^{3+} inhibited solution, showed the presence of cerium on the S phase intermetallic particles. Mapping showed the presence of Ce on the intermetallic particles adjacent to which pitting took place. This also verified the mechanism of inhibition of Ce^{3+} ion widely discussed in the literature where corrosion is a precursor to the inhibition by the Ce^{3+} cation [14, 16-18]. The oxygen reduction reaction on the noble intermetallic particles produces an alkaline interfacial electrolyte facilitating the deposition of a cerium compound.

Figure 3.4a shows the SEM micrograph and spot EDS analysis of the coupon immersed in the La^{3+} inhibited chloride solution. Big, flowery particles (~200 μm) which were probably precipitates of $La_2(CO_3)_3$ or $La(OH)_3$ are seen. A closer look at the copper map gives an idea of the distribution of intermetallic particles on the surface. The La map did not show any local islands of lanthanum precipitates on these intermetallics but precipitation and growth seemed to have occurred by a different mechanism. These large particles were not expected to contribute to corrosion inhibition, as they do not form any kind of physical barrier for the cathodic reaction supporting intermetallic particles. Al_2CuMg intermetallics were much smaller than these massive particles. Hence, no inhibition was seen by La^{3+} ion inhibitor.
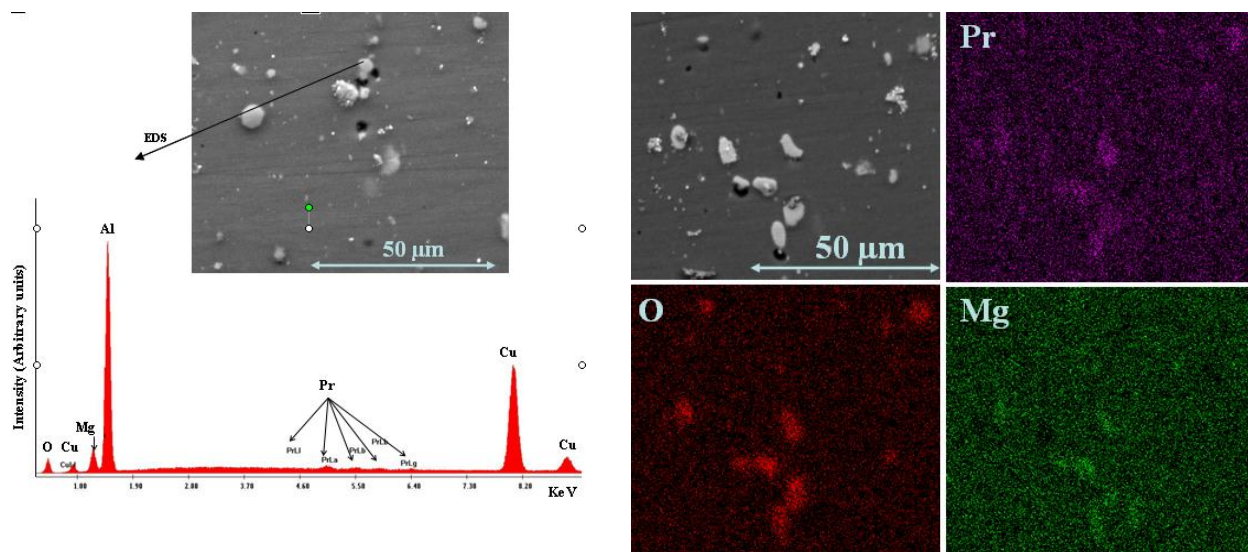
(a)   (b)

Figure 3.3. (a) SEM image of the AA 2024-T3 coupon exposed in 0.1M NaCl solution containing 300 ppm of Pr^{3+} cation for a period of 24 hours. (b) Backscattered electron image of the coupon immersed in Pr^{3+} inhibited solution and EDS mapping of the area in the image showing chemical maps of Pr, Mg and O.
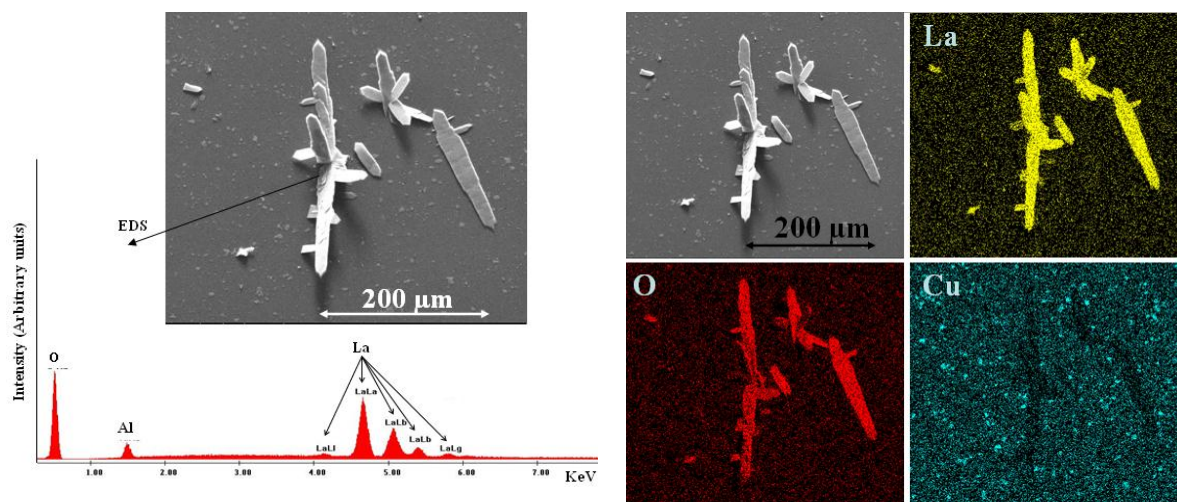
(a)   (b)

Figure 3.4. (a) SEM image of the AA 2024-T3 coupon exposed in 0.1M NaCl solution containing 300 ppm of La^{3+} cation for a period of 24 hours. (b) Backscattered electron image of the coupon immersed in La^{3+} inhibited solution and EDS mapping of the area in the image showing chemical maps of La, Cu and O.

5.3.1.3.4 Cathodic Polarization on Copper Rotating Disk Electrode. AA 2024-T3 is subjected to local cathodic corrosion. Cu-rich sites support the oxygen reduction reaction, which produces high local pH zones above and around the site. High pH promotes the selective dissolution of the

S phase and dissolution of Al matrix phase adjacent to the intermetallic particle. This leads to peripheral attack around the site or dealloying of the S phase leaving copper remnants behind. These intact Cu-rich remnants may further induce localized corrosion due to accelerated galvanic attack at their periphery in the matrix. The inhibition of oxygen reduction reaction on copper-containing intermetallics is important in reducing the corrosion rate of the alloy. Therefore, characterizing the oxygen reduction reaction kinetics on copper in chloride solutions containing inhibitor additions should shed light on the extent of inhibition caused by these cations on the 2024-T3 alloy.

The cathodic polarization curves of copper rotating disk electrode in blank 0.1M NaCl solutions were done at rotation rates ranging from 500 rpm to 2000 rpm. Polarization curves were collected immediately after conditioning the Cu electrode for 10 min at -620 mV_{SCE}. Slight deflection of the curves at -620 mV_{SCE} was seen due to the reduction of Cu oxide to Cu. In neutral chloride-only solutions, the polarization curves on copper show a rotation rate dependent cathodic current to a potential of -1.2 mV_{SCE} where the cathodic kinetics increase with a rotation rate increase. Cathodic polarization experiments were carried out on Cu RDE in the presence of 100 ppm of Ce^{3+}, Pr^{3+} and La^{3+}. A reduction in cathodic kinetics was observed by the addition of 100 ppm of the lanthanide chloride salts as the band of polarization curves shifted to lower current densities. The current-rotation rate dependence decreased for Ce^{3+} inhibitor and it was completely lost for the Pr^{3+} and La^{3+} inhibitors. The cathodic current seemed to decrease with increase in cathodic potential for Pr^{3+} and La^{3+}. After each experiment, the electrode showed a visible film completely covering the surface of the copper electrode suggesting an electrode blocking effect. The high alkalinity produced by the reduction of oxygen during the cathodic polarization, caused the deposition of the insoluble compound on the surface, thus reducing the oxygen reaction kinetics.

The potential-current behavior of the copper rotating disk at 2000 rpm is plotted in Figure 3.5 in the chloride-only and inhibited solutions for a comparison. Ce^{3+} reduced the ORR kinetics by less than half an order of magnitude of cathodic current while La^{3+} and Pr^{3+} reduced the cathodic current by more than half an order of magnitude. Kendig et al. had seen about half an order of magnitude of reduction in the ORR current in 5 wt% NaCl solution in the presence of 10 mM of Ce^{3+} inhibitor [9]. Of all the inhibitors, Pr was observed to provide the highest reduction in the ORR current up to cathodic polarizations of -1.1 V_{SCE}.
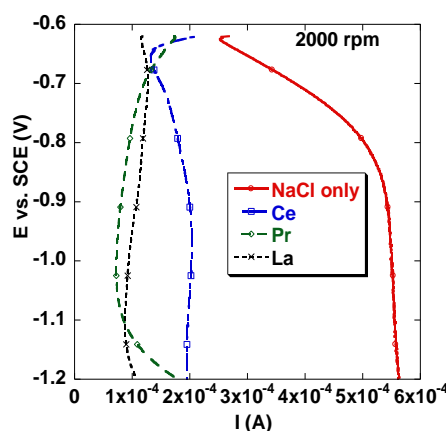
Figure 3.5. Comparison of the cathodic polarization curves on copper rotating disk electrode in chloride only solution and 100 ppm of REM cation (Ce, Pr, La) inhibited chloride solutions at 2000 rpm

5.3.1.4 Discussion

5.3.1.4.1 Inhibition of oxygen reduction reaction. Many researchers have reported the cathodic inhibition caused by the Ce^{3+} and La^{3+} cations [12-18, 27-29]. Cathodic polarization studies have verified the inhibition by these cations. It is found that Pr^{3+} acts by suppressing the oxygen reduction reaction. However, these cations did not provide anodic inhibition, which is assessed by a rise in the pitting potential or a reduction in the overall anodic kinetics after half an hour of immersion at the open circuit potential before polarization. The inhibition of the oxygen reduction reaction shifted the corrosion potential in the negative direction, thus decreasing the tendency of the alloy to undergo localized corrosion under free corrosion exposure.

The cathodic polarization data were used to extrapolate the corrosion rate with the aid of Gamry Echem Analyst^{TM} software. A tangent drawn approximately 100 mV below the OCP along the cathodic arm of the curve intersected the horizontal line drawn at OCP at a point. A vertical line drawn parallel to the potential axis (Y-axis) at this intersection point intersected the current density axis (X-axis) at a second point from where the corrosion current density (corrosion rate) was read. Figure 3.6 shows a plot of the corrosion rate of aluminum 2024 versus the concentration of cationic inhibitors as metal chlorides in 0.1M NaCl solution. The lanthanide cations exhibited concentration windows in which their inhibition is maximum. This range was typically 100 – 300 ppm. Similar results were seen by Hinton et al. where small concentrations of 100-1000 ppm of Ce and La chloride solutions showed maximum inhibition on AA 7075 alloy as obtained from free immersion studies [28]. Among all the lanthanides, the data here suggest that Ce^{3+} provides maximum inhibition by reducing the ORR kinetics by half an order of magnitude followed by Pr^{3+}. In the order of concentrations studied here, La^{3+} barely changed the corrosion rate of the 2024-T3 alloy even though it seems to provide good cathodic inhibition as reported elsewhere [16]. The solubility diagrams suggest that the natural pH of the solutions (pH 5.8 – pH 6) is slightly above the La^{3+} precipitation, but slightly below that for Ce^{3+} and Pr^{3+}. This could contribute to the relative inhibition seen by the three cations.
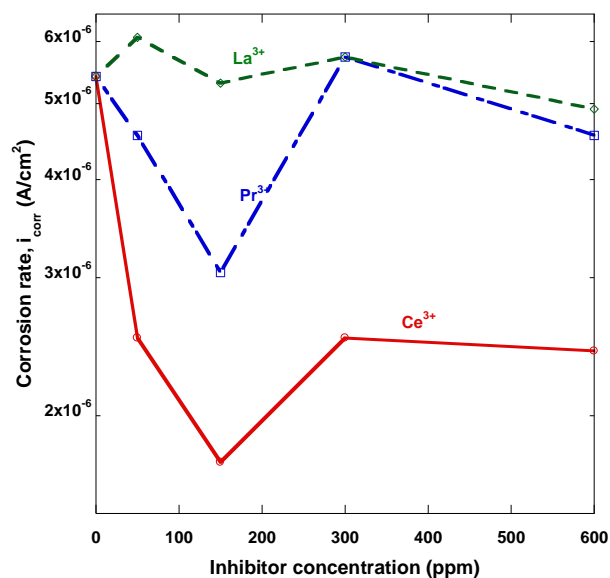
Figure 3.6. Comparison of the rates of corrosion at different rare earth inhibitor chloride concentrations (obtained from polarization studies)

5.3.1.4.2 Quantification of the reduction kinetics and the inhibition. The Levich representation of mass transport limited ORR on copper as a function of rotation rate at -850 mV bias and -900 mV SCE bias for chloride-only and inhibited solutions is shown in Figure 3.7. The linear dependence of I_L on $\omega^{1/2}$ in the chloride-only solution indicates that the reduction of oxygen on Cu is limited by diffusion [23]. The slope of the fit to the data for the uninhibited solution is represented by a constant, k, given by,

$$k = \frac{I_L}{A\omega^{\frac{1}{2}}} = 0.2nFC_B D_O^{\frac{2}{3}} \upsilon^{-\frac{1}{6}}$$

(eq. 3.1.2)

where A is the area of the Cu electrode exposed which is 0.196 cm^2 (5 mm diameter), I_L is the limiting current and all the other symbols carry the same meaning as explained above.

For an electrode area of 0.196 cm^2, an oxygen diffusion coefficient of 2.7 x 10^{-5} cm^2 /s [24], a kinematic viscosity of 0.01 cm^2 /s [25], and a bulk dissolved oxygen concentration of 2.2 x 10^{-4} moles/l, the value of 'n' obtained for the chloride-only solution was less than 4 from equation 2. This suggests that two possible routes exist for the electrochemical reduction of oxygen; a 2 electron and a 4 electron process. The oxygen diffused from the bulk to the surface could reduce to peroxide and the peroxide formed could get transported into the solution resulting in a 2 electron process. If the peroxide formed further reduces to hydroxide, this results in a 4 electron process [25, 30].

Assuming that lanthanide additions to the solution do not change the diffusion coefficient and the viscosity of solution, and further assuming that the ORR mechanism does not change and that the proportionality between the limiting current density and rotation rate remains, we could estimate the electrode area supporting the ORR with the addition of lanthanide additions. The precise values of the variables in the Levich equation might be debated, particularly in view of the addition of lanthanum cations to the solutions, but the magnitudes of the changes would be small and would not be expected to produce more than half an order of magnitude of reduction of the limiting current, I_L. For these reasons, we interpret the large change in I_L as an electrode blocking effect associated with the deposition of lanthanide compounds on the electrode surface.

The Levich representation of the polarization curves obtained in 100 ppm rare earth metal inhibited chloride solutions are also shown in the Figure 3.7. The slope of the respective lines of the inhibited solutions, k_{REM} is given by,

$$k_{REM} = \frac{I_L}{\omega^{\frac{1}{2}}} = 0.2 A_{REM} n F C_B D_O^{\frac{2}{3}} \upsilon^{-\frac{1}{6}}$$

(eq. 3.1.3)

where A_{REM} is the effective area of the Cu electrode supporting oxygen reduction. Assuming all the other parameters on the right hand side (RHS) of the equation 3.1.3 remain the same, the ratio of the slopes, R, is the ratio of the area of the copper electrode supporting ORR in the rare earth metal inhibited solution to the area of the copper electrode supporting ORR in the chloride-only solution. Equation 3.1.4 is obtained by taking a ratio of the equations 3.1.2 and 3.1.3. This ratio, at a constant rotation speed is essentially the ratio of the limiting currents or the rate of oxygen reduction reaction in the presence and absence of the inhibitor. Hence, this could quantify inhibition where low value of R implies good inhibition.

$$R = \frac{k_{REM}}{k} = \frac{A_{REM}}{A}$$

(eq. 3.1.4)

The Ce^{3+} cation gave an R value of 0.376. The La^{3+} cation gave an R value of 0.207 while the Pr^{3+} cation gave an R value of 0.171. Pr^{3+} exhibits the lowest R value and hence it is a better cathode blocker when compared to the others. La^{3+} also provided good inhibition and is comparable to that of Pr^{3+} and higher than that of Ce^{3+}. Kendig et al. found that the R value of a 0.01 M chromate solution in pH 6 chloride solution was determined to be 0.019 while the value of R for strontium chromate (pH 8.3 from Baker Colors) was found to be 0.002 [31]. On the basis of this comparison, the lanthanides are modest inhibitors of cathodic kinetics on copper. The cathodic polarization on the 2024 alloy showed higher inhibition of the cathodic kinetics by Ce^{3+} while Pr^{3+} showed best inhibition on copper. This is because of a contribution of numerous factors like the difference in experimental conditions, complex microstructure of 2024, etc. Mg-containing S phase particles are first anodic to the matrix while other alloying elements like Fe, Mn form the second most populated Al-Cu-Fe-Mn intermetallics, which could also influence the efficiency of inhibitors.
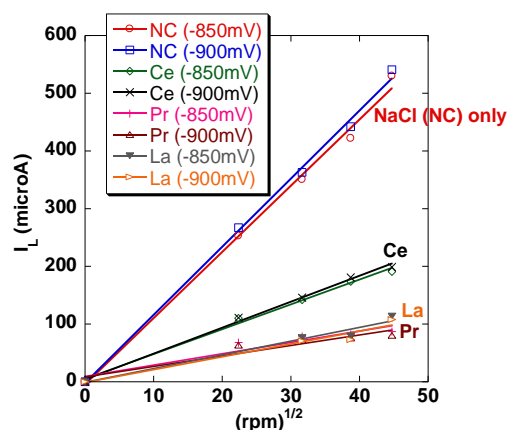
Figure 3.7. Levich representation of the oxygen reduction reaction kinetic data obtained from the polarization curves on Cu RDE in chloride only solutions and chloride solutions containing 100 ppm of the REM cations. (NC stands for 0.1M NaCl solution without any inhibitor additions). The two lines for each cation indicate the data extracted at either -850 mV_{SCE} or -900 mV_{SCE}.

Differences in the efficiency of the lanthanide inhibitors on different high strength alloys like AA 7075-T6, AA 5083 had been reported indicating that the lanthanide cations are substrate specific [11, 13, 15, 32]. Yasakau et al. found that AA 5083 alloy substrates immersed in 1 mM concentrations of La^{3+} in 0.05 M NaCl solution for a period of 14 days exhibited an order of magnitude higher total impedance and higher oxide resistance from Electrochemical Impedance Spectroscopic (EIS) measurements when compared to the substrates immersed in 1 mM concentrations of Ce^{3+} in 0.05 M NaCl solution [32]. Mishra et al. found that the polarization resistance from EIS measurements on AA 2014 substrates in 3.5 wt% NaCl solutions with $CeCl_3$ inhibitor additions at all concentrations (250 ppm - 1000 ppm) was half an order of magnitude higher than $LaCl_3$ inhibitor additions [13]. The corrosion rate of AA 7075 in 0.1 M NaCl solution after 21 days (determined from weight loss tests) was found to be lower for 100 ppm $CeCl_3$ additions than 100 ppm $LaCl_3$ additions [11].

5.3.1.4.3 Mechanism of inhibition. The copper-rich intermetallic particles play an important role in the overall corrosion of the high strength alloy, 2024-T3. The mapping of the intermetallic particles immersed in Ce^{3+} and Pr^{3+} inhibited solutions showed that magnesium was still intact after immersion for 24 hours. This is interesting as the coupons immersed in undoped solutions became completely devoid of magnesium in the intermetallic particles. Hence, Pr^{3+} suppresses the dissolution of the S phase by forming a film affecting the oxygen reduction kinetics, thus reducing the anodic kinetics. The mechanism of corrosion inhibition of the alloy by the Pr^{3+} ion in solution is very similar to that of the Ce^{3+} ion studied before.

The maps showed a uniform background layer of the rare earth metal cations on the surface and islands of the lanthanide oxide/hydroxide on the intermetallic particles. This background layer was reportedly formed after a few hours of immersion and the islands were formed with the more active anodic and cathodic sites present within the microstructure [33]. Cerium deposits were contained on the Mg-containing S phase particles and were absent on the Al-Cu-Mn-Fe particles.

Similar results had been reported by Yasakau et al.[16]. Pr^{3+} also exhibited a similar behavior where Pr deposits were more concentrated on the S phases while no deposits are seen on the Fe containing intermetallics.

Hinton et al. had seen similar dendritic or lenticular particles of lanthanum oxide/hydroxide on AA 7075-T6 alloy after immersing the alloy in La chloride inhibited solution for 48 h [14, 33]. The development of such larger particles is an indication of continued corrosion through the sub-microscopic pores in the protective film. Huge particles of about 200 μm of lanthanum oxide/hydroxide were seen suggesting that high localized regions of alkalinity must extend into the solution through these pores, sustaining the growth of these lenticular particles. Hence, La^{3+} is unable to hinder the submicroscopic corrosion while Ce^{3+} and Pr^{3+} are able to form a much more robust film suppressing the localized corrosion attack. Therefore, the extent of inhibition and microscopic features are subjective to the substrate and the type of the REM cation [33]. Electrochemical experiments proved that these can have a strong influence on the rate of the ORR on the metal substrate.

5.3.1.5 Conclusions

1. Rare earth metal cations suppress ORR to varying extents on 2024-T3 alloy. Electrochemical polarization data show that Ce^{3+} and Pr^{3+} have windows of concentration in which their corrosion rate was found to be minimal (100 ppm – 300 ppm). Ce^{3+} provides maximum inhibition by reducing the corrosion rate by half an order of magnitude followed by Pr^{3+}. La^{3+} barely changes the corrosion rate of the alloy.

2. Lanthanide inhibitors are modest inhibitors of cathodic kinetics on copper. Rare earth cations suppress ORR on Cu by more than half an order of magnitude. Among the cations, Pr^{3+} and La^{3+} are seen to be better cathode blockers than Ce^{3+}.

3. The mechanism of Pr^{3+} cation is very similar to that of the Ce^{3+} cation. Pr^{3+} suppresses the selective dissolution of Mg from the intermetallics by precipitating a barrier film on the S phase and shuts down the oxygen reduction kinetics. It could be potentially used as a corrosion inhibitor for 2024-T3 that is an alternative to chromates.

4. La^{3+} is not an effective inhibitor of localized corrosion of 2024-T3. It could be due to the low solubility of the cation under natural pH conditions. La^{3+} does not hinder the localized corrosion on the alloy as it forms huge deposits of La oxide/hydroxide across the surface, with no film formation on the Cu-rich sites.

5.3.2 - Evaluation of the corrosion inhibition of AA 2024-T3 alloy by the cationic inhibitor, Zn^{2+}

5.3.2.1 Introduction

Chromate pigments and primers are known to provide excellent corrosion protection to AA 2024-T3 [9, 10, 34]. However, the toxicity of chromates has led to the development of coating system components that provide useful levels of corrosion protection, but do not possess the toxic chemical hazards. Metallic zinc and zinc compounds are attractive inhibitors in this regard. They have been used to combat corrosion of many metals and their toxic hazard is much lower

than that of chromate[35]. Historically, there have been four different realms of Zn usage in combating corrosion, which includes pigments in organic coatings (Zn dust, Zn phosphates, Zn chromates, etc.) [36-44], zinc phosphate conversion coatings (ZPOs) [45-47], metallic coatings (electroplating, hot dipping) and soluble Zn^{2+} inhibitor compound additions to solution.

One third of the Zn metal produced is used in galvanization[48] which protects the substrate by acting as a sacrificial anode. It is not a good idea to galvanize Al alloys as they are susceptible to cathodic corrosion. The alkali produced by oxygen reduction on the cathodically polarized Al dissolves the passive film. Even though Al is cathodically polarized relative to its corrosion potential, it is still above its reversible potential and can oxidize. Aggressive pitting often results. In the potentiodynamic polarization experiments done by Zhang et al., it was seen that Zn layer on Zn clad Al 3103 became noble to the substrate in alkaline environments [49]. The phosphate conversion coatings based on divalent Zn^{2+} cations, were first developed as alternatives for Chromate Conversion Coatings (CCCs) on iron and steel substrates and are now being extensively studied on Al and its alloys [46, 50]. The phosphating film consists of $Zn_3(PO_4)_2 \cdot 4H_2O$ which is formed as a result of an increase in pH due to a simultaneous local anodic dissolution and hydrogen reduction at the nearby cathodic sites. This film increases both the resistance to localized corrosion and paint adhesion [45].

Soluble Zn^{2+} generally inhibits corrosion by forming an insoluble $Zn(OH)_2$ precipitate over the local cathodes which experience a local elevation of pH[51]. Buchheit et al. polarized AA 2024-T3 cathodically in 0.124M NaCl solution having Zn^{2+} [52]. These curves indicate a reduction in the limiting current density of the oxygen reduction reaction (ORR) with the increase in Zn^{2+} ion concentration. The release of Zn^{2+} from a hydrotalcite vanadate pigment may contribute to cathodic inhibition provided by vanadates, which were also released from the compound. Zn works well in combination with other compounds like polyphosphates and phosphonates to provide an effective multicomponent inhibition system for both ferrous and non-ferrous alloys. The addition of Zn to polyphosphates accelerates the protective film formation and enables multivalent metal ions to form cationic colloidal complexes which increase cathodic inhibition [51]. The Zn-phosphonate combination shows effective cathodic inhibition by forming a stable complex and counteracts the anodic nature of the phosphonates that attack the alloys when used alone [51, 53].

Corrosion inhibition Al and Al alloys by Zn^{2+} ion alone and its mechanism of inhibition is not widely reported in the literature and therefore warrants research to characterize the basic aspects of its inhibiting action. Zn^{2+} exhibits complex pH-dependent speciation in chloride solutions. In this study, polarization experiments were carried out at different Zn^{2+} ion concentrations to find the critical concentration required for inhibition. Rotating disk electrode experiments were carried out to quantify the extent of ORR (oxygen reduction reaction) inhibition. Scanning Electron Microscopy/ Energy Dispersive X-ray Spectroscopy (SEM/EDS) analysis of the free corrosion samples was done to characterize the protective film formed and understand the mechanism of localized corrosion inhibition. Electrochemical impedance was carried out to further understand the protectiveness of the film formed on the substrate by the zinc ion present in dilute chloride solutions of different pH. An attempt was made to understand the mechanism of inhibition at different pH by analyzing the i_{corr} data obtained from the impedance analysis.

5.3.2.2 Experimental

5.3.2.2.1 Materials and Chemicals. All experiments were carried out on 2 mm AA 2024-T3 sheet stock obtained from a commercial supplier. This alloy is a solution heat-treated, cold worked and stabilized with a nominal chemical composition of: 3.8-4.9% Cu, 1.2-1.8% Mg, 0.3-0.9% Mn, 0.5wt% Fe, 0.5wt% Si, balance being Al [1]. A few electrochemical experiments were carried out on the Zn containing Al alloy, AA 7075-T6 and is obtained from the same supplier. This alloy is artificially aged after solution heat treatment and has a nominal composition of 5.3%Zn, 2.4%Mg, 1.36%Cu, 0.24%Fe and the remainder being Al. All the chemicals used for the electrochemical experiments (zinc chloride, sulfuric acid, sodium hydroxide, sodium chloride) are of reagent grade and are obtained from commercial sources. Rotating disk experiments were carried out on 99.999% pure Cu electrodes. Deionized water of 18.2 MΩ.cm resistivity was used for preparing all aqueous solutions.

5.3.2.2.3 Sample preparation. AA 2024-T3 sheet was cut into 2 x 2 cm coupons for all the experiments. The samples used for polarization experiments and impedance measurements were abraded on 600 grit to 1200 grit paper in ethanol to avoid any corrosion prior to immersion. These samples were used immediately for polarization to avoid thickening of the aluminum oxide layer. The coupons used for exposure experiments and for surface and microscopic analysis were abraded with the SiC grit papers through to 1200 grit and then polished until 1 μm diamond paste. The backs of the samples were covered with an insulating tape to avoid any coupling between the two faces of the sample. The samples used for polarization, impedance and exposure experiments were ultrasonically cleaned to remove any residual debris attached to the sample during polishing. After the exposure experiments, the sample was washed with ethanol and air dried before any further analysis.

5.3.2.2.2 Potentiodynamic Polarization. Polarization of AA 2024-T3 coupons was carried out using a Gamry^{TM} Ref 600 potentiostat in conjunction with Gamry Framework software. This was done using a standard three electrode flat cell with a saturated calomel electrode (SCE) as the reference electrode and platinum mesh as the counter electrode and either AA 2024-T3 or AA 7075-T6 as the working electrode. The working electrode has an exposed area of 1 cm^2. Cathodic polarization was done in 0.1M NaCl solution with $ZnCl_2$ concentrations ranging from 0.1 mM to 50 mM. All the scans were repeated a minimum of three times and the open circuit potential (OCP) was monitored for 30 min prior to polarization. The cathodic scan was started at OCP and was stopped before any reduction of Zn^{2+} started (about -1.1 V$_{SCE}$). Anodic polarization was done at different Zn^{2+} ion concentrations ranging from 0.1 mM to 10 mM to investigate any changes in pitting potential, repassivation potential and/or reduction in anodic current density. Potentiodynamic polarization measurements were started at 20 mV below OCP, reversed at 1 mA/cm^2 and stopped at 20 mV below OCP. Polarization experiments were also carried out in 5 mM Zn^{2+} solutions whose pH was adjusted to 3, 4, 7 or 10 prior to the experiment. The pH was adjusted with drop by drop additions of sulfuric acid or sodium hydroxide solution. Measurements made in 0.1 M NaCl solutions without the inhibitor additions at different pH were used for comparison. The scan rate used was 0.5 mV/s for all the experiments.

5.3.2.2.4 Free corrosion exposure. AA 2024-T3 coupons were exposed to 40 ml of 0.1M NaCl solutions containing 5mM Zn^{2+} at pH 3, 4, 7 (natural pH) or 10 for a period of 24 hours. The

coupon was immersed with the polished surface facing upward and the back surface covered with insulting tape facing downward. Samples were also immersed in NaCl solutions without Zn^{2+} additions at different pH for comparison. At the end of the exposure, these samples were washed with ethyl alcohol and air dried. They were visually investigated and the microstructural differences were examined using a Quanta 200 Scanning Electron Microscope that has an EDS (Energy dispersive X ray spectroscopy) component attached to it that is used for chemical mapping on the surface.

5.3.2.2.5 Electrochemical Impedance Spectroscopy and surface analysis. Electrochemical Impedance experiments were carried out in electrolytes containing 5 mM concentrations of the Zn^{2+} cation added as zinc chloride in 0.1M NaCl solution adjusted to different bulk pH of 3, 4 or 7. Impedance spectra of the coupons immersed in Zn^{2+}- free solutions were also measured simultaneously. Three different kinds of cell environments were used – aerated, deaerated and decarbonated environments. A flat cell with a working electrode area of 1 cm^2 having a three electrode setup consisting of an SCE reference electrode and a platinum mesh counter electrode was used. Argon gas was bubbled into the electrolyte at a high flow rate for about an hour for deaerating the solution and then pumped into the flat cell. The gas was then bubbled at a small flow rate into the sealed setup for duration of 5 days. Decarbonation of solutions was accomplished by saturating the solutions using Zero Grade Air^{TM} (air free of CO_2 and hydrocarbons) for about an hour before the solution comes in contact with the sample. Impedance measurements were taken every 5 hours for a period of 5 days using an automatic sequence wizard enabled in the Gamry Framework software.

The 2024-T3 samples were exposed to inhibited solutions containing the same Zn^{2+} concentration of 5 mM at pH 3, 4 and 7 in the three different kinds of environments for a period of 5 days. The sample surface was then analyzed by x-ray diffraction (XRD) and by x-ray photoelectron spectroscopic (XPS) techniques. These experiments created a matrix of test samples and were carried out to supplement and aid the understanding of the influence of oxygen and carbon dioxide, if any, on the corrosion inhibition of the alloy by the zinc ion obtained from the electrochemical impedance exposure measurements at different pH.

5.3.2.2.6 Cathodic Polarization on copper rotating disk electrode (RDE). The preparation of the change disk copper electrode tip for rotating disk electrode was discussed in chapter 3 and is briefly described here. The copper disks of 5 mm diameter were cut by a low speed saw machine, embedded into the Teflon^{TM} tip and were polished together through to 1μm diamond paste using SiC grit papers and a specially designed holder. They were then polished in 0.05 μm colloidal silica. Cathodic polarization curves were run on the copper disk while rotating the electrode at rates from 300 to 8000 rpm in Zn^{2+} ion inhibited and chloride-only solutions using a modulated speed rotator from Pine Research Instrumentation. The cell used was a jacketed cell obtained from Gamry instruments with SCE (Saturated Calomel Electrode) as the reference electrode and coiled platinum wire as the counter electrode. The scan was started after conditioning the electrode at -0.62 V_{SCE} for 10 min and stopped at -1.1V_{SCE} before the Zn^{2+} reduction started. A scan rate of 0.5 mV/s was used for all the RDE experiments.

5.3.2.3 Instrumental

5.3.2.3.1 XRD. XRD of the surface films formed on the substrate by immersion in dilute NaCl solution with zinc ions at pH 3, 4 or 7 was carried out using Scintag XDS 2000 with Cu K_α radiation (λ = 1.5406 A°). The anode was operated at 45 kV and 20 mA with a scan rate of 1°/min. The diffraction pattern was analyzed and matched to a compound using Bruker Corporation's EVA^{TM} software.

5.3.2.3.2 XPS. XPS measurements were conducted on AA2024-T3 coupons (20 x 20 x 2 mm) to examine the composition of the surface film formed by the dissolved Zn species at different pH. A Kratos AXIS Ultra instrument controlled by a VISION^{TM} data system was used. A mono-chromatic Al K_α X-ray source was operated at 1486.6 eV and 150 W. Typical operating pressures were around 2×10^{-8} Torr. All the spectra collected were calibrated to the carbon 1s peak at 283.2.8eV.

5.3.2.3.3 Rotating Disk Electrode. A modulated speed rotator obtained from Pine Research Instrumentation with a change disk electrode tip was used and the rotator was connected to a CH Instruments bipotentiostat. A Cu rotating disk electrode was used to study the effect of a 1 mM Zn^{2+} ion addition on the oxygen reduction kinetics in aerated 0.1M NaCl solution. Cu was selected as an electrode material as a model to the Cu-rich intermetallic particles that serve as local sites for the oxygen reduction. The data were analyzed using the Levich equation [54]:

$$i_L = \frac{I_L}{A} = 0.2nFC_B D_O^{\frac{2}{3}} \upsilon^{-\frac{1}{6}} \omega^{\frac{1}{2}}$$

(3.2.1)

where i_L is the limiting current density in mA/cm^2, I_L is the limiting diffusion current, A is the area of the electrode (cm^2), D_o is the diffusion coefficient of O_2 (2.7×10^{-5} cm^{2}s^{-1}) [55], ν is the kinematic viscosity (0.01 cm^{2}s^{-1}), C_B is the bulk concentration of O_2 (7 ppm), ω is the rotation rate in rpm, and n and F represent the number of electrons exchanged in the cathodic reaction and Faraday's constant respectively. The bulk concentration of oxygen was determined from visual inspection using a dissolved oxygen test kit, Model 0-12 obtained from CHEMetrics, Inc. Initial conditioning of the Cu electrode was carried out at -0.62 V_{SCE} for 10 min to reduce any Cu present as oxide on the electrode surface. The scan was stopped before any reduction of Zn^{2+} had started.

5.3.2.3.4 Electrochemical experiments. All the electrochemical measurements on 2024-T3 coupons were carried out using a Gamry^{TM} Ref 600 potentiostat. A sinusoidal voltage of 10 mV about OCP was applied with frequency ranging from 10^5 to 10^{-2} Hz for the electrochemical impedance measurements. The spectra were fit and analyzed using Scribner Associates' ZView^{TM} impedance software. The data from the polarization curves was analyzed using the Gamry Echem Analyst^{TM} software.

5.3.2.3.5 SEM/EDS. Scanning electron microscope (SEM) was typically carried out using an accelerating voltage of 20 kV. Energy dispersive spectroscopy (EDS) is used for chemical mapping of a spot or an area on the surface for elemental analysis. Elemental mapping was used to characterize the relative concentration of these elements on the surface of exposed samples.

5.3.2.4 Results

5.3.2.4.1 Speciation in aqueous solutions . Speciation of Zn in dilute aqueous sodium chloride solutions was calculated using the thermodynamic simulation program, MEDUSA^{TM}(Make Equilibrium Diagrams Using Sophisticated Algorithms) developed at Inorganic Chemistry, Royal Institute of Technology (KTH), Stockholm, Sweden. MEDUSA has an embedded software named HYDRA that contains the database of chemical equilibrium constants with log K values at 25˚C. The starting concentrations of cations, anions and/or partial pressures of gases defining the aqueous solution chemistry are given as inputs in HYDRA. The pH-dependent solubility of Zn^{2+} considering hydroxide, chloride and carbonate anions are shown.

Figure 3.8a shows the speciation diagram of 5 mM concentrations of Zn^{2+} cation in an aqueous solution containing OH^- anions only. The concentration of different ionic species was plotted on a logarithmic scale as a function of solution pH. The red dashed line represents the total solubility and is approximately the sum of the concentrations of the dissolved species in the solution. The solubility remained high with soluble Zn^{2+} cations predominant in the low pH regions up to pH 7. The solubility reduced by about three orders of magnitude by the hydrolysis of Zn^{2+} cations leading to precipitation of Zn oxide (ZnO) at pH 7. The overall solubility remained low until pH 11.8 due to the sparingly soluble $Zn(OH)_2$. Further hydrolysis above pH 11.8 increased the solubility by forming $Zn(OH)_3^-$ and $Zn(OH)_4^{2-}$ anions.

Figure 3.8b shows the pH-dependent solubility diagram obtained by 100 mM NaCl additions in the aqueous system containing 5 mM Zn^{2+}. The black dotted line represents the total solubility for Zn^{2+} with Cl^- additions. The change in the total solubility of Zn^{2+} due to the addition of Cl^- anions is shown in the diagram by superimposing the total solubility of Zn^{2+} in the absence of Cl^- adopted from Figure 3.8a (red dashed line). Cl^- additions caused the total solubility to reduce at pH 6.7 instead of pH 7 as observed with no Cl^- additions (Figure 3.8a). The first drop in the solubility occurred due to the precipitation of insoluble $Zn_5(OH)_8Cl_2$ at pH 6.7 and the solubility further reduced at pH 8.7 due to the precipitation of sparingly soluble $Zn(OH)_2$. The limiting solubility of dissolved $Zn(OH)_2$ was a little less in the Cl^- containing solutions when compared to that of the solution with no Cl^- anion. The solubility starts to rise at pH 11.8 by forming $Zn(OH)_3^-$ and $Zn(OH)_4^{2-}$ anions.

Figure 3.8c shows the speciation diagram of 5 mM Zn^{2+} in aqueous solutions containing 100 mM NaCl with carbonate anions in the solution due to atmospheric CO_2 (partial pressure of CO_2 in air is $10^{-3.5}$ atm). The natural pH of the solution was slightly less than 7 and is shown in Figure 3.8c. The thick blue line represents the total solubility for Zn^{2+} with hydroxide, chloride and carbonate anions in the solution. The total solubility for Zn^{2+} with OH^- anions only (red dashed line) and both OH^- and Cl^- anions (black dotted line) were superimposed in Figure 3.8c. CO_3^{2-} anions reduced the total solubility above pH 6.7 by the precipitation of insoluble $Zn_5(OH)_6(CO_3)_2$. The solubility started to increase at pH 8.25 by further complexation with carbonates to form $Zn(CO_3)_2^{2-}$ anion. Overall, the carbonate additions reduced the pH range of solubility minimum compared to that observed in the absence of carbonates (Table 3.1). However, carbonates reduced the solubility by more than a half order of magnitude compared to the solubility profiles without carbonate additions.

(a)

(b)

114
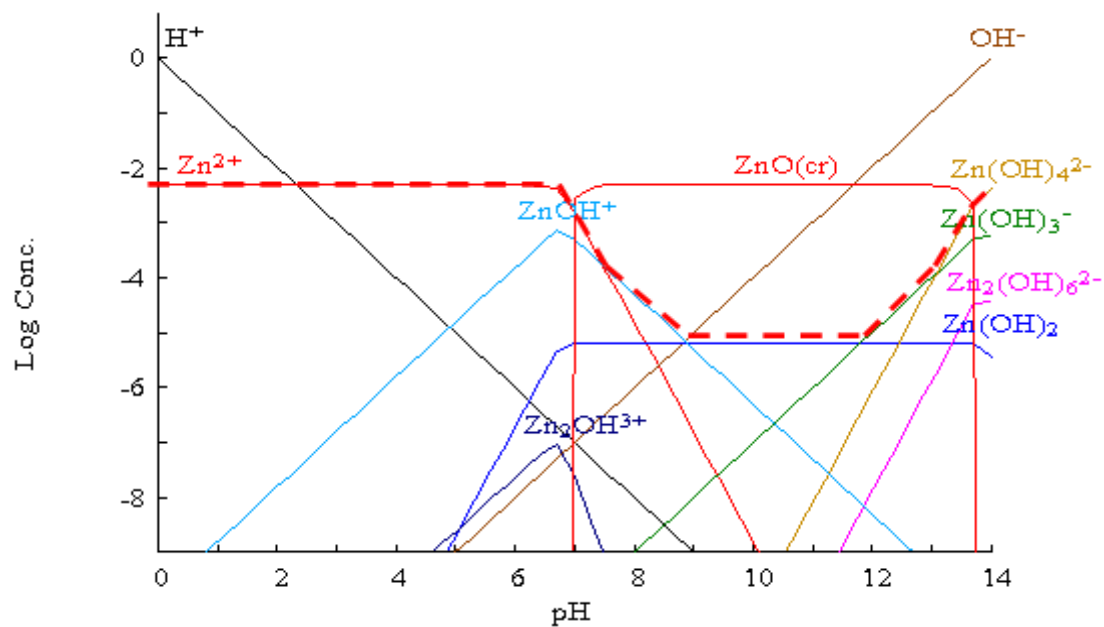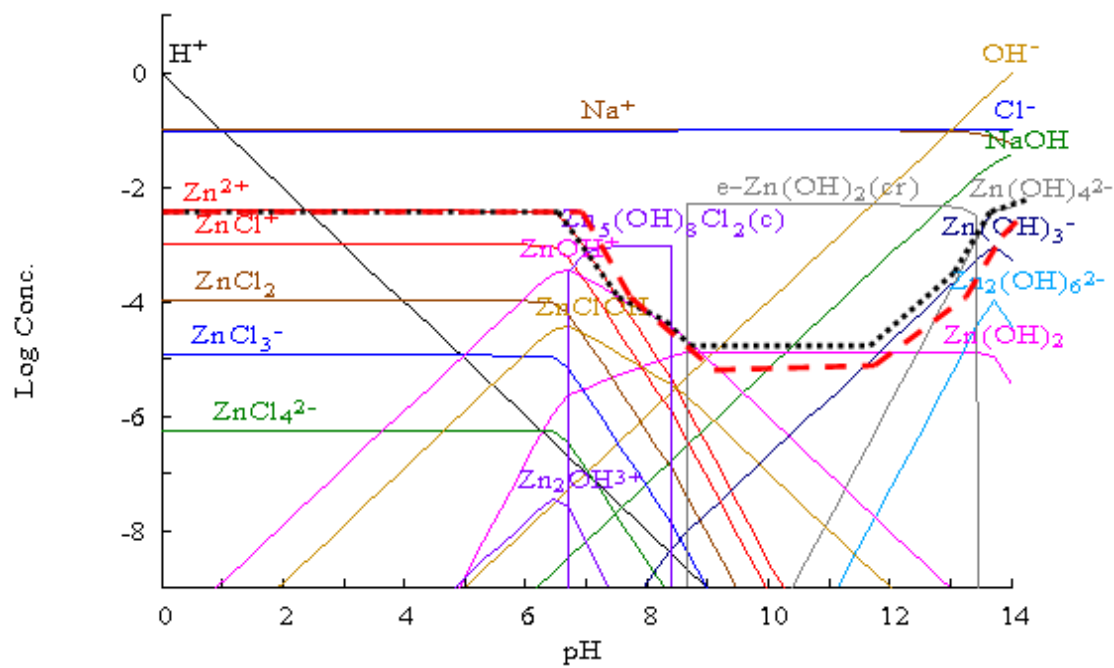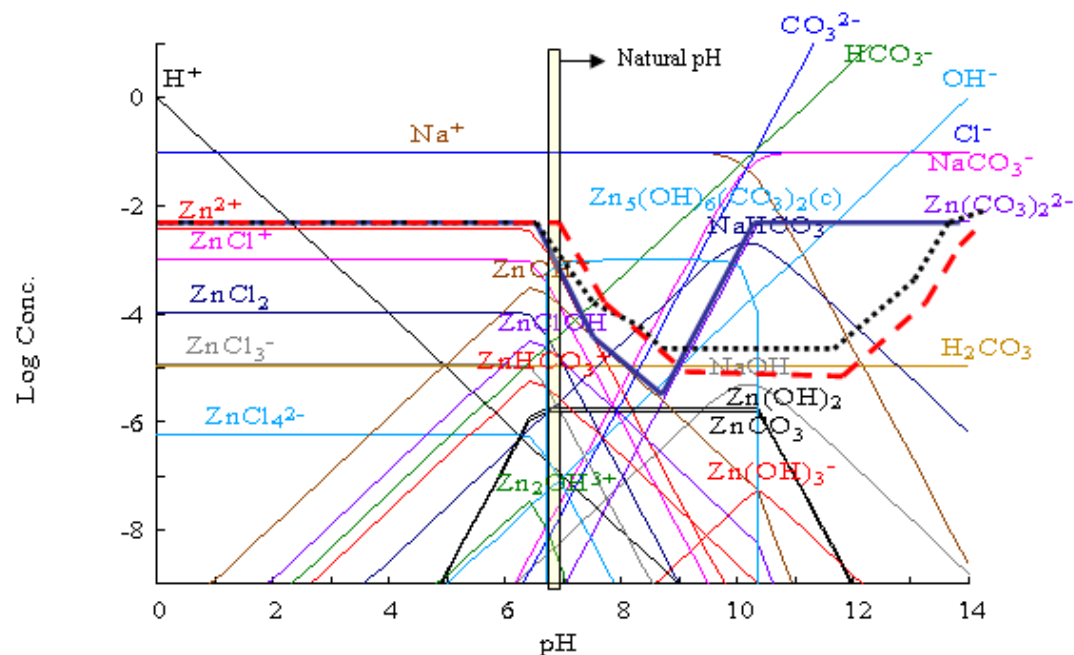
(c)

Figure 3.8. Speciation diagram of Zn species in the presence of (a) OH^- (b) OH^- and 100 mM [Cl^-] (c) atmospheric CO_2 (OH^-, Cl^- and CO_3^{2-} anions) in 5 mM of Zn^{2+} cation.

Table 3.1 also shows the solid species limiting the solubility of Zn^{2+} cations in the presence of OH^-, Cl^- additions and CO_3^2 additions. It is interesting to see that CO_2 is an important aspect of the solubility profile for Zn^{2+}. In aerated environments, Zn^{2+} ion inhibition is expected to occur in the solubility minimum by the precipitation of $Zn_5(OH)_6(CO_3)_2$.

Table 3.1. Solid species limiting the solubility of 5 mM of Zn^{2+} cation by considering different anion additions.

Anions	Solid precipitates	pH above which the solubility reduces	pH above which the solubility increases
OH^- anions only	ZnO	6.7	11.8
OH^- and Cl^- anions	$Zn_5(OH)_8Cl_2$, $Zn(OH)_2$	7	11.8
OH^-, Cl^- and CO_3^{2-} anions	$Zn_5(OH)_6(CO_3)_2$	7	8.2

5.3.2.4.2 Polarization in aerated sodium chloride solutions. Figure 3.9 shows cathodic and anodic polarization measurements carried out on aluminum 2024-T3 samples in aerated 0.1M NaCl solutions with concentrations varying from 0.1 mM (6.5 ppm) to 50 mM (3250 ppm) of zinc chloride. The natural pH of all these solutions was between 6 and 7. The purpose of these experiments was to verify the inhibition of oxygen reduction reaction by zinc as previously reported [52], investigate any anodic inhibition and determine the concentration at which the inhibition reaches its maximum. 0.1M NaCl solution was used as a control. Figure 3.9a shows

that Zn^{2+} ion suppressed the oxygen reduction reaction (ORR). Shift in the open circuit potential (OCP) towards negative values was seen which indicates a reduction in cathodic kinetics.

ORR is a mass transport limited reaction and the limiting current density of ORR decreased with an increase in Zn^{2+} ion concentration. This can happen only if precipitation by Zn^{2+} ion blocked the area supporting the ORR.

Figure 3.9b shows no change in pitting potential (E_{pit}) as Zn^{2+} ion concentration increases. Anodic inhibition as assessed by a reduction in the anodic kinetics or a shift in the pitting potential in the positive direction was not observed. However, an increased separation of OCP from the E_{pit} was observed with increasing Zn^{2+} ion concentration. This separation reached a maximum at around 5mM. This effect decreases the tendency for pit initiation and promotes corrosion resistance. Hence, Zn^{2+} ion in solution is a good cathodic inhibitor but does not provide anodic inhibition at any concentrations.

(a)   (b)
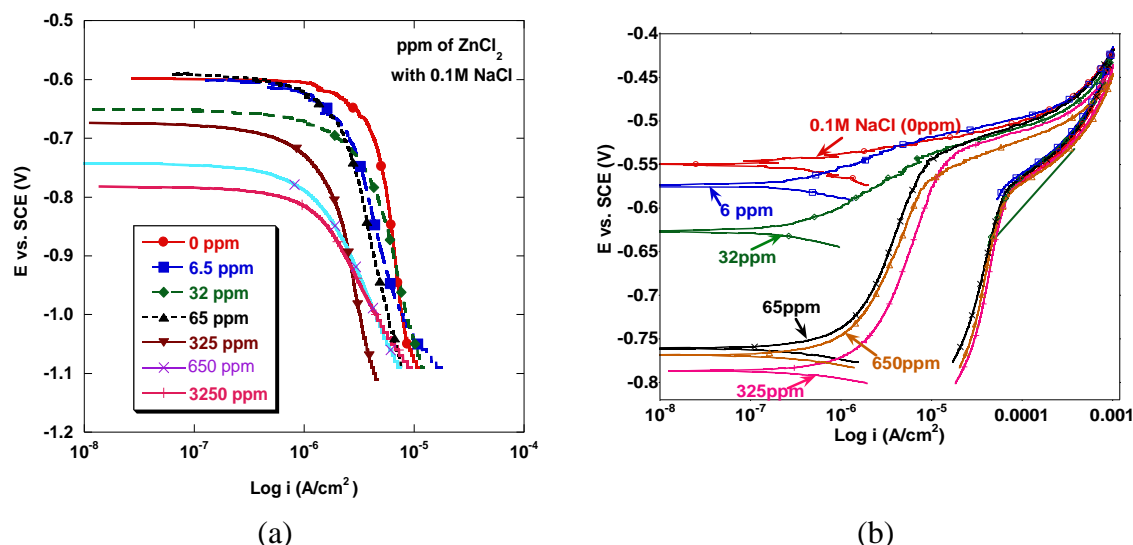
Figure 3.9. (a) Cathodic and (b) Anodic polarization curves of AA 2024-T3 in aerated 0.1M NaCl with different concentrations of zinc chloride (natural pH range $6 - 7$).

Suppression of ORR was also observed in zinc containing aluminum alloy, AA 7075-T6 in a manner similar to 2024-T3. Figure 3.10 shows that the limiting current density for the ORR was decreased by Zn^{2+} additions as low as 0.1 mM (6.5 ppm) and was decreased by an order of magnitude by a 5 mM Zn^{2+} additions (325 ppm). Zn^{2+} additions do not confer anodic inhibition on 7075.
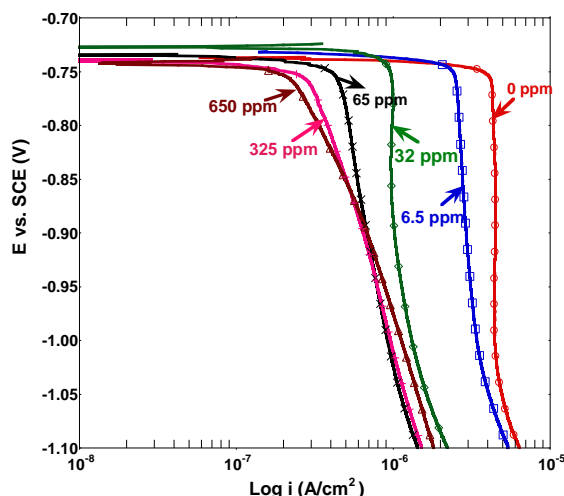
Figure 3.10. Anodic polarization curves of AA 7075-T6 in aerated 0.1M NaCl with different concentrations of zinc chloride (natural pH range 6 – 7)

The effect of pH on polarization behavior was also investigated. Figure 3.11 shows the cathodic polarization curves of aluminum 2024-T3 after 30 min OCP in 0.1M NaCl solutions with 5 mM Zn^{2+} at pH 3.95, 4.71, 7 (natural pH), 7.71, 9.8. No reduction in cathodic kinetics was observed at lower pH of 3 (not shown) and pH 3.95 and higher pH of 9.8 and pH 12.4 (not shown) compared to chloride-only solutions at the same pH while inhibition of ORR was seen at intermediate pH values of 4.71, 7 and 7.71. It has to be noted that pH values of 4.71 and 7 are outside the solubility minimum identified in Figure 3.8c. Experiments were also done to determine the effect of pH on the anodic polarization behavior. Inhibited solutions did not show any signs of anodic inhibition at any pH compared to the chloride-only solutions adjusted to the same pH.

Zn^{2+}-bearing solutions at pH 4.71, 7 and 7.71 that reduced cathodic kinetics have an interfacial electrolyte whose pH is pushed to the pH region of solubility minimum during the cathodic polarization. Hence, reduction in ORR kinetics occurs as the precipitated film forms a physical barrier on the ORR supporting copper rich sites. Solutions having a pH of 3 and 3.95 dissolve the passive film on the alloy surface activating the entire surface uniformly with little or no local alkalinity. The alkali generated by ORR is not sufficient to drive the pH to the pH region of solubility minimum and hence provide no cathodic inhibition. Solutions having a pH of 9.8 and 12.4 were cloudy with an insoluble zinc compound and could not suppress oxygen reduction as most of the zinc ion is exhausted in the formation of the hydroxide and/or carbonate. Inhibited solutions at any pH did not show any signs of anodic inhibition.

117

(a)

(b)

(c)

(d)

(e)
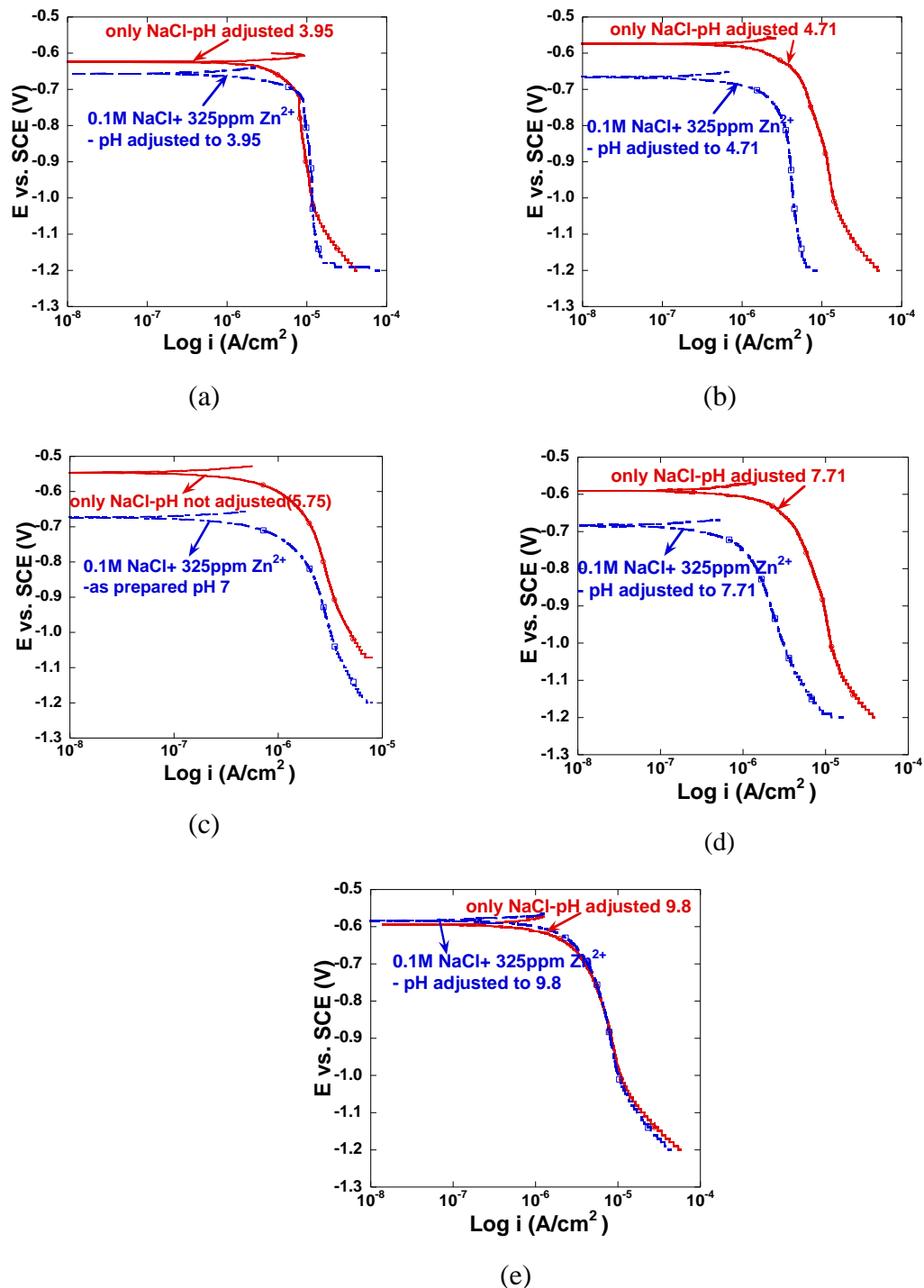
Figure 3.11. Cathodic polarization curves for 2024-T3 electrodes in aerated inhibited and uninhibited solutions adjusted to different pH (a) 3.95 (b) 4.71 (c) 7 (d) 7.71 (e) 9.8. The red curve represents plain 0.1M NaCl solutions while the blue curve represents chloride solutions with 5 mM Zn^{2+} ions.

5.3.2.4.3 Polarization on Cu RDE. The corrosion cell process on 2024-T3 in aerated environments is driven by oxygen reduction occurring on Cu-rich intermetallic particles. RDE experiments were carried out with pure Cu electrodes, which were used as a proxy for Cu-rich intermetallic particles. These experiments were conducted to systematically explore the effect of Zn^{2+} addition on ORR kinetics.

Figure 3.12a shows the polarization curves of Cu in 0.1 M NaCl solution with 1 mM (65 ppm) additions of Zn^{2+} at rotation rates ranging from 1000 to 8000 rpm, and Figure 3.12b shows the polarization curves of Cu in 0.1 M NaCl solution at rotation rates ranging from 300 to 6500 rpm. It was observed that the band of polarization curves in Zn^{2+}-bearing solutions are shifted to the left compared to those in chloride-only solutions. There was a reduction in the ORR current on copper in the Zn^{2+} inhibited solution, when compared to that of the chloride-only solution, of almost two orders of magnitude.. This is a much higher reduction than that resulting from lanthanides, where 100 ppm of lanthanides (Ce^{3+}, Pr^{3+} and La^{3+}) could suppress ORR by approximately half an order of magnitude, as shown in chapter 3. The slight deflection of the curves at -0.62 V_{SCE} was due to the reduction of Cu oxide to Cu. The curves in chloride-only solutions showed a rotation rate-dependent ORR current where the current density increased with the increase in rotation rate according to the Levich equation. The ORR current at -0.65 V_{SCE} to -0.85 V_{SCE} increased with the rotation rate in 1 mM Zn^{2+} solution but the current-rotation rate dependence disappeared at more active potentials.

(a)   (b)
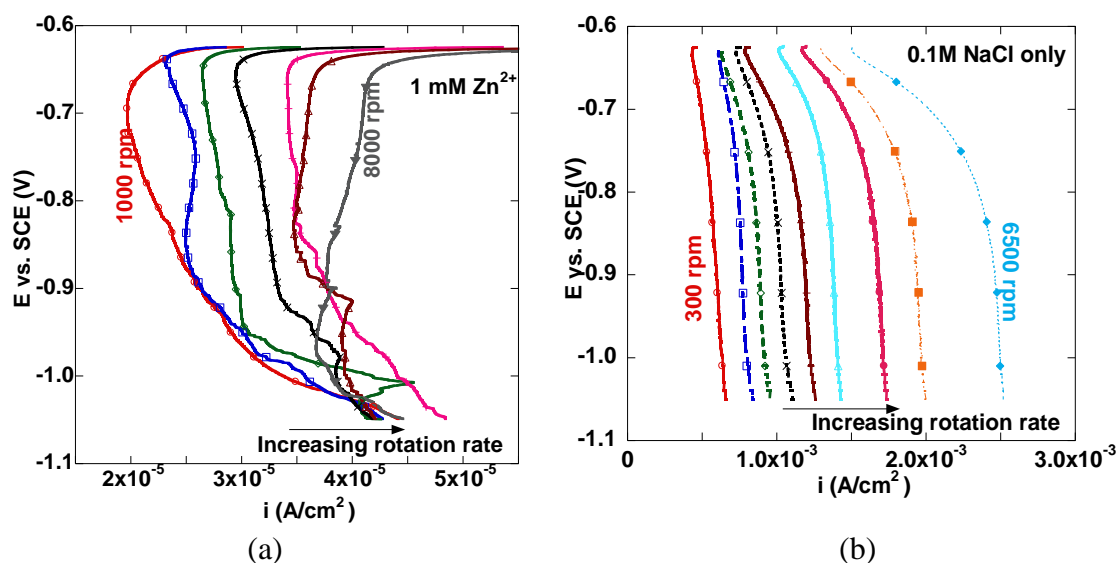
Figure 3.12. Cathodic polarization curves on Cu RDE in (a) 0.1M NaCl solution with 1mM (65 ppm) of Zn^{2+} ion added as zinc chloride (b) in 0.1M NaCl solution without Zn^{2+}

No visible film was seen on the copper surface after 2000 rpm rotation in 1 mM Zn^{2+} solution. Zn was also not detected in post-experiment EDS measurements on the electrode possibly due to the comparatively insensitive EDS detection limits.

X-ray photoelectron spectroscopy was conducted on the copper disk and the presence of Zn and O were observed in the survey scan. Chemical quantification using individual high energy resolved spectra for each element indicated presence of high concentrations of zinc and oxygen on the surface, a moderate concentration of chlorine and carbon and very low concentrations of

copper. The percentage of elements in the surface analysis is shown in Table 3.2. Fitting and area calculations were obtained by using CasaXPS^{TM} software developed by Casa Software Ltd. The carbon percentage shown corresponds to the $C_{carbonate}$. The high resolution spectrum of carbon indicated the presence of adventitious carbon (284.8 eV and 285.6 eV) originated from atmospheric contamination while a carbonate peak (289.3 eV) exists which could be either from zinc carbonate or zinc carbonate hydroxide [56].

Table 3.2. Chemical quantification analysis obtained from the XPS high resolution individual element spectra, performed on the the copper cylindrical disk that was rotated in a 1mM Zn^{2+} inhibited chloride solutions at 2000 rpm.

% Elements from XPS analysis				
Zn	Cu	O	Cl	C
24.6	1.8	58.6	6.1	8.9

(a)   (b)   (c)
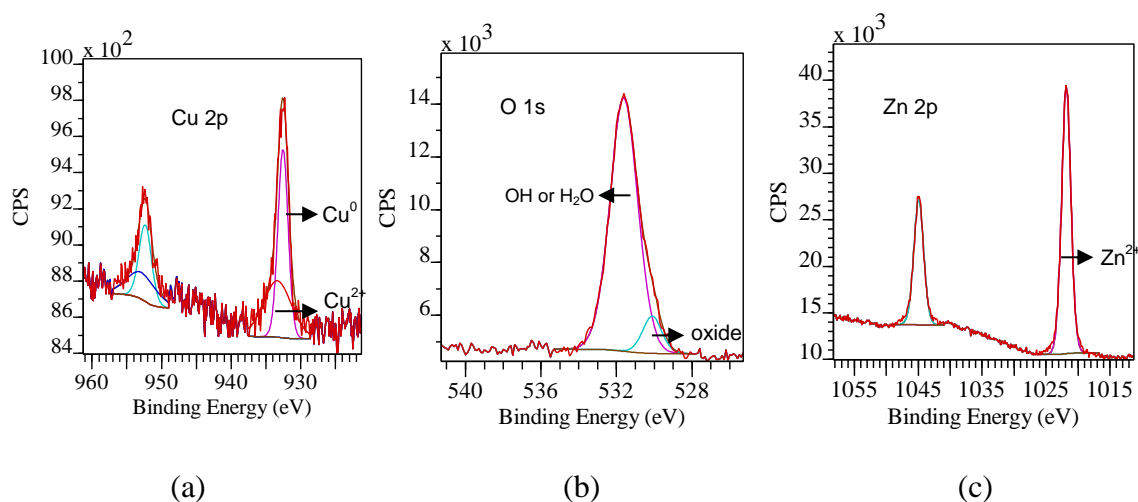
Figure 3.13. Cathodic polarization curves on Cu RDE in (a) 0.1M NaCl solution with 1mM (65 ppm) of Zn^{2+} ion added as zinc chloride (b) in 0.1M NaCl solution without Zn^{2+}

The high resolution spectrum for Cu shows two broad peaks corresponding to $2p_{1/2}$ and $2p_{3/2}$ electron configurations as shown in Figure 3.13a. Fitting of these peaks shows existence of both metallic copper and oxidized copper, which indicates that the surface film is extremely thin on the order of nanometers. The Cl 2p peak (not shown) showed two peaks due to spin-orbital splitting. Evaluation of the spectrum shows that the peak corresponds to inorganic chloride. The oxygen XPS spectrum in Figure 3.13b shows a high intensity peak at 531.6 eV, which corresponds to significant concentrations of a hydroxide and or a carbonate (but not to a metal oxide). The spectrum for Zn 2p in Figure 3.13c shows two peaks corresponding to $2p_{1/2}$ and $2p_{3/2}$ electron configurations. The $2p_{3/2}$ has a peak at 1021.8 eV binding energy which is consistent with a hydroxide ($Zn(OH)_2$) or carbonate hydroxide ($Zn_5(OH)_6(CO_3)_2$) or chloride hydroxide ($Zn_5(OH)_8Cl_2$) or carbonate ($ZnCO_3$).

Chemical quantification showed a measured Zn_{total}:Cl ratio of 4 and Zn_{total}:$C_{carbonate}$ ratio of 2.75 (equations 3.2.2 and 3.2.5). Equations 3.2.3 and 3.2.7 are obtained from the stoichiometric formula of the compound.

$$\frac{Zn_{total}}{Cl} = 4 \tag{3.2.2}$$

$$\frac{Zn_5(OH)_8Cl_2}{Cl} = \frac{1}{2} \tag{3.2.3}$$

From equations 3.2.2 and 3.2.3, equation 3.2.4 is obtained.

$$Zn_5(OH)_8Cl_2 = 0.12.Zn_{total} \tag{3.2.4}$$

Similarly,

$$\frac{Zn_{total}}{C_{CO_3}} = 2.75 \tag{3.2.5}$$

$$\frac{Zn_5(OH)_6(CO_3)_2}{C_{CO_3}} = \frac{1}{2} \tag{3.2.6}$$

From equations 3.2.5 and 3.2.6,

$$Zn_5(OH)_6(CO_3)_2 = 0.2.Zn_{total} \tag{3.2.7}$$

From equations 3.2.4 and 3.2.7, equation 3.2.8 is obtained.

$$\frac{Zn_5(OH)_6(CO_3)_2}{Zn_5(OH)_8Cl_2} = 1.45 \tag{3.2.8}$$

This indicates an excess of carbonate hydroxide species compared to the chloride hydroxide species. These results indicate the formation of a thin Zn-rich hydroxy carbonate film. Based on RDE measurements, this film inhibits ORR and the overall corrosion cell process on 2024-T3 (and probably 7075).

5.3.2.4.4 Free Corrosion morphology of aluminum 2024-T3 on exposure

Photographs of Al alloy 2024-T3 samples after free corrosion exposure in 0.1M NaCl solution with and without 5 mM of $ZnCl_2$ are shown in Figure 3.14. at open circuit potential for 22 hours at pH 4, 7(as prepared pH), and 10. The extent of inhibition depended strongly on solution pH. The coupons immersed in the chloride-only solutions turned brown and pitted.
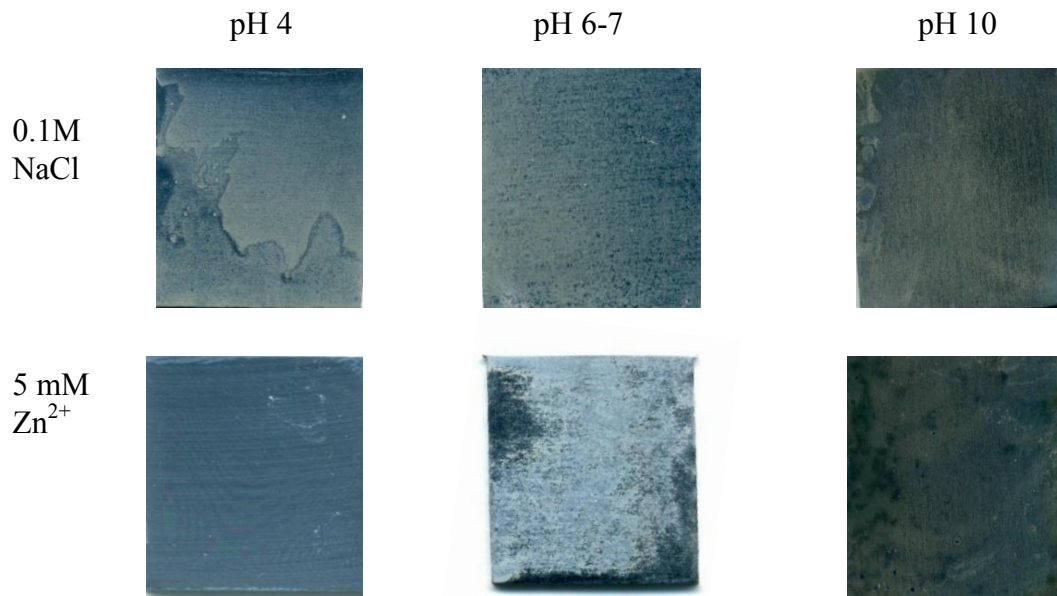
Figure 3.14. Free corrosion samples exposed in a solution containing inhibited and uninhibited 100 mM NaCl at pH as specified.

Very different results were found in the solutions where ZnCl$_2$ was added. At pH 7, the sample was covered with a white film with very little or no visible attack. At pH 10, the sample turned brownish. This is consistent with the cathodic polarization results where ORR inhibition was detected at pH 7 but not at pH 10.

Figure 3.14 shows that the sample exposed to the Zn^{2+}-bearing solution at pH 4 is completely unattacked. In fact, the surface retained its initial mirror finish during exposure. This observation contrasts the findings from cathodic polarization at pH 4 where no evidence of ORR inhibition was detected. Reconciliation of these findings is given in the next section.

Figure 3.15a shows the SEM/EDS analysis of the substrate immersed in the pH 7 Zn^{2+}-bearing solution. The surface was rich with crystalline deposits rich in Al, Zn, Cl and evidence of increased deposit density was seen over the intermetallic particles as shown in Figure 3.15a. Figure 3.15b shows the XRD film formed on the sample surface. XRD peaks corresponded to crystalline compounds, Al-Zn carbonate hydroxide (Zn$_6$Al$_2$(OH)$_{16}$CO$_3$.4H$_2$O), Al-Zn-Cu carbonate hydroxide (Cu$_2$Zn$_4$Al$_2$(OH)$_{16}$CO$_3$.4H$_2$O or Cu$_3$Zn$_3$Al$_2$(OH)$_{16}$CO$_3$.4H$_2$O). The broad peak at 2θ of 12° is from the plexiglass that was used to hold the aluminum substrate. The SEM images in Figures 3.2.8a and 3.2.8b showed that this crystalline film was densely populated over some of the active intermetallics (mainly Al$_2$CuMg intermetallics) and was seen to be open at pits and trenches around other S phase and Al-Cu-Mn-Fe intermetallics. Precipitation of this hydroxide occurs due to the local increase in pH at the cathodic sites caused by the ORR. This explains the cathodic inhibition seen in the polarization curves of the samples immersed in pH 7 Zn^{2+}-bearing solutions. Scatter in the OCP of the substrates immersed in the Zn^{2+}-containing solutions conditions during polarization experiments could be due to the varying amount of coverage of the substrate.
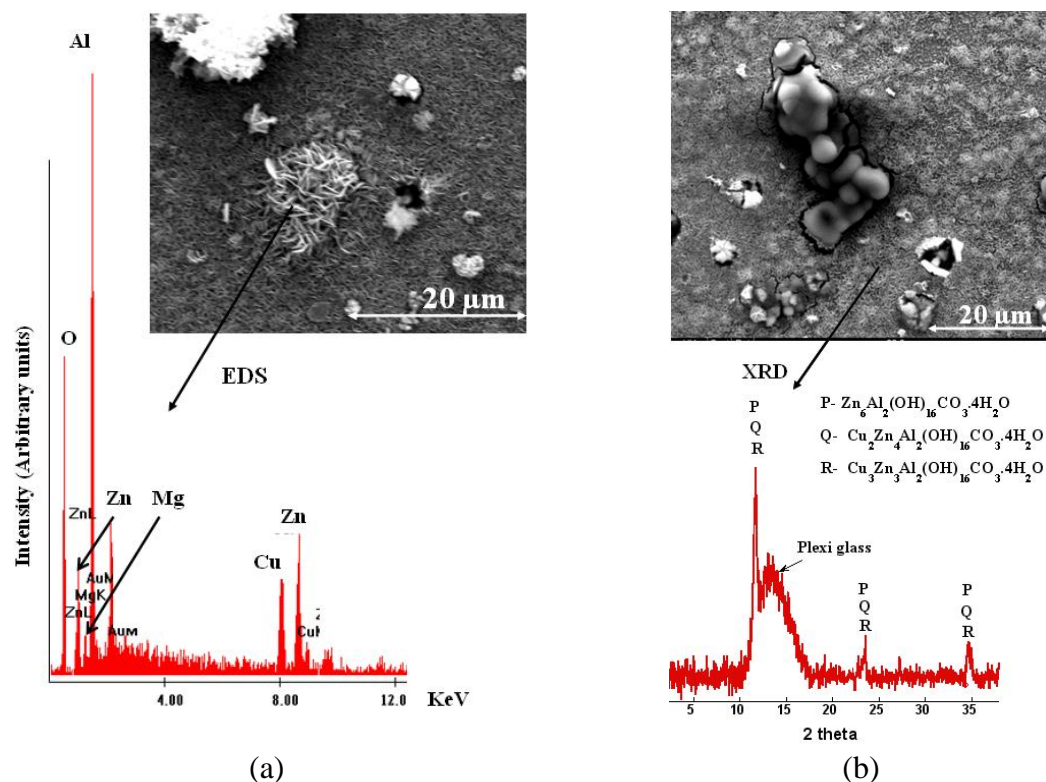
Figure 3.15. (a) (top) SEM image of the sample immersed in 0.1M NaCl + 5 mM Zn^{2+} for 22 hrs – as prepared pH 7. (Bottom) Spot EDS of the crystalline structures in the image (b) Another SEM image showing trenches and pits and XRD of the sample surface

Figures 3.16a and b show the SEM images of the samples immersed in pH 4 chloride solutions with and without 5 mM Zn^{2+} additions, respectively. The sample immersed in the solution with Zn^{2+} additions showed no pits while the one immersed in chloride-only solutions showed a heavily pitted surface. Figure 3.16c shows the chemical mapping of the sample immersed in the pH 4 solution with 5 mM of Zn^{2+} cation for 2 days. The Mg map showed intact Mg present in S phase particles (Al_2CuMg) suggesting that Zn^{2+} ions suppressed the dissolution of Mg from this phase even after 2 days of immersion. The Mg from the S phase was seen to be completely dissolved after 22 days of immersion of the control sample in uninhibited solution at pH 4. Zn maps showed the presence of Zn over the entire surface that suggests the presence of a film over the entire surface. This film was neither visible to the naked eye nor in the SEM analysis of the sample. The intermetallic particles appeared to be intact but there is no segregation of Zn detected over these intermetallic particles. EDS mapping lacks the sensitivity to detect thin films and deposits, hence, a detailed surface analysis is required to understand the interaction between the Zn^{2+} ion and alloy microstructure in pH 4 solutions.
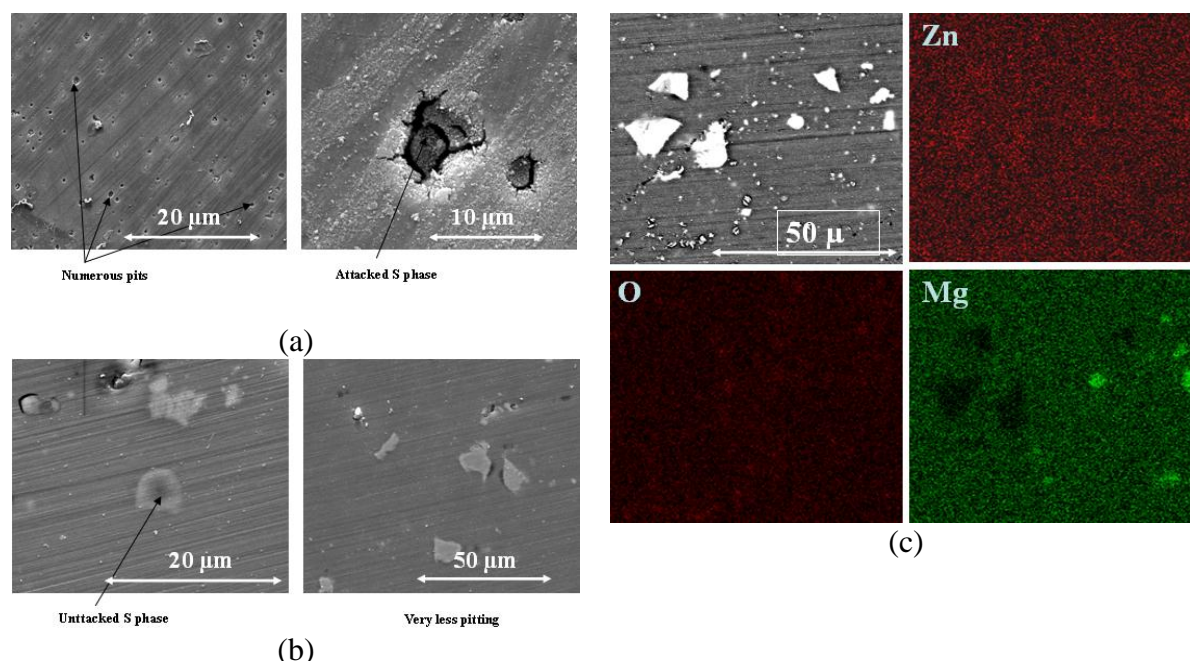
Figure 3.16. SEM images of the sample immersed in (a) pH 4 0.1M NaCl solution with no inhibitor showing heavily pitted surface(b) pH 4 0.1M NaCl solution with 5 mM Zn^{2+}(c) Backscattered electron image of the sample immersed in pH 4 0.1M NaCl solution with 5 mM Zn^{2+} and EDS Mapping of the area in the image showing maps of Zn, Mg and O

5.3.2.4.5 Sluggishness and Persistence of Zn^{2+} inhibition at pH 4. The cathodic polarization done in pH 4 chloride solutions with 5 mM Zn^{2+} additions after a short immersion time of 30 min at OCP did not show any inhibition as shown in Figure 3.11a. Figure 3.17 shows the polarization of the alloy samples immersed for longer times at OCP in pH 4 Zn^{2+}-bearing chloride solutions. This delayed cathodic polarization after longer immersion times of 42 hours OCP also showed no reduction in the reduction kinetics as seen in Figure 3.17a. Figure 3.17b shows the anodic polarization curves of AA 2024 seen after different immersion times and significant reduction of anodic kinetics was observed from 30 min to 90 hours of immersion at OCP before polarization. The sample in pH 4 chloride-only solution immersed for 30 min at OCP before anodic polarization was used for comparison. Anodic polarization also showed no anodic inhibition during polarization after an immersion time of 30 min in pH 4 Zn^{2+}-bearing solutions, but polarization after increasing immersion times indicated a gradual increase in the pitting potential and a significant reduction in anodic current density of about two orders of magnitude, suggesting that at pH 4, Zn^{2+} ion may be a slow acting anodic inhibitor. If so, short term tests may not adequately resolve this component of Zn^{2+} ion inhibition.

Samples immersed in pH 4 Zn^{2+}-inhibited solutions (5 mM Zn^{2+}) for 50 h and 19 days at open circuit potential were removed and then anodically polarized in 0.1 M sodium chloride solutions to test the persistency of the protection provided by the film formed in pH 4 Zn^{2+}-inhibited solutions. A negative control sample immersed for 30 min at OCP in 0.1M NaCl solution was polarized in the same chloride-only solution and a positive control sample immersed for 90 h in pH 4 Zn^{2+}-bearing solutions was polarized in the same inhibited solution. Figure 3.17c shows the anodic polarization curves of these samples. Significant reduction in anodic kinetics was observed after polarizing in chloride-only solutions and the reduction in kinetics was slightly

better than the positive control sample after 50 h immersion and markedly better than that of the sample polarized after immersion for 19 days. This shows the formation of a robust protective film that passivates the surface and the inhibition is increased, if not maintained with increase in exposure time.

(a)

(b)

(c)
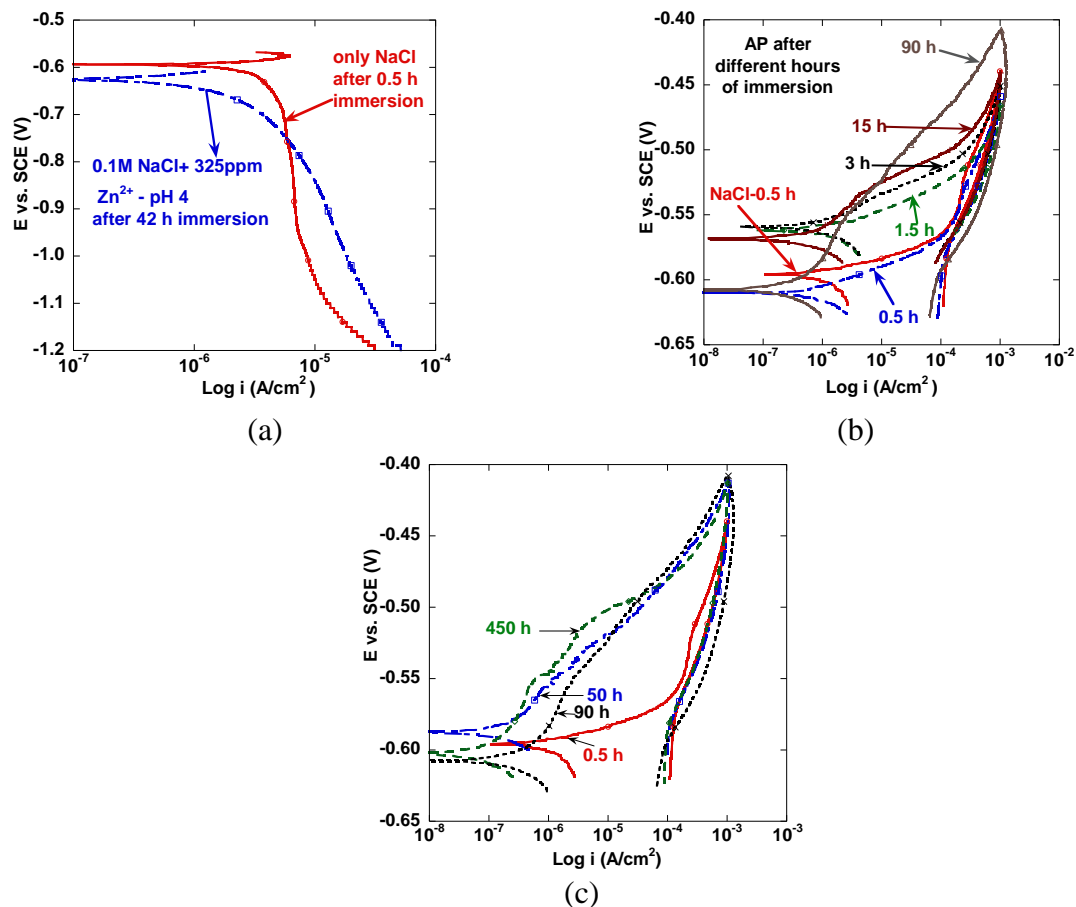
Figure 3.17. (a) Cathodic polarization curve in pH 4 0.1M NaCl solution with 5 mM Zn^2 after 42hrs immersion (blue curve) against the polarization curve in pH 4 0.1M NaCl solution after 0.5 hours of immersion (red curve) (b) Anodic polarization in pH 4 0.1M NaCl solutions with 5mM Zn^{2+} additions after different lengths of immersion time. (c) Anodic polarization of 2024-T3 in chloride-only solutions after different exposure times to test persistence

5.3.2.4.6 EIS

5.3.2.4.6.1 EIS spectra in aerated solutions. Electrochemical Impedance shed further light on the time evolution of the corrosion response with Zn^{2+} ion additions at near-OCP conditions EIS experiments consisted of immersion of samples in 0.1M NaCl solution containing 5 mM Zn^{2+} at pH 3, 4 and 7 (natural pH), and impedance spectra were recorded after various lengths of exposure time (5 hours to 7 days). EIS spectra of bare metal exposed to chloride-only solutions adjusted to the same pH were used for comparison.

The Nyquist plots of the immersed samples in Figure 3.18 show the increase in low frequency impedance with increase in exposure time with Zn^{2+} ion additions at all pH demonstrating the time-dependent evolution of Zn^{2+} inhibition. The effect of increased immersion times on the extent of inhibition was higher for pH 4 than for pH 7 and pH 3 Zn^{2+}-bearing solutions. The pH 4 Zn^{2+}-bearing solution exhibited more than an order of magnitude increase in the low frequency impedance after 7 days immersion when compared to 1 day immersion. This increase is however less than an order of magnitude for pH 7 and much less for pH 3 Zn^{2+}-bearing solutions.

All the samples in Zn^{2+}-bearing solutions exhibited higher impedance when compared to that of the samples immersed in chloride-only solutions at the same pH. The sample immersed in pH 4 Zn^{2+} solution had the highest impedance compared to the pH 7 and pH 3 Zn^{2+}-bearing solutions at the end of 7 days.

All of the spectra exhibited a single time constant behavior. In order to characterize the behavior of these systems, a simplified Randles circuit was used to fit the spectra as the system goes through a maximum in the phase angle response. This equivalent circuit consisted of a solution resistance (R_s), a double layer constant phase element (CPE_{dl}) and a polarization resistance (R_p). A CPE is used in the equivalent circuit models as the system does not exhibit a perfect capacitive behavior but acts as a 'leaky capacitor'. The true capacitance is derived from the CPE parameters using the equation [57]:

$$C_{dl} = Y^{\frac{1}{n}} R_p^{\frac{1-n}{n}}$$

(3.2.9)

Where Y and n represent the CPE constant and exponent respectively and C_{dl} is the extracted charge transfer capacitance. The polarization resistances are extracted and compared.

5.3.2.4.6.2 Evolution of Polarization Resistance in aerated, deaerated and decarbonated conditions. The evolution of polarization resistance with immersion time in aerated and deaerated 0.1M NaCl solutions with and without 5 mM Zn^{2+} additions at pH values of 3, 4 and 7 is shown in Figures 3.19a and 3.19b. Strong effect due to Zn^{2+} ion additions was observed in aerated conditions with a significant increase in polarization resistance compared to that of chloride-only solutions at the same pH. In contrast, Zn^{2+} ion additions in deaerated conditions did not show any effect on the polarization resistance compared to the chloride-only solutions. This shows that shutting down the supply of oxygen in de-aerated conditions is an important part of the effect. The pH 4 Zn^{2+}-bearing solution which exhibited the highest polarization resistance in aerated conditions compared to all the solutions with and without Zn^{2+} additions, is away from the solubility minimum predicted from the speciation diagram in Figure 3.8c. However, it exhibited lower polarization resistance in deaerated conditions compared to pH 7 Zn^{2+}-bearing solutions and pH 6 chloride-only solutions. Therefore, oxygen is necessary for the superior Zn^{2+} inhibition observed at pH 4.
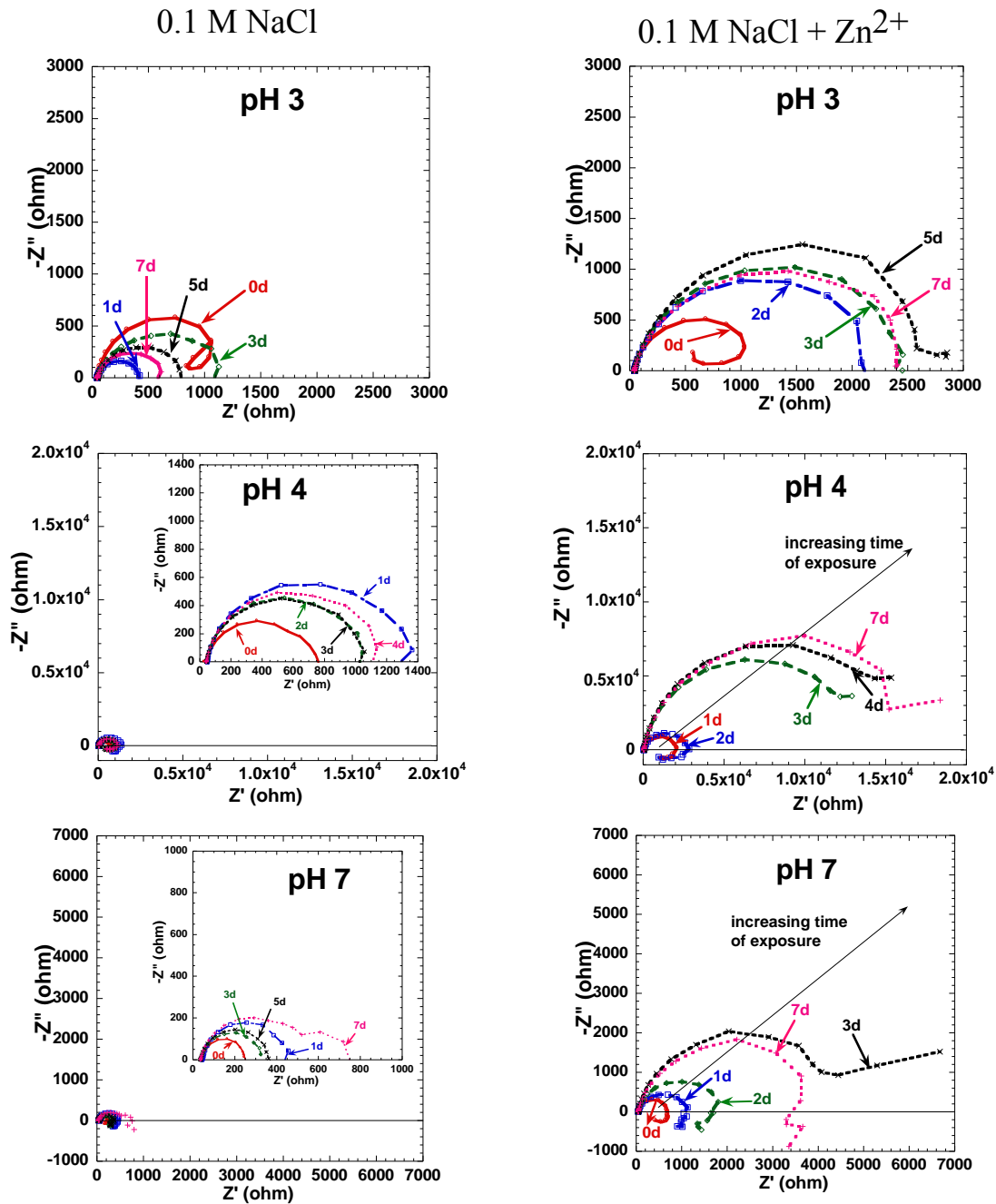
Figure 3.18. Nyquist plots of AA 2024-T3 samples immersed in different solutions during different days of exposure. Note that the plots at a single pH are plotted to the same scale for an easy comparison between the inhibited and the uninhibited case.
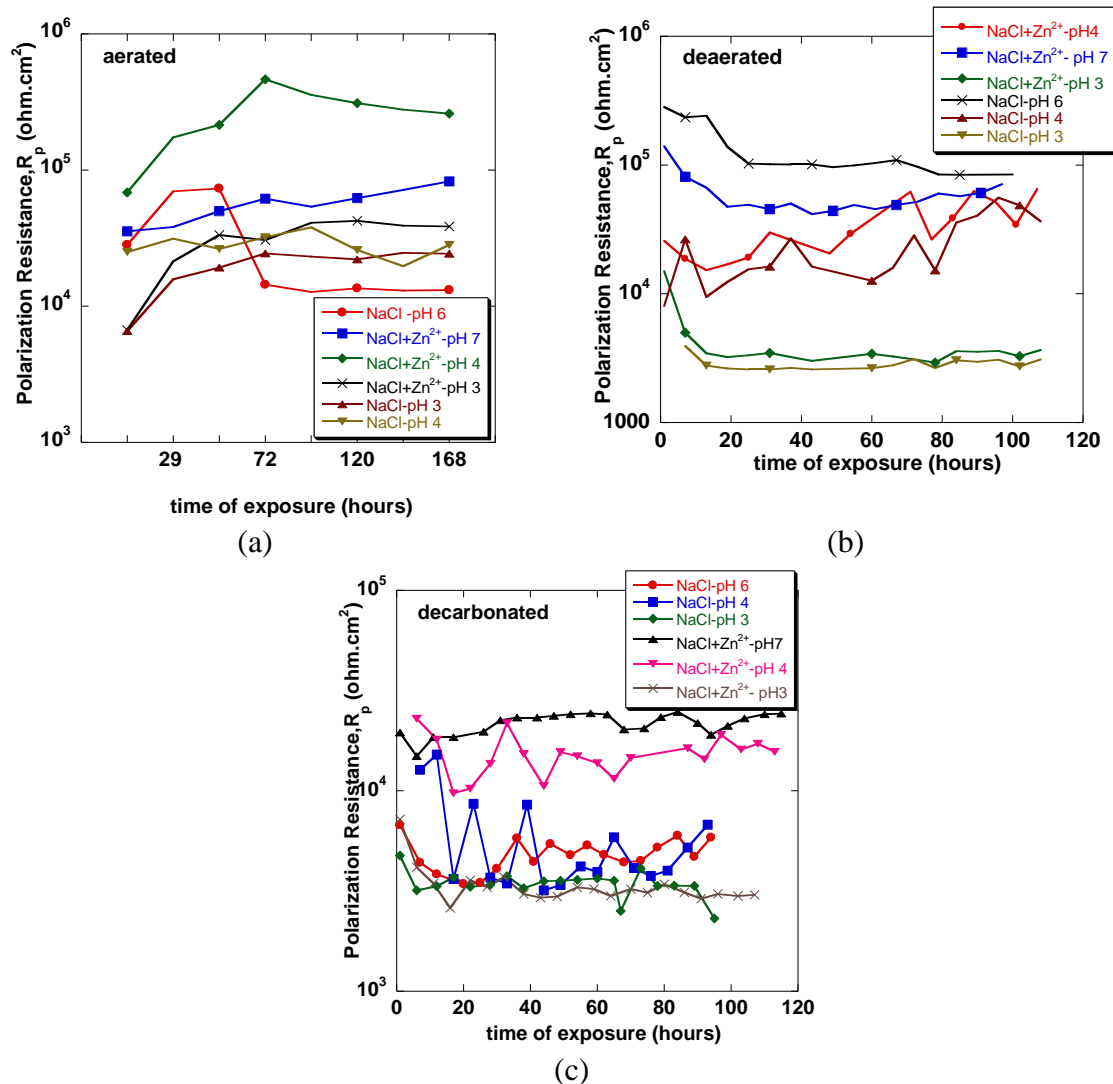
Figure 3.19. Polarization resistance of the samples exposed to 0.1M NaCl + 5 mM Zn^{2+} and NaCl-only solutions at pH 3,4 and 7 (natural pH) in (a) aerated (b) deaerated (c) decarbonated environments.

The polarization resistance vs. time of the samples immersed in decarbonated solutions with and without Zn^{2+} ion additions at different pH is shown in Figure 3.18c. Higher polarization resistance was exhibited by pH 7 Zn^{2+}-bearing solution compared to pH 4 Zn^{2+}-bearing solutions, in contrast to the aerated solutions where pH 4 Zn^{2+}-bearing solutions showed superior performance. This shows that CO_2-bearing precipitation is an important part of Zn^{2+} ion inhibition. Inhibition in the absence of CO_2 at pH 7 is closer to the solubility minimum shown in the Zn^{2+} speciation diagram in Figure 3.8b.

Higher polarization resistances of pH 7 and pH 4 Zn^{2+}-bearing decarbonated solutions compared to those in chloride-only solutions at the same pH, shows that there is some corrosion inhibition seen in the absence of CO_2. This could be due to Cl^- and OH^- -bearing precipitation forming $Zn_5(OH)_8Cl_2$ and $Zn(OH)_2$ as predicted by the Zn^{2+} speciation diagram in the absence of CO_2

(Figure 3.8b). However, no effect on the polarization resistance was seen with Zn^{2+} additions at pH 3.

3.2.4.7 Surface Analysis. Surface analysis of the samples immersed in 5 mM Zn^{2+} ion concentrations for a period of 5 days in different environments (aerated, deaerated and decarbonated) was done to characterize the differences in the surface film which led to the differences in impedance measurements and hence to aid in the understanding of the mechanism of inhibition by the Zn^{2+} ion at pH 4 and pH 7. X-ray diffraction of the sample surface was done to identify the chemical compounds and XPS, being a surface sensitive measurement was carried out to obtain a chemical composition with a detailed individual elemental analysis.
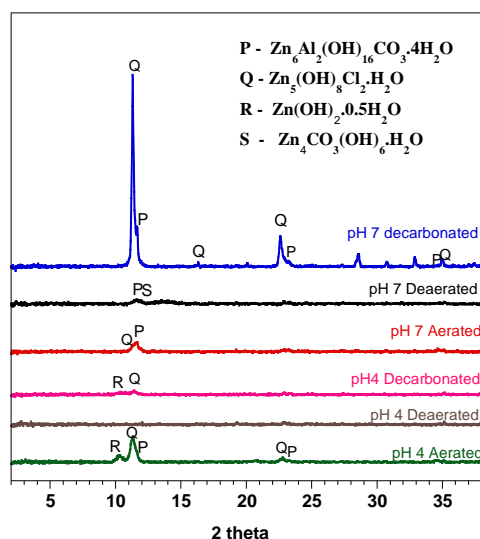
Figure 3.20. X-ray diffractograms of AA 2024-T3 coupons after immersion for 5 days in 0.1M NaCl + 5 mM Zn^{2+} solution in different environment

Table 3.3 shows the results for the elemental chemical quantifications of the surface film on AA 2024-T3 alloy immersed in the inhibited solutions in various environmental conditions. These were obtained from the analysis of the high resolution spectra. The percentage of carbon (C) shown correspond to the carbonate peak and the other carbon peaks were not accounted as they might be obtained from contamination during measurements. Figure 3.20 shows the x ray diffraction patterns of the samples exposed to various conditions. The assignment of the compounds was done using the JCPDS software and with the help of literature sources [56, 58].

5.3.2.4.7.1 Exposure to pH 7 inhibited electrolyte. Localized film formation on the sample could be seen visually. The XRD of the sample in Figure 3.20 shows peaks corresponding to two compounds, zinc aluminum carbonate hydroxide ($Zn_6Al_2(OH)_{16}CO_3.4H_2O$) and zinc chloride hydroxide ($Zn_5(OH)_8Cl_2.H_2O$). The relative XRD peak intensity of the Zn-Al carbonate hydroxide was higher than that of the zinc chloride hydroxide. As the XRD peak intensities are directly proportional to the concentration of the compounds, the film formed in aerated solutions at pH 7 contains predominantly Zn-Al carbonate hydroxide and low concentrations of Zn chloride hydroxide.

Table 3.3. Chemical quantification analysis obtained from the XPS high resolution individual element spectra, performed on the AA 2024-T3 samples exposed to different environments for a period of 5 days

% Elements from XPS surface analysis								
0.1M NaCl+ 5 mM Zn^{2+}	**Al**	**Zn**	**Cu**	**Mg**	**O**	**Cl**	**S**	**C**
pH 7 - Air	23.989	4.052	0.044	0.121	65.597	3.661	0.654	1.882
pH 7 - Air Free	21.268	3.949	0.112	0.528	67.622	4.459	-	2.062
pH 7 - CO$_2$ free	2.941	21.840	-	-	57.140	10.076	-	8.003
pH 4 - Air (white region)	22.346	5.306	0.074	-	66.583	1.170	2.737	1.783
pH 4 - Air (grey region)	26.622	1.551	-	-	65.250	1.775	2.000	2.803
pH 4 - Air Free	28.253	0.486	0.702	0.246	63.279	0.802	2.190	4.041
pH 4 - CO$_2$ free	24.081	2.985	-	-	64.627	4.828	2.078	1.401
Bare 2024 (Unexposed)	39.921	-	0.155	0.071	55.917	0.853	0.464	2.618

The Zn 2p3/2 peak obtained from the XPS measurement of the sample surface confirmed the presence of zinc element in the surface film with a binding energy corresponding to 1022.2 eV. This binding energy does not correspond to the oxide but to a hydroxy compound or a carbonate compound [56]. The high resolution Cl 2p spectrum showed increased levels of chlorine on the surface compared to the freshly prepared and unexposed 2024-T3 surface (Figure 3.21b). The binding energy of Cl peak, 198.6 eV, corresponded to an inorganic chloride, confirming that the signal is coming from the zinc chloride hydroxide. The O peak corresponds to that of a hydroxide or a carbonate and not to metal oxide. Evidence of oxidized copper and magnesium was seen on the surface (Mg peak shown in Figure 3.21c) supporting the idea that corrosion is the precursor to the precipitation of the zinc film. The aluminum signal from the unexposed surface was collected and is shown in Figure 3.21a. Al peaks from the unexposed surface were obtained at 74.6 eV and 71.8 eV which correspond to Al^{3+} and Al metal respectively. After immersion for 5 days in pH 7 Zn^{2+}-bearing solution, the signal from the metal peak disappeared with negligible change in the intensity of the Al^{3+} peak. It should be noted that, the chemical quantification results seen in Table 3.3 indicated that the surface film is rich in aluminum hydroxide and among the small percentage of zinc compounds, the Zn-Al carbonate hydroxide was higher in concentration when compared to the chloride hydroxide.
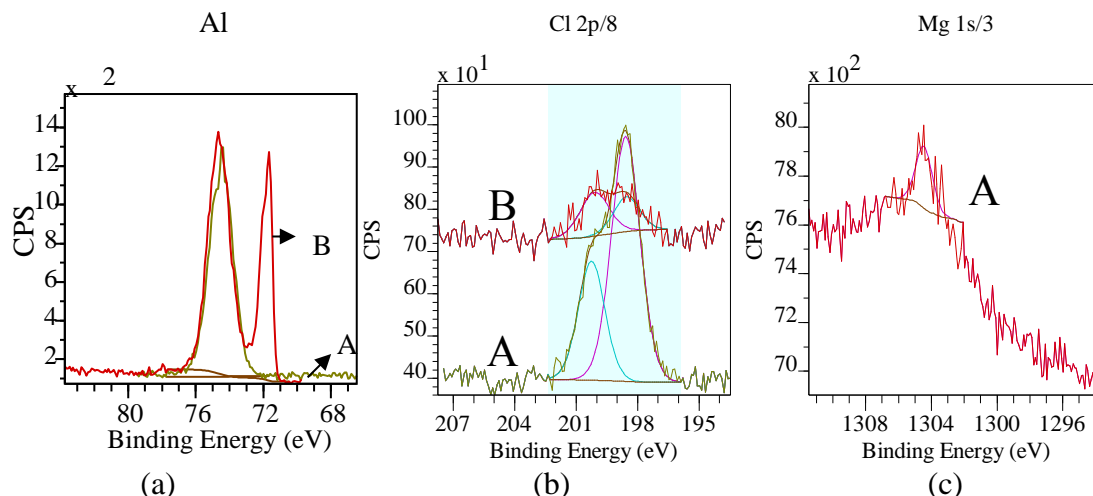
Figure 3.21. XPS peaks of (a) aluminum (b) chlorine (c) magnesium obtained from the surface of the coupon, A − exposed to chloride solution with 5 mM Zn^{2+} cation at pH 7 in Air for 5 days and B − Freshly prepared Bare 2024-T3 coupon unexposed.

The sample immersed in deaerated pH 7 Zn^{2+}-bearing solution for a period of 5 days showed visible attack and turned brownish. The XRD of the sample showed very low concentrations of zinc compounds and the peak analysis showed that they corresponded to $Zn_6Al_2(OH)_{16}CO_3.4H_2O$ and $Zn_4CO_3(OH)_6.H_2O$. High chloride concentrations were seen from XPS chemical quantification in Table 3.3, which could probably be from contamination as no peaks of any inorganic chloride were seen in XRD.

Figures 3.22a and 3.22b show the high resolution Cu 2p spectrum and Mg 1s spectrum obtained from samples immersed in pH 7 Zn^{2+}-bearing solutions in aerated and deaerated environments. Relatively higher amounts of oxidized Cu and Mg were seen on the air-free sample compared to that of the sample in air. This is consistent with the idea that Zn^{2+} ion doesn't inhibit corrosion in the absence of air.

The surface film formed in the absence of CO_2 in pH 7 Zn^{2+}-bearing solution contained predominantly Zn compounds (Al 2.94% and Zn 21.84 %) as opposed to the film formed in the presence of CO_2 (Al 23.98% and Zn 4.05%). The XRD of the sample showed strong intensity peaks of zinc compounds with high concentrations of $Zn_5(OH)_8Cl_2.H_2O$ compared to $Zn_6Al_2(OH)_{16}CO_3.4H_2O$. The relatively high concentration of the carbonate compound ($C_{carbonate}$% of 8 from Table 3.3) in a decarbonated environment is incongruent. The carbonate could either be from traces of carbonate anions in the electrolyte or it could be from the exposure of the sample to the air (for a short duration of 10 min) before introducing in the XPS vacuum chamber. XPS of the high energy resolved Al 2p spectra in Figure 3.22c showed very low intensity Al^{3+} peak obtained from the sample in CO_2 free solution while the sample in air (in the presence of CO_2), showed a strong Al^{3+} peak. The small intensity of the Al 2p peak could be from the Al in $Zn_6Al_2(OH)_{16}CO_3.4H_2O$. Thin surface films are known to provide more protection, thus, this extremely thick surface film of zinc compounds indicates higher amount of corrosion and does not seem to provide impedance to corrosion reactions.
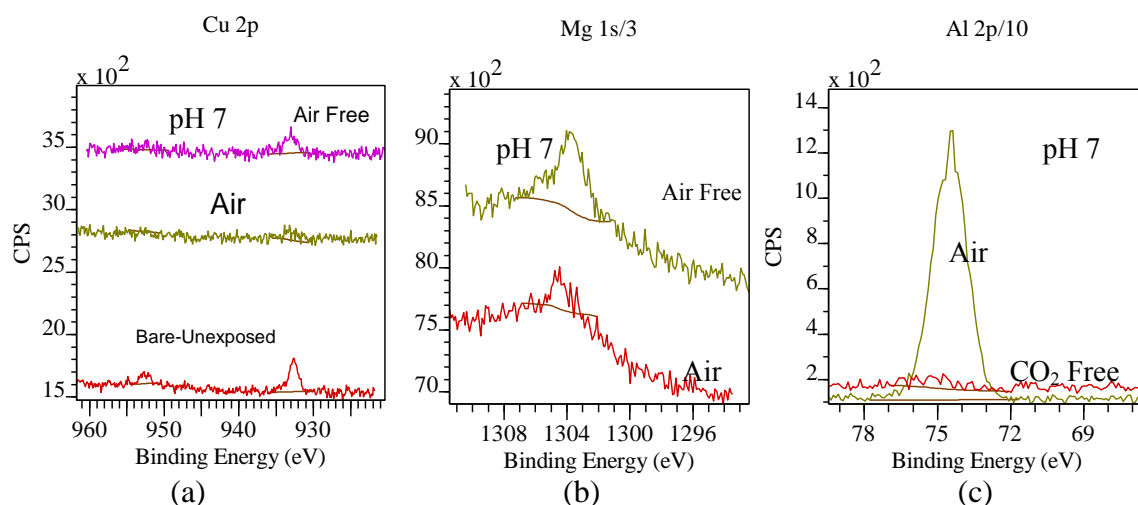
Figure 3.22. XPS peaks of (a) Copper (b) Magnesium obtained from the surface of the coupon exposed to chloride solution with 5 mM Zn^{2+} cation at pH 7 in air and air-free environments for 5 days (c) High resolution Al 2p peak obtained from the surface of the coupon exposed to chloride solution with 5 mM Zn^{2+} cation at pH 7 in air and CO_2-free environments for 5 days

5.3.2.4.7.2 Exposure to pH 4 inhibited electrolyte. The sample immersed in aerated conditions for 5 days showed two distinct regions – a white region where a film was seen and a grey shiny region. The XRD of the film in the white region showed peaks from three compounds, $Zn_5(OH)_8Cl_2.H_2O$, $Zn_6Al_2(OH)_{16}CO_3.4H_2O$ and $Zn(OH)_2.0.5H_2O$, among which $Zn_5(OH)_8Cl_2.H_2O$ was seen in relatively higher concentrations. This is in contrast to the film formed in aerated pH 7 solution where the concentration of the $Zn_6Al_2(OH)_{16}CO_3.4H_2O$ was higher compared to the $Zn_5(OH)_8Cl_2.H_2O$. There was no evidence of Mg over the entire surface (both the white and grey regions), indicating the suppression of Mg dissolution or complete dissolution of Mg by the Zn^{2+} ion in solution at pH 4. However, EDS mapping of the sample immersed in aerated pH 4 Zn^{2+}- bearing solution (Figure 3.16c) showed intact Mg in the S phase particles supporting suppression of Mg dissolution by Zn^{2+} ion. XPS is surface-sensitive with signal coming from less than 10 nm from the surface while EDS is not surface-sensitive as the signal comes from within 10 μm from the surface. Absence of Mg signal from the XPS peak suggests the coverage of the sample surface with a film.

Evidence of oxidized Mg on the surface in pH 7 aerated solutions shows the effectiveness of Zn^{2+} ion inhibition at pH 4 (Figure 3.23a). The grey region showed no evidence of copper but the white film region showed evidence of oxidized copper, which suggests that the white film formed as a result of higher corrosion activity. The sample in Figure 3.14 immersed for a day in pH 4 inhibited solution had a mirror finish with no presence of any white film. EDS mapping showed uniform presence of zinc on the surface. Increase in the immersion time for 5 days resulted in the formation of a white film at some regions on the surface and the film is rich in zinc element concentration. Thickening of zinc film usually started from the edges of the cut samples, which could be that the edges are more prone to corrosion. Differences in the electrochemical activity of the passivated surface and the rough edges could have resulted in corrosion closer to the edges and result in the white film formation.

132
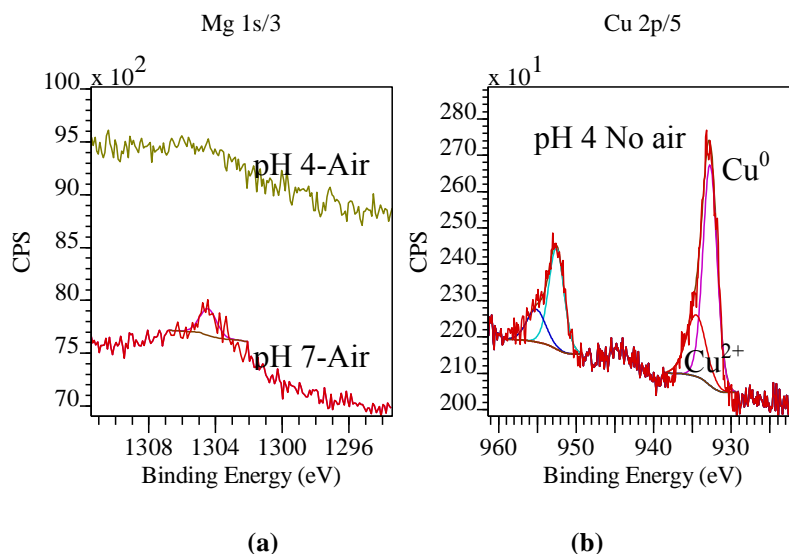
Figure 3.23. (a) High resolution Mg1s peak obtained from the surface of the coupon exposed to chloride solution with 5 mM Zn^{2+} cation at pH 7 and pH 4 in aerated environments for 5 days (b) Copper XPS peak obtained from the surface of the coupon exposed to chloride solution with 5 mM Zn^{2+} cation at pH 4 Air free condition for 5 days

The sample immersed in deaerated pH 4 Zn^{2+}-bearing solution showed a brown surface with visual signs of corrosion. Very low zinc element concentration was seen on the surface, which shows that oxygen is critical for the inhibition by zinc at pH 4. Significant amounts of copper (both oxidized and metallic) and oxidized magnesium were observed on the surface while no magnesium and negligible amounts of Cu were found in aerated conditions (Figure 3.23b).

The XRD of the surface film formed in decarbonated pH 4 solutions showed a different composition of the film which includes $Zn_5(OH)_8Cl_2.H_2O$, $Zn(OH)_2.0.5H_2O$ and negligible amounts of $Zn_6Al_2(OH)_{16}CO_3.4H_2O$. The film had a higher concentration of $Zn_5(OH)_8Cl_2.H_2O$ than the $Zn(OH)_2.0.5H_2O$ as deduced from the XRD peak intensities. No concentrations of oxidized metallic Cu or Mg were seen on the surface. This film differed from the film formed in air in that XPS showed a high concentration of Cl (3 times more) on the surface in the CO_2 free environment compared to air (Table 3.3).

5.3.2.5 Discussion

5.3.2.5.1 Zn^{2+} vs. Rare Earth Metal (Ce^{3+}, Pr^{3+}, La^{3+}) cations

5.3.2.5.1.1 ORR inhibition on 2024. Previous researchers have shown that Zn^{2+} cation suppresses cathodic kinetics on both aluminum alloys and ferrous substrates. Low concentrations of Zn^{2+} cation of 40 ppm in 0.003 M chloride was seen to increase the linear polarization resistance and decrease the corrosion potential on carbon steel in neutral solutions[53]. The cathodic inhibition by Zn^{2+} cation on AA 2024-T3 alloy was first studied by Buchheit et al. in 0.124 M NaCl solution and saw an order of magnitude of corrosion current at higher zinc ion concentrations of 0.05M, 0.15M and 0.25M[52]. This cathodic inhibition by Zn^{2+} was verified and similar results were observed where a decrease in corrosion potential was observed with the

increase in Zn^{2+} ion concentration, thus decreasing the susceptibility of the alloy to localized corrosion.
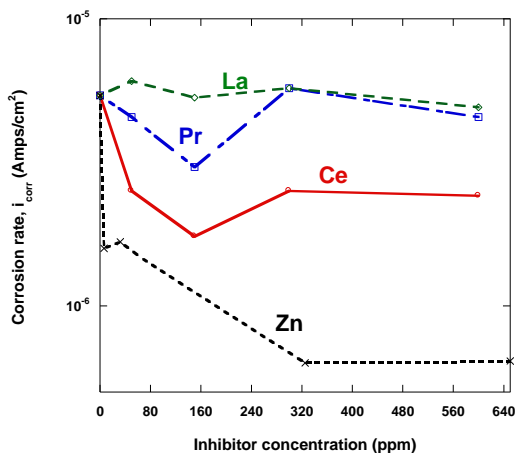
Figure 3.24. Comparison of the rates of corrosion at different inhibitor chloride concentrations (obtained from polarization studies)

The effect of Zn^{2+} concentration on the cathodic polarization response from 2024-T3 alloy and the extent of corrosion inhibition by Zn^{2+} ion when compared to REM cations is summarized in Figure 3.24. Corrosion current was obtained by the extrapolation of cathodic current from the cathodic polarization curves done in natural pH solutions with the help of Gamry Echem Analyst[TM] software (explained in part 3.1). The plot shows the corrosion rate of 2024 samples versus the concentration of cationic inhibitors added as metal chlorides in 0.1M NaCl solution. Zn^{2+} inhibits ORR when its concentration is as low as 6 ppm (0.1 mM) and reaches a maximum at around 325 ppm (5 mM) unlike the Ce^{3+} and Pr^{3+} cations which exhibit concentration windows in which their inhibition is maximum. This range is typically $100-300$ ppm. This means that excessive REM cation concentrations are not effective inhibitors while the inhibition by Zn^{2+} cation is still at its maximum at concentrations above 5 mM. This critical concentration of 5 mM for Zn^{2+} has been chosen for the speciation calculations and electrochemical experiments as mentioned above in solutions at different pH. Among all the cationic inhibitors, Zn^{2+} inhibited the cathodic kinetics to the maximum extent by almost an order of magnitude while the lanthanides suppress the kinetics by less than order of magnitude of current.

5.3.2.5.1.1 ORR inhibition on Cu RD. 1 mM Zn^{2+} additions to 0.1 M NaCl solution were observed to suppress the mass transport limited ORR kinetics on Cu RDE by about two orders of magnitude at 2000 rpm. Levich representations of ORR current as a function of rotation rate at a bias of 0.75 V, 0.8 V, 0.85 V, 0.9 V and1 V vs SCE for the chloride-only solutions and at a bias of 0.65 V, 0.675 V, 0.7 V, 0.725 V, 0.750 V vs SCE for with 1 mM Zn^{2+} additions is shown in Figure 3.25. As described in section 10.3.1.4.2, the ratio, R, which is the ratio of the slope of the Levich plots of the Zn^{2+}-bearing solution (k_{Zn}) to that of the slope of chloride-only solution (k), is a quantification factor where low value of R implies good corrosion inhibition. The slope of the fit of the chloride-only solution k is written as,

$$k = \frac{I_L}{\omega^{\frac{1}{2}}} = 0.2AnFC_B D_O^{\frac{2}{3}} \upsilon^{-\frac{1}{6}}$$

$$(3.2.10)$$

And the slope of the fit of the Zn^{2+}-bearing solution, k_{Zn}, is written as,

$$k_{Zn} = \frac{I_L}{\omega^{\frac{1}{2}}} = 0.2A_{Zn} nFC_B D_O^{\frac{2}{3}} \upsilon^{-\frac{1}{6}}$$

$$(3.2.11)$$

From equations 3.2.10 and 3.2.11,

$$R = \frac{k_{Zn}}{k} = \frac{A_{Zn}}{A}$$

$$(3.2.12)$$

where A_{Zn} is the effective area of the Cu electrode supporting oxygen reduction in the presence of Zn^{2+} cation in the solution . Again, equation 3.2.13 holds assuming that zinc additions to the chloride solution does not change the ORR mechanism (n is the same), diffusion coefficient of the oxygen and the kinematic viscosity of solution, and also that the proportionality between the limiting current density and rotation rate remains, leading to the effect caused by an electrode blocking phenomena associated with the deposition of zinc compound on the electrode surface.

The value of R was found to be 0.015 which means the effective area of the copper electrode supporting ORR in the Zn^{2+} inhibited solution is 0.015 times the area of the copper electrode supporting ORR in the chloride-only solution. This also means that 98.5% of the copper area was blocked by the zinc hydroxy compound. The R value of Zn^{2+} cation was about an order of magnitude higher than that of the REM cations where Ce^{3+}, Pr^{3+} and La^{3+} cations gave an R values of 0.376, 0.171and 0.207 respectively (see in chapter 3). This low value of R for Zn^{2+} was very close to the R value of a 0.01 M chromate solution in pH 6 chloride solution which was determined to be 0.019 by Kendig et al. However, strontium chromate (pH 8.3 from Baker Colors) exhibited an order of magnitude of lower R value of about 0.002 [31]. Based on this comparison, Zn^{2+} is a very effective inhibitor of cathodic kinetics on Cu while lanthanides proved to be modest inhibitors.

(a)   (b)
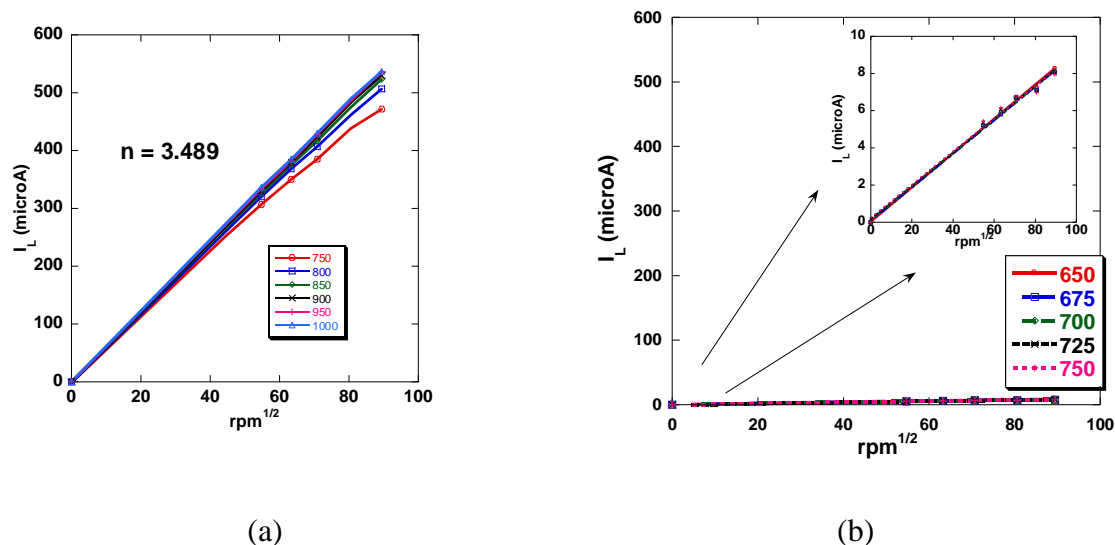
Figure 3.25. Levich representation of the oxygen reduction reaction kinetic data obtained from the polarization curves on Cu RDE in (a) chloride only solutions and (b) chloride solutions containing 1mM of the Zn^{2+} cation. Each straight line corresponds to the value of the limiting current extracted at the respective bias vs SCE shown in the legend box

5.3.2.5.2 Inhibition vs pH

5.3.2.5.2.1 Evolution of corrosion response. Figure 3.26 shows the comparison of cathodic corrosion current extracted from the cathodic polarization curves at -800 mV SCE which is in the mass transport ORR regime, in aerated 0.1M NaCl solutions with and without 5 mM Zn^{2+} additions at different pH ranging from 3 to 10. This potential value is chosen for comparison because this point is below the least corrosion potential observed. The maximum inhibition was observed at pH 7.7 in the solubility minimum as shown in the Zn^{2+} speciation diagram in Figure 3.8c. Garcia et al. made a similar comparison of the corrosion current of 2024 samples in 0.1 M NaCl solutions with and without 0.1 mM $CeCl_3$ as a function of pH [59]. The corrosion current was extracted from polarization experiments after 30 min. immersion at OCP. The trend observed was similar to the one seen in Figure 3.26 where maximum inhibition by Ce^{3+} cation was seen in neutral pH conditions close to the solubility minimum.

The trend in corrosion rate vs. pH seems to be very different from the impedance measurements done in aerated solutions at near-OCP conditions for a period of 5 days. The polarization resistance, R_p is inversely related to the corrosion current given by the Stern-Geary equation [60]. The values of R_p obtained from the impedance data were used to estimate the rate of corrosion of aluminum substrates at varying lengths of exposure time. Figures 3.2.20b and 3.2.20a show the trend in the corrosion rate of the samples immersed in aerated, solutions at pH 3, 4 and pH 7 solutions with and without 5 mM Zn^{2+} additions respectively. They were plotted to the same scale for easy comparison. The plot in aerated Zn^{2+}-bearing solutions exhibited a larger dip in the corrosion rate at pH 4 at all immersion times (6h – 168 h), in contrast to the corrosion rate vs. pH curve from polarization experiments (Figure 3.26) which showed a dip in the neutral pH conditions.
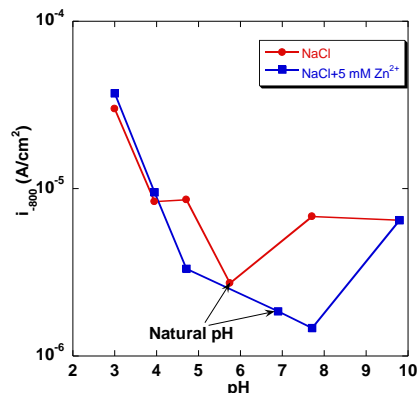
Figure 3.26. Current at -800 V SCE (i_{-800}) obtained for two solutions (0.1M NaCl with and without additions of 5mM Zn^{2+} inhibitor) at different pH. These data are obtained from polarization studies.

It was also observed that the effect of increased immersion times on the extent of inhibition was higher for pH 4 than for pH 7 Zn^{2+}-bearing solutions. However, in the polarization experiments, the samples were exposed 30 min. prior to running the polarization curves which is insufficient time for the Zn^{2+} ion in pH 4 solutions to suppress the corrosion kinetics as observed in impedance measurements (Figure 3.23a). This finding is interesting as it shows that polarization experiments done after short immersion times do not capture all the important aspects while testing new inhibitors.

5.3.2.5.2.2 Oxygen and CO_2 dependence. Figures 3.27, 3.28 and 3.29 show the trend in the corrosion rate of the samples immersed in aerated, deaerated and decarbonated solutions at pH 3, 4 and pH 7 solutions with and without 5 mM Zn^{2+} additions. The dip at pH 4 is lost in the deaerated conditions indicating that oxygen is an important part of this effect. In fact, the corrosion rates are higher at pH 4 Zn^{2+}-bearing solutions than at pH 7 Zn^{2+}-bearing solutions. As stated earlier, there is no effect of Zn^{2+} ion addition in deaerated conditions on the corrosion rate at all pH indicating that oxygen is required for Zn^{2+} inhibition. Al alloy dissolves in mildly acidic conditions with hydrogen reduction as the main cathodic reduction in deaerated conditions. Therefore, higher corrosion rates are seen in pH 4 solutions, which have higher concentration of hydronium ions. The susceptibility of the alloy to corrosion is suppressed due to the absence of oxygen and lesser concentration of hydronium ions at pH 7 and hence the alloy is more corrosion resistant with a more stable passive oxide at neutral pH.

137

(a)   (b)
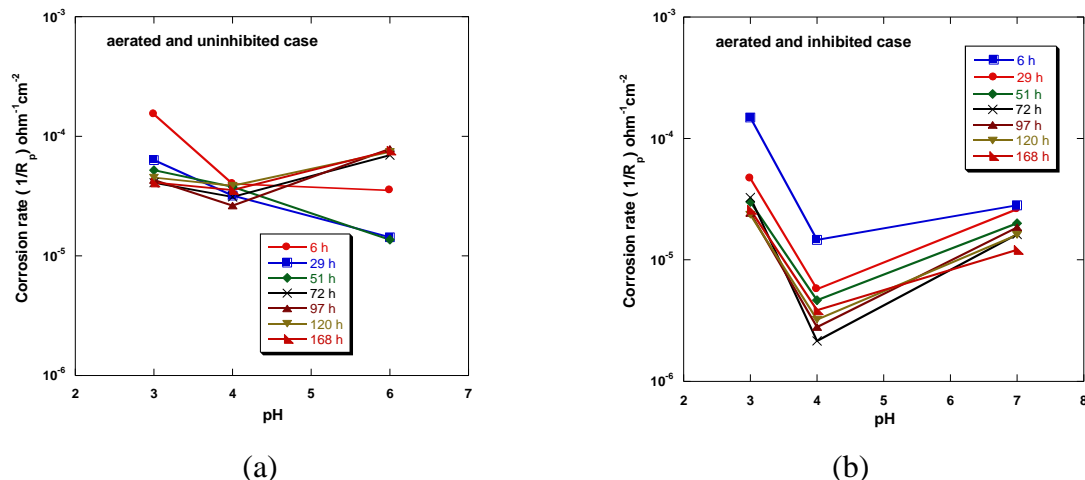
Figure 3.27. The corrosion rate of 2024-T3 coupons immersed in aerated (a) sodium chloride solutions (b) zinc containing sodium chloride solutions at different pH (obtained from the EIS measurements) .

(a)   (b)
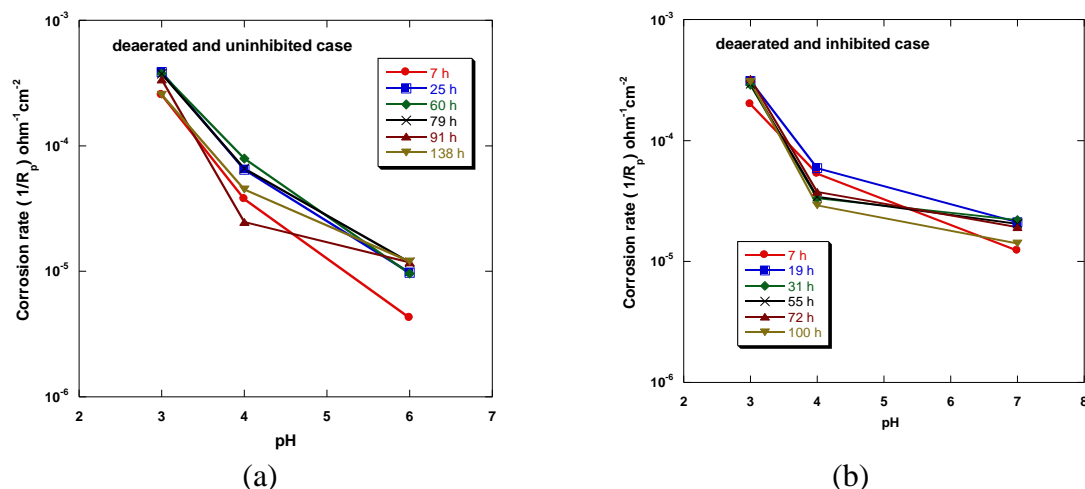
Figure 3.28. The corrosion rate of 2024-T3 coupons immersed in deaerated (a) sodium chloride solutions (b) zinc containing sodium chloride solutions at different pH (obtained from the EIS measurements) .

The dip in decarbonated pH 4 Zn^{2+}-bearing solutions disappeared with the inhibition at pH 4 being very similar to that at pH 7. Comparison between the corrosion rates of the alloy in aerated (with atmospheric CO_2) and decarbonated Zn^{2+}-bearing solutions in Figures 3.27b and 3.29b, shows that CO_2 does play an important role in aiding Zn^{2+} to provide corrosion inhibition. This effect is observed to be more pronounced in acidic solutions where the corrosion rate in decarbonated Zn^{2+}-bearing solutions was about an order of magnitude higher than the aerated Zn^{2+}-bearing solutions at both pH 3 and pH 4. Al alloy undergoes uniform corrosion and the entire surface supports cathodic reaction, thus producing alkalinity in the interfacial layer. This alkalinity deprotonates the carbonic acid and the bicarbonate anions to form carbonate anions which could react chemically with the Zn^{2+} cations and the dissolving Al metal cations, and forms a barrier to the corrosion reactions.
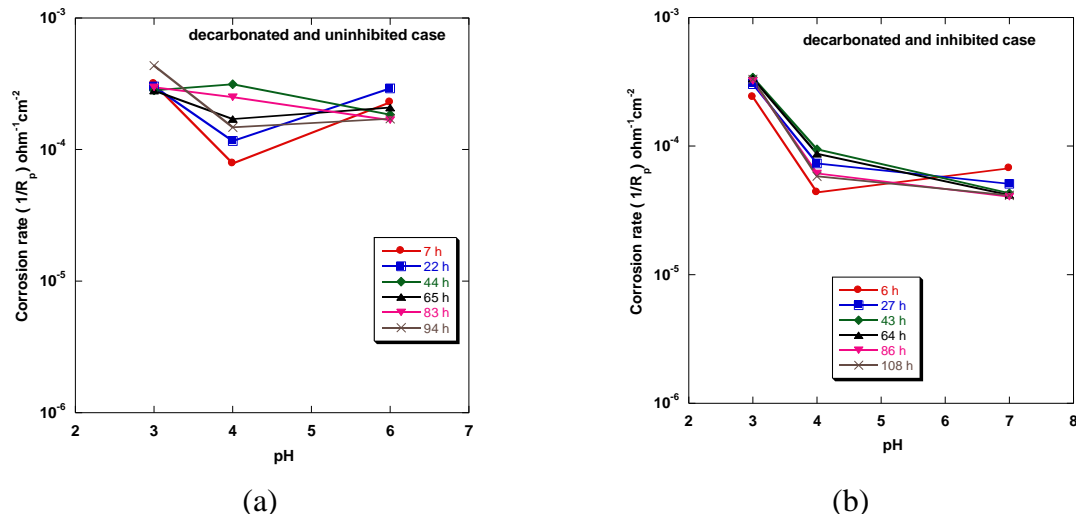
Figure 3.29. The corrosion rate of 2024-T3 coupons immersed in decarbonated (a) sodium chloride solutions (b) zinc containing sodium chloride solutions at different pH (obtained from the EIS measurements).

XPS surface analysis results are consistent with this idea where negligible carbonate hydroxide compound was seen on the sample in decarbonated pH 4 Zn^{2+}-containing solutions, in contrast to the aerated pH 4 Zn^{2+}-containing solution which had a relatively higher concentration of the carbonate compound. Hence, CO_2-bearing precipitation aids in retarding the corrosion reactions in Zn^{2+}-containing chloride solutions.

5.3.2.5.3 Mechanism of inhibition. A mechanism is proposed to explain the inhibition by the Zn^{2+} in acidic (pH 3), mildly acidic (pH 4) and neutral (pH 7) environments. AA 2024-T3 is passivated at pH 7 except at the intermetallic particles as the oxide film is much thinner at the intermetallic particles. The alloy is susceptible to localized corrosion due to galvanic coupling between the Cu-rich sites within the intermetallic particle and the anodic constituents of the active intermetallics or between the Cu-rich sites and the matrix surrounding the intermetallic particles. These Cu-containing particles support ORR and dissolve the matrix surrounding the particle leading to pitting or trenching of the alloy or dealloying of the active intermetallics [8]. ORR leads to an increase in alkalinity and drives the local pH on the intermetallic particle upwards. This local increase in pH lowers the solubility of Zn^{2+} cation adjacent to the intermetallic particles resulting in massive precipitation, which eventually leads to exhaustion of the Zn^{2+} ion. Corrosion process is followed by precipitation. Higher corrosion rate is seen at shorter periods of exposure time and then a decrease in the corrosion rate results due to increased precipitation with increase in exposure time as seen in Figure 3.27b. This decrease in the corrosion rate was observed after the formation of an effective physical barrier to ORR, which causes localized inhibition. The massive localized precipitation was evidenced in the SEM pictures of the free corrosion sample in pH 7 solution where the entire surface was covered with crystalline deposits of Zn-Al carbonate hydroxide. The deposits were densely populated over the intermetallics and had openings or defects at pits, trenches in and around the intermetallic particles, through which corrosion can continue to occur.

Al dissolves in acidic pH seen in the Pourbaix diagrams. The entire surface of the Al alloy is activated at pH 4 including the intermetallic particles and the matrix. The alloy is subjected to

139

uniform corrosion where the ORR is supported by the entire surface. Hence, the solubility of Zn^{2+} ion is reduced in the interfacial electrolyte but remains high in the bulk electrolyte due to a low pH of 4. This results in the formation of a uniform homogeneous thin film, which provides better inhibition. SEM analysis of the surface of the free corrosion sample immersed for a day showed a pit-free surface and EDS mapping of the surface showed the presence of this film with no preferential distribution over the intermetallic particles. The inhibition is not localized and the entire surface is passivated with a protective film, which resulted in higher polarization resistance during impedance measurements. This explains why reduced anodic kinetics were observed at longer immersion times before polarization in pH 4 solutions as seen in Figure 3.17b. Anodic polarization of 2024 leads to S phase dissolution and localized corrosion, thus reduction of anodic kinetics at longer immersion times indicates increase in resistance to S phase dissolution. It was interesting to see intact Mg in the Al-Cu-Mg intermetallics in the Mg map shown in Figure 3.16c of the sample immersed in pH 4 Zn^{2+}-bearing solution 2 days. The alloy is activated even at a low pH of 3 but the solubility of the zinc ion is high both in the interfacial electrolyte and bulk electrolyte as the pH is too acidic for the ORR to drive the pH of the interfacial electrolyte upwards. Hence, precipitation or film formation does not occur, thus providing poor or negligible inhibition.

The disappearance of the dip in corrosion rate in deaerated pH 4 Zn^{2+}-bearing solutions is consistent with the idea that an alkaline interfacial electrolyte forms in aerated pH 4 Zn^{2+}-bearing solutions in the presence of oxygen due to ORR. Boisier et al. have similarly observed higher film resistance at acidic pH of 4 in decanoate inhibited chloride solutions[61]. They explained that the surface acquires a positive charge at acidic pH as it is way below the isoelectric point of Al oxide (pH 9.5) and dissolution to Al^{3+} ions occurs. The negatively charged decanoate ions experience coulombic forces, which result in the formation of an organic film. Similarly, the hydroxyl ions produced by oxygen reduction and carbonate anions are attracted and react with the Zn and Al ions to form a stable protective film. Hence, preliminary steps of corrosive processes (oxidation and reduction) seem to be necessary for the inhibitor action to take place.

5.3.2.6 Conclusions

1. Potentiodynamic polarization experiments were carried out on AA 2024-T3 with varying concentrations of Zn^{2+} inhibitor (0.1 mM to 50 mM) and systematic variation of pH in 100 mM NaCl solutions after 30 min immersion at OCP. Results showed greatest suppression of oxygen reduction reaction in neutral chloride solutions (pH 7 and pH 7.7), which reached a maximum at a Zn^{2+} ion concentration of 5 mM. No inhibition was seen at either very high pH (10-12) or very low pH (3-4) while modest inhibition is seen at pH 4.7.

2. Anodic polarization experiments after 30 min immersion time, showed no anodic inhibition by Zn^{2+} ion in any concentration (0.1 mM – 10 mM) and at any pH. However, anodic polarization of samples immersed after longer immersion times (up to 4 days) in mildly acidic Zn^{2+} (pH 4) solutions showed significant reduction in anodic kinetics indicating that Zn^{2+} inhibition is sluggish and acts as a "slow anodic inhibitor".

3. In contrast to the polarization experiments, samples exposed to pH 4 chloride solutions with 5 mM Zn^{2+} additions showed complete suppression of dissolution of Al_2CuMg

particles compared to zinc-free solutions in the SEM studies. Also, EIS measurements showed that the sample exhibited highest polarization resistance, which increased with exposure time. Zn^{2+}-bearing solutions at pH 7 showed modest inhibition while the more acidic pH 3 solution showed negligible inhibition.

4. In deaerated solutions, no effect of Zn^{2+} ion additions on the corrosion rate of the alloy is seen because the ability to make the interfacial electrolyte alkaline is retarded in the absence of oxygen. This indicates that Zn^{2+} inhibition is strongly oxygen-dependent.

5. Absence of CO_2 affects inhibition at pH 4 with an increase in corrosion rate by an order of magnitude compared to that of the sample immersed in aerated pH 4 Zn^{2+}-containing solutions. The carbonate protective layer formed in aerated solutions is crucial for providing better protection of the substrate at pH 4. Thus, CO_2-bearing precipitation is an important part of Zn^{2+} ion inhibition at pH 4.

5.3.3 Bentonite pigments for corrosion inhibition of aluminum alloy 2024-T3

5.3.3.1 Introduction

AA 2024-T3 is a precipitation hardened alloy which is used in aerospace and military applications where stiffness, fatigue performance and good strength are required [62]. Addition of alloying elements such as copper, magnesium, manganese results in these superior mechanical properties with high strength to weight ratio. However, elemental additions lead to the formation of a heterogeneous microstructure containing constituent intermetallic particles that have different electrochemical properties compared to the matrix phase [7, 8, 62-65]. This leads to galvanic interactions within and around the intermetallic particles and makes the alloy highly susceptible to localized attack, which includes pitting, intergranular corrosion and stress corrosion cracking [3, 4, 6-8, 66]. Hence, the alloy needs to be protected with passivating corrosion inhibitors and by using organic or inorganic barrier coatings to increase the lifetime of the parts and reduce the maintenance costs. Barrier coatings suppress the diffusion of oxygen and aggressive electrolytes to the metal substrate beneath, thus reducing the corrosion of the alloy significantly. The flow of electrons to the metal is also inhibited by the barrier coatings [67]. Passivating inhibitors act by reducing and adsorbing (like chromates) or precipitating (like cationic cathodic inhibitors) on specific sites or exposed defects prone to corrosion. These protective films act in a similar way where the diffusion of oxygen and chloride ions is suppressed, thus, reducing the corrosion rate of the alloy. Therefore, full protection can be obtained by having a coating containing active inhibiting pigment.

Historically, chromate primers and conversion coatings have been used to protect Al alloys used in aerospace applications. Cr(VI) in a chromate conversion coating is released and diffuses to the exposed metal or a defect and reduces itself to form an irreversible Cr(III) hydroxide stifling all the corrosion reactions [68-71]. Cr(VI) species leach out from the sparingly soluble chromate in the primer at a defect when it comes in contact with a chloride solution and reduces to Cr(III) species, protecting the substrate metal beneath [72, 73]. The chromate protection scheme provided improved adhesion and excellent protection with a unique 'self-healing' ability in

corrosive environments. However, the toxic and carcinogenic nature of these chromate compounds has led to the development and deployment of 'green' inhibitors in coatings [9, 74-77]. Many compounds have been studied including vanadates, molybdates, tungstates, silicates, phosphates among the anionic inhibitors and rare earth metal cations, Zn^{2+}, Ca^{2+}, etc among the cationic inhibitors [27, 52, 75, 76, 78-80]. Much interest has been shown in developing and formulating coating systems whose performance matches that of chromated system. This has been difficult to achieve.

Many salts containing inhibitor compounds like vanadates, molybdates, rare earth cations etc., have solubilities that are higher than the critical concentration required for corrosion inhibition of the alloy [72]. Excessive pigment solubility leads to osmostic blistering in the presence of moisture, which is driven by the differences in the activity of water present within the blister and the outer environment [81]. Pigments having extremely low solubility should also be avoided as insufficient amounts of inhibitor are released, not reaching the critical concentrations necessary for inhibition. Some chromates, especially $BaCrO_4$ and $SrCrO_4$ satisfy these requirements where the solubility is sufficient to provide corrosion inhibition but not high enough to cause blistering [72]. Hence, pigments as effective as $SrCrO_4$ in providing inhibition and in the ideal solubility range still need to be identified.

Insoluble ion exchange compounds have been identified and proven to be 'pigment grade' compounds [52, 82-86]. The required amount of inhibitor cations or anions are held and delivered when they come in contact with an aggressive electrolyte. This takes care of issues related to solubility, thus avoiding leaching and osmotic blistering. Cationic inhibitors are incorporated into the cation-exchangeable bentonites while the anions are incorporated into the anion-exchangeable chloride-containing hydrotalcites. This study on cationic inhibitors focuses mainly on the cation exchangeable sodium bentonites.

Bentonite clays are layered compounds with an intrinsic property of cation exchange that occurs independent of pH [87-89]. They consist of extended two-dimensional layered hydrated aluminum silicates with a partial isomorphous substitution of Mg^{2+} for Al^{3+}[90]. This leaves a net negative charge of 0.67 units per unit cell. The chemical formula for bentonite representing one unit cell is, $[Si_8.(Al_{3.33}Mg_{0.67})O_{20}(OH)_4]$ $0.67M^{+n}$, where the cation M^{+n} compensates the anionic charge of the layers which is usually either Na^+ or Ca^{+2}. This cation is bound by electrostatic forces and it can be exchanged easily. Bentonites swell upon wetting and the amount of swelling varies inversely with the valence of the exchangeable cation [87-90]. The desired cation can be exchanged into the bentonite by repeatedly washing the bentonite with a salt solution followed by drying [91]. Powdered x-ray diffraction of the bentonite gives the basal 00*l* reflections from the separated layers and other peaks, which are characteristic of the mineral. Ion-exchange is detected by a shift in the basal 00*l* peak and this can be used as an indication for local environmental changes before the onset of corrosion.

Bohm et al. first used Ca and Ce bentonites as pigment primers in organic coated galvanized steel [92]. They exhibited good anti-delamination performance at the cut edge in salt spray tests, which goes as Ca bentonite ~ $SrCrO_4$ < Ce bentonite. AA 2024-T3 coupons coated with an epoxy containing Ce(III) bentonite pigment showed resistance to blistering and modest corrosion protection after 3000 h of salt spray exposure [80]. Williams et al. have shown that Ce bentonite

and Zn bentonite compounds have reduced the cathodic delamination on galvanized steel substrates [85, 86].

Previous studies suggest that bentonites can be potentially used as pigments to deliver inhibitors without triggering blistering due to excessive solubility. This chapter deals with a study of exchanged bentonite characterization and developing a framework in which bentonites are used as pigments in coatings. Rare earth metal and zinc inhibitor cations are exchanged into sodium bentonites, which deliver these ions when incorporated as pigments in organic resins like polyvinyl butyral (PVB) and polyvinyl alcohol (PVA) and epoxy. Material characterization of the pigments was done to confirm ion exchange and characterization of the corrosion inhibition of the painted coupons was assessed using accelerated salt spray exposure tests and impedance measurements.

5.3.3.2 Experimental

5.3.3.2.1 Materials and Chemicals. AA 2024-T3 was used as the substrate material and the sheet stock coupons of 2 mm thickness were obtained from a commercial supplier. This alloy is solution heat-treated and cold worked with a nominal chemical composition of 3.8-4.9% Cu, 1.2-1.8% Mg, 0.3-0.9% Mn with the remainder being aluminum. Sodium bentonite (BIG HORN$^{®}$ 200 from WYO-BEN, INC.) was used as an ion-exchanger. All the chemicals used for the bentonite synthesis and electrochemical experiments (chlorides of cerium, praseodymium, lanthanum and sodium, sodium metasilicate, polyvinyl alcohol (PVA), polyvinyl butyral (PVB), etc.) were of reagent grade and were obtained from commercial sources. Epoxy primer PD381-94, a commercial aerospace primer which has organic solvents and titanium dioxide solid dust of 3 - 7 wt% but no inhibitor pigments, was mixed with an EC-283 primer cure solution. The primer and cure solutions were obtained from Akzo Nobel^{TM}. Deionized water of 18.2 MΩ.cm resistivity was used for preparing all the aqueous solutions.

5.3.3.2.2 Bentonite synthesis, characterization. Cation exchange was carried out by treating 25 g of as-received sodium bentonite silicates with aqueous solutions of 250 ml of 0.2M rare earth metal (REM) chloride and Zn chloride solutions and stirred for a period of 48 hours. The solid was then washed repeatedly with deionized water for about four to five times until unreacted salts had been removed. The filtrate was sampled for the presence of the chloride ion by the silver nitrate test. Excess liquid was vacuum filtered from the solid and the pigment was finally washed with ethyl alcohol, redispersed and dried overnight in a low temperature furnace at 40°C. The exchanged bentonite pigment was ground using mortar and pestle and after which it was passed through an ASTM 230 mesh sieve.

X ray diffraction (XRD) of the powder was done to ensure that the exchange was accomplished. Thermogravimetric analysis (TGA) was carried out on the bentonite powders to determine their water content.

5.3.3.2.3 Cation Exchange Capacity (CEC). The amount of cations exchanged into bentonite is characterized by the cation exchange capacity (CEC). A standard method to determine this value is by the exchange with ammonium acetate method. This method has the disadvantage of being lengthy [93]. A quick and reproducible method of characterization is by copper triethylenetetramine [Cu(trien)$^{2+}$] exchange. The results obtained are in good agreement with the

ammonium acetate method [94]. A 0.01 M complex solution was prepared by adding 1.463g (0.01 mole) triethylenetetramine and 1.596g (0.01 mole) copper sulfate and diluted to 1 litre. 500 mg of the clay was dispersed in 40 ml of the complex solution and shaken for about 4 h. The solution was then centrifuged at 3000 g for 10 min and the concentration of the remaining complex in the solution was determined using UV-Visible spectroscopy.

5.3.3.2.4 PAR method for determining Zn^{2+} ion concentration and CEC for Zn^{2+} cation. Determination of the concentration of the Zn^{2+} cation can be done using many techniques like atomic absorption spectroscopy, neutron activation analysis and mass spectrometry. However, these techniques require expensive set-ups and have tedious sample preparations. Recently, Zn^{2+} ion concentration was determined by complexing it with 4-(2-pyridylazo) resorcinol (PAR), a good chelator of transition metal cations [95]. At pH values above 5, this compound complexes with Zn^{2+} to form a 2:1 complex which is a stable, colorful and water soluble complex. The $Zn(PAR)_2$ complex absorbs visible light and therefore UV-Visible spectroscopy can be used to detect and quantify the Zn^{2+} ion concentration [95]. The maximum absorbance peak for the PAR and $Zn(PAR)_2$ complexes were seen at 414 nm and 491 nm, respectively. The concentrations of the unknown Zn^{2+} solutions were obtained by determining the extinction co-efficient at the maximum absorbance peak of 491 nm. All the PAR solutions were prepared using a pH 10 phosphate buffer.

Sodium bentonite of 0.5 g was dispersed in 40 ml of 0.01 M $ZnCl_2$ at pH 6.5 and pH 5.5. The centrifuge tube was shaken for 4 hrs and then centrifuged. 1ml of clear solution was complexed with PAR solution and analyzed and back calculated to determine the Zn^{2+} concentration gone to intercalation.

5.3.3.2.4 Inhibitor release. Ce^{3+} and Pr^{3+} cation release from exchanged bentonites was studied by immersing 0.25 g of the bentonite pigment in 30 ml of 0.5M NaCl solution at pH 5.3 while Zn^{2+} release from Zn bentonite was studied by immersing 0.25 g of the pigment in 20 ml of 0.5 M NaCl solution. The bentonite was allowed to settle and the clear supernatant was used for the analysis of the lanthanide concentration using UV-Visible spectroscopy. Calibration curves of absorbance vs. concentration of Ce^{3+} and Pr^{3+} ions are constructed using standard solutions of known concentrations. The absorbance peaks of 221.8 nm and 444 nm are chosen for Ce^{3+} and Pr^{3+} respectively. The PAR method described in the above section is used for determining the concentration of Zn^{2+} cation released.

Quartz cuvettes of 1 cm square cross section were used. The analyte solution was poured back after every measurement to keep the volume of the electrolyte constant in order to avoid inconsistency in the measurements due to volume change. The spectroscopic measurement is taken periodically until a steady amount of concentration of the cation was seen to be present in the electrolyte

5.3.3.2.5 Preparation of AA 2024-T3 substrate. Al 2024-T3 coupons of approximately 3 x 5 in were cut for coating purposes. These aluminum substrates were subjected to a two-step cleaning procedure involving:

1) Degreasing for 2 minutes in an alkaline bath consisting of 32.4 g sodium metasilicate and 48 g sodium carbonate in 1000 ml deionized (DI) water at 65°C.

2) Deoxidizing for 3 minutes in an acidic bath consisting of 30 g SANCHEM 1000^{TM} and 72 ml nitric acid in 928 ml of DI water at 55°C.

The substrates were rinsed in continuous stream of DI water after each step and they were left to air dry at room temperature for about 24 h before coating application.

5.3.3.2.6 PVA/PVB/Epoxy coating preparation and application. PVA and PVB are hydrophilic polymer compounds due to the presence of hydroxyl groups. These polymer resins do not have significant barrier properties as they are water permeable. As a result, they enable quick screening of new inhibitor pigments during pigment evaluation. To form these coatings, 10 wt% PVB in methanol was stirred for 2 days, and used as the PVB resin and 4 wt% PVA in DI water was stirred overnight, and used as the PVA resin. Unpigmented epoxy coatings are obtained by mixing the epoxy primer (containing TiO_2 solids) with the curing solution in a 1: 0.67 ratio by weight. Pigmented PVA, PVB and Epoxy coatings were made by thoroughly mixing 5 wt% of bentonite pigments with the resin. The pigments added included Ce, Pr, La and Zn exchanged bentonites. The degreased and deoxidized aluminum alloy coupons were coated with a draw down bar. A tape was used to mask edges and control the variation in the thickness of the coating while drawing down the bar. The coated samples were allowed to cure at ambient temperature and humidity for about 48 hours for the PVA and PVB coatings while the epoxy coatings were allowed to cure for a period of one week. $SrCrO_4$ pigmented coatings of 5 wt% pigment loading were used as positive control samples. Neat organic resins without any pigment loading were used as a negative control sample. The list of all the coatings prepared and the notations used to represent them in the text and figures is given in Table 3.4. Two sets of samples were prepared for each pigment and resin combination. One sample was used for the electrochemical impedance measurements (EIS) and the other sample was used for the ASTM B117 salt spray exposure.

5.3.3.2.7 Characterization of coatings. EIS was used to characterize coated samples exposed to 0.5 M NaCl solution and salt spray exposure. Salt spray exposure was carried out according to ASTM B117 which specifies exposure to a salt fog obtained from 5 wt% NaCl solution in an enclosed chamber at a constant temperature of 35°C. The sides of the coated samples and the uncoated back surface were covered with a tape for the salt spray testing. This was done to cover the discontinuity of the paint at the edges and to avoid coupling between the two faces of the sample. The samples were then scribed from one corner to the opposite corner using a carbide scribe forming a cross mark, exposing the bare metal beneath the coating. The samples were assessed by visual inspection based on the relative blistering performance (B) and scribe protection (SP). A relative ranking from 1 to 5 is given to the coatings with rank "1" indicating the best performance coating compared to the others. For example, a coating with a blister rank "1" showed no blisters while a coating with a blister rank "5" showed numerous blisters through out the area.

EIS experiments were carried out in cells obtained by gluing polyvinyl chloride (PVC) hollow cylindrical tubes to the coated panels with a water proof silicone sealant. Cells were filled with 15 ml of 0.5 M NaCl solution. Platinum was used as the counter electrode while a saturated calomel electrode (SCE) was used as the reference electrode. The EIS measurements were taken at 0, 1, 2, 3, 7, 15 days of static immersion in 0.5 M NaCl solution to study the evolution of coating protection.

Table 3.4. List of all pigmented coatings.

#	Written as	Pigment	Wt% of pigment	Resin
1	Neat.PVA	-	-	PVA
2	SrCr.PVA	$SrCrO_4$	5	PVA
3	CeB.PVA	Ce bentonite	5	PVA
4	PrB.PVA	Pr bentonite	5	PVA
5	LaB.PVA	La bentonite	5	PVA
6	ZnB.PVA	Zn bentonite	5	PVA
7	Neat.PVB	-	-	PVB
8	SrCr.PVB	$SrCrO_4$	5	PVB
9	5CeB.PVB	Ce bentonite	5	PVB
10	5PrB.PVB	Pr bentonite	5	PVB
11	5LaB.PVB	La bentonite	5	PVB
12	5ZnB.PVB	Zn bentonite	5	PVB
13	10ZnB.PVB	Zn bentonite	10	PVB
14	20ZnB.PVB	Zn bentonite	20	PVB
15	30ZnB.PVB	Zn bentonite	30	PVB
16	Unpigmented.Ep	Non-inhibiting TiO_2 (T)	3-7	Epoxy(T)
17	SrCr.Ep	$SrCrO_4$	5	Epoxy(T)
18	5CeB.Ep	Ce bentonite	5	Epoxy(T)
19	5PrB.Ep	Pr bentonite	5	Epoxy(T)
20	5LaB.Ep	La bentonite	5	Epoxy(T)
21	5ZnB.Ep	Zn bentonite	5	Epoxy(T)
22	10ZnB.Ep	Zn bentonite	10	Epoxy(T)
23	20ZnB.Ep	Zn bentonite	20	Epoxy(T)
24	30ZnB.Ep	Zn bentonite	30	Epoxy(T)

5.3.3.3 Instrumental

5.3.3.3.1 XRD. X-ray diffraction of cation-exchanged bentonite powders was done to characterize and confirm the exchange of the inhibiting cations. The XRD equipment used was a

Scintag (now ThermoARL) Pad-V^{TM} and XDS 2000^{TM} diffractometer with a CuK$_\alpha$ radiation source (λ=1.5418 Å). The accelerating voltage was set at 45 kV and the current set at 20 mA. A MicroVAX^{TM} data acquisition system was used for recording the data. Using the continuous scan method, the measurement was taken at 2θ from 2˚ to 30˚ at 0.5˚/min. The resulting patterns were analyzed using EVA^{TM} software version 7.0 by DIFFRAC^{plus}.

5.3.3.3.2 UV-Visible Spectroscopy. Ultraviolet-visible spectroscopy of the aqueous analyte samples was carried out using a Perkin Elmer Lambda EZ201 spectrometer to determine the concentration of the inhibitor cations released from the exchanged benotnite pigments during immersion. It was also used to determine the cation exchange capacity of the sodium bentonite. This was done alongside a reference cuvette containing 0.5 M NaCl solution for the Ce^{3+} and Pr^{3+} cations while using a pH 10 phosphate buffer reference solution for the Zn^{2+} cation.

5.3.3.3.3 Thermo-Gravimetric Analysis (TGA). The interlayer and adsorbed water content of the bentonites was obtained using a Perkin Elmer TGA 7 Thermogravimetric analyzer with TAC 7/DS Thermal Analysis Instrument controller. A platinum crucible was used to hold the bentonite sample inside the furnace and it was operated from 30 ˚C to 250 ˚C at a heating rate of 10 ˚C.min^{-1}. The purging gas used was air with a flow rate of 40 ml.min^{-1}.

5.3.3.3.4 Electrochemical Impedance Spectroscopy. Electrochemical impedance of the coated aluminum substrates was performed in polyvinyl chloride (PVC) coupling cells (exposed area of 5.55 cm^2) in an aqueous 0.5M NaCl solution. The measurements were done using a Gamry^{TM} Ref 600 potentiostat. A sinusoidal voltage of 10 mV about OCP was applied with frequency ranging from 10^5 to 10^{-2} Hz. The spectra were fit using Scribner Associates' ZView^{TM} impedance software.

5.3.3.4 Results

5.3.3.4.1 Characterization of the Bentonites

5.3.3.4.1.1 X-ray Diffraction (XRD). Bentonite clays are a form of montemorillonite based on the di-octahedral pyrophillite structure. These are 2:1 layered hydrated silicates, which extend in two-dimensions. The cation is not a part of the layered structure but is intercalated between the aluminosilicate sheets by van der Waals forces of attraction and is therefore easily exchanged. The amount of swelling varies inversely with the valence of the exchangeable cation. Hence, the interlayer gallery spacing is not only dependent on the size of the cation but also on the amount of water associated with it.

The synthesis of cation-exchange bentonites from sodium bentonite was confirmed using X-ray Diffraction (XRD). Figure 3.30 shows the XRD patterns of the as-received and exchanged bentonites. The peak positions and shifts were similar to the patterns reported literature[80, 96] and indicated a successful exchange of the sodium cation for the inhibitor cation during synthesis.
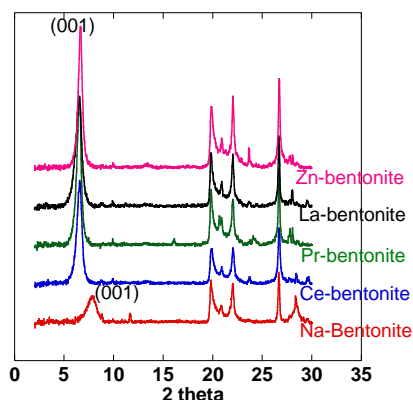
Figure 3.30. XRD patterns for as-received Wyoming sodium bentonite and synthesized exchange bentonites of Ce^{3+}, Pr^{3+}, La^{3+} and Zn^{2+}.

X-ray diffraction of the bentonite powder gives the basal (001) reflections at low 2θ originating from the layered structure and other peaks obtained at higher 2θ are from the structure within the alumino silicate layers of the compound that are characteristic of the mineral. The most intense reflections from the bentonites are obtained from the silicate layered sheets due to the large interplanar spacings and this occurs at low 2θ values referred to as the (001) basal reflections in Figure 3.30. Bragg's law can be used to determine the unit cell parameter, d, which is the total layer thickness that includes the gallery height combined with the thickness of the alumino silicate sheet [97].

Ion exchange was detected by a shift in the Bragg angle of the basal (001) peak of the (Ce, Pr, La. Zn)-bentonite compounds with respect to Na-bentonite, which indicated successful synthesis of the exchanged bentonites. The $d_{(001)}$ basal spacings of the hydrated interlayers obtained from the Bragg's law are given in Table 3.5. An increase in the $d_{(001)}$ basal spacing was observed from 11.19 Å in the sodium bentonite to about 13.5 Å for the exchanged bentonites. The trivalent cations of Ce and La showed a similar increase while the divalent Zn ion showed slightly less increase in the $d_{(001)}$ spacing compared to Ce^{3+} and La^{3+} cations. Pr^{3+} showed a slightly higher increase in $d_{(001)}$ spacing compared to the Ce^{3+} and La^{3+}. XRD does not tell us the nature of the exchangeable cation because they do not contribute to the diffraction intensities as illustrated elsewhere [98]. However, it is irrelevant in this case as the exchanged ion is known.

Other authors have observed changes in the $d_{(001)}$ interlayer spacing of sodium bentonite and calcium bentonite by the adsorption of alkali, alkaline earth, rare earth and transition metal cations [80, 96, 97]. Auboiroux et al. [96] saw a shift in the $d_{(001)}$ basal spacing of calcium bentonite after exchanging with Zn^{2+} cations and Pb^{2+} cations. The $d_{(001)}$ basal spacing of exchanged Zn^{2+} bentonite was shifted to 13.73 Å, which is about the same as the value calculated in Table 3.3.2 for Zn^{2+} bentonite [96].

Table 3.5. Characterization of bentonites for exchange cations using XRD and TGA

Cation-Bentonite	XRD-d_{001} basal spacing (Å)	Literature estimates for d-spacing (Å)	TGA- % Weight loss at 250˚C
Na^+	11.19	10.4	7.7
Ce^{3+}	13.44	14	10.5
Pr^{3+}	13.56	-	11.5
La^{3+}	13.44	-	10.9
Zn^{2+}	13.32	13.7	10

The increase in the interlayer spacing could be due to the formation of the bulky polynuclear complexes like the hydrolysis products in the interlamellar spacing of the clay upon intercalation of these cations in the galleries [96]. Thus, $d_{(001)}$ basal spacings of the exchanged clays would be different for each exchange cation. This change in the $d_{(001)}$ spacing is also the basis for corrosion sensing. An evolution of a new basal peak was seen when the sodium cations exchange for the cerium-bentonite pigment in the coating [80].

5.3.3.4.1.2 Thermogravimetric analysis (TGA). Thermogravimetric analysis of the bentonite clays was performed to assess the amount of interlayer water in the exchanged bentonite species. The TGA of the natural bentonite has three main steps of weight loss. The first step occurs in the temperature range (80˚C – 215˚C) and is due to the loss of adsorbed water and interlayer water. The second step (550 ˚C – 750˚C) and third steps (850˚C – 1050˚C) correspond to the crystal water and the collapse of the entire lattice [97, 99]. Hence, weight loss measurements were carried out only up to 250˚C.

The disadvantage with this technique is that the weight loss recorded is obtained both from the water in the interlayer as well as adsorbed water on the external surface area. The specifications provided by WYO-BEN, Inc. for the as-received bentonite show that the external surface area is 0.1 multiples of the entire surface area of the bentonite (external surface area and interlayer surface area). This means that one-tenth of the total weight loss obtained corresponds to the weight loss due to adsorbed water. It was found that the external surface area of each exchanged bentonite varied with the interlayer cation and it varied from 0.04 to 0.1 multiples of its total surface area with Na bentonite having the highest external surface area of 0.1 multiples of its total surface area [97].

The weight loss curves from the TGA analyses are shown in Figure 3.31 and the percentage of weight loss at 250˚C is shown in the Table 3.5. The exchange bentonites showed higher total weight losses (>=10%) compared to sodium bentonite (7.7 %). Assuming the highest contribution of total weight loss from the adsorbed water on the external surface area (0.1 multiples) of the exchanged bentonites, they still showed higher weight losses due to water from the interlayer spacing.
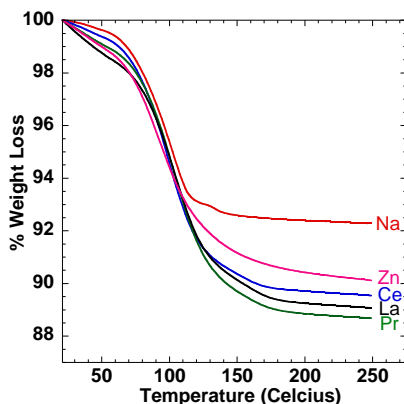
Figure 3.31. Weight loss analyses for as-received Wyoming sodium bentonite and synthesized exchange bentonites of Ce^{3+}, Pr^{3+}, La^{3+} and Zn^{2+}.

The total weight loss trend among the exchanged bentonites is similar to that of the trend in the hydrated interlayer spacing values shown in Table 3.5 with Pr bentonite showing the highest weight loss and the Zn bentonite exhibiting the lowest weight loss. The hydration energy of a cation is defined as the ratio of the charge of the cation to its radius. The higher the hydration energy, the more the water molecules surround the cation in the closest coordination sphere and the more strongly the water molecules are held by the cation. Na^+, Ce^{3+}, Pr^{3+}, La^{3+} cations all have similar ionic radii at about 1 Å [100], but the basal spacings of the exchanged lanthanide bentonite species are higher than that of the sodium bentonite. The charge:radius ratio is higher for the trivalent REM cations compared to the univalent sodium cation leading to accommodation of more water molecules, thus expanding the d-spacing. The ionic radius of the Zn^{2+} cation on the other hand is lower at about 0.74 Å and has a higher basal d-spacing than the Na bentonite (radius of Na^+ = 1 Å) . This is again due to the higher charge:radius ratio for the Zn cation causing an expansion in the d-spacing. The TGA results support these findings. Similar results were seen by Cuadros et al. where a slightly higher d-spacing for Li-smectite compared to Na-smectite was seen as Li cation has a higher hydration energy due to the smaller radius of the Li cation[97]. Hence, the amount of water adsorbed by the bentonites depends on the cation exchange and it modifies the interlayer surface area creating water complexes with different number of water molecules and/or spatial conformation.

Higher number of water molecules maybe released from the exchanged pigments when these pigments are incorporated into the coatings. This might have an impact on the corrosion inhibition caused by the pigments.

5.3.3.4.2 Capacity of Bentonites. The cation exchange capacity (CEC) experiments were carried out by copper triethylenetetramine $[Cu(trien)^{2+}]$ exchange into sodium bentonite.   The complex showed a maximum absorption peak at 577 nm and the extinction co-efficient was determined to be 152.87 $mol^{-1}cm^{-1}$ at 577 nm, which agreed well with the value found in the literature [94]. The calculations lead to a CEC value of 84.82 meq/100g for the sodium bentonite. Most of the authors report CEC values for the dried clay. Hence, CEC value adjusting for the water content in the dried bentonite at 250 ˚C was 91.97 meq/100g. This value fell within the CEC range of 80 to 150 meq/100g calculated for bentonites [101].

The ion-exchange ability of the Na-bentonite for the Zn^{2+} cation was also tested by the PAR method. The calibration curve for the $Zn(PAR)_2$ complex was obtained from 491 nm peak by using standard solutions. The exchange capacity values of Na benonite for Zn^{2+} cation obtained by dispersion in pH 5.5 $ZnCl_2$ solution for the undried and dried bentonites are 80 meq/100g and 86.7 meq/100g, respectively, while the values from a pH 6.5 $ZnCl_2$ solution for the undried and dried bentonites are 67.71 meq/100g and 73.4 meq/100g respectively.

5.3.3.4.3 Inhibitor release from the bentonite pigments. UV-visible spectroscopy was used to track the amount of exchanged cations (Ce^{3+}, Pr^{3+}, Zn^{2+}) released from the synthesized bentonite pigments to know whether sufficient concentration of the inhibitor cations is released for corrosion inhibition.

Figure 3.32a shows the release kinetics of the Zn^{2+} cation from exchanged Zn bentonite exposed to 0.5M NaCl solution. It suggests that the release is a diffusion-controlled process with a cumulative amount released at the end of 168 h of 52 meq/100g. This shows that not all the exchanged Zn^{2+} is released upon immersion in 0.5 M NaCl solution, which was also reported elsewhere [102]. A 52 meq/100g corresponds to a Zn^{2+} cation concentration of 3.25 mM released from 0.25 g of exchanged Zn bentonite immersed in 20 ml of solution.

Figures 3.32b and 3.32c show the kinetics of release of Ce^{3+} and Pr^{3+} ions from the bentonite pigments. Pr^{3+} ion release shows a steady release except at 24 h and equilibrates to 40 meq/100g at the end of 168 h. This corresponds to a Pr^{3+} ion concentration of 1.11 mM (156 ppm) released from 0.25 g of exchanged Pr bentonite immersed in 30 ml of solution. This is lower than the equilibrium milliequivalents of the Zn^{2+} cation released. Very strong initial release of about 66 meq/100g is seen for the Ce^{3+} cation and it is seen to decrease to 39 meq/100g at the end of 327 h. This peculiar behavior of Ce^{3+} cation release was also seen in a previous work [80]. A 39 meq/100g corresponded to Ce^{3+} ion concentration of 1.08 mM (151 ppm) released from 0.25 g of exchanged Ce bentonite immersed in 30 ml of solution.

The amount of cations released after a period of 2 weeks gives the fraction of inhibitor released from the total reservoir of the inhibitor contained in the pigment. At a CEC value of 85 meq/100g, the fraction of the reservoir was higher for Zn^{2+} cation at 0.61 compared to Ce^{3+} and Pr^{3+} cations (0.46 and 0.47).

(a) (b) (c)
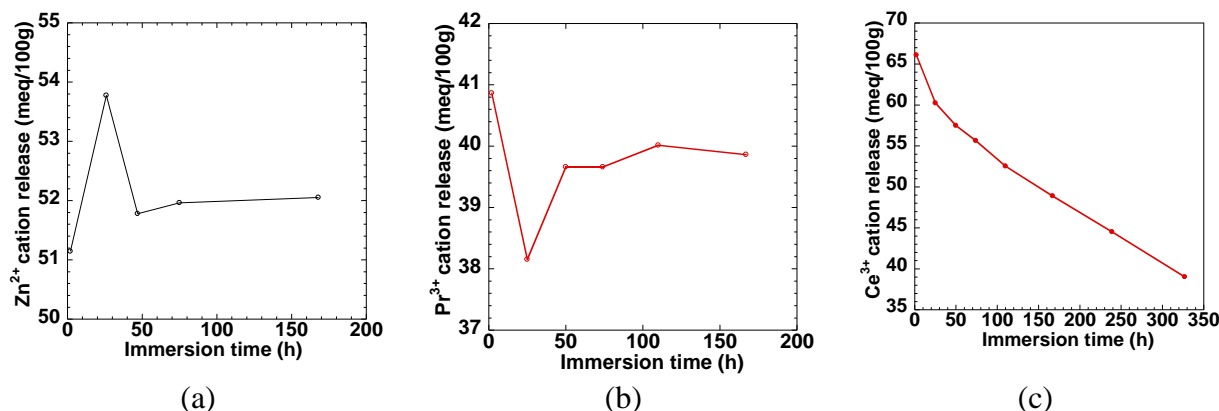
Figure 3.32. Concentration of (a) Zn^{2+} (b) Pr^{3+} (c) Ce^{3+} ions released from bentonite immersed 0.5 M NaCl solution, expressed in milliequivalents/100g.

5.3.3.4.4 Electrochemical Impedance Spectroscopy. Electrochemical impedance measurements on coated AA 2024-T3 panels were done to assess the protective ability of the coating by monitoring the coating characteristics with time on static immersion in an aggressive 0.5 M NaCl electrolyte. Most of the pigmented model coatings prepared with PVA and PVB resins exhibited a two-time-constant behavior with a few exceptions. The EIS response was interpreted using a damaged coating equivalent circuit models [103] as shown in Figure 3.33. In this model, the capacitances were replaced by constant phase elements (CPEs). In some cases, there were two fully resolved arcs and a partially resolved third arc in the Nyquist plots for these coatings. This third partially resolved arc in the Nyquist plot is associated with the diffusive reactance in the interface [104]. The evolution of characteristic resistances and capacitances, each describing a physical phenomenon are extracted and compared for every coating system in order to determine coating degradation. Figure 3.33a shows a model representing a coating system with pores and defects exposing the metallic substrate beneath. The resistance of the polymer coatings is relatively large making them difficult to identify and therefore, they essentially become an open in the circuit. The true value of the capacitance is extracted from the CPE using the following equation[105]:

$$C = Y^{\frac{1}{n}} R^{\frac{1-n}{n}}$$

(eq. 3.3.1)

where R is the resistance in parallel to the capacitance. A Finite Length Warburg element, which terminates in a open circuit is used to represent the diffusive component in the pore when needed.

The simplified circuits, which provided good data fitting are shown in Figures 3.33b and 3.33c. The magnitude of total impedance at 0.01 Hz (lowest frequency), the coating capacitance, the defect capacitance and the pore resistance values were extracted using the simplified circuit. The simplified circuit in Figure 3.33b was used when the third arc in the Nyquist plot is not fully resolved due to the presence of diffusion along with charge transfer reactance.

5.3.3.4.4.1 EIS of PVA coatings pigmented with exchanged bentonites. Figure 3.34a shows the Bode magnitude and phase angle plot for the PVA coating pigmented with 5 wt% Pr bentonite (PrB.PVA) and is presented here as an example of a coating with exchanged bentonites. The resistive behavior at high frequencies ($10^5 - 10^4$ Hz) is well resolved and represents the solution resistance. The capacitive behavior from $10^4 - 10^{-1}$ Hz was not very well resolved to show the PVA capacitance and the defect capacitance. The magnitude of impedance in the Bode magnitude plot in this frequency region decreases indicating an increase in the capacitance, which could be due to water uptake and localized corrosion. The faradaic resistance was seen at 10^{-1} Hz by the huge change in the slope of the Bode magnitude plot and the phase angle peak approaching resistive values. The final low frequency region from $10^{-1} - 10^{-2}$ Hz, here is from the diffusive reactance in the pore. No inhibition by this coating was observed probably because there is either no release or too little release of the Pr^{3+} cation.
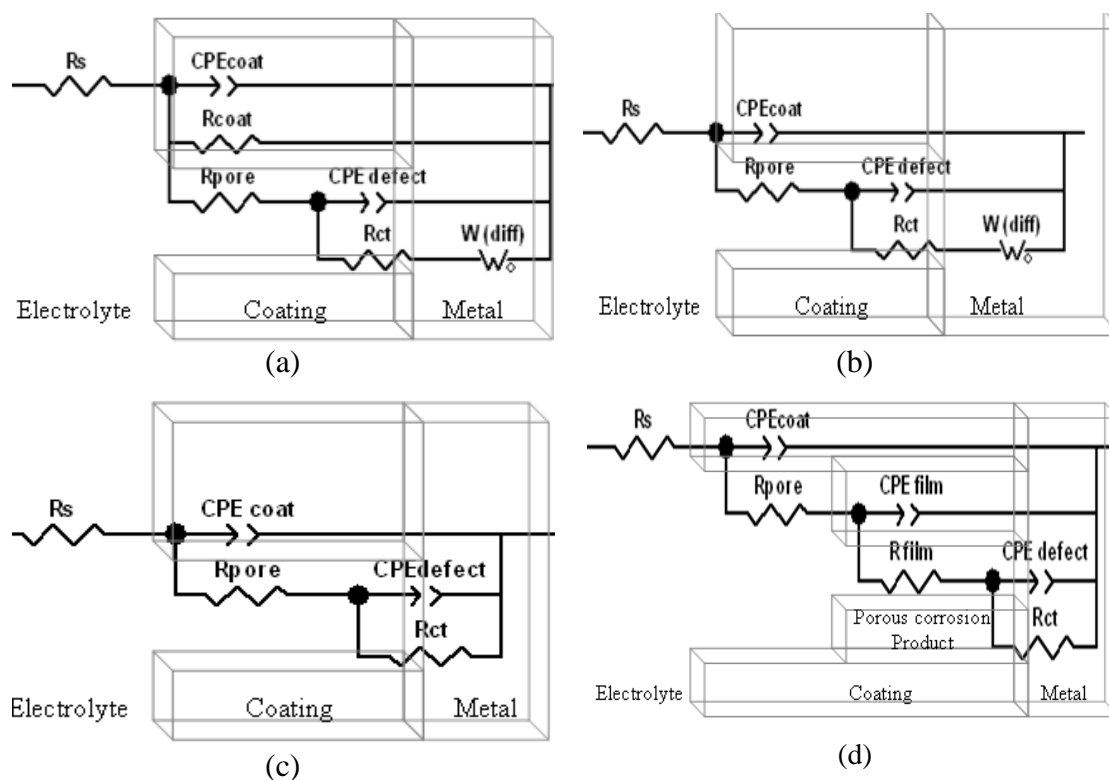
Figure 3.33. (a) An explicit equivalent circuit of a coating that exhibited two time constant behavior and diffusion at low frequencies. (b) Simplified circuit of a coating that exhibited two time constant behavior and diffusion at low frequencies. (c) Simplified circuit of a coating used to fit the data that exhibited two time constant behavior(d) Simplified circuit of a coating used to fit the data that exhibited three time constant behavior

Figure 3.34b shows the Bode and phase angle plot of the SrCrO$_4$ pigmented PVA coating (SrCr.PVA). It is different from the other spectra of pigmented bentonites as the spectra are very stable with no change in response over 173 h. The phase angle response grew increasingly capacitive at low frequencies indicating strong interfacial passivity. This implies that SrCrO$_4$ releases CrO$_4^{2-}$ and Sr^{2+} ions that reinforce the natural passivity of aluminum. This happened despite the fact that SrCrO$_4$ additions degrade the barrier properties of the neat resin.

All the spectra were fitted using the simplified two time constant circuit and the evolution of fit parameters is compared for the pigmented PVA coatings. Figure 3.35a shows the total magnitude of impedance at low frequency (10^{-2} Hz) relative to the neat PVA and SrCr.PVA controls. The low impedance of Neat.PVA indicates that it has low barrier properties. The SrCr.PVA coating had the highest impedance of 1.6 x10^6 Ω.cm^2 and none of the pigmented coatings performed as well as the SrCr.PVA standard. SrCrO$_4$ pigment showed excellent performance despite the low barrier properties of the PVA resin. Bentonites did not lower the already low barrier properties as ZnB.PVA (1.05 x10^5 Ω.cm^2) and PrB.PVA (5.8 x10^4 Ω.cm^2) performed relatively better than the neat PVA coating (2.87 x10^4 Ω.cm^2) at the end of 173 h. Bentonites also do not reinforce passivity.

153

(a)   (b)
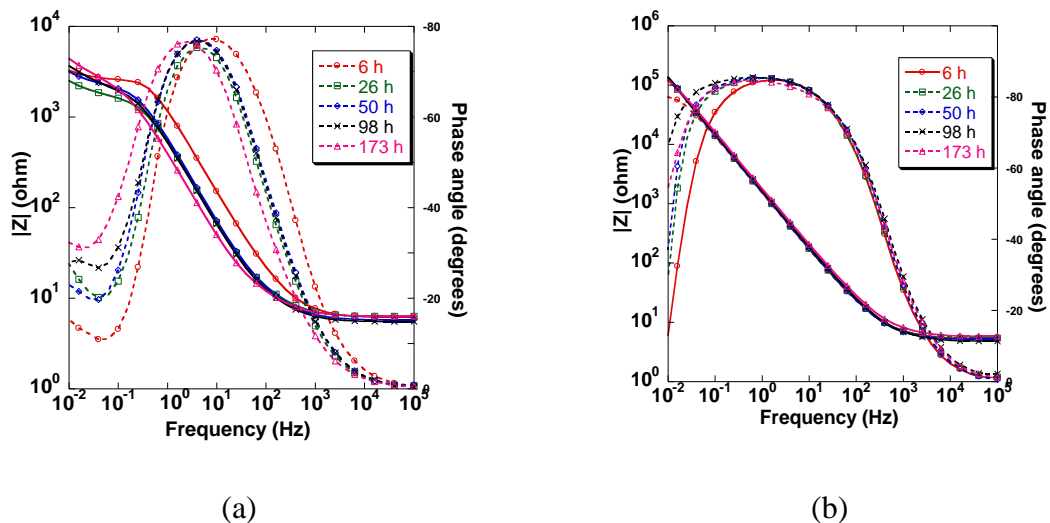
Figure 3.34. Bode magnitude and phase angle plots of (a) PrB.PVA (b) SrCr.PVA (SrCrO$_4$ pigmented) coating upon static exposure to 0.5M NaCl solution for a period of 1 week (173 h). The area exposed to the solution was 14.5 cm^2.

Figure 3.35b shows the trend in PVA coating capacitances with time. SrCr.PVA control showed the smallest coating capacitance (2.87 x10^{-6} F.cm^{-2}) compared to the other pigmented coatings, which fell in between 1 x10^{-5} F.cm^{-2} and 2 x10^{-5} F.cm^{-2} at the end of 173 h. These values of capacitances are not consistent with polymer coatings that are dielectric barriers which would give coating capacitance values of 1-10 nF.cm^{-2}. PVA essentially acts like a gel and these capacitances correspond to the capacitance of the gel. All the coatings showed an overall increase in coating capacitance with time with SrCr.PVA as an exception. This suggests localized corrosion for the neat PVA and bentonite pigmented coatings and passivity for SrCrO$_4$.

(a)   (b)
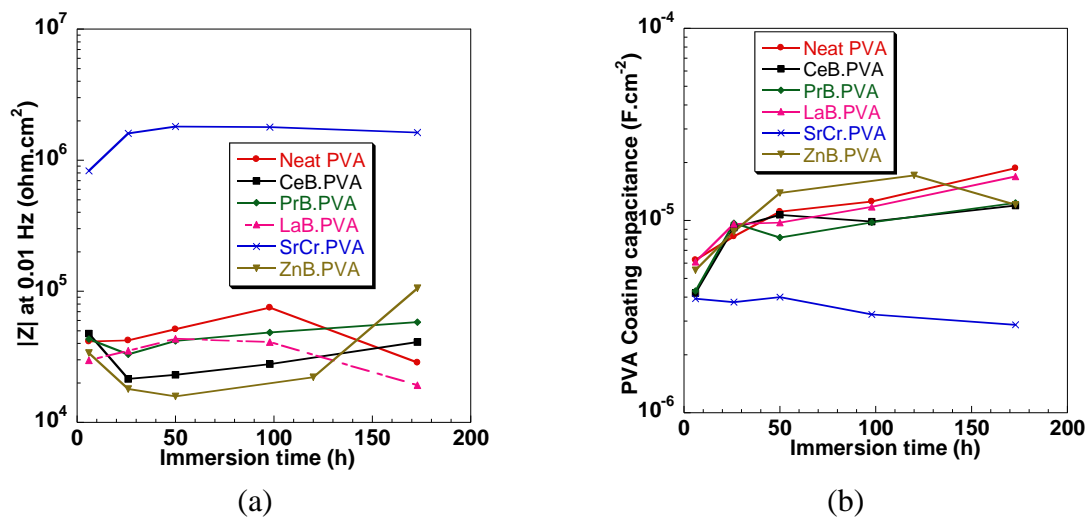
Figure 3.35. (a) Total impedance (b) Capacitances of PVA coatings pigmented with exchange bentonites and SrCr.PVA standard, subject to static immersion in 0.5 M NaCl.

154

5.3.3.4.4.2 EIS of PVB coatings pigmented with exchanged bentonites. Figure 3.36 shows the Bode magnitude and phase angle plots for 5ZnB.PVB pigmented coating and it was chosen to plot as it was similar to the other bentonite pigmented PVB coatings with neat PVB and SrCr.PVB as the exceptions. The solution resistance was absent and the PVB coating capacitance dominated the higher frequency region ($10^5 - 10^2$ Hz). A resistive plateau representing pore resistance slowly resolved at 22h of immersion at intermediate frequencies ($10^3 - 10^1$ Hz) in the Bode magnitude region and is seen to decrease with time. The emergence of the resistive plateau suggests the onset of localized corrosion and the water reaches the interface and contacts the surface by 22 h. At lower frequencies ($10^1 - 10^{-1}$ Hz), the double layer capacitance associated with the pore was seen. The diffusive reactance in the pore is seen at 10^{-2} Hz and decreased with increase in exposure time. This suggests that little inhibition is provided by the Zn bentonite pigments when added to a PVB coating. This could be because the Zn^{2+} release is either too small an amount or there is no release at all. All the spectra are fit using a two time constant circuit and the fit parameters are extracted and compared.

Figure 3.37a shows a plot of the total magnitude of impedance of the coatings at 0.01 Hz relative to the neat PVB and SrCr.PVB control. High total impedance of neat PVB coatings indicates that PVB is a better barrier compared to PVA resin. None of the bentonite pigments performed as well as the SrCr.PVB standard (3.1 x10^6 Ω.cm^2) and their impedances were more than an order of magnitude lower than that of SrCr.PVB at the end of 168 h of exposure. High stable impedances of SrCr.PVB coating at all times suggests strong reinforced interfacial passivity and superior inhibition by the chromates, despite degrading the barrier properties of PVB. The impedances of the bentonite PVB coatings rapidly decreased during the first 24 h of exposure and remained much lower than neat PVB coatings showing that bentonites did not promote passivity. This also suggests that bentonites significantly degrade the barrier properties of PVB.
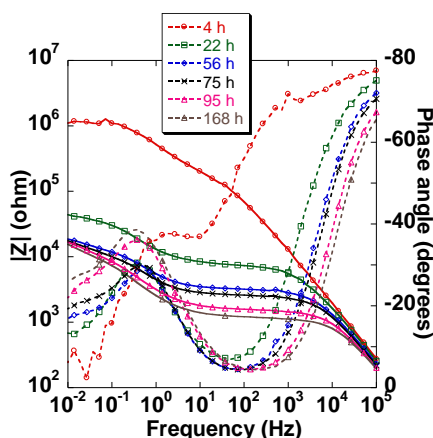
Figure 3.36. Bode magnitude and phase angle plots of 5ZnB.PVB (5 wt% Zn bentonite) coating upon static exposure to 0.5M NaCl solution for a period of 1 week (168 h). The area exposed to the solution was 5.55 cm^2

Figure 3.37b shows the PVB coating capacitance over a period of 167 h relative to the controls. Neat PVB showed the lowest capacitance at (6.15 x10^{-10} F.cm^{-2}) while all the other coatings including SrCr.PVB fell between 1.5 x10^{-9} F.cm^{-2} and 2.51 x10^{-9} F.cm^{-2} with 5PrB.PVB

exhibiting the least value in the range. The trend in the coating capacitances suggests no water uptake by the PVB coatings at 5 wt% loading levels.

(a)   (b)
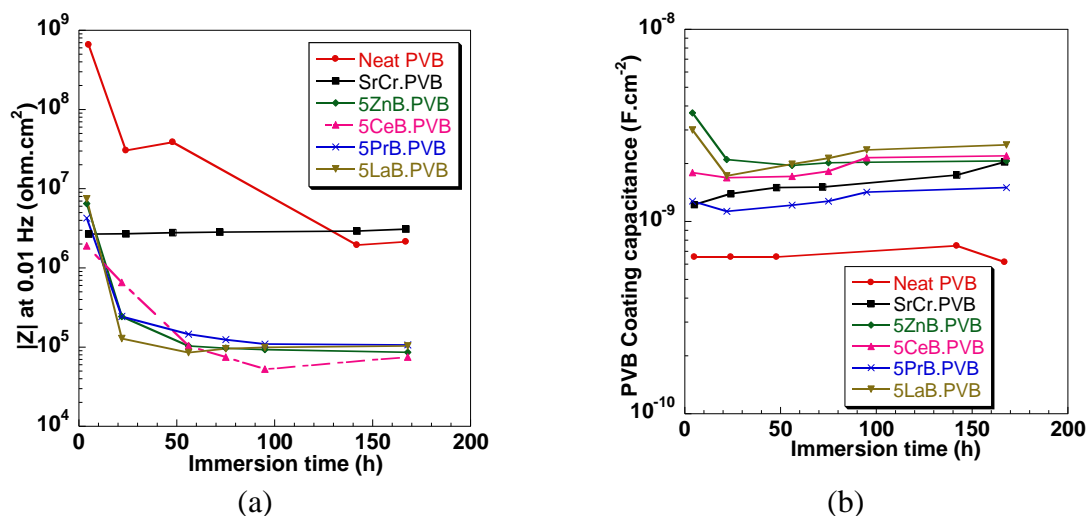
Figure 3.37. (a) Total impedance (b) Capacitances of PVB coatings pigmented with exchange bentonites and SrCr.PVB standard, subject to static immersion in 0.5 M NaCl.

The effect of increasing pigment loading levels on the PVB coating characteristics was investigated. All the spectra exhibited a two time constant behaviour and the characteristic parameters were compared. SrCr.PVB containing 5 wt% of $SrCrO_4$ pigment was used as the positive control. Figure 3.38a shows the total magnitude of impedance at low frequency for all the coatings with the Zn bentonite pigment loadings varying from 5 wt% to 30 wt% relative to SrCr.PVB standard. None of them performed as well as the SrCr.PVB standard. Increase in the pigment loading concentrations, did not improve the low frequency impedance, in fact decreased the magnitude of impedance at the end of 168 h. This indicates that increase in pigment loadings further degraded the barrier properties of PVB and did not provide passivation of the interface. It also suggests that the Zn^{2+} ion release is suppressed in the PVB resins and the release is not triggered with an increase in Zn bentonite loadings in the resin.

Figure 3.38b shows the variation in pore resistance with time for the coatings. Increase in the Zn bentonite loadings in PVB reduced the pore resistances indicating increased corrosion of the substrate. This suggests that bentonite pigments are essentially acting as defects in the PVB resin without releasing the inhibitor cation. It could be that higher bentonite concentrations in PVB led to higher number of defects in the coatings, thus leading to low impedance response. Overall, increasing the pigment loading, did not improve the coating performance, in fact, deteriorated the coating characteristics.

156
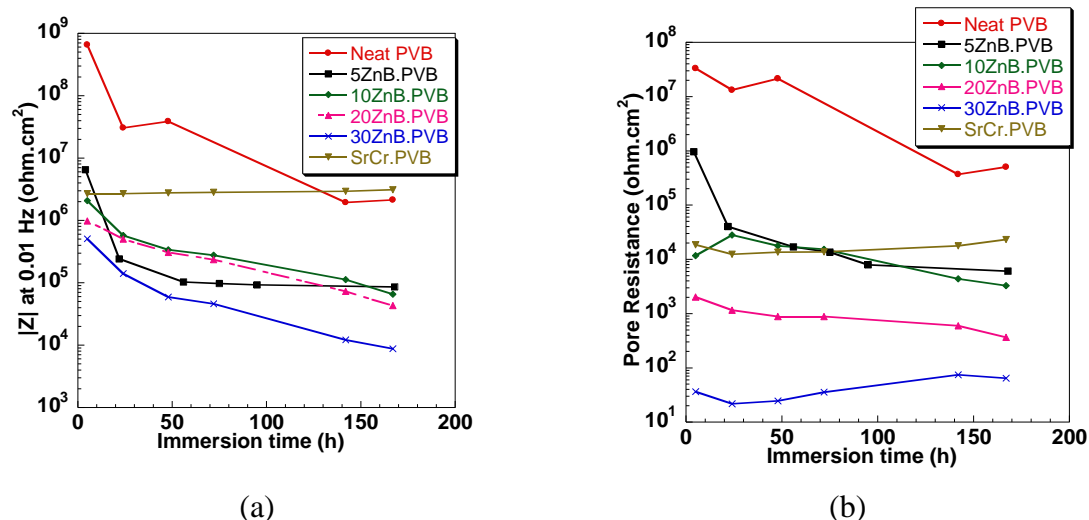
Figure 3.38. (a) Total impedance (b) Capacitances of PVB coatings pigmented with 5 to 30 wt% of Zn bentonite and SrCr.PVB standard, during static immersion in 0.5 M NaCl.

5.3.3.4.4.3 EIS of epoxy coatings pigmented with exchanged bentonites. The impedance spectra of epoxy coatings initially exhibited a two time constant behavior, which later evolved into a three time constant spectra after continued exposure for more than a week. Figure 3.39 shows the Bode magnitude and phase angle plot for the unpigmented epoxy coating immersed in 0.5M NaCl solution for a period of 336 h. Three-time constant behavior were shown by 5LaB.Ep, 5CeB.Ep and 5PrB.ZnB and SrCr.Ep at increased exposure times while 5ZnB.Ep exhibited two time constant behavior throughout its immersion time. The magnitude of impedance at high frequencies (10^5 to 10^2 Hz) in the Bode phase angle plot, reduced as a result of increased water uptake and localized corrosion beneath the coating [106, 107]. This is in contrast to the PVB coatings, which did not show changes in the coating capacitances with time suggesting no water uptake. The presence of solids like TiO_2 in the unpigmented epoxy coating increased the permeability of the epoxy coating enabling water uptake. However, 5 wt% bentonite pigments in neat PVB resin did not seem to enable water uptake by the PVB resin. It was not possible to calculate the water uptake of the epoxy coating from these data as it occurred within one day of immersion and was not captured.

The resistive plateau in the Bode magnitude plot in Figure 3.39 corresponding to pore resistance disappeared (100 Hz) after 168 h of exposure and showed the rise of a new capacitive peak (10^2 to 10^1 Hz) associated with capacitance responses from either new defects or a porous corrosion product in the existing defect. The double layer capacitance and charge transfer resistance in the defect beneath the corrosion product dominates the low frequency region. Simplified two time constant circuit shown in Figure 3.33c and simplified three time constant circuit shown in Figure 3.33d are used to fit the spectra and the coating characteristic parameters are extracted and compared with time.
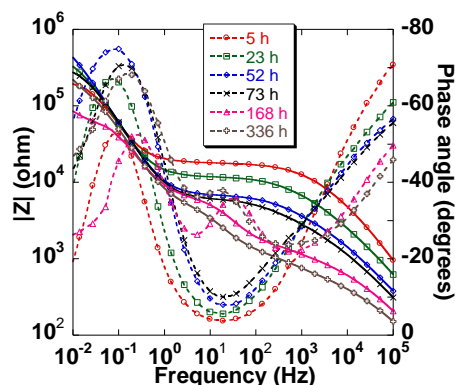
Figure 3.39. Bode magnitude and phase angle plots of Neat Epoxy coating upon static exposure to 0.5M NaCl solution for a period of 2 weeks (336 h). The area exposed to the solution was 5.55 cm^2

Figure 3.40a shows the total magnitude of impedance at 0.01 Hz of the coatings relative to the SrCr.Ep standard. Better response was seen from the bentonite pigmented coatings at the end of 680 h with the impedance of 5ZnB.Ep (1.51 x10^6 Ω.cm^2) and 5LaB.Ep (1.79 x10^6 Ω.cm^2) in the same order of magnitude as SrCr.Ep (2.48 x 10^6 Ω.cm^2). Interestingly, Ce and Pr bentonite pigments showed inferior performance compared to the other bentonites. The water uptake by the pigmented coatings is causing the release of the Zn^{2+} and La^{3+} cations from the pigments and promoting passivity of the interface.

Figure 3.40b shows the variation in coating capacitances with time over 680 h relative to the SrCr.Ep control. There is some incongruence in the interpretation as the coating capacitances of the bentonites are too high on the order of 10^{-7} to 10^{-8}, which cannot be coating capacitances. As a check, the dielectric constant of a coating with thickness, t, is given by $\varepsilon = Ct/A\varepsilon_o$, where C is capacitance, A is area and ε_o is 8.85 x 10^{-12} F/m. The thickness of the plain epoxy coating was measured to be approximately 35 μm and the area of the exposed coating was 5.55 cm^2. Assuming the increase in capacitance during initial exposures up to 2 days is due to diffusional water uptake, the capacitance vs. t$^{1/2}$ curve was extrapolated to obtain the capacitance of the epoxy coating before exposure (t=0). The capacitance of the unpigmented epoxy coating was found to be 7.8715 x 10^{-11} F/cm^2. The dielectric constant of the epoxy coating was found to be 3.1 which lies in the range of dielectric constants of polymers of 3 – 10 [108]. The thickness of 5 wt% Ce bentonite pigment loaded epoxy coating was measured to be 55 μm and the capacitance of 5 wt% Ce bentonite pigment loaded epoxy coating was determined to be 2.162 x 10^{-9} F/cm^2. This gave a dielectric constant 130.43, which suggests that this value of capacitance does not correspond to that of the coating. Therefore, this implies that the high frequency capacitive response from the bentonite coatings except 5LaB.Ep was from the mixed capacitances of the coating and defects in the coating. It has to be noted that, despite bentonites degrading the barrier properties, Zn bentonite and La bentonite performed comparably to SrCr.Ep.
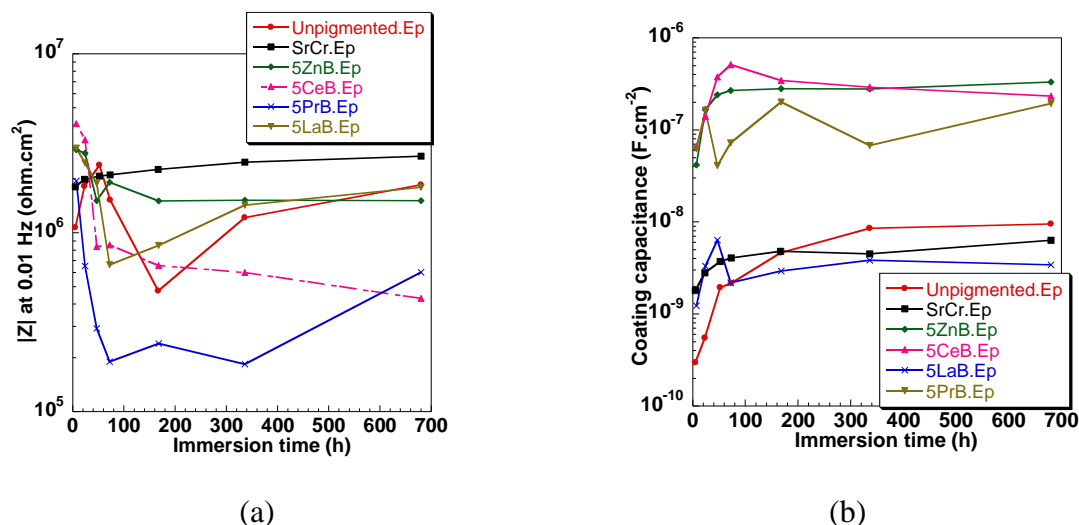
Figure 3.40. (a) Total impedance (b) Capacitances of epoxy coatings pigmented with exchange bentonites and SrCr.Ep standard, subject to static immersion in 0.5 M NaCl.

The pigment loading levels of Zn bentonite pigment added to the epoxy was increased from 5 wt% to 30 wt% and its effect on the coating characteristics were investigated. SrCr.Ep was used as the positive control and unpigmented.Ep was used as the negative control. All the pigmented bentonite coatings exhibited a two time constant behavior and they were fit using the simplified equivalent circuit. Figure 3.41 shows the variation in the magnitude of total impedance at low frequency of Zn bentonite coatings relative to the SrCr.Ep standard. Increasing the pigment loadings up to 30 wt% from 5 wt% decreased the total impedance by about two orders of magnitude, much similar to the case observed in increasing Zn bentonite loadings in PVB coatings. Release of Zn^{2+} cation was observed as the solution at the coating turned cloudy with the hydrolysis of the Zn^{2+} cation at localized defects. However, it was different from the PVB case that the release of the cations was suppressed in the PVB resin due to no water uptake. It could be that, increasing the pigment concentrations in epoxy, increases the total number of localized defects in the coating. Hence, even though release is seen, significant destruction of barrier properties causes increased localized attack.
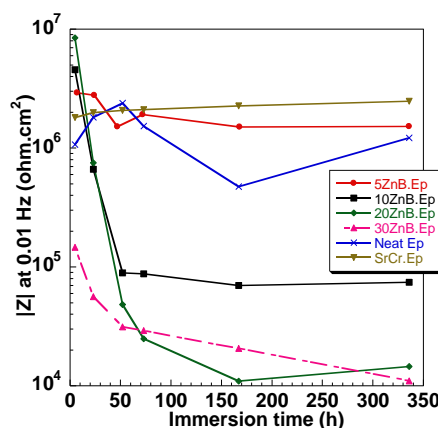
Figure 3.41. Total impedance of epoxy coatings pigmented with 5 to 30 wt% of Zn bentonite and SrCr.Ep standard, during static immersion in 0.5 M NaCl.

159

5.3.3.4.5 Salt Spray Exposure of bentonite pigmented coatings. Figure 3.42a shows the PVB coated samples with 5 wt% pigment loadings after exposure in a salt spray chamber for 336 h and Figure 3.42b shows the PVB coated samples with increased Zn bentonite pigment loading levels after exposure in salt spray for 72 h. The relative ranking for the blistering (B) of the coatings and their scribe protection (SP) are given on the top right hand corner for each sample. A ranking of "1" for the blisters indicates that there are no blisters on the surface, "3" indicates a few blisters on the surface while "5" indicates more number of blisters on the surface. Similar ranking was used for the scribe protection while a ranking of "1" shows good protection through out the scribe with no corrosion product, "3" indicates partial area of the scribe protected with shiny metal and "5" indicates no scribe protection. The SrCr.PVB standard showed the best performance with no blisters (rank 1) and full protection of the scribe (rank 1). All the samples in Figure 3.42a showed varied amount of blistering from ranks 2 to 5 and none of them showed full scribe protection. 5ZnB.PVB performed much better with a blistering rank of 2 compared to the 5PrB.PVB (blister rank 3), Neat.PVB (blister rank 5) and other pigmented bentonites ((blister rank 5). However, Neat PVB, 5ZnB.PVB and 5PrB.PVB showed some signs of filiform corrosion. 5ZnB.PVB and 30ZnB.PVB exposed for 72 h (Figure 3.42b) performed relatively better compared to Neat.PVB while 10ZnB.PVB and 20ZnB.PVB showed excessive blistering.

(a)   (b)
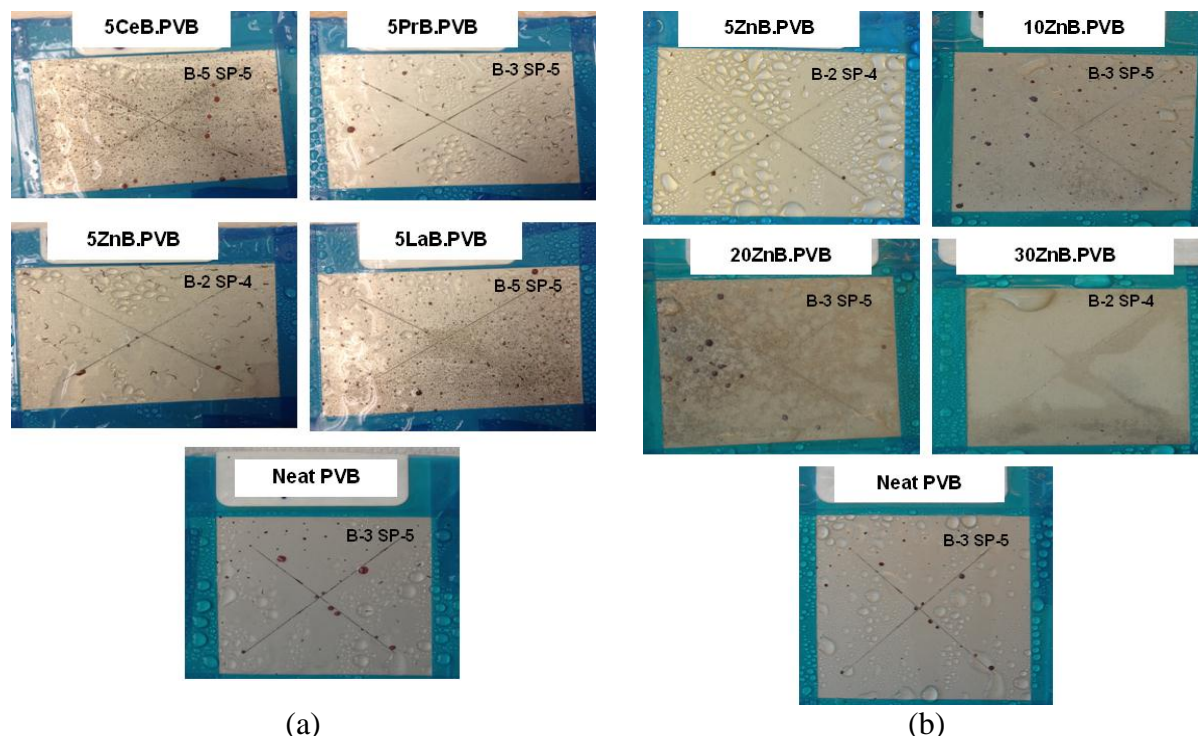
Figure 3.42. AA 2024-T3 samples coated with (a) PVB pigmented with exchanged bentonites of 5 wt% (b) PVB pigmented with Zn bentonite of increasing loading levels The scribed samples were exposed to the salt spray for a period of 336 h in (a) and for a period of 72 h in (b). The rankings are given in the top right hand corner with "1" indicating the best performance

Figure 3.43 shows the pigmented bentonite coatings in epoxy after 680 h of exposure in the salt spray. The same ranking system was used. The control unpigmented.Ep was seen to blister while all the exchanged bentonites added in 5 wt% concentration did not blister. However, all the

160

pigmented coatings exhibited partially attacked scribes and an attacked area around the scribe, with the exception of 5LaB.Ep which did not show any attack around the scribe. SrCr.Ep performed the best with no blistering and provided excellent scribe protection. Increasing the loading concentration of Zn bentonite caused heavy attack on the scribe and delamination.

(a)   (b)
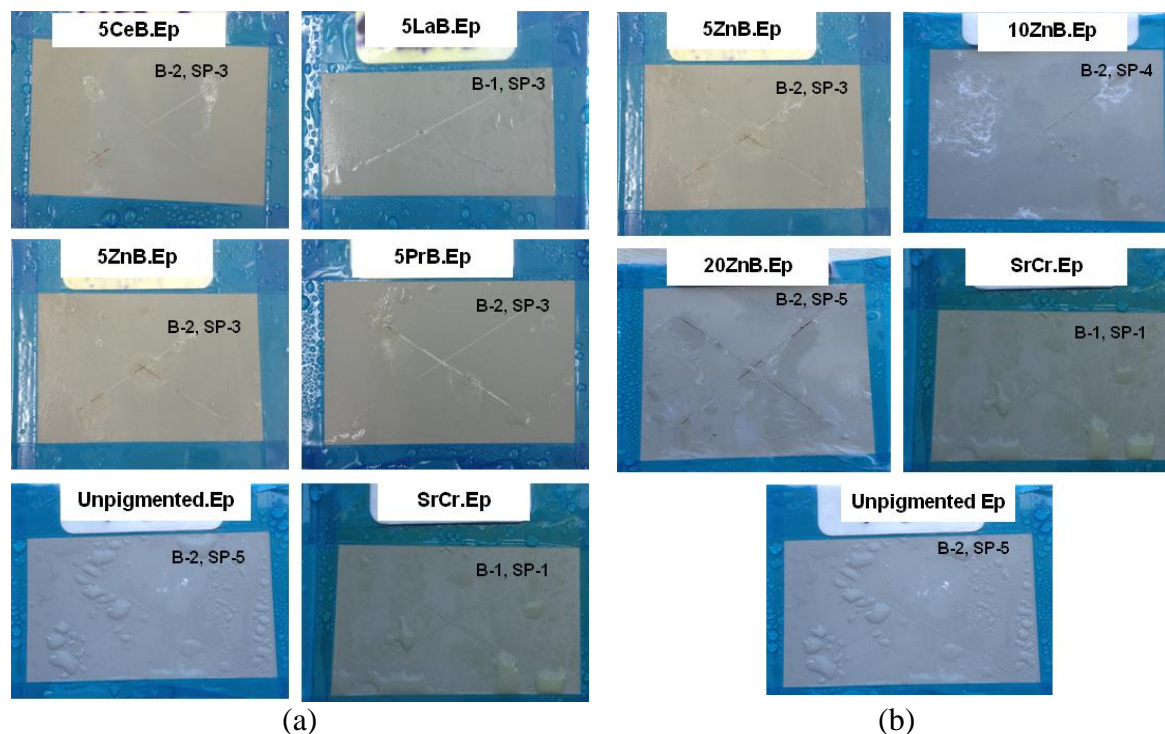
Figure 3.43. AA 2024-T3 samples coated with (a) Epoxy pigmented with exchanged bentonites of 5 wt% (b) Epoxy pigmented with Zn bentonite of increasing loading levels The scribed samples were exposed to the salt spray for a period of 680 h. The rankings are given in the top right hand corner with "1" indicating the best performance.

5.3.3.5 Discussion

Neat resin coatings usually possess good barrier properties. Pigmented coatings are very different from the neat resin coatings as they disturb the continuous polymer network and degrade the barrier properties of the coating. Therefore, pigments increase the permeability of the coating. The release of inhibitor cations from bentonites to promote interfacial passivity depends on the water uptake by the coating. After water uptake by the coating, substrate passivity should occur for the pigment to be a candidate.

The bentonite pigment performance in three different kinds of resins was demonstrated. PVA resins, being hydrophilic and water soluble, takes up a lot of water and they essentially, behaved like gels. Impedance results showed that PVA exhibited very low barrier properties. Bentonites did not passivate the interface and also did not already lower the weak barrier properties. It suggests that not enough inhibitor cation was released to completely passivate the surface. In contrast, $SrCrO_4$, promoted interfacial passivity, despite the low barrier properties of PVA. PVB exhibited excellent barrier properties and the coating capacitances do not suggest water uptake by the resin with and without 5 wt% bentonite pigment additions. This implies that the inhibitor

cations had not been released and bentonites essentially act like defects on the substrate, causing increasing localized corrosion. Increased pigment loadings worsened the barrier properties of PVB and exhibited increased corrosion of the substrate. $SrCrO_4$ pigmented PVB coatings on the other hand showed superior performance and strongly passivated the interface. This is observed because, $SrCrO_4$ pigment leaches out of the coating and reduces to Cr^{3+} at defects.

Epoxy resins on the other hand, had non-inhibiting solids like TiO_2 in them. This significantly increased the water uptake of the neat epoxy coatings. This is the reason why there was better response observed from La and Zn bentonite pigments in the epoxy coatings and they also promoted interfacial passivity, comparable to $SrCrO_4$.

Among all the pigments added in PVB coatings, Zn bentonite pigment added in low concentrations of 5 wt% performed relatively better compared to the other exchanged bentonites. The impedances of PVB loaded with Zn bentonite were similar to other bentonites but the salt spray tests of the PVB based coatings also showed that 5 wt % Zn bentonite performed much better and suppressed blistering of PVB. Among the pigmented epoxy coatings, La and Zn bentonites showed superior performance with their impedance in EIS measurements closer to strontium chromate. La and Zn bentonites in epoxy coating provided partial scribe protection but La bentonite epoxy coating did not show any attack around the scribe unlike Zn bentonite. The superior performance of La bentonite is not understood at this point. The release experiments showed that a higher fraction of the total Zn^{2+} inhibitor reservoir in the Zn bentonite pigment was released which was 0.61, in contrast to Ce and Pr bentonites whose fractions of the total inhibitor release was 0.46. Chapter 4 discussed that Zn^{2+} cations are better cathodic inhibitors of AA 2024 when compared to rare earth metal (REM) cations. Hence, higher interfacial passivity was promoted by Zn bentonite pigments.

The existence of any correlation between the impedance data and the scribe protection in salt spray exposure generally depends on the mechanism of inhibition by the inhibitors in the coating. $SrCrO_4$ is known to inhibit corrosion at the scribe by the transportation of mobile chromate ions that are leached out of the coating, to the exposed metal and undergo reduction. However, the mechanism of Zn bentonite pigment is very different. Zn^{2+} cations should be released from the bentonite pigment present in the coating adjacent to the exposed metal, and then precipitate by an increase in the localized pH as a result of corrosion. The pH dependence and sluggish kinetics of inhibition by the Zn^{2+} ion seen in chapter 4 could be the reason why there is no scribe protection seen even though a high impedances and pore resistances are recorded.

The salt spray results are very different from what the static exposure experiments suggest from the impedance measurements. It could be because, salt spray has a thin layer of moisture and has a lot more supply of oxygen and carbonate anions than in the bulk volumes of sodium chloride solutions in static immersion. Zn bentonite in PVB performs much better in salt spray tests as Zn^{2+} requires CO_2 for precipitation and it is available in much more quantities in the salt fog than in static immersion.

5.3.3.6 Conclusions

1. Exchange bentonites of Ce, Pr, La and Zn were synthesized and their characterization by XRD showed a shift in their basal d_{001} spacings indicating successful exchange of the sodium cation for the inhibitor cation during synthesis. The trend in the d-spacing increase for the bentonites was Pr > Ce = La > Zn. TGA analysis until 250˚C showed higher loss in wt% for the exchanged bentonites indicating that the number of water molecules associated with the interlamellar space has increased. This is the cause for the increase in d-spacing. The trend for the d-spacing increase correlated well with the TGA weight loss measurements

2. Sodium bentonite exhibited a Cation Exchange Capacity (CEC) of 85 meq/100g. Release measurements confirmed inhibitor cation (Ce^{3+}, Pr^{3+}, Zn^{2+}) release. The fraction of reservoir of the inhibitor in the bentonite was relatively high for Zn bentonite at 0.61 and it was 0.46 and 0.47 for Ce and Pr bentonites. This could be one of the reasons why Ce and Pr bentonites performed inferior to the Zn bentonites in the impedance and salt spray tests.

3. La and Zn bentonites showed better performance compared to the other exchange bentonites when incorporated into epoxy coatings with total impedance magnitude in the same order as the $SrCrO_4$ standard. The presence of TiO_2 solids increased the permeability of the epoxy resin and impedance suggested strong water uptake by the epoxy coatings, enabling La^{3+} and Zn^{2+} cation release and promoting interfacial passivity.

4. EIS measurements showed that PVA behaved like a gel and exhibited very low barrier properties. Bentonites did not passivate the interface suggesting that not enough inhibitor cation was released to completely passivate the surface. EIS on the PVB coatings on the other hand suggested no water uptake due to which the inhibitor cation was not released. Bentonites degraded the barrier properties of PVB and provided no inhibition.

5. Salt spray exposures showed that Zn bentonite incorporated into PVB performed relatively better compared to the neat PVB and other pigmented bentonites with very few blisters. La bentonite incorporated in epoxy coatings showed no attack around the scribe compared to other pigmented epoxy coatings. However, all the pigmented epoxy coatings showed partial scribe protection.

5.3.4 References

1. I.J.Polmear, Light Alloys Metallurgy of the Light Metals, p. 362, Arnold, London (1995).
2. Z. Szklarska-Smialowska, Corrosion Science, 41, 1743 (1999).
3. T. Suter and R. C. Alkire, Journal of the Electrochemical Society, 148, B36 (2001).
4. J. O. Park, C. H. Paik, Y. H. Huang and R. C. Alkire, Journal of the Electrochemical Society, 146, 517 (1999).
5. C. M. Liao, J. M. Olive, M. Gao and R. P. Wei, Corrosion, 54, 451 (1998).
6. P. Leblanc and G. S. Frankel, Journal of the Electrochemical Society, 149, B239 (2002).
7. R. G. Buchheit, L. P. Montes, M. A. Martinez, J. Michael and P. F. Hlava, Journal of the Electrochemical Society, 146, 4424 (1999).

8.   R. G. Buchheit, R. P. Grant, P. F. Hlava, B. McKenzie and G. L. Zender, Journal of the Electrochemical Society, 144, 2621 (1997).
9.   M. W. Kendig and R. G. Buchheit, Corrosion, 59, 379 (2003).
10.   M. Kendig, S. Jeanjaquet, R. Addison and J. Waldrop, Surface & Coatings Technology, 140, 58 (2001).
11.   B.R.W. Hinton, N.E. Ryan, D.R. Arnott, P.N. Trathen, L. Wilson and B. E. Williams, Corr. Austral, 10, 12 (1985).
12.   D. R. Arnott, B. R. W. Hinton and N. E. Ryan, Materials Performance, 26, 42 (1987).
13.   A. K. Mishra and R. Balasubramaniam, Corrosion Science, 49, 1027 (2007).
14.   B. R. W. Hinton, Journal of Alloys and Compounds, 180, 15 (1992).
15.   A. Aballe, M. Bethencourt, F. J. Botana and M. Marcos, Journal of Alloys and Compounds, 323-324, 855 (2001).
16.   K. A. Yasakau, M. L. Zheludkevich, S. V. Lamaka and M. G. S. Ferreira, The Journal of Physical Chemistry 110, 5515 (2006).
17.   A. J. Aldykiewicz, H. S. Isaacs and A. J. Davenport, Journal of the Electrochemical Society, 142, 3342 (1995).
18.   A. J. Aldykiewicz, A. J. Davenport and H. S. Isaacs, Journal of the Electrochemical Society, 143, 147 (1996).
19.   M. A. Jakab, F. Presuel-Moreno and J. R. Scully, Journal of the Electrochemical Society, 153, B244 (2006).
20.   X. Yu and C. Cao, Thin Solid Films, 423, 252 (2003).
21.   X. Yu, C.Cao and Z.Yao, Mater.Sci.Lett., 19, 1907 (2000).
22.   V. Mansfeld and F. Wang, Brit.Corr.Jour., 29, 194 (1994).
23.   A. J. Bard and L. R. Faulkner, Electrochemical methods : fundamentals and applications, p. 833, Wiley, New York (2001).
24.   G. W. Hung and R. H. Dinius, J. Chem. Eng. Data Journal of Chemical & Engineering Data, 17, 449 (1972).
25.   R. Procaccini, S. Ceré and M. Vázquez, Journal of Applied Electrochemistry, 39, 177 (2009).
26.   C. F. Baes and R. S. Mesmer:, The Hydrolysis of Cations, p. 245, John Wiley and Sons, Inc., New York, (1976).
27.   D. R. Arnott and B.R.W. Hinton, Microstructural Sci., 17 (1989).
28.   N. E. Ryan,. B.R.W. Hinton, D.R. Arnott, P.N. Trathen, L. Wilson, B.E. Williams, Corr. Austral, 10 (1985).
29.   B. R. W. Hinton, D. R. Arnott and N. E. Ryan, Metals Forum, 7, 211 (1984).
30.   H. Wroblowa, H. Yenchipan and G. Razumney, Journal of Electroanalytical Chemistry Journal of Electroanalytical Chemistry, 69, 195 (1976).
31.   K. Martin and H. Melitta, Electrochemical and Solid-State Letters, 8, B10 (2005).
32.   K. A. Yasakau, M. L. Zheludkevich and M. G. S. Ferreira, Journal of the Electrochemical Society, 155, C169 (2008).
33.   B. R. W. Hinton and D. R. Arnott, Microstructural Sci., 17, 311 (1989).
34.   P. Schmutz and G. S. Frankel, Journal of the Electrochemical Society, 146, 4461 (1999).
35.   G. J. Fosmire, American Journal of Clinical Nutrition, 51, 225 (1990).
36.   A. Kalendova, P. Kalenda and D. Vesely, Progress in Organic Coatings, 57, 1 (2006).
37.   A. Kalendová, Progress in Organic Coatings, 46, 324 (2003).
38.   M. Leclerq, European Coatings Journal, 3, 106 (1991).

39. M. Mahdavian and M. M. Attar, Progress in Organic Coatings, 53, 191 (2005).
40. A. Amirudin, C. Barreau, R. Hellouin and D. Thierry, Progress in Organic Coatings, 25, 339 (1995).
41. A. Kalendova, Anti-Corrosion Methods and Materials, 49, 173 (2002).
42. B. D. Amo, R. Romagnoli, V. F. Vetere and L. S. Hernandez, Progress in organic coatings, 33, 28 (1998).
43. A. Kalendová, Pigment & Resin Technology, 31, 381 (2002).
44. A. Kalendová, Anti-Corrosion Methods and Materials, 49, 364 (2002).
45. K.Ogle and M.Wolpers, in ASM Handbook: Corrosion:Fundamentals, Testing and Protection, p. 712, ASM International (2003).
46. D. Susac, X. Sun, R. Y. Li, K. C. Wong, P. C. Wong, K. A. R. Mitchell and R. Champaneria, Applied Surface Science, 239, 45 (2004).
47. D.B.Freeman, Phosphating and Metal Pretreatment, Cambridge, Endland (1986).
48. Zinc, in, p. http://www.stormwaterx.com/Resources.aspx, StormwaterRx LLC.
49. X. Zhang, S. Lo Russo, A. Miotello, L. Guzman, E. Cattaruzza, P. L. Bonora and L. Benedetti, Surface and Coatings Technology, 141, 187 (2001).
50. A. S. Akhtar, P. C. Wong, K. C. Wong and K. A. R. Mitchell, Applied Surface Science, 254, 4813 (2008).
51. B. P. Boffardi, in ASM Handbook: Corrosion:Fundamentals, Testing and Protection, p. 902, ASM International (2003).
52. R. G. Buchheit, H. Guan, S. Mahajanam and F. Wong, Progress in Organic Coatings, 47, 174 (2003).
53. H. S. Awad, Anti-Corrosion Methods and Materials, 52, 22 (2005).
54. A. J. Bard and L. R. Faulkner, Electrochemical methods : fundamentals and applications / Allen J. Bard, Larry R. Faulkner, p. 718, Wiley, New York (1980).
55. G. W. Hung and R. H. Dinius, Journal of Chemical and Engineering Data, 17, 449 (1972).
56. S. Schurz, G. H. Luckeneder, M. Fleischanderl, P. Mack, H. Gsaller, A. C. Kneissl and G. Mori, Corrosion Science, 52, 3271.
57. G. J. Brug, A. L. G. van den Eeden, M. Sluyters-Rehbach and J. H. Sluyters, Journal of Electroanalytical Chemistry, 176, 275 (1984).
58. Y. Li, Corrosion Science, 43, 1793 (2001).
59. S. J. Garcia, T. H. Muster, O. Ozkanat, N. Sherman, A. E. Hughes, H. Terryn, J. H. W. de Wit and J. M. C. Mol, Electrochimica Acta, 55, 2457 (2010).
60. G. A. L. Stern M, J. of the Electrochemical Society, 104, 56 (1957).
61. G. Boisier, N. Portail and N. Pebere, Electrochimica Acta, 55, 6182 (2010).
62. I.J.Polmear, Light Alloys Metallurgy of the Light Metals, Arnold, London (1995).
63. T. H. Muster, A. E. Hughes and G. E. Thompson, in Corrosion Research Trends, I. S. Wang Editor, p. 35, Nova Science Publishers, Inc. (2007).
64. C.-M. Liao and R. P. Wei, Electrochimica Acta, 45, 881 (1999).
65. R. G. Buchheit, Journal of the Electrochemical Society, 142, 3994 (1995).
66. C. M. Liao, J. M.Olive, M.Gao and R. P.Wei, Corrosion, 54, 451 (1998).
67. R. L. Twite and G. P. Bierwagen, Progress in Organic Coatings, 33, 91 (1998).
68. P. L. Hagans and C. M. Haas, in ASM Handbook : Surface Engineering, p. 405 (1994).
69. A. E. Hughes, R. J. Taylor and B. R. W. Hinton, Surface and Interface Analysis, 25, 223 (1997).
70. H. Stunzi and W. Marty, Inorganic Chemistry, 22, 2145 (1983).

71.   L. Xia and R. L. McCreery, Journal of the Electrochemical Society, 145, 3083 (1998).
72.   J. Sinko, Progress in Organic Coatings, 42, 267 (2001).
73.   L. Xia, E. Akiyama, G. Frankel and R. McCreery, Journal of the Electrochemical Society, 147, 2556 (2000).
74.   R. G. Buchheit and A. E. Hughes, in ASM Handbook, S. D. Cramer and B. S.Covino Editors, p. 720 (2003).
75.   B. R. W. Hinton, Metal Finishing, 89, 55 (1991).
76.   B. R. W. Hinton, Metal Finishing, 89, 15 (1991).
77.   P.O'Brien and A.Kortenkamp, Transition Metal Chemistry, 20, 636 (1995).
78.   K. D. Ralston, Chromate-free corrosion inhibition of aluminum alloys vanadates and anionic exchange clay pigments, in Materials Science and Engineering, p. 234, Ohio State University, Columbus, Ohio (2008).
79.   K. D. Ralston, S. Chrisanti, T. L. Young and R. G. Buchheit, J. Electrochem. Soc. Journal of The Electrochemical Society, 155 (2008).
80.   S. Chrisanti, The application of ion-exchanged clay as corrosion inhibiting pigments in organic coatings, in Materials Science and Engineering, Ohio State University, Columbus, Ohio (2007).
81.   L. A. van der Meer-Lerk and P. M. Heertjes, J.Oil.Colloid.Chem. Assoc., 62, 256 (1979).
82.   S. P. V. Mahajanam and R. G. Buchheit, Corrosion, 64, 230 (2008).
83.   G. Williams and H. N. McMurray, Electrochemical and Solid State Letters, 6, B9 (2003).
84.   H. N. McMurray and G. Williams, CORROSION -HOUSTON TX-, 60, 219 (2004).
85.   G. Williams, H. N. McMurray and M. J. Loveridge, Electrochimica Acta, 55, 1740 (2010).
86.   G. Williams, H. N. McMurray and D. A. Worsley, Journal of the Electrochemical Society, 149, B154 (2002).
87.   D. H. Solomon and D. G. Hawthorne, Chemistry of pigments and fillers, Wiley, New York (1983).
88.   H. v. Olphen, An introduction to clay colloid chemistry, for clay technologists, geologists, and soil scientists, Interscience Publishers, New York (1963).
89.   R. E. Grim, Clay mineralogy, McGraw-Hill, New York (1968).
90.   G. W. Brindley and G. Brown, Crystal structures of clay minerals and their X-ray identification, Mineralogical Society, London (1980).
91.   J. Adams, Journal of Catalysis Journal of Catalysis, 58, 238 (1979).
92.   S. Bohm, H. N. McMurray, D. A. Worsley and S. M. Powell, Materials and Corrosion Materials and Corrosion, 52, 896 (2001).
93.   L. P. Meier, Clays and Clay Minerals Clays and Clay Minerals, 47, 386 (1999).
94.   L. Ammann, F. Bergaya and G. Lagaly, Clay Minerals, 40, 441 (2005).
95.   L. Szabó, L. Leopold, B. Cozar, N. Leopold, K. Herman and V. Chiş, Central European Journal of Chemistry, 9, 410 (2011).
96.   M. Auboiroux, P. Baillif, J. C. Touray and F. Bergaya, APPLIED CLAY SCIENCE, 11, 117 (1996).
97.   J. Cuadros, American Journal of Science, 297 (1997).
98.   J. C. Taylor and C. E. Matulis, Powder diffraction., 9, 119 (1994).
99.   L. Zhirong, M. Azhar Uddin and S. Zhanxue, Spectrochimica Acta Part A: Molecular and Biomolecular Spectroscopy, 79, 1013.

100. F.Liebau, Structural Chemistry of Silicates, p. 347, Springer-Verlag, Berlin Heidelberg (1985).
101. D. Dermatas and M. S. Dadachov, Applied clay science., 23, 245 (2003).
102. M. M. Elgabaly and H. Jenny, The Journal of Physical Chemistry, 47, 399 (1943).
103. W. S. Tait, An introduction to electrochemical corrosion testing for practicing engineers and scientists, p. 138, PairODocs Publications, Racine, Wis. (1994).
104. R. Cottis and S. Turgoose, Electrochemical impedance and noise, NACE International, Houston, TX (1999).
105. G. J. Brug, A. L. G. van den Eeden, M. Sluyters-Rehbach and J. H. Sluyters, Journal of Electroanalytical Chemistry Journal of Electroanalytical Chemistry, 176, 275 (1984).
106. F. Wong, Application of layered double hydroxides as corrosion sensing pigments in coatings, in Materials Science and Engineering, The Ohio State University, Columbus (2004).
107. D. M. Brasher and A. H. Kingsbury, J. Appl. Chem. Journal of Applied Chemistry, 4, 62 (2007).
108. Dielectric Constant, in, p. http://my.execpc.com/~endlr/dielectric_const_.html, StormwaterRx LLC.

5.4 Task 4: Paint adhesion strength and mechanism

5.4.1 Objective

The objective of this work is to evaluate the effect of various commercial surface treatments on the adhesion of paint coatings.

5.4.2 Background.

Surface treatments are known to be critical to the corrosion performance of coated Al substrates. The focus of the effects of the treatments is typically how they provide corrosion protection and sometimes active corrosion protection. For instance, chromate conversion coatings alone provide active corrosion protection. However, paint coatings will only protect if they adhere to the substrate and the role of surface treatments in promoting adhesion is not known. Furthermore, there is a lack of knowledge of what controls adhesion strength of coating to substrate. There are many techniques to evaluate adhesion. But, most are performed in dry conditions, are not reproducible or quantitative. The Blister Test is an adhesion tester developed by Dannenberg circa 1950 [1] offers several advantages [2]. There is no contamination of the system by an adhesive placed on top of the coating. Engineering analysis of the system is possible. Finally, the blister test can be performed wet or without liquid contact.

Adhesion strength assessed by fracture energy, G_a, can be determined from pressure, P, and blister radius, a:

$$G_a = \left(\frac{(Pxr)^4}{17.4xExt} \right)^{\frac{1}{3}} \quad \text{(Eq. 4.1)}$$

where P is critical internal pressure, E is tensile Young's modulus of the adhering layer, t is thickness of the layer, G_a is adhesion strength of the layer to a rigid substrate, and r is the blister radius.

5.4.3 Materials and Methods.

5.4.3.1 The Blister Test

The Blister Test (BT) apparatus has been modified and improved as the project progressed. A schematic of the latest setup is shown in Figure 4.1. The BT involves pressurization of a hole in a substrate using a fluid to create a blister at the substrate/coating interface. During this process, the diameter of the blister and its pressure are recorded until the complete delamination of the coating occurs. For this purpose, the setup contains a programmable syringe pump (KD Scientific), which is connected to the sample holder by a stainless steel tube. A T-valve is used between these two parts of the setup to feed the syringe with electrolyte when the BT needs to be conditioned for a new test. The pressure is recorded versus time using a pressure transducer (Omegadyne). The sample holder has a cubic shape and is made of polycarbonate. It is designed to accommodate a reference and counter electrode for electrochemical measurements. It has connections for the syringe pump and the pressure transducer. The largest hole is for attachment

of the coated sample, which is tightened down with the help of a plastic coated C-shaped stainless steel sheet and four screws. All tubing and tubing accessories are made of stainless steel.

The setup also has an environmental chamber made of polycarbonate, which is attachable on top of the sample holder. This chamber is sealed against the sample holder using an o-ring. The relative humidity of the air flowing through the chamber can be controlled by the solution in washing bottles and is measured by a sensor in a downstream mini-chamber. Unless otherwise noted, water saturated air is pumped through the chamber using an aquarium pump and two washing bottles during all BT experiments.

The environmental chamber has a quartz window in the upper face to allow viewing and recording of the blister growth with a CCD camera attached to a face-down stereoscopic microscope (SZX12 OLYMPUS). The syringe pump is controlled by a program written in DasyLab software. The BT can be set up to run in Constant Infusion (CI) rate mode or Constant Pressure (CP) mode. The infusion/withdrawal rates, target pressure and other variables can be adjusted in the program. Unless otherwise mentioned, all the CI experiments used an infusion rate of 0.050 mL/h, with DI water as the pressurizing fluid.
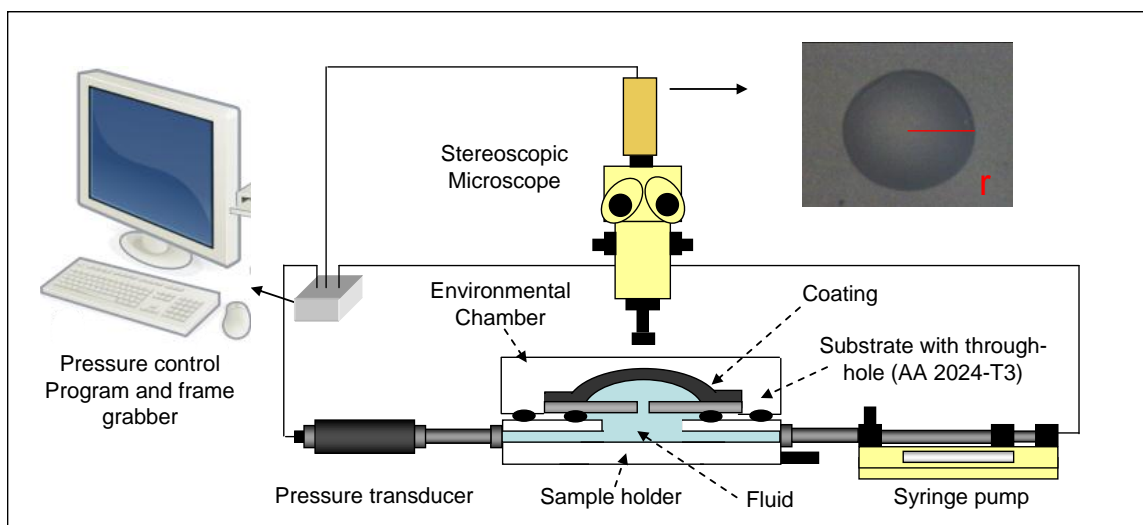
Figure 4.1. Schematic of the Blister Test.

5.4.3.2 The Galvanic Blister Test

The Galvanic Blister Test (GBT) is a CPBT where the pressure is achieved by a column of 5 wt% NaCl inside a SS316 tube that is galvanically coupled to the sample. The sample holder is placed upside down to avoid gas accumulation at the surface, which would disrupt the electrochemical reactions taking place in the system. A chloridized silver wire is used as reference electrode. The electrolyte is circulated through the system using a fixed-flow peristaltic metering pump (Fisher Scientific) at a rate of 37 L/hr to avoid gas bubble accumulation.

5.4.3.3 Coated Samples for BT and GBT experiments

AA2024-T3 was used as substrate. The BT sample dimensions are 30 x 30 x 1.3 mm. Different approaches were attempted for preparation of a through hole in samples for the blister test. The goal is to have a high quality coating spanning a through-hole in the sample. It is possible either to drill a hole through the substrate and then coat, or to do the reverse, i.e., coat a sample and then create a hole in the substrate. Methods for the first approach were investigated by plugging the drilled hole with a wax or cork, or covering the hole with a polished scotch tape disc and then applying the coating. Various approaches were used to create a through-hole in a non-tape coated sample, including electrical discharge machining, nano-milling machining, and milling combined with electrodissolution machining. Figure 4.2 shows schematic illustrations of the different approaches.

a.1. Cork Plugging	a.2. Wax Plugging	a.3. Polished Scotch tape covering
b.1. Electrical Discharge Machining	b.2. Nano-milling Machining	b.3. Milling + Electrodissolution Machining
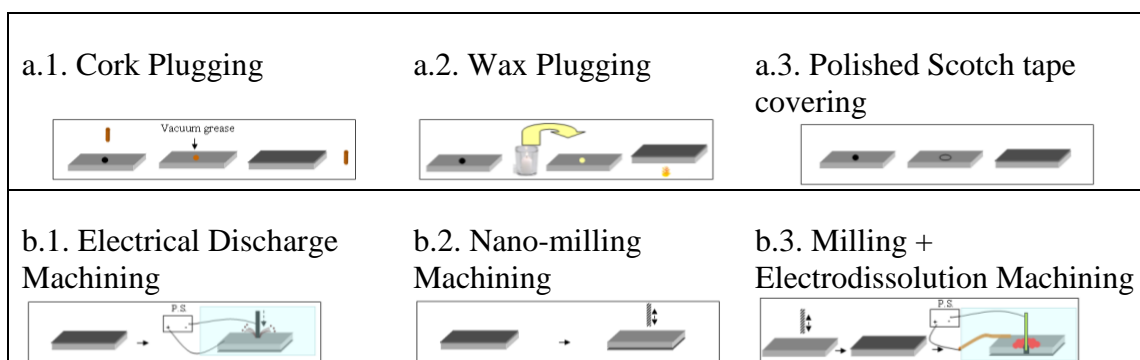
Figure 4.2. Schematic depictions of the different approaches used for sample preparation for the Blister Test, where a) the sample is coated after a pre-drilled hole is made and b) a hole is created in a pre-coated sample.

In the case of the first type of approach, the cork and wax plugging produced a non-uniform coating with a thinner layer over the hole than on the rest of the substrate, resulting in primer fracture at defects on the hole edge upon pressurization rather than adhesive failure at the substrate/coating interface. The thinner coating over the hole probably resulted from the low surface tension of the primer on the materials used to plug the hole. Samples prepared using a polished scotch tape disc to cover the hole, followed by coating application, fractured at the edge of the tape. Regarding the approach of creating a hole in a pre-coated sample, electrical discharge machining was found to be uncontrollable. In some cases the hole did not reach the interface between coating and metal, and in other situations the coating was perforated. Nano-milling machining led to the formation of flaws at the edge of the hole and primer fracture at the edge of the blister. The combination of milling and electrodissolution, described presently, was found to give the best results.

A schematic of the sample preparation steps is shown in Figure 4.3. A hole was milled in the center of one side of the substrate to a depth of about 0.9 mm (leaving about 0.4 mm in thickness under the hole). The other side of the substrate was then prepared for coating. Some samples were abraded randomly or in an aligned matter using silicon carbide papers grit or of 180, 600, or 1200 grit, depending on the scope of the specific experiment. A MultiPrep[TM] System with DP-

Lubricant Blue (Struers) was used for abrasion. Samples were ultrasonically cleaned using acetone for 1 minute.

Samples were treated and coated by NAVAIR in Patuxent River, MD. Turco 4215 NC-LT and Turco Smut Go NC (Henkel Corp.) were used as cleaner and deoxidizer, respectively. Different conversion coatings (CCs) were used in this investigation, including Alodine 5700, NCP (Ti based non-chromium CC, Henkel Corp.), SurTec 650, TCP (trivalent chromium CC, SurTec), and Alodine 1200S, CCC (chromate CC, Henkel Corp.). The immersion times and temperatures are shown in Table 4.1. After the samples are treated, coating application takes place after 24 h to allow the CC layer to stabilize and dehydrate.
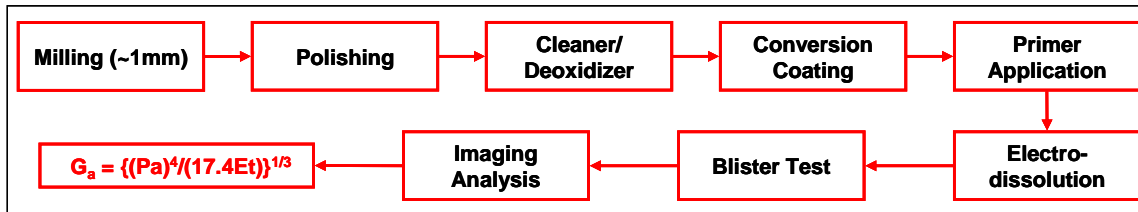
Figure 4.3. Schematic of sample preparation procedure for the BT and GBT.

Table 4.1. Immersion times and temperatures.

Commercial Solution	Immersion Time (minutes)	Temperature (°C)
Turco 4215 NC-LT	5	48.89 (120 F)
Turco Smut Go NC	1	24.44 (76 F)
Alodine 5700	5	23.89 (75 F)
SurTec 650	5	24.44
Alodine T5900	3	23.89

Several coatings were used for this research: 15 wt% PVB, Blank Primer PD381-94, acetoacetate primer Aviox® CF 37619, and epoxy primer Aviox® CF 37124 (all from Akzo Nobel Corp.). The acetoacetate primer is a ketac system (ketimine/acetoacetate) designed for aerospace applications. After the sample was cured (7-14 days in air) the bottom of the milled hole was dissolved to create a through-hole using an electrodissolution process. A potential of 2.125 V vs SCE was applied to the AA2024-T3 sample in 0.5 M NaCl solution. The sample was masked by first placing a sticker of 3 mm in diameter inside the hole. The hole perimeter was highlighted using a marker and the sticker was then removed. The area outside the drawn hole was then masked with red lacquer carefully using a very fine brush. A stainless steel rod coated on the side but with a bare tip was used as a counter electrode. The counter electrode was positioned very close to the area to be electrodissolved without touching it. Short electrodissolution steps were performed with rotation of the flat cell between steps to ensure a more rounded hole. The first step was approximately 70 s and the following steps were 5-30 s. Once the through hole was achieved, the size was measured between every step using an optical microscope until a diameter of 3 mm was achieved.

5.4.3.4 Fastener/Plate galvanic samples and measurements

The galvanic samples were designed and prepared by NAVAIR. AA2024-T3 sheets (15 x 10 x 0.7 cm) were used for the experiments. Eight holes were drilled in each sample. Then the sample was wiped with acetone, cleaned using Turco 4215 NC and Turco Smut Go, and treated with SurTec 650. After 24 hours, the acetoacetate primer mentioned above was applied using a spray gun. Half of the samples were top coated. After the coating system was cured, scribes were made in the bottom row of holes. Different types of fasteners were tightened to the AA2024-T3 sheet using nuts in the back side. Two types of samples were made depending on the type of fasteners attached. Type A contained Ti 6-4 and SS316 fasteners, while Type B had AA2024-T3 and no fasteners.

The galvanic samples were exposed to ASTM B117 for 567 hours. Potential measurements were performed across the scribes using a Scanning Kelvin Probe (SKP) at different exposure times. The line scans were performed above and below the scribed fasteners at 0.9 and 1.2 cm away from the center of the fasteners. The SKP tip, a SS304 wire with a diameter of approximately 189 μm, was calibrated prior to every measurement using a Cu/CuSO$_4$ system. The RH inside the SKP chamber was controlled at 98 % by purging air saturated with DI water through the chamber. After each SKP measurement of the galvanic samples and at the end of exposure in the salt fog chamber, pictures were taken to determine the extent of attack in the samples depending on fastener type and presence of exposed underlying metal. In addition, the volume material lost due to corrosion was determined using the optical profilometer.

Electrochemical experiments on the galvanic samples were performed at room temperature using a Gamry Reference 600 with Framework^{TM} software and a Saturated Calomel Electrode, SCE, as reference electrode. The Open Circuit Potentials (OCPs) of the different fasteners were measured before exposure. Cathodic polarization experiments were carried out on fasteners at a potential scan rate of 0.167 mV/s. The cell was a plastic tube glued to the coated sample using silicone sealant and the electrolyte was 5 wt % NaCl, which is what is used in the ASTM B117 chamber.

5.4.3.5 Other Adhesion Tests

The pull-off tests were performed following the ASTM D4541-09 Standard Test Method for Pull-Off Strength of Coatings Using Portable Adhesion Tester. The adhesion tester used was a PosiTest$^®$ AT (DeFelsko Corporation). The dolly diameter was 20 mm. The dollies were abraded with Scotch Brite^{TM} sponge. Ten passes were made rotating the dollies 90° after each pass. Then the dollies were wiped clean using acetone. A similar cleaning procedure was performed on the coated samples but without spraying acetone directly into the coated sample to avoid swelling of the coating. The dolly was glued to the coated sample using an epoxy. A thin layer of the epoxy was applied to the base of the dolly from the inside out, avoiding bubble entrapment inside the epoxy. Then the dolly is placed on top of the coated sample and slightly pushed from the center to the periphery until epoxy was pushed out from the interface. This step helps to prevent entrapped bubbles in the joint and ensures a complete layer of epoxy in the interface between dolly and primer. Then a clear tape was used to hold the dolly in place by taping the dolly to the table. After the epoxy cured, the extra epoxy and coating system next to the dolly was removed using a cutting tool to avoid incorporating the fracture energy of both materials to the measurement. Finally, the actuator was placed on the dolly, making sure that the actuator had a

good grip on the dolly, the equipment was zeroed and the hydraulic pump was activated by pumping the level. The pull rate must be kept at approximately 100 psi/s. Then, the measurement was recorded and pictures were taken from the failure surfaces for analysis.

The tape test was performed following the ASTM D3359-09 Standard Test Method for Measuring Adhesion by Tape Test. Samples were exposed to DI water at 60°C for four days before performing the test. After exposure, the samples were dried with a Kimwipe and the ASTM D3359 guidelines were followed to perform the test. Six incisions ¾ inch long were created in a parallel manner having 2 mm of separation between each incision. Then six more incisions were created with the same characteristics, but perpendicular and centered to the first ones. Then the debris was cleaned with a dry Kimwipe and 3M 250 tape was placed on top of the incisions. A roller with a weight of 4 ½ pound was rolled above the tape ten times to press the tape against the sample. Finally, the tape was manually removed at 180° direction in one motion. The surface was photographed for each sample and the delaminated area was calculated using the Clemex Vision software. The samples were classified following the standard classification in terms of delaminated area percent.

5.4.3.6 Other measurements

The Young's modulus is a parameter needed to calculate the adhesion strength of primers to the substrate. This parameter was determined from tensile tests performed on at least four samples of the specific primer. The samples were prepared by mixing the components of the coating in the appropriate ratio followed by pouring it in a Teflon mold that has a groove of 50 x 25 x 0.25 mm. After it was cured, the sample was removed carefully using a blade and tweezers. Then an aluminum template 2 mm thick with a 20 mm gauge length was used to give a dog bone shape to the primers. The samples were placed between the two templates and it is kept in place using two 3 mm dermal punches (Acuderm Inc.). The punches are introduced carefully to avoid primer stretching. Surgical blades (Bard-Parker No. 15) were used to cut shape using a single cut to avoid defects that could create stress concentration. Before performing the tensile test, the thickness of the primer was measured. The primer was placed between two glass slides of known thickness and the thickness was measured using a digital micrometer. The tensile test was performed using a load cell (TestResources, Model 1000R12) and a force transducer with a capacity of 50 lbf (TestResources, model SM-50-294) at a strain rate of 0.1667 inch/s, as recommended by the ASTM D882-10 standard test method for tensile properties of thin plastic sheeting.

A Veeco Contour GT-K optical profilometer and the metrology application Visio64[TM] v5.30 (Bruker) were used to assess the average roughness and real surface area (including roughness) of the different substrates after abrasion. Four measurements were taken using a 5X objective and a 1.0 multiplier, resulting in a field of view with dimensions 0.96 x 1.28 mm^2. The images were adjusted by using the terms removal option in the software, specifically the tilt only mode to produce a plane fit and avoid any calculation error due to an inherent tilt.

Thickness measurements were performed using the Elcometer® 456 Basic ferrous and non-ferrous coating thickness gage.

5.4.4 Results and Discussion.

5.4.4.1 Effect of coating thickness on stress at fracture of blank primer.

Blistering is unfortunately a common phenomenon in coated samples. Most of the primers used in aerospace application are solvent-based epoxy primers, which are characterized by having low elongation and high stiffness and therefore they are brittle. The purpose of primer application is to create a pigmented slightly permeable barrier that adheres to the substrate. The pigments are present for corrosion inhibition and therefore the primer needs to be slightly permeable for the pigment to solubilize and inhibit corrosion of the substrate. However, blisters can be created due to an internal pressure, which can be driven by osmotic blistering. A blister in a coated sample can be assumed to be a spherical cap. If the pressure inside the blister increases, the stress can reach the fracture stress and produce at least a microdefect, which will expose the substrate to the corrosive environment. Therefore, the stress at fracture is an important mechanical property of the primer that needs to be studied and no other test offers a better simulation of a blister than the BT.

Samples were coated with blank primer for this specific study. The substrate was cleaned and deoxidized 24 hours prior to primer application. Coated samples of different thicknesses were prepared by applying several layers of primer. Figure 4.4 shows representative behavior of the coated samples during the BT. The primer fractured for all of these samples. From the Griffith's failure criterion, a crack will propagate if the strain energy release rate is equal or larger than a critical value. In this specific case, the crack is defined as the location where de-adhesion of the organic coating from the substrate occurred. Therefore, it is expected that the pressure x radius product, pxr, would reach a critical value that would be kept constant if the energy is continually supplied to the system. When that critical value is reached and maintained, the crack propagates. This critical value should be achieved at the highest pressure. However, the product Pxr increased during the test without reaching a plateau and the radius started increasing after 10,700 seconds, before reaching the maximum pressure. This onset of blister growth before the maximum pressure has been found by other authors. Gent [3], Kappes [4], and Wang [5] found it in pressure-sensitive tapes adhered to PMMA and Teflon, carbon steel, and PMMA respectively. This behavior has been related to the visco-elastic properties of the adherent layer. The criterion that will be used to determine adhesion strength will be to take the maximum pxr value. Nevertheless, there is not enough data to make these calculations due to the primer fracture. The pressure and radius at rupture were used to calculate the stress at fracture, which is calculated using the following equation [2],

$$\sigma = \frac{pa}{2t} \qquad \text{(Eq. 4.2)}$$

where σ is the stress in the blister, p is the pressure inside the blister, a is the radius of the sphere, and t is the primer thickness. The sphere radius can be calculated from the radius of the blister area on the substrate, r, and the blister height h:

$$a = \frac{\left(r^2 + h^2\right)}{2h} \qquad \text{(Eq. 4.3)}$$

The height can be calculated taking into account the spherical cap volume V_{SC}, the infusion rate, and time until failure as follows,

$$V_{SC} = \frac{\pi h}{6}\left(3r^2 + h^2\right) \qquad\qquad \text{(Eq. 4.4)}$$

$$V_{SC} = 0.050 mL/h \times t(h) \times \frac{1cm^3}{1mL} \times \frac{1m^3}{1\times10^6 cm^3}$$

The effect of coating thickness on pressure and stress at fracture are shown in Figure 4.5. The results elucidate the positive effect of coating thickness on the pressure at fracture. The pressure increases strongly with the coating thickness. However, the stress at fracture shows to be independent on coating thickness.

(a)   (b)
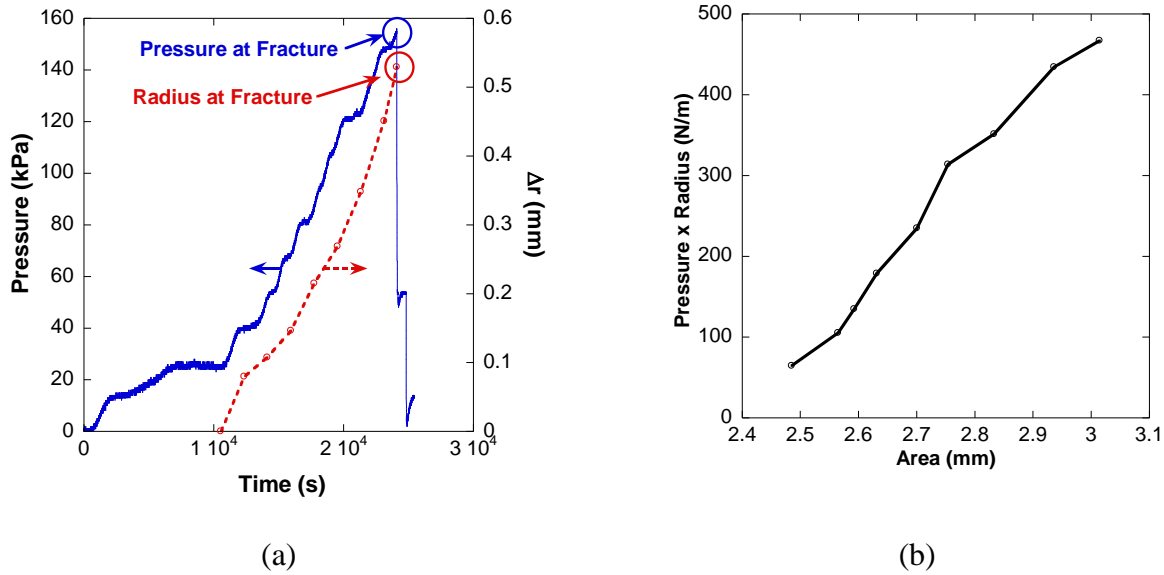
Figure 4.4. Blister Test data representative of samples coated with blank epoxy. (a) pressure and radius difference versus time and (b) pressure x radius product versus area.

5.4.4.2 Effect of substrate roughness and topography distribution on adhesion strength

5.4.4.2.1 Random Abrasion

AA2024-T3 samples having different roughness and topography distribution were coated with 15 wt% PVB. Figure 4.6 shows the data gathered for a sample abraded randomly using 600 grit silicon carbide paper. No coating fracture was observed; instead delamination of the PVB from the substrate occurred. The delaminated part of the substrate was observed under the optical microscope and no polymer residue was found. The pressure increased to a maximum and then decreased (Figure 4.6a). The onset of blister growth took place before the maximum pressure and also before the maximum Pxr product was reached (Figure 4.6b). The same behavior was found previously with the blank primer (Section 5.4.4.1) and also by other authors [3-5]. The

175

delamination kinetics, represented by the slope of the curve of radius vs. time, shows that the delamination is faster at the beginning and then slows down, probably due to a lack of driving force since the fluid is pumped at a low rate of 0.050 mL/h. Assuming that the blister behaves as a spherical cap, the height of the blister would tend to increase at the beginning until delamination starts. The increased blister radius results in a decrease in blister height to accommodate the fluid volume. The behavior is exhibited by all the samples.
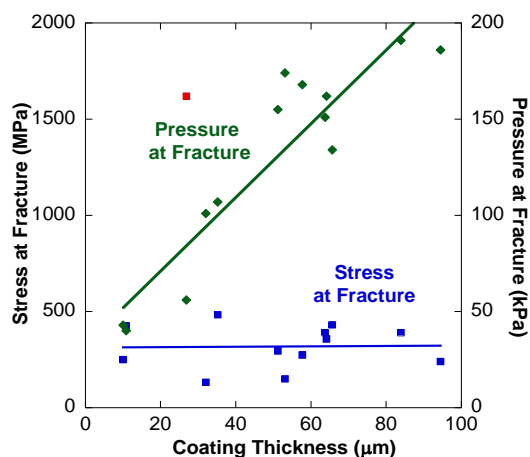
Figure 4.5. Effect of coating thickness on the pressure and stress at fracture of blank primer.

(a)   (b)
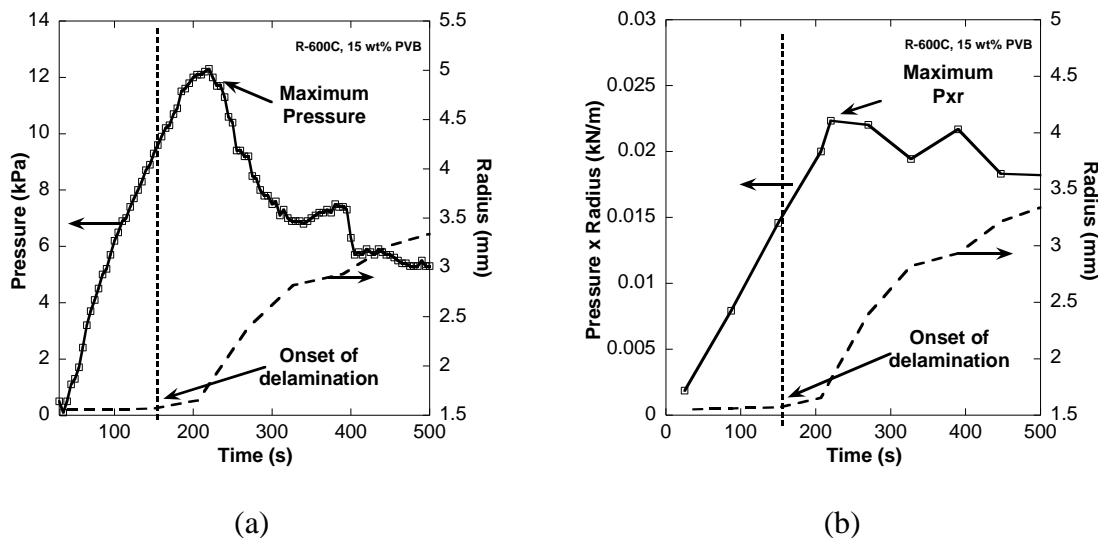
Figure 4.6. Blister Test data of a sample abraded using a 600 grit silicon carbide paper in a random manner and coated with 15 wt% PVB. (a) Pressure and radius difference versus time and (b) Pressure x Radius product versus area.

Figure 4.7 displays the results of the Pxr product for the randomly abraded samples using different grit papers. As explained above in Section 4.4.1, the Pxr value used for the adhesion strength calculations is the maximum one for each test. The product increased and reached a

plateau but then decreases as the radius increased. At this point, the radius increase produced a high reduction in pressure since the infusion rate was constant and low (0.050 mL/h). However, the radius kept increasing as shown in Figure 4.6b. The results of repeated experiments with the same conditions were found to be very reproducible. The effect of different surface roughness is evident and will be discussed below.
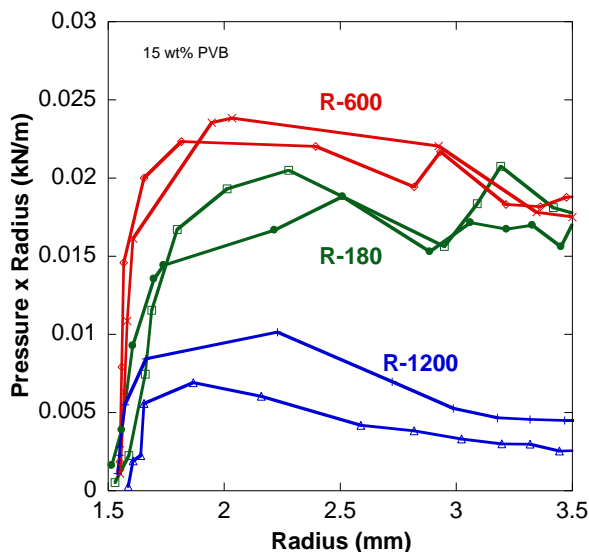
Figure 4.7. Pressure x radius values in terms of radius for samples randomly abraded with different grits and coated with 15 wt% PVB.

The adhesion strength was calculated using Eq. 4.1 and is presented in Table 4.2 along with the measured values of Pxr, coating thickness, and roughness. As expected, the R-180 (random abrasion at 180 grit) samples showed the highest roughness and R-1200 samples showed the lowest roughness. The grit number is inversely proportional to the grit size. The roughness difference between R-180 and R-600 is small, even though the silicon carbide particles are very different in size. As shown in Figure 4.8, the adhesion strength was lowest for the smoothest surface, R-1200. However, the adhesion strength for the R-600 samples was somewhat larger than that for the R-180 samples, even though the R-180 samples were rougher. It is expected that adhesion strength should increase with increasing roughness based on the results of others. It is unknown why the measured adhesion strength was highest for the R-600 sample. However, as shown in Figure 4.8, it is possible that the results for the R-180 and R-600 samples represent scatter and that the roughness and adhesion strengths are not statistically different. More experiments with different roughness values are required.

5.4.4.2.2 Aligned Abrasion

Table 4.3 shows the roughness, coating thickness, measured values of Pxr, and adhesion strength for samples abraded in aligned manner with 180, 600 and 1200 grit paper. The behavior of these samples was similar to that of random abraded samples in that the blister started growing before the maximum pressure was reached. The plot of Pxr product vs. radius is shown in Figure 4.9. In this case, the adhesion strength increased monotonically with roughness, as expected. The roughness values for samples abraded with 600 and 180 grit papers in an aligned fashion were

177

significantly different, unlike what was found for the randomly abraded samples. This probably allowed for the development of a clear relation between roughness and adhesion strength, as shown in Figure 4.10

Table 4.2. Surface roughness, real surface area, coating thickness, product of pressure x radius, and adhesion strength, G_a, of randomly abraded samples tested with the BT. Repeated measurements for each grit are shown.

Samples	Roughness (µm)	Coating Thickness (µm)	Pxr (N/m)	G_a (J/m^2)
R-180	0.353	10.13	18.82	0.89
R-180	0.417	11.88	20.50	0.97
R-600	0.327	11.90	22.33	1.24
R-600	0.306	12.73	23.84	1.14
R-1200	0.036	12.88	10.15	0.27
R-1200	0.026	12.88	6.909	0.18
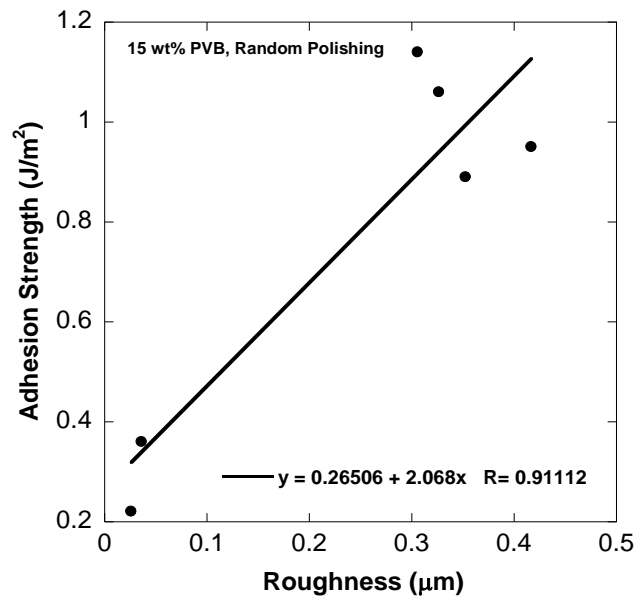
Figure 4.8. Effect on roughness on adhesion strength of PVB to non-cleaned randomly abraded AA2024-T3.
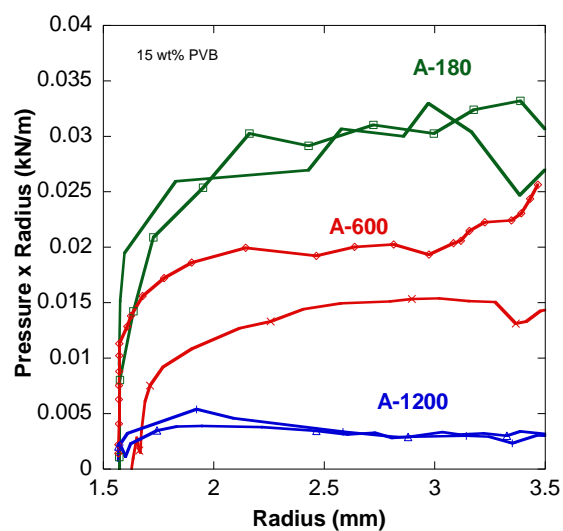
Figure 4.9. Pressure x radius values in terms of radius for samples abraded in an aligned manner with different grits and coated with 15 wt% PVB.

Table 4.3. Surface roughness, real surface area, coating thickness, product of pressure x radius, and adhesion strength, G_a, of aligned abraded samples tested with the BT. Repeated measurements for each grit are shown.

Samples	Roughness (μm)	Coating Thickness (μm)	Pxr (N/m)	G_a (J/m^2)
A-180	1.236	12.5	32.98	1.76
A-180	1.324	13.95	37.85	2.04
A-600	0.551	13.10	25.66	1.24
A-600	0.433	11.1	15.40	0.66
A-1200	0.095	10.13	5.38	0.17
A-1200	0.169	11.23	3.89	0.11
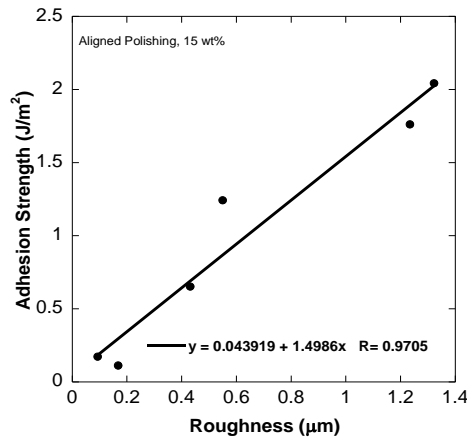
Figure 4.10. Effect on roughness on adhesion strength of PVB to non-cleaned aligned abraded AA2024-T3.

5.4.4.2.3 Comparison between Random and Aligned Abrasion

Abrasion removed the original oxide present on the surface of rolled AA2024-T3 sheets, leaving behind a fresh surface characterized by valleys and peaks. The random abrasion produced a surface with grooves oriented in all directions, while the aligned abrasion oriented the grooves in a unidirectional way (Figure 4.11). These two abrasion methods created samples with different roughness (Figure 4.12), blister shape (Figure 4.13), and adhesion strength (Figures 4.8 and 4.10).
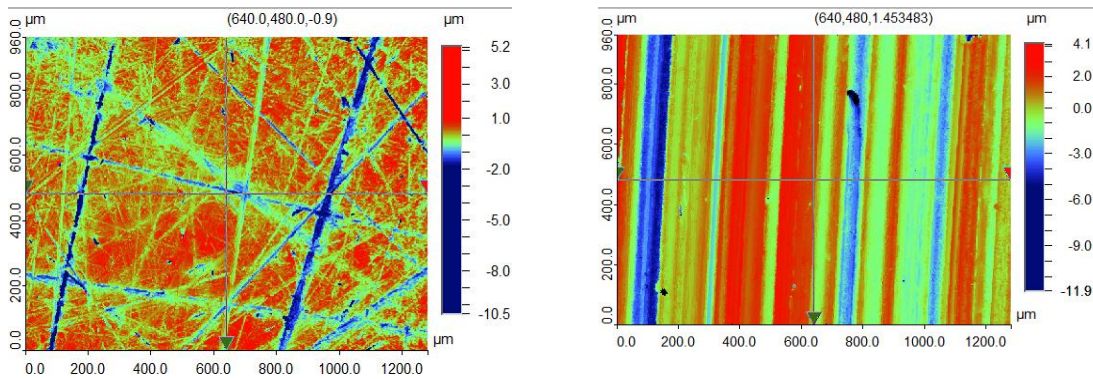
Figure 4.11. Surface morphology for (a) randomly abraded AA2024-T3 and (b) aligned abraded AA2024-T3 using 180 grit.

The surface morphology depended on the abrasion method and grit number. Even though the same grit SiC papers were used for the two different abrasion methods, the average roughness obtained was different, as shown in Figure 4.12. The substrates abraded in an aligned manner had higher average roughness values than the substrates abraded randomly. And the difference increased as the grit number decreased. Random abrasion removes material faster than aligned abrasion because the rotatory motion of the sample results in continual cross abrasion of grooves.

In contrast, the aligned abrasion is accomplished by unidirectional motion of the sample on the SiC paper.
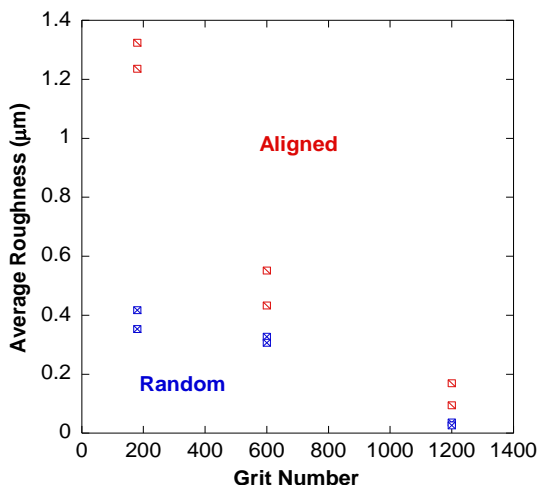
Figure 4.12. Average Roughness of Randomly and aligned abraded AA2024-T3 using different grit numbers.

The abrasion manner also affects the blister shape. Figure 4.13 displays images of blisters for samples prepared by the two different methods and different SiC papers. The blisters grew in the direction of the abrasion features. In the case of samples abraded in an aligned manner, the unidirectional grooves led to faster growth in the abrasion direction and therefore elongated blisters, while the samples abraded in a random manner resulted in rounder and more uniform blisters. The calculation of adhesion strength requires a blister radius. For these elongated blisters, an average radius was determined from the blister area. The groove peaks are barriers for delamination, while the valleys do not offer much resistance. The peeling angle was shown by Gent and Hamed to affect the amount of plastic strain in the primer [6]. Figure 4.14 shows a schematic of the portion of the primer under plastic strain for a peeling angle of 90° and 180°. The highlighted areas represent the portions that are plastically strained in the primer. The primer peeled at 90° experiences less plastic strain than the primer peeled at 180°. These two extreme cases show that the plastic strain increases with the peeling angle.

Delamination in a valley and up the side of a peak in an aligned abraded sample are shown schematically in Figure 4.15. The peeling angle is larger when the blister is growing towards the peaks than when the blister is growing through the valleys. Therefore, when the blister is growing towards the peak, more energy from fluid pressurization is used to plastically deform the larger volume of paint than when the blister is growing through the valleys. Less energy remains to produce delamination up the peaks so the delamination rate is slower up the peaks than along the valleys and the blisters are elongated in shape. Elongated blisters were also observed for aligned abraded samples with the blank epoxy primer.

181
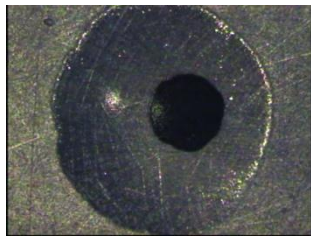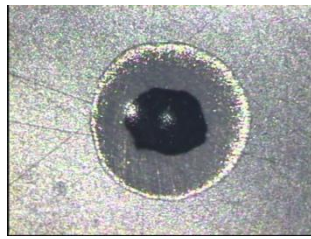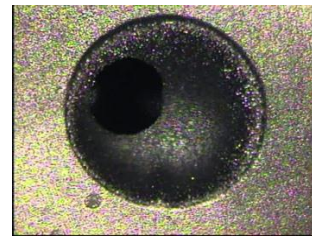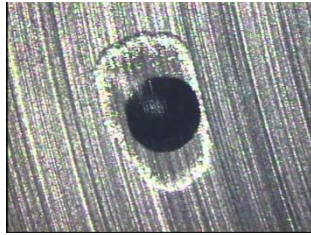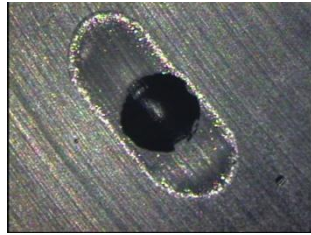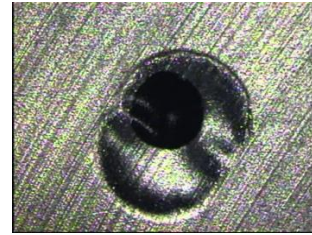
Figure 4.13. Blister shape during the BT for samples (a.1) randomly abraded 180 grit, (a.2) randomly abraded 600 grit, (a.3) randomly abraded 1200 grit, (b.1) aligned abraded 180 grit, (a.2) aligned abraded 600 grit, and (a.3) aligned abraded 1200 grit.
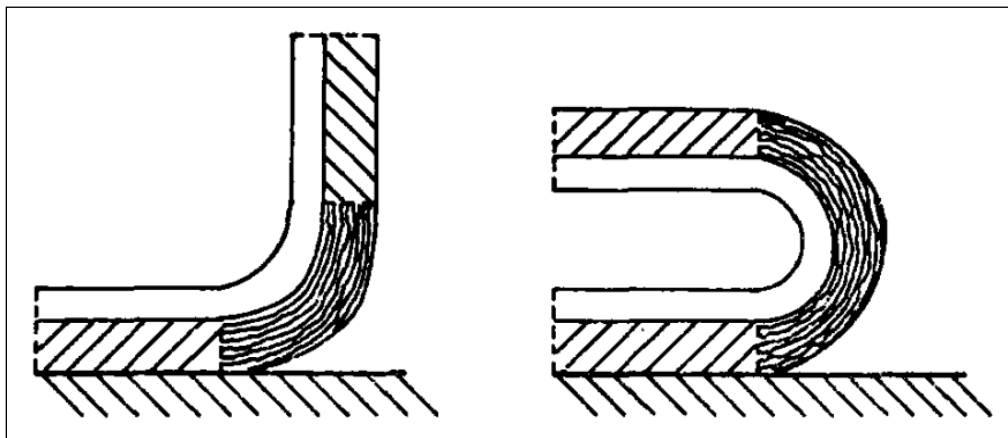
Figure 4.14. Schematics of the dependence of the portion of the primer under plastic strain on the peeling angle [6].

(a)   (b)
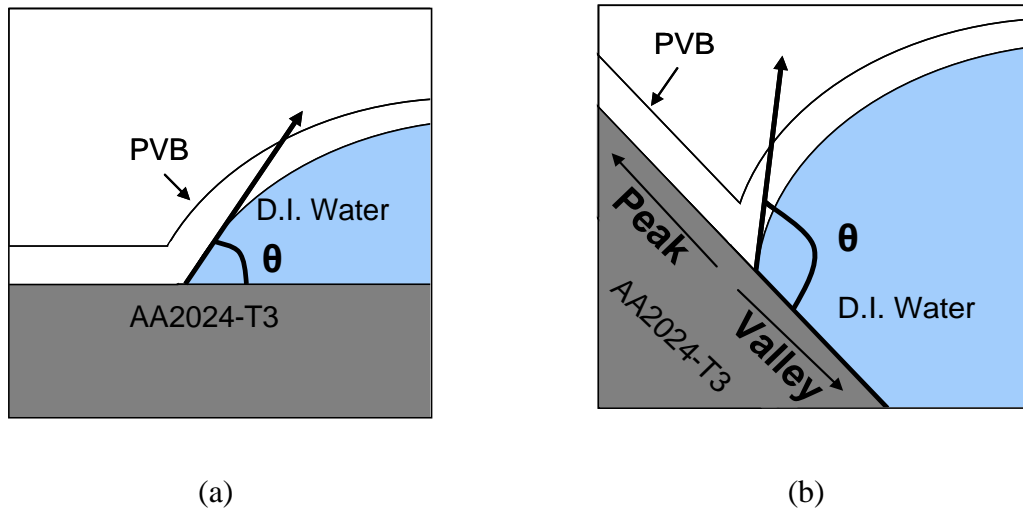
Figure 4.15. Peeling angle of two different scenarios: a) blister growing through the
valleys and b) blister growing towards the peaks.

Figure 4.16 displays the adhesion strength as a function of roughness for samples with aligned
and random abrasion. The randomly abraded samples exhibit the higher adhesion strength at
similar levels of roughness. As shown previously, the valleys are the preferred pathways for
blister growth and the peaks are barriers due to the higher plastic strain experimented by the PVB
under these circumstances.
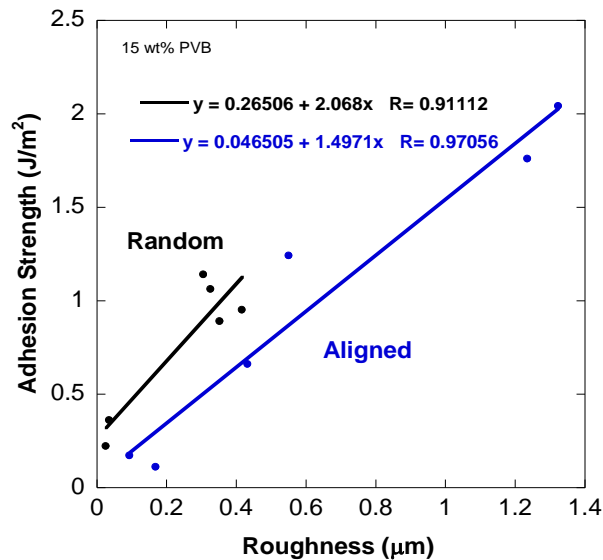
Figure 4.16. Adhesion strength as a function of roughness for randomly and aligned abraded
samples

5.4.4.3 Methods for accelerated adhesion degradation

Different approaches were taken in an attempt to accelerate coating adhesion degradation for the epoxy/AA2024-T3 interface. The first approach was to increase the ionic conduction of the pressurizing fluid to allow electrochemical corrosion to exist. However, the blister growth behavior was found to be the same for blank epoxy coated on randomly abraded substrates at 600 grit when pressurizing with DI water or 0.5 M NaCl solution.

The second approach consisted of constant pressure experiments at 100 kPa with DI water or 0.5 M NaCl solution to allow more time for degradation of the interface to occur. The blister growth behavior was the same with the different pressurizing fluids (Figure 4.17). No more data was gathered after 5000 s for the sample exposed to 0.5 M NaCl because the primer fractured.
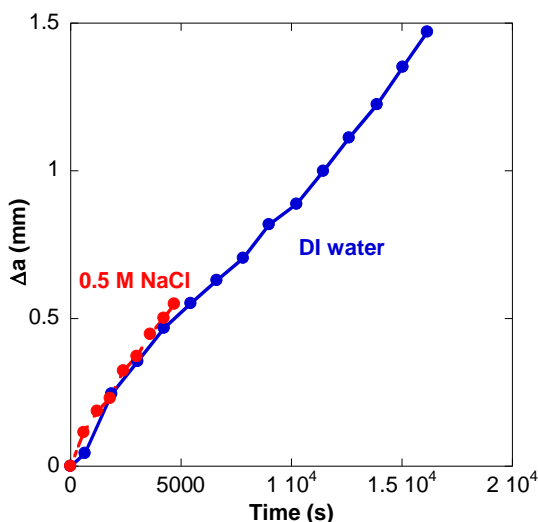
Figure 4.17. Blister growth for as received blank coated AA2024-T3 samples exposed to constant pressure BT using DI water and 0.5 M NaCl as pressurizing fluids.

High pH solutions were also attempted because aluminum is amphoteric so corrodes at high pH and polymers also degrade at high pH. NaOH solution with a pH of 10 or 11 was used at a pressure of 100 kPa on samples that were chemically cleaned and CC treated. No delamination was observed after 7 days. The pH decreased during the test, reaching values of 7.4 and 9.3 for initial pH values of 10 and 11, respectively. The alkaline solution did not accelerate adhesion degradation.

Simultaneous application of electrochemical techniques during the constant pressure BT was also tried. Potentiodynamic BT tests with 5 wt% NaCl were performed to see if there is a critical potential that would define the onset of blister growth. The BT was carried out initially at a constant infusion rate of 0.1 mL/h until the pressure reached the target value of 0.1 bars, which took 900 s, Figure 4.18. After another 600 s, potentiodynamic polarization was started at 0.167 mV/s in the anodic direction from the OCP. When the polarization scan was initiated, the pressure increased abruptly and the syringe pump control program was not able to maintain de pressure in the system. This pressure increase was caused by hydrogen evolution at the WE, which accompanies pitting in Al. Blister growth took place beyond this point. It is not certain if

the electrochemical activity aided the de-adhesion more than just in a mechanical way associated with the pressure increase. Because the controlled could not maintain the pressure during anodic polarization, no further tests with potentiodynamic polarization were performed.
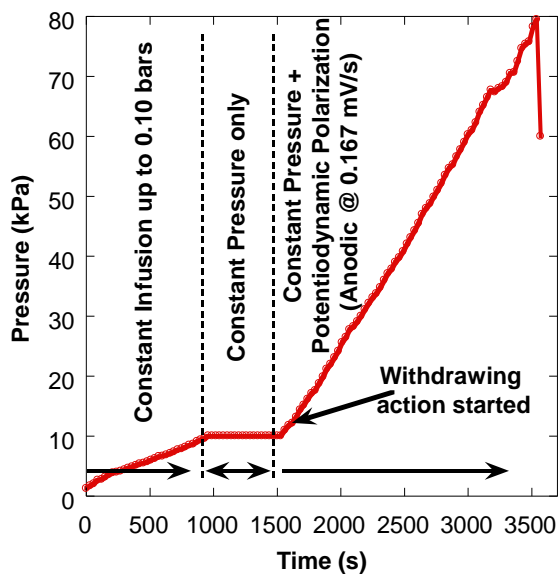
Figure 4.18. Blister growth for as received blank coated AA2024-T3 samples exposed to constant pressure BT using DI water and 0.5 M NaCl as pressurizing fluids.

Another approach for degrading adhesion involved pre-exposure of a sample to ASTM B117 for a month. The surface was cleaned, deoxidized, treated with CCC, and coated with epoxy/amine primer. As will be shown below, this coating system was found to have the best adhesion among the samples coated with this primer. After the salt spray exposure, the BT was performed using DI water at a constant infusion rate of 0.050 mL/h. No decrease in adhesion was found. A more aggressive condition is needed to degrade the interface.

As will be shown below, galvanic coupling greatly accelerated corrosion of coated Al alloy samples during exposure to ASTM B117 conditions. The galvanic BT setup was described above. It couples the Al alloy substrate to a SS316 tube that contains 5 wt% NaCl and creates hydrostatic pressure. However, the galvanic coupling was too aggressive, causing excessive dissolution of the AA2024-T3. A much higher column of 5 wt% NaCl is needed to achieve a high constant pressure and increase the mechanical nature of the exposure. A hydrostatic approach to keep the pressure constant is the best approach because it can allow the hydrogen gas evolved at the working electrode to escape. To create a hydrostatic pressure of 100 kPa (1 bar), a column approximately 10 m tall is needed, which is too unwieldy for laboratory investigations. More detail of galvanic coupling effects is given in the next section.

The last approach tested was based on water uptake by organic coatings during exposure to high temperature water. The details of the approach and the outcomes will be addressed below.

5.4.4.4 Mechanism of Corrosion and Adhesion Degradation during Galvanic Coupling

Matzdorf and Nickerson at NAVAIR found that different coating systems on AA2024-T3 galvanically coupled to uncoated SS and Ti fasteners experienced significant degradation after three weeks exposure to ASTM B117. These results correlated well with long-term beach exposure. The same type samples design with acetoacetate primer was studied using the Scanning Kelvin Probe to investigate the degradation mechanism.

The corrosion evolution in scribed areas during the first 68 hours of exposure in ASTM B117 is displayed in Figure 4.19. Coating degradation near the SS316 fasteners was present after only 1 day of exposure. Degradation near the Ti fastener was evident after 33 hours for the sample with no top coat. For the case of the AA2024-T3 fastener or no fastener, no degradation was observed after only 68 h except for a small area in the sample with an AA2024-T3 fastener and no top coat that appeared after 46 hours. However, this degraded area did not grow so it could have been a defect that was created during sample manipulation. Figure 4.19a shows that the top coated sample with an SS316 fastener had less coating degradation area than the sample without a top coat, even though the pictures where taken at longer exposure time. A noticeable difference between these coating systems is that the sample that was only primed had complete loss of primer in the affected areas, while the primed and top coated samples show blistering without complete removal of the coating system. This is probably due to the better mechanical properties that the top coats normally exhibit.

The coating degradation produced after 567 hours in ASTM B117 is shown in Figure 4.20. The extent of coating degradation was strongly dependent on the fastener material with SS316 > Ti >> AA 2024-T3 ≈ No fastener. The top coated samples had less degradation. The exposure of the underlying metal at a scribe was found to accelerate attack. Type A sample without topcoat showed less attack near the SS316 fastener without scribes compared to the scribed area next to the SS316 fastener.

The underlying AA2024-T3 corrosion is key for understanding the galvanic coupling mechanism. The volume of AA2024-T3 lost during exposure was calculated by optical profilometry after removing the coating, Table 4.4. The AA2024-T3 corrosion strongly depended on the presence of scribed area, fastener, and fastener material. In the case of the scribed areas the ranking in terms of material loss is the following SS316 > Ti 6-4 > AA2024-T3 ≈ no fastener, while for non scribed areas the Ti 6-4 fastener galvanic effect decreased, giving the following trend: SS316 > Ti 6-4 ≈ AA2024-T3 ≈ no fastener. These results correlate with the visual observations. The none-scribed areas have less loss of material than the scribed areas, and again the area surrounding the SS316 fasteners was most affected. For the areas surrounding the Ti and AA2024-T3 fasteners, the loss of material was higher for the top coated samples than for the only primed samples. However, the opposite was observed for SS316. When no galvanic coupling was present, the addition of the top coating to the coating system increased corrosion resistance.
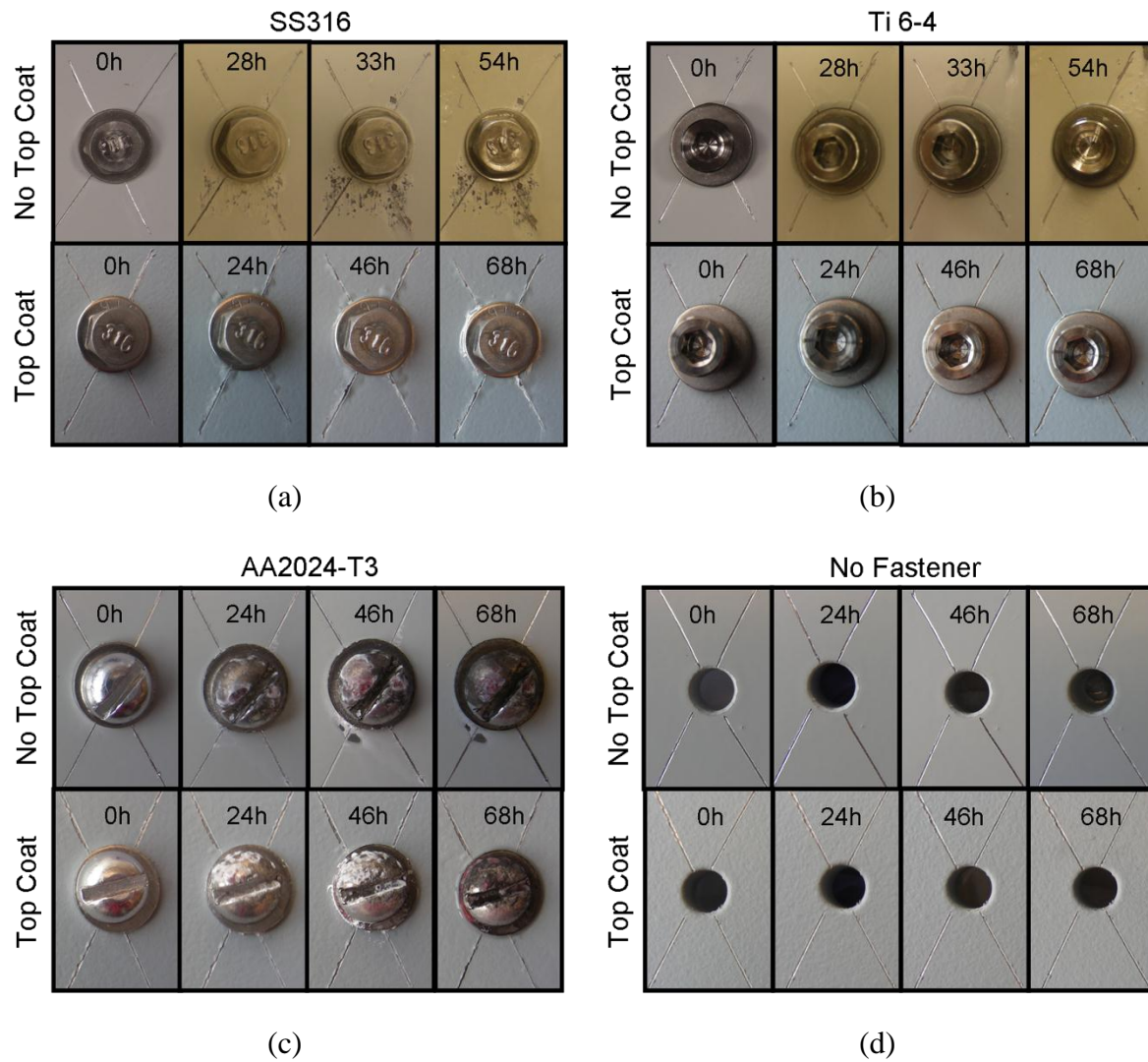
Figure 4.19. Coating degradation evolution in scribed areas during the first 68 hours of ASTM B117 exposure for (a) SS316, (b) Ti 6-4, (c) AA2024-T3, and (d) no fasteners.
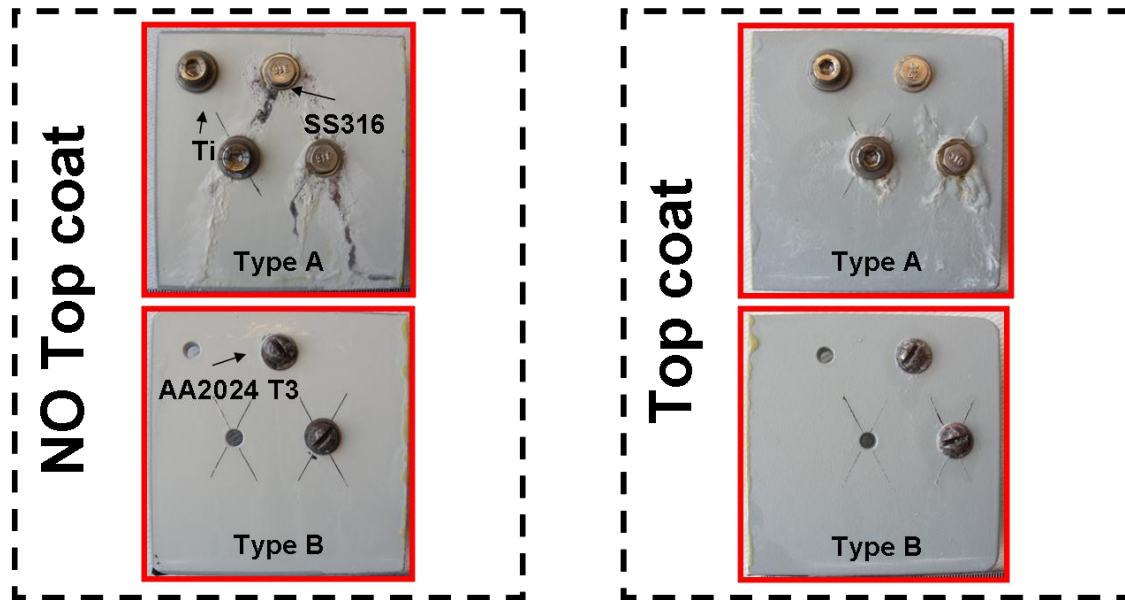
Figure 4.20. Coating degradation after 567 hours in ASTM B117.

Table 4.4. AA2024-T3 volume lost during exposure of coated samples to ASTM B117.

		Type A (mm^3)		Type B (mm^3)	
		Ti 6-4	SS316	AA2024-T3	No fastener
Primer	No Scribe	0.94	13.08	0.71	0.97
	Scribed	7.87	25.80	1.14	1.34
Primer +	No Scribe	1.89	2.78	0.86	0.72
Top Coat	Scribed	8.55	24.34	1.00	0.97

As described in the experimental section, the SKP was used to measure the potential at scribes after varying exposure times in B117. The minimum potential across the scribes generally decreased with exposure time, Figure 4.21. Furthermore, the minimum potential was lower for scribes near the fasteners that caused the worst galvanic corrosion. For non-top-coated samples the potential trend was SS316 < Ti 6-4 < No fastener ≈ AA 2024-T3. These observations are opposite to what would be expected from standard galvanic coupling theory, which states that the potential of the more active material in a galvanic couple should increase. However, no trend was found when a top coat was included in the coating system.
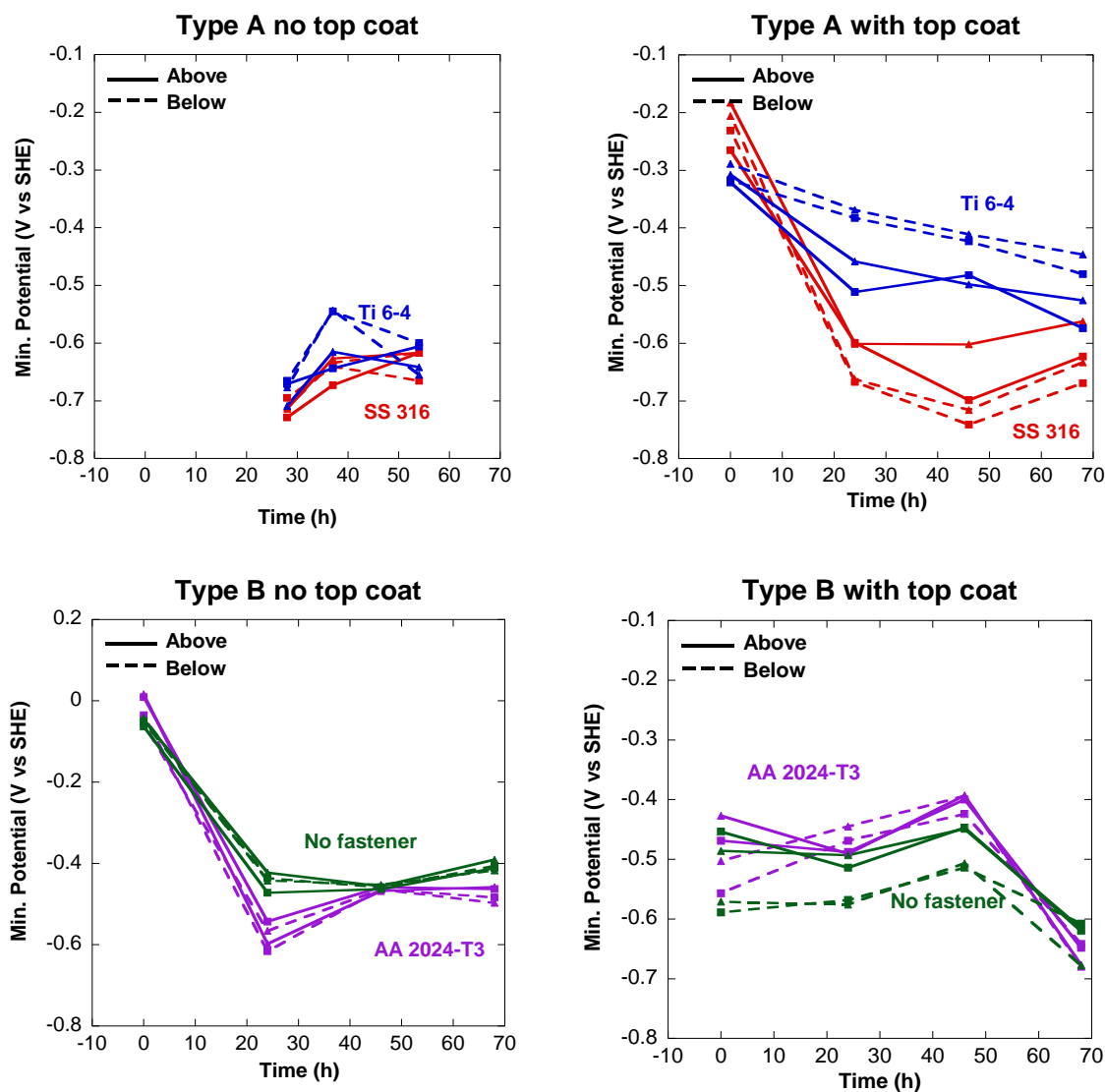
Figure 4.21. Minimum potential across the scribes with exposure time.

Cathodic polarization curves were measured on the various fasteners in 5 wt % NaCl solution. The OCPs were found to be -0.700, -0.572, and -0.488 V vs SCE for the AA2024-T3, SS316, and Ti 6-4 fasteners, respectively. These results indicate, from a thermodynamic point of view, that AA2024-T3 is the most active fastener followed by SS316, with Ti 6-4 being the most noble. Therefore, the highest potential difference existed in the AA2024-T3/Ti 6-4 couple. This means that the thermodynamic driving force for galvanic corrosion is greatest for this couple. However, the data clearly show that the worst galvanic attack was for the AA2024-T3/SS316 couple.

The cathodic polarization curves provided clarifying information, Figure 4.22. Note that the current in these curves is not normalized by area, but is current per fastener to show the amount of current available from each fastener. All of the curves exhibit limiting current density associated with the reduction of dissolved oxygen in this aerated environment. The order of the

cathodic reaction magnitude was the same as the extent of attack seen after exposure in B117: SS316 > Ti > AA2024. The curves for SS316 and Ti cross so that the current at most potentials was larger for SS316 despite having a lower OCP than Ti. The larger cathodic current from SS316 fasteners is the reason why it generated the worst galvanic attack when exposed in close proximity to AA2024 in the scribe during exposure in B117. The larger cathodic current activated the Al alloy surface, causing breakdown of the passive film and the initiation of localized corrosion. Activation of passive metals like Al always results in a decrease in the potential, which is the reason why the potential measured by the SKP was lowest for the case exhibiting the most galvanic interaction. In summary, these experiments show that galvanically accelerated corrosion of Al alloys is controlled by the available cathodic current.
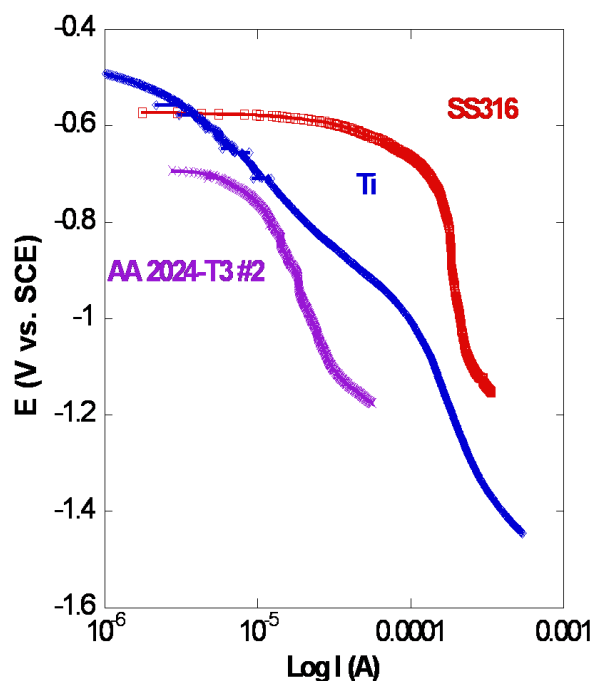
Figure 4.22. Cathodic Polarization of fasteners in 5 wt % NaCl solution.

5.4.4.5 Water Uptake Prior to Constant Infusion Blister Testing

Constant Infusion BTs after immersion in 60°C DI water were carried out with the expectation that water uptake would degrade adhesion and decrease the pressure sustained by the coating system before delamination. However, the opposite was observed as shown in Figure 4.23. The pressure reached after exposure was greater than 350 kPa, which is more than 3 times the highest pressure sustained by the coating system during the constant infusion BT without pre-exposure in hot water. Furthermore, permeation of water through the coating during the test was observed. The blister was able to sustain such high pressures that water was forced through the intrinsic porosity and droplets were observed to form on the outer surface. Some samples delaminated during the BT, but others did not. Furthermore, the samples that delaminated also generated blisters during the hot water exposure. During the BT, these blisters joined with the large artificial blister created by the sample preparation so it was not possible to interpret the data for assessment of adhesion strength. The fact that the coating systems that exhibited blistering after

exposure in hot water also delaminated after exposure during the BT (see Table 4.5) indicates that osmotic blistering is related to the adhesion strength of the coating.

More experiments were performed to investigate what changes allowed the blisters to sustain the high pressure following hot water immersion. The same coating system was pre-exposed to DI water at room temperature or air at 60°C for four days prior to BT. The sample exposed to hot air exhibited the same behavior of pressure vs time as the sample without exposure (brown and green lines in Figure 4.24a). For both cases, the pressure increased to a maximum of about 90 kPa and then decreased as the coating delaminated. The sample exposed to room temperature DI water sustained a higher pressure (>130 kPa), but then the primer fractured. This behavior is similar to the sample pre-exposed to 60°C DI water, except that the fracture occurred at a lower pressure for the room temperature exposed sample. The product Pxr is proportional to adhesion strength according to Eq. 4.1, so the product can be evaluated even though there was little blister growth for the water-exposed samples. The magnitude of Pxr for the various conditions followed this trend: 60°C DI water > RT DI water > 60°C oven ≈ no exposure. In contrast to epoxy primers, curing of the Ketac system used (ketimine/acetoacetate) is enhanced in the presence of moisture because water activates the blocked ketimine to initiate the polymerization process. Therefore, the samples exposed to water, either at room temperature or at 60°C, could have higher crosslink density than the sample exposed in hot air and the sample not exposed. An increase in cross-linking during the water exposure could explain why the water exposed samples sustained higher pressures in the BT whereas the 60°C oven exposure exhibited the same pressure response as the unexposed sample. High temperature increases the water diffusion coefficient [9] and also increases the cross-linking reaction rate.
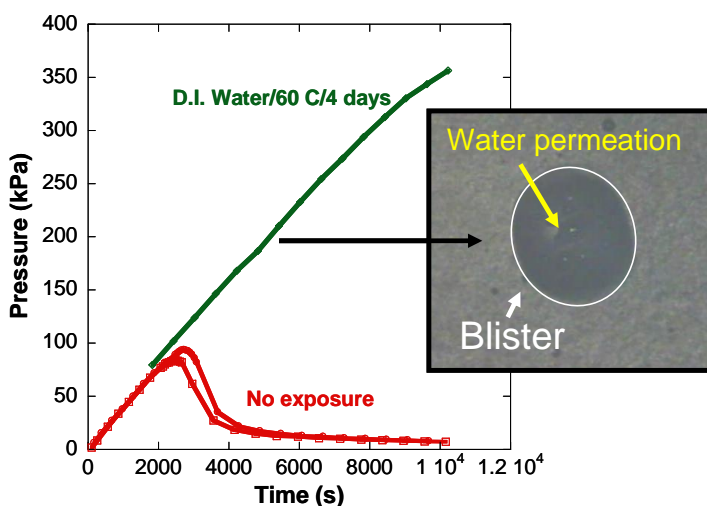
Figure 4.23. Effect of immersion of coated sample in DI water at 60°C on the pressure sustained during the BT.

Table 4.5. Resemblance between the occurrence of osmotic blistering after exposure and the presence of adhesive failure during BT.

Coating Systems	Blistering after exposure?	Adhesive failure during BT after exposure?
A	No	No
B	**Yes**	**Yes**
C	No	No
D	**Very little**	**Very little**
E	No	No
F	**Yes**	**Yes**
G	**Yes**	**Yes**
H	**Yes**	**Yes**

(a)   (b)
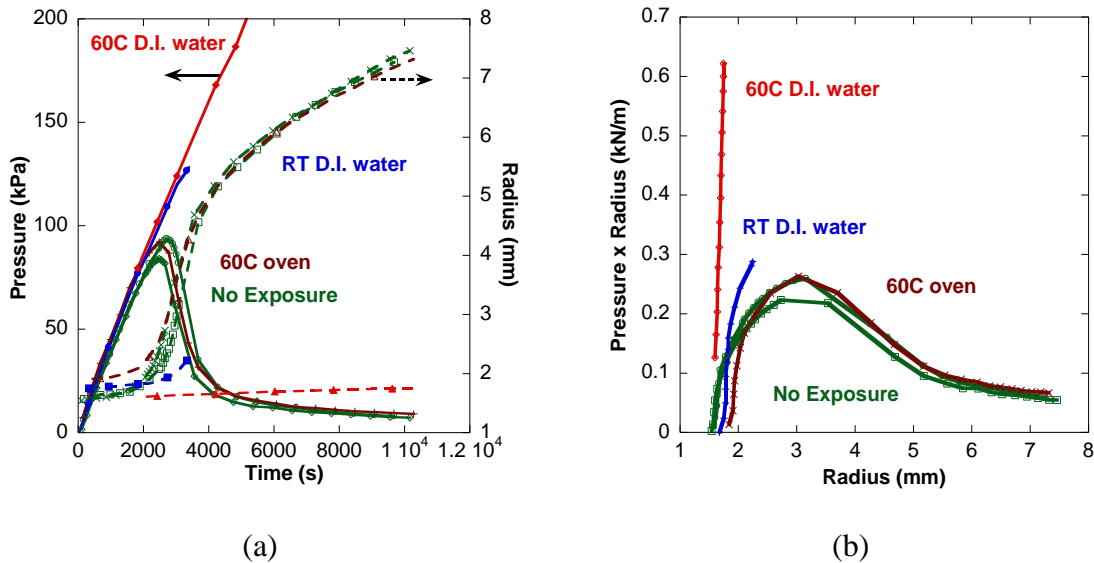
Figure 4.24. Effect of exposure conditions prior to BT on adhesion strength of a sample coated with acetoacetate.

Tensile tests performed on the samples of the Ketac coating after the different exposures indicated differences in mechanical response that correlate with the BT data. The stress-strain curves for the non-exposed primer and the one exposed to the oven at 60°C were essentially straight lines until the point of fracture, Figure 4.25. This is the characteristic response of a brittle polymer. In contrast, the primer films pre-exposed to water, either at RT or 60°C, exhibited two linear regions in the stress-strain curves, where the slope decreased after a critical point. This behavior is characteristic of a bimodal network [7]. The Young's modulus of the water-exposed films were larger than those not exposed to water, probably because of the higher cross-linking described above [8]. The ranking of Young's modulus was: 60°C DI water (624.77 MPa) > RT DI water (114.11 MPa) > 60°C oven (45.86 MPa) ≈ no exposure (37.72 MPa). However, the

slope of the sample exposed to hot DI water changed to a value very close to that of the non-exposed sample. Because the coating fractured before reaching the maximum Pxr value and the large difference in the stiffness of the primers exposed to the different conditions, the effect of pre-exposure temperature and environment on adhesion strength cannot be assessed. However, the results indicate that cross-linking degree is an important factor in the adhesion of coating systems.
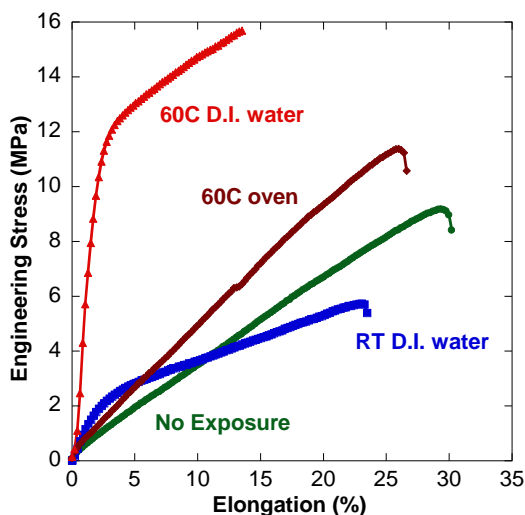
Figure 4.25. Tensile test results for thin primers non-exposed, exposed to room temperature DI water, hot air at 60°C, and DI water at 60°C during four days.

The same behavior was observed for samples that were cleaned, deoxidized, pretreated with NCP, and coated with the pigmented epoxy primer (Figure 4.26). The pressure sustained by the primer increased when the primer was previously exposed to DI water at 60°C for four days. Also, no blister growth was observed. It is not expected that water exposure accelerates the curing of the epoxy primer as it did for the Ketac primer. However, the high temperature could have accelerated curing of the epoxy. Experiments are underway to understand the effect of the pre-exposure to 60°C DI water on the epoxy primer.

5.4.4.6 Comparison between the Blister Test and other adhesion tests

ASTM D4541, the dolly pull-off test is very inefficient for the measurement of adhesion strength. Several glues such as Belzona, Araldite 907, and Super Glue (cyanoacrylate) were used to attach the dollies to the samples. Two curing times, 1 day and 7 days, were allowed before performing the pull-off test. One day is not enough for the Super Glue to fully cure as shown by the presence of liquid in the interface after the test was performed. The failure found in samples neither cleaned nor pretreated was a mixture of adhesive/cohesive failure in all the interfaces with little or no adhesive failure when Belzona or super glue was used (Figure 4.27(a), (b), and (c)). The measurements performed using this standard do not represent the adhesion strength of acetoacetate to AA2024-T3. In contrast, the BT results in adhesive failure. The failure was observed using an optical microscope. The surface was shiny with no presence of organic polymer (Figure 4.27(d)). In addition the results were reproducible.
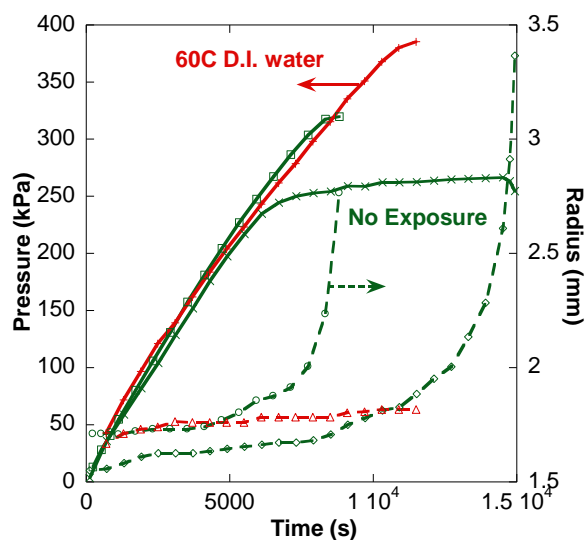
Figure 4.26. Effect of exposure conditions prior to BT on adhesion strength of a sample cleaned, deoxidized, pretreated with NCP and coated with AVIOX CF 37124.
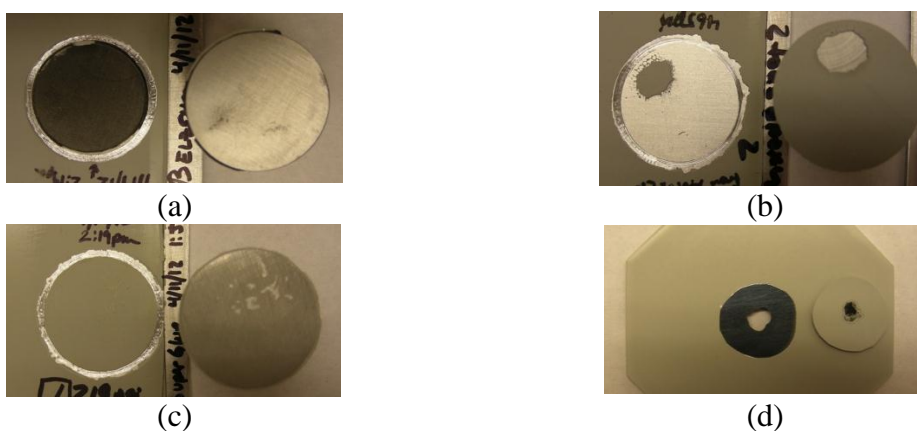
Figure 4.27. Failure morphologies of coated samples after Pull-Off test when (a) Belzona, (b) Araldite 907, and (c) Super glue are used to attach the dolly to the substrate; and after (d) BT.

ASTM D3359 is the cross-hatch tape test. Samples of 7 different coating systems were exposed to DI water at 60°C for four days before performing this test. Details of these coating systems are not given because these samples were contaminated by Si as described below. Any comparison of the different systems is complicated by the contamination. However, a comparison of the results of the BT and the tape test for each system is valid. The tape test samples were classified following the standard classification shown in Figure 4.28 and the results are displayed in Figure 4.29. All of the samples were classified "3B" except for coating system 2 and one of the samples of coating system 6, which were classified as "4B" because the delaminated area percent was below 5. Any differences between the coating systems are not discernable with this technique.

194

The values of delaminated area percent for duplicate tape test experiments are given in Table 4.6. These data are highly scattered. Also given in this table are the values of adhesion strength determined from analysis of BT experiments on the same coating systems. The scatter of the adhesion strength data is significantly less than that of the tape test data. Therefore, the BT is a better technique because it gives a quantitative value of adhesion strength, the measurements are reproducible, and the different coating systems are discernable, while the tape test is qualitative, does not differentiates between coating systems, and is not reproducible.

Figure 4.28. Classification of adhesion test results related to the percent area removed after the test ASTM D3359.
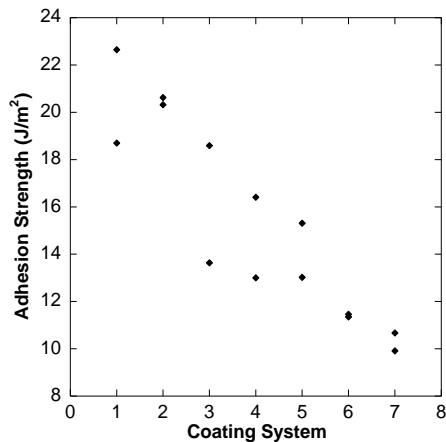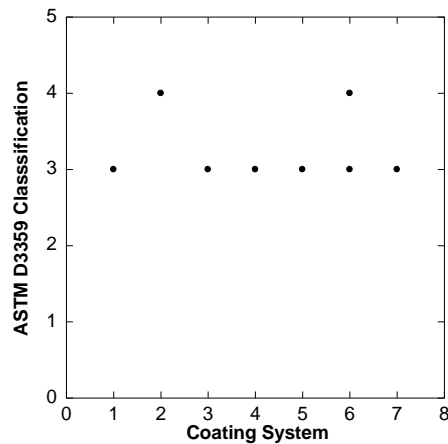
(a)   (b)

Figure 4.29. Comparison between (a) the adhesion strength results obtained from the BT and (b) the classification of adhesion test results from the test ASTM D3359.

Table 4.6. Results of area delaminated for different coating systems from the Tape Test and BT after four days exposure in 60°C DI water.

Coating Systems	Tape Test Delaminated Area (%)	Blister Test Adhesion Strength (J/m^2)
1	8.40	22.65
1	11.27	18.70
2	2.61	20.63
2	1.84	20.32
3	12.32	18.59
3	5.53	13.63
4	13.94	16.41
4	9.98	13.00
5	12.87	15.31
5	4.22	13.03
6	6.79	11.35
6	3.96	11.46
7	11.80	9.91
7	12.48	10.67

5.4.4.5 Effects of Cleaning/Deoxidizing and CC on Adhesion Strength

5.4.4.5.1 Epoxy/AA2024-T3 interface

Samples were abraded randomly using 600 grit SiC paper, ultrasonically cleaned with acetone for 1 minute, and sent to NAVAIR for cleaning, CC treatment, and coating application (details are given in Section 5.4.3.3). Half of the substrates were cleaned/deoxidized and the other half of the substrate matrix was not. This was done to analyze the effect of cleaning/deoxidizing on the adhesion strength of epoxy primer to AA2024-T3. A full factorial matrix of samples with different combinations of treatments was tested using the CIBT. The relative humidity of the air flowing through the chamber was controlled using saturated NaCl solution in washing bottles and measured to be 75% by a sensor in a downstream mini chamber. Results for one sample are shown in Figure 4.30. The behavior shown is representative of the other samples. The pressure increased until the primer fractured. The epoxy primer ruptured after only a small amount of adhesive failure occurred. Blister growth initiation before maximum pressure was observed as shown previously for other primers. Also, the maximum Pxr value was not achieved. However, enough delamination occurred to be able to rank the coating systems by taking into account the pressure at which delamination started (Figure 4.31). This type of plot helps to elucidate the effect of surface treatment on adhesion strength. The pressure increased at a constant radius until blister growth started. The pressure and blister radius then both increased until the pressure remained constant and fracture occurred or the pressure then decreased followed by primer fracture. The maximum pressure will be used as a critical variable to rank the different surface treatments. The sample that was cleaned/deoxidized but not pretreated reached the lowest maximum pressure among the coated samples tested. Therefore, CCs improve adhesion of epoxy to the substrate. The delamination pressure results show that the adhesion strength for cleaned/deoxidized samples followed the trend: No CC < NCP ≈ TCP < CCC, while for non-

cleaned/deoxidized samples, CCC < NCP ≈ TCP. Cleaning and deoxidizing does not seem to have a big impact in the adhesion strength of epoxy to the substrate for samples treated with NCP and TCP. However, the CCC samples exhibit an improvement of approximately 35%.

(a)   (b)
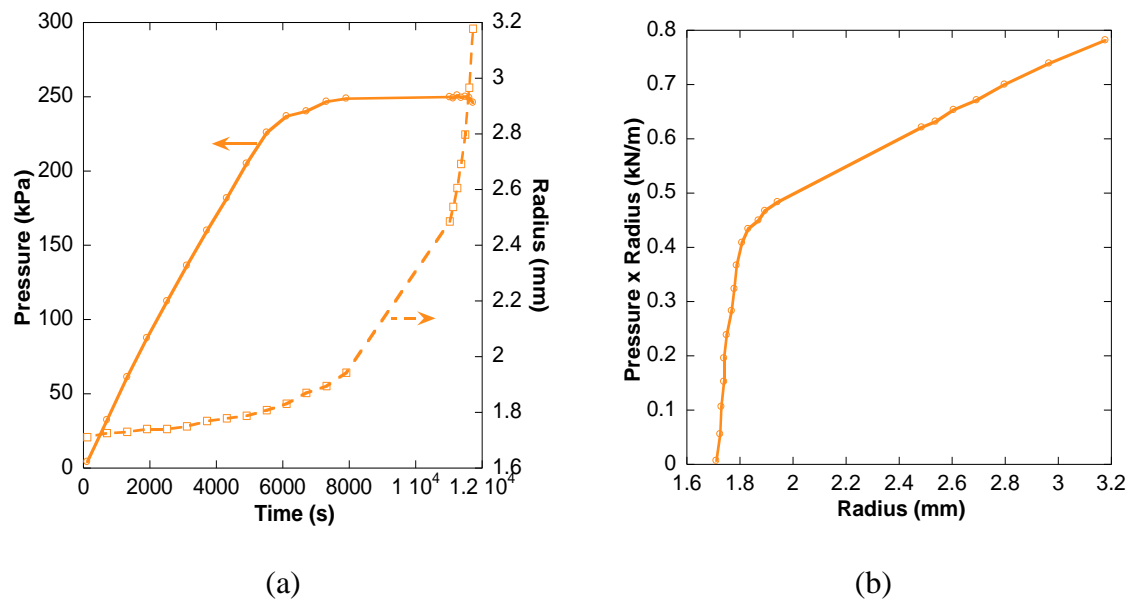
Figure 4.30. BT results related to (a) the behavior of pressure and radius versus time and (b) pressure x radius trend for sample cleaned, deoxidized, treated with CCC and coated with epoxy.
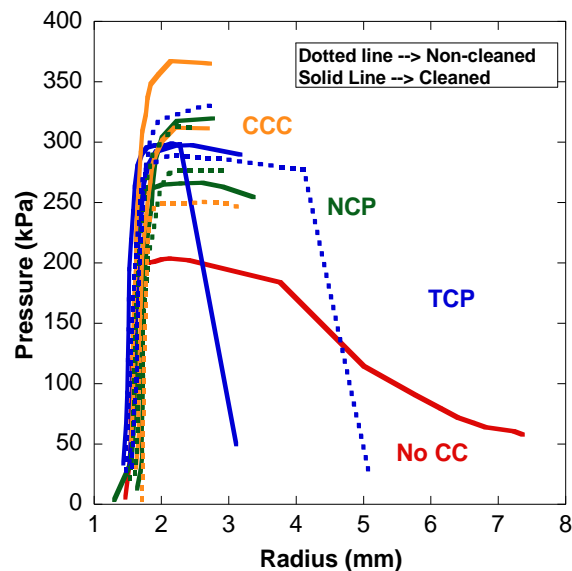
Figure 4.31. Pressure versus radius for full factorial of AA2024-T3 samples coated with epoxy.

5.4.4.5.2 Acetoacetate/AA2024-T3 interface

CIBT experiments were performed on samples prepared by NAVAIR. A full factorial matrix of cleaning/deoxidizing and CC treatments followed by application of acetoacetate was studied. Figure 4.32 shows the pressure and radius versus time and also Pxr product versus radius for a sample that was not cleaned/deoxidized or pretreated. This behavior is representative of the rest of the samples. The same behavior found previously for primers that adhesively failed during BT was exhibited by these samples. Namely, blister growth started before the maximum pressure, a pressure peak was observed, blister growth kinetics were fast at the beginning of adhesive failure followed by a decrease, and Pxr exhibited a peak, Figure 4.33. All samples delaminated without fracturing except for the NCP samples, which fractured after little delamination. The NCP samples that were not cleaned/deoxidized reached the maximum Pxr value before fracturing, but the cleaned/deoxidized samples did not. Pretreatment improved adhesion strength of acetoacetate to non-cleaned/deoxidized samples in the following order: no CC < TCP < CCC < NCP. The cleaning/deoxidizing step improved adhesion for no CC, NCP, and TCP samples, but it deleteriously affected the CCC samples. Adhesion strength for cleaned/deoxidized samples followed: No CC < CCC < TCP < NCP. The adhesion strength values for each coating system are shown on Figure 4.34. The dotted arrows in the samples cleaned/deoxidized and treated with NCP mean that the adhesion strength of that sample is higher than the value shown. The maximum Pxr could not be measured due to primer rupture, as explained previously. The cleaning/deoxidizing step increased adhesion strength of the samples with no CC by a factor of approximately 2. The same trend was found for the TCP sample although the improvement was not as high as for the no CC samples. No effect of cleaning/deoxidizing on NCP samples was observed. However, the samples cleaned/deoxidized and treated with NCP fractured before the adhesion strength could be assessed. Cleaning/deoxidizing decreased the adhesion strength of CCC samples, but, in general, cleaning/deoxidizing and CC were found to improve adhesion.

(a)   (b)
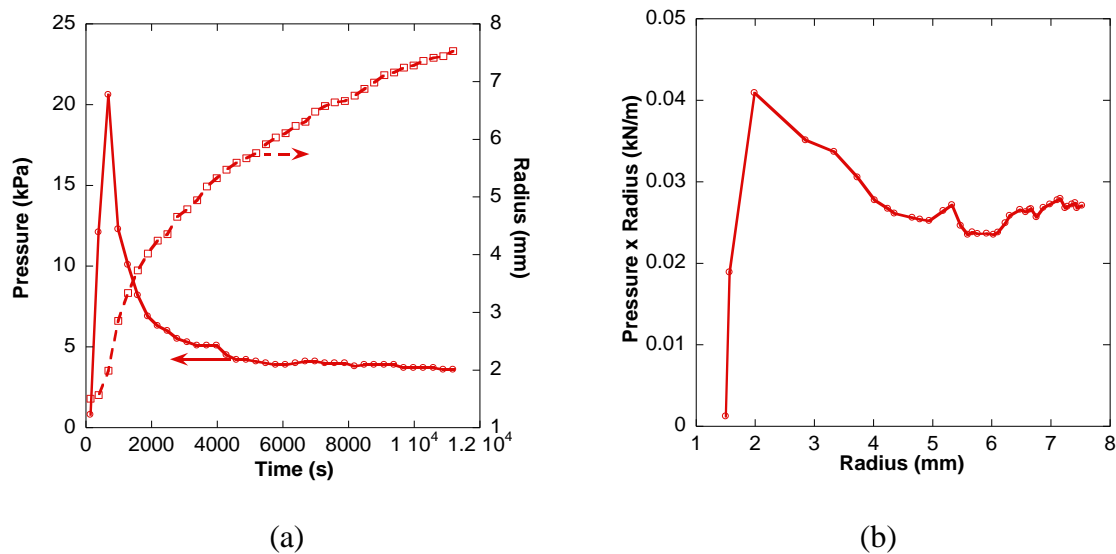
Figure 4.32. BT results related to (a) the behavior of pressure and radius versus time and (b) pressure x radius trend for sample neither cleaned/deoxidized, nor treated, and coated with acetoacetate.
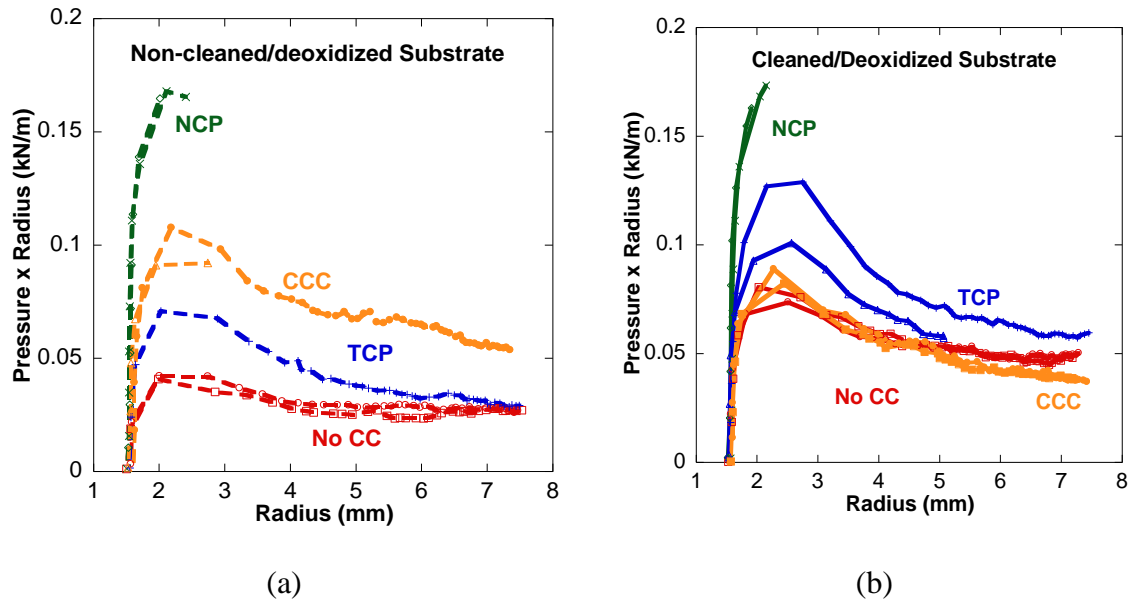
Figure 4.33. Pressure x radius trend for samples (a) non-cleaned/deoxidized and (b) cleaned/deoxidized and coated with acetoacetate.
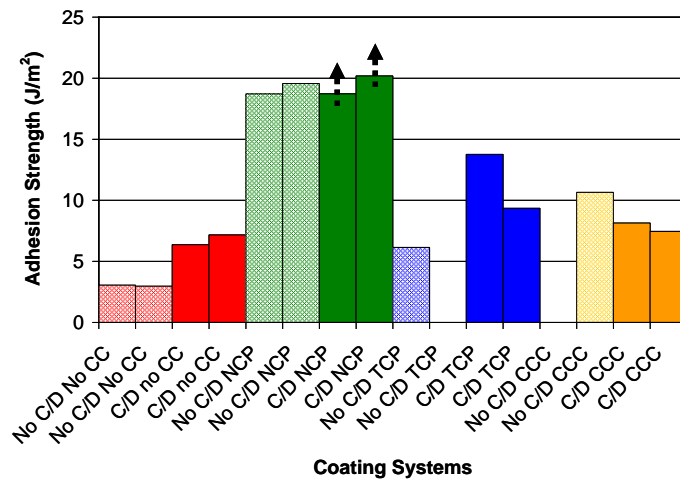
Figure 4.34. Effect of cleaning/deoxidizing and CC on the adhesion strength of acetoacetate to AA2024-T3. C/D means cleaned/deoxidized.

5.4.4.6 Effect of Sample Contamination

280 samples were abraded randomly using 600 grit SiC papers and taken to NAVAIR for treatment and coating application. A full factorial matrix was prepared taking into account cleaning/deoxidizing or no cleaning/deoxidizing and different CC (Section 4.3.3). These samples

were created to study a number of parameters: adhesion after immersion in hot DI water (60°C) using the constant infusion BT; adhesion using standard techniques such as ASTM D 4541 (pull-off test) and ASTM D3359 (tape test); corrosion resistance through ASTM B117, filiform corrosion, and EIS measurements at different times of exposure to 5 wt% NaCl; and surface characteristics of the treated surface prior to primer application using XPS, optical profilometer, and contact angle measurements using DI water. However, the samples were contaminated during the processing at NAVAIR. Figure 4.35 shows the results from the BT. Delaminated area was observed under an optical microscope for all the samples and no primer residue was found. The samples exhibited adhesive failure without fracture. As described above, previous experiments performed using acetoacetate, the same primer used for this batch of samples, showed that cleaning/deoxidizing step improved adhesion for samples non-treated with CC and samples treated with NCP and TCP. However, this was not observed in this batch of samples. The maximum Pxr value decreased for NCP and TCP when the cleaning/deoxidizing step was included in the coating process. In addition, the adhesion strength values were very different from those calculated from the first batch of samples. The maximum Pxr value was measured and used for adhesion strength calculations taking into account the primer thickness and Young's modulus. Table 4.7 displays the adhesion strength values obtained from the old and the new samples. The values for the same coating system were very different. The only two coating system that had similar adhesion strength were those that were neither cleaned nor deoxidized but treated with NCP and the cleaned/deoxidized and treated with TCP. The values of adhesion strength between batches differed by at least 8.79 J/m^2 for the rest of the coating systems. Therefore, the new coating systems obtained must be different from the old ones, even though the same commercial solutions were used in their preparation.
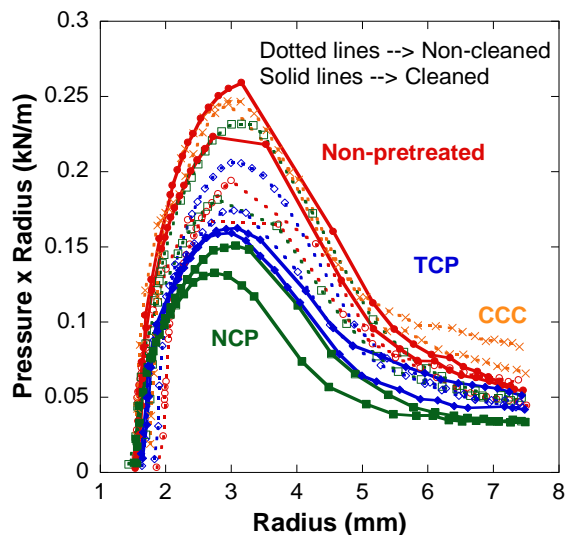
Figure 4.35. Pressure x radius trend for samples (a) non-cleaned/deoxidized and (b) cleaned/deoxidized and coated with AVIOX CF 37619.

Table 4.7. Adhesion Strength values calculated from BT data for old and new samples batch coated with acetoacetate.

Coating Systems	Adhesion Strength (J/m^2)	
	Old Batch	New Batch
No Cl/Deox No CC	15.31	3.05
No Cl/Deox No CC	13.03	2.96
No Cl/Deox NCP	18.59	18.71
No Cl/Deox NCP	13.63	19.56
No Cl/Deox TCP	16.41	6.13
No Cl/Deox TCP	13.00	-
No Cl/Deox CCC	20.63	-
No Cl/Deox CCC	20.31	10.65
Cl/Deox No CC	22.65	6.36
Cl/Deox No CC	18.70	7.16
Cl/Deox NCP	9.91	18.71
Cl/Deox NCP	10.67	20.18
Cl/Deox TCP	11.35	13.76
Cl/Deox TCP	11.45	9.33
Cl/Deox CCC	18.59	18.71
Cl/Deox CCC	13.63	19.56

Samples were immersed in DI water at 60°C prior to performing the tape test (ASTM D4541). Figure 4.36 shows images of the samples following the hot water exposure. All the samples except for the non-cleaned/non-pretreated sample developed blisters. The blisters ranged from less than 0.5 mm to 3 mm in diameter. The blisters in the non-cleaned/deoxidized samples treated with CC were very small (<0.5 mm). The samples treated with NCP had the highest number of blisters. When the cleaning and deoxidizing steps were part of the coating process, the blistering increased, which is opposite of what is expected. Blistering even increased for samples that were cleaned/deoxidized and then coated with primer (no CC) compared to samples that were just coated with no pretreatment at all. The cleaned/deoxidized sample without CC treatment developed dispersed 0.5 mm diameter blisters. The sample that was cleaned/deoxidized/NCP exhibited blisters with diameters from 0.5 to 2 mm. The biggest blisters (2-3 mm in diameter) were found in the cleaned/deoxidized/TCP sample, but the number of blisters was small. There were only 1 to 4 big blisters per sample. The cleaned/deoxidized/CCC sample was similar to the one cleaned without any CC treatment. The order in terms of number of blisters was NCP > TCP > No CC ≈ CCC. These observations, in terms of the deleterious effect of cleaning/deoxidizing step, agree with the adhesion strength results of NCP and TCP samples.

XPS analysis was performed on all of the uncoated samples, and the results of the quantitative analysis of the spectra are given in Table 4.8. The CCC layer was thick as evidenced by the absence of an Al peak. Cu was completely removed by TCP and CCC. Also, the Cr present in the cleaned CCC layer was 31% Cr(VI). This percentage was 35at % when the sample was

cleaned. The samples pretreated with TCP had Cr mainly in the form of $Cr(OH)_3$. Interestingly, Si was present in all the samples. Si 2s peaks were used instead of Si 2p peaks for quantification of the Si concentration, even though Si 2p peaks are larger and are normally used for quantification. Inelastic scattering masked the Si 2p peaks for the sample without any treatment, so the 2s peaks were used for all of the analyses. Figure 4.37(a) shows spectra in the binding energy range of the 2s and 2p peaks. Figures 4.37(b) and (c) show a magnification of the region where the two characteristics peak should appear. Figure 4.37(c) clearly shows the non-asymmetric peak characteristic of inelastic scattering, masking the 2p peak, while Figure 4.37(b) shows the symmetric peak 2s. As mentioned, all samples have Si on the surface, but the sample with the lowest Si concentration is the one without any treatment and the non-cleaned/deoxidized sample treated with NCP. The cleaning/deoxidizing process increases Si content for Non-CC and NCP samples, while it remains approximately constant for TCP and decreases for CCC samples. These results indicate that the surfaces were contaminated by Si and this contamination might be the reason for the blistering and poor performance of the second batch of samples. However, the XPS detection limit of the XPS is known to be $0.1 - 1$ %, which is the range of these measurements. Therefore, even though the analysis indicates Si contamination, the technique sensitivity makes the determination not totally certain. The cleaning solution is silicate-based and B. Nickerson at NAVAIR has indicated that Si contamination degrades coating performance even though this has not been reported in the literature. The effects of a silicate cleaner on TCP were studied in this project and are reported in the Task 1 section of this report. Electrochemical Impedance, Scanning Electron Microscopy/Energy Dispersive Spectroscopy, Transmission Electron Microscopy, and XPS were used to characterize the TCP formation on AA2024-T3 after cleaning a silicate-based or a non-silicate based solution. The characteristics of the treated samples were similar and it was determined that the silicate-based cleaner did not have a major influence on the TCP film. However, primed samples were not investigated, so the effect of Si might be limited to adhesion of the organic coatings.

Detailed analysis of the NAVAIR processes found that the process used for these samples did not follow the standard protocol. In particular, the water rinse step after the cleaning/deoxidizing step was performed at room temperature during the winter season (67 F $\approx$ 19.44°C), instead of using warm water as specified by the cleaner supplier technical process bulletin. The MSDSs of the various baths indicate that the cleaner is the only one containing Si. If the room temperature water rinse, left Si residue on the samples, then it is possible that Si could have been transferred to the tanks containing the CC solutions during sample processing. This could explain why a high Si concentration was found even for the samples that were not cleaned/deoxidized. Another factor is that the primer thickness of the new batch was more than three times that of the old samples. The coating applicator indicated that he had to deposit a thick coating because the paint was not wetting, which is another indication of surface contamination. The difference in thickness for the two batches might indicate that there was a difference in the extent of curing. However, the cleaning/deoxidizing step and adhesion strength ranking should have been the same. In conclusion, all of the information indicates that the second batch of samples was contaminated by Si in the production line and that this contamination degraded the performance of the samples.
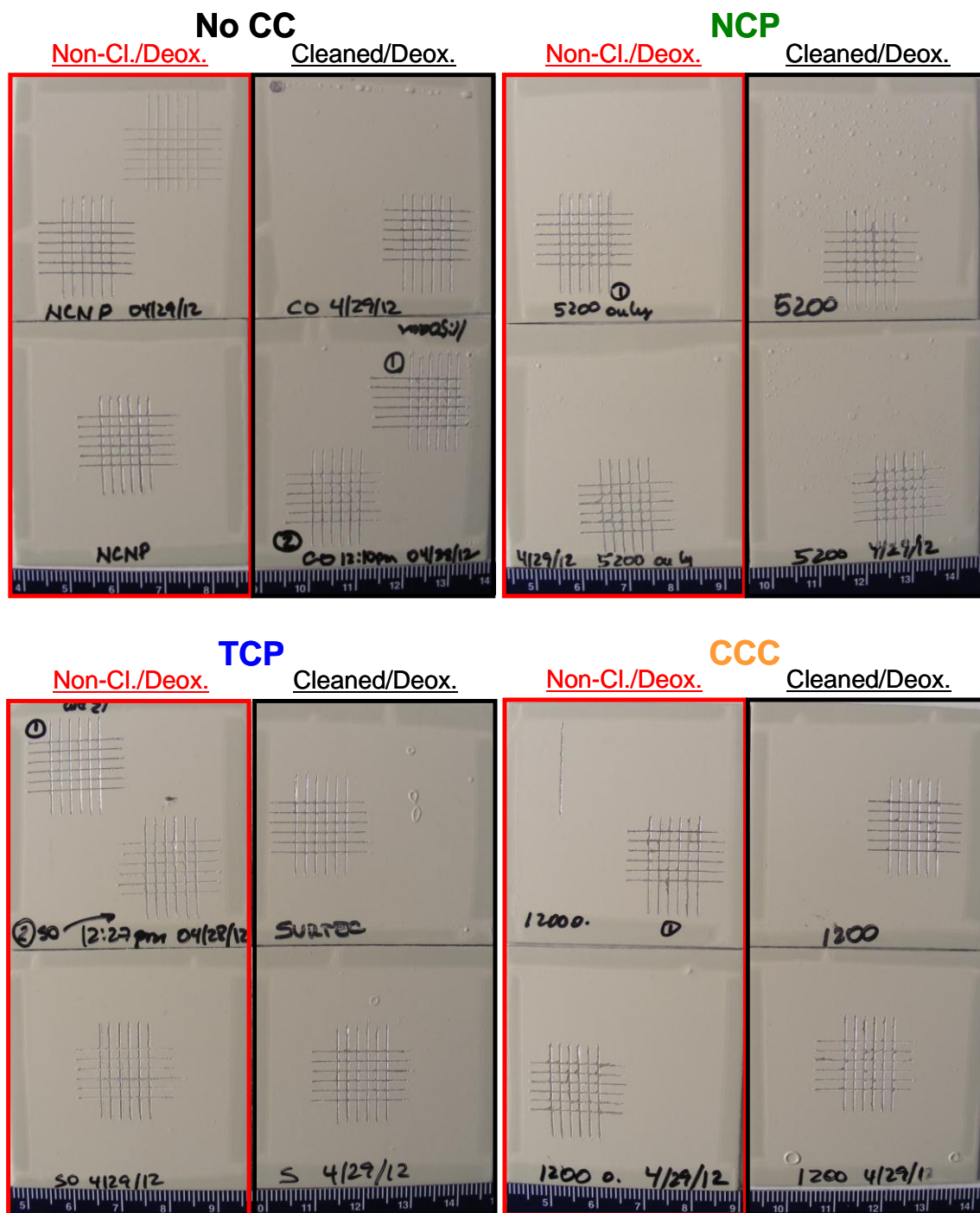
Figure 4.36. Photographs of acetoacetate coated samples after exposure to DI water at 60°C.

Table 4.8. XPS results from different treated AA2024-T3 after 24 hours of treatment step (old batch).

Sample	Atomic Percent (%)										
	F	O	N	C	Fe	Cr	Si	Ti	Cu	Zr	Zn	Al
NC/DNCC	0.00	32.6	0.57	35.6	0.00	0.00	0.34	0.00	0.17	0.00	0.32	30.4
C/DNCC	4.13	33.7	0.59	32.5	0.00	0.00	0.98	0.00	0.24	0.00	0.00	27.6
NC/DNCP	7.61	27.7	1.99	47.2	0.00	0.00	0.34	1.85	0.30	0.16	0.06	12.8
C/DNCP	7.82	25.5	2.28	47.6	0.00	0.00	0.78	1.35	0.82	0.12	0.09	13.7
NC/DTCP	5.91	32.5	1.05	46.6	0.00	2.09	0.71	0.00	0.00	7.51	0.00	3.67
C/DTCP	8.59	36.1	0.55	36.9	0.00	2.73	0.69	0.00	0.00	9.16	0.00	5.19
NC/DCCC	1.87	25.9	12.3	49.4	2.01	7.86	0.66	0.00	0.00	0.00	0.00	0.00
C/DCCC	1.36	25.0	11.9	51.9	1.75	7.59	0.44	0.00	0.00	0.00	0.00	0.00

NC/DNCC: non cleaned/deoxidized, non CC; C/DNCC: cleaned/deoxidized, non CC; NC/DNCP: non cleaned/deoxidized, NCP; C/DNCP: cleaned/deoxidized, TCP; NC/DTCP: non cleaned/deoxidized, TCP; C/DTCP: cleaned/deoxidized, TCP; NC/DCCC: non cleaned/deoxidized, CCC; C/DCCC: cleaned/deoxidized, CCC
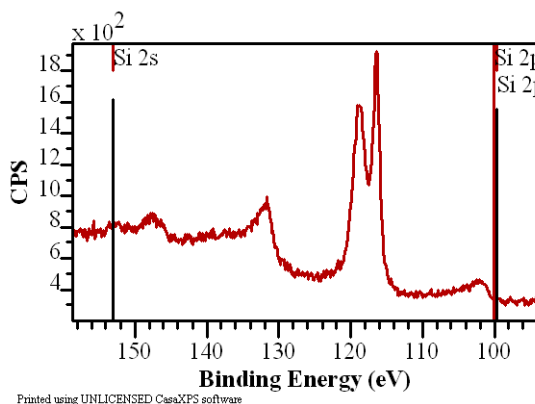
(a)
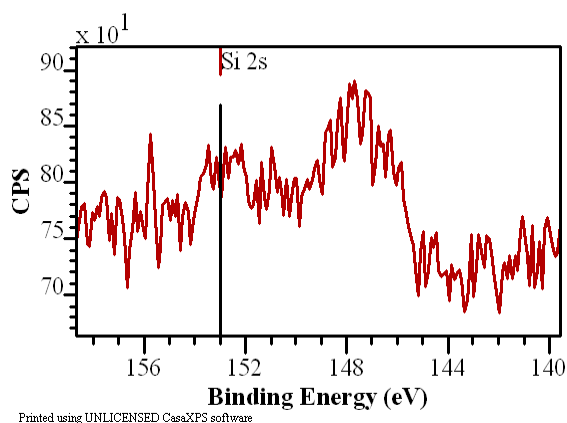
(b)
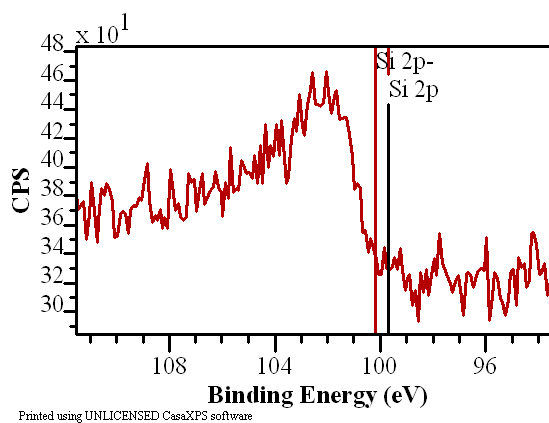
(c)

Figure 4.37. XPS signal measured from a non-treated sample, showing the (a) Si 2s and 2p peaks and a magnification of each one, respectively (b) and (c) (old batch).

5.4.5 Conclusions and Implications for Future Research.

- The blister test (BT) is a very versatile technique that allows calculation of stress at fracture and adhesion strength. The adhesion strength results from the BT are reproducible and help to discern the effects of different surface treatments on adhesion. The best method to prepare samples for the BT is milling followed by electrodissolution.

- Roughness degree and surface topography are very important factors for adhesion strength of PVB to AA2024-T3. Adhesion strength increases with roughness and surface area due to a larger interaction in the primer/substrate interface. Randomly abraded samples have higher adhesion strength than randomly abraded samples.

- Numerous approaches were tested to sample adhesion strength using the BT after adhesion degradation of the interface. However, no adhesion strength degradation was found.

- Galvanic coupling of SS316 fasteners to AA2024-T3 activates the underlying metal due to the high cathodic current on the fastener. The minimum potential along the scribe tends to decrease with increased galvanic coupling owing to activation of the aluminum alloy. This contradicts the typical assumptions of galvanic coupling. The galvanic interaction and coating degradation varies with different fastener materials according to SS316 > Ti 6-4 > AA2024-T3 ≈ No fastener. The material loss also confirms this trend.

- Mechanical properties of primers and effects of exposure are very important for determining adhesion strength performance.

- Regarding other adhesion techniques, the pull-off test does not produce adhesive failure across the entire interface. Therefore, the results do not represent true adhesion strength. The tape test is very qualitative and does not discern between the effects of different coating systems on the adhesion performance. In contrast, the BT produces adhesive failure of the primer studied, is very reproducible and is able to show adhesion strength difference between different coating systems.

- Conversion coating treatment improves the adhesion strength of acetoacetate and epoxy coatings on AA2024-T3. Cleaning and deoxidizing improves adhesion of acetoacetate samples for all conversion coatings except for chromate conversion coatings. For epoxy coatings the addition of the cleaning/deoxidizing step improves the adhesion strength of the chromate conversion coating samples, but no effect is noticeable for titania based coatings and trivalent chromium process coatings.

- Si contamination seems to affect deleteriously the adhesion strength and resistance of coating systems to osmotic blistering.

5.4.6 Literature cited

1. H. Dannenberg, *Measurement of adhesion by a blister method*, Journal of Applied Polymer Science **14** (1961), 125-134.

2. J. A. Hinkley, *A blister test for adhesion of polymer films to SiO₂*, Journal of Adhesion **16** (1983), 115-126.

3. A. N. Gent and L. H. Lewandowski, *Blow-off pressures for adhering layers*, Journal of Applied Polymer Science **33** (1987), 1567-1577.

4. M. Kappes, G.S. Frankel and N. Sridhar, *Adhesion and adhesion degradation of pressure sensitive tape on carbon steel*, Progress in Organic Coatings **69** (2010), 57-62.

5. C. Wang, *Measurements of interfacial strength from the blister test*, Journal of Applied Polymer Science **73** (1999), 1899-1912.

6. A. N. Gent and G. R. Hamed, *Peel mechanics*, Journal of Adhesion **7** (1975), 91-95.

7. L. H. Sperling, "Mechanical behavior of polymers," *Introduction to physical polymer science*, John Wiley & Sons, Inc., New Jersey, 2006.

8. Z. W. J. Wicks, F. N. Jones, S. P. Pappas and D. A. Wicks, *Organic coatings science and technology*, John Wiley & Sons, Inc., New Jersey, 2007.

9. D. A. Porter and K. E. Easterling, *Phase transformations in metals and alloys*, Stanley Thornes Ltd, 2001.

5.5 Task 5: Inhibitor Activation and Transport in the Primer Layer

5.5.1 Objective

The objective of this task is to gain an understanding of the nature of the range of effective anticorrosion pigments available in anticorrosion primers, to elucidate the solubility equilibria of these compounds, and to determine and explain their transport properties in primer films.

5.5.2 Background

A key aspect of the corrosion performance of painted, high strength aluminum alloys is the behavior of the corrosion inhibitor in the paint primer layer. Soluble inhibitive species are typically generated from parent pigment particles dispersed in the primer layer. The solubility equilibria of these species are critical, and are understood to be strongly affected by the polyelectrolyte environment of the primer film. Once solubilized, the inhibitive species must then be transported through and from the primer layer to be available to passivate exposed metal. An understanding of the solubility and transport effects in chromate-free primer systems must also account for the reactive aging of the pigment particles themselves, and the chemical and structural evolution of the primer film and its incorporated filler materials.

5.5.3 Materials and Methods

5.5.3.1 Identification of candidate pigments for study

High performance anticorrosion primers and pigments were identified through surveys of recent literature and interviews with aerospace industry materials engineers. Samples of eight chromate-free inhibitor technologies were obtained, as shown in Table 5.1, for identification of active anticorrosion pigments.

Table 5.1. Chromate-free inhibitor systems characterized.

Chromate-free system	Form obtained			
	Liquid primer	Panel	Post- salt spray panel	Isolated pigment
Cytec BR6700-1 adhesive bond primer		X	X	
DEFT 02GN083 paint primer	X	X		
DEFT 02GN084 paint primer	X	X		
DEFT 44GN098 paint primer	X	X	X	
Hentzen 16708/709 paint primer	X	X	X	
PPG RW-4057-64 paint primer	X	X		
Sherwin Williams cm0481968 paint primer	X	X		
UTC EcoTuff™ Pigment				X

Whenever possible, samples were obtained as a liquid primer, a cured primer applied to 2024-T3 Al, and a cured primer / 2024-T3 test panel exposed to ASTM B117 salt spray testing. Liquid primer samples were sought to allow for elemental identification of inhibitive compounds, and to permit isolation of the pigment for specific compound analysis by x-ray diffraction. The use of

cured primer samples on test panels allows for the identification of the particle size of the constituents in the pigment system. Post-salt spray samples allow for the identification of elements unique to the pigment system that have migrated and deposited in the scribe region.

A protocol for chromate-free inhibitor identification was established, as shown in Figure 5.1. Liquid samples were vacuum dried to enable identification of the elemental constituents by SEM / EDX. A second liquid sample was washed in methanol and filtered to isolate the pigments in a form that enabled dry grinding for compound analysis by x-ray diffraction. When possible, the scribe regions of post salt-spray samples were examined in plan view and cross section to identify unique elements in the primer system that may have migrated and deposited on the actively-corroding surface. Finally, cured free bodies of the primer samples were cast, cured and water-extracted, with the water extract analyzed by FTIR and GC/MS for evidence of organic corrosion inhibitors.
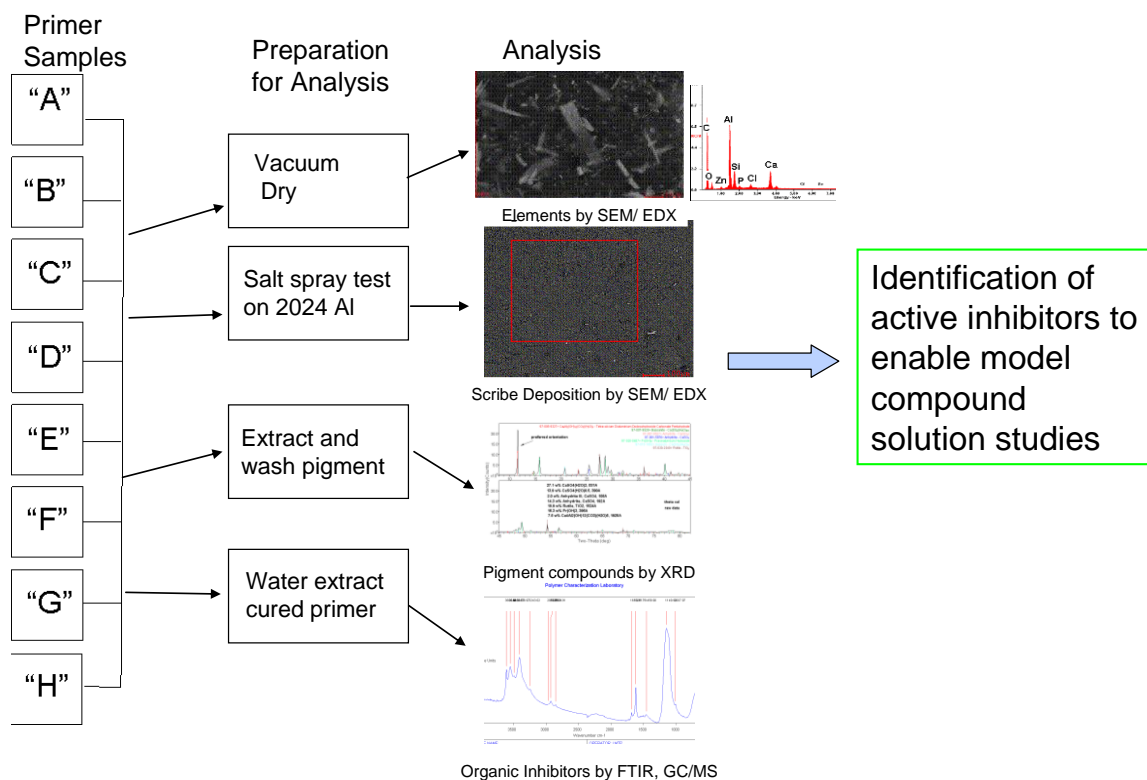
Figure 5.1. Protocol for chromate-free inhibitor identification.

5.5.3.2 Corrosion Inhibitor Solubility Testing

The solution behavior of corrosion inhibitors provides insight into the mode of corrosion inhibition delivered and the response of the inhibitor system to environmental factors, while providing necessary information to assess the transport mechanisms and ageing characteristics of the coating system.

A controlled atmosphere and temperature solubility measurement apparatus was constructed. In this apparatus, excess amount (0.4 gram) of pigment samples are introduced into 50 ml of test

solution for equilibration at controlled temperature, with agitation provided by either air or nitrogen bubbling, and allowed to equilibrate. The tests solutions are HCl, DI water, and NaOH, with and without NaCl additions. A period of 20 h is allowed for equilibration. Solution aliquots are withdrawn from resulting equilibrated slurries by syringe sampling through the gas inlet line. The samples are prepared for analysis by syringe filtering through 20 nanometer media, and stabilized in nitric acid solution. Spectroscopic standards are matched to the salt matrix of the test solution; slurries equilibrated in 1 M NaCl solution were analyzed using standards prepared with 1 M NaCl incorporated. The technique utilized is Inductively Coupled Plasma – Atomic Emission Spectroscopy (ICP-AES). The apparatus and procedure are further described in Figure 5.2.

In most cases, corrosion inhibitor model compounds were obtained as reagents from chemical suppliers. In the case of praseodymium hydroxide, the lead time to purchase reagent material was prohibitive, so a small quantity of $Pr(OH)_3$ was synthesized. In this procedure, praseodymium chloride was titrated with a slight excess of potassium hydroxide solution to precipitate $Pr(OH)_3$. The precipitate was centrifugally separated, decanted, added to deionized water through seven purification cycles before drying at 80º C. The synthesis procedure is summarized in Figure 5.3. The resulting crystalline product was confirmed to be $Pr(OH)_3$ by x-ray diffraction, with purity estimated as 99% by SEM / EDX, with the balance of impurities residual chloride. Testing of the solubility properties of this material are currently in progress.

The apparatus and measurement protocol were initially tested on the strontium chromate pigment system. Strontium chromate slurries were found to equilibrate within 20 hours at ambient temperature, and to be recovered in concentrations that closely agree with published values.

5.5.3.3 Spatial Mapping of Inhibitors in Primer Films

Three spatial mapping techniques were assessed for the characterization of inhibitor distributions in primer films. As shown in Table 5.2, Energy Dispersive X-ray Spectroscopy (EDXS) was found to be the most informative survey technique for primer samples, due to its spatial accuracy, relative speed and moderate sample preparation requirements. Auger Electron Spectroscopy (AES) mapping was found best suited for fine-scale mapping of pigment particle surfaces, while X-ray Photoelectron Spectroscopy / Electron Spectroscopy for Chemical Analysis (XPS /ESCA) was found best suited for chemical state maps at relative coarse resolutions. The measurement techniques applied to spatial mapping of inhibitor fields are summarized in Table 5.2.

Statistical techniques were applied to the data in the inhibitor field maps to reveal and quantify spatial and chemical distribution trends. The most informative of these is the isolation of horizontal (in the primer plane) and vertical (through the primer plane) line scans from the maps, for application of correlation analysis to the element pairs within each line scan.

Solubility test set-up

Thermocouple

manifold

Water bath for temperature control

Test flask

Syringe for in-situ sampling
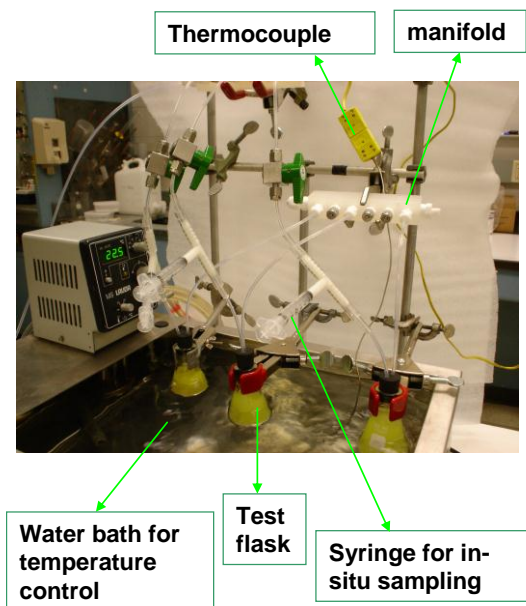
Experimental procedure

Solution preparation with different pH in HCl, DI water, and NaOH w/wt NaCl

↓

Sample added in solutions with different pH

↓

Equilibrate pigment slurries 20 hours under test conditions

↓

In-situ syringe sampling and filtration

↓

ICP-AES analysis
- *STD solution prepared in DI+HNO3 for samples tested without NaCl*
- *STD solution prepared in NaCl+HNO3 for samples tested with 1M NaCl*

Figure 5.2. Apparatus and method for inhibitor slurry testing.

KOH (0.035mol)

PrCl$_3$ (0.01mol)

Pr(OH)3 precipitation

Centrifuge wash

80C dry overnight

Pr(OH)$_3$ powder

Pr(OH)$_3$ synthesis set-up

Chemical reaction:

PrCl$_3$ + 3KOH ⟶ Pr(OH)$_3$↓ + 3KCl
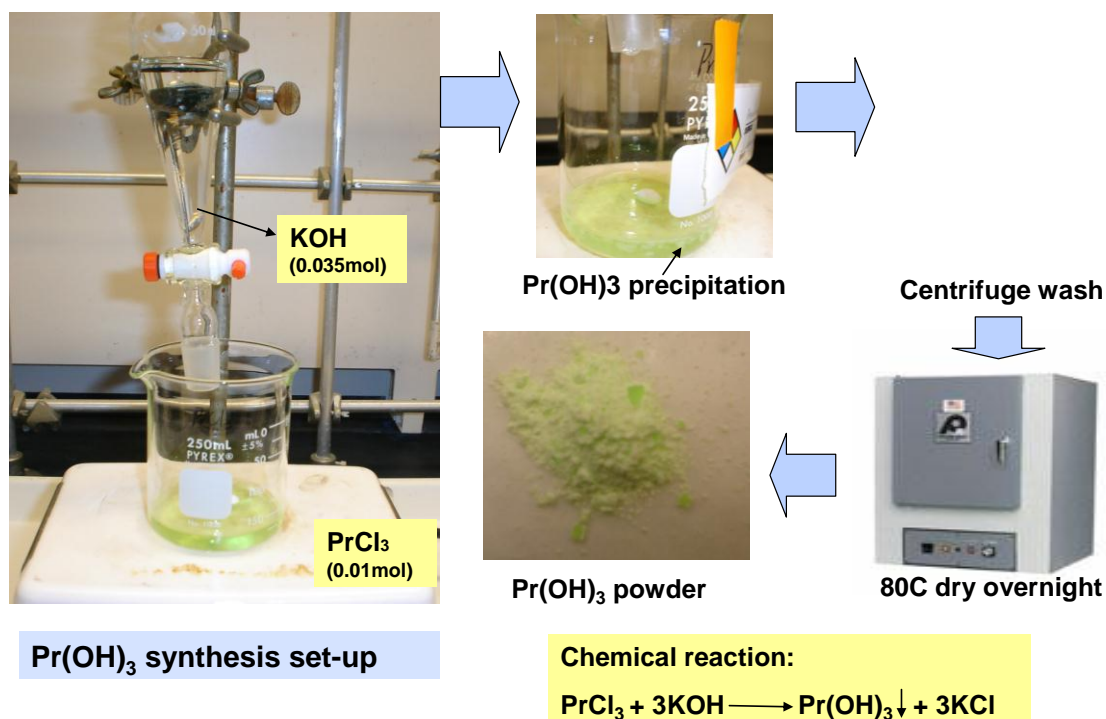
Figure 5.3. Synthesis procedure for Pr(OH)$_3$.

Table 5.2. Techniques applied to spatial mapping of inhibitor fields in primers

	Energy Dispersive X-ray Spectroscopy (EDXS)	Auger Electron Spectroscopy (AES)	X-ray Photoelectron Spectroscopy/Electron Spectroscopy for Chemical Analysis (XPS/ESCA)
Signal Detected:	Characteristic x-rays	Auger electrons from near surface atoms	Photoelectrons from near surface atoms
Elements Detected:	B-U	Li-U	Li-U Chemical bonding information
Detection Limits:	0.1 – 1 at%	0.1 – 1 at% sub-monolayer	0.01 - 1 at% sub-monolayer
Depth Resolution:	0.5 – 3 µm	20 – 200 Angstrom (Profiling Mode)	20 - 200 Angstroms (Profiling Mode)
			10 - 100 Angstroms (Surface analysis)
Imaging/Mapping:	Yes	Yes	Yes
Lateral Resolution/Probe Size:	>=0.3 µm	>=0.2 µm (LaB6 source)	10 µm - 2 mm
		>=100 Å (field emission)	
Characteristics:	Quick, "first look" analysis	Small area analysis (as small as 30 nanometers)	Chemical state identification on surfaces
	Versatile, inexpensive, and widely available	Excellent surface sensitivity	Depth profiling with matrix-level concentrations
	Quantitative for some samples (flat, polished, homogeneous)	Good depth resolution	Oxide thickness measurements

5.5.3.4 Water and inhibitor transport studies in primer films

Both through-plane and in-plane water transport studies were completed through representative films including Teflon sheet, Akzo Nobel PD381-94 base (chromate pigment omitted) and Deft 02-GN-084 and 44-GN-098 primers. Through-plane measurements were conducted by the gravimetric procedure described in ASTM D1653 [1]. The apparatus and method used are summarized in Figure 5.4.

In-plane transport properties are of particular importance in primers, as through-plane diffusion of inhibitors is defeated in most cases by topcoat systems designed as environmental barriers. In-plane measurements were made using a capacitance monitoring technique in a radial diffusion cell, which provided good agreement with microbalance measurements of water loss.

A commercial non-chromated, two component, epoxy polyamide primer for aerospace application, Deft-44-GN-098, manufactured by Deft Industries, was used for these in-situ capacitance measurements. To prepare free primer films, a wet paint mixture was applied by doctor-knife casting into glass substrates covered with an adhesive Teflon tape. The primer films were cured under air at room temperature for a minimum of two weeks. After curing, the films with thickness ranging from 200 to 300 µm were removed carefully from the glass substrates, and stored in a vacuum oven for one week at room temperature to remove any volatiles remaining from the curing processes.

$$J = D \bullet \frac{\partial C}{\partial x}$$

$$\frac{dC(x,t)}{dt} = \frac{\partial J}{\partial x} = D \bullet \frac{\partial^2 C(x,t)}{\partial x^2}$$

Liner region data used for WVTR calculation

$$Q(t \rightarrow \infty) = \frac{DC_1}{l}(t - \frac{l^2}{6D})$$

Lag-time $= l^2/6D$

$$C(x,t) = C_1(1 - \frac{x}{l}) - \frac{2C_1}{\pi}\sum_{n=1}^{\infty}\frac{1}{n}\sin(\frac{n\pi x}{l})e^{-Dn^2\pi^2 t/l^2}$$

$$Q(t) = \int_{t'=0}^{t} J(x=l,t)dt' = \frac{DtC_1}{l} - \frac{lC_1}{6} - \frac{2lC_1}{\pi^2}\sum_{n=1}^{\infty}\frac{(-1)^n}{n^2}e^{-Dn^2\pi^2 t/l^2}$$
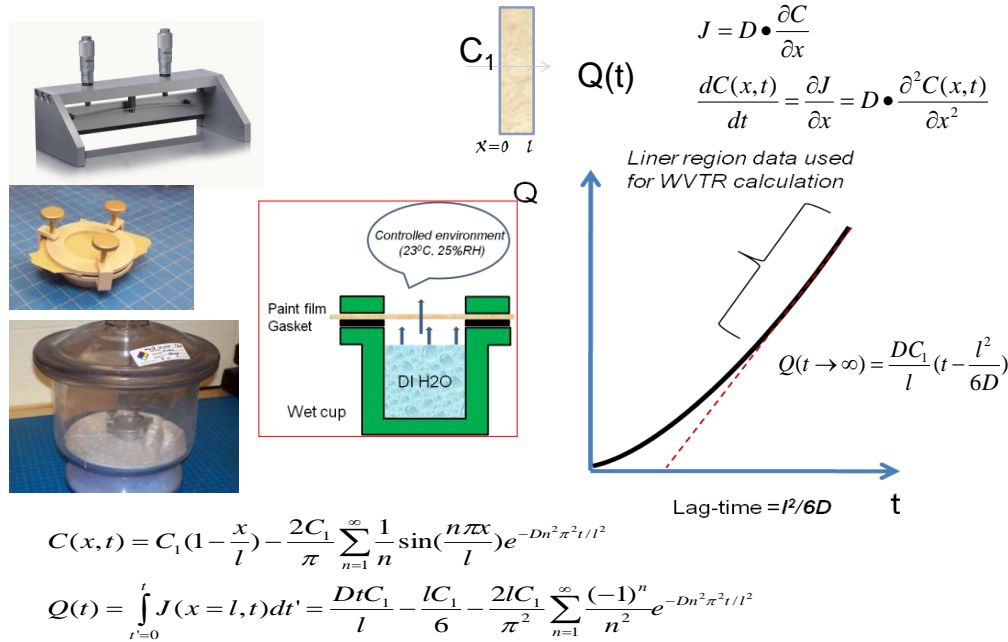
Figure 5.4. Apparatus and approach for through-plane water vapor transport measurement in primers.

The specimen for capacitance measurement consists of a free primer film placed between two Cu foil tapes, or coated with conductive silver paste on both surfaces, defining the film capacitor electrode surface of about 20 cm^2. The paint film has a circular center area (~ 10 cm^2) removed, allowing directly exposure to water vapor from one side. The specimen was clamped and sealed with water vapor resistant gasket to the open mouth of a Payne permeability cup containing water and the assembly was placed in a test chamber with a temperature and humidity controlled at 23^{0}C (+/- 10^{0}C) and 25% RH (+/-1% RH). Figure 5.5 (a, b) shows a schematic of the paint primer film geometry and experimental apparatus for in-situ capacitance measurements.

(a)   (b)
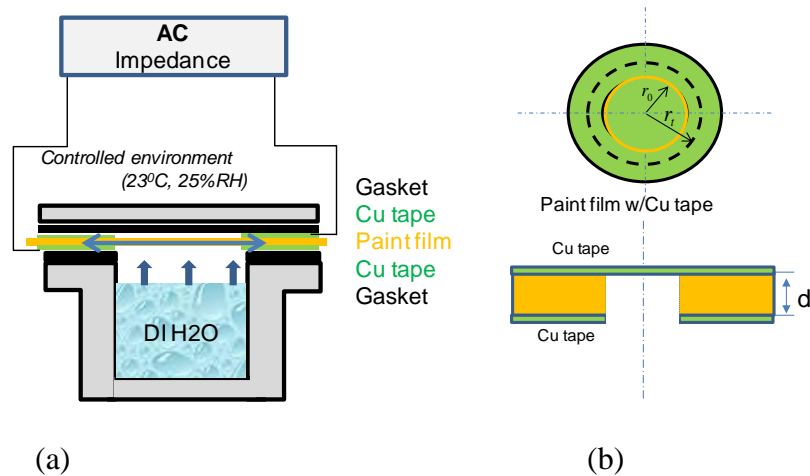
Figures 5.5. (a) Experimental set-up for in-situ measurement of lateral water (vapor) transport, (b) Tested film specimen configuration.

The capacitance was determined by Electrochemical Impedance Spectroscopy (EIS). The EIS measurements were made using a two electrode arrangement by a Solartron potentiostat (SI-1287) equipped with a high-frequency response analyzer (SI-1255B). The measurement was conducted in the frequencies ranging from 106 Hz to 1K Hz with an acquisition rate of 10 points per decade, and a 5 mV (vs reference electrode) AC perturbation potential applied. No DC bias voltage was applied.

For validation purposes, gravimetric measurements were also performed for one selected sample in conjunction with the capacitance measurements. The weight change of the primer film sandwiched between two Cu tapes was measured over time using a precision balance to an accuracy of 0.01 mg.

5.5.3.5 Inhibitor transport measurements

A two compartment cell was used to measure the leaching of inhibitors from free primer films and the transport rates of inhibitors through model primer films as a function of pH. The apparatus used is shown in Figure 5.6. As shown in Figure 5.6, a tested paint film with exposed areas of about 20 mm in diameter was inserted between two glass chambers, where one side (referred to as the receptor), is filled with DI water (~ 120 ml) and the other side (referred to as the donor) contains inhibitor (Pr^{3+}) solution (~ 120 ml) with initial pH range from 2 to 8. A small amount of solution was taken periodically from the receptor side in order to determine the Pr concentration by ICP technique.

In addition, 2024-T3 aluminum alloy samples were exposed to dilute salt water solutions (0.035Wt% NaCl) in a cell containing free films of Pr-based corrosion inhibitive primer. The electrochemical corrosion properties (corrosion current, corrosion potential, pitting potential) of the aluminum alloy samples were monitored with exposure times up to 200 hours.
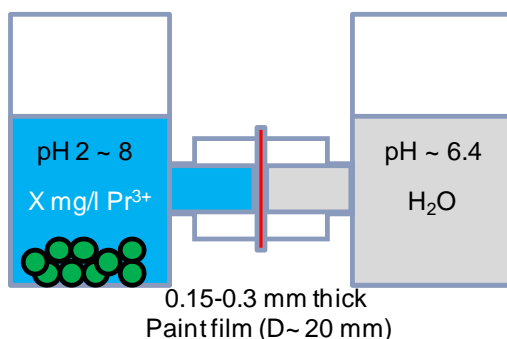
Figure 5.6. Two-compartment cell for inhibitor transport studies.

5.5.3.6 Migration of inhibitors in electric fields

One hydrated samples of Deft 02GN084 primer film sample was electrically biased at 10 V DC between copper electrodes for up to five days and characterized by XPS surface analysis for Pr content in the near surface region of the two electrodes.

5.5.3.7 Nanopore structure characterization of primer films

The nanopore structure of primer film samples was investigated by Positron Annihilation Lifetime Spectroscopy (PALS). The samples tested are listed in Table 5.3, including both freshly-prepared and aged for water-borne primer Deft-44-GN-098. For solvent-borne one, only the aged film was tested by PALS.

Table 5.3. Primer systems characterized by PALS

Primer	Chemical	Sample name	Curing time	Note
Deft-02-GN-084	Solvent-	Deft-084-aged	Aged > 1year	Film prepared in April 2010
Deft-44-GN-098	Water-borne	Deft-098-aged	Aged > 1year	Film prepared in April 2010
		Deft-098-7day	7-days	
		Deft-098-21day	21-days	
		Deft-098-24 day (backside)	24-days	Film prepared in Feb. 2012

Two types of positron annihilation lifetime spectroscopy techniques were used, including positron annihilation lifetime measurements (PAL) for bulk free volume and Doppler broadening of energy spectra (DBES), coupled with a slow positron beam to examine the free-volume depth profiles near surface. The standard PAL technique uses high energy positrons that penetrate deeply (on the order of a few hundred μm) into primer films, and therefore, provides the average properties of bulk films, with no ability to study the influence of surfaces or films thickness on free volume, while the DBES measures radiation near the 511keV where a major contribution comes from para-Positronium (p-Ps). For DBES experiments, a slow positron beam source (0-30keV) was used to selectively control the positron implantation depth, which enables the free volume to be studied as a function of distance from the surface, allowing the nature of the free volume profiles near the film surface to be characterized.

5.5.4 Results and Discussion

5.5.4.1 Identification of Candidate Pigments for Study

The corrosion inhibitors identified in the samples are summarized in Table 5.4. All sample obtained as commercial primers were found to contain one or more recognized cathodic or anodic corrosion inhibitors. No organic corrosion inhibitors were detected in any of the samples tested by FTIR and GC/MS analysis of water extracts.

The primers from Deft contained varying amounts of praseodymium hydroxide, a recognized rare earth metal (REM) cathodic corrosion inhibitor, in combination with calcium sulfate. Praseodymium, calcium and sulfur were detected in the scribe region after salt spray testing. The EcoTuff pigment contains cerous citrate, another recognized REM cathodic inhibitor, in

combination with zinc molybdate, a recognized anodic corrosion inhibitor. The primer sample from PPG contained only magnesium hydroxide as a recognizable inhibitive compound. The magnesium hydroxide in this system is assumed to function as a pH buffer, a chloride scavenger and perhaps to precipitate as a cathodic corrosion inhibitor in arresting corrosion. Magnesium hydroxide was also detected in the sample from Hentzen, in combination with alkaline earth silicates, which are recognized anodic corrosion inhibitors. The primer sample from Cytec contained an alkaline earth silicate in combination with zinc phosphate, believed to be a cathodic inhibitor. The primer from Sherwin Williams contained aluminum phosphate and zinc oxide, both recognized as cathodic corrosion inhibitors.

Table 5.4. Corrosion inhibitors detected.

Material Characterized	Active corrosion inhibitor
Cytec BR6700-1	Calcium silicate, zinc phosphate
Deft 02GN083	Praseodymium hydroxide
Deft 02GN084	Praseodymium hydroxide
Deft 44GN098	Praseodymium hydroxide
Hentzen 16708/709	Calcium and magnesium silicate, magnesium hydroxide
Sherwin Williams CM0481968	Zinc oxide, aluminum phosphate
PPG RW-4057-64	Magnesium hydroxide
EcoTuff™	Cerous citrate, zinc molybdate

5.5.4.2.1 Corrosion Inhibitor Solubility Effects by Model Pigment

Calcium silicate ($CaSiO_3$)

Alkali earth silicates were determined to be the principal corrosion inhibitor in two of the primer systems evaluated in our experiments as well as being a source of the corrosion-inhibiting silicate anion complex. Calcium silicate ($CaSiO_3$) is strongly alkaline. A reagent grade $CaSiO_3$ pigment with Ca/Si ratio of 1:1 was chosen to serve as a model for solubility study of these systems. The solubility of $CaSiO_3$ at various conditions is summarized in Table 5.5 and discussed below.

$CaSiO_3$Atmosphere effect

The calcium silicate model pigment demonstrated a distinct reaction when sparged with air, resulting in a decreased Ca/Si ratio compared to those obtained in N_2 sparged as shown Table 5.5. Compared to the same pH in N_2, the concentration of calcium is 5-20% lower in air while 5-7 times higher for silicon without the existence of sodium chloride. This is presumed due to reaction of dissolved calcium with carbon dioxide in the air to form insoluble calcium carbonate, accompanied by the liberation of a silicic acid product as shown in the Reactions 1-6. In aqueous solution, $CaSiO_3$ dissociates to form calcium cations and silicate ions according to Reaction (1). In air atmosphere, the CO_2 dissolved in water reacts with calcium ions to precipitate $CaCO_3$ as

indicated in Reaction (2). The $CaCO_3$ precipitation makes the solubility equilibrium of $CaSiO_3$ (Reaction 1) move to the right, which results in less Ca and more Si detected in the solution.

Table 5.5 Solubility data of $CaSiO_3$ at 20°C, 24 h at various conditions

| | Air | | | | | | N_2 | | | | | |
| | 0M NaCl | | | 1M NaCl | | | 0M NaCl | | | 1M NaCl | | |
pH	Ca, mmol	Si, mmol	Ca/Si	Ca, mmol	Si, mmol	Ca/Si	Ca, mmol	Si, mmol	Ca/Si	Ca, mmol	Si, mmol	Ca/Si
3	2.1739	7.5233	0.3	5.4290	5.9537	0.9	2.3686	1.4456	1.6	4.3915	2.7813	1.6
7	1.4114	6.1387	0.2	4.6353	5.1088	0.9	1.8060	1.2415	1.5	3.4164	2.4436	1.4
10	1.5572	7.0066	0.2	4.8893	4.8471	1.0	1.9329	1.1716	1.6	3.9583	2.6409	1.5

CaSiO₃ solubility results_20°C_24hours

Under nitrogen sparging the lack of CO_2 introduced into the solution resulted in a higher pH than in air as shown in Figure 5.7. The produced SiO_3^{2-} may react with H^+ in the solution according to Reaction 5. The pKa of silicic acid is around 9.2. At relatively high pH, $CaOH^+$ (Reaction 5) is the dominant calcium species in the solution, which provides a higher soluble calcium concentration. Combining these two factors, the ratio of Ca/Si in N_2 is higher than 1. However, the exact formula of the formed compounds in the solution under N_2 remains unknown. This reaction is of continued interest as it illustrates both an ageing characteristic of pigments of this class, and the generation of a silicic acid reaction product that may have unique secondary inhibitive properties.

CaSiO₃ pH effect

In air without NaCl, a great deal of more silicon is dissolved than calcium due to the initially precipitation formation of $CaCO_3$. However, around 30% more calcium is observed in acidified solution than in neutral and alkaline solutions, which may be due to the redissolution of the $CaCO_3$ precipitation under high acidity based on the reaction shown in Reaction 3. As a comparison, $CaCO_3$ cannot be redissolved in NaOH solution while $Ca(OH)_2$ precipitation may occur. However, due to the lower Ksp of $CaCO_3$ than $Ca(OH)_2$, the $CaCO_3$ deposition was favored [2,3]. In 1M NaCl environment, due to the strong ionic strength from NaCl, dissolvable Na_2SiO_3 and $CaCl_2$ may be formed. Therefore, almost the equally dissolved Ca and Si are detected in the solution as the Ca/Si ratio in Table 5.5.

CaSiO₃ NaCl effect

NaCl has two major effects on the $CaSiO_3$ system. In the N_2 sparged condition, the presence of NaCl increases the concentrations of both calcium and silicon by a factor of two. This effect has been noted by Glasser et al. [4] in studies of the stability of cement components. In air, due to the CO_2 effect, without presumably NaCl, the Ca/Si ratio is near 0.3. The possibility that NaCl

tends to prevent the precipitation of $CaCO_3$ due to the formation of soluble species of $CaCl^+$ is disproven by OLI thermodynamic simulations, as shown in Figure 5.8. The solubility of calcium in alkaline solution increases in 1M NaCl under both air and N_2 condition compared to that in solution without NaCl. This increase in calcium concentration due to the presence of NaCl is attributed to the "electrolyte shielding effect" described below.
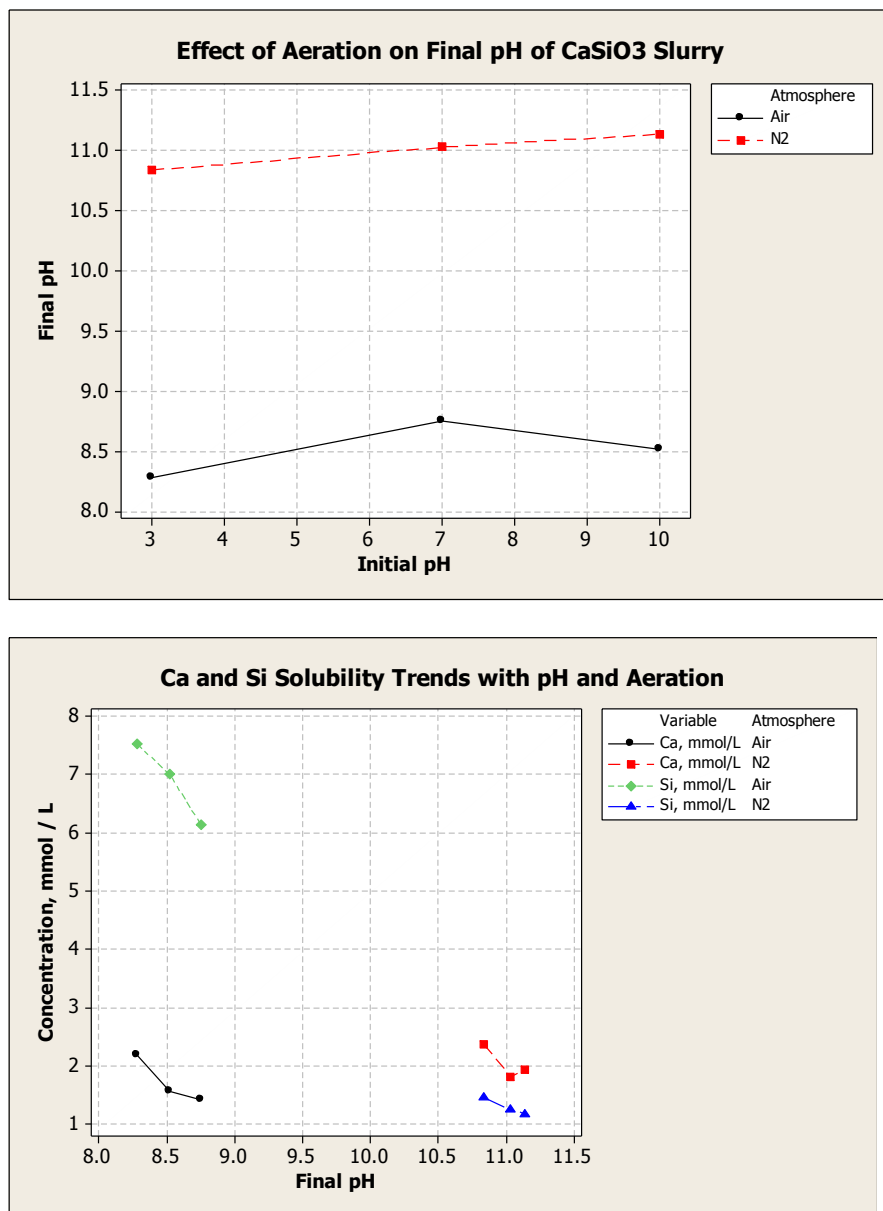
Figure 5.7 Solubility of calcium silicate at various conditions.
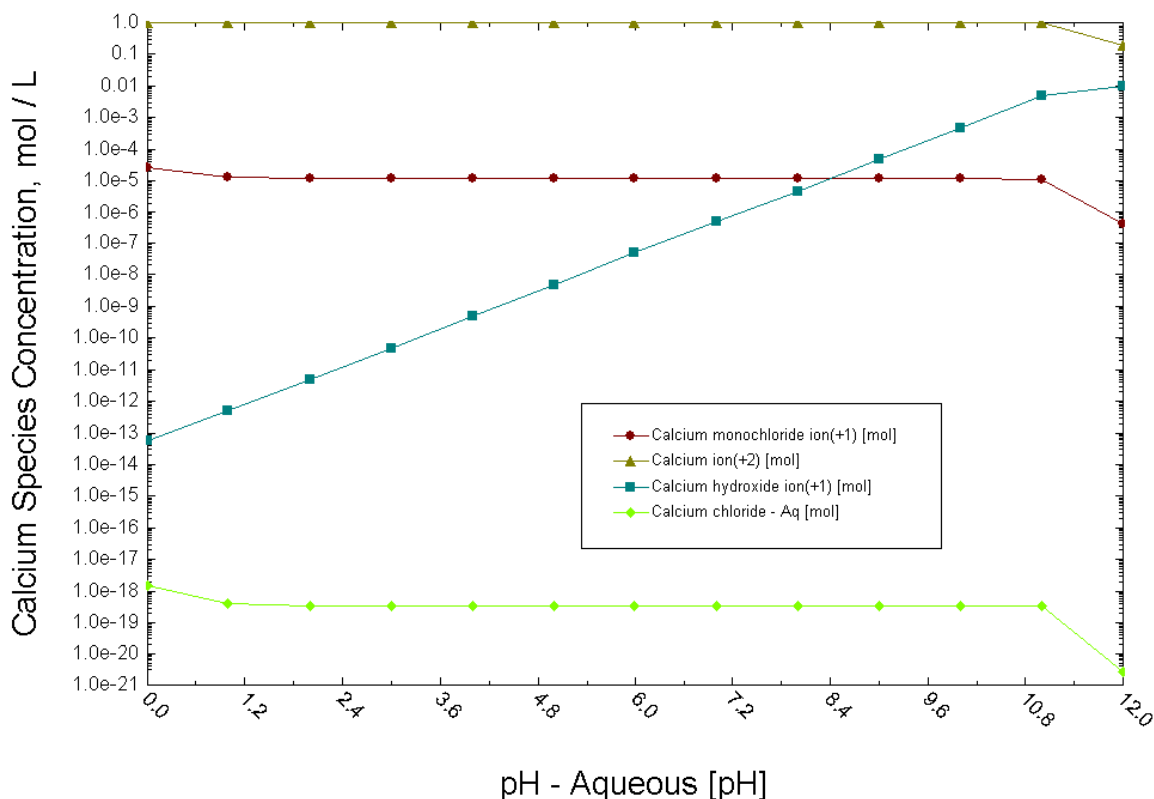
Figure 5.8 Predicted calcium speciation in chloride environments.

$$CaSiO_3 \longrightarrow Ca^{2+} + SiO_3{}^{2-} \qquad (5.1)$$
$$Ca^{2+} + CO_3{}^{2-} \longrightarrow CaCO_3 \downarrow \qquad (5.2)$$
$$2H^+ + SiO_3{}^{2-} \longrightarrow H_2SiO_3 \qquad (5.3)$$
$$H_2SiO_3 \longrightarrow SiO_2 + H_2O \qquad (5.4)$$
$$Ca^{2+} + OH^- \longrightarrow CaOH^+ \qquad (5.5)$$
$$Ca^{2+} + 2OH^- \longrightarrow Ca(OH)_2 \qquad (5.6)$$
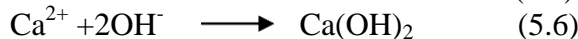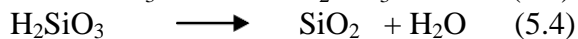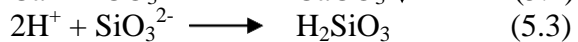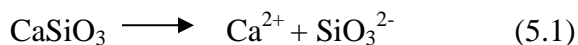
Pr(OH)₃

In the case of praseodymium hydroxide, a small quantity of $Pr(OH)_3$ was synthesized in the lab. In this procedure, praseodymium chloride was titrated with a slight excess of potassium hydroxide solution to precipitate $Pr(OH)_3$. The precipitate was centrifugally separated, decanted, added to deionized water through purification cycles before drying. The resulting grey green powder was confirmed to be $Pr(OH)_3$ crystalline product by x-ray diffraction, with purity estimated as 99% by SEM / EDS. In solubility measurement, since $Pr(OH)_3$ is a base, no test was carried out in pH=3 solution due to the neutralization reaction.

Pr(OH)₃ pH effect

Alkaline affects praseodymium solubility when its counter ion is OH- because solubility of $Pr(OH)_3$ is expressed as a solubility product, Ksp. The relevant solubility expression is:

$$Ksp = [Pr^{3+}][OH-]^3$$

Where square brackets indicate activities, although in this simplified illustration of solubility products the concentration is substituted for activity. If OH^- is introduced into the system, the praseodymium solubility will significantly be depressed due to the three magnitude of hydroxide ion concentration. In air without NaCl interference, 9x reduction of solubility was obtained for praseodymium. However, under N_2 sparging conditions, a small decrease in praseodymium concentration was detected. This is believed to be due to the formation of the $PrCO_3^+$ species in the aerated solution as shown in the stability diagram shown in Figure 5.9.

$Pr(OH)_3$ Atmosphere effect

The main effects from solubility testing of praseodymium hydroxide – based inhibitor slurries are shown in Table 5.6 and Figure 5.9. Saturating the slurry with air has a strong effect on promoting $Pr(OH)_3$ solubility, which is believed to be due to the acidification of the slurry from dissolved CO_2 as indicated in Table 5.6. However, the references are not sensitive to discriminate the effect of pH and dissolved CO_2 on the praseodymium solubility.

The Ksp of $Pr(OH)_3$ is around 10^{24}. Therefore, at pH=9, the solution activity of Pr+ is theoretically near 10^{-6} mmol/L. In air, due to the decreased pH of the dissolved CO_2 in the solution, the soluble $PrHCO_3^{(+2a)}$ as shown in Figure 5.9 may be formed which results in the a little higher solubility of $Pr(OH)_3$ than that in N_2 sparged conditions, as shown in Table 5.6. However, in the pH 10 solutions in the absence of NaCl, the solubility of is too low to be accurately measured by ICP, so the solubility difference measured in air and N2 at pH=10 is not regarded as experimentally significant.

Table 5.6. Pr solubility under various conditions.

Dissolved $Pr(OH)_3$ at various conditions, mmol/L				
	Air		N_2	
pH	0M NaCl	1M NaCl	0M NaCl	1M NaCl
7	0.000639	0.036491	0.000099	0.0007664
10	0.000071	0.014179	0.000213	0.0010219
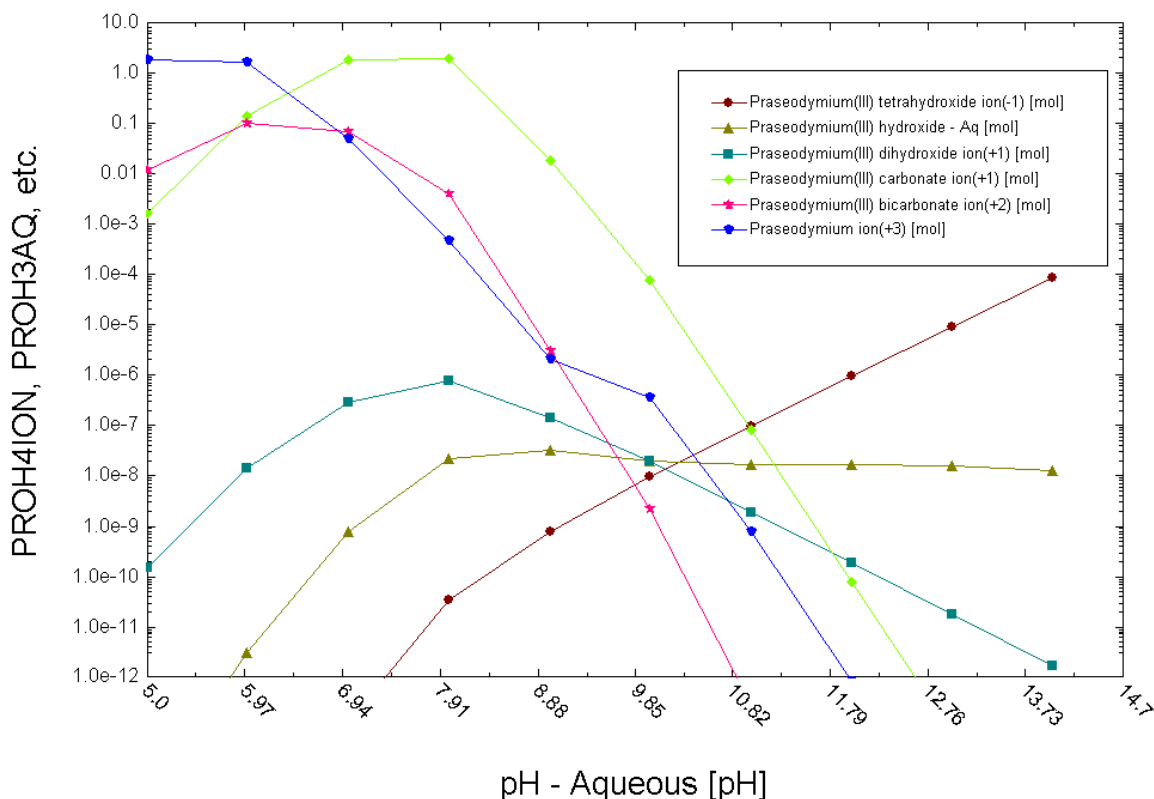
Figure 5.9: Pr speciation in the presence of CO_2 (OLI Stream Analyzer)

Pr(OH)$_3$ NaCl and CaSO$_4$ effect

As seen in other pigment systems, the electrolyte "salt effect" serves to increase the solubility of Pr(OH)$_3$. The pigment systems primers were found to contain calcium sulfate compounds in varying degrees of hydration. The moderate solubility of CaSO$_4$ compounds (typical Ksp of 5x 10^{-5}) and the recognized corrosivity of the sulfate anion toward aluminum alloys suggests that this pigment additive is not included as an inert filler, and that its presence may serve a functional purpose that outweighs its potential for supporting corrosion damage as a source of sulfate ions. For this reason, solubility studies of the recognized active praseodymium hydroxide corrosion inhibitor were expanded to determine the effect of the calcium sulfate pigment constituent. Interestingly, the addition of sulfur (as calcium sulfate) has a strong effect to increase the solubility of Pr(OH)$_3$ although the effect is not as strong as NaCl as shown in Table 5.7. Without NaCl, the solubility of Pr(OH)$_3$ was increased 10 times with the presence of CaSO$_4$. In a solution with 1M of NaCl, the dissolved Pr^{3+} is slightly lower than that with the existence of both NaCl and CaSO$_4$. This is attributed to the ionic strength change with the addition of the NaCl in the solution.

EcoTuff®

The EcoTuff® pigment system contains a cerous citrate cathodic corrosion inhibitor and a zinc molybdate compound that is expected to contribute both cathodic (from Zn^{2+}) and anodic (from

MoO_4^{2-}) inhibition to the system. The citric acid anion system is a recognized metal complexing agent and, as a poly acid, is expected to introduce pH-sensitivity into the solubility characteristics of the system. As can be seen in initial data presented in Table 5.7, the Zn and Mo concentrations display initial pH sensitivities that are consistent with their classifications as cathodic and anodic corrosion inhibitors, respectively. The effect of pH on the solubility of Ce in this system is not evident over the relatively small range of near-neutral terminal pH values obtained in initial testing. Both the pH buffering and relative insensitivity of Ce solubility are attributed to the presence of Ce in solution as the citric acid complex. Both Mo and Ce exhibit electrolyte-enhanced solubility, while Zn does not, perhaps indicating a relatively lower charge on the zinc species in solution.

Table 5.7. Effect of salts on $Pr(OH)_3$ solubility.

Dissolved $Pr(OH)_3$ in Air_20^{o}C_pH7, mmol/L			
	Pr	Ca	S
0M NaCl	0.00064	0.00	0
0M NaCl-CaSO$_4$	0.00768	41.11	42.26
1M NaCl	0.03649	0.00	0
1M NaCl-CaSO$_4$	0.01418	108.54	103.23

EcoTuff® atmosphere effect

Cerium citrate dissociates in the solution based on Reactions 7-15. Therefore, the dissolution equilibrium is between the cerium citrate molecule and two ions, Ce^{3+} and citrate ions. The differences between air and N_2 conditions are mainly due to two factors: dissolved CO_2 and O_2. If no reaction between the dissociated ions and these two dissolved gases, the solubility of the materials should be close in air and N_2. Otherwise, depending on the specific reactions, materials will show various solubilities under these two environments.

The solubility of cerium in air and N_2 without NaCl is very close in pH=3 solution. When pH increases to 7 or 10, due to the absence of CO_2 and consequently no enough neutralization for OH- in the solution, cerium precipitates as hydroxide. Therefore, the solubility of cerium species under N_2 sparging is only 60% of that in air as shown in Table 5.8. Although solubilized Ce^{3+} in the solution can be oxidized to Ce^{4+} cations with oxygen in air based on Reaction 9 to promote the solubility of Ce^{3+}, it was not observed in the current system. Additionally, no carbonate precipitation of cerium is predicted based on the Pourbaix diagram (Figure 5.10).

Table 5.8. Ecotuff ® solubility characteristics.

EcoTuff® solubility test_20°C_24hrs			
pH Solubility, mmol/L	3	7	10
Ce-Air-0M NaCl	0.1126	0.1511	0.1257
Zn-Air-0M NaCl	2.0272	0.9514	0.9116
Mo-Air-0M NaCl	0.0830	0.2464	0.2050
Ce-Air-1M NaCl	0.5407	0.5918	0.5743
Zn-Air-1M NaCl	0.7834	0.5091	0.5839
Mo-Air-1M NaCl	0.7106	0.9737	1.0086
Ce-N$_2$-0M NaCl	0.1331	0.0862	0.0742
Zn-N$_2$-0M NaCl	1.3308	0.4324	0.1960
Mo-N$_2$-0M NaCl	0.2722	0.2166	0.2973
Ce-N$_2$-1M NaCl	0.1361	0.3802	0.2661
Zn-N$_2$-1M NaCl	1.2208	0.5145	0.7005
Mo-N$_2$-1M NaCl	0.3655	0.7386	0.5238
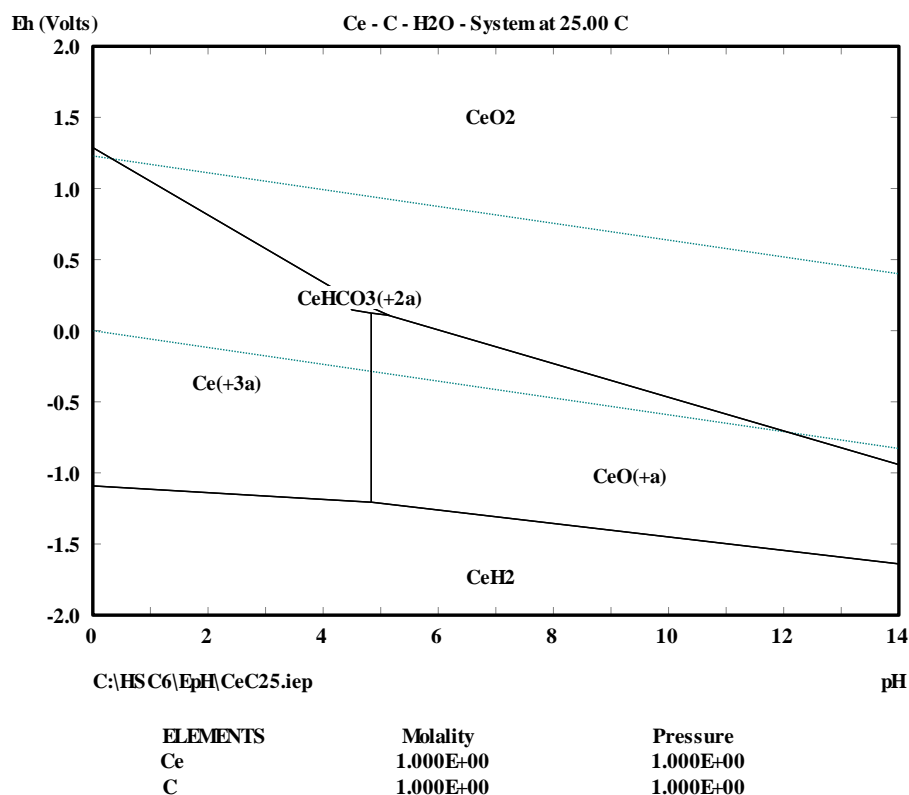
Figure 5.10. Pourbaix diagram for Ce in the presence of CO_2.

Zinc molybdate is reported to be similar to strontium chromate in its solubility properties [5]. The associated zinc molybdate equilibrium is shown Reaction 5.11. In the case of zinc, CO_2 neutralizes the OH^- which precipitates zinc as zinc hydroxide (Reaction 13). As a result, more soluble zinc is observed in air especially in alkaline condition around 4 times higher than in N_2. In addition, due to the lower Ksp of $Zn(OH)_2$ ($3x10^{-17}$) [6] than zinc carbonate ($1.46x10^{-10}$), no zinc carbonate precipitation is predicted in the system. The presence of CO_2 affects the solubility of molybdenum as shown in Reaction 12 as well. The formation of polymeric molybdate moves the dissolution equilibrium of zinc molybdate (Reaction 11) to the right side, which also contributes to the higher solubility of zinc in air. However, the polymeric molybdate may precipitate, especially under acidic condition as shown in Table 5.8. Otherwise, the concentrations of zinc and molybdenum are close to each other.

EcoTuff® pH effect

Generally, with the increase of pH in the starting solution, more cerium hydroxide precipitation is observed. This is confirmed in N_2 condition. However, in air, due to the existence of CO_2 and O_2, the system mechanism is more complicated. The increased protonation of citric acid with pH is believed to stabilize the Ce^{3+} complex against precipitation from the solution.

In pH=3 solution, a weak acid of citric acid may be prepared due to the existence of hydrogen ions (Reaction 10). As a result, the dissociation equilibrium of cerium citrate moves to the right side. In addition, in acidic solution, the lack of OH^- removes the possibility of $Ce(OH)_3$ precipitation. Combining these two factors, in pH=3 solution, similar dissolved cerium was found in either air or N_2 sparged conditions. This is in agreement with the experimental data. Although it is a relatively strong base, $Ce(OH)_3$ has a very low solubility. At pH=7.26, the precipitation of $Ce(OH)_3$ can be observed as shown in Reaction 8. Therefore, with the increase of pH in the starting solution, the precipitation of $Ce(OH)_3$ takes place which results in a decreased solubility of cerium. This is in a great agreement with the data collected in N_2 environment.

Similar to cerium, zinc ions tend to form deposition as hydroxides in solutions with increased pH as shown in Reaction 13. This results in the right movement in the dissociation equilibrium of $ZnMoO_4$ (Reaction 11) and provides a higher solubility of molybdate as is observed in N_2 condition. However, in air, due to the presence of CO_2, OH^- has been neutralized and as a consequence, the precipitation of zinc hydroxide decreases which leads to less dissolution of molybdenum compared to N_2 condition. The pH measurement after tests confirmed the assumption: the pH is slightly acidic, around 6.5 in N_2 while the value is around 7.5, more alkaline in air.

EcoTuff® NaCl effect

NaCl increases the solubility of cerium and molybdenum greatly. However, the solubilities of zinc and molybdate do not vary in proportion. The effect of NaCl on the solubility of zinc is attributed to the low valance state of zinc species in solution. This is attributed to electrolyte shielding as described below.

$$CeC_3H_5O(COO)_3 \longrightarrow Ce^{3+} + C_3H_5O(COO)_3^{3-} \qquad (5.7)$$
$$Ce^{3+} + 3OH^- \longrightarrow Ce(OH)_3 \downarrow \qquad (5.8)$$
$$4Ce^{3+} + 4OH^- + O_2 + 2H_2O \longrightarrow 4Ce(OH)_2^{2+} \qquad (5.9)$$
$$C_3H_5O(COO)_3^{3-} + H^+ \longrightarrow HC_6H_5O_7^{2-}/ H_2C_6H_5O_7^- \qquad (5.10)$$
$$ZnMoO_4 \longrightarrow Zn^{2+} + MoO_4^{2-} \qquad (5.11)$$
$$7MoO_4^{2-} + 8H^+ \longrightarrow Mo_7O_{24}^{6-} + 4H_2O \qquad (5.12)$$
$$Zn^{2+} + 2OH^- \longrightarrow Zn(OH)_2 \qquad (5.13)$$
$$Zn(OH)_2 + 2OH^- \longrightarrow Zn(OH)_4^{2-} \qquad (5.14)$$
$$Zn^{2+} + CO_3^{2-} + O_2 + H_2O \longrightarrow Zn_3CO_3(OH)_2 \qquad (5.15)$$
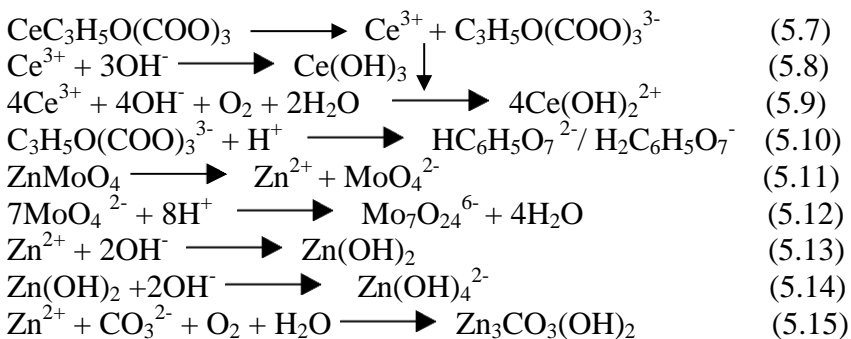
5.5.4.2.2 Corrosion Inhibitor Solubility Effects by Environmental Factor

CO_2 effect

In our study, the differences in solubilities of inhibitors of interest in various atmospheres are mainly due to the dissolved CO_2 in the solutions. The CO_2 dissolved in the testing solutions significantly affects the solubility of the different species in the system due to the two possible important roles: 1. dissolved CO_2 may form H_2CO_3, whose pH of saturated solution is around 5.656; 2. reactions between CO_2 and the species in the solution.

In the investigation of $Pr(OH)_3$ solubility, the solution pH was lowered because of the dissolution of CO_2 compared to that in N_2 atmosphere. As a result, a more soluble species presumed $PrCO_3^+$ was formed which significantly makes the solubility equilibrium of $Pr(OH)_3$ move to the right. Therefore, the measured solubility of this inhibitor was much higher than in N_2 condition.

In the case of $CaSiO_3$, the Ca^{2+} cation reacts with CO_3^{2-} anions produced from dissolution of CO_2 in the solution, which results in a new precipitation of $CaCO_3$ as shown in Reaction 2. This process consequently increased the concentration of dissolved silicates. The dissolved silicon formed a secondary inhibitive species of silicic acid in the solution. However, calcium concentration in air soaking condition is lower than that in nitrogen condition due to the initial precipitation of $CaCO_3$ production regardless of different initial pH values.

EcoTuff® is composed of two main inhibitive compounds and an organic polyacid. Since the pH of saturated CO_2 solution is around 5.65 and no new species is formed in between carbonate and cerium, there is not difference in the solubilities of cerium in the solution at pH=3 in air and N_2 condition. However, when pH is raised to 7 or 10, cerium precipitates as hydroxides due to the absence of CO_2 and resulting higher pH. As a consequence, the solubility of cerium species in N_2 condition is only 60% of that in air as calculated in Table 5.8. Another active inhibitive species, Zn^{2+} cations, has more complicated relations with carbonate and hydroxide ions as indicated in Reactions 13-15, acidification from the presence of CO_2 prohibits the precipitation of Zn(OH)2 and leads to a higher solubility in aerated conditions.

Electrolyte effects

The presence of a salt that has no ion in common with the solute has an effect on the solubility equilibrium known as "salt effect". The salt effect of the ionic strength of the solution tends to decrease the activity coefficients of ionic sources in solution so that the equilibrium, expressed as a concentration quotient, changes. In the current study, NaCl has been found to have a strong shielding effect on the studied inhibitors due to the "salt effect". The salt shielding effect can be partially explained by Debye-Huckel equation as shown below:

$$\lg \gamma = -0.5102 * Z^2 * I^{\frac{1}{2}}$$

where $I = \sum m_i Z^2$.

Under the same temperature, pH, and in N_2 condition, the solubilities of the active inhibitive species, such as praseodymium for $Pr(OH)_3$, are greatly increased by the presence of 1 M NaCl. In $Pr(OH)_3$, the presence of NaCl increases the concentration of praseodymium 5-8 times regardless the effect from CO_2. Based on Debye-Huckel equation, without other factors, the praseodymium concentration should increase around 6 times. Similarly, in the calcium silicate system, a doubling of solubility was observed under the same condition with NaCl in the solution compared to the measurements without NaCl. This is close to the factor of 3 increase in solubility predicted by theory. Similar results consistent with theoretical predictions were obtained for cerium in EcoTuff® pigment.

Internal reactions

In addition to the effects of dissolved CO_2 and electrolyte strength, the other important factor influencing the solubility of corrosion inhibitors is the internal reactions for certain inhibitors. For example, the concentration of praseodymium increased with the presence of the other secondary pigment calcium sulfate.

The mechanism for solubility promotion of praseodymium by calcium sulfate is believed to reside in the thermochemical stability of praseodymium sulfate and its ion complexes, as shown in Figure 5.11. Two sulfate ion complexes of praseodymium are predicted, with the monosulfate cation $Pr(SO_4)^+$ predominating. The aggregate increased solubility of these two sulfate complexes stand in good agreement with the measured increased in Pr solubility in the presence of calcium sulfate.

While the thermochemical explanation for Pr solubility promotion by sulfate is relatively straightforward, its implications to the service life of these coatings include the consumption of the facilitating sulfate compound and the fate of calcium compounds in the primer layer, and the ionic current reversal of $PrSO_4^+$ and $Pr(SO_4)_2^-$ species in response to local electric fields.

5.5.4.3 Spatial Mapping of Inhibitors in Primer Films

Figure 5.12 shows a series of EDXS maps obtained from Deft 44GN098 primer samples applied to Alodine 600-treated 2024-T3 Al before and after 2000- hour salt spray testing. By inspection, the as-prepared samples show distinct calcium sulfate and praseodymium hydroxide pigment particles. After 2000-hour neutral salt spray exposure, the calcium sulfate particles are significantly less distinct, and an elevated concentration of praseodymium is evident in the primer matrix. Calcium and sulfur appear in association with praseodymium.
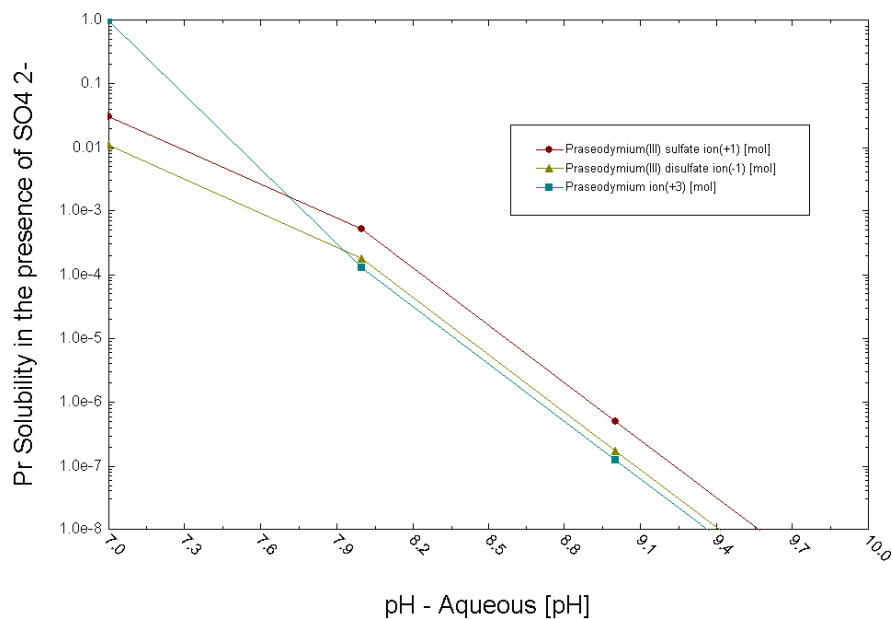
Figure 5.11. Pr speciation in the presence of calcium sulfate (OLI Stream Analyzer).
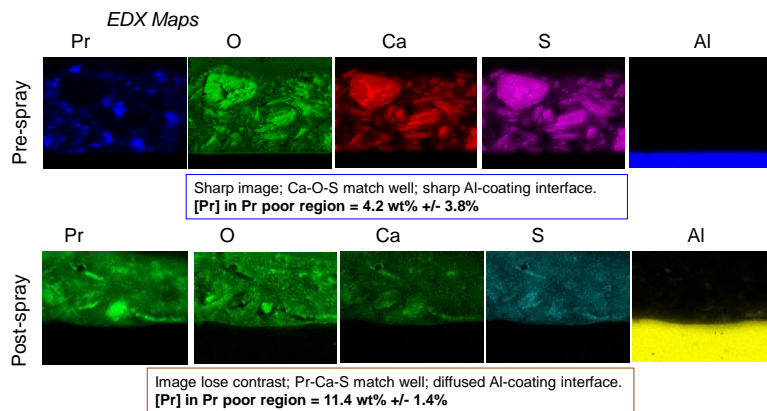
Figure 5.12. EDXS Inhibitor Mapping of Deft 44GN098 primer before (above) and after (below) 2000-hour ASTM B117 salt spray test.

Statistical techniques were applied to the data in the inhibitor field maps to reveal and quantify spatial and chemical distribution trends. The approach taken, as shown in Figure 5.13, is to isolate horizontal (in the primer plane) and vertical (through the primer plane) line scans from the maps, and to apply correlation analysis to the element pairs within each line scan.

226

This approach yields two figures of merit for each element pair in each line scan: the Pearson product moment (r^2) is a robust measure of the variation in the concentrations of the element pairs that can be attributed to linear covariation, with the regression slope for each element pair as a second measure of covariance with greater sensitivity but potentially lower confidence. These figures of merit can be used to compare inhibitor distributions in primer films as a function of either exposure history or distance from the substrate or air-interface of the primer film.
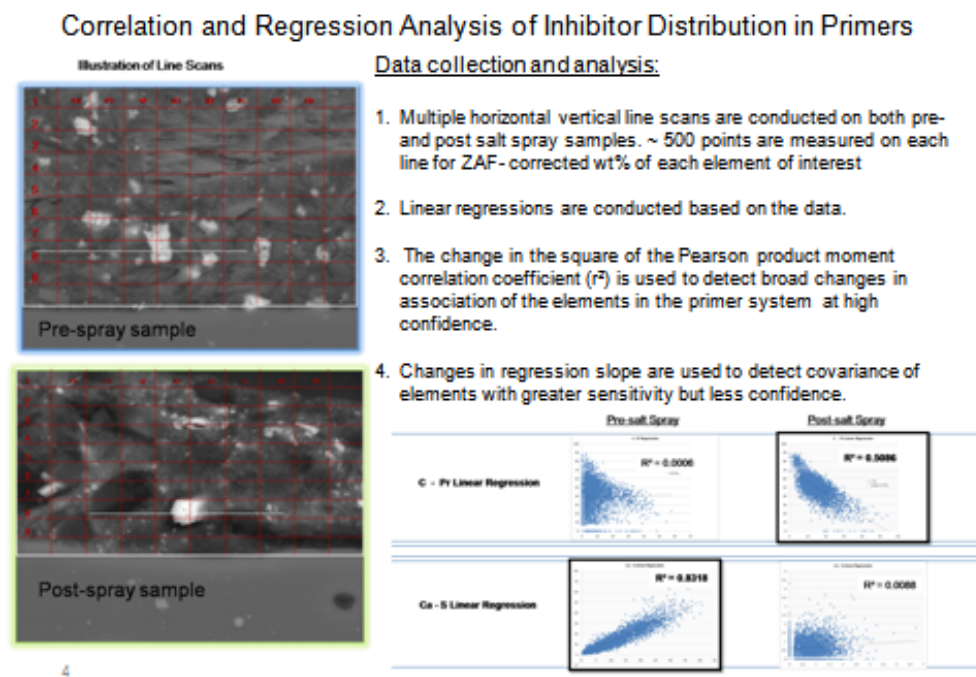
Figure 5.13. Statistical treatment of inhibitor spatial maps.

Figure 5.14 shows the results of applying the higher confidence figure of merit, r^2, to describe correlation in the pairs of elements shown in spatial map of the Deft GN44098 primer shown in Figure 5.13. The y-axis of this Figure shows the change in the r^2 parameter produced by the salt spray test as measured in the sets of horizontal and vertical line scans. This analysis shows the positive correlation of praseodymium with the carbon of the primer matrix produced by the salt spray test, the strong de-correlation of calcium with sulfur, and the drop in correlation of both calcium and sulfur with the carbon matrix following the salt spray test. This is interpreted as the mobilization of praseodymium through the primer matrix, the dissolution of parent $CaSO_4$ pigment particles, and an overall loss of both calcium and sulfur in the primer matrix produced by the salt spray test.

Analyzing the data of Figure 5.13 by the regression slopes of element pairs reveals additional interactions, as shown in Figure 5.15. In this Figure, the y-axis is the change in slope of the element pair regression lines produced by the 2000-hour salt spray test. This treatment reveals a proportional covariation developing between praseodymium and both sulfur and calcium as a consequence of the salt spray test. This is explainable by the formation of praseodymium sulfate

compounds with local deposition of a calcium reaction product. The full nature and morphology of these internal reaction products are not currently understood.
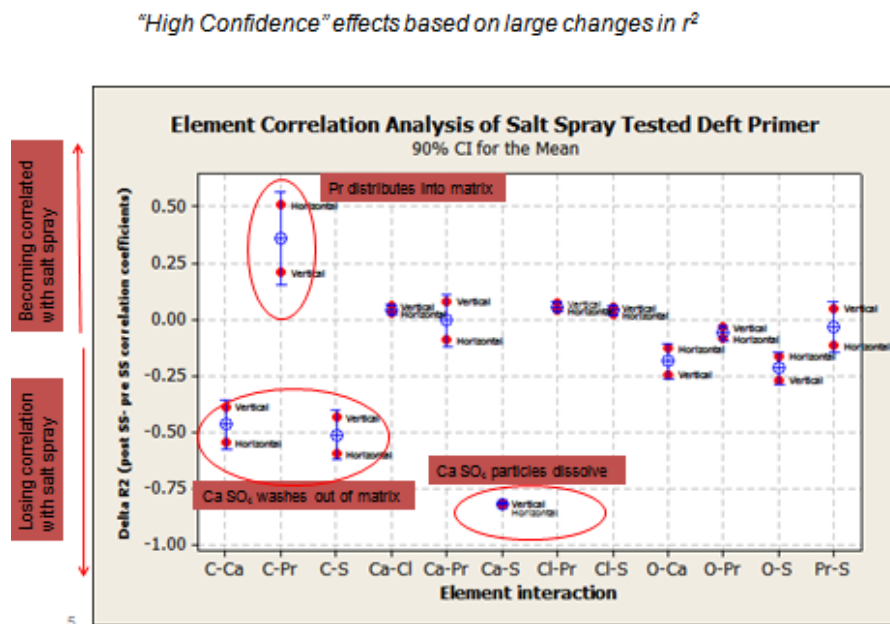
Figure 5.14: Element interactions produced in Deft 44GN098 primer by 2000-hour salt spray test (r^2 analysis)
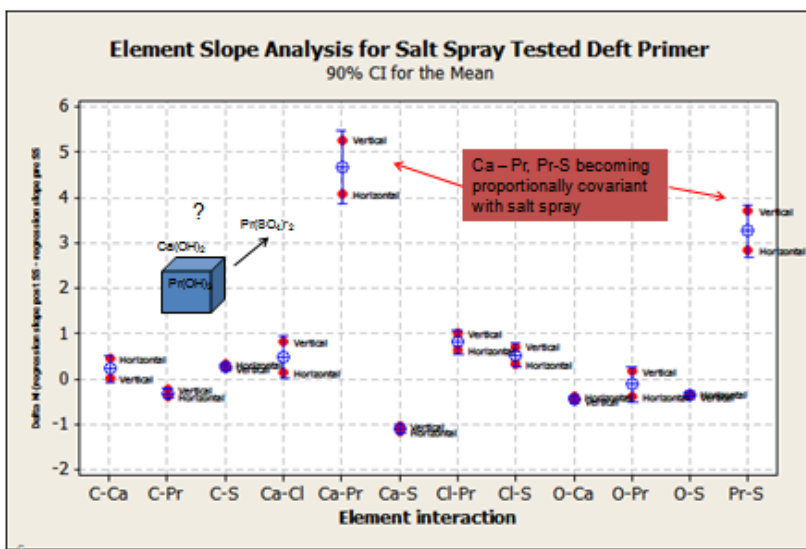
Figure 5.15. Element Interactions produced in Deft 44GN098 Primer by 2000-hour salt spray test (slope analysis).

Inhibitor mapping of the Hentzen 16708/709 primer after 2000-hour salt spray exposure, as shown in Figure 5.16, shows apparent partial dissolution of parent calcium silicate particles and distribution of calcium and silicon into the primer matrix. This primer also showed, in Figure 5.17, a coincidence of through-film gradients of chlorine and titanium following the salt spray test, with the highest concentrations near the air / primer interface.

Calcium, Silicon Distribution in Hentzen 16708/709 Primer Depth after Salt Spray Testing
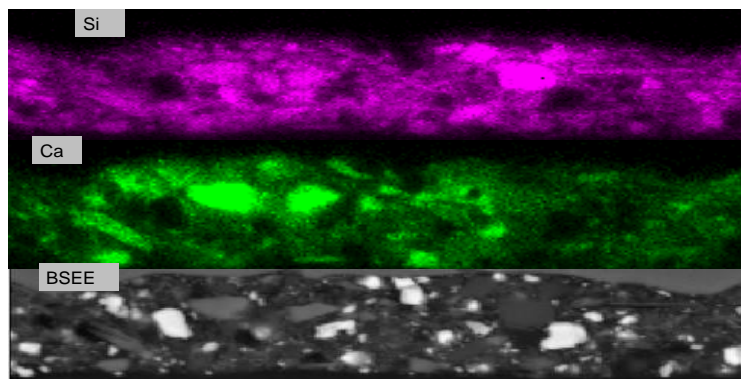
Figure 5.16. Distribution of Calcium Silicate produced by Salt Spray Exposure of Hentzen16708/ 709 Primer.

Figure 5.17. Through-film association of chlorine and titanium in Hentzen16708/709 primer following salt spray exposure.

Two samples of EcoTuff-inhibited epoxy primers were evaluated after one year ASTM B117 salt spray exposure. This inhibitor system includes cerium citrate as a cathodic corrosion inhibitor, and zinc molybdate, calcium silicate and optionally strontium tungstate, as anodic corrosion inhibitors. As shown in Figure 5.18, both primer variants exhibited dissolution of cerous citrate and calcium silicate parent particles, and diffusion of Ce, Ca and S into the primer matrix. The pigment variation that included strontium tungstate demonstrated a complete loss of molybdate after the test.

Figure 5.18. Inhibitor maps from Ecotuff® -inhibited primer samples after 1-year salt spray exposure: inhibitor package including strontium tungstate (top), without strontium tungstate (bottom).

The molybdate loss in the strontium tungstate-bearing primer is attributed in part to the reaction of strontium ions with zinc molybdate to form a stable strontium molybdate complex. This complex is predicted to form, as shown in Figure 5.19, under conditions of alkaline pH.
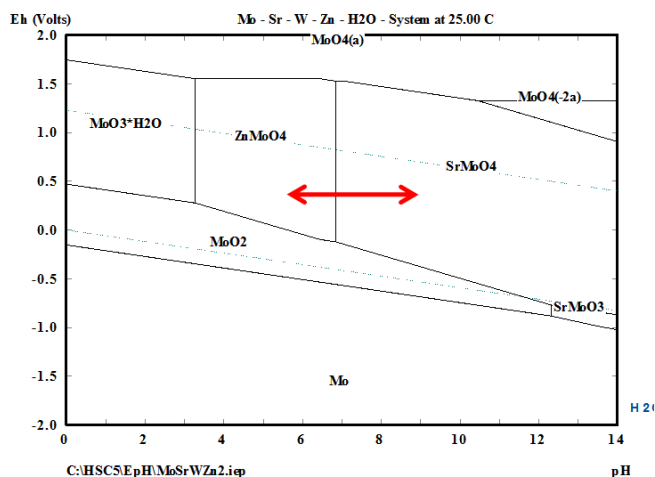
Figure 5.19. Instability of zinc molybdate in the presence of strontium.

In summary, work to date has shown that EDXS spatial mapping of inhibitor fields in primers after simulated weathering confirms some effects, such as silicate distribution and sulfate-assisted mobilization of Pr, that are predictable from solubility measurements, while revealing additional processes, such as chloride ion / titanium interactions and internal reactions of multi-inhibitor systems.

5.5.4.4 Water and inhibitor transport studies in primer films

Application of a standard technique, ASTM D1653-03 [1], "Standard Test Methods for Water Vapor Transmission of Organic Coating Films" established that nonchromate primers are relatively permeable to water vapor (50-100 g/m^2day at 25 um thickness) in the through-plane axis, and that water vapor permeation rates of water-reducible primers can exceed 400 g/m^2day in a state of incomplete cure after drying for 7 days. These effects are shown in Figure 5.20.

The capacitance technique is based on the assumptions that the change in capacitance is due entirely to the water uptake and diffusion into the film. Two models were proposed to understand the effect of the water permeation in coatings on the capacitance measurements [x]. One is discrete model (DM) where the water is uniformly distributed across the film, and the other is continuous model (CM) where a variable water distribution is present in the film.

For a thick paint film like one (about 200 to 300 um) used in this work, the water concentration distribution C(r,t) is not uniform across the film, Figure 5.21(a). According to the CM model, the film can be divided in many parallel infinitesimal thick layers, and each can be represented by a simple equivalent circuit consisting of a resistance dR, in parallel with a capacitance dC, as shown in Figure 5.21.

One-week cure may be insufficient for thick films (~10 mils) of certain primers
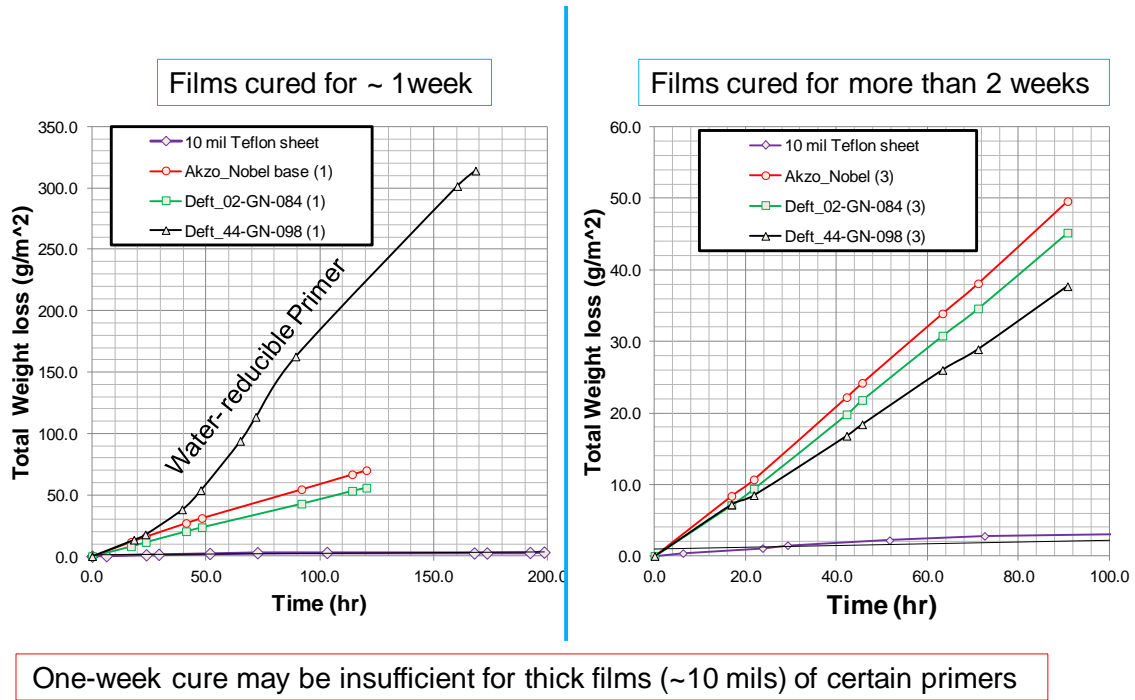
Figure 5.20. Through-plane transport of water vapor through primer films.

(a)

(b)
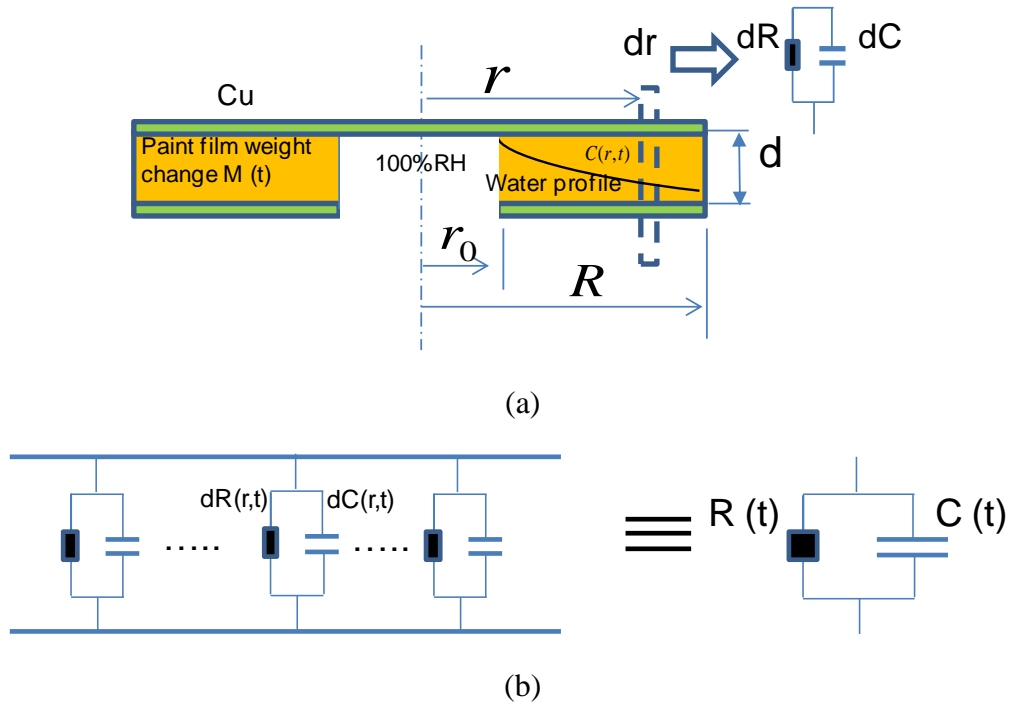
Figure 5.21. (a) Schematic representation of a tested primer film, (b) Equivalent circuit model for the film during in-plane water transport.

The capacitance dC is given by

$$dC = \frac{\varepsilon_0 \varepsilon(r,t) * 2\pi r}{d} dr \tag{5.1}$$

The resistance dR is given by

$$dR = \frac{\rho(r,t)}{2\pi r * dr} d \tag{5.2}$$

where $\rho(r,t)$ and $\varepsilon(r,t)$ are the resistivity and dielectric constant of the paint film, respectively, ε_0 is the dielectric constant of vacuum (8.854 x 10^{-14} F/cm), d is the film thickness, and dr is the infinitesimal thickness.

The total capacitance of the coated film at time t, Ct, can be calculated by integrating Eq.5.1 over the entire electrode areas of the film as follows:

$$C_t = \int_{r_0}^{R} dC(r,t) = 2\pi \int_{r_0}^{R} \frac{\varepsilon_0 \varepsilon(r,t)}{d} * rdr = \frac{2\pi\varepsilon_0}{d} \int_{r_0}^{R} \varepsilon(r,t) * rdr \tag{5.3}$$

The total resistance of the coated film, R(t), can be computed by integrating Eq.5.2 over the entire coated areas of the film, as follows:

$$\frac{1}{R(t)} = \frac{2\pi}{d} \int_{r_0}^{R} \frac{r}{\rho(r,t)} dr \tag{5.4}$$

In order to relate the dielectric constant of the paint film, $\varepsilon(r,t)$, to the water concentration profile $C(r,t)$, the Brasher-Kingsbury equation is used as follows:

$$\varepsilon(r,t) = \varepsilon_{dry} \times \varepsilon_w^{\phi(r,t)} \tag{5.5}$$

$$\phi(r,t) = \frac{C(r,t)}{\rho_w} = \frac{\ln[\frac{\varepsilon(r,t)}{\varepsilon_{dry}}]}{\ln \varepsilon_w} \tag{5.6}$$

$$\varepsilon(r,t) = \varepsilon_{dry} \exp[\frac{\ln \varepsilon_w}{\rho_w} * C(r,t)] \tag{5.7}$$

where $\phi(r,t)$ is the local water volume fraction of each infinitesimal thick layer, ρ_w is the density of water in the film, ε_{dry} and ε_w are the dielectric constant of the dry film and of pure water, respectively.

By substituting Eq. 5.7 into Eq.5.3, the total capacitance, C(t), then becomes

$$C_t = \frac{2\pi\varepsilon_0\varepsilon_{dry}}{d}\int_{r_0}^{R} r * \exp[\frac{\ln\varepsilon_w}{\rho_w}C(r,t)]dr \qquad (5.8)$$

Note that using expansion of the exponential term in a MacLaurin series, Equation 5.8 becomes

$$C_t = \frac{2\pi\varepsilon_0\varepsilon_{dry}}{d}\int_{r_0}^{R} r * \{1 + \frac{\ln\varepsilon_w}{\rho_w}C(r,t) + \frac{1}{2}[\frac{\ln\varepsilon_w}{\rho_w}C(r,t)]^2 + \frac{1}{6}[\frac{\ln\varepsilon_w}{\rho_w}C(r.t)]^3 + \cdots\}dr$$
$$(5.8-1)$$

The total amount of water transported into the film at time t, M(t), is given by

$$M(t) = \int_{r_0}^{R} 2\pi r * C(r,t)dr \qquad (5.9)$$

By substituting Equation 5.9 into Equation (5.8-1), then

$$C_t = C_0 + \frac{\varepsilon_0\varepsilon_{dry}\ln\varepsilon_w}{2d\rho_w}M(t) + \frac{\pi\varepsilon_0\varepsilon_{dry}}{d}(\frac{\ln\varepsilon_w}{\rho_w})^2\int_{r_0}^{R} r[C(r,t)]^2 dr + \cdots$$
$$(5.8-2)$$

For the case where lne/pw << 1, the second-order term of the series can be neglected, then

$$\frac{C_t - C_0}{C_\infty - C_0} = \frac{M(t)}{M(\infty)} \qquad (5.10)$$

Equation 5.10 suggests that the normalized capacitance change from impedance measurements will exhibit the same as the gravimetric measurements.

Radial Diffusion

Given the paint film specimen configuration it is expected that the mass transport of water over time in-plane direction is a radial diffusion process. Assuming that the in-plane water transport follow Fick's second law :

$$\frac{\partial C(r,t)}{\partial t} = D[\frac{\partial^2 C(r,t)}{\partial r^2} + \frac{1}{r}\frac{\partial C(r,t)}{\partial r}] \qquad (5.11)$$

For non-steady state, the water concentration C(r,t) is given by [7]:

234

$$C(r,t) = C(r_0)[1 - \frac{2}{r_0} \sum_{n=1}^{\infty} \frac{\exp(-D\alpha_n^2 t)J_0(r\alpha_n)}{\alpha_n J_1(r_0\alpha_n)}] \qquad (5.12)$$

where J1(x) is the Bessel function of the first order and a is the root of the Bessel function of the first kind of order zero.

$$\frac{M(t)}{M(\infty)} = 1 - \sum_{n=1}^{\infty} \frac{4}{r_0^2 \alpha_n^2} \exp(-D\alpha_n^2 t) \qquad (5.13)$$

where $M(t)$ is the total amount of water vapor diffused into the film at time t, $M(\infty)$ the total amount of water vapor when the film is fully saturated with water vapor (steady state radial diffusion).

For a small time we have [7]

$$\frac{M(t)}{M(\infty)} = \frac{4}{\pi^{1/2}} \bullet \frac{(Dt)^{1/2}}{r_0} - \frac{Dt}{r_0^2} - \frac{1}{3\pi^{1/2}} \bullet \frac{(Dt)^{3/2}}{r_0^3} - \ldots \qquad (5.14)$$

Combining Equations 5.14 and 5.10, for a short time approximation, we obtain

$$\frac{C_t - C_0}{C_\infty - C_0} = \frac{M(t)}{M(\infty)} = \frac{4}{\pi^{1/2}} \bullet \frac{(Dt)^{1/2}}{r_0} - \frac{Dt}{r_0^2} - \frac{1}{3\pi^{1/2}} \bullet \frac{(Dt)^{3/2}}{r_0^3} - \ldots\ldots \qquad (5.15)$$

Equation (5.15) shows that the diffusivity D can be found by numerical analysis of experimental results from capacitive or gravimetric measurements.

It must be pointed out that in deriving equation (5.14), the diffusion is assumed as a non-steady state in an infinite medium, i.e. the outer radius of the paint film is infinite large. As will discussed later, for a finite radial diffusion where the outer radium of the circular cylinder is limited by the size of the tested paint film, the equation (5.14) is valid only up to a point when the diffusion reaches its steady state.

At the beginning of the water vapor exposure, the impedance measurements reveal a fully capacitive behavior. Figure 5.22 shows representative data in the form of Bode impedance and phase angle plots for the primer films under different exposure time, using Ag past or Cu tape as contact electrodes. As shown in Figure 5.22, the films exhibit pure capacitive behavior (slope of -1, and phase angle close to -90 degree) at the beginning (t=0), but begins to deviate from pure capacitive behavior after 24 hr water vapor exposure. The reason for this deviation is the decreasing ionic resistance of the paint film as it becomes hydrated by the water, creating the RC equivalent circuit shown in Figure 5.21b. The film is equilibrated with water vapor after 500 hrs of exposure as evidenced by no significant changes in the measured impedance and phase angle plots.

Another way to interpret above EIS spectra change is to determine the capacitance at a fixed frequency. In this work, the film capacitance was calculated at a fixed frequency of 100 KHz. At

such a high frequency, as shown in Figure 5.21, the film can be represented by a simple equivalent circuit consisting of a resistance R, in parallel with a capacitance C determined by the following equation:

$$C = \frac{-Z''}{2\pi f (Z'^2 + Z''^2)}$$

(5.16)

where Z' and Z" are the real and imaginary part of impedance measured at a fixed frequency of 100 KHz. Table 5.9 shows the initial film capacitance calculated from the EIS data measured using Cu or Ag paste as contact electrodes, respectively. Using these initial film capacitance and corresponding film geometries, the dielectric constant for each film was calculated by the following equation

$$\varepsilon = \frac{d}{\varepsilon_0 A} C_0 = \frac{d}{\pi \varepsilon_0 (R^2 - r_0^2)} C_0$$

(5.17)

where A is the area of the test film covered with Cu or Ag paste whose inner and outer radii are r and R respectively, and ε_0 is the dielectric constant of vacuum (8.854 x 10^{-14} F/cm), d is the film thickness, and Co is the initial film capacitance measured by EIS. To verify the capacitance measurements, 10 mil thick Teflon films from Dupont was also tested using both Cu and Ag paste as contact electrodes. As shown in Table 5.9, the value of dielectric constant of Teflon film measured using Cu tape as contact electrodes is very close to that reported by DuPont [8]. The value of the dielectric constant for the aerospace primer films is about 3-4. Comparing to the measurements using Cu tape, both Teflon and aerospace primer films showed a slightly higher dielectric constants from the measurements using Ag paste as contact electrodes, indicating that some residual water or solvent from Ag paste was absorbed by the films during the experiment or retained from the curing process. Therefore, Cu tape is preferred to Ag paste as a contact material for paint film capacitance measurements.

Table 5.9. Dielectric constants of films calculated from capacitance measurements using Ag paste or Cu tape as contact electrodes.

Film	Thickness (mm)	Contact Electrode	C_0 (F)	ε (Calculated)	ε (Literature)
Aerospace primer	0.268	Ag (paste)	2.95E-10	4.56	3 ~ 4
	0.330	Cu tape	1.65E-10	3.13	
	0.300	Cu tape	2.17E-10	3.75	
Teflon	0.260	Ag (paste)	1.62E-10	2.48	2.06 [8]
	0.260	Cu tape	1.34E-10	2.13	

(a)

(b)

Primer film w/ Cu tape

(c)

Primer film w/ Cu tape

(d)
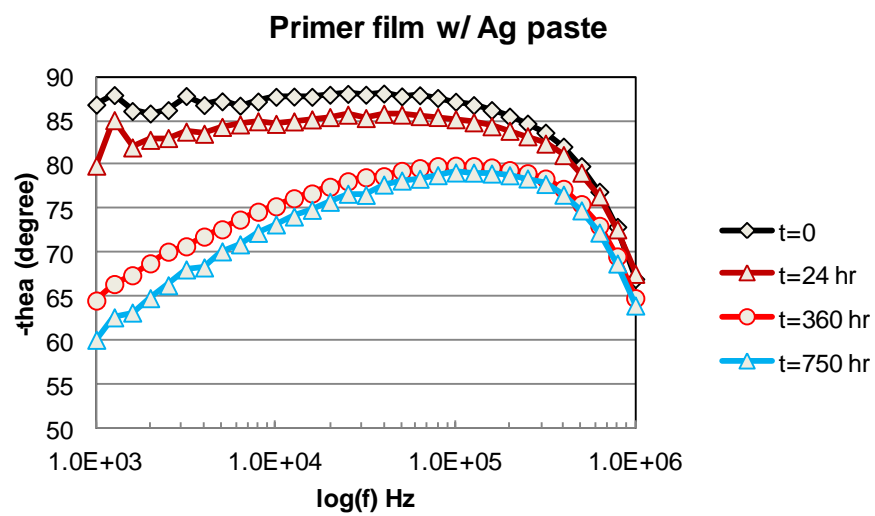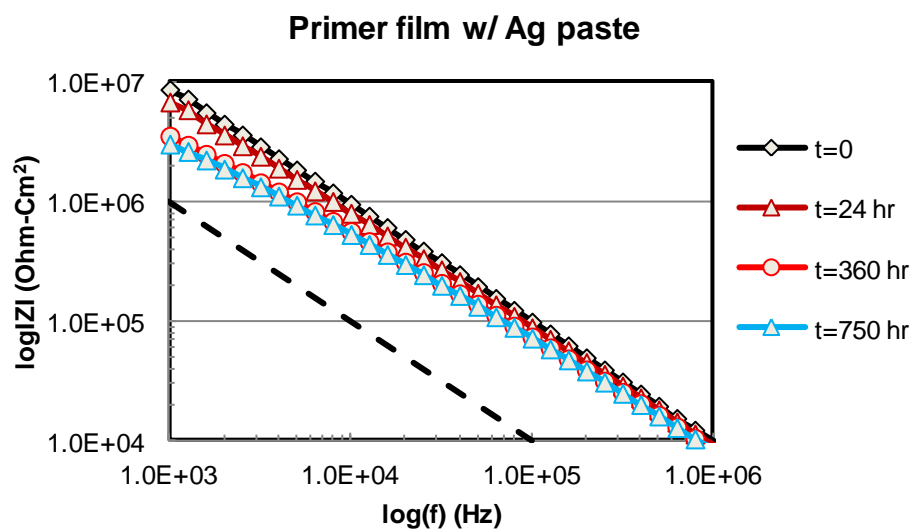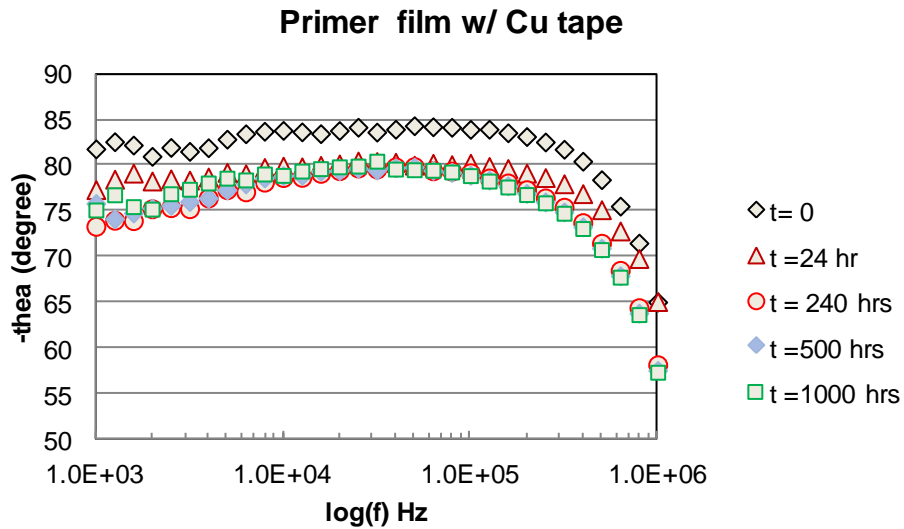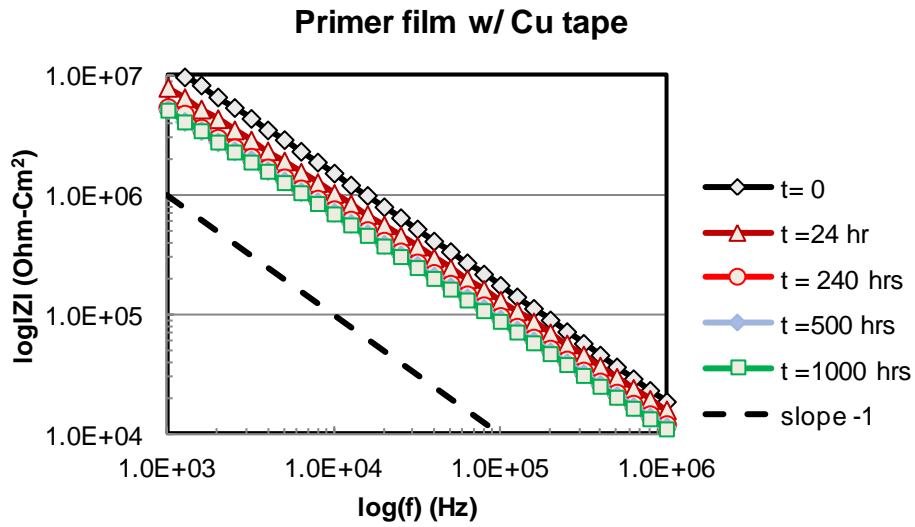
Figure 5.22. Bode plots showing (a, c) Impedance of aerospace primer film at different exposure time, (b, d) Phase angle plot of measured impedance at different exposure time, using Ag paste and Cu tape, respectively.

Figure 5.23 shows typical capacitance evolution as a function of the square root of the exposure time for the primer films, measured using Ag paste and Cu tape as the contact materials,

respectively. The capacitance was observed to increase linearly with the square-root of the exposure time from the initial primer film capacitance C_0 to an equilibrium value of the film capacitance $C\infty$, as shown with arrows on the left and right scales, respectively in Figure 5.25. Two different water vapor transport phases are clearly distinguished: a linear increase of the film capacitance to the square root of the time in the initial stage, which is believed due to the in-plane water vapor transport by non-steady radical diffusion, followed by the appearance of a plateau where the film is fully saturated with moisture, indicating that water vapor transport is occurring at the rate dictated by steady state radial diffusion. Interestingly, the capacitance time decay plots shown in Figure 5.25 are consistent with the models of water (liquid) uptake and transport (through–plane) reported in organic coatings [9]. Noteworthy is that a clear plateau in the capacitance time decay plot must be observed in order to exact the water vapor transport properties from capacitance measurements.
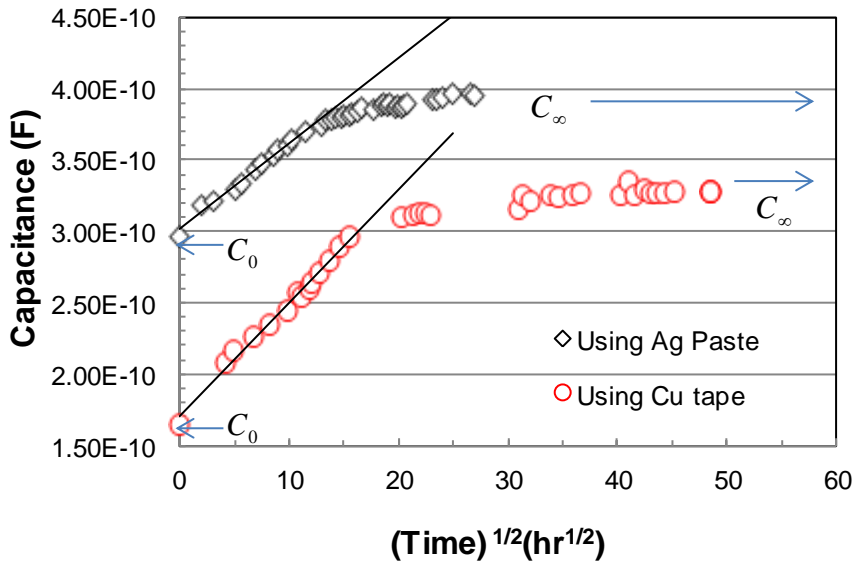
Figure 5.23: Capacitance changes as a function of the square root of the exposed time for primer films measured by Ag paste and Cu tape, respectively.

The capacitance data plotted in Figure 5.23 can also be arranged as the normalized capacitance change $(C_t-C_0)/C_\infty-C_0)$ as a function of the square root of the exposure time. As discussed above, if the radial diffusion of water vapor in a film follows Fick's Laws, all capacitance data plotted as the normalized capacitance change $(C_t-C_0)/C_\infty-C_0)$ must lie on a unique curve as described by Equation (5.14) for a small time:

$$\frac{M(t)}{M(\infty)} = \frac{4}{\pi^{1/2}} \bullet \frac{(Dt)^{1/2}}{r_0} - \frac{Dt}{r_0^2} - \frac{1}{3\pi^{1/2}} \bullet \frac{(Dt)^{3/2}}{r_0^3} - \ldots\ldots$$

(5.18)

239

These results are shown in Figures 5.24(a) and (b) for the primer films measured by Ag paste and Cu tape, respectively. Fitting Equation (5.14) by adjusting the value of diffusivity D to the capacitance data gives diffusion coefficient of about 7.5 and 8.5 x 10-7 cm^2/s for primer films w/ Ag paste and Cu tape, respectively. Note that both diffusivity curves of the equation (5.14) match well with the capacitance data from the initial stage of the water vapor transport when the film capacitance changes linearly to the square root of the exposure time. There exists significant discrepancies between the experimental data and the diffusivity curve described by Equation (5.14), indicating that water vapor transport is no longer under non-steady state diffusion after the initial stage.
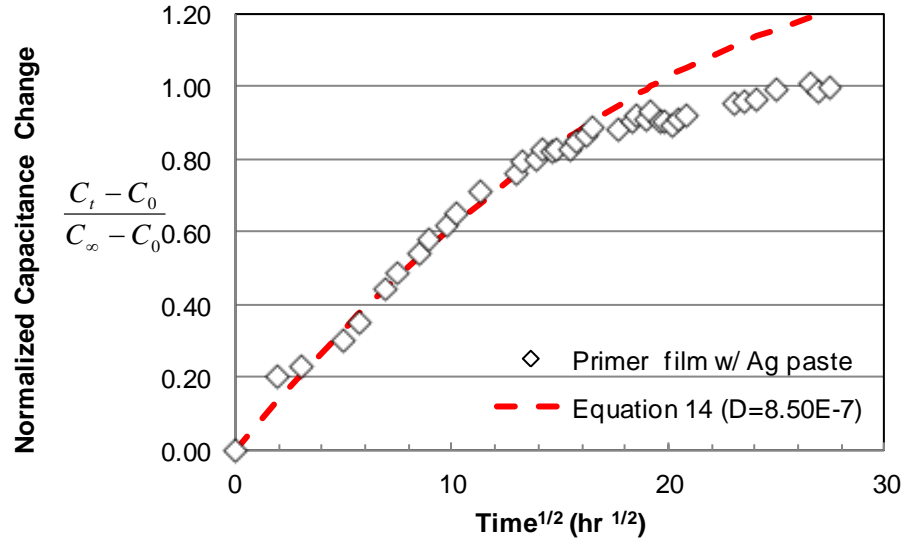
(a)
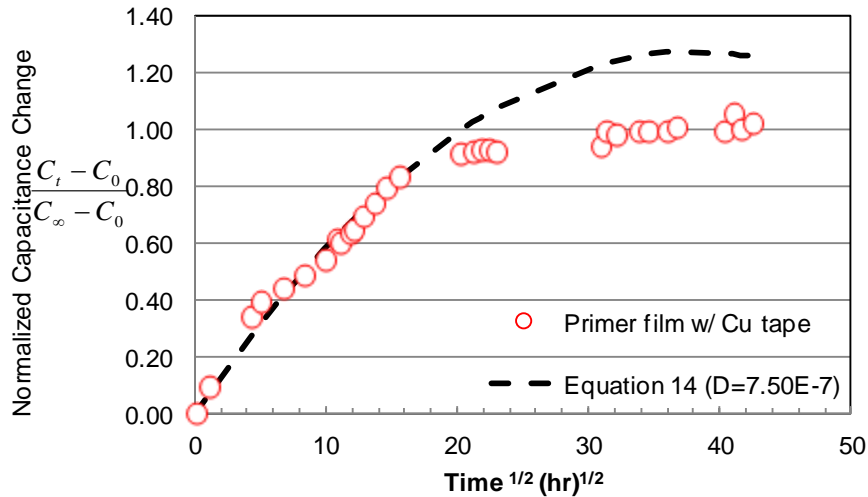
(b)

Figure 5.24: Normalized capacitance measured using Ag paste (a) or Cu tape (b) as contact materials. The dotted lines were determined using Equation (5.14) giving the best fit to the experimental data.

240

For the purpose of validation, the weight loss of one selected paint film sample was measured along with the capacitance measurement. Figure 5.25 shows both capacitance and gravimetric data as a function of the square root of the exposure time. Both the capacitive and gravimetric measurements show two distinct stages: an initial linear increasing to the square root of the exposure time, followed by the appearance of a plateau where both capacitance and weight gain reaches their equilibrium values. Note that the transition timing point for both capacitance and gravimetric data from the linear to the plateau match well each other, indicating that the coating capacitance change is well correlated with the amount of in-plane water vapor transported in paint films.
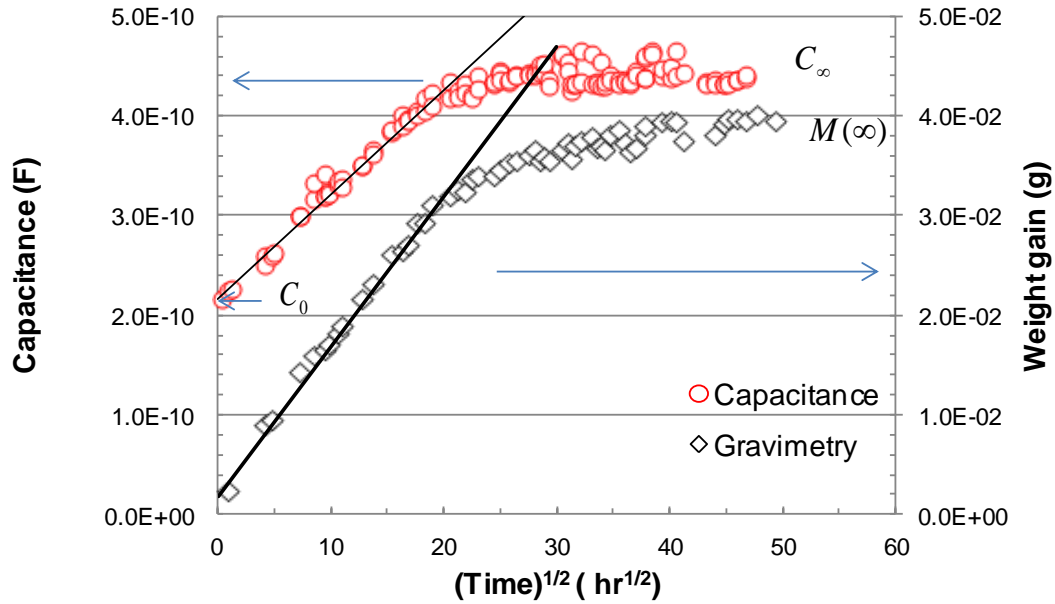
Figure 5.25: Capacitance and mass change as a function of the square root of the exposure time for the primer film measured w/ Cu tape as contact materials.

Now a direct comparison between capacitance and gravimetric measurements can be made. Both capacitance and gravimetric data plotted in Figure 5.25 can be re-arranged as the normalized capacitance/weight change $(C_t-C_0)/C_\infty-C_0)$, and $M(t)/M(\infty)$, and the results are plotted in Figure 5.26 as a function of the square root of the exposure time. The results show that there is reasonable agreement between the capacitance and gravimetric measurements. Figure 5.26 also validates the equation (5.10) in experimental, showing that the normalized capacitance change can be equally translated into the normalized mass change from gravimetric measurements.

By comparison of the in-plane and through plane diffusivity values for water, it is apparent that water vapor transport is considerably higher in-plane compared to through-plane. This effect is attributed to the nanopore structure of primer films, as described below.
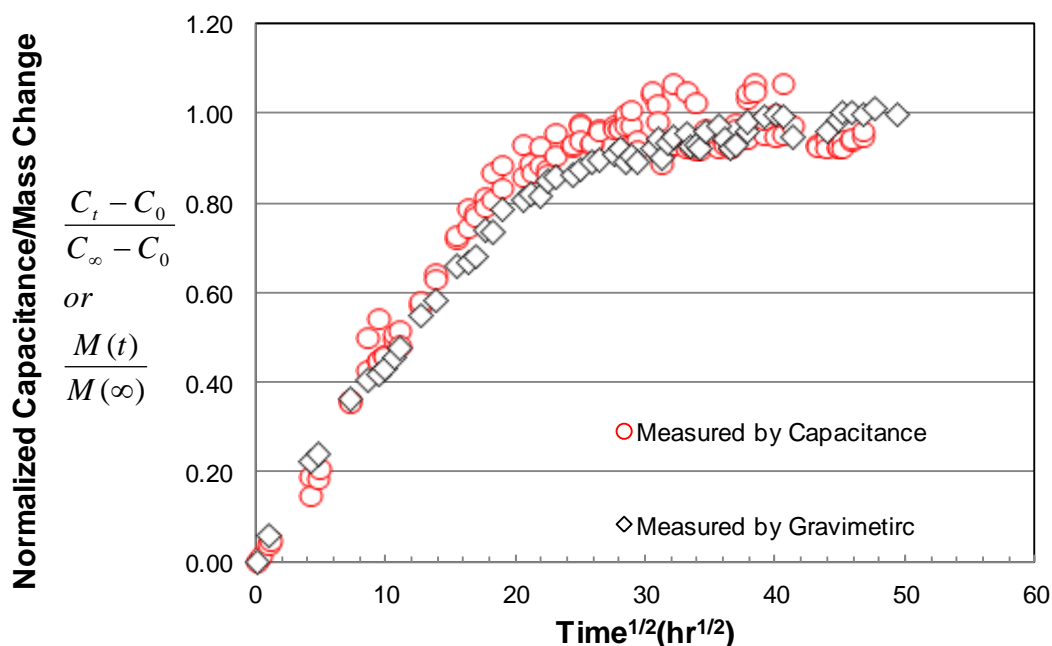
Figure 5.26: Normalized capacitance and mass change as a function of the square root of the exposure time for the primer film measured w/ Cu tape as contact materials.

A series of diffusivity curves described by equation (5.14) can be computed using water vapor diffusivity D as an adjustable parameter. The solid lines in Figure 5.27a and b represent the best agreements between the experimental and computed data, giving the diffusion coefficients of about 4.0 and 5.0 x 10^{-7} cm^2/s, respectively. These results also indicate that there is agreement between the capacitance and gravimetric measurements, which supports the suitability of the capacitance technique for in-plane water transport measurement in the paint film. As discussed above, a significant deviation from the theoretical curves computed for an infinite geometry is observed for long exposure times when water vapor diffusion reaches a steady state.

Table 5.10 summarizes the diffusion coefficients obtained for water vapors in aerospace primer films. The value of diffusion coefficient derived from capacitance measurement is in good agreement with one obtained from gravimetric method. The relatively close agreement between the particle-filled Ag paste and solid adhesive Cu tape measurements indicates that water vapor transport at the interfaces is not a controlling factor.

	(a)		(b)
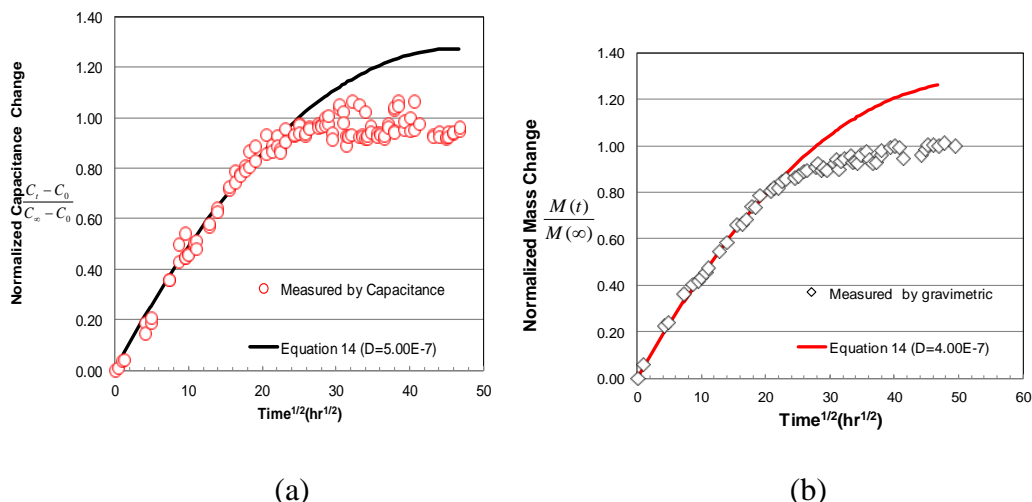
Figure 5.27. (a, b) Normalized mass (a) and capacitance (b) measured using Cu tape as contact materials. The solid lines were determined using Equation (5.14) giving the best fit to the experimental data.

5.5.4.5 Inhibitor transport measurements

The transport of praseodymium ions through aerospace primer films is extremely slow. As shown in Figure 5.28, only trace amounts of Pr are recoverable in a two-compartment diffusion cell in a timeframe of three months. The rate of transport is increased when the originating cell is acidified, and when the soluble Pr concentration in the originating cell is elevated. Overall, the diffusivity of Pr is estimated to be lower than 10^{-10} cm^2/s.

Table 5.10. In-plane diffusion coefficients estimated from capacitance and gravimetric methods.

Paint Films	In-plane Diffusion Coefficient ($x10^{-7}$ cm^2/sec.)			
	Thickness (mm)	Electrode	Capacitance technique	Gravimetric
Aerospace primer	0.268	Ag-paste	8.5	-
	0.330	Cu tape	7.5	-
	0.300	Cu tape	5.5	4.0

243

Inhibitor (Pr^{3+}) Diffusion Through Paint Films

Pr^{+3} transport is significantly slower than water transport through primer films

~ 120 ml

pH 2 ~ 8
X mg/l
Pr^{3+}

pH ~ 6.4

H$_2$O

0.15-0.3 mm thick
Paint film (D~ 20 mm)
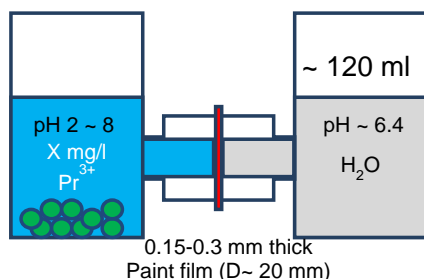
Assuming Fick's diffusion, given D, Pr diffusion across the film (~ 0.3 mm thickness) is estimated as follows:

D (cm^2/s)	Time (hr)	
~ 10^{-7}	~ 2.5	
~ 10^{-8}	~ 25	
~ 10^{-10}	~ 2500	

Donor Side (Pr^{3+} Source)			Paint Film d (mm)	Receptor Side (Pr^{3+} Transported) by ICP			
Pr^{3+} Source	[Pr^{3+}] (ppm)	pH	0.15 ~ 0.3	1 day	1 month	2 month	3 month
Deft paint films	~ 0.3	7.8	Model epoxy	< 0.1	< 0.1	< 0.1	< 0.1
Pr(OH)$_3$	~ 5	6.4	Model epoxy	< 0.1	< 0.1	< 0.1	< 0.1
	~ 100	2.0		< 0.1	< 0.1	0.16	0.22
	0	6.4	Deft film	< 0.1	< 0.1	< 0.1	< 0.1
	~100	2.0		< 0.1	0.12	0.20	0.25
PrCl$_3$*xH$_2$O	~ 50	5.5	Deft film	< 0.1	0.14	0.18	0.24
	~130	5.5		< 0.1	0.16	0.20	0.25

Figure 5.28. Pr inhibitor diffusion through paint films.

The electrochemical behavior of 2024-T3 Al in a dilute salt solution containing free films of a Pr-base inhibitive primer is shown in Figure 5.29 as a function of time. No significant indication of corrosion inhibition was detected in this test.

5.5.4.6 Migration of inhibitors in electric fields

We used XPS to explore the oxidation states and compositional changes of inhibitor species (Pr) in primer films. XPS spectra of Pr 3d from both sides of Deft 02-GN-084 primer film, after being exposed to 10 V DC for 120 h, are shown in Figure 5.30 (a-b). The detailed shape of Pr 3d$_{5/2}$ peaks can be fitted by a multipeak Gaussian deconvolution procedure to extract the peak position and intensities. Both sides of the sample showed a peak at about 933eV. The negative side showed a 928 eV peak where the positive side did not. The positive side showed a peak in the 935 eV range that was not seen on the negative side. The position of the measured Pr 3d$_{5/2}$ peak may reflect the weighted average of two different oxidation states of Pr, associated with two binding energies. It was reported that the 3d$_{5/2}$ binding energy is 935.2 eV for Pr^{4+} and 933.2 eV for Pr^{3+} [10,11]. This would imply that the post-DC biased primer film surfaces consist of two different charge states of Pr-ion, and that Pr^{3+} is dominated on the negative side as a result of

Pr ion migration in electrical fields. A sample of laboratory synthesized $Pr(OH)_3$ was also analyzed in the XPS and the general peak shape (Figure 5.30c) matches the results obtained from the negative electrode side of the primer film. However, there is an approximately 0.6 eV difference in the lower binding energy peak.
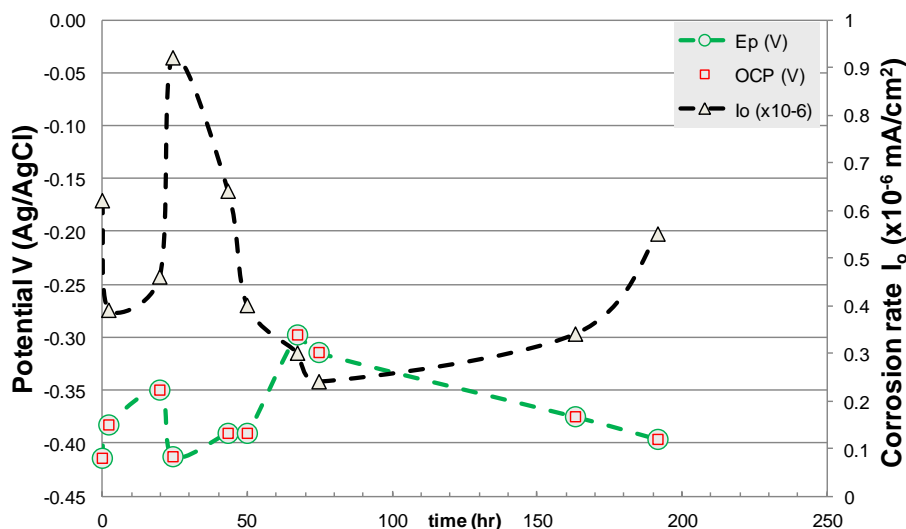
Figure 5.29. Effect of Pr inhibitor leaching on AA2024-T3.

To get a semi-quantitative comparison of Pr concentration between the positive and negative sides, the primer film was sputtered using the ion gun for 8 minutes (approximately 20 nm on Ta_2O_5 standard) on both the positive and negative electrode sides. Analysis shows the negative side continues to demonstrate a Pr peak in the range of 928 eV while the positive side does not, and both sides had peaks in the 933 eV range. Figure 5.31a and b shows the semi-quantitative results of different elements obtained from the XPS survey scan on the Deft primer film after 20 nm sputtered. The negative side shows a significant higher in both Pr and S than those from the positive side, which further indicates that Pr-ions migrated from the positive side to the negative side.

The interpretation we place on this is that, in the hydrated primer film, the cation complex $PrSO_4^+$ predominates over the anion complex $Pr(SO_4)_2^-$ consistent with the thermochemical prediction shown in Figure 5.11. The cation complex of Pr will be favorably transported to cathodic sites, such as intermetallic particles, on the alloy surface by the local ionic current, where alkaline hydrolysis is expected to precipitate a locally-passivating $Pr(OH)_3$ film. Similarly, the anion complex $Pr(SO_4)_2^-$ should be favorably transported to anodic sites such as active pits where it is expected to remain in solution. Regulation of the positive charge of the soluble Pr complex is a strategy to consider in further improvements to this inhibitor family.
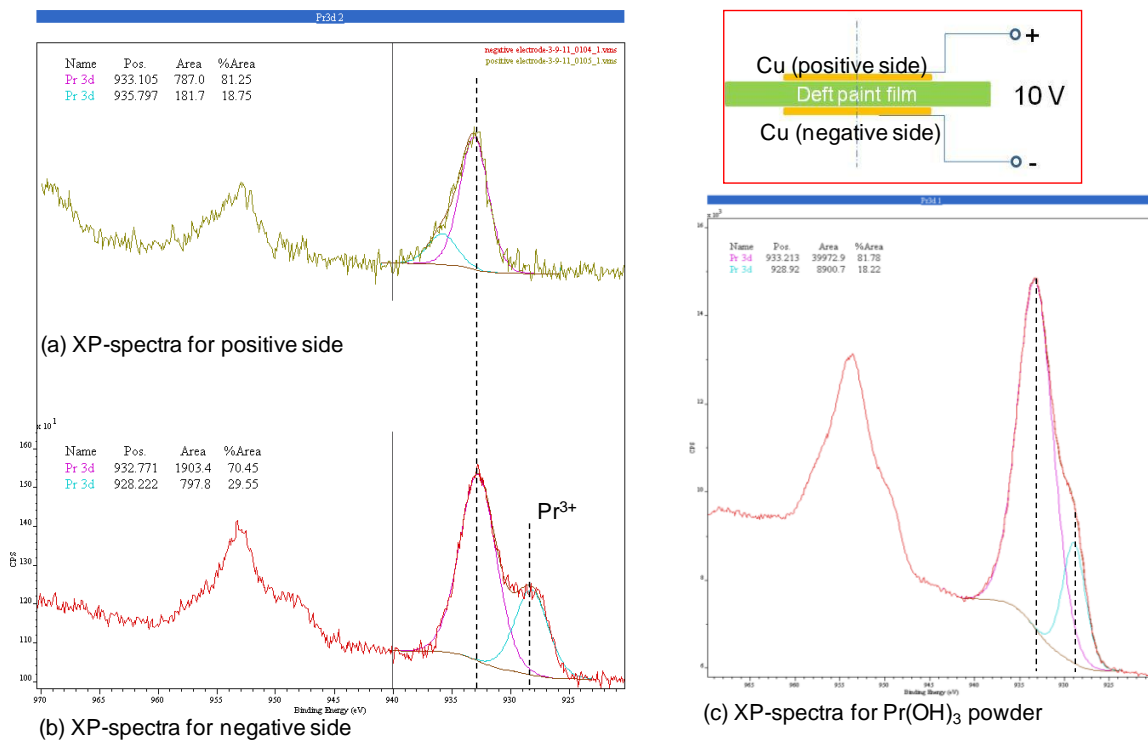
Figure 5.30. The XPS spectra of Pr 3d for the Deft primer film after being electrically biased at 10V DC for 120 hrs, high resolution XP-spectrum of (a) positive side; (b) negative side; in comparison with the corresponding Pr 3d spectrum of (c) $Pr(OH)_3$ powder.
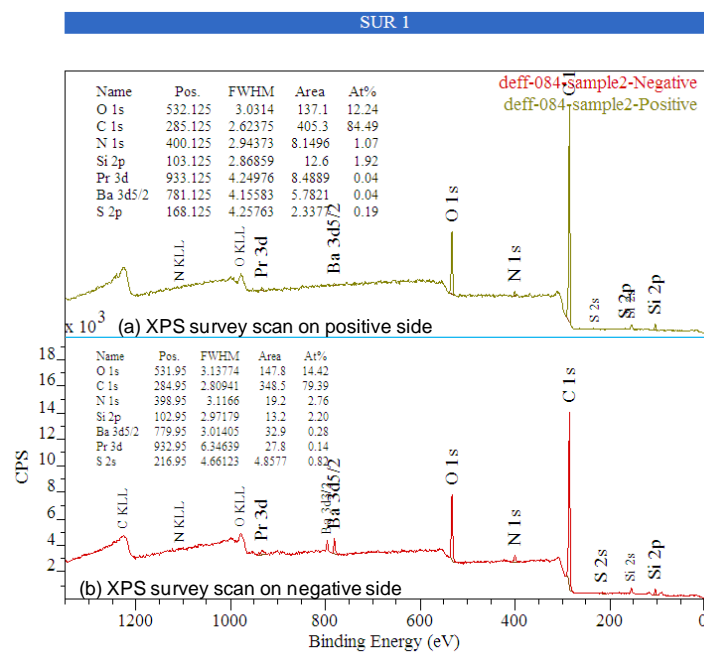
Figure 5.31. The XPS survey scan on the Deft primer film after 20 nm sputtered (a) positive side; (b) negative side, showing a significant higher content in Pr and S than those on the positive side.

5.5.4.7 Nanopore structure characterization of primer films

<u>Bulk Free Volume</u>

In standard PAL, one uses the well-established relationship between ortho-Positronium (o-Ps) pick-off lifetime (τ_3 in a few ns) and spherical free-volume hole radius R (in a few Å), as defined by the following semi-empirical equation [5.12-5.15]:

$$\tau_3 = 0.5 \cdot \left[1 - \frac{R}{R_0} + \frac{1}{2\pi} \sin\left(\frac{2\pi R}{R_0} \right) \right]^{-1} \qquad [5.19]$$

where, τ_3 (o-Ps lifetime) and R (hole radius)are expressed in ns and nm units, respectively, and R_0=R+DR where DR is a constant for an electron layer thickness (1.66 Å).

Similarly, the free-volume hole size V_h is defined as the following Eq:

$$V_h = \frac{4 \cdot \pi \cdot R^3}{3} \qquad [5.20]$$

Lifetime measurements of the positron in primer films also allow the estimation of the fractional free volume, ffv(%), by using the semi-empirical equation [5.16]:

$$ffv(\%) = A \times I_3 \times V_h \qquad [5.21]$$

where I_3 is the relative intensity of the o-Ps lifetime component, V_h is the free volume of the single hole (in nm^3), and A is the normalization constant.

The positron lifetime spectra were analyzed using the PATFIT-88 package program. The measured PALS spectra were well resolved into three components (τ_1, τ_2 and τ_3) with their intensities (I_1, I_2, and I_3) after the background and positron source correction was subtracted. As discussed above, the third component τ_3 (the longest-lived component) is assigned to the pick-off annihilation of ortho-Positronium (o-Ps) in the free volume holes within the films. Since the cast primer films have a thickness ranging between 240 and 370 mm. Two pieces of identical primer film samples are stacked together to assure a suitable thickness (> 300 mm) for average lifetime measurement. The stacked film samples were oriented to have both the front faces (face-to-face) toward the positron source. After analysis of the front face, the same sample was reoriented to have the reverse faces towards to the positron source (back-to-back), or to have a mixed faces (mixed faces). In addition, samples were also analyzed before and after exposure to beam conditions, labeled as before and after vac. in the sample orientation column of the table. The results of bulk PALS measurements are presented in Table 5.11 and Table 5.12. Only the lifetimes and the intensities of the longest-lived component of the positron lifetime spectrum have been summarized because they were used to calculated the free volume radius, R, free volume size, Vh, and fractional free volume, ffv(%) values according to the Eq. [5.17-5.19].

As shown in Tables 5.11 and 5.12, there is almost no effect of the beam exposure on the bulk free volume measurements. Also it seems that there is no significant influence of sample orientation on the bulk free volume results except for those freshly prepared Deft-098 samples, indicating that the nature of heterogeneity exists in the freshly-prepared water-borne Deft-098 films. The average free volume radius R for a spherical hole was estimated to be 0.300 nm for aged Deft-084 films, 0.285 nm for aged Deft-098 films, respectively.   In comparing the results of the same Deft-098 sample with different curing time, 7-day vs. 21-day, the average free volume radius R was estimated to be about 0.295 nm for the 7-day cured sample, showing only a little larger than that of the 21-day cured condition with the average free volume radius of 0.286 nm, very close to that of the aged Deft-098 film.

Table 5.11. Bulk free volume results for both Deft-084 (aged > 1year) and Deft-098 (aged> 1year).

PAL run	Sample orientation	Deft-084 (aged > 1year)				Deft-098(aged > 1year)			
		τ3 (ns)	I3 (%)	R (Å)	ffv (%)	τ3 (ns)	I3 (%)	R (Å)	ffv (%)
1	Mixed faces, before vac.	2.13	7.58	2.97	1.50				
2	Mixed faces, before vac.	2.21	7.04	3.04	1.50				
3	Face-to-face, before vac.	2.21	6.55	3.04	1.39	1.98	8.01	2.84	1.38
4	Back to back before vac.	2.17	7.28	3.01	1.49	2.04	5.94	2.89	1.08
5	Face-to-face, after vac.	2.18	7.22	3.02	1.50				
6	Back to back after vac.	2.14	6.19	2.98	1.24				
Avg	Face-to-face			3.03	1.44			2.84	1.38
Avg	Back-to-back			3.00	1.37			2.89	1.08
Avg	Mixed faces			3.01	1.50				

Table 5.12. Free volume results for Deft-098(aged> 1year), Deft-098(7-day) and Deft-098(21-day).

PAL Run	Sample orientation	Deft-098(aged > 1year)				Deft-098(7-day)				Deft-098(21-day)			
		τ3 (ns)	I3 (%)	R (Å)	ffv (%)	τ3 (ns)	I3 (%)	R (Å)	ffv (%)	τ3 (ns)	I3 (%)	R (Å)	ffv (%)
1	Face-to-face, before vac.	1.98	8.01	2.84	1.38	2.14	9.23	2.98	1.84	2.00	11.22	2.86	1.98
2	Back to back before vac.	2.04	5.94	2.89	1.08	2.10	6.52	2.94	1.25	1.99	6.83	2.84	1.19
3	Face-to-face, after vac.					2.08	10.44	2.93	1.98	2.01	10.28	2.86	1.82
4	Back to back after vac.					2.10	5.66	2.95	1.09	2.02	6.83	2.87	1.22
Avg	Face-to-face			2.84	1.38			2.95	1.91			2.86	1.90
Avg	Back-to-back			2.89	1.08			2.94	1.17			2.86	1.20

It has been suggested [14] that molecular transport (diffusion) through glassy polymer depends strongly on the amount of free volume or space not occupied by polymer chains. Free volume, whether static voids created by inefficient chain packing or transient gaps generated by thermally

induced chain segments rearrangements, presents diffusing molecules with a low resistant pathways for transport. Diffusion occurs only when the motion of the polymer chains results in a free volume hole large enough for the penetrant to enter. As reported previously, and shown in Figure 5.32, Deft-098 film showed a significant drop in water vapor transport rate when the curing time increased from about 1-week to 2-weeks while Deft-84 showed only a slight decrease in water transport rate with an increase in curing time from five days to ten days. Beyond this point, the water transport rate seems little change with curing time for both Deft primer films. The water vapor transport behavior of the systems makes it appear that the Deft-098 may experience great changes in the amount (or the size) of free volume during the early curing stage.

From the bulk free volume measurements in Tables 5.11 and 5.12, it appears that the early curing stage from 7-day to 21-day does not produce any significant changes in both free volume radius R and fractional free volume ffv(%). In other words, the variations of these values are not large enough to support that there is any correlations between the free volume and water vapor transport properties. It is possible that water vapor may respond differently to changes in polymer structure because of its ability to interact strongly with the polymer via hydrogen bonding. To further explore the nature of the free volume distribution within the primer films, the coupling of PALS with a variable mono-energetic positron bean source was performed on those bulk PAL tested film samples.
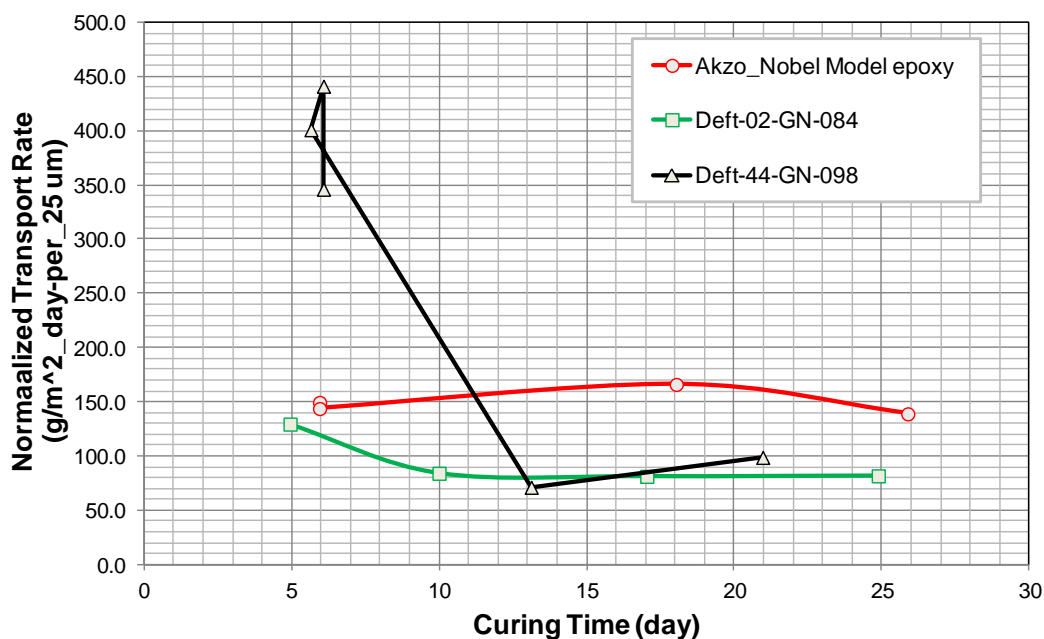
Figure 5.32. The effect of curing time on normalized water vapor transport rates.

Free-Volume Depth Profile

249

When a positron with well-defined energy is injected from a vacuum into a polymer, it either reflects back to the surface or penetrates into the polymer. The fraction of positrons penetrating the polymer substrates increases rapidly as a function of positron energy. The mean implantation depth of the positron as a result of inelastic interactions with polymer molecules is given in nm by [17]:

$$d(E) = \left(\frac{400}{\rho}\right) \cdot E^{1.6}$$ [5.22]

where r is the polymer density in g/cm^3, and E is the incident energy in keV.

In DBES, the obtained DBES spectra were characterized by an S-parameter, defined as a ratio of integrated counts between E_1=509.41 and E_2=512.59 keV (the central part) to the total counts after the background is properly subtracted, expressed as follows [17]:

$$S = \frac{\sum_{E_1}^{E_2} N(E_i)}{\sum_{Ei=0}^{\infty} N(E_i)}$$ [5.23]

Since the S parameter represents the relative value of the low momentum part of positron-electron annihilation radiation, it is sensitive to the change of the positron and Positronium (Ps) states due to microstructural changes. When the positron and Ps are localized in a hole or free volumes with finite size, the observed S-parameter is a measure of the momentum broadening according to the uncertainty principle: a larger hole results in a larger S parameter value and the amount of *para*-Positronium (*p*-Ps, singlet state). The S parameter has been successfully used in detecting free volume depth profile in polymeric systems.

Figure 5.33a shows the S parameter curve versus positron energy for Deft-084 (aged >1year) sample. The solid line in the plot represents the mean depth (using Eq. [5.22]) of positron penetration a function of energy. As shown in Figure 30, S parameter significantly varies with positron incident energy. At very low energy, S increases as positron energy increases, reaches a maximum at approximately 2.5 keV (at the depth about 100 nm from the surface). The S parameter shows decreasing with the positron energy with larger than 4 keV. This decrease is attributed to the effect of the pigments such as TiO_2 in the film as Ti contains high-momentum d electrons. Then, the S parameter decreases gradually, and finally reaches close to a constant value after 20 keV.

The S-parameter depth profile curve as shown in Figure 5.33b is typical for slow positron data near the surface of polymers, which contain a large fraction of sub-nanometer defects. As the positron penetrates further into the bulk, an increased Ps formation is also expected, mainly due to the S parameter from p-Ps annihilation in polymers. On the other hand, the S parameters decreases in solids, which do not contain a large fraction of defects, such as oxides or semiconductors. This occurs because as the positron energy increases, there is a decrease in free Ps escaping from the surface.

The presence of a peak in S parameter depth profile is an indication of a multilayer structure in the film from annihilation characteristic difference between those layers. From the variation of S parameter depth profile in Figure 5.33b, it suggests that there exists approximately 100 nm of polymer skin from the surface of the aged Deft-084 primer film. Inside the polymer skin there exists an intermediate transition layer (about 0.1-2.5 mm thickness) where pigments start to disperse with the polymer and other additives. Beyond the transition layer it is the bulk layer of the primer film where the S-parameter remains close to a constant with the depth.
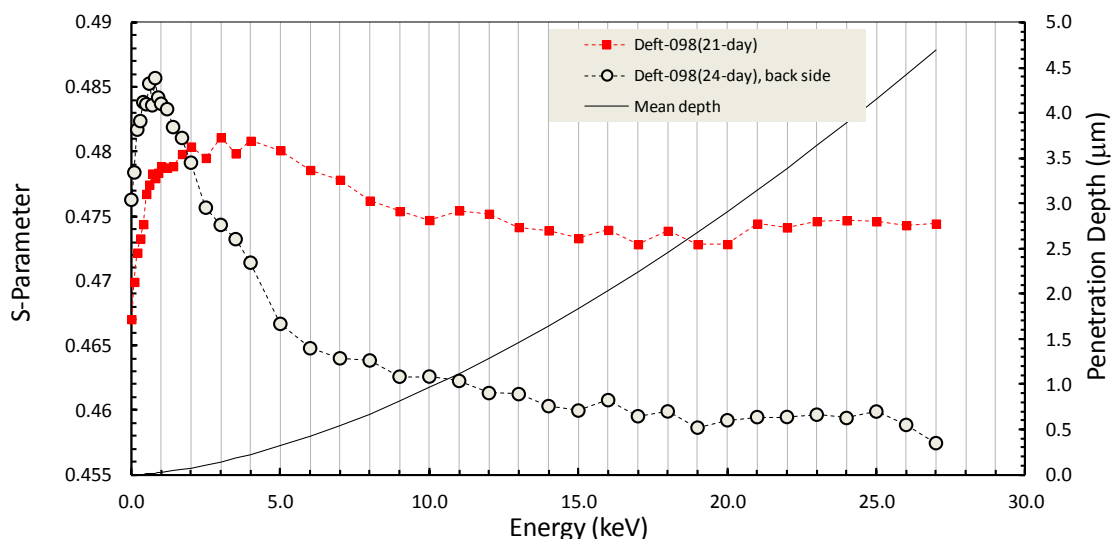
(a)
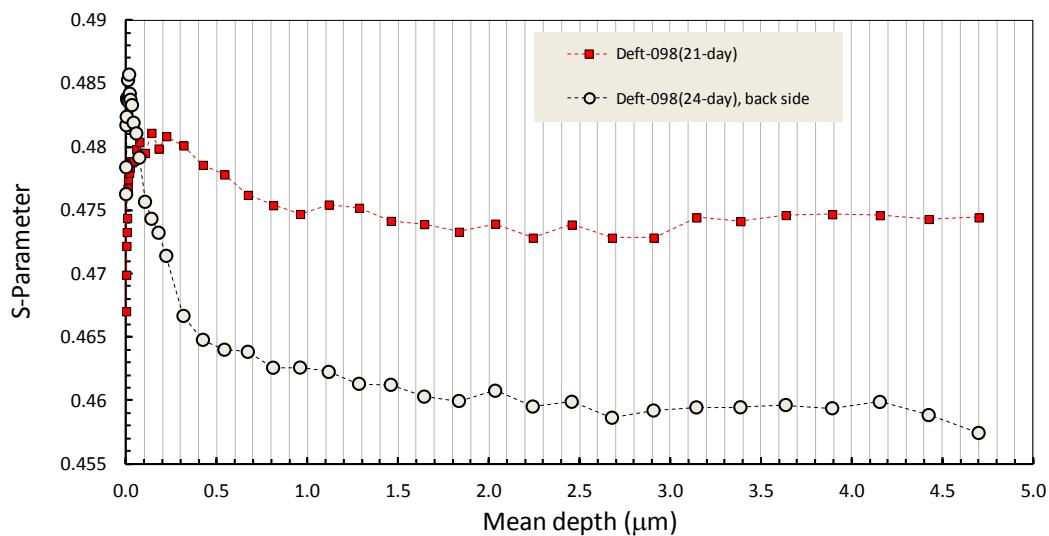
(b)

Figure 5.33. S parameter for aged Deft-084 film (a) as a function of positron incident energy (b) as a function of mean depth.

Figure 5.34a and b show the S-parameter energy and depth curves for the same water-borne Deft-098 primer film sample cured for 7-day and 21-day at room temperature, respectively. It is apparent that the variations of the S-parameter follow the same trends as those observed in solvent-based Deft-84 films aged for more than one year. There is an initial increase in the S parameter to a maximum value. The film also consists of three different layer structures near the surface: a polymer skin, an intermediate transition and bulk layer. It seems that there is no significant effect of curing time on film nanopore structure as identified from the S-parameter depth characteristics.
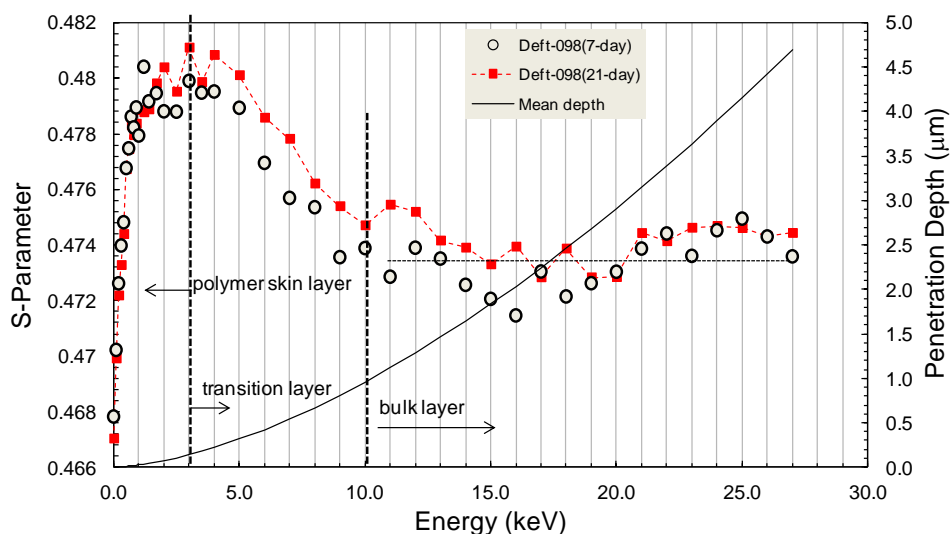
(a)
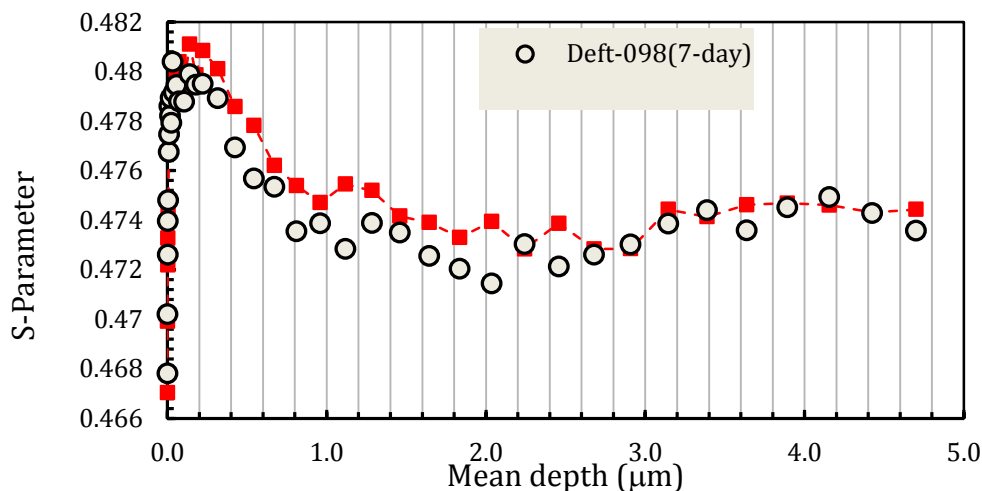
(b)

Figure 5.34. S parameter for 7 and 10 day cured Deft-084 film (a) as a function of positron incident energy (b) as a function of mean depth.

Figures 5.35a and 5.33b show the S-parameter energy and depth curves for the same water-borne Deft-098 primer film sample cured for 21 days at room temperature. From 5.35b, the "back" side of the sample (interface with the substrate during curing) has a much lower density of nanopores arranged closer to the surface compared to the "front" side or air interface.
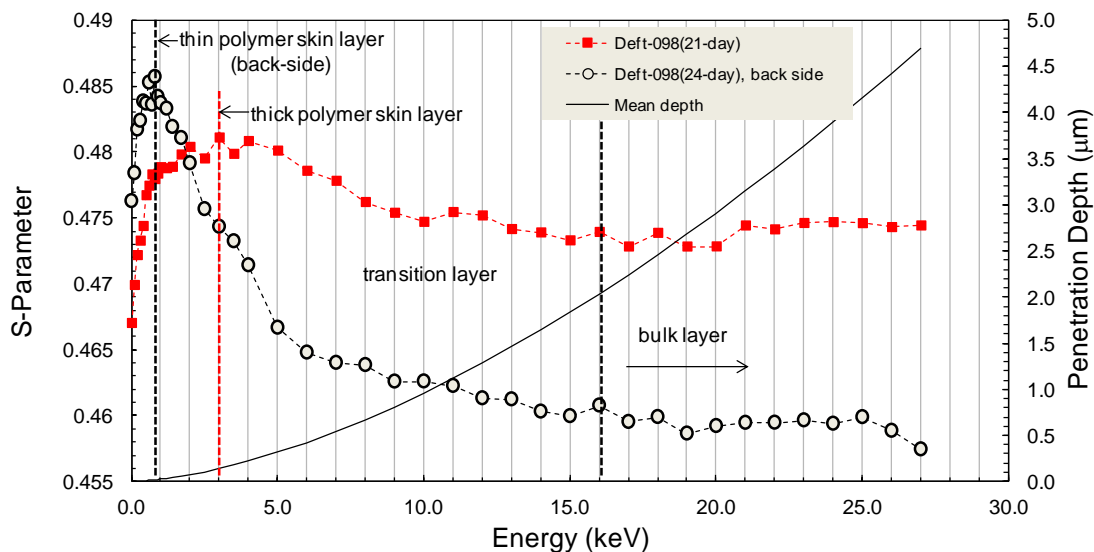
(a)
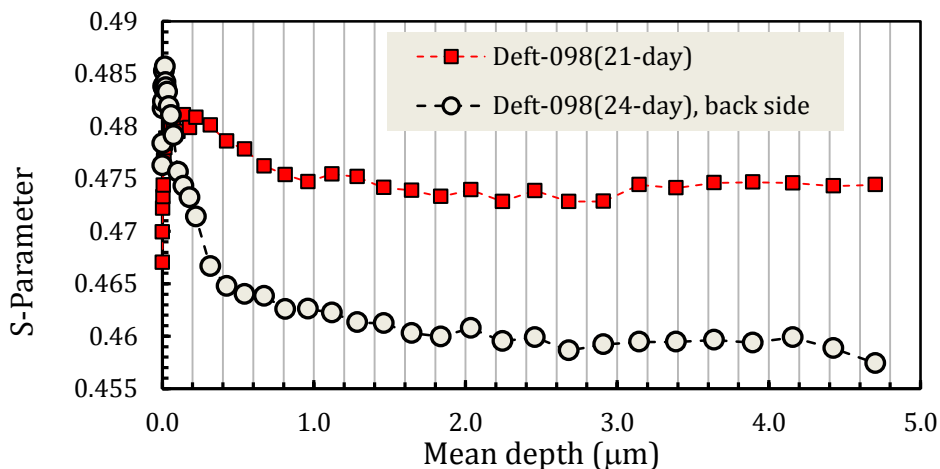
(b)

Figure 5.35. S parameter for 21 and 24 day cured Deft-084 film (a) as a function of positron incident energy (b) as a function of mean depth.

The R parameter is also obtained from DBES spectra. The R parameter is defined as the ratio of the total counts from the valley region with an energy with a width between 364.2 keV and 496.2 keV (which is from 3γ annihilation) and the total count from the 511 keV peak region with a

width between E_1= 504.35 and E_2= 517.65 keV (which is from 2γ annihilation). The R parameter provides information about the existence of large pores (nm to μm), where *o*-Ps undergoes 3γ annihilation while the S- parameter is from o-Ps 2γ radiation (pick-off annihilation) in free volumes (Å to nm) in a sample. As shown in Figures 5.36 (a) and (b), there is almost the same for R-parameters for the same water-borne Deft-098 primer film samples cured for 7-day and 21-day at room temperature, respectively. In other words, it implies that there is no significant effect of curing time on film structure in term of large pores (nm to μm). In addition, from Figures 5.37a and b, a direct comparison of the R-parameter depth curve shows some difference between the front face-oriented and back-side for Deft-098 sample, indicating that on the surface of the back-side there exist much larger sized pores than the front surface.
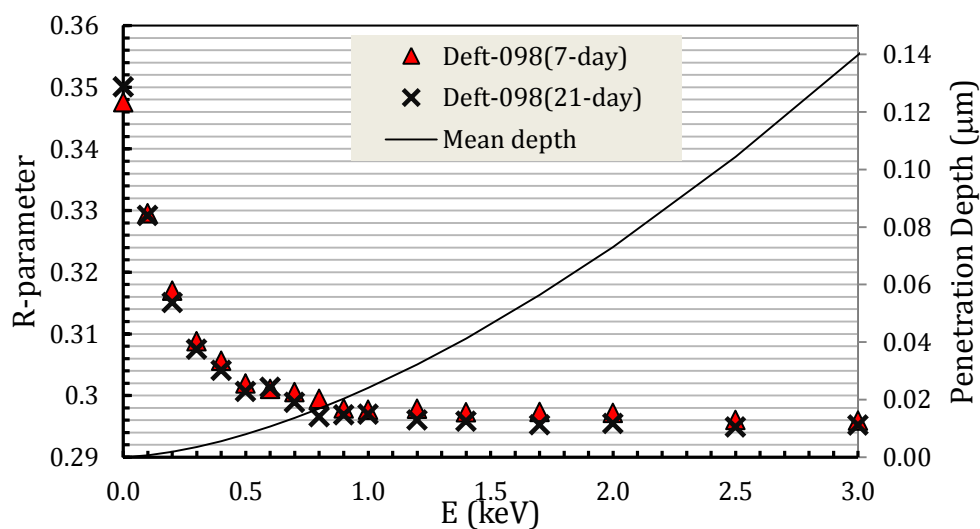
(a)
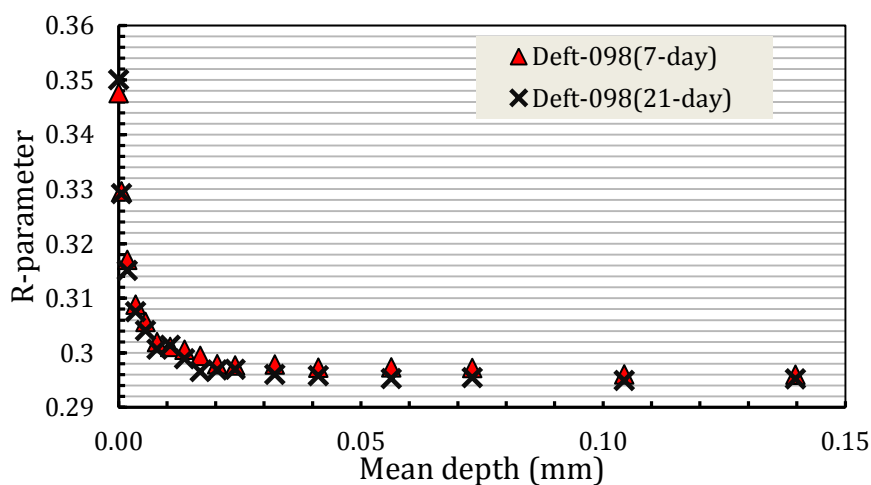
(b)

Figure 5.36. R parameter for 7 and 21 day cured Deft-084 film (a) as a function of positron incident energy (b) as a function of mean depth.

254
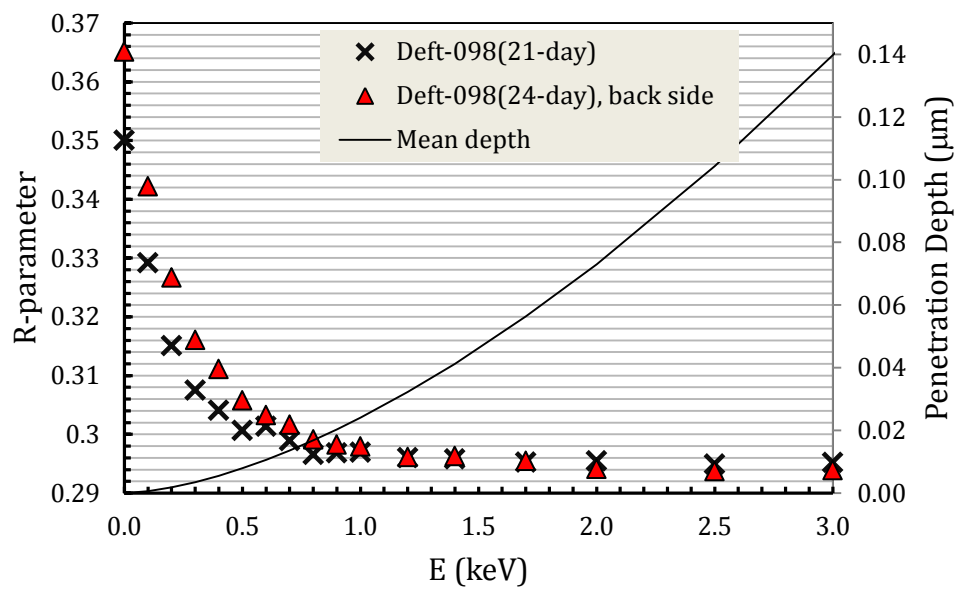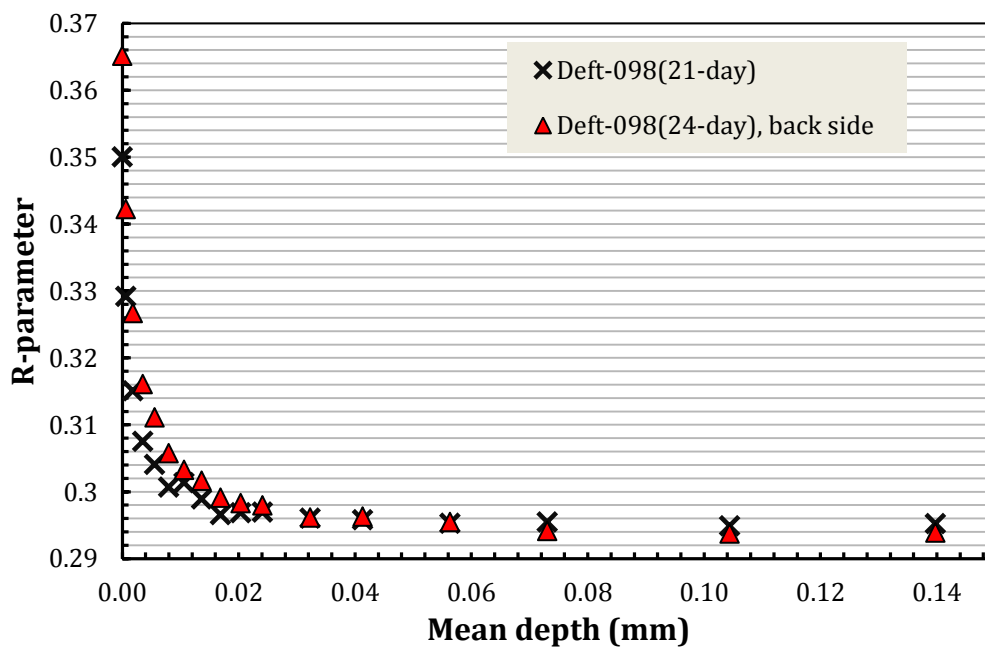
Figure 5.37. R parameter for 21 and 24 day cured Deft-084 film (a) as a function of positron incident energy (b) as a function of mean depth.
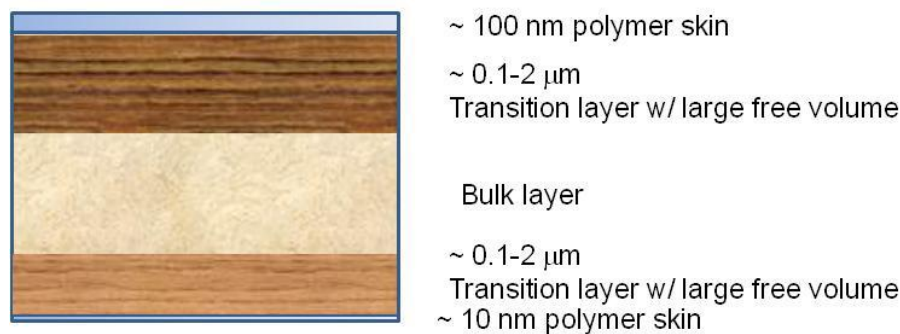
Figure 5.38. Schematic of proposed multiple-layer structure for cast primer films.

In summary, from the variations of the *S* parameter and the R-parameter together with bulk free volume measurements we propose a multiple-layer structure model for cast free primer films, composed of a polymer skin layer near the surface, an intermediate transition layer, and bulk layer, as schematically shown in Figure 5.38 for solvent and water-borne primer films. Because of relatively large free volume (i.e. large R radius and ffv(%)) associated with transition layer below the skin layer, the primer films are expected to show strong anisotropic behavior of water vapor transport in term of in-plane versus through-plane water vapor transport rates, as reported previously.

5.5.5 Conclusions and Implications for Future Research

The conclusions drawn from this task are that the activity of modern chromate-free pigments depends on reactions both with their environment and with their internal co-pigments. The knowledge gained of these reactions and their importance will be of value in both the modeling of present-day inhibitive coatings and in designing future generations of protective coatings systems. For example, the $Pr(OH)_3$ inhibitive pigment was found to be activated in the primer through reaction with a support pigment, $CaSO_4$, to produce both the cationic and anionic praseodymium sulfate complexes, of which only the cation complex is presumed to be an active inhibitor. The effectiveness of an inhibitive coating system also strongly depends on the transport characteristics of the coating matrix. Existing primer systems were found to transmit water vapor at high rates, but to transport inhibitive species at very slow rates that may be sub-optimal. The rate of water vapor and presumably inhibitor transport in primer films was found to be highly isotropic in a manner that is consistent with the nanopore structure detected in primer films. The existence of this transport network and its apparent tractability to alteration creates the prospect for the engineering of controlled transport properties into future generations of primer films.

5.5.6 Literature Cited

1. *ASTM, D1653, Standard Test Methods for Water Vapor Transmission of Organic Coating Film (2008).*

2. J. J. Chen, et al. Cement and Concrete Research. 34 (2004) 1499.

3. R. C. Newton, et al. Geochimica et Cosmochimica Acta, 70 (2006) 5571.

4. F. P. Glasser, et al. Advances in Cement Research. 17 (2005) 57

5. T. M. Letcher, "Thermodynamics, solubility, and environmental issues", P 130.

6. http://www.ktf-split.hr/periodni/en/abc/kpt.html

7. J. Crank, The Mathematics of Diffusion, Oxford University Press, 1975.

8. 8. Dupont Corp. Website:

9. http://www2.dupont.com/Cabling_Solutions/en_US/assets/downloads/h26580.pdfF. Deflorian, L. Fedrizzi, S. Rossi, et al., Electrochimica Acta 44, (1999) 4243

10. D. D. Sarma and C. N. R. Rao, J. Electron Spectrosc. Relat. Phenom. 20, 25 (1980)

11. A. Fissel, J. Dabrowski, and H. J. Osten, Journal of Applied Physics, Vol.91, No. 11 (2002)

12. S. J. Tao, J. Chem. Phys. 56 (1972) 5499

13. M. Eldrup, D. Lightbody, J. N. Sherwood, Chem. Phys. 63, 51(1981)

14. Z.F. Wang, B. Wanga, N. Qia, X.M. Ding, J.L. Hu, Materials Chemistry and Physics, 88 (2004) 212–216

15. S. Sellaiyan, S V Smith, A. E. Hughes, A Miller, D. R. Jenkins and A. Uedono, Journal of Physics: Conference Series 262 (2011) 012054

16. A. Danch, W. Osoba, Fibres and Textiles in Eastern Europe, Vol.11, No. 5 (2003) 126-127

17. H. Cao, R. Zhang, C. S. Sundar, J.-P. Yuan, Y. He, T. C. Sandreczki, and Y. C. Jean, Macromolecules, 31 (1981) 6627-6635

5.6 Task 6: Interactions between polymer matrix, pigment, surface treatment, and alloy

Objectives
The objective of this task was to use electrochemical testing, exposure testing, and destructive forensic techniques based on electron microscopy to evaluate the corrosion protection and corrosion protection mechanisms of emergent chromium-free coating systems.

5.6.1 Evaluation and Ranking of Emergent Cr-Free Corrosion Resistant Coatings

5.6.1.1 Introduction

5.6.1.1.1 Coating systems considered. Cr-free coatings are being developed as alternatives to Cr-containing coatings for corrosion protection of aluminum alloys such as AA7075-T6 [1-3]. A simplified coating system comprises a pre-treatment and a primer. Among the different commercially available Cr-free coatings, several have been selected for a characterization of their protectiveness on high strength aluminum alloys. Zirconium-based [3-5] and trivalent chromium (Cr^{3+}) based chemistries [6, 7] have been used as pre-treatments or conversion coatings and lanthanide-based pigments such as Ce, La or Pr [8-11] and Si-oxoanions compounds such as $CaSiO_3$ or $MgSiO_3$ [2] have been used as pigments in the primers.

Zirconium-based and Cr^{3+}-based conversion coatings form very stable oxide films that provide an adherent surface for subsequently applied organic coatings and provide some barrier corrosion protection [3, 7]. By immersing galvanized steel samples in a silane-based solution containing 1×10^{-3}M $Zr(NO_3)_3$, Trabelsi and co-workers were able to form a stable Zr-based coating which, when exposed to 0.5M NaCl, showed an increase in the total impedance response [4]. The increase in the total impedance was attributed to the presence of ZrO_2 which reduced coating porosity and conductivity; therefore improving the barrier characteristics of the coating.

A proprietary trivalent chromium conversion coating applied to AA2024-T3 and subjected to salt spray testing showed an increase in the impedance response in the lower frequency range (< 1Hz) when compared to control samples [12]. The increase was attributed to the creation of a more continuous Cr_2O_3 oxide layer or possibly to some localized corrosion inhibition by Cr^{3+} species.

Lanthanide-based coatings offer protection to the substrate by creating a precipitated oxide barrier layer and also by providing some localized corrosion inhibition [8]. A study by Breslin and Geary showed that a Sn-Zn alloy passivated with a Ce surface conversion treatment achieved a level of corrosion protection similar to those found for chromate treatments [9]. Potentiodynamic polarization of Mg-alloys samples treated with Ce and Pr coatings (immersion in 5×10^{-4} mol/dm^3 of $Ce(NO_3)_3$ or $Pr(NO_3)_3$ at room temperature for 5 minutes) showed a decrease in the anodic and cathodic currents when tested in a borate buffer solution (0.15 mol/dm^3 H_3BO_3 and 0.05 mol/dm^3 $Na_2B_4O_7$ at pH=8,5) [13].

Si-oxoanion based coatings are believed to protect the aluminum metal by offering corrosion inhibition through a buffering effect [2]. It has been found that slurries produced by excess

pigment of $CaSiO_3$ with initial pH of 3, 7 and 10 reached a final pH of 8.0 to 8.5 when in contact with air (pers. comm. M. Jaworowski). A Si-oxoanion based coating applied to an aluminum alloy will maintain the solution pH near the substrate-coating interface at a near neutral pH therefore maintaining substrate passivation.

5.6.1.1.2 Characterization of corrosion protection. The corrosion resistance of coated aluminum alloys can be characterized by different methods. Field exposures are the most direct assessment of coating performance. Such exposures are also considered to be the most relevant exposure regimen to service conditions. However, exposures under these conditions are slow to develop corrosion in the case of excellent coating systems and, for this reason; such exposures are impractical in many cases. Detailed assessments of corrosion other than by visual inspection are often not done so as to avoid initiating or accelerating corrosion. As a result, detailed characterization is almost always postmortem in nature, and limited in its ability to diagnose root causes of failure.

To generate results more quickly, damage accumulation can be accelerated by increasing the aggressiveness of the environment. Salt spray exposure testing carried out according to ASTM B 117 in an example of a widely used accelerated test for coated metals of many different types [14]. ASTM B 117 is a standardized test which consists of exposure of coated panels to a salt spray, 5 wt% NaCl, in an enclosed chamber held at 35ºC. Although the exposure times are reduced by this method, the primary method for characterizing accumulated damage is visual examination by an evaluator. Such assessments are subjective and regularly draw criticism.

Accelerated exposure tests, like salt spray are also criticized because they do not replicate many service exposure conditions very well. How salt spray results translate to performance of a coated metal system is rarely known with confidence. This has tended to limit application of the test method to process and material qualification, and prevents its use for forecasting coating lifetimes; which is a significant limitation.

In recent years attempts to modify salt spray exposure testing to more accurately replicate service exposure conditions have been explored with some success by the use of cyclic wet/dry test, such as norms ASTM G85 and ASTM D5894 [15, 16]. ASTM G85 considers the exposure of a coating in a controlled wet/dry environment. The cycle consists of salt fog exposure at 25ºC for 1 hour followed by a drying-off period of 1 hour at 35ºC. UV radiation has also been found to be of importance to replicate service exposure [17]. ASTM D5894 is a cyclic UV radiation at 60ºC for 4 hours followed by water condensation at 50ºC for another 4 hours. Yang and co-workers used ASTM D5894 standard to characterize blistering formation of polyurethane coatings on AA2024-T3 in service life conditions [18]. Although the use of these modified salt spray exposures replicate service conditions more accurately, the information collected is still qualitative in nature and therefore a more quantitative analysis is desired. One such an analysis is the electrochemical impedance spectroscopy technique.

Electrochemical impedance spectroscopy (EIS) is an excellent small-signal electrochemistry-based method for characterizing corrosion damage accumulation on coated metals. It is sensitive to physical and chemical changes in the coating well before they are visually identifiable. EIS and the analysis methods that derive from it are complex, the measurement equipment is

expensive and extensive analyst training is needed to interpret the resulting data. For these reasons EIS is not a routine tool for the coatings industry. Nonetheless, it is a method that offers quantitative information and can be used in conjunction with field or accelerated exposure protocols to characterize damage accumulation.

Equivalent circuit (EC) modeling is the basis for much interpretation of EIS data collected for coated metals. The evolution in time of EC elements, such as resistors and capacitors, can give information on the corrosion protection given by a coating and can be used to characterize aspects of coating performance [19]. The circuit shown in Figure 6.1 can be used to model the response of a bare metal protected by a porous coating.

To assess the extent of coating delamination, Mansfeld proposed that the delamination area, A_{del}, could be extracted from a ratio of measured capacitances [20]:

$$\frac{C_{dl}^0}{C_{dl}} = A_{del}$$

(eq. 6.1.1)

where C_{dl}^0 is the area-specific value for the metal-coating interface capacitance (F/cm^2) and C_{dl} (F) is extracted from the EC fitting of measured data from a coated metal sample experiencing coating disbondment. The model proposed by Mansfeld assumes that the change in C_{dl} is due to a change in the delaminated area and that changes in solution chemistry or the metal interface change C_{dl}^0 during the course of the disbondment process. This model was implemented by Deflorian and co-workers to monitor the adhesion of different aluminum pre-treatments [21]. The authors found a good correlation between dry adhesion (measured with a pull-off test) and that given by A_{del}. Also, they were able to establish a ranking among pre-treatments based on A_{del}.

Mansfeld and co-workers also used the change in the pore resistance (R_{pore}) to evaluate breakdown of the corrosion protection by polymer coatings in aluminum and steel alloys [22]. They concluded that breakdown was caused by the short circuiting of the coating which is measured by a decrease in the R_{pore} value. In this method, R_{pore} is used as the parameter to measure coating degradation. Corrosion protection characterization by the R_{pore} method and the delaminated area method are based on EC modeling.

Using EIS data, collected after 24 hours of exposure in 0.5M NaCl in the input layer of an Artificial Neural Network (ANN), Kumar and co-workers used ANN to predict visual degradation of a set of coated metals exposed to 1500 hours in a salt spray chamber [23]. They found a correlation between ANN predicted and visually observed times to failures with a R^2 of 0.90. The authors also found that information contained in the phase angle parameter at low or intermediate frequencies was more relevant than any other EIS-derived parameter.

The objective of this work was to assess the protectiveness of several emergent coating systems using EIS-based analysis of samples subjected to ASTM B117 exposure. This approach allowed a detailed assessment of the relative protectiveness of emergent Cr-free coating systems and

allowed a comparison of the different EIS-based assessment methods that have been proposed for coated metal systems.

5.6.1.2 Experimental

5.6.1.2.1 Materials and coating procedures. Fifteen commercially available coatings were applied to alloy AA7075-T6 (5.3%Zn, 2.4%Mg, 1.36%Cu, 0.24%Fe, 0.04%Si, 0.18%Cr, 0.025%Mn, balance Al). All the samples were prepared at Patuxent River Naval Air Station using standard military depot methods. Each coating system consisted of a pre-treatment or conversion coating and a primer. Five commercial conversion coatings and three primers were used. Fourteen nominally identical samples were tested for each coating combination to allow for serial removal and an assessment of the time-dependent evolution of degradation. This yielded a total of 210 samples tested. The five commercial surface pre-treatments used were: Alodine 5700, T5900, Boegel 8500, PreKote, and Metallast EPA.

Alodine 5700 is a very dilute form of Alodine 5200, which is a fluorozirconate bath that also contains Ti. T5900-TCP is a trivalent chromium conversion coating process. The bath is a dilute solution where 1 wt% of the total composition is Cr-III basic sulfate and potassium hexafluorozirconate solution. Metallast-EPA is also a trivalent chromium fluorozirconate conversion coating bath with a proprietary organic corrosion inhibiting additive. PreKote is a non-chromic alkali soap cleaner with silane adhesion promoter and inorganic inhibitor. Boegel 8500 is a dilute aqueous mixture of zirconium alkoxide and a silane coupling agent.

The processing parameters for all 5 surface pre-treatments can be found in Table 6.1. All surface coatings were allowed to air dry for 24 hours at ambient laboratory conditions before priming.

The three primers used were: Deft02GN084, Hentzen 16708TEP, and Sicopoxy 577-630. All primers were epoxy-based. Deft02GN084 primer includes pigments of $Pr(OH)_3$, $CaSO_4$ and TiO_2 where $Pr(OH)_3$ is considered the active inhibitor. Hentzen primer includes $BaSO_4$, TiO_2, SiO_2 and $CaSiO_3$ pigments where Ca and Mg silicates are considered to be active inorganic inhibitors. Sicopoxy is a Zn-based organic primer. All primers were mixed and applied per manufacturer's instructions. They were sprayed and air dried at ambient laboratory conditions for 24 hours, before being force cured at 150º F for 48 hours. Each sample was identified by assigning the first letter of both conversion coating and primer, for example AA7075 substrate treated with **T**5900 and **D**eft02GN084 was named 7075-**TD**.

5.6.1.2.2 Exposure testing. Exposure testing was carried out to assess the relative corrosion protection of the various coating systems. Exposures were carried out in salt spray chamber running under norm ASTM B117 (5% NaCl at 35ºC) for different exposure times [14]. Exposure times were chosen according to a logarithmic function of time (1, 2, 4, 6, 8, 10, 24, 48, 96, 192, 336, 432, 600 and 720 hours). The exposure time in salt spray needed for a particular sample to show any visual sign of failure was taken as the time to failure (TTF). A sample was considered to fail if any visual signs of blistering, localized corrosion or general corrosion were detected with the unaided eye. Crevice and blistering within 0.35 inches of the sample edge was attributed to variations in the coating associated with the sample edge and therefore was not

considered as coating failure. If no failure was present at the end of the exposure, a TTF of > 1000 hours was assigned.

Table 6.1. Processing parameters for the 5 surface pre-treatment used: Alodine 5700, T5900-TCP, Metalast-EPA, PreKote and Boegel 8500.

Alodine 5700, T5900-TCP and Metalast-EPA	PreKote	Boegel 8500
- Panels were solvent wiped with acetone - Cleaner: Turco 4215 NCLT non-silicated, non-etching 5 min. at 130º F. - Deoxidizer: Turco Smut Go 30 sec. at RT - Immersion on Alodine 5700, Alodine T5900 or Metallast solution bath - 2 min. at RT - Following each step of the process, the panels were double rinsed in DI water.	- The PreKote was prepared following the USAF T0 1-1-8 instructions [28] - 3-step cyclic process - Each step consisted of a manual scrub followed by product application, followed by a dry/rinse. - During each scrubbing phase, the panels were scrubbed immediately following the spray application of the PreKote solution.	- Cleaner: Turco 4215 NCLT for 5 minutes at 135F - Warm double tap water rinse - Deoxidizer: Turco Smut Go for 30 sec at RT - Cold double tap water rinse Spray application of Boegel at 20º angle for 5 minutes allowing the panels to drain off -The panels were not rinsed following the spray application of Boegel

5.6.1.2.3 EIS measurements. Immediately after salt spray exposure, an EIS measurement was performed for each sample type. Measurements were collected after 1, 2, 4, 6, 8, 10, 24, 48, 96, 192, 336, 432, 600 and 720 hours of exposure. EIS measurements were performed over the frequency range of 100 kHz to 10 mHz using a Gamry Reference 600 (Gamry Instruments Inc.) at the OCP. Measurements were made using a sinusoidal voltage perturbation of 10mV. Fitting to the equivalent circuit shown in Figure 6.1 was done by using a complex non-linear least squares regression in Zview v3.1c software (Scribner Associates, Inc.). Constant phase elements (CPE) were used to characterize interfacial reactances. Extraction of the true capacitance value was performed by the Brug equation [24]:

$$C = Y_0^{\frac{1}{\alpha}} R^{\frac{1-\alpha}{\alpha}} \qquad \text{(eq. 6.1.2)}$$

where R is the resistance parallel to the CPE. The resistance associated to faradic processes (R_f) together with the pore resistance (R_{pore}) were added together in a term called the corrosion resistance R_{corr}:

$$R_{corr} = R_{pore} + R_f \qquad \text{(eq. 6.1.3)}$$

The solution resistance (R_{sol}) value was always very small compared to R_{corr} and was ignored.

Kramers-Kronig (K-K) transformations were applied to the measured data to assess whether or not invalid EIS data was collected [25, 26]. Particularly, a frequency range where the EIS data did not follow the K-K transforms was determined from the K-K analysis. The remaining valid frequency range was then used to fit the EIS data into the EC showed in Figure 6.1. In this work, the regression of process models was the chosen method to validate the EIS data collected and an explanation can be found elsewhere [27].
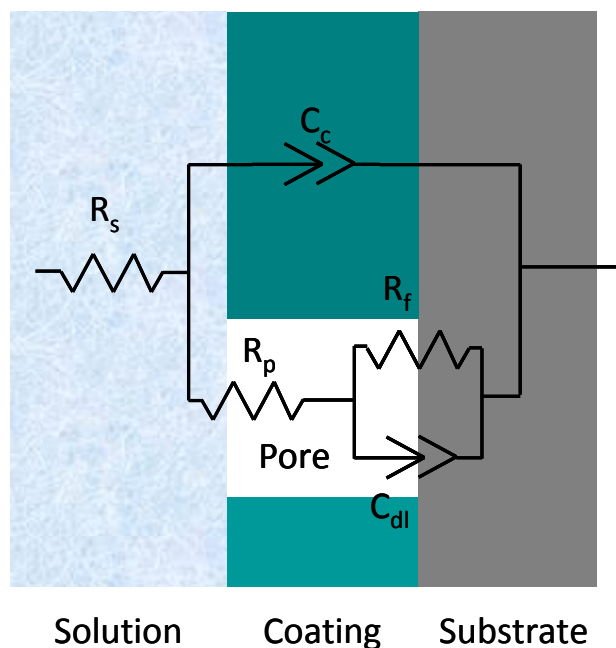
Figure 6.1. Equivalent circuit used for modeling of EIS data.

5.6.1.3 Results

5.6.1.3.1 Exposure testing. Figure 6.2 shows the results of the exposure testing for the 15 coating systems examined. Results are reported as time to failure (TTF) indicating the first instance of any form of visual degradation in the coating. Three main observations can be made. First, Metallast and PreKote conversion coatings, regardless of the primer used, failed at exposure times of less than 196 h. Second, combinations of Alodine, Boegel and T5900 conversion coatings combined with Deft or Hentzen primers showed good corrosion resistance at longer exposure times. In fact all of these samples, except the sample with the Alodine conversion coating and the Hentzen primer, showed no indications of corrosion after 1000 hours of exposure. Third, samples prepared with Sicopoxy primers all failed in 196 hours or less of exposure irrespective of the type of conversion coating used.

263
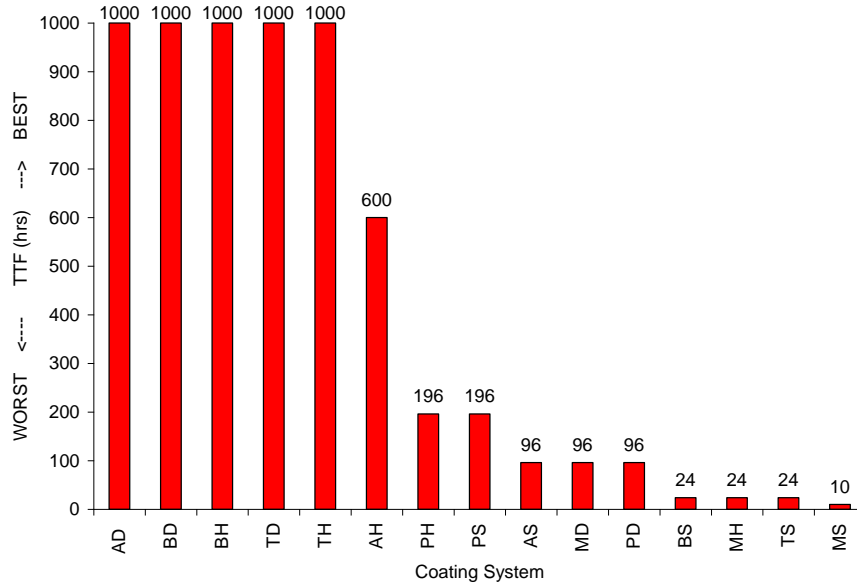
Figure 6.2. Visual time to failure TTF for all 15 samples. Any sign of corrosion (blistering, localized or uniform) was considered failure.

Figure 6.2 also shows that of the 15 coating systems tested, samples either survived 1000 hours with no evidence of coating damage, or showed such evidence in less than 196 hours of exposure. Using this strongly segregated data set enables a comparison to be made among the various types of impedance-based methods for assessing coating system performance.

5.6.1.3.2 Impedance-based analyses of coating systems. The analysis of coating systems was done using the corrosion resistance R_{corr}, the metal-coating interface capacitance C_{dl}, and the delaminated area A_{del}. Also, a new approach using ANN fed with only phase angle at low frequencies was used. The ANN output parameter was time to failure in hours and the calculation process is described in section 6.2 of this report.

A step-by-step analysis for a single sample is shown first, followed by the analysis for all the samples. This analysis was performed as an example to show the calculations of how R_{corr}, C_{dl} and A_{del} were obtained. The sample chosen for the single analysis was Alodine 5700 conversion coating and Hentzen 16708TEP primer (7075-AH).

The Bode plot for sample 7075-AH (Figure 6.3) shows a shift of the total impedance response in all of the frequency ranges to lower values as a function of exposure (solid arrow). In particular, the magnitude of the impedance at low frequency (0.01Hz) shows a decrease of 2 orders of magnitude in the total length of exposure, where the larger decrease is seen before and after 288 h. Also, the change in the slope shifts to higher frequencies as the exposure time increases (dashed arrow).
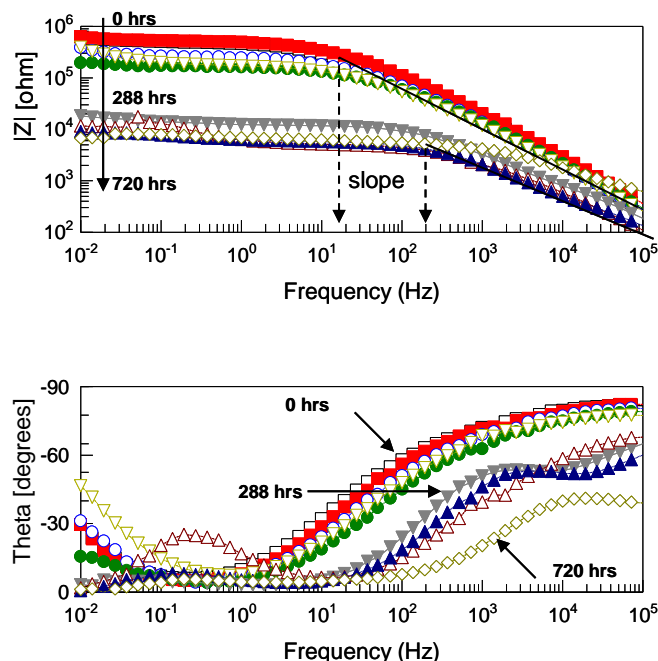
Figure 6.3. Bode plot for sample 7075-AHN after exposure to salt spray for 30 days. Solid arrows show the evolution of the systems as a function of time. Dashed arrows show the shift to higher frequencies of the change in the slope as the exposure time increases (EIS test area was 13.2 cm^2).

The phase angle for sample AA7075-AHN in Figure 6.3 deviates from the ideal capacitive response (phase shift of -90º) at early exposure time suggesting that the coating is not perfect and defects are present. Also a shift from -90º to more positive values is seen as the exposure time increases. The shift to more positive values is considered as an indication of the decrease in the protectiveness of the coating. The phase angle response at frequencies lower than 1 Hz shows a tendency to reach values close to -90º for short exposure times, but as the exposure time increases, it drops closer to 0º. The drop at low frequencies after 288 h is related to the drop in the total impedance and consequently to a drop in the coating protection.

The Nyquist plot for sample 7075-AHN (Figure 6.4) shows the system response as a function of exposure time. The intersection in the x-axis further away from the origin is assumed to be the response of the coating pore resistance. As exposure time increases, the intersection of the semi-circle with the x-axis moves closer to the origin, which indicates a reduction in R$_{pore}$ value. The height of the semi-circle (maximum y-axis value) gives information on the coating capacitance response. The height decreases as a function of exposure. The decrease indicates that the capacitance of the system increases, suggesting incorporation of water in the coating. At 288 hours (Close up in Figure 6.4) a second semi-circle is observed. The semi-circle closer to the origin is attributed to the coating-dielectric response and the one further away is attributed to the coating-metal interface. Again, as exposure time increases, both semi-circles shrink. For the coating-metal semi-circle, the decrease is attributed to both an increase in the double layer capacitance and a decrease in the faradaic resistance.

265
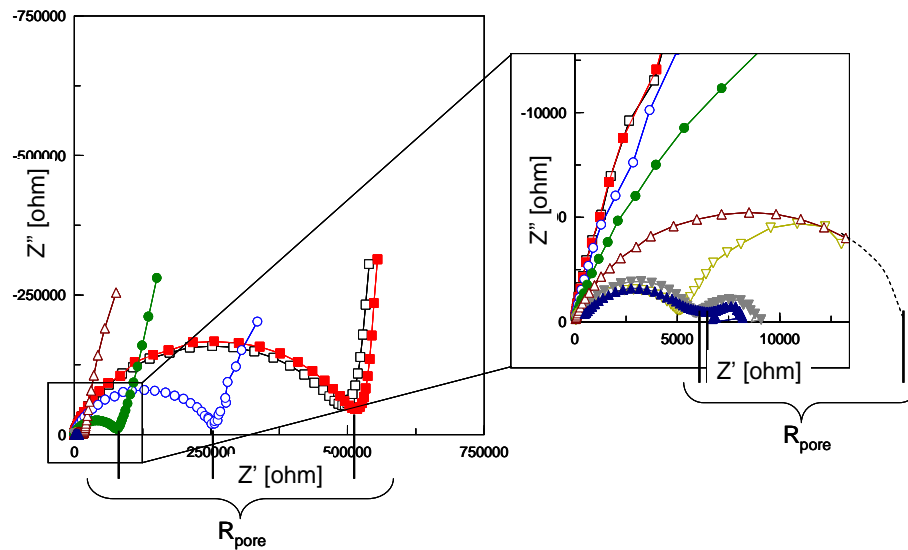
Figure 6.4. Nyquist plot for sample 7075-AHN after exposure to salt spray chamber for 30 days (720 hours). The intersection of the semi-circle with the x-axis can be used as a graphic representation of the R_{pore} value (EIS test area was 13.2 cm^2).

The regression of process model method (K-K transforms) was used in conjunction with the EC shown in Figure 6.1 to determine a valid frequency range where EIS data could be modeled [27]. After the modeling was done, true capacitance values for C_{coat} and C_{dl} were extracted from the constant phase element using the Brug method (equation 6.1.1) [24]. The evolution of the system was then evaluated by plotting the passive elements C_{coat}, C_{dl}, and R_{corr} as a function of exposure time.

In Figure 6.5 both capacitance responses (C_{coat} and C_{dl}) had a decrease at earlier exposure times reaching a plateau at 10^{-8} F after 2 h of exposure while the total impedance, R_{corr}, remained at 10^6 ohm·cm^2. After 288 h exposure, C_{dl} increased more than 3 orders of magnitude together with a decrease of 1 order of magnitude in R_{corr}. The variation of C_{coat} was less than one order of magnitude throughout the duration of the experiment and is not discussed further.
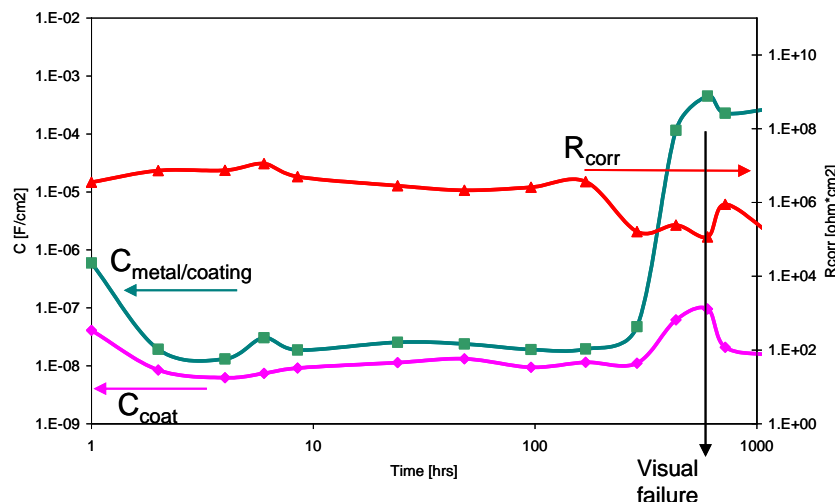
Figure 6.5. EIS modeling for sample AA7075 treated with Alodine conversion coating and Hentzen primer (AA7075-AHN). Solid arrow represents the time needed in salt spray chamber for the sample to present visual (un-aided eye) signs of corrosion (EIS test area was 13.2 cm^2).

In this work, R_{corr}, C_{dl}, and the percentage of delaminated area A_{del} were used in the coating performance characterization. The time needed for R_{corr} to drop below 10^7 ohm·cm^2 was used as a degradation parameter of the coating barrier properties. Similar to R_{corr}, the time needed for C_{dl} to show a marked increase was recorded and used to calculate the percentage of delaminated area A_{del} (equation 6.1.2). The larger the value of %A_{del} is, the worse the adhesion between coating and substrate.

To conclude the step-by-step analysis, sample AA7075-AHN needed only 1 hour to show an R_{corr} value below 10^7 ohm·cm^2. Also, the noticeable change in C_{dl} was after 432 hours with an A_{del} of 7.49. The time to failure given by ANN was 213 hours. All four coating performance parameters (R_{corr}, C_{dl}, A_{del} and ANN) were used to comment on the corrosion behavior of the coatings (see discussion section).

5.6.1.3.3 Comparison of impedance based methods for assessing coating systems. A comparison between the visual TTF and R_{corr}, C_{dl}, A_{del} and ANN results allows an evaluation of the effectiveness of each parameter to assess coating performance.

The total impedance response R_{corr} for all samples tested, grouped by primer, can be seen in Figures 6.6-6.8. R_{corr} value among coatings showed variations from less than one order of magnitude to almost 5 orders of magnitude in the 30-day exposure period. A compilation of the time needed for R_{corr} to drop below 10^7 ohm.cm^2 can be seen in Table 6.2.

Several key observations can be made. First, the Deft primer showed a constant decrease in the R_{corr} value except for TCP and Metallast conversion coatings. All samples showed an R_{corr} value lower than 10^7 ohm·cm^2 in less than 2 hours, except for TCP and Metallast that showed an increase in the barrier properties of the coating after 48 hours exposure. For those samples treated with Hentzen primer, TCP conversion coating showed a marked decrease from 10^{10} ohm·cm^2 to 10^6 ohm·cm^2 after 30 days exposure. Alodine, Metallast, PreKote and Boegel

267

conversion coatings showed similar behavior, starting between 10^7 - 10^6 ohm·cm^2 and dropping one order of magnitude for the first three, while Boegel showed a drop of more than 2 orders of magnitude at the end of the exposure. Sicopoxy samples started with an R_{corr} value between 10^6 - 10^7 ohm·cm^2. Sicopoxy primer together with Metallast conversion coating showed almost no change or even a slight increase in the R_{corr} after 30 days exposure. Boegel conversion coating showed a decrease of less than one order of magnitude for the duration of the exposure. The Sicopoxy and TCP combination showed a drop in the R_{corr} after 24 hours followed by an increase in R_{corr} after 196 hours. PreKote and Alodine both showed a decrease in the R_{corr} after 10 hours and 96 hours respectively.
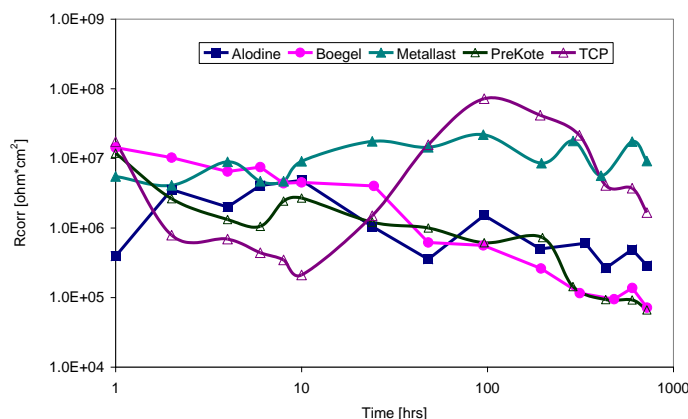
Figure 6.6. R_{corr} response for samples treated with Deft primer and 5 different conversion coatings: Alodine, Boegel, Metallast, PreKote and TCP (EIS test area A=13.2 cm^2).
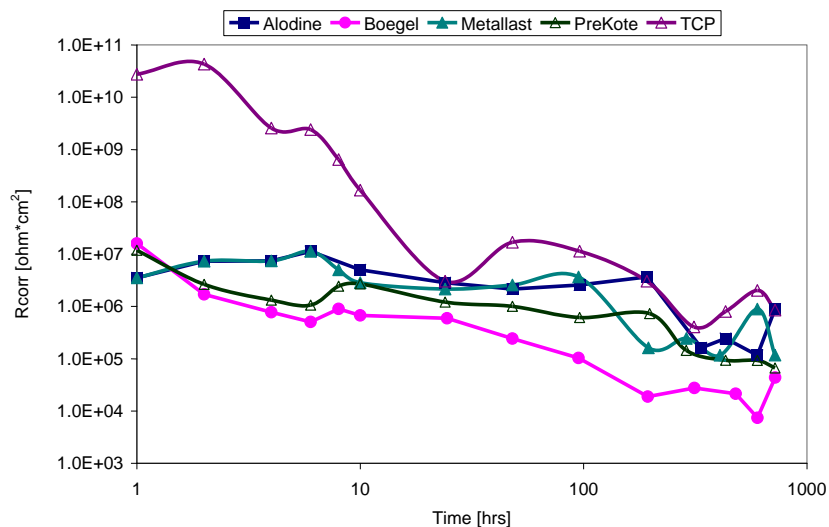
Figure 6.7. R_{corr} response for samples treated with Hetnzen primer and 5 different conversion coatings: Alodine, Boegel, Metallast, PreKote and TCP (EIS test area A=13.2 cm^2).
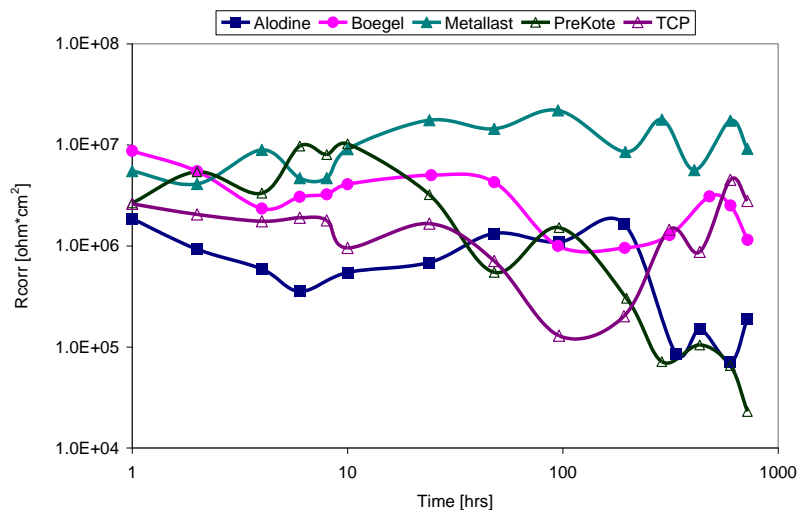
Figure 6.8. R_{corr} response for samples treated with Sicopoxy primer and 5 different conversion coatings: Alodine, Boegel, Metallast, PreKote and TCP (EIS test area A=13.2 cm^2).

The metal-coating capacitance response C_{dl} for all samples tested, grouped by primer, can be seen in Figures 6.9-6.11. The time needed for the C_{dl} to show a noticeable increase is compiled in Table 6.2 together with the delaminated area parameter A_{del}. As expected from the higher sensitivity of the EIS technique compared to the visual examination with the un-aided eye, the time needed for C_{dl} to increase was always less than or equal to TTF. Samples treated with Metallast pre-treatment and Sicopoxy or Hentzen primers deviated from the expected behavior, i.e. showed visual signs of corrosion sooner than a change in the capacitance response. Future research is needed to assess the reason of this deviation.
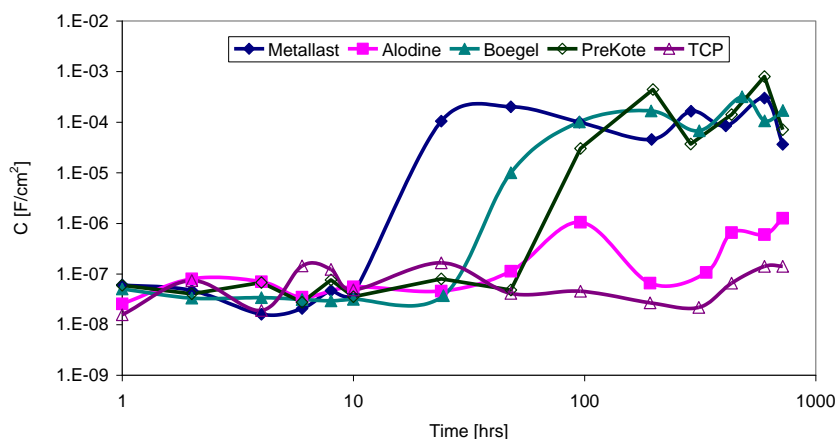
Figure 6.9. Metal-Coating capacitance response (C_{dl}) for samples treated with Deft primer and 5 different conversion coatings: Metallast, Alodine, Boegel, PreKote and TCP (EIS test area A=13.2 cm^2).
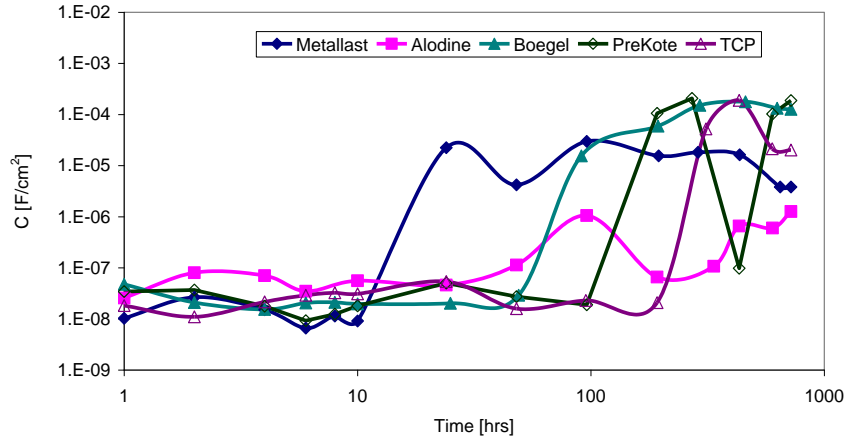
Figure 6.10. Metal-Coating capacitance response (C_{dl}) for samples treated with Hentzen primer and 5 different conversion coatings: Metallast, Alodine, Boegel, PreKote and TCP (EIS test area A=13.2 cm^2).
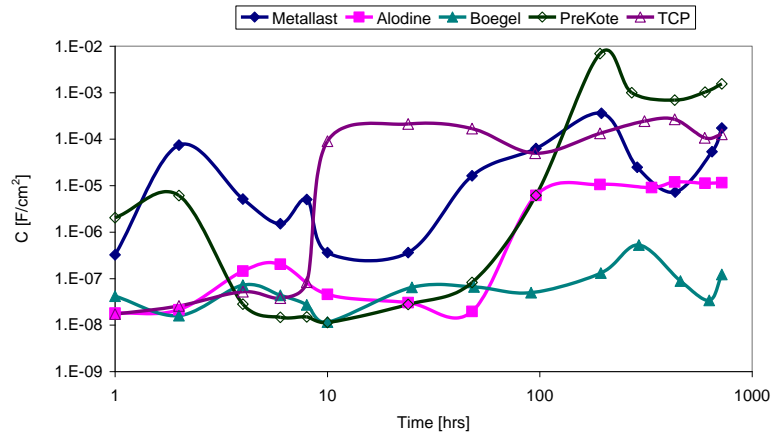
Figure 6.11. Metal-Coating capacitance response (C_{dl}) for samples treated with Sicopoxy primer and 5 different conversion coatings: Metallast, Alodine, Boegel, PreKote and TCP (EIS test area A=13.2 cm^2).

A correlation between the visual examination TTF and both impedance based parameters and ANN parameters can be extracted from Table 6.2. Three main conclusions can be extracted. First, the A_{del} and R_{corr} both showed a weak correlation to the visual TTF parameter. For example, sample BH has a TTF of 1000 hours and a A_{del} of 3.86 and sample PS has a TTF of 196 hours and a A_{del} of 3.89. Second, C_{dl} showed a linear correlation with samples that had a TTF below 720 hours (Figure 6.12) but a weak correlation was found for those samples that did not showed signs of visual failure. Third, the ANN parameter was found to have the best linear correlation and it was selected as the parameters to rank the performance of the coatings (Figure 6.13).

Table 6.2. Parameters used as coating degradation indicators.

Sample	TTF	Exposure needed to show an increase in the C_{dl}	$\dfrac{C_{dl}^0}{C_{dl}} = A_{del}$	Exposure needed for R_{corr} to drop below 10^7 ohm.cm^2	ANN prediction
	v	[hours]	% A_{del}	[hours]	[hours]
AD	1000	*	*	1	780
BD	1000	48	1.08	1	931
BH	1000	48	3.86	10	1059
TD	1000	---	<0.06%	**	813
TH	1000	310	3.39	192	975
AH	600	432	7.49	1	213
PH	196	196	6.83	10	186
PS	196	196	3.89	24	137
MD	96	24	6.83	1	74
PD	96	96	28.66	2	72
AS	96	96	6.16	192	158
BS	24	---	<0.03%	***	15
MH	24	96	1.93	48	23
TS	24	10	5.86	1	18
MS	10	196	23.32	96	13

* Sample showed cycles of increase decrease value of % A_{del}

** Showed an increase in the R_p between 24 and 196 hours

*** R_p value oscillated between 10^6 and 10^7 ohm.cm^2
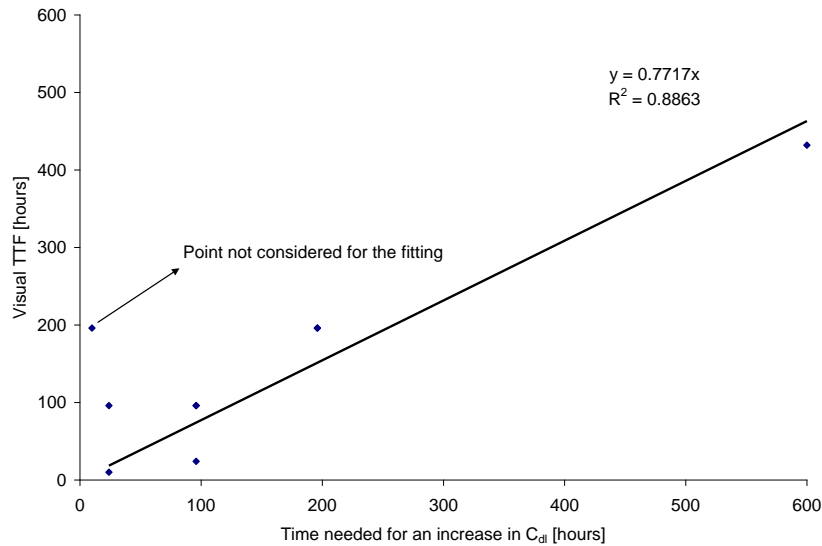
Figure 6.12. Linear regression between the time needed for C_{dl} to show an increase and the TTF extracted for visual (un aided eye) examination of samples after exposure to salt spray chamber.
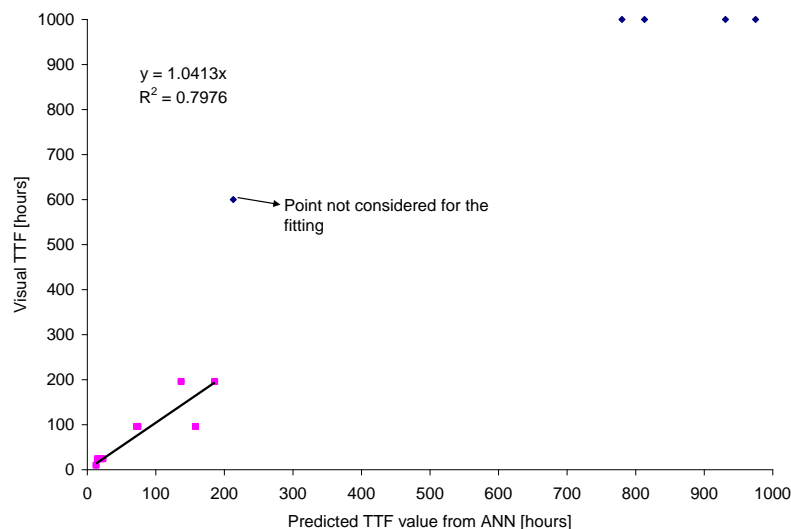
Figure 6.13. Linear regression between the TTF predicted by ANN and the TTF extracted for visual (un-aided eye) examination of samples after exposure to salt spray chamber.

5.6.1.4 Discussion

5.6.1.4.1 Deft 02GN084. Samples prepared with the Deft primer showed the best TTF in salt spray testing. Deft primer samples showed low values in the R_{corr} parameter, which were attributed to mild or weak barrier properties, indicating that metal protection is attributed mainly to inhibition properties. As presented in the results section, samples treated with Deft primer (with the exception of TCP and Metallast conversion coating) showed an R_{corr} value below 10^7 ohm.cm^2 suggesting mild to weak barrier properties. The R_{corr} value for TCP conversion coating showed an improvement in the barrier response (increase in the R_{corr} value) at intermediate exposure times but the value still remained closed to 10^7 ohm.cm^2 also suggesting weak barrier properties. The increase observed for Metallast suggests mild barrier properties. Visual examination showed that samples treated with Deft primer and PreKote (TTF = 96) or Metallast (TTF = 96 h) pre-treatments both showed signs of corrosion after 96 hours of exposure. On the other hand, samples treated with Deft primer and Alodine, Boegel or TCP pre-treatments showed no signs of visual corrosion. Assuming that the combination of any conversion coating treated with Deft primer has weak or mild barrier properties, the good visual performance (TTF = 1000 h) is attributed to an inhibition mechanism.

The inhibiting power of Pr for aluminum alloys has been studied at the Fontana Corrosion Center at OSU (pers. comm. A. Chilukuri). Cathodic polarization on AA2024-T3 substrates in aerated 0.1M NaCl solution with Pr-chloride salts in various concentrations showed that Pr^{3+} exhibited a window of concentration between 100 to 300 ppm. At those concentrations, the corrosion rate of the substrate showed a minimum. The reduction in the corrosion rate was attributed to a reduction of the ORR caused by precipitation of Pr-species in the substrate cathodic particles.

The protection given by Zr-based pre-treatments such as Alodine and Boegel showed synergy when presented with the inhibition power of Pr contained in the Deft primer. TCP pre-treatment, which has Zr and Cr^{3+} as main elements, also showed good performance. The poor performance

of Metallast pre-treatment, which has Cr^{3+} and a proprietary organic corrosion inhibitor as main elements, can be attributed to some antagonism between the main pre-treatment elements and the Pr contained in Deft primer. PreKote pre-treatment, which contains a silane coupling agent and a proprietary organic corrosion inhibitor, when combined with Deft primer did not perform as well (TTF = 96 h). Serious blistering was observed in the surface of samples treated with PreKote suggesting coating adhesion was compromised.

5.6.1.4.2 Hentzen 16708TEP. Hentzen-primed samples mainly showed small values of R_{corr}, which is attributed to weak barrier properties while the good visual performance suggested strong inhibition properties comparable to that of Deft primer. Only TCP pre-treatment showed good barrier properties for a large part of the duration of the experiment reaching R_{corr} values lower than 10^7 ohm.cm^2 only after 288 hours. All other pre-treatments showed mild to weak barrier properties (R_{corr} lower than 10^7 ohm.cm^2).

The weak barrier properties and the good visual performance of Boegel, TCP (TTF = 1000 h) and Alodine (TTF = 600 h) pre-treatment can be explained by Si-oxoanions present in the primer. It has been suggested that the main elements in Hentzen primer, Ca and Mg silicates, protect the aluminum substrate against pitting by a buffering effect (pers. comm. M. Jaworowski).

A synergy similar to that of Deft primer is seen with Hentzen primer. The Si-oxoanions combined with the Zr and Cr element present in the Boegel, TCP and Alodine pre-treatments gave good protection to the metal substrate. A weak protection is obtained when PreKote or Metallast pre-treatments are combined with Hentzen primer.

Sicopoxy 577-630. Regardless of the pre-treatment used, Sicopoxy-primed samples showed the lowest values for the visual performance (TTF < 19 h) among the samples tested. Boegel, TCP and Metallast showed TTF of 24 hours, while Alodine and PreKote showed a slight improvement of 96 and 196 hours. All conversion coatings treated with Sicopoxy primer showed weak to mild (R_{corr} of 10^7 ohm.cm^2 or lower) barrier properties being mild only for those samples treated with Metallast conversion coating.

The Zn present in Sicopoxy primer seems to offer limited metal protection suggesting that no synergy exists between the Zr, Cr^{3+} or Si-oxyanions present in the pre-treatments.

5.6.1.4.3 Ranking. The time needed for R_{corr} to drop below 10^7 ohm$^.$cm^2, which was considered as a parameter to characterize the corrosion performance of coatings exposed to salt spray chamber (Table 6.2), showed a weak correlation with the visual parameter TTF. Therefore, and for the case of the coatings tested, R_{corr} must be used with caution when interpreting coating performance.

The time needed for a sample to show an increase in the C_{dl} together with the percentage of delaminated area attributed to that particular time were also considered as a parameter (Table 6.3). For those samples that failed before 720 hours (TTF < 720 h) the change in C_{dl} showed a linear correlation with samples that failed the visual TTF with an $R^2 = 0.88$ (Figure 6.12). Therefore, the metal-coating interface response C_{dl} could have been used to characterize coating

performance for samples that failed during the length of exposure but it could not be used for samples that did not fail. The percentage of delaminated area A_{del} was calculated using Equation 6.1.1 at the time when C_{dl} showed an increase. Although both parameters are related, a clear correlation between the visual TTF and the A_{del} cannot be extracted, suggesting that for the purpose of this experiment, the delaminated area method is also a weak parameter to measure coating performance.

Artificial neural networks (ANN) were used to predict visual TTF based only on phase angle information. The predicted TTF values for the samples tested were calculated previously and can be seen in Table 6.2. The information obtained by ANN correlates with the visual TTF with an R^2 of 0.79, Figure 6.13. The value of R^2 was calculated for only the samples that failed before 720 hours as was done for C_{dl}. Although the R^2 for ANN is smaller than that of C_{dl}, ANN provided a correlation with the visual TTF even for samples that did not fail. Also, ANN parameter gave a predictive time to failure after finalization of the test where visual examination could only assess that the samples did not fail.

From all the EIS parameters available to characterize coating degradation, R_{corr} showed a weak correlation with visual TTF, C_{dl} showed a strong correlation with samples that fail (TTF < 720 h) but was unsuccessful for samples that did not fail.

ANN parameter, which it was explicitly derived to predict TTF based on phase angle information, showed the best correlation with all samples (failed or not) and therefore was selected as the parameter to characterize coating performance. A rank of the coating tested was obtained based on ANN parameter. Among all the samples tested Boegel 8500 conversion coating and Deft02GN084 showed the best performance with a predicted TTF of 1059 and those treated with Metallast and Sicopoxy 577-630 showed the worst performance.

5.6.1.5 Conclusions

- EIS combined with visual examination after accelerated salt spray exposure was used to analyze coating performance.

- A relationship between the chemical composition of the coatings and the coating performance was established.

- R_{corr}, defined as the sum of the pore resistance, the r defect resistance together and the solution resistance was a weak predictor of coating performance in exposure testing.

- The metal-coating interface capacitance C_{dl} parameter showed strong correlation with the visual TTF for only those samples that failed during exposure.

- The percentage of delaminated area $\%A_{del}$ parameter showed weak correlation with the visual examination.

- Prediction of the TTF obtained by ANN fed with phase angle information showed strong correlation with the visual TTF for all samples tested.

- A ranking among coatings was obtained using the ANN parameter. The combination of Boegel 8500 conversion coating with Deft02GN084 primer ranked first among the emerging corrosion resistance coatings tested.

5.6.1.6 References

1. Cohen, S. M., *Review - Replacement for Chromium Pretreatments on Aluminum.* Corrosion, 1995. **51**(1): p. 71-78.
2. Sinko, John, *Challenges of Chromate Inhibitor Pigments Replacement in Organic Coatings.* Progress in Organic Coatings, 2001. **42**: p. 267-282.
3. Kendig, M. W. and Buchheit, R.G., *Corrosion Inhibition of Aluminum and Aluminum Alloys by Soluble Chromates, Chromate Coatings, and Chromate-Free Coatings.* Corrosion, 2003. **59**(5): p. 379-400.
4. Trabelsi, W., Triki, E., Dhouibi, L., et al., *The use of pre-treatments based on doped silane solutions for improved corrosion resistance of galvanised steel substrates.* Surface & Coatings Technology, 2006. **200**(14-15): p. 4240-4250.
5. Dufek, E. J. and Buttry, D. A., *Inhibition of O-2 reduction on AA2024-T3 using a Zr(IV)-Octadecyl phosphonate coating system.* Electrochemical and Solid State Letters, 2008. **11**(2): p. C9-C12.
6. Pearlstein, F and Agarawala, S, *Trivalent Chromium Conversion Coating for Aluminum.* US PATENT, 1994. **5,304,257**.
7. Pearlstein, F. and Agarwala, V. S., *Trivalent Chromium Solutions for Applying Chemical Conversion Coatings to Aluminum-Alloys or For Sealing Anodized Aluminum.* Plating and Surface Finishing, 1994. **81**(7): p. 50-55.
8. Hinton, B. R. W., Arnott, D. R., and Ryan, N. E., *The Inhibitino of Aluminum-alloy Corrosion by Cerous Cations.* Metals Forum, 1984. **7**(4): p. 211-217.
9. Breslin, C.B. and Geary, M., *Influence of Rare-Earth Metal Passivation Treatments on the Dissolution of Tin-Zinc Coatings.* Corrosion 1998. **54**(12): p. 964-970.
10. Aldykiewicz, A. J., Isaacs, H. S., and Davenport, A. J., *The Investigation of Cerium as a Cathodic Inhibitor for Aluminum-Copper Alloys.* Journal of the Electrochemical Society, 1995. **142**(10): p. 3342-3350.
11. Buchheit, R.G., Mamidipally, S.B., Schmutz, P., et al., *Active Corrosion Protection in Ce-Modified Hydrotalcity Conversion Coatings.* Corrosion, 2002. **58**(1): p. 3-14.
12. Nickerson, B.C., Matzdorf, C.A., and Lipnickas, E., *Evaluation of Modified Zirconium Trivalent Chromium Conversion Coatings by Accelerated Corrosion and Electrochemical Techniques* Tri-Service Corrosion Conference Proceedings, 2005.
13. Rudd, A.L., Breslin, C.B., and Mansfeld, F., *The Corrosion Protection Afforded by Rare Earth Conversion Coatings Applied to Magnesium.* Corrosion Science, 2000. **42**: p. 275-288.
14. ASTM, *ASTM B117-03 Standart Practive for Operating Salt Spray (Fog) Apparatus*, in *Annual Book of ASTM Standards*. 2003, ASTM: Philadelphia, PA.
15. ASTM, *ASTM D5894 - Standard Practice for Cyclic Salt Fog/UV Exposure of Painted Metal*, in *Annual Book of ASTM Standards*. 2005, ASTM: Philadelphia, PA.

16. ASTM, *ASTM G85 - Standard Practice for Modified Salt Spray (Fog) Testing*, in *Annual Book of ASTM Standards*. 2009, ASTM: Philadelphia, PA.

17. Yang, X. F., Vang, C., Tallman, D. E., et al., *Weathering degradation of a polyurethane coating.* Polymer Degradation and Stability, 2001. **74**(2): p. 341-351.

18. Yang, X. F., Tallman, D. E., Bierwagen, G. P., et al., *Blistering and degradation of polyurethane coatings under different accelerated weathering tests.* Polymer Degradation and Stability, 2002. **77**(1): p. 103-109.

19. Kendig, M. and Scully, J., *Basic Aspects of Electrochemical Impedance Application for the Life Prediction of Organic Coatings on Metals.* Corrosion, 1990. **46**(1): p. 22-29.

20. Mansfeld, F., *Use of Electrochemical Impedance Spectroscopy for the Study of Corrosion Protection by Polymer Coatings.* Journal of Applied Electrochemistry, 1995. **25**: p. 187-202.

21. Deflorian, F. and Fedrizzi, L., *Adhesion characterization of protective organic coatings by electrochemical impedance spectroscopy.* J. Adhesion Sci. Technol., 1999. **13**(5): p. 629-645.

22. Mansfeld, F., Kendig, M.W., and Tsai, S., *Evaluation of Corrosion Behavior of Coated Metals With AC Impedance Measurements.* Corrosion, 1982. **38**(9): p. 478-485.

23. Kumar, G. and Buchheit, R.G., *Use of Artificial Neural Network Models to Prodict Coated Component Life from Short-Term Electrochemical Impedance Spectroscopy Measurements.* Corrosion, 2008. **64**(3): p. 241-254.

24. Brug, G. J., Vandeneeden, A. L. G., Sluytersrehbach, M., et al., *The Analysis of Electrode Impedance Complicated by the Presence of a Constant Phase Element.* Journal of Electroanalytical Chemistry, 1984. **176**(1-2): p. 275-295.

25. Macdonald, D.D., Sikora, E., and Engelhardt, G., *Characterizing electrochemical systems in the frequency domain - A review.* Electrochimical Acta, 1997. **43**(1-2): p. 87-107.

26. Esteban, J. M. and Ozarem, M.E., *On the Application of the Kramers-Kronig Relations to Evaluate the Consistency of Electrochemical Impedance Data.* J. Electrochem. Soc., 1991. **138**(1): p. 67-76.

27. Orazem, Mark E. and Tribollet, Bernard, *Electrochemical Impedance Spectroscopy - Chapter 22 (p. 443).* The Electrochemical Society Series, ed. ECS. 2008.

28. USAF, *Technical Manual: Application and Removal of Organic Coatings, Aerospace and Non-Aerospace Equipment (Chapter 3 - p.13-14).* USAF T0 1-1-8. 2008.

5.6.2 Electrochemical Impedance Spectroscopy (EIS) Study to Predict Long-term Performance of Cr-Free Coatings on Aluminum Alloys Using Artificial Neural Networks (ANNs)

5.6.2.1 Introduction

Chromate-bearing coating systems provide excellent corrosion protection to high strength aluminum alloys used in condensing atmospheric exposure conditions. However, the toxic hazard associated with corrosion-inhibiting chromates is unacceptably high, which has prompted the development of alternate coating formulations for corrosion resistant coatings that do not use toxic forms of chromate [1, 2]. Accelerated exposure testing is the most widely used method for evaluating the protectiveness of coating systems. Among these, the salt spray exposure test described in ASTM B117 is common for testing the corrosion resistance of coated aluminum alloys [3]. Development of corrosion damage requires long exposure times ranging up to thousands of hours for some of the very best coating systems. Long test times delay coating development and qualification activities and there is a desire across the coatings community for shorter length tests that determine coating performance. There is also a desire for a shorter test that allows an estimation of useful coating life in service.

Electrochemical impedance spectroscopy (EIS), combined with equivalent circuit (EC) modeling of the EIS response, has been shown to be a powerful approach for characterizing the extent and nature of the corrosion protection provided by coating systems [4, 5]. Recently, efforts were made to correlate results from long-term exposure testing to results from much shorter exposures combined with EIS characterization. Buchheit [6] and later Leggat [7] related EIS data collected on ranges of different coating systems after 24 hours immersion in 0.5M NaCl to the salt spray performance after 168 hours. Although the interpretations were debated [8], the authors found that a general relationship existed between coating system performance in salt spray exposure and the total impedance value extracted from EC modeling of the EIS data. In similar fashion, Bierwagen *et al.* used an accelerated thermal cycling corrosion test together with EIS data to characterize the performance of a pigmented ($SrCrO_4$) water-borne coating in AA2024-T3 and AA7075-T6 [9]. In this study it was found that the less the change in any EC modeling parameter (pore resistance, metal-coating interface capacitance and coating capacitance) upon cyclic exposure, the better the corrosion resistance. Although the ECs used in these studies were closely related to generally accepted physical interpretations of the corrosion mechanisms for coated metals, there are implicit and unverified assumptions about the nature of the physical and chemical changes in the coating and the damage occurring that go along with use of these models. One central assumption is that the total measured impedance of a coated metal sample is inversely related to the overall corrosion rate of the system. This assumption is questionable for coating systems that do not exhibit a clearly resolved faradaic resistance-dominated impedance at low frequencies. This situation arises when chromate primers are applied to aluminum alloys.

To avoid the assumptions associated with the application of EC models to EIS data, Kumar introduced a fresh approach in relating EIS results to long-term exposure test results [10]. In this work, artificial neural networks (ANN) approaches were used to find relationships between impedance magnitude or phase angle EIS data and the salt spray results for a range of conversion coated aluminum alloys. The impedance magnitude and phase angle information were

normalized, but otherwise not transformed through modeling of any type. Among the various models tested, an ANN trained with only phase angle information collected after 24 hours of exposure, related well enough to time to failure in salt spray that the relationship allowed prediction of salt spray performance from the short-term EIS measurement.

In this work, which follows the approach introduced by Kumar, an attempt is made to predict salt spray performance of commercially available organic coating systems after 720 hours exposure by using an ANN trained with EIS data collected at less than 48 hours. In doing so, an empirical but predictive short-term characterization is developed. In this work, direct inputs from EIS spectra were selected based on a sensitivity analysis, which allowed an estimation of which parts of the EIS spectrum were most significant in forecasting time to failure in the exposure test.

ANNs are massively parallel mathematical processing algorithms that emulate aspects of neural processing in the human brain. ANNs excel in recognizing patterns in complex data sets without knowing governing relationships among them beforehand [11]. A feed-forward fully-connected architecture is a commonly used ANN architecture. This architecture consists of an input layer, a hidden layer and an output layer [12]. Each layer is formed by one or more neurons. Each neuron is mathematically connected to all other neurons in the adjacent layers. The network prediction is based upon a feed-forward process in which data is fed in the input layer and thru mathematical operations in the forward direction and an outcome is obtained. The cognitive power of ANN is based on the network architecture (number of layers and neurons in each layer), the training and validation routines, and the type of input variables [13]. Although neural networks have the power to discriminate between noisy input variables and significant ones, assessing the significance between input variables prior to using them in an ANN leads to simpler and more able models. It also allows an understanding of which input variables are most significantly related to the output variables [14, 15]. Sung studied how the accuracy of an ANN changed when the network was trained with data input pruned from a larger data set. Three different pruning methods were explored: sensitivity analysis, change of the means square error, and the method of fuzzy curves [16], with the latter approach being most efficient while retaining acceptable model performance.

The method of fuzzy curves [14, 17, 18] for evaluating the significance of input variables to an ANN model prediction is an adaptation derived from fuzzy set theory [19]. Fuzzy set theory, in contrast to a classic crisp set theory, is based on the idea of graded set membership, which can be represented by a mathematical membership function [20]. This mathematical function transforms the input variables into values between zero and one (fuzzy set) instead of only zero and one (crisp theory). This fuzzy set is used to determine the relative significance among input variables.

In this work, a range of ANN models were constructed and evaluated for relating EIS data to data from exposure testing. Sensitivity analyses based on the method of fuzzy curves were carried out to pre-prune and simplify models. Pruned ANN models have been trained, validated and assessed for their ability to predict long term exposure testing.

5.6.2.2 Experimental

5.6.2.2.1 Coating system description. Thirty commercially available coatings were applied to AA7075-T6 and AA2024-T3 sheet stock samples. Figure 6.14 illustrates the range of coatings tested in this study. All samples were prepared at the Patuxent River Naval Air Station. Each coating system consisted of a conversion coating and a primer. Each primer and conversion coating combination was prepared with and without a clear polyurethane topcoat. Table 6.3 shows coating thickness by sample. Thickness measurements were performed five times for each coating using a coating thickness gauge Elcometer Model 456 with an associated error of less than 4 μm. Five (18cm x 4cm) panels for each coating system were shear cut to form 14 (5cm x 4cm approximately) nominally identical samples, resulting in a total of 840 total tested samples. Each sample was exposed to salt spray for characterization.
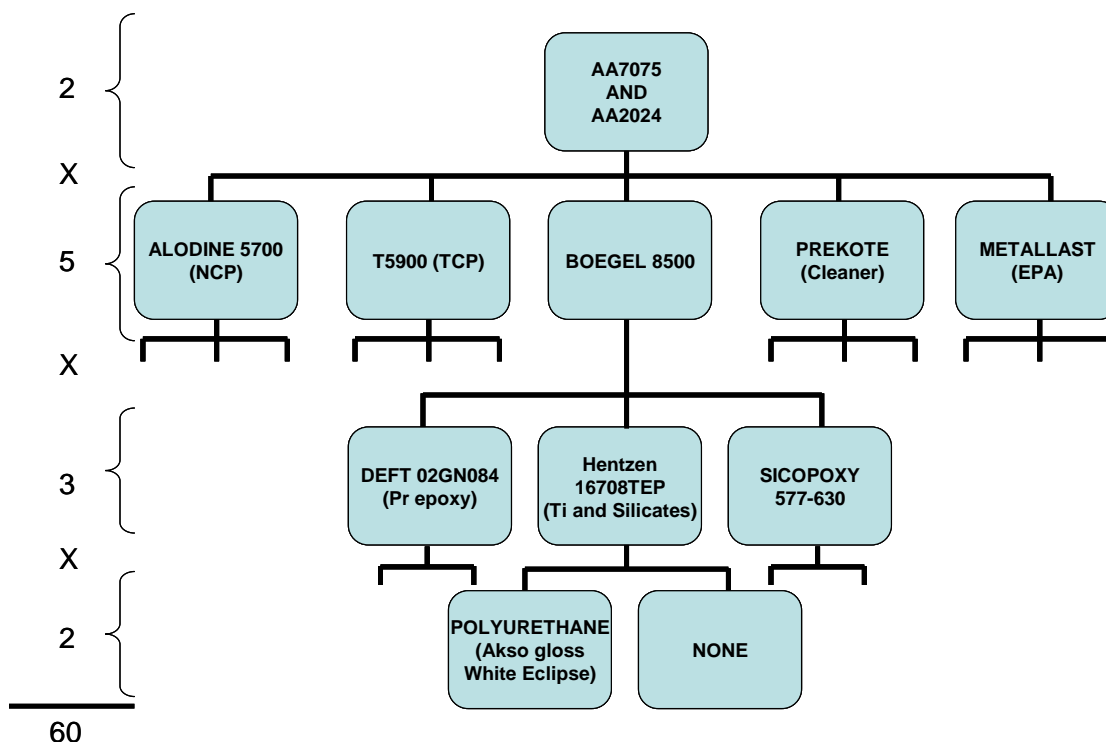
Figure 6.14. Diagram showing all 60 coating system used. Two metal substrates: AA7075-T6 and AA2024-T3. Five conversion coatings (Alodine, TCP, Boegel, PreKote and Metllast), three primers (Deft, Hentzen, and Sicopoxy) and two finishing procedures, with and without a polyurethane top coat.

Five (5) commercial surface treatments were used: Alodine 5700, T5900, Boegel 8500, PreKote, and Metallast EPA. Alodine 5700 is a very dilute form of Alodine 5200 (90% is water), which is a fluorozirconate conversion coating with a Ti base.   T5900-TCP (tri-valent chromium conversion coating process) is a dilute solution where 1%wt of the total composition is Cr-III sulfate basic and potassium hexafluorozirconate.   Metallast-EPA is a trivalent chromium fluorozirconate conversion coating with a proprietary organic corrosion-inhibiting additive. PreKote is a non-chromate alkali soap cleaner with silane adhesion promoter and inorganic inhibitor. Boegel 8500 is a dilute aqueous mixture of zirconium alkoxide (zirconia alkoxide stabilized with acidic acid) and a silane coupling agent. The processing used to apply each of the

5 surface pre-treatments can be found in Table 6.4. All spray-applied coatings were allowed to air dry for 24 hours at ambient laboratory conditions before being individually wrapped in tech-wipes and hermetically bagged.

Table 6.3. Coating thickness. Thickness measurements were performed five times for each coating using coating thickness gauge Elcometer Model 456 with an associated error of less than 4 μm. Sample IDs defined in the text below.

Sample	Thickness	Sample	Thickness μm
7075_ADN	20.00	2024_ADN	37.30
7075_AHN	18.75	2024_AHN	35.13
7075_ASN	23.22	2024_ASN	25.48
7075_BDN	21.03	2024_BDN	29.43
7075_BHN	28.14	2024_BHN	39.62
7075_BSN	18.29	2024_BSN	24.01
7075_MDN	30.54	2024_MDN	33.18
7075_MHN	36.25	2024_MHN	28.24
7075_MSN	22.58	2024_MSN	26.23
7075_PDN	29.04	2024_PDN	32.17
7075_PHN	28.04	2024_PHN	43.08
7075_PSN	21.18	2024_PSN	23.42
7075_TDN	19.83	2024_TDN	34.37
7075_THN	35.20	2024_THN	32.28
7075_TSN	17.41	2024_TSN	29.79
Average	**24.63**		**31.58**
7075_ADP	43.69	2024_ADP	64.17
7075_AHP	45.58	2024_AHP	61.24
7075_ASP	73.17	2024_ASP	75.07
7075_BDP	62.40	2024_BDP	64.23
7075_BHP	66.68	2024_BHP	82.40
7075_BSP	78.83	2024_BSP	78.14
7075_MDP	65.92	2024_MDP	77.08
7075_MHP	62.67	2024_MHP	71.25
7075_MSP	57.66	2024_MSP	79.38
7075_PDP	56.07	2024_PDP	65.17
7075_PHP	72.66	2024_PHP	69.09
7075_PSP	66.85	2024_PSP	62.37
7075_TDP	55.13	2024_TDP	68.67
7075_THP	72.11	2024_THP	77.40
7075_TSP	67.43	2024_TSP	75.40
Average	**63.12**		**71.41**

Table 6.4. Processing parameters for the 5 surface pre-treatment used: Alodine 5700, T5900-TCP, Metalast-EPA, PreKote and Boegel 8500.

Alodine 5700, T5900-TCP and Metallast-EPA	PreKote	Boegel 8500
- Panels were solvent wiped with acetone - Cleaner: Turco 4215 NCLT non-silicated, non-etching 5 min. at 130º F. - Deoxidizer: Turco Smut Go 30 sec. at RT - Immersion in Alodine 5700 - 2 min. at RT, Alodine T5900 - 2 min. at RT - Metallast EPA - 2 min. at RT Following each step of the process, the panels were double rinsed in DI water.	- The PreKote was prepared following the USAF T0 1-1-8 instructions [32] - 3-step cyclic process; Each step consisted of a manual scrub followed by product application, followed by a dry/rinse. - During each scrubbing phase, the panels were scrubbed immediately following the spray application of the PreKote solution.	- Cleaner: Turco 4215 NCLT for 5 minutes at 135F - Warm double tap water rinse - Deoxidizer: Turco Smut Go for 30 sec at RT - Cold double tap water rinse Spray application of Boegel at 20º angle for 5 minutes allowing the panels to drain off - The panels were not rinsed following the spray application of Boegel

The three primers used were: Deft 02GN084, Hentzen 16708TEP, and Sicopoxy 577-630. Deft02GN084 is a 2-part epoxy primer mainly composed of $Pr(OH)_3$, $CaSO_4$, TiO_2 where $Pr(OH)_3$ is considered the active inhibitor. The Hentzen primer is an epoxy-based primer with Si-oxoanion pigments, where $CaSiO_3$ is considered to be the active inorganic inhibitor. Sicopoxy 577-630 is a Zn-rich epoxy primer. All primers were mixed and applied per manufacturer's instructions. They were then sprayed and air-dried at ambient laboratory conditions for 24 hours, before being force cured at 150º F for 48 hours.

Also, two finishing procedures were considered: one with a polyurethane topcoat and one without. Panels that received a topcoat were air-dried at ambient laboratory conditions for 24 hours before topcoat application, and after application they followed the same air dry and force cure procedure as the primer.

Each sample was identified by first assigning the aluminum alloy used for the substrate, such as AA2024 and AA7075 followed by three letters (7075-*xxX* or 2024-*xxX*). The first two letters '*x*' represents the conversion coating and primer in that order, while '*X*' represents the presence (P) or not (N) of a polyurethane top coat. For example, aluminum alloys AA7075 treated with **T**5900 conversion coating, **D**eft02GN084 primer and a polyurethane coating was named 7075-

TDP. While AA2024 treated with **A**lodine 5200 conversion coating, **H**entzen primer and no topcoat was label 2024-**AHN**.

5.6.2.2.2 Time to failure variable (TTF). Coated samples were subject to cabinet exposure conditions consistent with practices described in ASTM B117. The exposure time needed for a particular coating system to show any visual signs of failure was considered the output variable time to failure (TTF). There were 14 different exposure times (14 individual samples) for each coating system where visual examination was performed. Once a coating system showed a sample that failed after time *t* all subsequent samples of the same coating system were considered to have failed at the same *t* time. A sample was considered to fail if any visual signs of blistering, localized corrosion or general corrosion were detected. Crevice and blistering in the edge of the samples was not considered to be a coating failure. The different surface finishes of the coatings, i.e. color, roughness, and gloss; did not influence the visual characterization. If a sample failed after time t (TTF = t) the subsequent samples also to the coating system.

Because a number of specimens did not fail within the 720 hours of the exposure test, the TTF data set is right-handed censored. In our study a *death* or *failure* was assigned to any system that failed before the end of the exposure (TTF < 720 h) while those samples that did not fail were considered a *loss* (TTF > 720 h). A Kaplan-Meier survival analysis approach was used to correctly account for censoring in the data set [21-23]. A full mathematical description of the analysis can be found elsewhere [24]. The Kaplan and Meier analysis (K-M), is a non-parametric modeling method. To apply the analysis, the TTF data was first scaled and divided into time intervals t_i or survival increments so that samples that failed were separated from those that did not in a known fashion (e.g. samples that survived 100% of the total exposure time were grouped together, the same for 90%, 80%, 70%, etc). The second step consisted of estimating the proportion of samples that survived (p_i) in each particular time interval (t_i) using the following expression:

$$p_t = \frac{P_{t=i}}{P_{t=i-1}}$$

(eq. 6.2.1)

where P_t is the number of samples that still had not failed at t_i and have survived after t_{i-1}. In the last step, the population of surviving coatings beyond a time t is estimated by the product of each p_i from all intervals prior to *t*.

In order to perform the survival analysis, and considering that for each sample 14 independent measurement were acquired, the TTF variable was represented as 14 vectors with the form <T, S>, where T represents the exposure time and S the survival status [25]. A value of 1 for S represents a loss, while a value of 0 represents a failure. For example, a sample that failed at 600 hours, will have 14 vectors associated with it, such as: <1 h,1>; <2 h,1>; … ;<336 h,1>; <432 h,1>; <600 h,0> and <720 h,0>.

The K-M analysis was performed using JMP 8® Statistical Discovery software, (SAS Institute Inc.). From the software, the population of surviving coatings beyond 720 hours was obtained. If the population of surviving coatings given by the K-M analysis is different from the

population of total TTF vectors <720 h,1> then the population of TTF vectors was changed so as to reach the same value as the one predicted by K-M.

5.6.2.2.3 Electrochemical Impedance Spectroscopy (EIS). All 840 samples were subjected to salt spray exposure according to ASTM B117 [3]. Samples were extracted from the chamber at regular intervals, examined for visual signs of corrosion and subjected to an EIS measurement. No further testing was done. After extraction of salt spray, samples were rinsed in distilled water and air-dried for a minute before exposure to 100 ml of 0.5 M NaCl solution. Samples were allowed up to 30 minutes in solution to reach a steady open circuit potential (OCP). An EIS spectrum was acquired after OCP stabilization. EIS was collected at the OCP with a voltage signal of 10mV. The frequency range used was 100 kHz to 10 mHz, with a sample acquisition rate of 7 points per decade. As a result, the spectra collected comprised 49 independent frequencies.

The EIS parameters used to train the various ANN models were the real and imaginary components of the impedance, the total impedance and phase angle. The exposure time in the salt spray chamber (*exposure time*) was also considered as an input variable in some models. The four EIS parameters extracted from each spectrum at each individual frequency together with *exposure time* were used as the input layer on the ANN to characterize coating performance.

5.6.2.2.4 Data pre-processing. In this work, all variables used in ANN training and sensitivity analyses were normalized to range between 0 and 1. Normalization was done using either a linear or logarithmic rule, depending on how well the values were distributed. For the phase angle data, a linear normalization function was used:

$$x' = \frac{x - x_{min}}{x_{max} - x_{min}}$$

(eq. 6.2.2),

where x, x_{min}, and x_{max} are the actual, minimum, and maximum values of the variable being normalized and x' is the normalized value. For real, imaginary and total impedances, a logarithmic normalization rule was used:

$$x' = \frac{\log(x) - \log(x_{min})}{\log(x_{max}) - \log(x_{min})}$$

(eq. 6.2.3).

5.6.2.2.5 Artificial neural networks. An artificial neural network was constructed, trained and validated to predict salt spray TTF from EIS data. ANN models were trained and validated though repeated presentation of example data sets. Among the different ANN architectures available, a fully connected feed-forward network was trained using a back-propagation of error method network was used [12]. Once trained the model was used to predict an output on the basis of presentation of a single EIS input dataset.

The fully connected feed-forward architecture is widely used for relating data sets characterized by wide dispersion [10, 26]. The architecture of the ANN used in this work consisted of three main layers: input layer, hidden layer and an output layer, which is shown in Figure 6.15 [27].

The input layer consisted of EIS parameter phase angle at specific frequencies given by the fuzzy sensitivity analysis. The output layer consisted of the time to failure variable, TTF. Each layer is connected by mathematically weighted links.
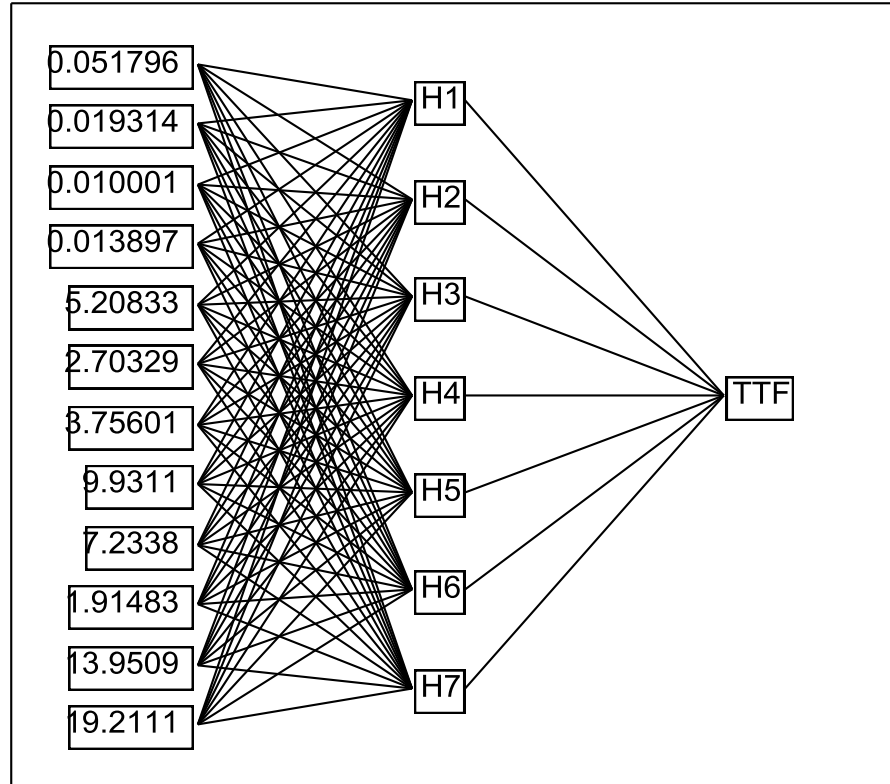
Figure 6.15. Feed-forward ANN diagram showing the architecture of the network: 12 input variables 7 hidden neurons and the time to failure TTF output.

The 840 data sets collected were partitioned to support training, validation and testing of the various ANN models. The majority of the data, 499 spectra were used for model training, 257 were used for validation and 84 were reserved for testing. Training was done using 66% of the data (499 EIS spectra) using a supervised learning routine [27]. The supervised learning routine used known data in both input and output layers to empirically determine the weight links connecting each layer. The weight factors were obtained by a process known as back-propagation of error, which is a minimization of the errors on the links backwards through the model from output to input [12]. To avoid underfitting or overfitting the data, the training and validation routines were run for models with different numbers of hidden neurons until the minimum error between predicted and given output for both training and validation routines was obtained. The network that best predicted the TTF observations had 7 hidden neurons.

5.6.2.2.6 Sensitivity analysis. In order to analyze the relative significance of an input variable (x_i) on the outcome (y) a sensitivity analysis based on the method of fuzzy curves was used [17]. In this study, 197 input variables comprised the impedance magnitude, the real and imaginary

components of the impedance and the phase angle at each frequency of the frequency domain. For each variable, 14 independent measurements were acquired, each at a different exposure time. Each measurement (p) of that input variable (x_i) was scaled to range between 0 and 1 and the degree of membership $\varphi_i(x_i)$ for each measurement at each input was computed using a Gaussian function:

$$\varphi_{ip}(x_i) = \exp\left[-\left(\frac{x_{ip} - x_i}{b}\right)^2\right]$$

(eq. 6.2.4)

where the constant b was given a value of 20% of the average of that particular input variable, p ranged from 1 to Q where Q represent the total number of independent measurements and i is the number of inputs [17].

To determine the extent to which an input variable affected the model output, graded or fuzzy membership function describing each input variable was defuzzified using the centroid defuzzification process [28]. In this method, a fuzzy parameter $c_i(x_i)$ was obtained by:

$$c_i(x_i) = \frac{\sum_{p=1}^{Q} \varphi_{ip}(x_i) * y_p}{\sum_{p=1}^{Q} \varphi_{ip}(x_i)}$$

(eq. 6.2.5)

where y_p is the output value of the p measurement. When the output y_p is sensitive to a change in the variable x_i, the membership function $\varphi_{ip}(x_i)$ and output value, y_p, will scale together resulting in a large range for the product of $\varphi_{ip}(x_i)*y_p$ and a large value for the fuzzy parameter $c_i(x_i)$. The range $c_i(x_i)$ over the range of the input variable x_i is directly proportional to the product $\varphi_{ip}(x_i)*y_p$. Therefore as the range of the $c_i(x_i)$ increases, the significance of input variable x_i on the output y also increases. Variables with the largest $c_i(x_i)$ range this exert the greatest influence on the value of the output. Inputs with small ranges have a small significance and are candidates for pruning from the model.

5.6.2.3 Results

5.6.2.3.1 EIS results. Two sets of EIS spectra from a single sample type are shown in Figures 6.16 and 6.17 to illustrate the evolution in the EIS response. These spectra are for AA7075 with Alodine 5200 conversion coating, a Hentzen 16708TEP primer, and a polyurethane topcoat (sample AA7075-AHP), and AA7075 with PreKote pre-treament, a Sicopoxy 577-630 and a polyurethane topcoat (sample AA7075-PSP) respectively. The AA7075-AHP sample showed no signs of visual corrosion over the course of the exposure, while AA7075-PSP showed visual failure after 196 h. Although both samples showed a decrease in the low frequency impedance as a function of exposure from a value of 10^8 ohm·cm^2 to 10^4 ohm·cm^2, the way in which this happened is different for each sample. Sample AA7075-AHP showed a constant value of the total impedance until 10 hours of exposure followed by a drop of two orders of magnitude. The AA7075-PSP sample showed a more progressive decrease during the experiment. Another

distinction between these two samples is the break in the slope of the impedance magnitude plot. Sample AA7075-AHP showed a break on the slope at lower frequencies than those presented by AA7075-PSP.
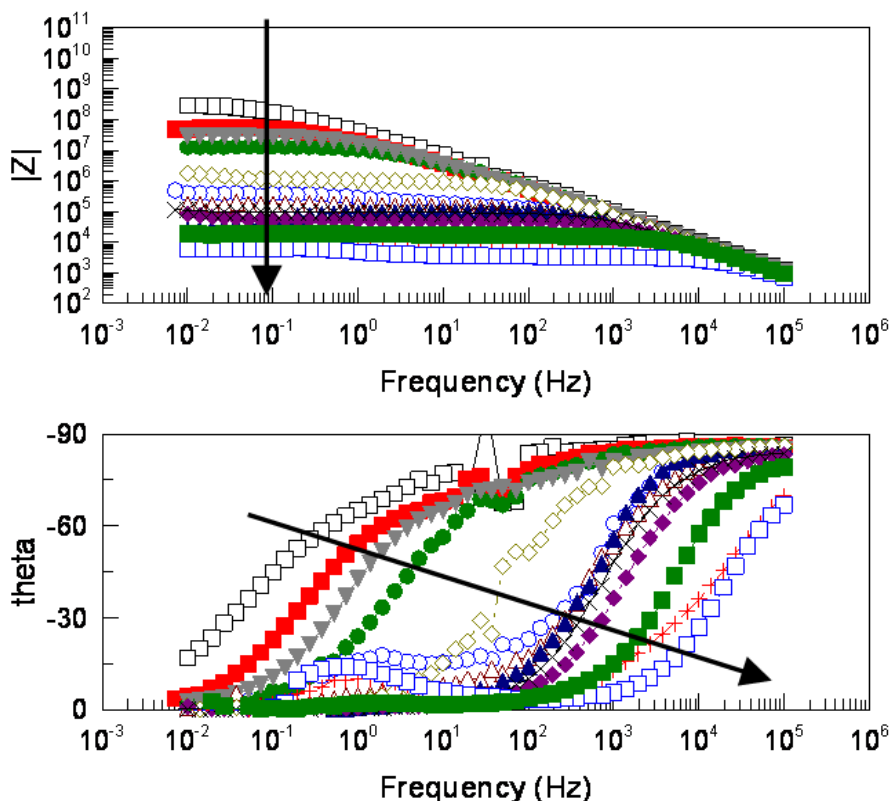
Figure 6.16. EIS spectra for sample AA7075 treated with PreKote surface pre-treatment, Sicopoxy 577-630 primer and a polyurethane top coat (7075-PSP) after exposure to salt spray chamber for 30 days (arrows point in the direction of increasing exposure time). Sample showed visual signs of corrosion after 196 hours (TTF=196 h) (EIS test area was 13.2 cm^2).

The Bode phase angle plots also showed differences. Both samples showed a single time constant at short exposure times. At longer exposure times, the phase angle shifted from near -90º to more positive values. Sample AA7075-PSP showed a more progressive transition than AA7075-AHP. Also, AA7075-PSP showed a second time constant (decrease in the phase angle to more negative values) at long exposure that was not present in AA7075-AHP.
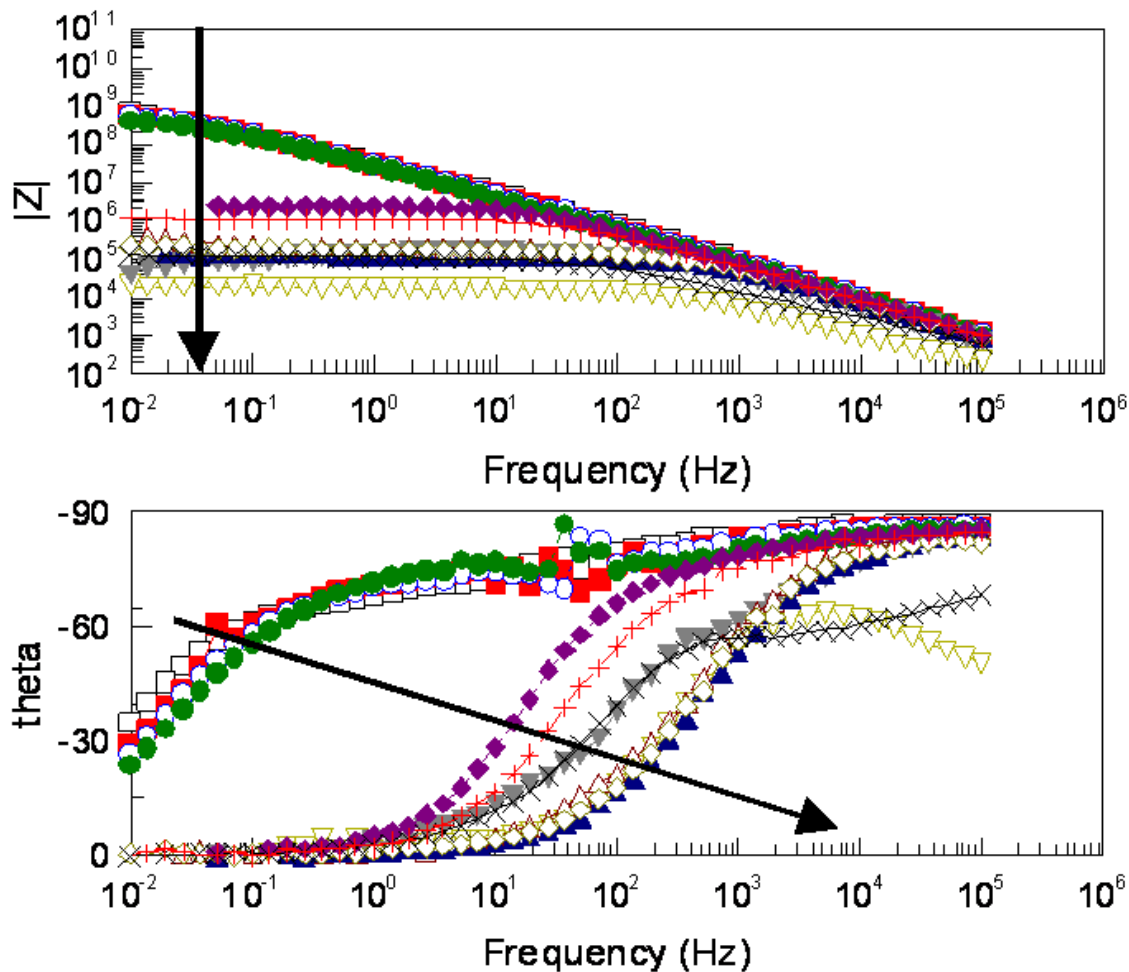
Figure 6.17. EIS spectra for sample AA7075 treated with Alodine 5700 conversion coating, Hentzen 16708TEP primer and a polyurethane top coat (7075-AHP) after exposure to salt spray chamber for 30 days (arrows point in the direction of increasing exposure time). Sample showed no visual signs of corrosion (TTF>720 h) (EIS test area was 13.2 cm^2).

These changes in the patterns of the Bode magnitude and phase angle plot over the course of the exposure experiment clearly differentiated these two samples. Through proper training, an ANN can be taught to recognize these patterns and their changes and associate them to corresponding results from an exposure experiment. When these patterns are sufficiently learned, the ANN can be supplied with EIS data and then estimate an outcome in exposure testing based on its previous learning experience.

5.6.2.3.2 Time to failure. The time needed for any signs of visual corrosion (TTF) to appear after salt spray exposure was collected for all 60 coatings and is shown Table 6.5. Of the coating systems tested, 32 did not fail after 720 hours resulting in a poorly distributed data set, known as a right-censored data set with a surviving fraction of 0.553. The use of a neural network as a non-linear pattern recognition tool requires that the data to be used is well distributed so as to model the non-linearity. In our case, the data as collected by the TTF needed to be corrected.

Table 6.5. Time needed in salt spray chamber (ASTM B117) for visual failure (TTF). Any sign of generalized corrosion, pitting or blistering on the surface was considered as a failure.

SAMPLE	TTF (hours)	SAMPLE	TTF (hours)
7075_ADN	---	2024_ADN	600
7075_AHN	600	2024_AHN	---
7075_ASN	96	2024_ASN	432
7075_BDN	---	2024_BDN	192
7075_BHN	---	2024_BHN	---
7075_BSN	24	2024_BSN	24
7075_MDN	96	2024_MDN	---
7075_MHN	24	2024_MHN	432
7075_MSN	10	2024_MSN	96
7075_PDN	96	2024_PDN	192
7075_PHN	196	2024_PHN	192
7075_PSN	196	2024_PSN	24
7075_TDN	---	2024_TDN	---
7075_THN	---	2024_THN	---
7075_TSN	24	2024_TSN	24
7075_ADP	---	2024_ADP	---
7075_AHP	---	2024_AHP	---
7075_ASP	---	2024_ASP	---
7075_BDP	---	2024_BDP	---
7075_BHP	600	2024_BHP	720
7075_BSP	---	2024_BSP	---
7075_MDP	600	2024_MDP	192
7075_MHP	---	2024_MHP	---
7075_MSP	---	2024_MSP	---
7075_PDP	196	2024_PDP	---
7075_PHP	288	2024_PHP	---
7075_PSP	196	2024_PSP	192
7075_TDP	---	2024_TDP	---
7075_THP	---	2024_THP	---
7075_TSP	---	2024_TSP	---

To correct for the right-censoring of the data, a Kaplan-Maier survival analysis was performed (Figure 6.18) [21]. By this analysis, the surviving fraction was found to be 0.305. In order to account for the censored data, both fractions were made to be equal. Consequently, the population of 32 samples that did not fail was reduced to only 17 samples. Therefore, only 17 samples with a TTF of 720 hours were used in the training of the ANN instead of the 31 available.
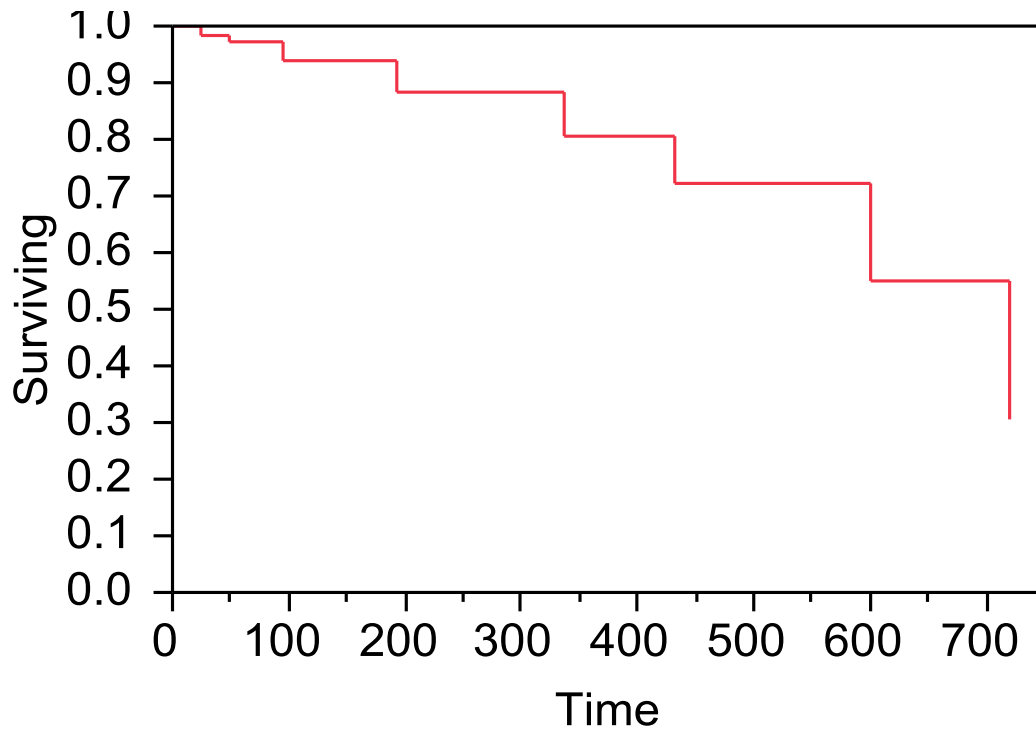
Figure 6.18. Kaplan-Meier survival analysis for the data set.

5.6.2.3.3 ANN model input sensitivity analysis. Figures 6.19 – 6.21 show the results from defuzzification of the EIS-TTF data. The figures show the fuzzy parameter $c_i(x_i)$ range for each input variable examined. Because the input data was associated with measurements at discrete frequencies in the measured frequency domain, it is possible to determine what parts of an EIS spectrum were most important for correctly predicting time to failure.
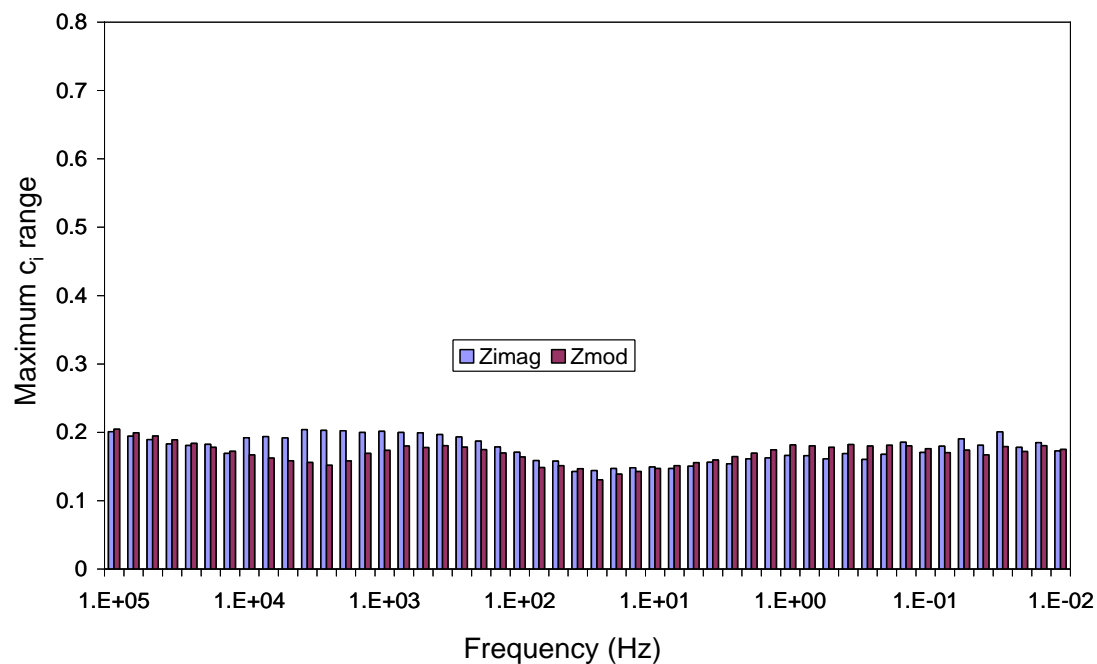
Figure 6.19. Maximum fuzzy parameter c_i range for EIS parameters Z_{mod} and Z_{imag} as a function of frequency.
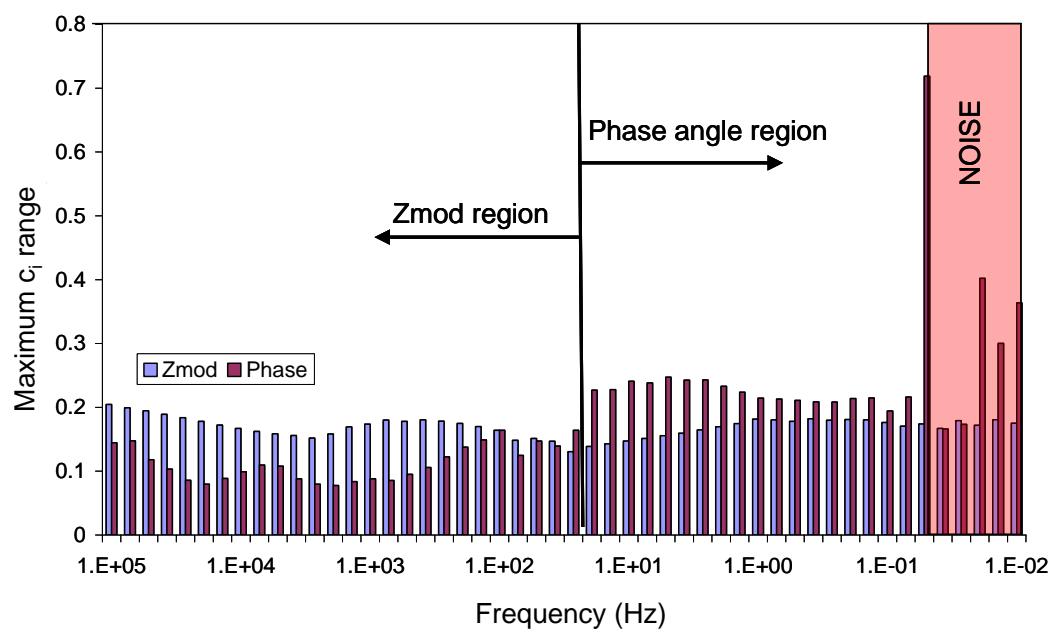
Figure 6.20. Maximum fuzzy parameter c_i range for EIS parameter phase angle and Z_{mod} as a function of frequency.
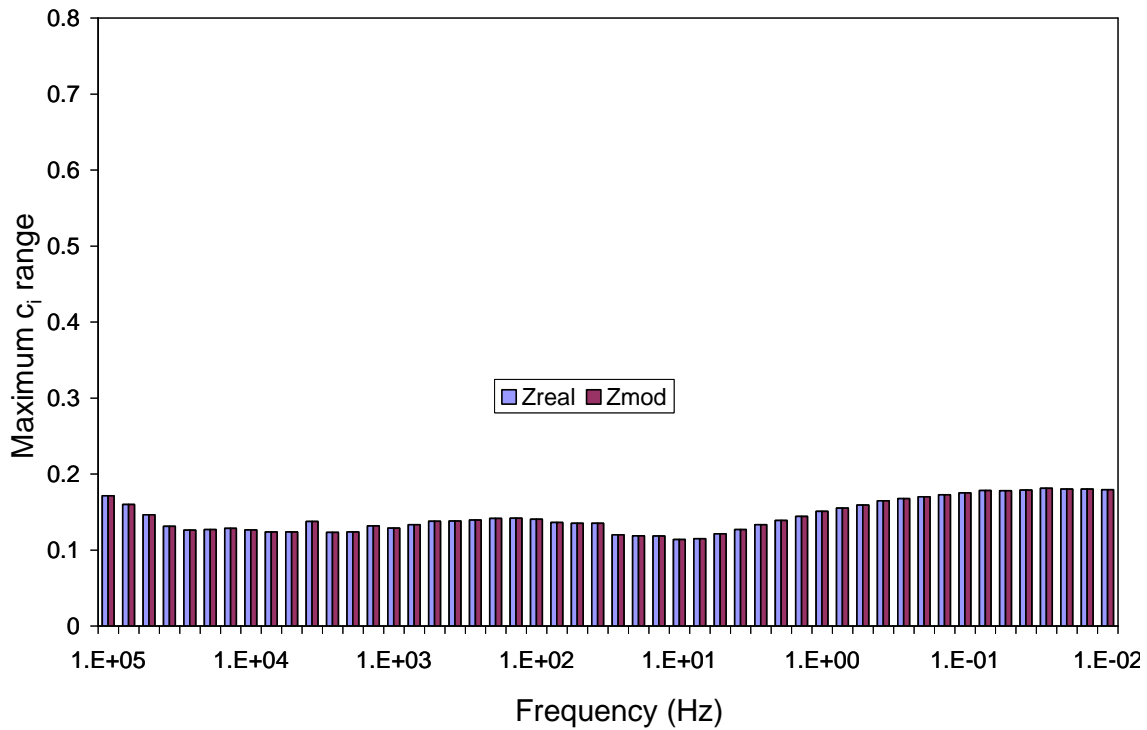
Figure 6.21. Maximum fuzzy parameter c_i range for EIS parameter Z_{real} and Z_{mod} as a function of frequency.

The most relevant EIS parameter was the phase angle at frequencies lower than 20 Hz. The real component of the impedance, Z_{real} was found to have the least influence. The imaginary component of the impedance, Z_{imag}, and the magnitude of the total impedance, Z_{mod}, seem to be the most significant variables at frequencies higher than 20 Hz. Although no considerable differences can be appreciated between Z_{mod} and Z_{imag}, it can be seen that the imaginary component is more significant than the total magnitude at intermediate frequencies while total magnitude is more significant at frequencies greater than 10 kHz.

The fuzzy parameter c_i for the phase angle showed that this particular EIS variable influenced the outcome the most (Figure 6.20) and therefore seems to be the best parameter for estimating TTF. The frequency domain in the figure can be divided in three regions. The vertical line at frequency of 20 Hz, divides the frequency region where phase angle dominates the response. Between 20 Hz and 50 mHz, the phase angle response dominates the TTF output but at lower frequencies the sensitivity is affected by noise present in the EIS data.
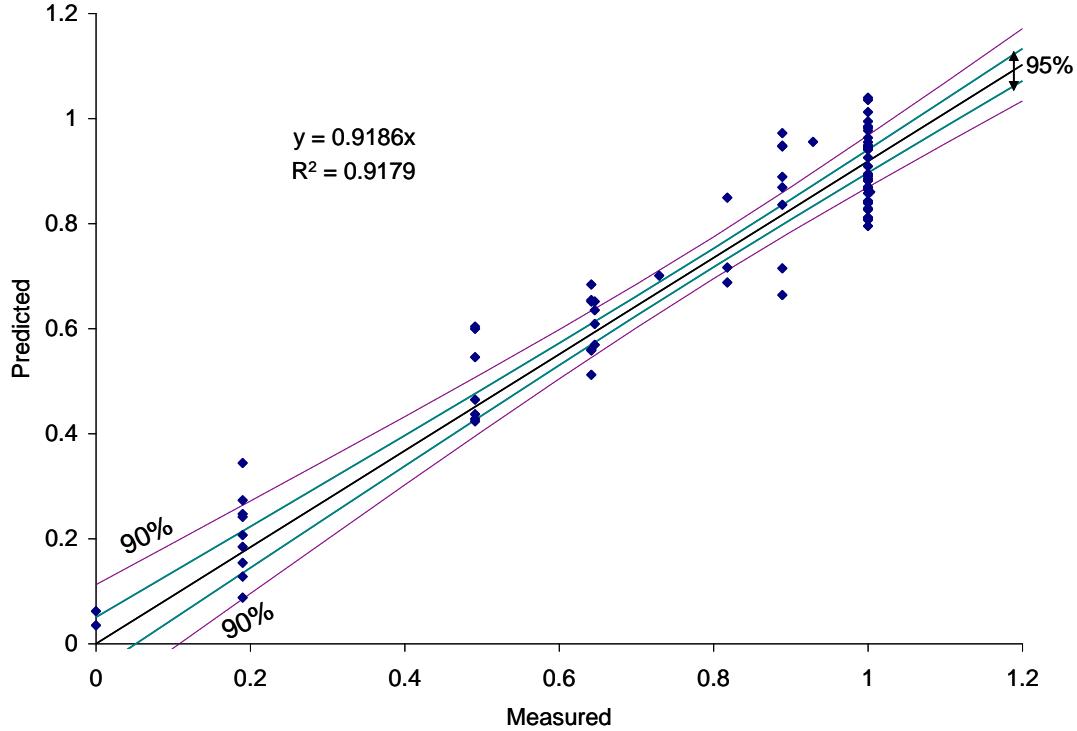
Figure 6.22. Normalized predicted vs. measure data. Prediction was done by a 7 hidden neurons ANN fed with phase angle information at 12 different frequencies. Confident intervals of 95% and 90% are also shown.

5.6.2.3.4 Artificial neural network construction, training and prediction. The number of neurons used in the hidden layer of the various ANN models explored was determined by systematically changing the number of hidden neurons, then training and validating the model. Configurations that gave the lowest error in the training and validation routines were adopted. Table 6.6 shows results of the best models.

Table 6.6. Parameters used for ANN prediction where M is the number of hidden neurons, and the coefficient of determination for the training set and validation set, R^2 and VR^2 respectively.

Input variables	# input variable	Best (90%)		
		M	R^2	VR^2
Real component of the impedance	49	12	0.42	0.40
Phase angle	49	14	0.75	0.64
Phase angle ($c_i > 0.208$)	21	9	0.82	0.79
Phase angle ($c_i > 0.227$)	12	7	0.88	0.86
Phase angle ($c_i > 0.243$)	6	8	0.91	0.84

The type and number of input neurons were selected based on the sensitivity analysis. The analysis showed that the most significant EIS input parameter category was phase angle data and that the real component of the impedance was the least significant. Two ANN models were constructed and tested using information obtained from the phase angle and real component. The output error in the validation routine was lower for the phase angle ($R^2 = 0.64$) than that for the real component ($R^2 = 0.40$).

The sensitivity analysis applied to the phase angle data input allowed elimination of comparatively insignificant phase angle information to further reduce the number of phase angle inputs. Models with pruned input layers were constructed. Pruning was carried out by eliminating phase angle inputs with fuzzy parameters with range values of 0.20, 0.22 and 0.24. This led to three different models with input layers 21, 12 and 6 input neurons respectively. In Table 6.6 the error associated with each model shows that an improvement is obtained from reducing the number of input neurons from 21 to 12 but the ability to correctly predict TTF diminishes if the number of input neurons drops to 6. On the basis of these exercises, the best architecture for the ANN had 12 input neurons (phase angle at 12 different frequencies between 20Hz and 50mHz), 7 hidden neurons, and the TTF output neuron (Figure 6.15).

Before training of the network, the training data set has to be trimmed to account for the censored data. This was done by randomly removing 14 EIS spectra from the training set that had a TTF of more than 720 hours (lost data). This reduced the number of training data from 499 to 485 EIS spectra. The validation set was not modified.

The ability of the ANN to predict TTF was tested using the reserved test data set. Predictions correlated well with actual outcomes. In Figure 6.22 the TTF predicted from the model is plotted against the actual TTF values in the test data set. A linear fit applied to the results yielded a line with a slope close to 0.918 and a correlation coefficient of 0.917. In this plot an ideal prediction would be characterized by a line passing from the origin with a slope of 1.0 and a correlation coefficient of 1.0.

The prediction can be evaluated by confidence intervals. The 90% and 95% confidence intervals are also shown in Figure 6.22. The prediction made by ANN at short exposures fell inside the 90% confidence interval except for one sample where the predicted TTF (0.347) was higher than the measured TTF (0.19) by 0.157. Considerably more of the predictions fell outside of the confidence interval at longer exposure times. It is worth mentioning that more than 60% of those predictions were empirically obtained by ANN using EIS data collected before 48 hours of exposure. For those samples that did not fail after 720 hours exposure more than 50% fell inside the 90% confidence interval.
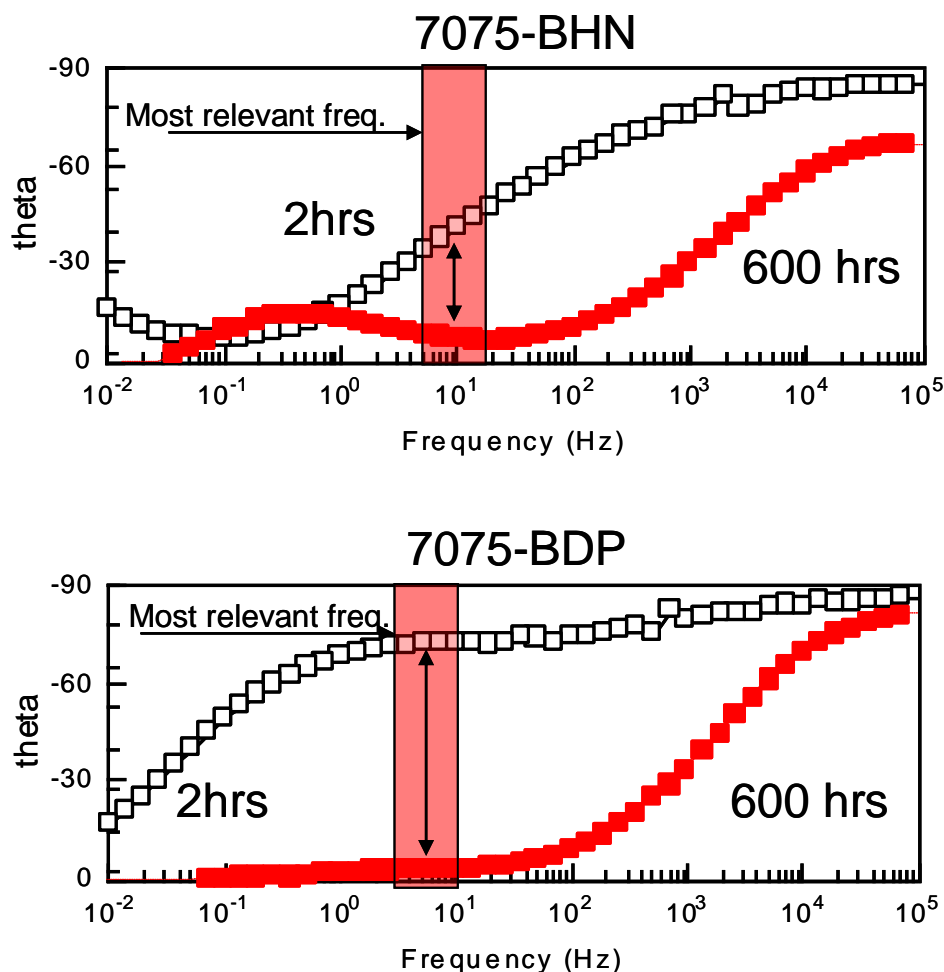
Figure 6.23. Two commercial samples 7075-BDP and 7075-BHN both with a visual TTF=1000 hours (B: Boegel 8500, D: Def 02GN084, P: Polyurethane and N: No top coat). Phase angle information was collected at 2 and 600 hours of exposure.

5.6.2.4 Discussion

5.6.2.4.1 Sensitivity analysis. The sensitivity analysis allowed a quantitative assessment of the significance of a large input data vector. This allowed pruning of the input to generate simpler models that retained acceptable degrees of prediction. Because the input data was derived from spectroscopy data it was possible to associate predictive significance to portions of the spectrum.

Interestingly, the fuzzy parameters for the phase angle variable in this study revealed that the most relevant frequencies in influencing the TTF value were 0.07Hz and 0.05Hz, followed by a range of frequencies between 0.5Hz and 20Hz, see Figure 6.20. The phase angle values associated to those frequencies correspond to a minimum on the phase angle curve and could be associated to the breakpoint frequency method, BFM.

The BFM method, introduced by Haruyama *et al.* [29] and later modified by Mansfeld and Tsai has been proposed as an estimator of the area of delaminated metal without the need of modeling EIS spectrum into an equivalent circuit [30, 31]. The original or modified BFM model relates the frequency at 45° ($f_{45°}$) or minimum phase-angle (f_{min}), to the delaminated coated area. An increase in both, $f_{45°}$ or f_{min}, is associated with an increase in the defect area and therefore to a decrease in the corrosion protection.

The phase angle response at the frequencies given by the fuzzy sensitivity analysis can be used to predict evolution on the defect area coating response. Figure 6.23 shows the phase angle response of commercial samples 7075-BDP and 7075-BHN. Although both samples showed no signs of corrosion at the end of the experiment (TTF = 1000 h), sample 7075-BDP shows twice the difference in the phase angle between 2 and 600 hours of exposure when compared with 7075-BHN. This difference suggests a markedly larger increase in the defect area for sample 7075-BDP than 7075-BHN.
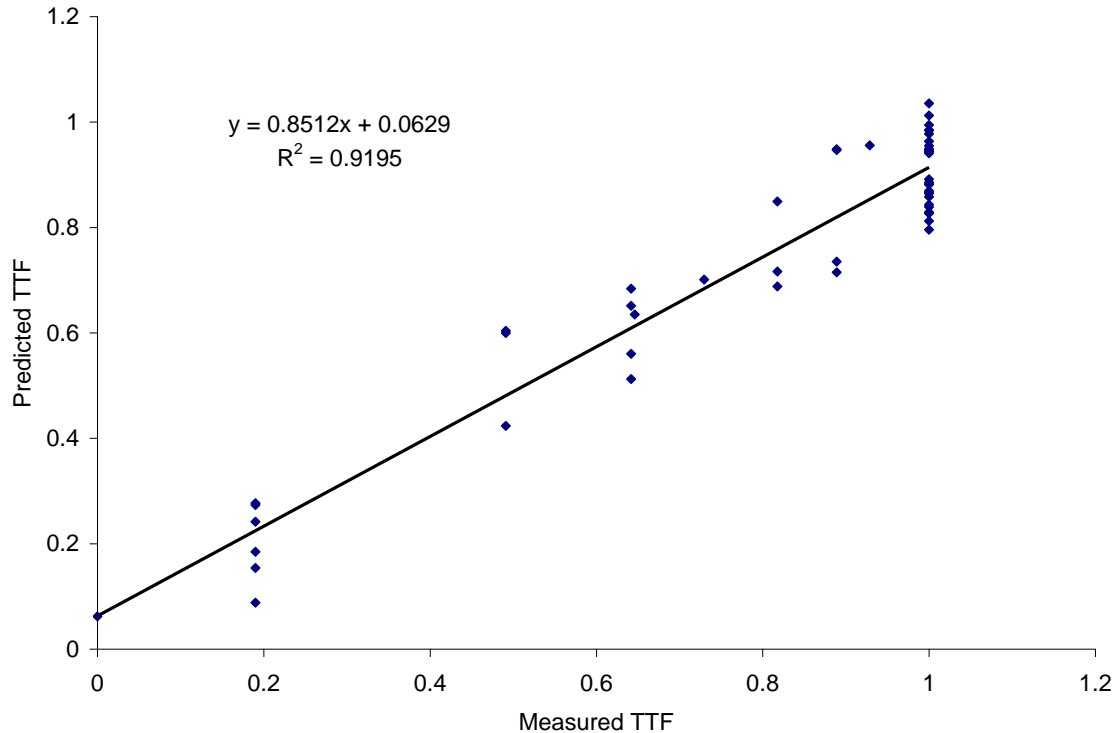
Figure 6.24. P-normalized predicted vs. measure data. Prediction was done by a 7 hidden neurons ANN fed with phase angle information collected before 48 hours exposure to ASTM B117.

Fuzzy analysis showed that the most relevant frequencies used to model TTF contained information about the evolution of defects. If one assumes that coating performance is then connected to the evolution of defects, and considering that defects are present at the time of coatings application, long-term TTF prediction from short-term exposure should be possible.

5.6.2.4.2 ANN development. There is interest in accelerated testing for coating performance predictions. Previous studies have shown that long-term predictions from short-term EIS measurement are possible. The first long-term predictions were done on the basis of EIS modeling using EC [6]. The EC parameter values obtained in the modeling were then fed into a regression model used to predict performance. More recently, Kumar and Buchheit used EIS data, with no modeling, to predict long-term performance [10]. They fed EIS data, which were randomly selected to cover all frequency ranges, into 4 different feed-forward ANNs. The best long-term prediction was achieved by an ANN fed with 10 phase angle values. The authors performed a sensitivity analysis and found out that among all four EIS parameters (Z_{mod}, Z_{imag}, Z_{real}, and phase angle) the phase angle was the most relevant EIS parameter. Our approach used a sensitivity analysis (fuzzy curves) to discriminate the most relevant input variables. Fuzzy curve analysis was able to discriminate among not only the EIS parameters but also among the frequencies, which allowed pruning of the EIS data. Although more ANN were constructed using different EIS parameters or combinations, the pruned ANN fed with the most relevant variables given by the fuzzy analysis showed the best prediction. The prediction accuracy of the pruned neural network presented in the result section showed an R^2 of 0.92 between measured and predicted TTF values for the 10% of data in the test data set. Roughly 66% of the test data set was collected before 48 hours of chamber exposure including exposure times of only 1 hour. The other 34% included spectra ranging from 96 hours to 720 hours. From Figure 6.24 it is evident that EIS spectra collected before 48 hours exposure can accurately predict coating performance up to 720 hours of exposure.

The pruned neural network presented in the result section was used to predict corrosion performance of chromium systems with an associated error of less than 4%. Previously collected phase angle information for samples AA7075-T6 and AA2024-T3 treated with and without a chromium conversion coating and with a chromium-containing primer after 48 and 1000 hours of salt spray exposure was fed in the pruned neural network. All chromium systems showed no signs of visual corrosion and therefore a visual TTF of 1 was given. The predicted TTF values obtained by the pruned neural network ranged from 0.96 to 1.02 for all the chromium systems.

Although the results from this research can only be related to coating performance in a salt spray exposure, the process involved in the prediction, i.e. pruning of the data and construction of an ANN, can be considered to be general and is ultimately applicable to predicting coating performance in service.

5.6.2.5 Conclusions

- Fuzzy curve analysis was used to discriminate the significance of EIS-based input data in the output variable. From the analysis, discrimination was not only among the type of EIS parameters, i.e. Z_{mod}, Z_{imag}, Z_{real}, or phase angle, but also among the frequencies.

- The most significant variables to influence the TTF extracted from fuzzy analysis were those attributed to the phase angle response at low frequencies.

- The most significant frequencies were those ranging from the upper breakpoint frequency to about 50 mHz; a range which is related to the evolution of coating defects.

- A pruned ANN was successfully constructed and trained using the most significant variables to predict time to failure of coating exposed to ASTM B117 salt spray.

- ANN showed proficiency in predicting long-term exposure TTF from short-term exposure EIS results.

5.6.2.6 References

1. Haley, P. J., *Pulmonary Toxicity of Stable and Radioactive Lanthanides.* Health Physics, 1991. **61**(6): p. 809-820.
2. Koplan, Jeffrey P., *Toxicological Profile for Chromium (p. 1-11)*, U.S.D.O.H.A.H.S.-A.f.T.S.a.D. Registry, Editor. 2000: Atlanta, GA.
3. ASTM, *ASTM B117-03 Standart Practice for Operating Salt Spray (Fog) Apparatus*, in *Annual Book of ASTM Standards*. 2003, ASTM: Philiadelphia, PA.
4. Kendig, M., Mansfeld, F., and Tsai, S., *Determination of the Long term Corrosion Behavior of Coated Steel With A.C. Impedance Measurements.* Corrosion Science, 1982. **23**(4): p. 317-329.
5. Mansfeld, F., Kendig, M.W., and Tsai, S., *Evaluation of Corrosion Behavior of Coated Metals With AC Impedance Measurements.* Corrosion, 1982. **38**(9): p. 478-485.
6. Buchheit, R.G., Cunningham, M., Jensen, H., et al., *A Correlation Between Salt Spray and Electrochemical Impedance Spectroscopy test Results for Conversion-Coated Aluminum Alloys.* Corrosion, 1998. **54**(1): p. 61-72.
7. Leggat, R.B., Taylor, S.R., Zhang, W., et al., *Corrosion Performance of Field-Applied Chromate Conversion Coatings.* Corrosion, 2002. **58**(3): p. 283-291.
8. Mansfeld, F., *A Discussion: A Correlation Between Salt Spray and Electrochemical Impedance Spectroscopy Test Results for Conversion-Coated Aluminum Alloys.* Corrosion, 1998. **54**(8): p. 595-597.
9. Bierwagen, G. P., He, L., Li, J., et al., *Studies of new accelerated evaluation method for coating corrosion resistance - thermal cycling testing.* Progress in Organic Coatings, 2000. **39**: p. 67-78.
10. Kumar, G. and Buchheit, R.G., *Use of Artificial Neural Network Models to Predict Coated Component Life from Short-Term Electrochemical Impedance Spectroscopy Measurements.* Corrosion, 2008. **64**(3): p. 241-254.
11. Kröse, Ben and Smagt, Patric van der, *An Introduction to Neural Networks (p.13-15)*. 8th edition ed. 1996.
12. Gurney, Kevin, *An Introduction to Neural Networks (Chapter 1 - p.1-6)*. 1997, Boca Raton, FL: CRC Press.
13. Bishop, Christopher M., *Neural Networks for Pattern Recognition (Chapter 3 - p.77)*. 11th ed. 1995.

14. Lin, Y., Cunningham-III, G.A., and Coggeshall, S.V., *Using Fuzzy Partitions to Create Fuzzy Systems from Input-Output Data and Set the Initial Weights in a Fuzzy Neural Network.* IEEE Transactions on Fuzzy Systems, 1997. **5**(4): p. 614-621.

15. Sinha, S. K., *Probabilistic Neural Network for Reliability Assessment of Oil and Gas Pipelines.* Computer-Aided Civil and Infrastructure Engineering, 2002. **17**: p. 320-329.

16. Sung, A. H., *Ranking importance of input parameters of neural networks.* Expert Systems with Applications, 1998. **15**(3-4): p. 405-411.

17. Lin, Y. and Cunningham-III, G.A., *A New Approach to Fuzzy-Neural System Modeling.* IEEE Transactions on Fuzzy Systems, 1995. **3**(2): p. 190-198.

18. Lin, Y., Cunningham-III, G.A., and Coggeshall, S.V., *Input Varaible Identification - Fuzzy curves and fuzzy surfaces.* Fuzzy Sets and Systems, 1996. **82**: p. 65-71.

19. Zadeh, L. A., *Fuzzy Sets.* Information and Control, 1965. **8**(3): p. 338-&.

20. Mendel, J. M., *Fuzzy Logic Systems for Engineering: A tutorial.* Proceedings of the IEEE, 1995. **83**(3): p. 345-377.

21. Stajduhar, I., Dalbelo-Basic, B., and Bogunovic, N., *Impact of censoring on learning Bayesian networks in survival modeling.* Artificial Intelligence in Medicine, 2009. **47**(3): p. 199-217.

22. Faraggi, D. and Simon, R., *A Neural-Network Model for Survival-Data.* Statistics in Medicine, 1995. **14**(1): p. 73-82.

23. Kaplan, E.L. and Meier, P., *Nonparametric Estimation From Incomplete Observations.* Journal of the American Statistical Association, 1958. **53**(282): p. 457-481.

24. Susarla, V and Ryzin, J. Van, *Nonparametric Bayesian Estimation of Survival Curves from Incomplete Observations.* Journal of the American Statistical Association, 1976. **71**(356): p. 897-902.

25. Delaurentiis, M. and Ravdin, P. M., *A Technique for Using Neural-Network Analysis to Perform Survival Analysis of Censored-Data.* Cancer Letters, 1994. **77**(2-3): p. 127-138.

26. Pintos, S., Queipo, N.V., Rincón, O. Troconis de, et al., *Artificial Neural Network Modeling of Atmospheric Corrosion in the MICAT project.* Corrosion Science, 2000. **42**: p. 35-52.

27. Marini, F., *Artificial neural networks in foodstuff analyses: Trends and perspectives - A review.* Analytica Chimica Acta, 2009. **635**: p. 121-131.

28. Reyes, Carlos Andres Peña, *Coevolutionary Fuzzy Modeling.* 2004: Springer-Verlag Berlin Heidelberg.

29. Hirayama, R and Haruyama, S, *Electrochemical Impedance for Degraded Coated Steel Having Pores.* Corrosion, 1991. **47**(12): p. 952-958.

30. Tsai, C.H. and Mansfeld, F., *Determination of Coating Deterioration with EIS: Part II. development of a Method for Field Testing of Protective Coatings.* Corrosion, 1993. **49**(9): p. 726-737.

31. Mansfeld, F., *Use of Electrochemical Impedance Spectroscopy for the Study of Corrosion Protection by Polymer Coatings.* Journal of Applied Electrochemistry, 1995. **25**: p. 187-202.

32. USAF, *Technical Manual: Application and Removal of Organic Coatings, Aerospace and Non-Aerospace Equipment (Chapter 3 - p.13-14).* USAF T0 1-1-8. 2008.

33. Brug, G. J., Vandeneeden, A. L. G., Sluytersrehbach, M., et al., *The Analysis of Electrode Impedance Complicated by the Presence of a Constant Phase Element.* Journal of Electroanalytical Chemistry, 1984. **176**(1-2): p. 275-295.

5.6.3 Characterization of Pigment Dissolution in Coatings

5.6.3.1 Introduction. Primer coatings are applied to metals and alloys to provide corrosion prevention. Primers improve adhesion of subsequently applied paints and can actively inhibit corrosion through incorporation of embedded inhibitive pigments. Pigment particle dissolution releases ionic species that work as corrosion inhibitors. Chromate is considered to be one of the most effective inhibitors for aluminum alloys. It provides both anodic and cathodic inhibition. However, chromates are toxic and cause cancer. Thus, the use of chromate pigments is restricted. Chromate-free pigments have and continue to be developed. Currently, there are some commercially available chromate-free primers, but the fundamental understanding of how they function is underdeveloped.

5.6.3.2 Materials and Methods

5.6.3.2.1 Coating Systems. A chromate and several Cr-free primers were examined in this study as shown in Table 6.7. The three chromate-free epoxy based primers used were Deft 02GN084, Hentzen 16708 TEP, and Sicopoxy 577-630. With the help of energy dispersive x-ray analysis (EDX) mapping and other information collected, the details of the primer formulations were developed. Deft 02GN084 is a high-solids epoxy-polyamide non-chromate primer. It is a solvent-based paint and mainly containing PrO_x, $CaSO_4$, TiO_2 pigment carriers. Among these three compounds, PrO_x is considered to be the inhibitor providing active corrosion prevention, which could be Pr_2O_3 or Pr_6O_{11}. Both of these compounds can decrease the corrosion current by at least one magnitude at pH = 5, 6 and 7. And they also increase passive region and shift open circuit potential (OCP) to be more negative by dissolution and reprecipitation as praseodymium hydroxide or praseodymium hydroxide carbonate. $CaSiO_3$ is considered to be the primary inhibitor within the Hentzen 16708 TEP primer, which is epoxy-based. $BaSO_4$ and SiO_2 are also present in this coating. Sicopoxy 577-630 is known as a Zn-rich epoxy primer, but no Zn-rich particles were found by EDX mapping. $CaSiO_3$ and $BaSO_4$ are found in Sicopoxy 577-630. All primers were mixed and applied following manufacturer's instructions. They were then sprayed and kept in lab fume hood for 24 h to get air-dried. Afterwards, primers were cured at 65.5º C for 48 hours. The thickness of these chromate-free is very similar and range from 20 to 30 μm.

A polyurethane topcoat was applied after the primers were coated. Samples with primers and topcoat were air-dried for 24 hours at room temperature, and then similar curing procedure was implemented as the process of curing chromate-free primers. Average thickness of the topcoat was about 40 μm.

Half primed samples were top-coated. Within this experiment, samples coated with Hentzen had polyurethane topcoat. So did samples with Sicopoxy. However, samples with Deft 02GN084 had no topcoat.

The chromate coating systems were prepared by Naval Air Station Patuxent River, MD. The coating system was composed of chromate conversion coating, chromate primer and topcoat. The chromate conversion coating was Alodine 1200S (MIL-DTL-81706 Type I, chromate control). The chromate primer was a solvent-based PPG CA7233 (MIL-PRF-23377 Type I, Class

C control). The inhibiting pigment in PPG CA7233 was soluble strontium chromate, which produces Cr^{6+} and Sr^{2+} ions by pigment dissolution to inhibit corrosion. The topcoat was a two-component polyurethane (PPG CA 8211/F36375 (MIL-PRF-85285 Type IV). The chromate primer and topcoat were sprayed according to standard procedures. The primed panels were allowed to cure for 24 hours at room temperature before applying topcoat, and then cured for 14 days at room temperature before further use.

Table 6.7: Phases within tested primers

Primer	Possible Inhibiting Pigments
Deft 02GN084	$Pr(OH)_3$, $CaSO_4$ and TiO_2
Hentzen 16708 TEP	$CaSiO_3$, $BaSO_4$ and SiO_2
Sicopoxy 577-630	$CaSiO_3$ and $BaSO_4$
Chromate Primer	$SrCrO_4$, SiO_2 and TiO_2

5.6.3.2.2 Salt Spray Exposure. The size of AA2024-T3 samples for salt spray was 125 x 75 mm. These samples were exposed in a salt spray chamber (Q-FOG, Inc.). Before salt spray exposure, black electrical tape was used to wrap edges of the samples so as to prevent corrosion from the edges of samples.

Coupons with primers were put on slotted frame to orient them at an angle slightly off vertical during exposure. The exposure followed ASTM B117, which prescribes use of a solution of 5% sodium chloride at 35 °C. Samples were exposed for 90 days. Two sets of samples with a chromate primer and topcoat were exposed. One set was in salt fog for 30 days and the other one for 90 days. Only the set exposed for 30 days was tested in this experiment. Chromate-free primers exposed in ASTM B117 for 30 days as part of a previous study. Unexposed samples of each coating systems also were obtained and examined as controls.

5.6.3.2.3 Sample Mounting and Polishing. Exposed samples were cut into 12x6 mm pieces and mounted within epoxy. Samples were polished using successively finer SiC grit papers starting at 240 and finishing with 1200 grit (Buehler Inc.). DP-Lubricant Blue (Struers A/S), a non-water based fluid was sprayed for lubrication and preventing samples attack by water. Diamond paste 1μm and 3 μm (Buehler Inc.) were used with micro diamond compound extender (LECO Corporation) on a microcloth for final polishing. Between each grinding, the samples were rinsed with ethanol and dried with air. Surfaces were examined under optical microscopy to assure readiness for further preparation. After final polishing, samples were cleaned ultrasonically to remove polishing residue. To facilitate SEM imaging, a thin gold coating was applied by a Pelco Model 3 sputter coater (Schneider Electric). A colloidal graphite (Ted Pella Inc.) was brushed all over the mount surface to increase the overall conductivity and prevent charging. With the help

of sputtering gold and carbon paint, the mounted samples were examined under SEM without charging.

5.6.3.2.4 Focused Ion Beam (FIB) Trenching. Focused ion beam (FIB) was used to create cross sections for analysis since ion beam milling caused limited damage to the surface. Samples were prepared using FEI Helios 600. When trenched, samples were placed horizontally (Figure 6.25). Titled cross sections were prepared by ion beam milling craters. The size of the observed area was approximately 30 µm by 25 µm. Identical beam voltage and current were applied when trenching different samples (30 kV, 21nA for trenching and 16kV, 4.7nA for surface cleaning) to assure similar damage to different samples. Two cross sections were prepared on each coating system of every exposure time.
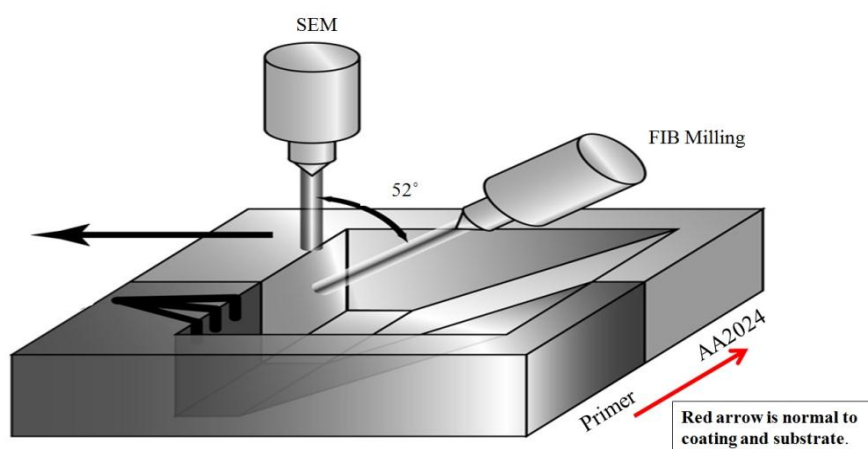
Figure 6.25. Position of samples when trenched by FIB.

5.6.3.2.5 Scanning Electron Microscopy (SEM) and Energy Dispersive X-ray (EDX) Mapping. A FEI/Philips XL-30 environmental scanning electron microscope (ESEM) equipped with energy dispersive spectroscopy was used to observe FIB-prepared cross sections. Energy dispersive X-ray (EDX) elemental maps were collected on samples using a 12 keV accelerating voltage and a spot size of 3-5. Pigment particle types within primers were identified by collocation of element maps with SEM images, along with product specification information. There was no gold coating and carbon paint on the surface of prepared cross sections as they were milled away by focused ion beam when trenching, so the results of EDX maps were not affected by them.

5.6.3.2.6 Image Analysis by Matlab™ Program. In order to analyze EDX mapping data to assess pigment dissolution, a Matlab™ program was developed based on elemental X-ray signal intensity. In this approach, the absolute value of elemental X-ray signal intensity could not be used as concentration directly. The X-ray signal intensity is an accumulation of counts at each image point at characteristic energy range. The higher the concentration, the greater is the

301

number of counts. However, the counts could not be converted to concentration, so the signal intensity indicated only the relative magnitude of elemental concentration at each pixel.

In this analysis there was no correction for absorption atomic number or fluorescence. A technique was developed to make comparative assessments of particle dissolution. The average (Ave) of the elemental X-ray signal intensity in a fixed area on a particle was used to estimate particle dissolution. Increasingly larger areas with radii of 5, 10 and 15 pixels were analyzed depending on the size of the particle. The center of the circle in which analysis was conducted was set as that with the highest average signal intensity across the selected pigment within radius of 5 pixels. The center selected did not only rely on its own intensity value, but the intensity values of the pixels around it. This method eliminated the possibility of selecting single pixel with unusually high intensity, which might not have seen the real center of the particle. When selecting a single particle for analysis, it was found that sizes and shapes of the particles were varied, even though the particles had similar elemental types. In order to limit the differences caused by shape and size, the pigments selected were larger than 30 pixels in any direction and the shape was close to spherical. However, the size of pigments could not be too large in case that the center of the pigments did not dissolve during exposure due to its large size. As an example, the fixed area for calculating average of calcium intensity within Hentzen 16708 TEP was shown in Figure 6.26. A similar evaluation was done for calcium and praseodymium within Deft 02N084, and barium within Sicopoxy 577-630. For the deft primer, the size of praseodymium-enriched pigments was small, so the radius of fixed area was limited to 5 and 10 pixels respectively. The percentage decrease of elemental signal intensity within fixed area was collected in order to see whether particle dissolved and soluble products spread out through the surrounding polymer. The calculation for estimating decrease in elemental signal intensity was:

$$\text{Percentage Residual (PR)} = \left(1 - \frac{2I_b - I_5}{I_5}\right) \times 100\% \qquad \text{(eq. 6.3.1)}$$

where I_5 is the average signal intensity of the fixed area within radius of 5 pixels and I_b is the average signal intensity of within radius of 10 or 15 pixels depending on the area selected. The smaller the percentage residue, the higher the dissolution rate during the same amount of time. Calculations were carried out for each element on multiple particles. Only the values of average percentage decrease (APD) are shown in Tables 6.8—6.11. Average intensity of the fixed area of particles within each primer is shown in Appendix 6A.
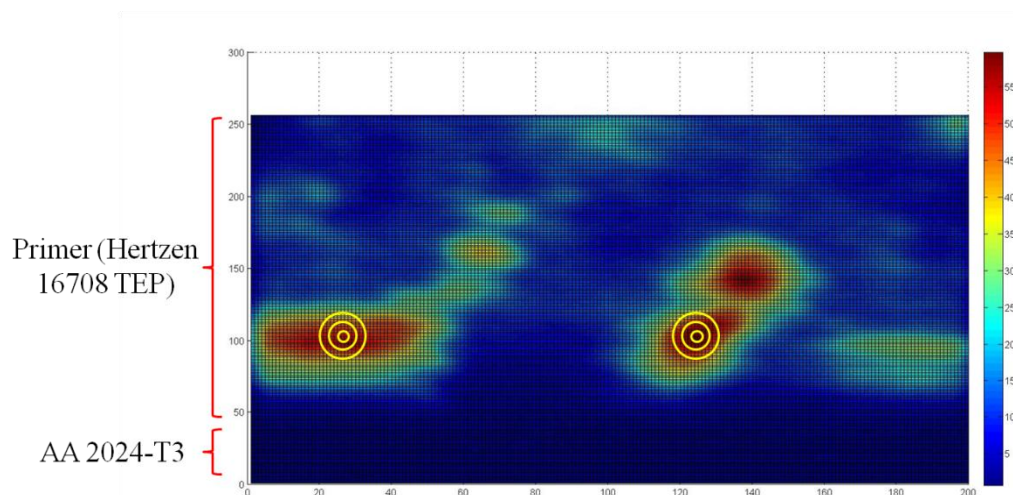
Figure 6.26. Cross-sectional view of calcium intensity profile of primer (Hentzen 16708 TEP) after 30-day exposure. Yellow circles mean increasingly larger areas with radii of 5, 10 and 15 pixels.

5.6.3.3 Objective. This study is to characterize essential aspects of active corrosion protection in primer coatings focusing on pigment dispersion and dissolution.

5.6.3.4 Results and Discussion

5.6.3.4.1 Cross Section by FIB Milling. A 25 x 30 μm cross-sectional area was made by FIB trenching on a chromate primer. Cross sections of other primer coatings were prepared by FIB milling as well. In Figures 6.27 through 6.30, it can be seen that the size of pigment particles varied in the range from 0.5 to 10 μm, and the shapes of particles were quite irregular.

5.6.3.4.2 EDX Mapping. EDX mapping was done on cross sections to determine particle identification. SEM images and EDX maps for primers examined are collected

In Figure 6.27, Cr and Si were identified in the unexposed chromate coating. Cr and Si both appeared in the mapping images. This was consistent with the information provided by Naval Air Station Patuxent River and confirmed the existences of chromate. Since K series X-ray emission energy of Sr was much large than 12 keV, the energy used in EDX, X-ray of Sr was not collected. By comparing the EDX maps and secondary electron (SE) images, the location of $SrCrO_4$ pigments could be determined by the location of Cr element in EDX maps. The size of chromate pigments ranged from 1-5 μm. The distance between two nearby individual chromate particles was quite small, about 1 to 2 μm. In the mapping image, chromium covers majority of area of the cross section and revealed the high volume concentration of chromate pigments. Nearby chromate pigments connected together. In Figure 6.28 and 6.29, the general intensity of chromium X-ray was quite high. This revealed the overall high concentration of chromium distributed within the primer. In addition, there was an inherent Cr-rich layer that appeared at the coating-metal interface, which was due to the chromate conversion coating since the coating was not exposed at all.

Oxygen was found to be collocated with Si and the particles were identified as SiO_2 (Figure 6.27). SiO_2 flake is widely used as pigment within primers. The size of SiO_2 particles was in the range of 1 to 5 μm. TiO_2 particles were identified from the collocation of Ti and O. They spread widely across the cross section, but had low volume fraction. The size of TiO_2 particles was very small and hard to be pointed out within SE image.
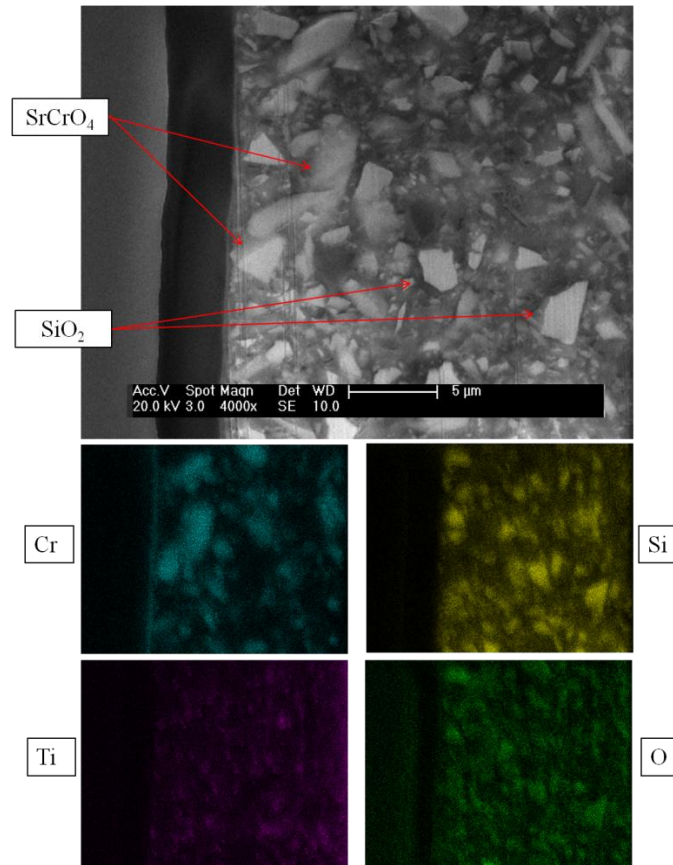
Figure 6.27. SEM and EDX mapping images of unexposed PPG EDWE 144A with conversion coating and phase identification
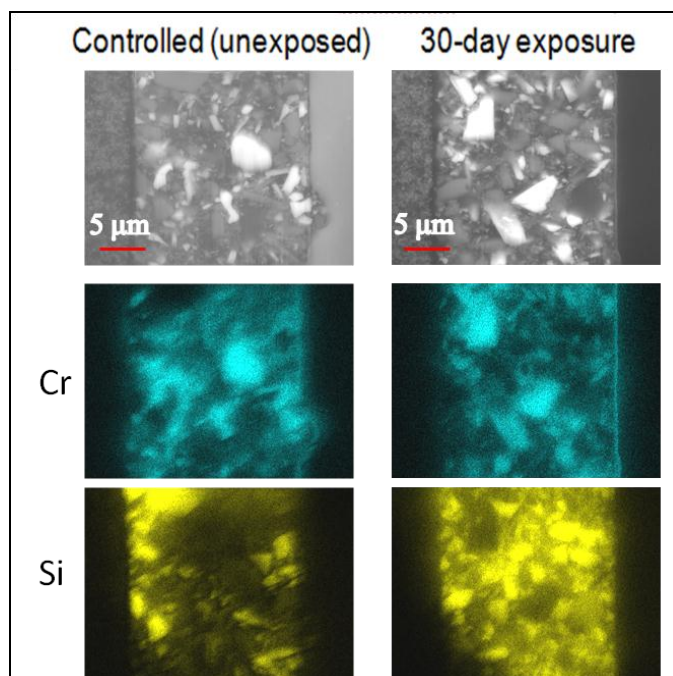
Figure 6.28. EDX maps of primer cross sections by FIB (PPG EDWE 144A)
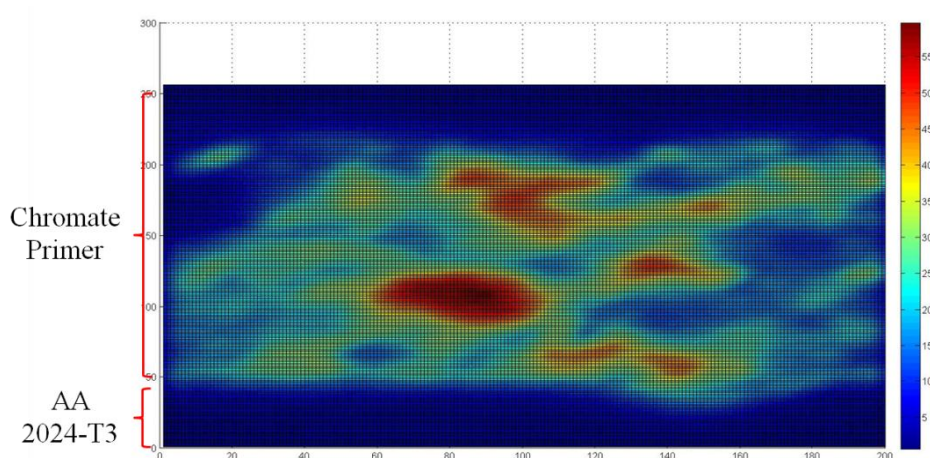
Figure 6.29. Cr elemental X-ray intensity map on PPG EWDE 144A by Matlab$^{\text{TM}}$ program.

In unexposed Deft 02GN084 (Figure 6.30), there was calcium, silicon, titanium and praseodymium, which was consistent with the product information. The overlap of Ca and S indicated the existence of $CaSO_4$. This phase appears as dark grey particles in the BSE image. $CaSO_4$ pigment particles were much larger than other types of particles within Deft primer. TiO_2 was determined from EDX mapping of elemental Ti. It was distributed all over the cross section as small clusters. In the BSE image, $Pr(OH)_3$ appears as the bright spots as Pr has the highest atomic number among the primary elements. In comparison with chromium in chromate primer,

the volume fraction of praseodymium was much smaller than chromium. Praseodymium was not detected at the coating-metal interface, even after ninety-day exposure (Figure 6.31). In another words, very little praseodymium appeared to reach the coating–metal interface. This lack of interaction may be due to a lack of inhibitive ion release or poor transport through the resin phase.
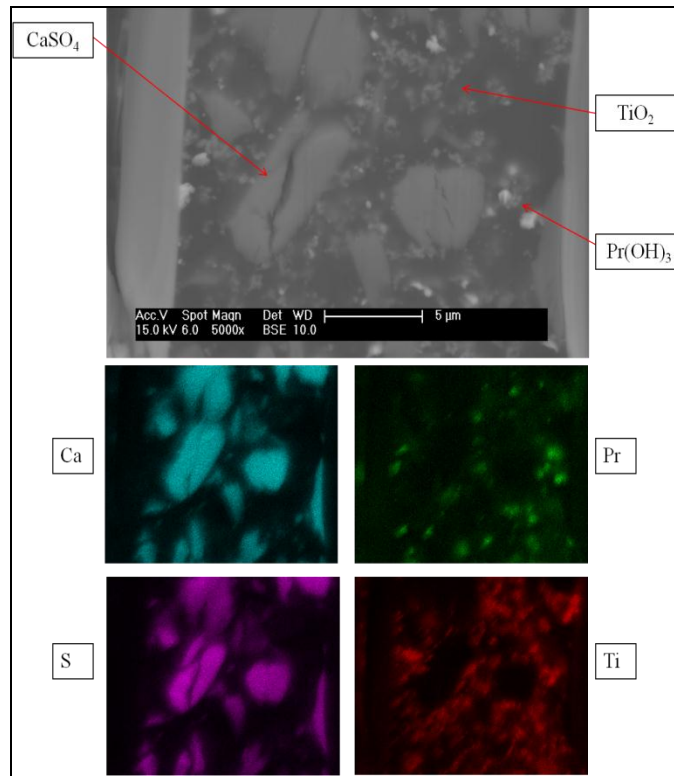
Figure 6.30. SEM and EDX mapping images of unexposed Deft 02GN084 and phase identification.
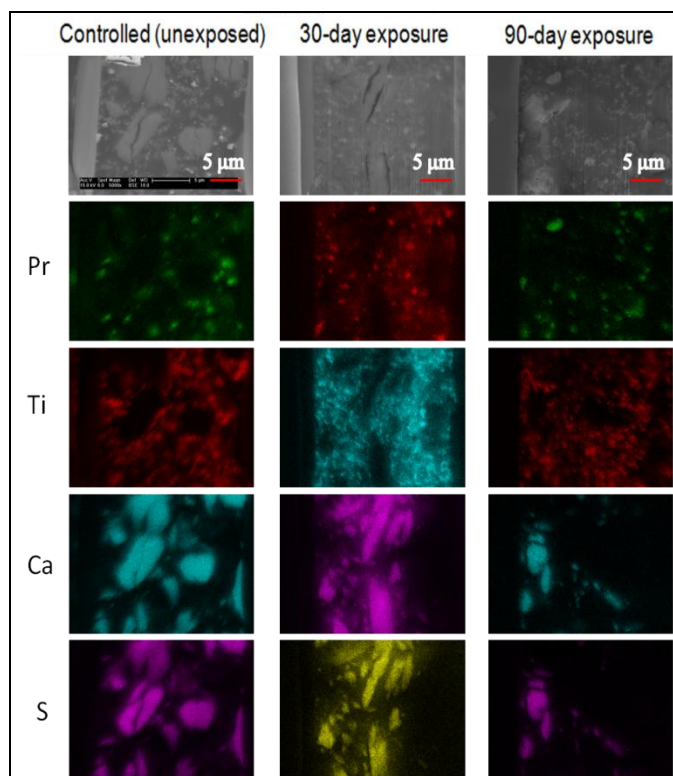
Figure 6.31. EDX maps of primer cross sections by FIB (Deft 02GN084).

Particles in Hentzen 16708 TPE and Sicopoxy 577-630 were identified as described above. In the BSE image of Hentzen 16708 (Figure 6.32), the brightest particles were identified as $BaSO_4$ due to the overlap of Ba and S. The size of $BaSO_4$ particles was about 1 to 3 μm. Overlapping of Ca and Si confirmed the existence of $CaSiO_3$. $CaSiO_3$ pigments were bright gray. $CaSiO_3$ is thought to be the inhibitor, but most of Ca element was far away from the interface, and particles were isolated from each other. Apparently, no calcium layer formed at the interface at the end of ninety-day test (Figure 6.33). In terms of the amount of calcium on the cross sectional area, it was more than praseodymium, but still less than chromium. The area of Si was much larger than that of Ca. This could be explained by existence of SiO_2 particles, which were dark gray.
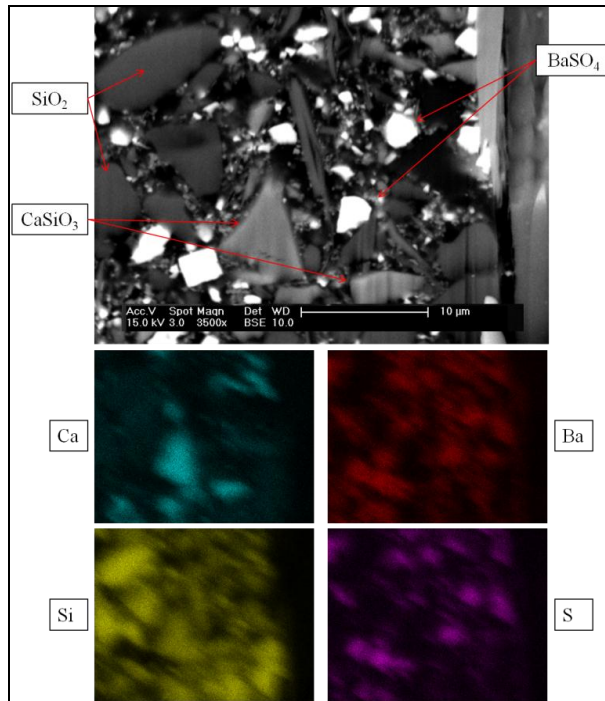
Figure 6.32. SEM and EDX mapping images of unexposed Hentzen 16708 TEP and phase identification.
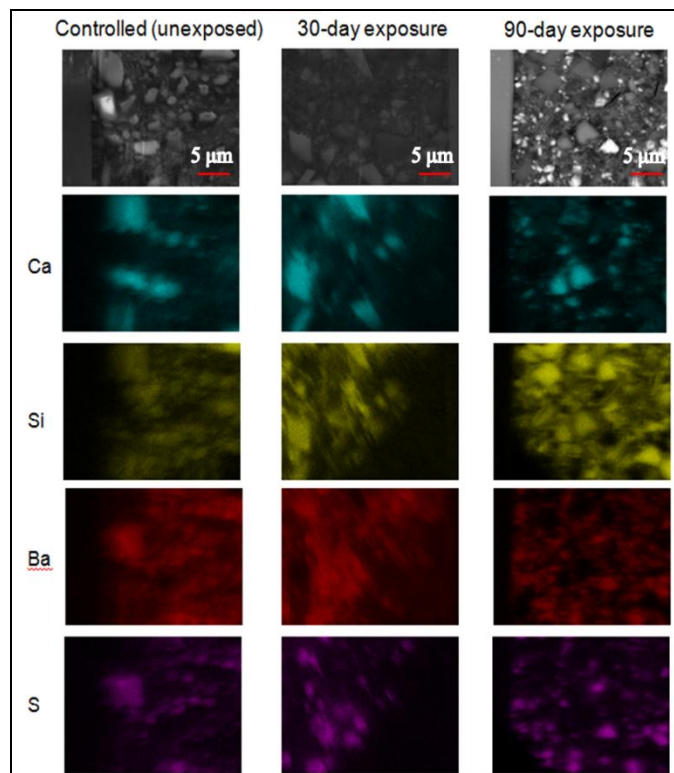
Figure 6.33. EDX maps of primer cross sections by FIB (Hentzen 16708 TEP).

In Figure 6.34, Ca and Si existed and were collocated in the mapping images. This demonstrated the existence of $CaSiO_3$. However, only several $CaSiO_3$ particles were seen on the cross section and none of them were larger than 1 μm. Ba and S overlapped and were prevalent in the primer. This reflected that there was $BaSO_4$ in this primer and it appeared to be a primary inhibitor in view of its prevalence. The volume fraction of barium was the largest among the three particles types. However, the amount of barium was still not as great as chromium in the chromate primers. And the intensity of barium was smaller than chromium, which meant lower concentration when comparing (Figure 6.28 and 6.34). And no clear barium layer was observed at the interface, as well as after long time exposure (Figure 6.35). Beside phase identification, EDX maps of primers as a function of exposure time showed there was no obvious dissolution and dispersion of any inhibitive species that could be identified by visual assessment alone (Figure 6.31, 6.33 and 6.35).
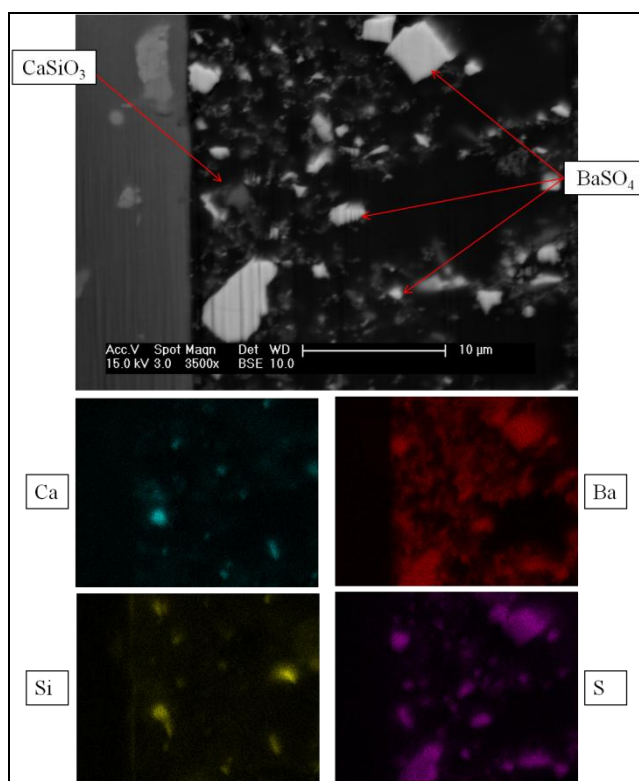
Figure 6.34. SEM and EDX mapping images of unexposed Sicopoxy 577-630 and phase identification.
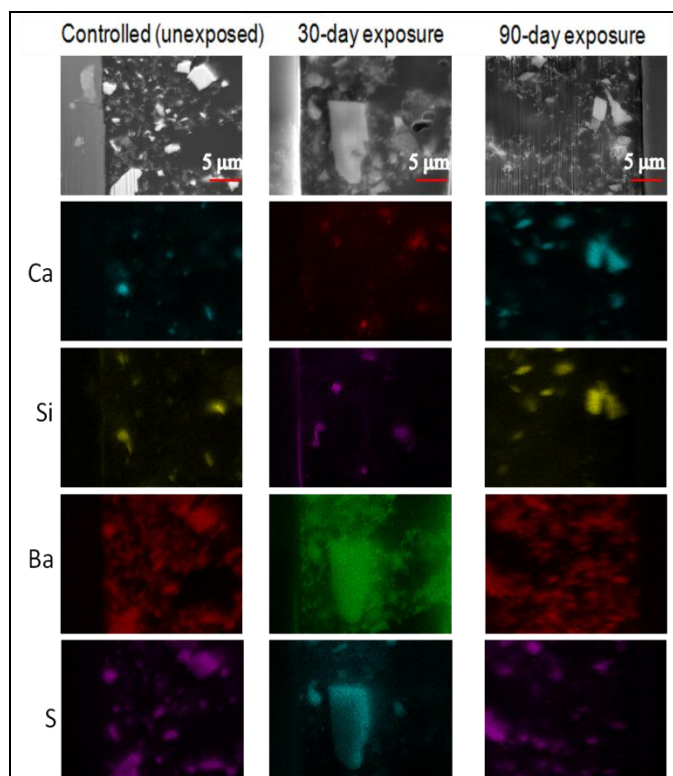
Figure 6.35. EDX maps of primer cross sections by FIB (Sicopoxy 577-630).

5.6.3.4.3 Image Analysis by Matlab. The percentage residual (PR) of chromium X-ray intensity within chromate primer was similar with increasing exposure time as the pigments were connected and mixed together and the distribution of chromium intensity was quite even across the cross sectional area. Therefore, PR could not be used to indicate the dissolution of chromate as there was almost no change of PR after exposure. However, in terms of isolated pigment particles, analyses were carried out to determine if the dissolution of pigment particles could be detected.

The average PR (APR) of calcium X-ray intensity within Hentzen 16708 TEP in a fixed area was calculated and is collected in Table 6.8. With increasing exposure time, APR of calcium intensity within fixed area of a single pigment particle decreased. As seen in Table 6.8, it fell from 84 to 71 percent after 90-day exposure indicating that the intensity of calcium dropped dramatically within same fixed area (15 pixels) after exposure. Similarly in Table 6.9, PR of calcium X-ray intensity decreased from 75 to 62 percent after salt spray test. All those above demonstrated calcium ion dissolved away from the center of the pigment particle during exposure regardless of the presence of a topcoat. The results of praseodymium from analysis of the Deft coating followed the same trend, (Table 6.10) reducing from 79 to 66 percent when comparing data from unexposed and 90-day exposed sample. Barium within Sicopoxy 577-630 also dissolved as its APR went down from 83 to 72 percent (Table 6.11).

Table 6.8. Average percentage residual of calcium X-ray intensity within fixed area of topcoated Hentzen 16708 TEP with, (a) unexposed, (b) 30-day exposure, (c) 90-day exposure.

Exposure Time No. of Pixels	Average Percentage Residual (%)		
	Unexposed	30 days	90 days
5			
10	93	92	87
15	84	80	71

Table 6.9. Average percentage residual of calcium X-ray intensity within fixed area of Deft 02G084, (a) unexposed, (b) 30-day exposure, (c) 90-day exposure.

Exposure Time No. of Pixels	Average Percentage Residual (%)		
	Unexposed	30 days	90 days
5			
10	88	82	80
15	75	64	62

Table 6.10. Average percentage residual of praseodymium X-ray intensity within fixed area of untopcoated Deft 02N084, (a) unexposed, (b) 30-day exposure, (c) 90-day exposure.

Exposure Time No. of Pixels	Average Percentage Residual (%)		
	Unexposed	30 days	90 days
5			
10	79	71	66

Table 6.11. Average percentage residual of barium X-ray intensity within fixed area of topcoated Sicopoxy 577-630, (a) unexposed, (b) 30-day exposure, (c) 90-day exposure

Exposure Time / No. of Pixels	Average Percentage Residue (%)		
	Unexposed	30 days	90 days
5			
10	93	91	85
15	83	81	72

From the analysis above, barium, calcium and praseodymium all dissolved during exposure since the APR of each element decreased with increasing exposure time. However, the rate of pigment dissolution was different and was affected by existence of topcoat. With topcoat applied, the APR in the circle with radius of 15 pixels hardly changed after 30-day exposure for Hentzen. In Table 6.8, with the existence of topcoat, APR of calcium X-ray intensity only decreased by 4% after 30-day exposure, whereas the APR of calcium intensity dropped from 75% to 64% without application of topcoat during the same period of time (Table 6.9). The average decrease rate of APR in the absence of topcoat was almost 2.5 times as that when there was topcoat during the first 30 days. However, there was only 2% drop from 30 to 90 day exposure for calcium with no topcoat in the next sixty days, while average percentage decrease of calcium still went down by 4.5% per 30-day exposure with the presence of a topcoat. The decrease of APR when a topcoat was absent was only one quarter of that with topcoat in the later sixty-day exposure. Regarding the non topcoated samples, calcium intensity decrease rate in the first 30 days was ten times larger than that in 30 to 90 day period, while the change of APR was very stable, 4% less per 30 days during the exposure when there was topcoat. This result expressed that calcium dissolved quickly at the beginning, but slowed down if there is no topcoat. And the case involved with topcoat showed the dissolution of calcium was restricted constantly.

For the primed-only coating, the APR of praseodymium decreased by 8% after 30-day exposure, but by just 5% from 30 to 90 day exposure. Dissolution of praseodymium was to calcium in that dissolution was strong initially and diminished gradually.

The APR of intensity of barium dropped only 2% in the first 30 days. Then it fell by 9% for the next 60 days. The dissolution rate increased, but only by 2.5%. Therefore, we can say that under aggressive environment pigments dissolved very fast and then slowed down. This may be because water could easily penetrate through the primer and dissolve the pigments. Thus, dissolution is strong at short times and then slows down. This also aligns with the idea of a driving force for dissolution that is proportional to concentration gradient. Dissolution of inhibiting ions was fast when the concentration gradient was large at the beginning and then become very slow as the gradient decreased. However, the pigments with topcoated primer dissolved very slowly and constantly. Water permeation required for pigments dissolution was

strictly limited due to the barrier property of topcoat. Barium dissolution rate increased as time passed by. This may result from more water penetrating topcoat with increased exposure time.

5.6.3.5 Conclusions and Implications for Future Research. Observations showed a greater concentration of chromate pigment particles in chromate primers than any other pigments particles in compared chromate-free primers. By visual assessment, the volume fraction of praseodymium was smallest within Deft 04GN098. Barium on Sicopoxy had the highest volume fractions inhibitor compound particles and its volume fractions were close to, but not as great as that of chromium within PPG CA7233. The amount of pigments within primers may be a critical factor for primer protection. In addition, none of these three non-chromate primer coatings formed a concentrated protective layer at the interface as the chromate conversion coating. Meanwhile, chromate pigments were close to each other. The distance between two nearby individual chromate particles was quite small, about 1 to 2 μm. In the mapping image, chromate pigments connected with each other and Cr element blended together through the outlay of the coating to the coating-metal interface, so they were able to form a channel providing inhibitive ions to coating-metal interface. However, similar type of active pigment within chromate-free primers was isolated and far apart, so it was difficult for the inhibitive ion to form a channel and transform through epoxy to the interface.

Although the pigments did not perform as well as chromate within PPG CA7233, they still dissolved during the exposure. When primer coated samples were exposed to an aggressive environment, the APR of elemental X-ray intensity in a fixed area decreased as exposure time increased. This indicated the dissolution of tested element. However, the rate of dissolution was influenced by the existence of topcoat. When there was no topcoat, the dissolution of pigments was fast at the beginning, but slowed down. For the instance of the presence of only primer, water moisture easily penetrated the primer and helped dissolve the pigment. Then the dissolution slowed down as the concentration gradient became smaller as pigments dissolved. However, the dissolution rate of pigments was similar along the whole exposure if there was topcoat. This appears to be due to the barrier property of topcoat, which constraints the water penetration.

This study showed the differences between chromate and chromate-free primers in terms of morphology and chemistry. It showed an influence of the topcoat on pigment dissolution. Meanwhile, it expressed the dissolution of the inhibiting pigment quantitatively. However, the data from analysis of Matlab$^{\text{TM}}$ program does not equate to the concentration of inhibiting species. Thus, only the trend of dissolution could be inferred; not true rate of dissolution and dispersion.

5.6.4 Quantitative Evaluation of Corrosion in Exposure Test Samples

5.6.4.1 Introduction. Weight loss is one of the most extensively used methods for measuring corrosion. In this approach, a sample with known exposure area and mass is exposed in an environment for a certain amount of time. The mass loss is measured after withdrawing the sample and removing the corrosion product. Weight loss is more commonly used for uniform

corrosion than for localized corrosion. The mass loss of localized corrosion is minimal and hard to measure, even though the corrosion is serious. The corrosion rate can be estimated based on the weight lost, exposure time and area. However, weight loss of substrate material may not be able to be obtained accurately if coatings are applied to the substrate, as the coatings must be removed carefully. The corrosion rate will be larger than its actual value if the weight of coating were not eliminated from the total weight loss. Therefore, it is necessary to develop a method measuring material loss directly after exposure without considering the impact of coatings.

5.6.4.2 Materials and Methods

5.6.4.2.1 Coating Composition. The samples were prepared by Naval Air Station Patuxent River MD. They were 155.3 x 79.2 x 6.5 mm and made of AA2024-T3. Eight holes were drilled on each panel at first (Figure 6.36). Then four kinds of surface treatment and six types of primer combinations were applied. Half of each sample had topcoat above primer coating, but the other half only had primer and surface treatment. After the panels were painted, scribes were applied manually using a carbide-tipped stylus in an "X" pattern across the holes before fasteners were installed. Two types of fasteners were mounted on the samples through the holes. The positions of fasteners mounted were shown in Figure 6.36. Overall, there were 96 types of coating and fastener combinations shown in Figure 6.37. Then scratches were made across bottom four holes. Each coating system was applied on two panels. One group of samples was exposed by following ASTM B117 for 500 h, and the other one by following ASTM G85 for 360 h. Scribes were applied manually using a carbide-tipped stylus in an "X" pattern across the fastener holes before fasteners were installed. Before the panels were processed and painted, the holes were put in the galvanic panels.
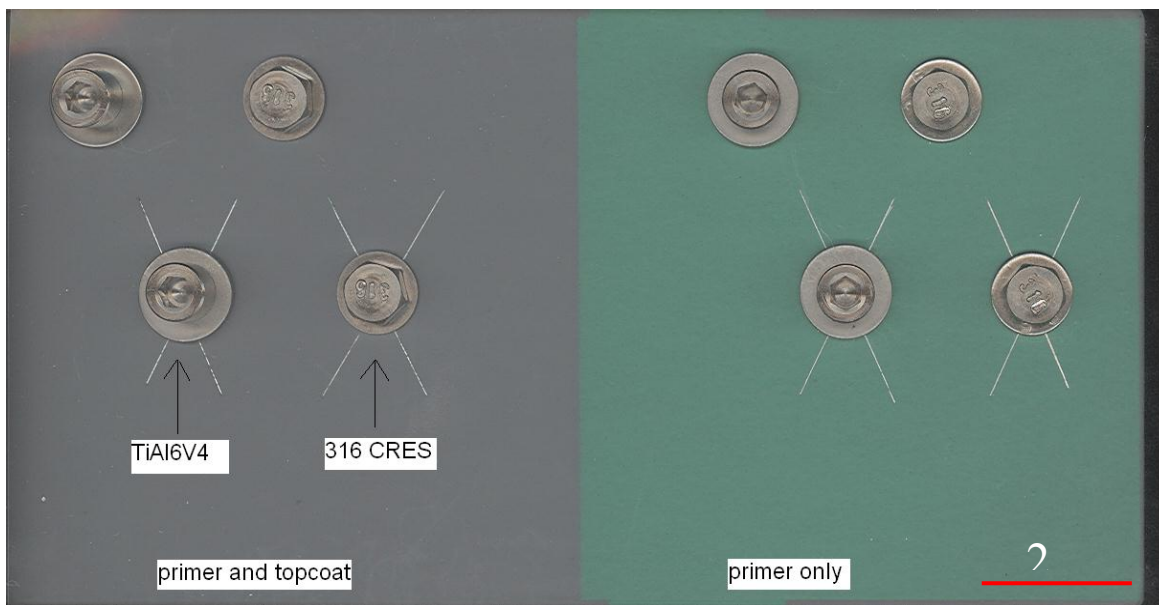
Figure 6.36. Positions of fasteners mounted.
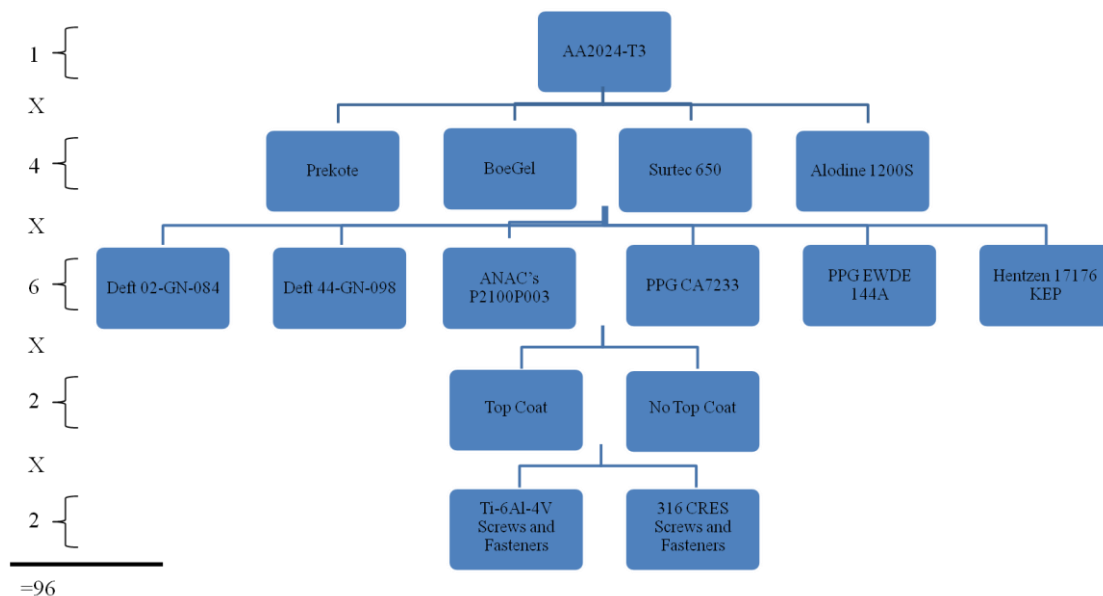
Figure 6.37. Coating systems in detail.

The four surface treatments used were PreKote, Boegel, Surtec 650 and Alodine 1200S. PreKote is a chromate-free inorganic inhibitor and also silane adhesion promoter. Boegel also is an adhesion promoter. Surtec 650 is a liquid concentrate based on trivalent chromium that could passivate aluminum. Alodine 1200S is a chromate-containing pretreatment. All test panels were surface treated following regular process. The six primers used are Deft 02-GN-084, Deft-44-GN-098, ANAC's P2100P003, PPG CA 7233, PPG EWDE 144A and Hentzen 17176 KEP. All primer paint were two-part epoxy-amides based paints, with part A (epoxy) and a part B (amide) mixed prior to painting. Deft 02GN084 was introduced in section 6.3. It is a high-solids epoxy-polyamide non-chromate primer. It is a solvent based paint. Praseodymium hydroxide is considered to be the active inhibitor. The primer's thickness was about 23.6μm. Deft 44-GN-098 is also a non-chromate primer qualified to MIL-PRF-85582 Class N Type I. Praseodymium compound is thought to be the inhibitor. It was 22μm thick which is thinner than Deft 02-GN-084. The difference between this primer and Deft 02-GN-084 is that Deft 44-GN-098 is a water-based paint, but Deft 02-GN-084 is a solvent-based. "ANAC" P2100P003 refers to Akzo Nobel Aerodur MgRP003 (P003). It is reported to be a solvent-based paint with a Mg-pigment phase. Magnesium within the primer will be sacrificially corroded to protect the aluminum alloy substrate. This is a non-chromate paint as well. The average thickness was about 25-30μm. Hentzen 17176 KEP is a solvent based paint. It is a non-chromate paint with thickness of 22μm. PPG CA7233 (MIL-PRF-23377 Type I, Class C control) and PPG EWEDA144A (MIL-PRF-85582 Type I, Class C1 control) are both chromate primers. PPG CA 7233 is solvent based while PPG EWEDA is water based. Their thicknesses were approximately 23μm.

Half of each sample was with topcoat. The topcoat a two-component polyurethane (PPG CA 8211/F36375 (MIL-PRF-85285 Type IV). The average dry thickness of the topcoat was 50μm. Panels were primed and top-coated according to standard procedures. The primed panels were allowed to cure for 24 hours at room temperature before applying topcoat, and then cured for 14 days at room temperature before further use.

315

The two types of fasteners were made of Ti-6Al-4V and 316 CRES. Ti-6Al-4V is composed of 6% aluminum, 4% vanadium, 0.25% iron, 0.2% oxygen, and titanium for the rest. It is used extensively in aerospace, medical and marine due to its high strength and good corrosion resistance. Stainless steel 316 CRES has 16 to 18% chromium and 2 to 3% molybdenum. The addition of molybdenum increases its corrosion resistance, particularly to pitting and crevice corrosion in chloride environment. Both of the fastener induced galvanic corrosion of aluminum alloys in these tests. When the samples were received, the fasteners were already taken out. The paint was stripped off by immersion in paint stripper PR-3505 MIL-R-81294 (Eldorado Chemical Company, Inc) for an hour. However, some coating remnants were remained on the substrate and needed to be cleaned.

5.6.4.2.2 Sample Cleaning. Due to the size of the samples, they were cut into half for ease of cleaning. Original weights were recorded before cleaning. One half of a sample was immersed in concentrated nitric acid (sp gr 15.6) to remove corrosion product. The amount of acid for each cleaning was about 100 mL to assure that the substrate was totally immersed. The acid was replaced if the cleaning process lasted more than an hour since nitric acid would start to attack the substrates as it decomposed. Decomposition was identified as the solution changed from colorless to yellow. During immersion, the coatings lost adhesion with the substrates and were suspended within the acid.

Weight change was measured every 10-15 minutes during cleaning. The cleaning process was terminated when the weight loss was within 0.01 gram between two consecutive weight measurements. Before each weight measurement, rinsing and drying were necessary. Immersed samples were rinsed in continuous streams of deionized water. Samples were then dried with a paper towel and compressed air. Samples were checked visually to make sure there were no white solid corrosion products within the scratches.

5.6.4.2.3 Volume measurements of material lost. An optical profilometer was used to measure the volume of material lost due to corrosion. After cleaning, the volume of material lost around the scribed area was measured to characterize the extent of corrosion. As the weight of the sample before exposure was not known, weight loss was not known. A technique called optical profilometry (OP) was utilized in this study that was able to measure the depth of corrosion and test the surface morphology profile. A stitching function was used as the area measured was much larger than that of a single OP measurement. Multiple partially overlapping measurements were matched together to form a single dataset The area measured by stitching function was in the range from 20 x 20 mm to 40 x 40 mm depending on the actual condition of corrosion. The volume was calculated after the morphology profile of corroded area around each hole at the bottom row. There were situations that uniform corrosion spread out which caused corroded area around nearby holes intersect. In order to deal with the intersection, the corroded area was separated from the middle if it was around two nearby screw holes at the bottom row.

When morphology measurements were accomplished, artificial zero height needs to be set up manually since OP software automatically sets the mean of all measured height as zero height, which may be not equivalent to the height of the intact substrate surface. After setting the zero height manually, the volume could be calculated.

Each corrosion volume of scribed area was measured twice and then the average value was collected. The overall results of samples with different coating and fastener systems are presented in Tables 6B.1 and 6B.4, in Appendix 6B to this section, for both exposure conditions. In addition, the corrosion volume was plotted by the category of material of fastener, surface treatment, primer and existence of topcoat respectively to see the impact of each factor on efficacy of corrosion prevention. Y axis was corrosion volume. The ordinate value plotted on the x-axis was calculated as follows:

$$X = \frac{n}{N+1}$$
(**eq.** 6.4.1)

where n was number of individual observations within each category and N is total number of observations. X was in the range from 0 to 1. Then number of counts falling in top, mid and bottom thirty two were collected in terms of material of fastener, surface treatment, primer and existence of topcoat. It was based on rank of corrosion volume from small to large.

5.6.4.2.4 Measurements of Corrosion Area. In order to measure the corrosion area of each sample, corroded surfaces of all cleaned samples were scanned. The scanned pictures were analyzed by an image analyzing software called Clemex Vision (Clemex Technologies Inc.). The scale bar was calibrated appropriately and then lines were drawn at the boundary of corrosion. The boundary was determined as the juncture of blurry corroded surface and uncorroded bright metal surface. Then the software is able to tell the corrosion area based on previous calibration. The area of screw holes was subtracted in the reported corrosion area. The area of the screw hole is about 24 mm^2. The results of corrosion area measurements were shown in Table 6B.3 and 6B.6 for both exposure environments.

5.6.4.2.5 Calculation of Corrosion Rate. The equation of corrosion rate (R) used was:

$$R = \frac{V}{tA} \times 8760$$
(**eq.** 6.4.2)

where V was volume of material loss, t the exposure time and A corrosion area. The unit of R was mm/yr. The results of corrosion rate were listed in Table 6B.2 and 6B.4 for ASTM B117 and G85. The corrosion rate was plotted as the way of plotting corrosion volume by the category of material of fastener, surface treatment, primer and existence of topcoat respectively to see the impact of each factor on protecting substrate AA2024-T3. Corrosion rate was also plotted as corrosion volume.

5.6.4.3 Objective. This objective of this study was to demonstrate the use of optical profilometry (OP) to estimate volume and mass loss to compare the efficacy of different coating combinations, even though there is no information prior to exposure available but only the samples after exposure. This study focuses on quantifying corrosion of primed and painted AA2024-T3 samples after cabinet exposure testing.

5.6.4.4 Results and Discussion. In general, samples exposed in ASTM B117 for 500 h had greater material loss than those exposed in ASTM G85 for 360 h (Figure 6.38). The corrosion volume was in the range from 0.9 to 29.4 mm^3.
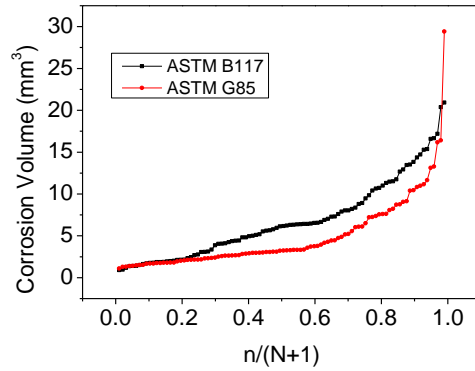
Figure 6.38. Corrosion volume in ASTM B117 and G85.

In terms of the corrosion rate, about 40% had similar corrosion rate regardless of exposure condition (Figure 6.39). In the other 60% cases, the corrosion rate of samples exposed to ASTM B117 was greater than that exposed to ASTM G85. The corrosion rate ranged from 0.48 to 4.8 mm/yr.
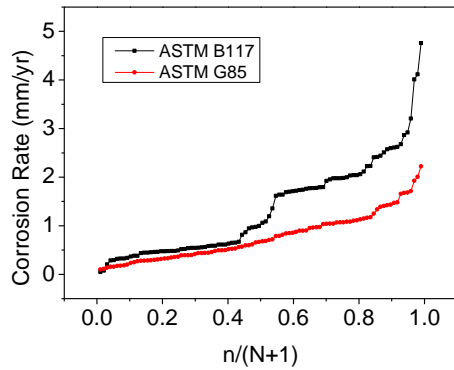
Figure 6.39. Corrosion rate in ASTM B117 and G85

The corrosion area of half samples was close no matter which exposure condition the samples were immersed in (Figure 6.40). However, for the other half of the cases examined, samples within ASTM G85 has obvious larger corrosion area that those within ASTM B117. The values of corrosion area were between 11 and 1200 mm^2.
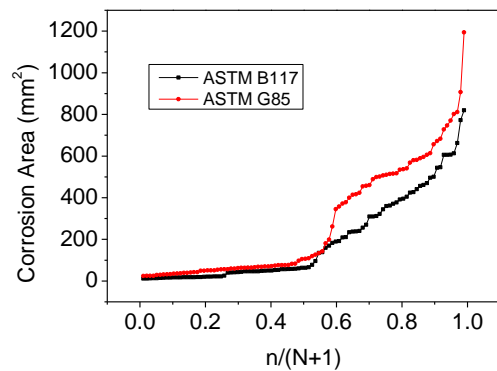
Figure 6.40. Corrosion area in ASTM B117 and G85.

5.6.4.4.1 Types of corrosion. In both ASTM B117 and G85, the samples with PreKote or Boegel as surface treatment ended up with corrosion in a small area tightly close to the scribes (Table 6.12), while the samples with Surtec 650 or Alodine 1200S all resulted in being corroded in a relative large area. PreKote and Boegel were chromate-free pretreatments. Surtec 650 and Alodine 1200S are two types of pretreatments involving with chromium. The results in Table 6.12 proved the types of corrosion did not depend on experiment environment, the existence of topcoat, choices of primer and fastener material. The explanation was that chromate pretreatment became a fundamental part of the metal surface and provided good adhesion and bonding properties for paints and coatings. Therefore, the excellent adhesion and bonding between pretreated surface and coating prevented the infiltration of water and oxygen, which resulted in corrosion in a very limited area. In contrast, the two adhesion promoters, PreKote and Boegel, were not able to provide as great adhesion properties as chromate surface pretreatment.

5.6.4.4.2 Corrosion of Samples Exposed in ASTM B117 and ASTM G85.

a. Effect of fasteners. In Figure 6.41, the corrosion volume of samples exposed in ASTM B117 was listed by material of fasteners. The corrosion volume around Ti-6Al-V4 fasteners was smaller than that around 316 CRES fasteners regardless of coatings applied as the line labeled as 316 CRES were far above Ti-6Al-4V line in terms of y axis. However, the corrosion rate did not follow the same trend as corrosion volume. Figure 6.42 showed the corrosion rate caused by both fasteners was very close. The corrosion volume caused by 316 CRES was bigger than that by Ti-6Al-4Vwhile the corrosion rate was very close, so the corroded area affected by 316 CRES was larger than that by Ti-6Al-4V. This also was confirmed the corrosion area measurements in Figure 6.43. The line referred as 316 CRES was always above that as Ti-6Al-4V. All in all, the reason why galvanic corrosion between 316 CRES and AA2024-T3 was stronger than that between Ti-6Al-4V and AA2024-T3 was due to the larger corrosion area not corrosion rate.

Table 6.12. Collection of corrosion type.

Surface Treatment	Primer	Corrosion Type			
		ASTM B117		ASTM G85	
		Corrosion in wide area	Corrosion in small area	Corrosion in wide area	Corrosion in small area
PreKote	Deft 02-GN-084	√		√	
	Deft 44-GN-098	√		√	
	ANAC's P2100P003	√		√	
	PPG CA7233	√		√	
	PPG EWDE 144A	√		√	
	Hentzen 17176 KEP	√		√	
Boegel	Deft 02-GN-084	√		√	
	Deft 44-GN-098	√		√	
	ANAC's P2100P003	√		√	
	PPG CA7233	√		√	
	PPG EWDE 144A	√		√	
	Hentzen 17176 KEP	√		√	
Surtec 650	Deft 02-GN-084		√		√
	Deft 44-GN-098		√		√
	ANAC's P2100P003		√		√
	PPG CA7233		√		√
	PPG EWDE 144A		√		√
	Hentzen 17176 KEP		√		√
Alodine 1200S	Deft 02-GN-084		√		√
	Deft 44-GN-098		√		√
	ANAC's P2100P003		√		√
	PPG CA7233		√		√
	PPG EWDE 144A		√		√
	Hentzen 17176 KEP		√		√

Figure 6.41. Corrosion volume listed by fastener type in ASTM B117 for 500 h.

Figure 6.42.Corrosion rate listed by fastener type- ASTM B117 for 500 h
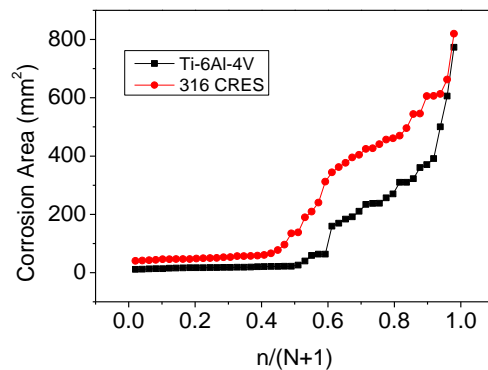
Figure 6.43. Corrosion area listed by fastener type in ASTM B117 for 500 h.

For samples exposed in ASTM G85 for 360 h, the corrosion volume was plotted by type of fastener. And the overall results followed the same trend as that in ASTM B117. The corrosion volume around Ti-6Al-V4 fasteners was smaller than that around 316 CRES fasteners regardless of coatings applied (Figure 6.44). The area affected by 316 CRES fasteners was larger than that by Ti-6Al-4V fasteners (Figure 6.45). However, the corrosion rate was very close (Figure 6.46). This confirmed the conclusion above that galvanic corrosion between 316 CRES and AA2024-

T3 were stronger than that between Ti-6Al-4V and AA2024-T3 due to the corrosion area, but not corrosion rate.
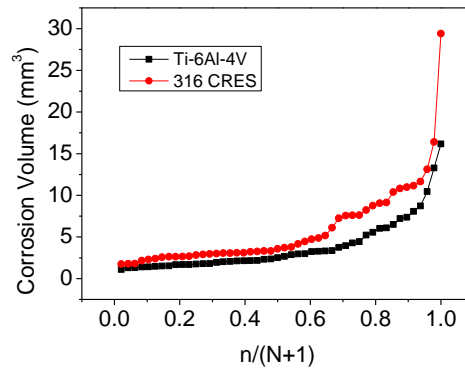
Figure 6.44. Corrosion volume listed by fastener type in ASTM G85 for 360 h.

Figure 6.45. Corrosion rate listed by fastener type- ASTM G85 for 360 h
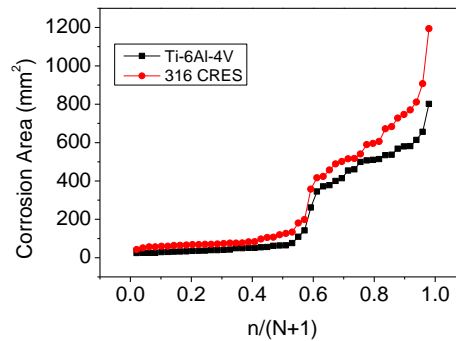
Figure 6.46. Corrosion area listed by fastener type in ASTM G85 for 360 h.

b. Efficacy of Surface Treatment. In Figure 6.47, Surtec 650 and Alodine 1200S, two types of surface treatments involving with chromium, provided better protection than the other chromium-free surface treatment in ASTM B117, as the samples with those two surface treatments had smaller volume of material lost. However, the results of corrosion rate were opposite to what the corrosion volume expressed (Figure 6.48). It was mainly due to the corrosion area. Samples with Alodine 1200S or Surtec 650 were corroded in the area close to

scratches while PreKote or Boegel coated samples were corroded in an extensive area. The corrosion area of samples applied with PreKote or Boegel was always larger than that with Surtec 650 or Alodine 1200S (Figure 6.49). Although samples coated with Surtec 650 or Alodine 1200S had high corrosion rate, they seriously limited the corrosion area and resulted in small corrosion area in comparison with PreKote and Boegel. Thus, a conclusion could be drawn within this experiment that the corrosion area dominated the performance of surface treatment, but not corrosion rate. In general, samples with Alodine 1200S or Surtec 650 were small in corrosion area, but high in corrosion rate. As the corrosion area was the dominative factor when considering surface treatment, samples treated with Alodine 1200S and Surtec 650 still have smaller corrosion volume than those with PreKote or Boegel.
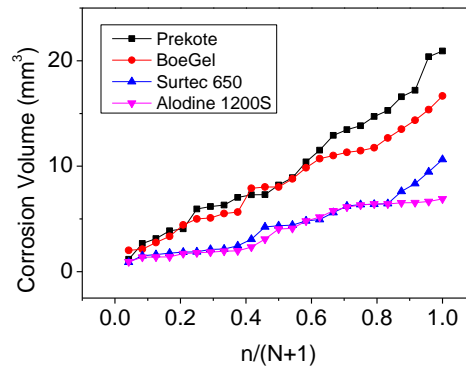
Figure 6.47. Corrosion volume listed by surface treatment ASTM B117 for 500 h
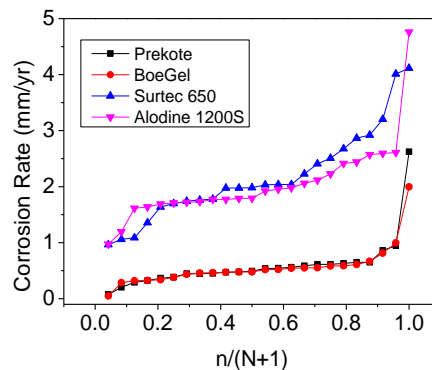
Figure 6.48. Corrosion rate listed by surface treatment in ASTM B117 for 500 h.
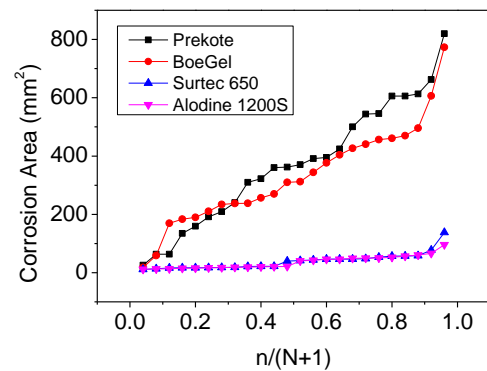
Figure 6.49. Corrosion area listed by surface treatment in ASTM B117 for 500 h.

For samples exposed to ASTM G85 for 360 h, Alodine 1200S, the surface treatments involving chromate, provided the best protection than the other surface treatment in terms of corrosion volume (Figure 6.50). The corrosion area of samples applied with PreKote or Boegel was much larger than that with Surtec 650 or Alodine 1200S (Figure 6.51). Although samples coated with Surtec 650 or Alodine 1200S had high corrosion rate (Figure 6.52), they seriously limited the corrosion area and resulted in small corrosion area in comparison with PreKote and Boegel. Thus, a similar conclusion could be drawn that the corrosion area dominated the performance of surface treatment, but not corrosion rate. This was consistent with the conclusion described in the condition of ASTM B117. In general, samples with Alodine 1200S or Surtec 650 were small in corrosion area, but high in corrosion rate. As the corrosion area was the dominant factor when considering surface treatment, samples treated with Alodine 1200S and Surtec 650 still have smaller corrosion volume than those with PreKote or Boegel.
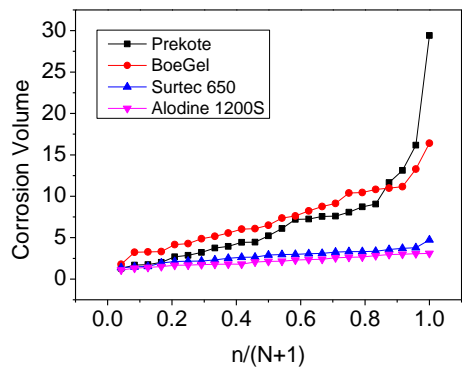
Figure 6.50. Corrosion volume listed by surface treatment in ASTM G85 for 360 h.
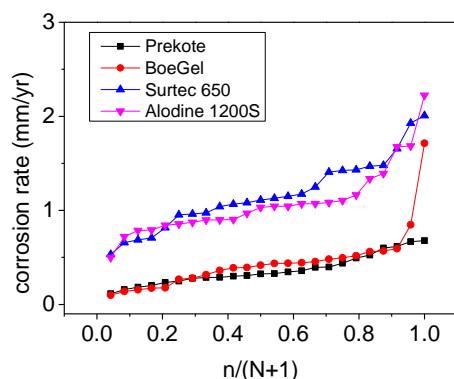
Figure 6.51. Corrosion rate listed by surface treatment in ASTM G85 for 360 h.
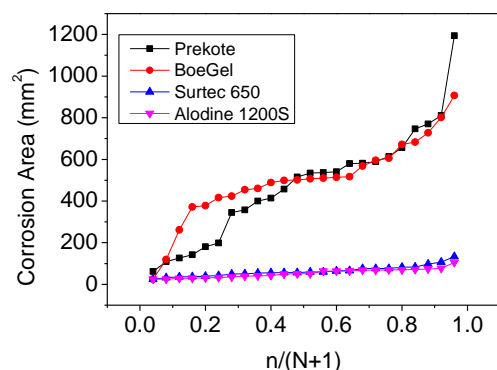
Figure 6.52. Corrosion area listed by surface treatment in ASTM G85 for 360 h.

c. Efficacy of Primers. In Figure 6.53, ANAC's P2100P003 and Deft 44-GN-084 were more effective as the corrosion volume of samples with these two was generally smaller than that with the other four primers. The performances of these two primers were better than the other primers. PPG EWDE 144A and Henzten 17176 KEP were the worst among these six primers as the lines standing for them in Figure 6.53 were always above other lines. Aside from that, about half of samples applied with those two primers were ranked in the worst thirty-two, while only two samples applied with PPG EWDE 144A and four with Henzten 17176 KEP were in the top thirty two. In addition, results of corrosion rate in Figure 6.54 did not fully comply with results in Figure 6.53. Corrosion rate of samples coated with PPG CA7233 was overall the lowest. However, PPG CA 7233 did not perform best. Corrosion area of samples coated with PPG CA 7233 was larger than that with ANAN's P2100P003 (Figure 6.55). The corrosion volume was determined by both corrosion rate and corrosion area. Thus, Deft 44-GN-098 and ANAC's P2100P003 performed best when considering corrosion volume. PPG CA7233 coated samples had the lowest corrosion rate and samples with the other five types generally had similar corrosion rate. ANAC's P2100 and PPG 7233 had better impact in terms of limiting corrosion area. In addition, the effect of applying different kinds of primers on corrosion was not as strong as different types of surface treatments or fasteners.
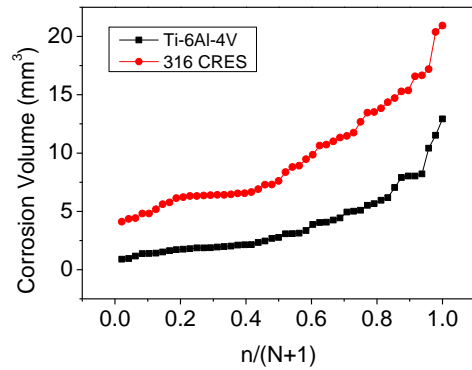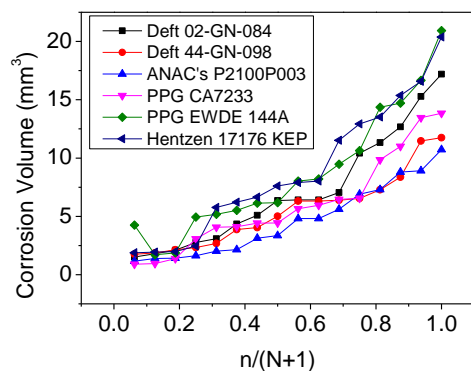
Figure 6.53. Corrosion volume listed by primer in ASTM B117 for 500 h.
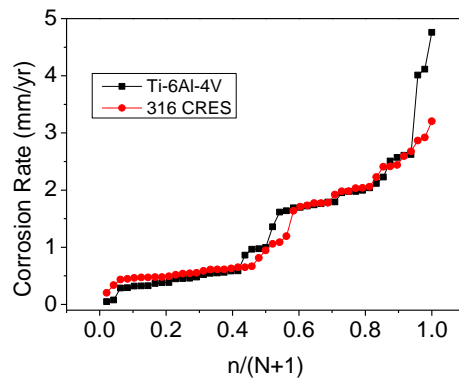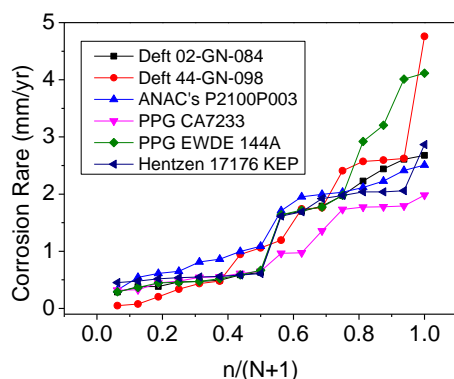

Figure 6.54. Corrosion rate listed by primer in ASTM B117 for 500 h
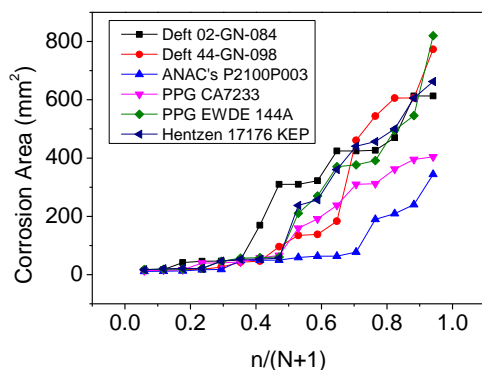
Figure 6.55. Corrosion area listed by primer in ASTM B117 for 500 h.

For samples exposed to ASTM G85 for 360 h, material lost of samples with each primer varied in a large range (Figure 6.56). All primers were able to protect samples fairly well and keep the corrosion volume lower than 5 mm^3 within the first four tenth of samples. However, PPG EWDE 144A and Hentzen 17176 KEP did not always perform that well. As seen in Figure 6.56, PPG EWDE 144A and Hentzen 17176 KEP protected the substrate poorly in some cases. In Figure 6.56, largest corrosion volume for samples painted with PPG EWDE 144A was 29.4 mm^3 and

with Hentzen 17176 KEP was 16.4 mm^3, while Deft 44-GN-098 and ANAC's P2100P003 provided excellent anticorrosive effect and kept the corrosion volume smaller 0.5 mm^3 in every scenario. Deft 02-GN-084 and PPG CA7233 were not as great as the best two, but they were still able to remain corrosion volume not over 1 mm^3. Regarding corrosion rate, five lines mingled and crossed over in most cases except the one labeled as PPG EWDE 144A which was high above (Figure 6.57). In terms of corrosion area, samples with Deft 44-GN-098 and PPG EDWE 144A had generally the smallest and largest corrosion area (Figure 6.58). The effects of the other four primers on corrosion area were not very different. However, smaller corrosion area did not always mean smaller corrosion volume. Neither corrosion rate or corrosion area was quite prevalent on determination of the extent of corrosion when considering effects of primer. Generally speaking, ANAC's P2100P003 and Deft 44-GN-098 provided the best overall protection, while PPG EWDE 144A and Hentzen 17176 KEP had the poorest influence on AA 2024-T3. PPG EDWE 144A coated samples had the highest corrosion rate, while samples with the other five types generally had similar corrosion rate. Deft 04-GN-098 performed best on limiting corrosion area. In addition, all of the six primers performed quite well in their best 40% conditions.
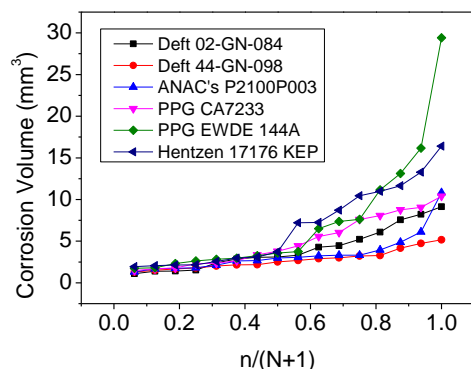
Figure 6.56. Corrosion volume listed by primer in ASTM G85 for 360 h.
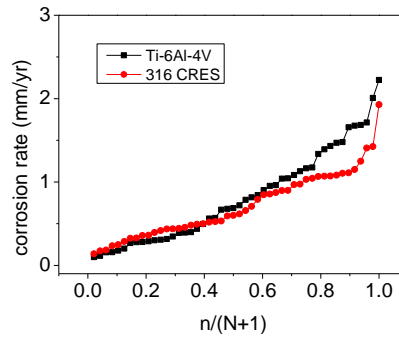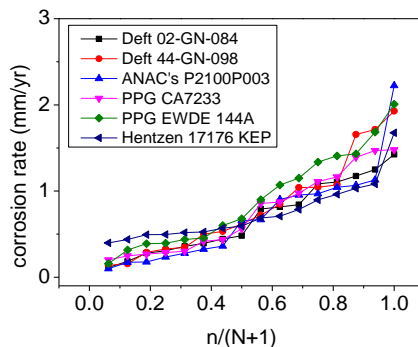

Figure 6.57. Corrosion rate listed by primer in ASTM G85 for 360 h
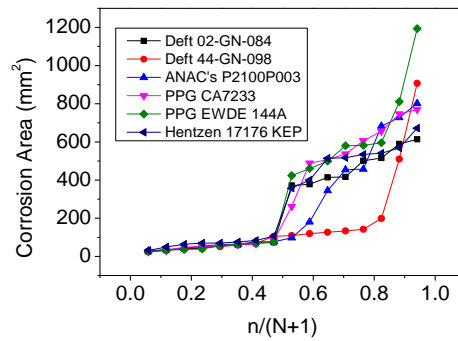
Figure 6.58. Corrosion area listed by primer in ASTM G85 for 360 h.

d. Efficacy of Topcoat. Figure 6.59 reflected that the corrosion volume of samples with topcoat was not necessarily smaller than that with primer only as lines was close to each other and intersected several times. This reason for this was that values of corrosion rate of samples with and without topcoat were quite similar (Figure 6.60). So were the values of corrosion area (Figure 6.61). Therefore, applying topcoat does not guarantee a better protection against corrosion in ASTM B117.
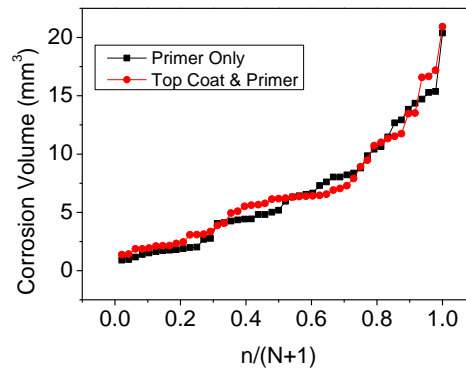
Figure 6.59. Corrosion volume listed by topcoat in ASTM B117 for 500 h.
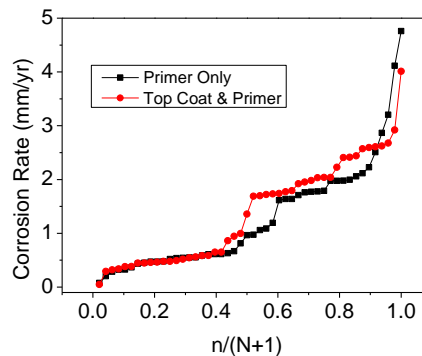
Figure 6.60. Corrosion rate listed by topcoat in ASTM B117 for 500 h
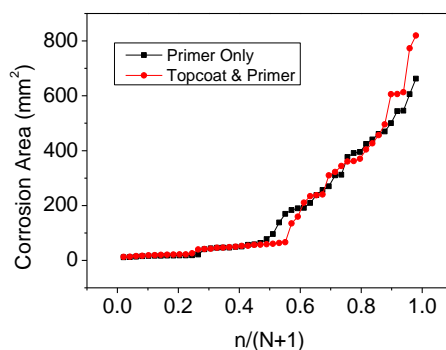
Figure 6.61. Corrosion area listed by topcoat in ASTM B117 for 500 h.

For samples exposed in ASTM G85 for 360 h, the corrosion volume of samples with topcoat was very close to that with primer only (Figure 6.62). What happened upon corrosion rate and area was identical to corrosion volume (Figure 6.63 and 6.64). Usually topcoat was expected to retard the corrosion rate. This could be due to barrier property of the topcoat. However, topcoat's superior barrier property limits the water diffusion, which results into limited dissolution of pigments. And most primers require water penetration to dissolve the pigments in order to release inhibitors. Then the inhibitors reach metal-coating interface to prevent corrosion. In this experiment, all the coatings were scribed. Since the coatings were scribed which means the pigments within primers could reach water moisture, the barrier property of topcoat would be lost. Then the anticorrosive ability would fully reply on the surface pretreatment and primer. Therefore, there is no obvious increase in corrosion prevention with topcoat.
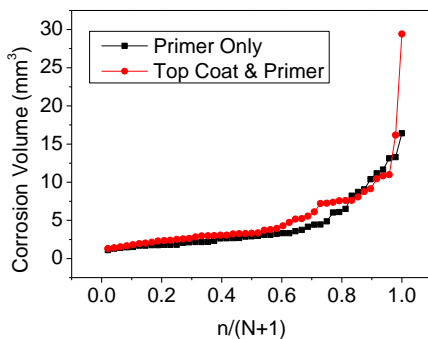
Figure 6.62. Corrosion volume listed by topcoat in ASTM G85 for 360 h
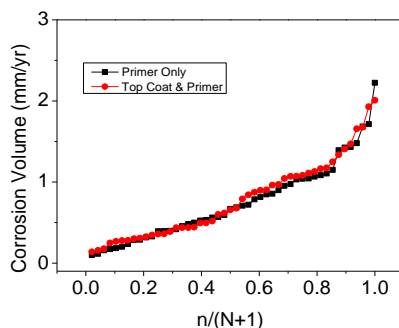
Figure 6.63. Corrosion rate listed by topcoat -ASTM G85 for 360 h
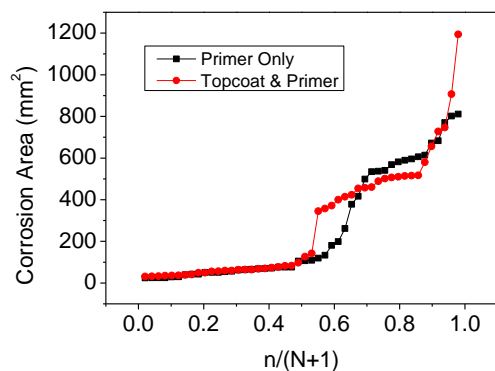
Figure 6.64. Corrosion area listed by topcoat in ASTM G85 for 360 h.

5.6.4.5 Conclusions and Implications for Future Work

5.6.4.5.1 Types of Corrosion. Within this study, corrosion type was mainly controlled by the surface treatment, but not fastener, primer and topcoat. Corrosion was always limited in the area close to scribes on the samples with Alodine 1200S and Surtec 650, while corrosion in a wide area occurred on the samples with PreKote and Boegel. This showed that chromium-containing surface treatments were able to restrict the corrosion in a small area by forming great adhesion and bonding with the coating above, so that the infiltration of water and oxygen through metal-coating interface was diminished which resulted in limitation on corrosion expansion. However, the non-chromate pretreatments were not capable of forming as strong adhesion as chromate pretreatments with paints above. Therefore, they cannot limit the expansion of corrosion.

5.6.4.5.2 Effect of Fastener Material. Under both exposure conditions, corrosion volume caused by 316 CRES was larger than that by Ti-6Al-4V. However, the corrosion rate of samples mounted with these two fasteners was very similar in each environment. In order to end up with more serious corrosion, the corrosion area influenced by 316 CRES was much larger than that by Ti-6Al-4V. Therefore, galvanic corrosion between 316 CRES and AA2024-T3 were stronger than that between Ti-6Al-4V and AA2024-T3 due to corrosion area, not corrosion rate.

5.6.4.5.3 Effect of Surface Treatment. With respect to corrosion volume, Alodine 1200S and Surtec 650 provided better protection than PreKote and Boegel. However, the corrosion rate of samples with the chromium-containing was much larger since the corrosion area was restrained. In contrast, samples with PreKote and Boegel has more material lost, but at a slow rate. The restriction of corrosion area outperformed the effect of differences of corrosion rate. Thus, the corrosion volume of samples with Alodine 1200S and Surtec 650 was smaller.

5.6.4.5.4 Effect of Primer Type. In ASTM B117, Deft 44-GN-098 and ANAC's P2100P003 performed best when considering corrosion volume, while samples with Hentzen 17176 KEP and PPG EWDE 144A had very large volume of material lost. However, the corrosion volume did not trend with either corrosion rate or corrosion area. Therefore, neither of these factors was determining corrosion volume. It was necessary to consider both corrosion rate and relative corrosion area together in order to understand the effect of primers. With regards to corrosion

rate, PPG CA7233 coated samples had the lowest corrosion rate and samples with the other five types generally had similar corrosion rate. ANAC's P2100 and PPG 7233 had better impact in terms of limiting corrosion area. In addition, the effect of applying different kinds of primers on corrosion was not as strong as different types of surface treatments or fasteners.

In ASTM G85, Deft 44-GN-098 and ANAC's P2100P003 were the best since they were able to keep both corrosion volume and corrosion rate smaller than that of the other four. The other four could restrict the corrosion volume, but not for every coating combination. Deft 02-GN-084 and PPG CA7233 were not as great as the first two, but they were still able to restrain the corrosion volume to less than 10 mm^3. Both Hentzen 17176 KEP and PPG EWDE 144A were inferior primers since over half of cases ended up with large corrosion volumes. In addition, all of the six primers performed quite well in the best 40% conditions. However, the corrosion volume did not fully comply with the results of either corrosion rate and corrosion area which is similar to the outcome in ASTM B117. Therefore, none of those two factors was ruling the corrosion volume. It was necessary to consider both corrosion rate and relative corrosion area together in order to understand the effect of primers. In aspect of corrosion rate, PPG EDWE 144A coated samples had the highest corrosion rate and samples with the other five types generally had similar corrosion rate. Deft 04-GN-098 performed best in limiting corrosion area.

5.6.4.5.5 Effect of Topcoat. Topcoating did not provide assurance of better protection in both exposure conditions. All in all, the general performance of sample with topcoat was close to that without topcoat. This may be due to scratches which made the topcoat lose its barrier property. In this case, corrosion prevention fully depended on surface treatment and primer coating. That is probably why no obvious increase in protection was seen when a topcoat was present.

Appendix 6A

Table 6A.1. Calcium x-ray intensity within fixed area of top-coated Hentzen 16708 TEP, (a) unexposed, (b) 30-day exposure, (c) 90-day exposure.

Exposure Time No. of Pixels	Unexposed				30-day		90-day	
5	62	57	53	41	51	48	55	50
10	58	53	49	38	46	44	47	40
15	53	48	46	31	41	38	34	30

Table 6A.2. Calcium x-ray intensity within fixed area of untopcoated Deft 02-GN-084, (a) unexposed, (b) 30-day exposure, (c) 90-day exposure

Exposure Time No. of Pixel	Average Intensity					
	Unexposed		30-day exposure		90-day exposure	
5	46	47	58	57	41	26
10	41	41	46	48	30	23
15	35	35	38	36	20	20

Table 6A.3. Praseodymium x-ray intensity within fixed area of untopcoated Deft 02-GN-084, (a) unexposed, (b) 30-day exposure, (c) 90-day exposure.

Exposure Time No. of Pixels	Average Intensity					
	Unexposed	30-day exposure		90-day exposure		
5	44	46	44	45	27	
10	35	34	31	26	20	

Table 6A.4. Barium x-ray intensity within fixed area of topcoated Sicopoxy 577-630, (a) unexposed, (b) 30-day exposure, (c) 90-day exposure.

Exposure Time No. of Pixels	Average Intensity					
	Unexposed		30-day exposure		90-day exposure	
5	49	44	61	48	37	36
10	46	41	56	43	32	30
15	40	37	51	38	27	25

Appendix 6B

Table 6B.1. Corrosion volume of samples in ASTM B117 for 500 h.

Surface Treatment	Fastener / Primer	Corrosion Volume (mm^3)			
		Primer Only		Topcoat & Primer	
		Ti-6Al-4V	316 CRES	Ti-6Al-4V	316 CRES
PreKote	Deft 02-GN-084	10.4	15.3	7.0	17.2
	Deft 44-GN-098	2.7	6.3	3.9	7.3
	ANAC's P2100P003	1.2	7.3	3.1	8.9
	PPG CA7233	6.0	13.8	4.1	13.5
	PPG EWDE 144A	8.2	14.7	6.2	20.9
	Hentzen 17176 KEP	12.9	20.4	11.5	16.6
Boegel	Deft 02-GN-084	2.8	12.7	5.1	11.3
	Deft 44-GN-098	5.0	11.5	2.1	11.8
	ANAC's P2100P003	2.0	8.8	3.4	10.7
	PPG CA7233	4.4	9.9	5.7	11.0
	PPG EWDE 144A	8.0	14.4	5.5	16.7
	Hentzen 17176 KEP	8.0	15.4	7.9	13.5
Surtec 650	Deft 02-GN-084	1.5	4.4	2.1	6.4
	Deft 44-GN-098	1.8	8.4	1.9	6.4
	ANAC's P2100P003	1.6	4.8	2.2	5.6
	PPG CA7233	0.9	4.4	3.1	6.5
	PPG EWDE 144A	4.3	10.6	4.9	9.5
	Hentzen 17176 KEP	1.9	7.6	2.5	6.2
Alodine 1200S	Deft 02-GN-084	1.8	6.4	3.1	6.4
	Deft 44-GN-098	4.0	6.5	2.3	6.3
	ANAC's P2100P003	1.4	4.8	1.4	6.9
	PPG CA7233	1.0	4.1	1.4	6.6
	PPG EWDE 144A	1.7	5.2	1.9	6.1
	Hentzen 17176 KEP	2.0	6.7	1.9	5.8

Table 6B.2. Corrosion area of samples in ASTM B117 for 500 h.

Surface Treatment	Fastener / Primer	Corrosion Area (mm^2)			
		Primer Only		Topcoat & Primer	
		Ti-6Al-4V	316 CRES	Ti-6Al-4V	316 CRES
PreKote	Deft 02-GN-084	322	613	310	424
	Deft 44-GN-098	26	135	606	544
	ANAC's P2100P003	64	240	63	209
	PPG CA7233	159	362	192	395
	PPG EWDE 144A	371	820	391	546
	Hentzen 17176 KEP	360	606	500	662
Boegel	Deft 02-GN-084	234	427	170	470
	Deft 44-GN-098	773	606	183	461
	ANAC's P2100P003	59	344	18	190
	PPG CA7233	310	404	238	312
	PPG EWDE 144A	211	496	270	377
	Hentzen 17176 KEP	237	457	256	441
Surtec 650	Deft 02-GN-084	22	42	13	47
	Deft 44-GN-098	19	47	18	138
	ANAC's P2100P003	17	48	11	78
	PPG CA7233	40	57	16	44
	PPG EWDE 144A	22	57	18	58
	Hentzen 17176 KEP	21	53	17	47
Alodine 1200S	Deft 02-GN-084	21	46	18	50
	Deft 44-GN-098	16	43	15	96
	ANAC's P2100P003	13	50	12	49
	PPG CA7233	14	66	17	41
	PPG EWDE 144A	19	61	18	46
	Hentzen 17176 KEP	20	53	22	57

Table 6B.3. Corrosion rate of samples in ASTM B117 for 500 h.

Surface Treatment	Fastener / Primer	Corrosion Rate (mm/yr)			
		Primer Only		Topcoat & Primer	
		Ti-6Al-4V	316 CRES	Ti-6Al-4V	316 CRES
PreKote	Deft 02-GN-084	0.59	0.63	0.38	0.49
	Deft 44-GN-098	0.08	0.2	2.62	0.95
	ANAC's P2100P003	0.32	0.61	0.86	0.65
	PPG CA7233	0.54	0.61	0.45	0.65
	PPG EWDE 144A	0.37	0.47	0.29	0.45
	Hentzen 17176 KEP	0.45	0.54	0.56	0.48
Boegel	Deft 02-GN-084	0.29	0.47	0.38	0.46
	Deft 44-GN-098	0.48	0.44	0.05	0.34
	ANAC's P2100P003	2	0.81	1	0.55
	PPG CA7233	0.33	0.55	0.32	0.48
	PPG EWDE 144A	0.52	0.67	0.46	0.59
	Hentzen 17176 KEP	0.55	0.61	0.58	0.52
Surtec 650	Deft 02-GN-084	1.98	1.64	1.7	2.68
	Deft 44-GN-098	1.76	1.06	1.74	2.41
	ANAC's P2100P003	2.51	1.09	2.23	2.03
	PPG CA7233	0.97	1.78	1.36	1.98
	PPG EWDE 144A	4.11	3.2	4.01	2.92
	Hentzen 17176 KEP	1.98	2.87	2.04	2.04
Alodine 1200S	Deft 02-GN-084	1.79	2.23	2.61	2.44
	Deft 44-GN-098	4.76	1.19	2.57	2.6
	ANAC's P2100P003	2.12	1.71	1.95	2.41
	PPG CA7233	0.98	1.77	1.79	1.73
	PPG EWDE 144A	1.64	1.98	1.72	1.77
	Hentzen 17176 KEP	1.61	2.06	1.69	1.92

Table 6B.4. Corrosion volume of samples in ASTM G85 for 360 h.

Surface Treatment	Fastener / Primer	Corrosion Volume (mm³)			
		Primer Only		Topcoat & Primer	
		Ti-6Al-4V	316 CRES	Ti-6Al-4V	316 CRES
PreKote	Deft 02-GN-084	2.9	4.5	5.2	7.6
	Deft 44-GN-098	1.3	2.7	2.0	3.2
	ANAC's P2100P003	1.7	1.7	3.9	6.1
	PPG CA7233	4.4	9.05	8.1	7.6
	PPG EWDE 144A	3.8	13.1	16.2	29.4
	Hentzen 17176 KEP	8.7	11.7	7.2	7.2
Boegel	Deft 02-GN-084	6.1	8.2	4.3	9.1
	Deft 44-GN-098	1.8	4.2	3.3	5.2
	ANAC's P2100P003	3.2	4.9	3.3	10.8
	PPG CA7233	6.0	10.4	5.6	8.8
	PPG EWDE 144A	6.5	11.2	7.4	7.6
	Hentzen 17176 KEP	13.3	16.4	10.5	11.0
Surtec 650	Deft 02-GN-084	1.4	3.3	1.5	3.1
	Deft 44-GN-098	2.2	2.9	2.5	4.7
	ANAC's P2100P003	2.1	3.3	3.0	2.6
	PPG CA7233	1.5	2.7	3.4	3.8
	PPG EWDE 144A	2.3	3.6	3.0	3.3
	Hentzen 17176 KEP	2.2	3.1	1.9	3.7
Alodine 1200S	Deft 02-GN-084	1.1	3.1	1.4	2.4
	Deft 44-GN-098	1.5	2.2	1.7	3.0
	ANAC's P2100P003	2.7	1.8	1.3	3.1
	PPG CA7233	1.7	1.8	2.4	2.3
	PPG EWDE 144A	1.8	2.6	1.8	2.8
	Hentzen 17176 KEP	2.1	3.0	2.1	2.6

Table 6B.5. Corrosion area of samples in ASTM G85 for 360 h.

Surface Treatment	Fastener / Primer	Corrosion Area (mm^2)			
		Primer Only		Topcoat & Primer	
		Ti-6Al-4V	316 CRES	Ti-6Al-4V	316 CRES
PreKote	Deft 02-GN-084	414	516	614	590
	Deft 44-GN-098	142	127	109	199
	ANAC's P2100P003	345	457	62	181
	PPG CA7233	656	747	537	770
	PPG EWDE 144A	580	1194	582	811
	Hentzen 17176 KEP	400	357	535	541
Boegel	Deft 02-GN-084	372	502	378	417
	Deft 44-GN-098	510	907	25	120
	ANAC's P2100P003	455	728	802	683
	PPG CA7233	507	489	262	606
	PPG EWDE 144A	461	423	499	596
	Hentzen 17176 KEP	514	517	568	672
Surtec 650	Deft 02-GN-084	32	60	42	57
	Deft 44-GN-098	37	60	51	133
	ANAC's P2100P003	64	97	54	76
	PPG CA7233	56	83	24	66
	PPG EWDE 144A	36	56	39	76
	Hentzen 17176 KEP				
		49	83	76	107
Alodine 1200S	Deft 02-GN-084	41	73	25	68
	Deft 44-GN-098	39	68	51	106
	ANAC's P2100P003	35	77	29	42
	PPG CA7233	49	64	29	51
	PPG EWDE 144A	33	64	25	71
	Hentzen 17176 KEP	31	70	64	70

Table 6B.6. Corrosion rate of samples in ASTM G85 for 360 h.

Surface Treatment	Fastener / Primer	Corrosion Rate (mm/yr)			
		Primer Only		Topcoat & Primer	
		Ti-6Al-4V	316 CRES	Ti-6Al-4V	316 CRES
PreKote	Deft 02-GN-084	0.11	0.18	0.31	0.36
	Deft 44-GN-098	0.29	0.33	0.35	0.62
	ANAC's P2100P003	0.67	0.23	0.28	0.33
	PPG CA7233	0.20	0.29	0.30	0.25
	PPG EWDE 144A	0.16	0.39	0.68	0.60
	Hentzen 17176 KEP	0.40	0.52	0.44	0.49
Boegel	Deft 02-GN-084	0.39	0.48	0.28	0.44
	Deft 44-GN-098	1.71	0.85	0.16	0.14
	ANAC's P2100P003	0.10	0.17	0.18	0.36
	PPG CA7233	0.56	0.42	0.27	0.44
	PPG EWDE 144A	0.32	0.46	0.39	0.44
	Hentzen 17176 KEP	0.57	0.59	0.49	0.52
Surtec 650	Deft 02-GN-084	0.82	1.42	1.17	1.25
	Deft 44-GN-098	1.04	0.53	1.66	1.93
	ANAC's P2100P003	0.95	1.07	1.13	0.66
	PPG CA7233	1.48	0.97	1.47	1.11
	PPG EWDE 144A	1.43	1.15	2.01	1.41
	Hentzen 17176 KEP	0.69	0.71	0.96	1.08
Alodine 1200S	Deft 02-GN-084	1.08	1.10	0.84	0.79
	Deft 44-GN-098	0.72	0.50	1.04	1.07
	ANAC's P2100P003	2.22	1.04	0.90	0.97
	PPG CA7233	1.39	0.86	1.16	0.87
	PPG EWDE 144A	1.68	0.90	1.34	1.07
	Hentzen 17176 KEP	0.79	1.03	1.68	0.90

5.7. Task 7: Characterization of Local Environments in Coating Systems

5.7.1 Objectives and Background

The objective of this research is to develop a technique to supplement traditional investigation approaches for characterizing corrosion of coated metals. Studies reported here focus on the effects of the metallurgical aspects of thin films and the local environments in organic coatings on pit formation, pit growth kinetics and pit morphology.

Much effort has been applied to characterizing the effect potential, pH and chloride concentration on localized corrosion of bulk materials. This work has extended to studies of the influence of these variables on pit current densities [1]. In such studies, the determination of active pit surface area is critical for accurately calculating the anodic current density [2]. However, pit area is difficult or impossible to determine for 3D pit morphologies [3]. Most investigators assume that pits are hemispherical. However Hisamatsu et al. studied the growth of a single pit in stainless steel and cross-sectioned the pit after it grew for sometime. It was found that the pit depth was much less than the pit mouth radius [4]. In order to develop precise models of pit morphologies, some researchers have simulated pitting corrosion by using a 2D model that involves deposition of thin films on inert substrates [1-3]. Since pits can rapidly penetrate the thickness of the film and then grow outward in an easily measureable way, thin film pitting provides a unique opportunity to study pit propagation in situ. Frankel found that under potential-controlled conditions, both current density and pit morphology depended on the applied potential [2]. At high potentials, pit growth is fast and rounds pits prevail as dissolution is controlled by mass transport. Mass transport-controlled growth is reflected by constant current density over a range of potentials. At low potentials, thin film pits exhibit convoluted morphologies and dissolution occurred under ohmic control where the current density increases linearly with potential.

Measurement of pit growth under open circuit conditions is very difficult to study because pit growth rates are much slower [5]. Open circuit potential (OCP) pit growth is "natural" as the cathodic current resource derives solely from the cathodic reaction that occurs on the sample itself. This is an important aspect of experiments aimed at studying the effect of coatings and inhibitors where inhibition of the cathodic reaction is one of the primary strategies for controlling corrosion. Generally speaking, OCP pit morphology is more variable because it is constrained by the rate of the supporting cathodic process [1]. Results show that pit morphologies range from fractal-like patterns to smooth circular walls depending on the specific environmental conditions. For example, high concentrations of Fe^{3+} provided the additional cathodic reaction which lead to a circular pit growth front in the pitting of iron. However, the anodic current density reaches a limiting value when the cathodic reaction is controlled by mass transport. Fractal patterns arise when the local convention of hydrogen bubbles dilutes the aggressiveness of the solution at the vicinity of the active pit surface resulting in the passivation of that area.

In the case of Al alloys, additions of Cu to Al matrix are known to increase the susceptibility pitting corrosion in thin films by affecting the oxide layer thickness and integrity [6-7]. The formation of constituent θ phase (Al_2Cu) also acts as cathodic reduction site, increasing the corrosion rates and as a result, the distribution and microstructure of Cu in Al-Cu thin films has been studied [8]. Conversely, when Cu is retained in solid solution, it acts as a pitting inhibitor.

Results show that the morphology of 50 nm sputtered Al-Cu thin films exposed to solution developed pits with fractal-like patterns and the precipitates caused more convolution in shape compared with pure Al thin films [9].

The application of coatings on metal surfaces confers protection against corrosive environments. About 90% of metals and alloys used in engineering application are covered with coatings [1]. The use of EIS to study the protection of metals and alloys by organic coatings has also been focused in the area of undercoating corrosion. In order to directly obtain visual signs of corrosion underneath the coating systems, some researchers have used translucent coatings and performed EIS to study the undercoating corrosion. However, since most coating systems are multilayered, or opaque, a large number of coatings are difficult to characterize by these methods. On the other hand, some researchers have mechanically removed the coatings after performing EIS measurements in order to assess the corrosion at the interface. However, the destructive nature of this method limits its use. One possibility of resolving this problem is by using metallic thin films as substrates. Since the thinness of the metallic layer leads to rapid penetration followed by constrained lateral spread, the corrosion process underneath the coating can be directly observed and the kinetics of corrosion can be assessed.

5.7.2 Materials and Methods

5.7.2.1 Sample preparation. Al thin films approximately 800 nm thick were deposited on a transparent 75 x 25 x 1mm glass slides of size using a 99% pure aluminum source in a vacuum electron beam evaporator. The average deposition rate was 10Å/s at an evaporation pressure of about 3×10^{-6} Torr.

The Al-4.9wt.%Cu thin films 800nm in thickness were deposited on the same transparent glass slide by physical vapor deposition using an Al-4wt.%Cu target. The deposition rate was 1.8Å/s at 5.5×10^{-7} Torr.

Two types of Al-Cu thin films were used. "As-deposited" samples were tested as fabricated without any further heat treatment. The "artificially aged" samples heat treated at 190°C for 24 hours to induce precipitation of θ phase.

Application of coatings experiments was carried out using a spin coater. Coatings were applied using a rotation rate of 250 RPM for 5 minutes. In several instances, a neat epoxy primer PD381-94 (Aerospace blank coating-no inhibitor) from Akzo Nobel was used. Other coatings used are described later. In order to simulate a coating with defects, an artificial defect through the coating around 0.1mm in diameter was made in the middle of the sample. The side and top view of the sample is shown in Figure 7.1.

After demonstrating the utility of this fabrication approach for idealized coating systems, methods were extended to the preparation of new and more realistic coating systems.

5.7.2.2 Pretreatment. Sputtered thin Al and Al alloy films were degreased for several seconds in a solution comprising 1.0 L deionized of (DI) water containing 48.0g Na_2CO_3 and 32.4g Na_2SiO_3

at 65°C. After using DI water to rinse the thin films, they were deoxidized for 3 minutes in a solution comprising 1.0 L of DI water, 30.0g Sanchem 1000^{TM} and 72.0 mL HNO_3 at 55°C.

Several different primer coatings were evaluated. The first was a chromium-free primer Deft 02GN084, which was a 2-part epoxy primer pigmented with a blend of $PrO/Pr(OH)_3$, $CaSO_4$, and TiO_2. The second was a home-made primer comprising a neat epoxy and a $SrCrO_4$ pigment.

A polyurethane Eclipse® high solids polyurethane aircraft topcoat was used in certain experiments. This is a chemically cured, low VOC topcoat designed to provide premium gloss.

These coating systems were applied by drawdown bar. Coating thickness was determined by optical profilometry. The Deft coatings were around 7μm thick and $SrCrO_4$ primer coatings were around 3μm thick. Top coats were around 15μm thick.

5.7.2.3 Instrumental. A schematic of the DOI fixture is shown in Figure 7.1a. A polymethylmethacrylate cell with an o-ring and an exposed area of about 1cm^2 was placed on top of the sample. A backing plate of plexiglass was attached to the bottom of the cell was used to hold the sample. In the middle of the plate a hole was made in order to allow the microscope directly capture images. A transmitted light source located above the sample was used for illumination. A QImaging Go-3 color CMOS camera attached to an Olympus SZ61 stereomicroscope was located underneath the electrochemical cell and the sample. As corrosion progressed, the thin sputtered film was perforated and transmitted light passed through the sample to the camera. The progression of corrosion was recorded by Template^{TM} video recording software. Selected images of pit shape and size were collected using KMPlayer ^{TM} and VideoMatch ^{TM} frame grabbing. Analysis of the collected images was conducted using ImageJ ^{TM}.

The technique has been extended to minimize crevice corrosion (as suggested in Figure 7.1b) during the experiments. Figure 7.2 illustrates a modified experimental setup. In this modification electrical tape was applied to the sample as a mask on top of any coating. The exposure area was reduced from 1.0 to 0.3 cm^2. A PVC tube with a diameter lager than the exposure area was glued on top of the tape. A new and more robust cell and camera fixture was developed and deployed to facilitate long-term experiments. All the experiments were terminated before the pits undercut the mask.
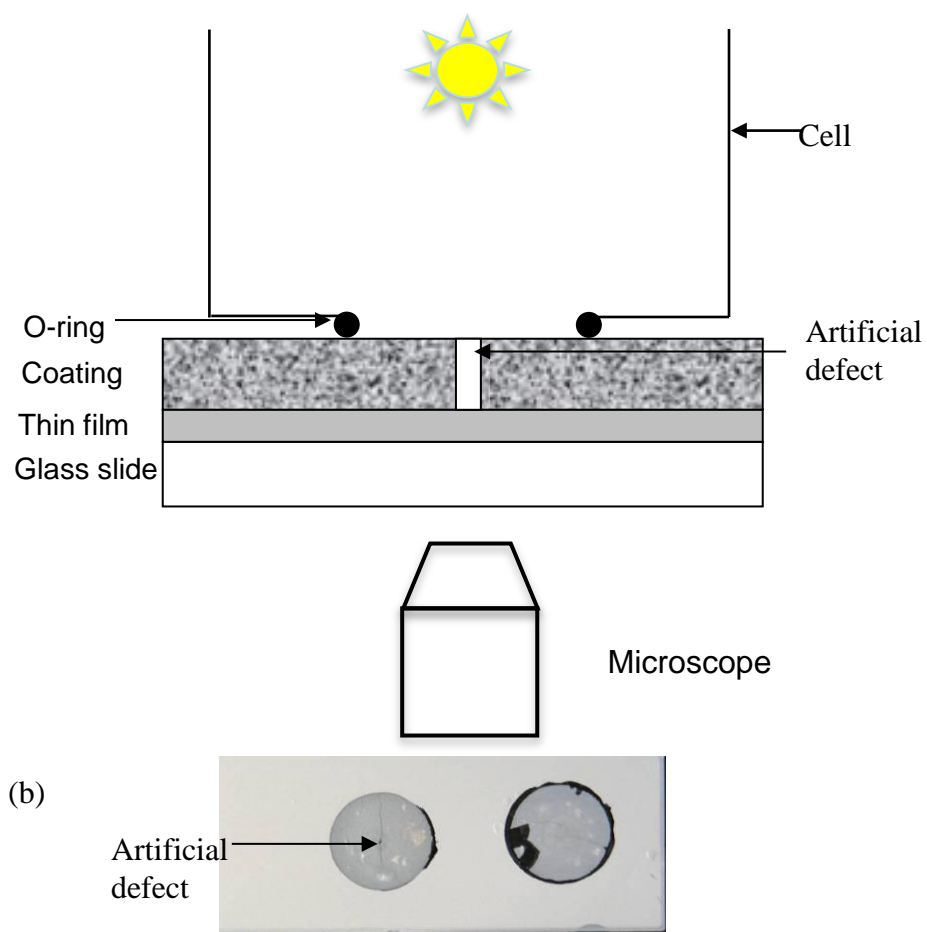
Figure 7.1. a) instrumental configuration with the side view of the sample, b) top view of the sample, inside of the circle is the o-ring area exposed to the electrolyte, after conducting the experiment, only the coating and corrosion product left attached to the glass slide. Out side of the o-ring is the neat epoxy.
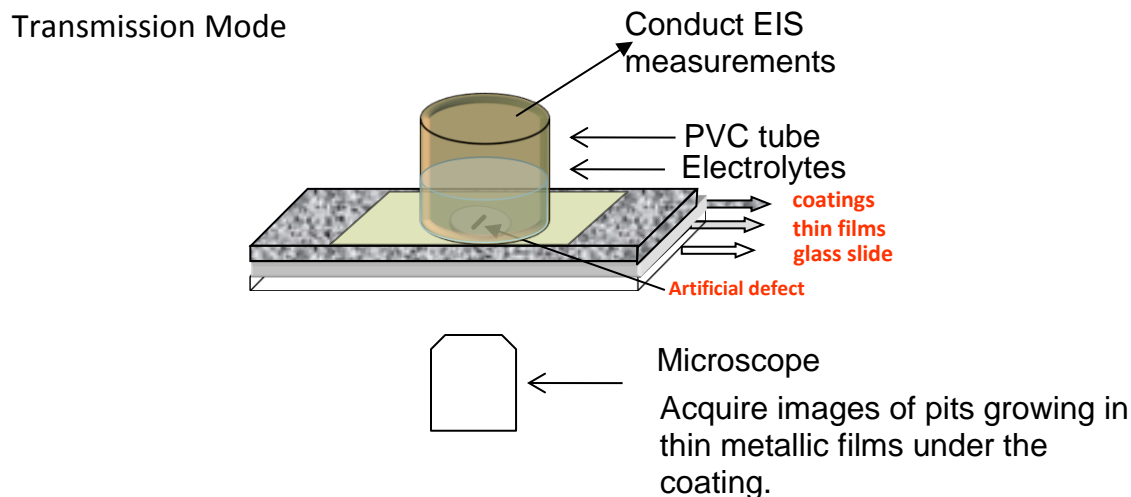
Figure 7.2. Instrumental configuration of the DOI setup.

5.7.2.4 Electrochemical Experiments. Electrochemical impedance spectroscopy (EIS) was carried out using a Gamry Ref 600 potentiostat during exposure and imaging experiments to relate the extent and nature of pitting corrosion to periodically measured EIS spectra. A standard three-electrode setup was used consisting of a saturated calomel reference electrode and a platinum mesh counter electrode. Experiments were carried out in naturally aerated 0.3M HCl and 0.5 M NaCl solutions.

In these experiments, the open circuit potential was monitored for 20 minutes before conducting the EIS measurement. The measurements themselves were performed at a frequency range of 10^5 to 10^{-2} Hz using a 10mV sinusoidal voltage perturbation applied with respect to OCP.

5.7.3 Results and Discussion

5.7.3.1 Pure Al thin films under neat epoxy coatings in 0.3M HCl. Experiments were conducted on the pure Al thin films coated with neat epoxy which were exposed to 0.3M HCl. The evolution of undercoating corrosion morphology is shown in Figure 7.3. The evolution of corrosion followed a general sequence of events. First, the pits activated and quickly penetrated the thin film. Once they reached the substrate, through-pits were formed. However, instead of growing from the artificial defect, the pits nucleated at two different locations simultaneously. Pits often passivated temporarily once formed. The second stage of growth involved uniform corrosion. Shortly after localized pits initiated, uniform corrosion of the thin film was detected. This manifested as a gradual brightening of the Al thin film without perforation.

Hydrogen gas bubbles were observed throughout the corrosion process. When uniform corrosion started to occur, many small bubbles nucleated across the surface of the coated sample. Because these bubbles were out of focus, they appear to be attached to the top of the polymer coating and in the bulk electrolyte. These bubbles are distinct from larger hydrogen bubbles in pitted regions

343

under the coating. Undercoating bubble from hydrogen gas coalesces under the coating and does not escape through the small defect in the organic coating. Such bubbles are in the plane of focus and clearly under the organic coating (Figure 7.3).

The final stage of corrosion in these experiments involves complete dissolution of the thin Al film and a decrease in of hydrogen gas generation as the thin film becomes completely dissolved.
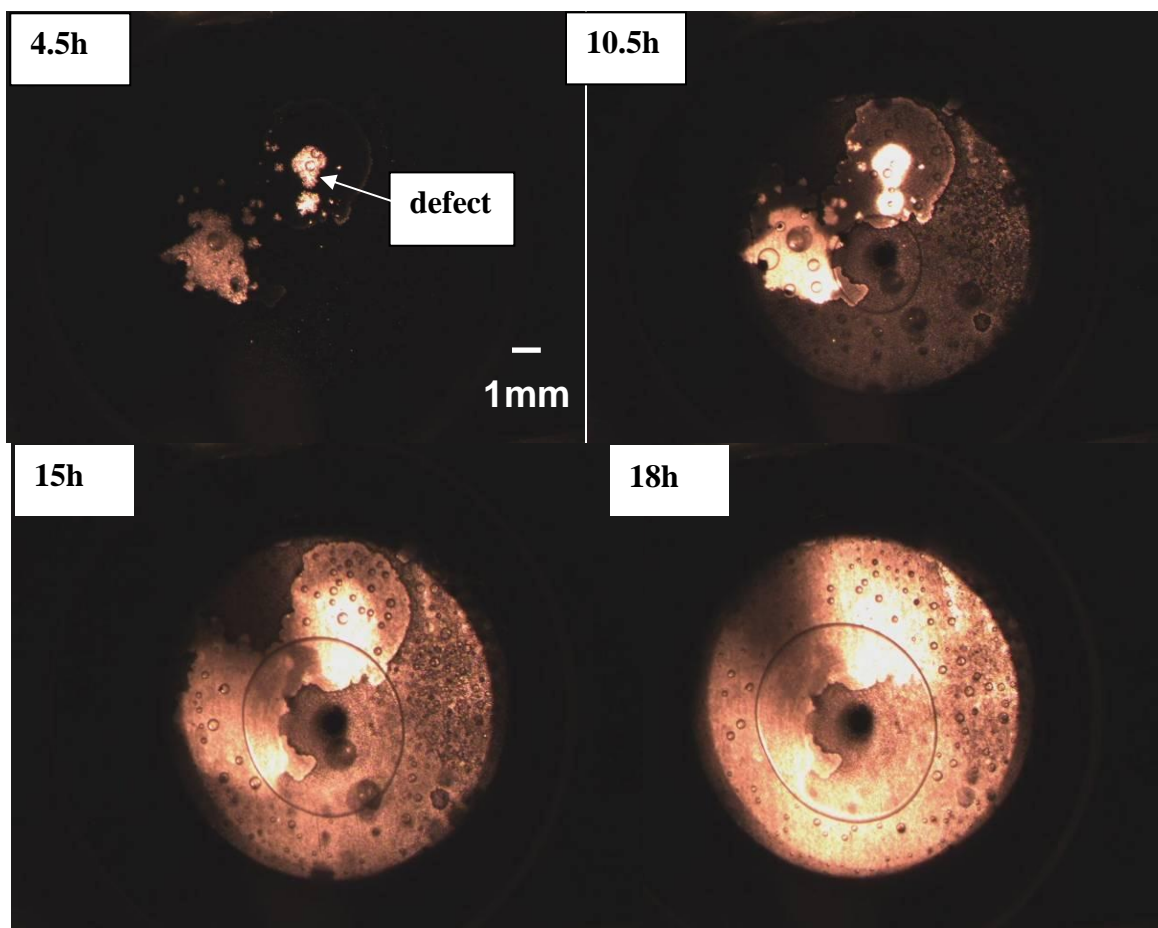
Figure 7.3. Sequence of images taken of the evolution of aluminum thin film with neat epoxy coating exposed to 0.3M HCl solution.

EIS spectra collected during these exposure experiments exhibits only one broad time constant. Due to the intentional defect present in the samples from the outset of the exposure, the HCl solution immediately contacts the Al thin film and the measured impedance is dominated by the defect impedance. Measured spectra were fit with a simplified Randles circuit model from which the polarization resistance (R_p) and sample capacitance (C) were estimated. The variation in polarization resistance and capacitance as function of exposure time are shown in Figure 7.4. There are three distinct regimes in both data sets that can be discriminated based in part by variations in the fitted R_p and C parameters and partly by visual observations from DOI. At early times, corrosion is activating and increasing. R_p is observed to fall and the sample capacitance increases. DOI shows multiple corrosion sites nucleating and growing. This regime is termed "activation". At intermediate times, R_p is steady at a low value and capacitance is steady at

relatively high values. This response is consistent with "propagation" of corrosion. Because the corrosion process is occurring under free corrosion conditions the corrosion rate in this regime may be limited by factors that control cathodic reaction kinetics. At the end of the exposure period, DOI shows that pit sites have consumed large amounts of the metallization with general thinning attacking the remainder. In this regime, R_p is observed to increase and C decreases in a manner that is consistent with "exhaustion" of the corrosion process due to complete consumption of the Al metallization.
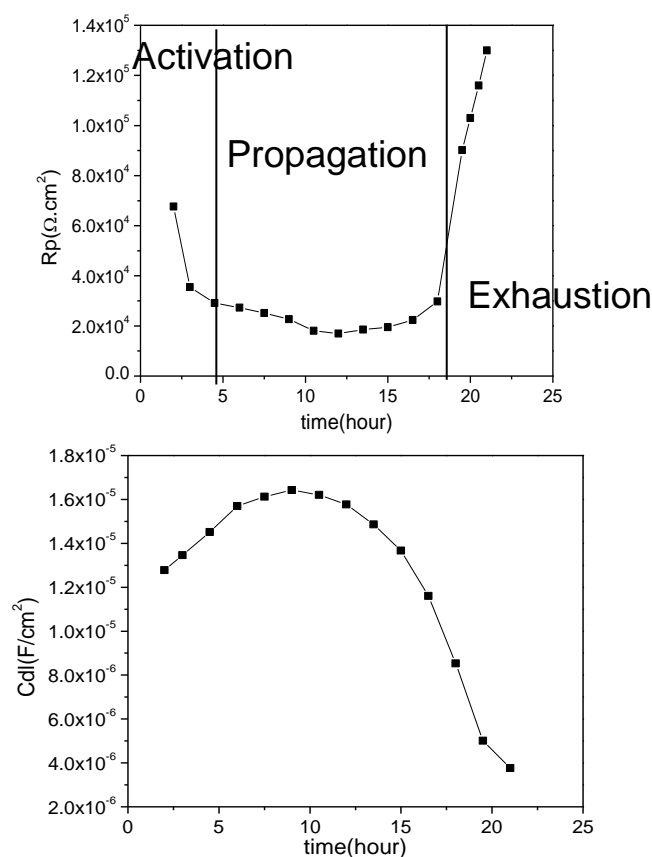
Figure 7.4. (a) Polarization resistance, R_p, and (b) capacitance, C, of an Al thin film metallization with neat epoxy coatings over top. This sample was exposed to 0.3M HCl.

Figure 7.5 is a chronological sequence of images showing the nucleation and growth of pits in an Al thin film covered by a neat epoxy resin during exposure to a 0.5 M NaCl solution. The images show pit morphologies that are round and smooth. Pits appear to have nucleated at random locations across the sample and were not necessarily associated with the intentional defect introduced before the exposure. Pits grew in short episodes separated by long periods of passivity. As time elapsed, the pits connected with one another until the aluminum layer was completely dissolved. As was the case in 0.3M HCl exposures, gas bubble formation and trapping under the coating was observed.

The growth of single pits was episodic. In this experiment, the first pit nucleated when the sample was exposed to the solution for 17 hours and grew for a short period of time (30 minutes)

345

after which the pit passivated for 7 hours. Moreover, the first pit was still passive (i.e. the pit size did not change) during growth periods for the second and third pits. This suggests that there is a limitation on the cumulative dissolution rate, or the ability to generate and sustain a critical local environment chemistry that is imposed by the cathodic reaction.
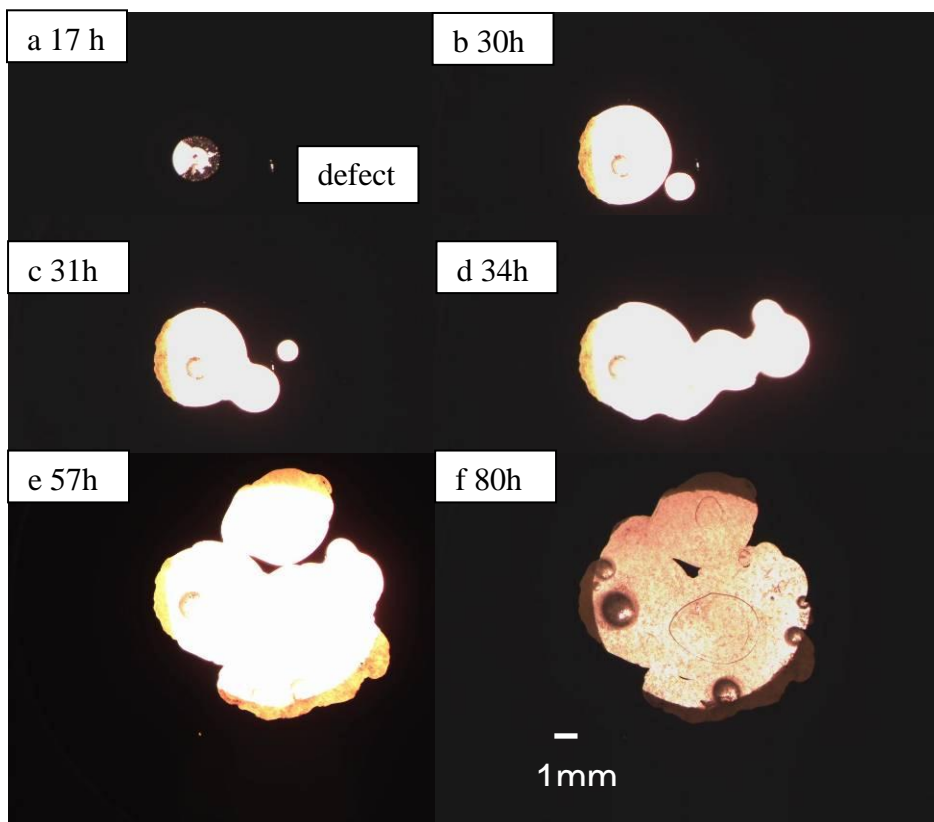
Figure 7.5. Sequence of images taken of the evolution of aluminum thin film under a neat epoxy resin during exposure to a 0.5M NaCl solution.

In the case of samples with neat epoxy coatings exposed to 0.5M NaCl, pit morphologies were observed to be smooth and in some cases nearly round. The nucleation and coalescence of multiple pits, each growing intermittently and at different rates complicates determination of pit perimeter, area and current density throughout the entirely of the experiment. However, at short exposure times, before pits coalesced, quantitative analyses are possible. Figure 7.6 shows the variation in pit perimeter and pit area for the three pits shown in Figure 7.5 prior to their coalescence.

(a)

(b)
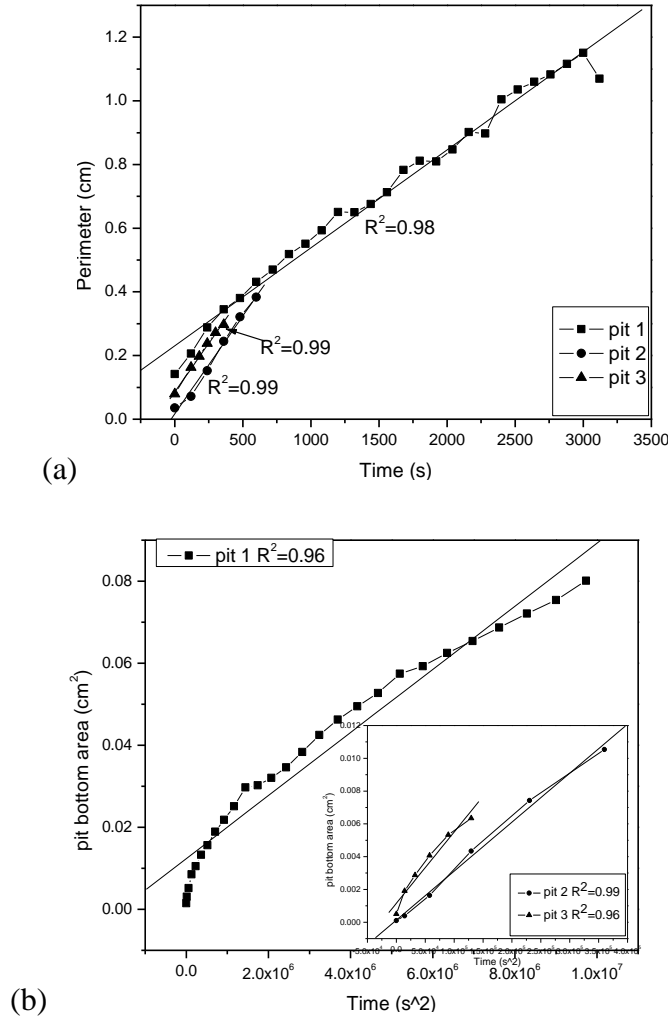
Figure 7.6. Pit perimeter (a) and pit bottom area (b) as a function of time by the image analysis. The closed symbols indicate the original data, the regular lines are the linear fitting results.

After an initial induction period, the pit perimeter and pit bottom area were observed to vary linearly with time and time squared, respectively. The pit perimeter, P was linearly dependent on time, t, according to,

$$P = C_1 \cdot t \qquad\qquad (eq.\ 7.1)$$

where C_1 (cm/s) is a constant whose value is estimated from the slope of the data shown in Figure 7.6a. The pit bottom area, A was linearly dependent on the square of time, t^2, according to,

$$A = C_2 t^2 \qquad\qquad (eq.\ 7.2)$$

where C_2 (cm^2/s^2) is a constant whose value is estimated from the slope of the data shown in Figure 7.6b. From Faraday's Law, and the constant terms in equations 7.1 and 7.2, the anodic current density, i_a (A/cm^2), can be estimated as,

$$i_a = \frac{2n\rho F C_2}{MC_1}$$

(eq. 7.3)

where ρ is the density of Al (g/cm^3), n is equivalents of change per mole of Al reacted (eq/mol), M is molar mass of Al (g/mol) and F is Faraday's constant (C/eq).

Using this approach, the anodic current densities of the three pits were estimated to be 1.45A/cm^2, 2.81 A/cm^2 and 4.12 A/cm^2, respectively. For comparison, Al thin film pits growing under potential control exhibit anodic current densities ranging from 18-30 A/cm^2 [2]. Not surprisingly, pits grow much slower under OCP conditions under an organic coating.

5.7.3.2 Al-Cu thin films under neat epoxy in 0.5M NaCl. The DOI experimental setup was modified to facilitate long-term exposure experiments as described earlier. In these experiments, comparisons were made of the pit morphology and pit growth kinetics for as-deposited Al-Cu solid solutions versus samples that were artificially aged for 24 hours at 190°C. Heat treatment produced a dispersion of Al$_2$Cu (θ phase), which precipitated out from the matrix as indicated by x-ray diffraction (XRD) characterization (Figure 7.7).

Both the as-deposited and artificially aged Al-Cu thin films coated with a neat epoxy resin were exposed to aerated 0.5M NaCl solution. These experiments were terminated before one of the pits undercut the mask. A comparison of pit morphologies that develop in as-deposited and aged thin films is shown in Figure 7.8.
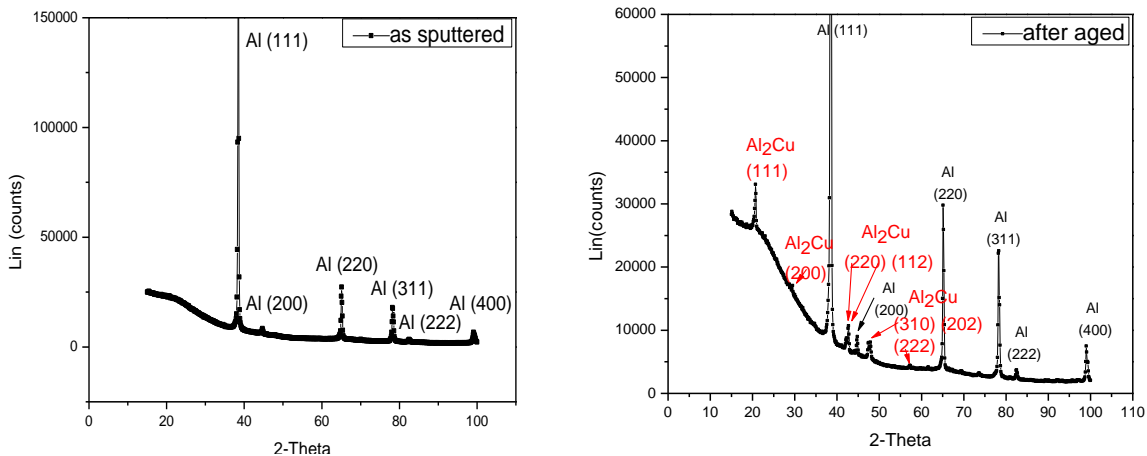

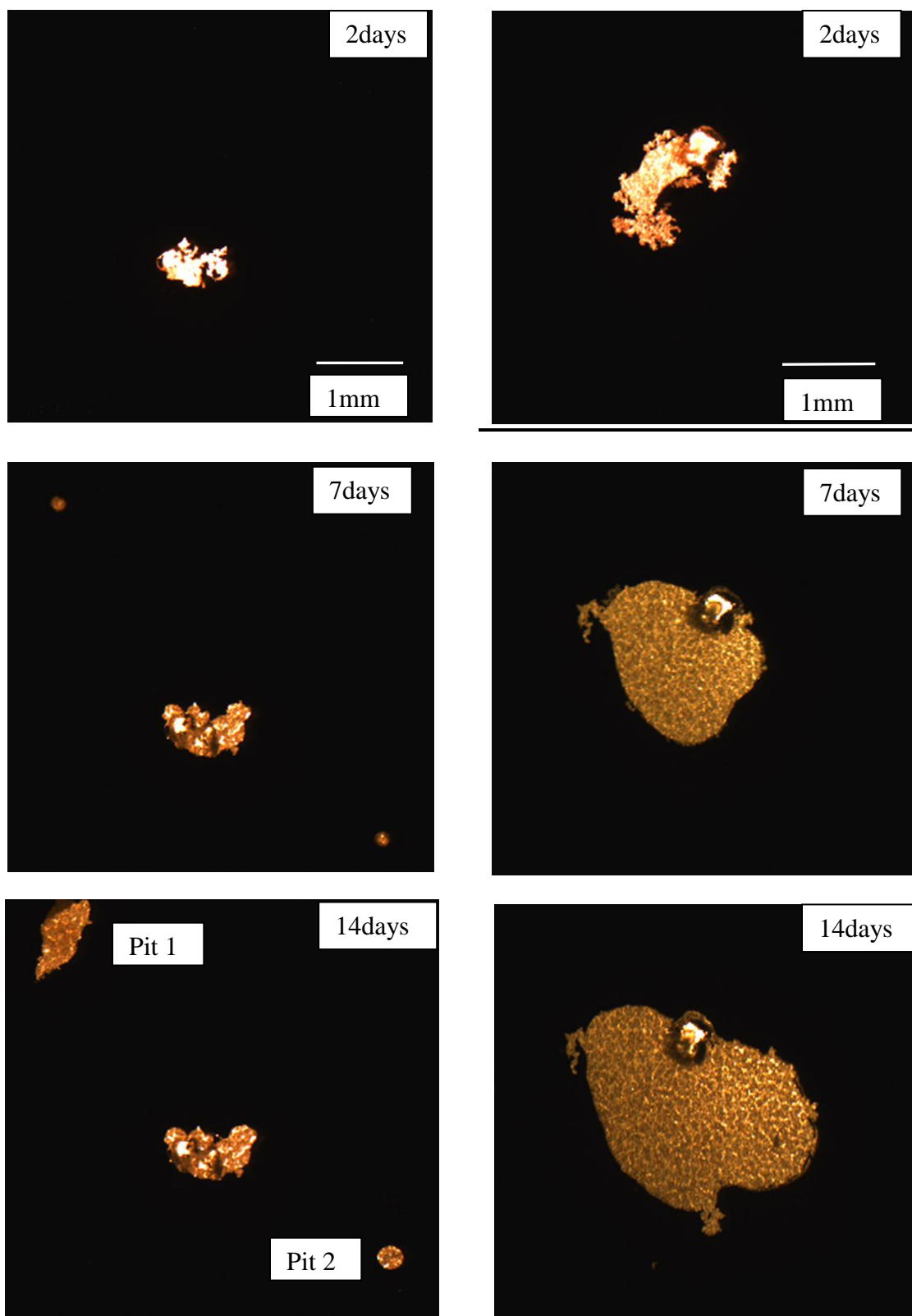Figure 7.7. XRD results of as-deposited Al-Cu thin films (left) and aged Al-Cu thin films (right).

Figure 7.8. Pit morphologies developed under neat epoxy resins applied to "as-deposited" (left) and aged Al-Cu thin films (right) at different exposure times.

Under the same neat epoxy resins, Al-Cu thin films produce different pit morphologies and different growth kinetics depending on metallurgical conditions and pit age. In the example shown in Figure 7.8, pits nucleated at intentionally introduced defects. In the as-deposited case nucleation occurred first at an artificial defect and rapidly passivated. Two new pits nucleated subsequently. After 14 days, three small, passivated pits were present. In the case of the aged sample, a single pit nucleated at the defect site and grew in one direction until the pit front became smooth. The pit then grew outward radially from its perimeter. As a result a single large pit grew in the case of the aged sample. This behavior is consistent with an inhibiting effect on localized corrosion by Cu retained in solid solution in the as-deposited sample. In this case, pit stability is reduced resulting in multiple pit attempts and multiple small pits relative to the aged case.

The neat epoxy coating was removed after exposure by using the PR-3500 Aircraft Epoxy paint remover. Scanning electron microscopy (SEM) was carried out to analyze the pit area under the coating. Results are shown in Figures 7.9 and 10. Pit bottoms in the as-deposited sample in Figure 7.9a contained concentric rings of corrosion and contaminant product. Inner rings contained corrosion product and solution contaminants. The outer rings closest to the pit wall contained Cu-rich dendrites that had formed by dissolution and replating [10]. These may have played a role in passivating the pit wall surface, thereby interrupting pit growth and preventing the formation of large pits.

Inside of the pit, there was undissolved Al-Cu thin film. The gap was rich in Al, Si and O. The other element such as Ca, Na, K et al. were from the glass slide substrates doped with these elements. In the aged thin film as shown in Figure 7.10, the pit was also passivated when the experiment terminated. Compared with the as-deposited condition, the Cu rich ring was discontinuous and the gap between the ring and the matrix was wider. Since all the pits were passivated with a gap at the corrosion front, it is believed that the gap had a contribution on the passivation of the pits.

Figure 7.10 shows pits formed in aged thin films. These pits also show rings of corrosion product on the pit bottoms with Cu dendrites near the pit wall. In this case the dendrites are more coarse and the dendrite layers are thicker. However the dendrite layer appears to be less continuous that is observed in the as-deposited case. In regions where the layer is broken, the pit wall corrodes into the matrix. This morphology suggests Cu dissolution and replating as is the case in the as-deposited sample, but a different pit morphology perhaps due to a lesser degree of Cu dendrite layer continuity along the corroding pit wall.

Pits growing in Al-Cu alloys think films under free corrosion conditions do not grow perimeters that increase linearly with time or with areas that increase linearly with t^2. To determine pit current densities, the variation in pit perimeter and pit area with time was fitted to polynomial functions, which were then substituted into equation 7.3.

The anodic current density from equation 7.4 is not a constant but is a function of time. Figures 7.11 a and b show the perimeter and area of the pit indicated as "pit 1" in the as-deposited Al-Cu thin film in Figure 7.8. The red curves indicate the polynomial fit. The anodic current density of
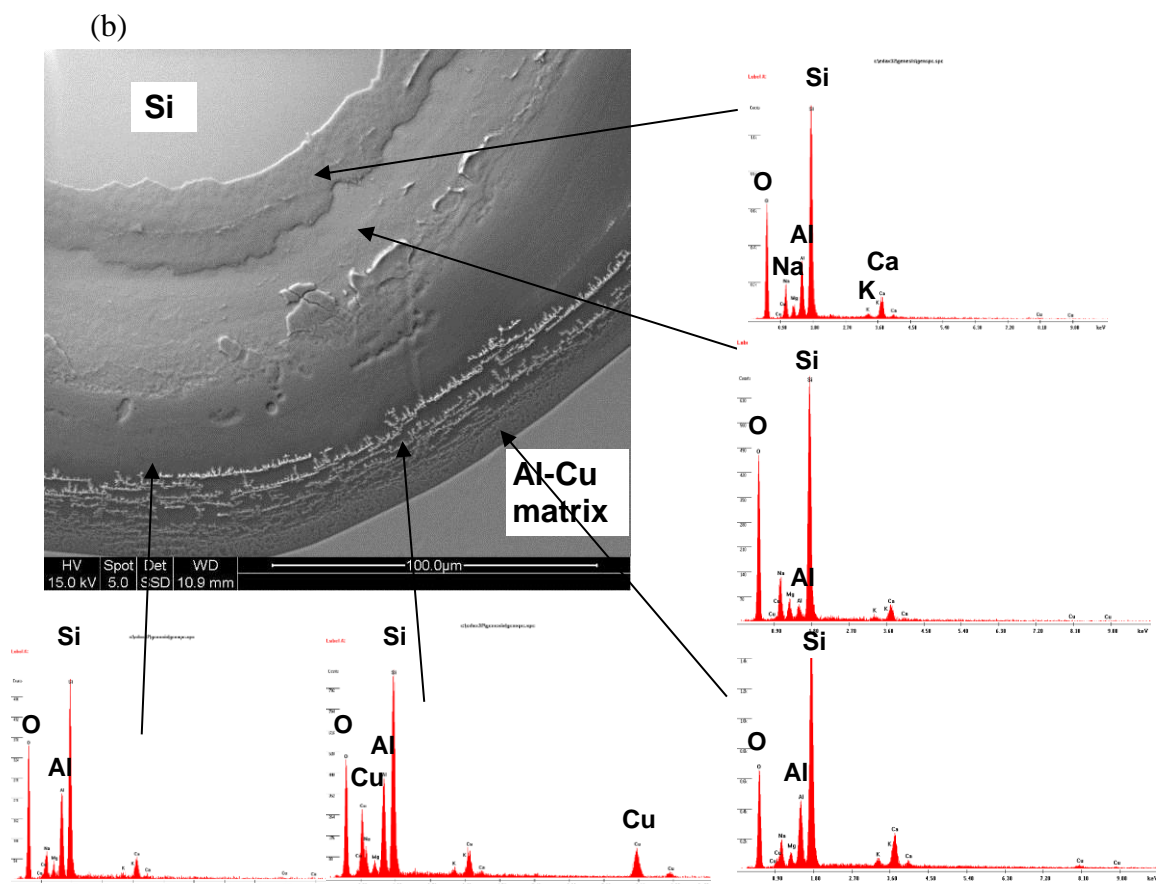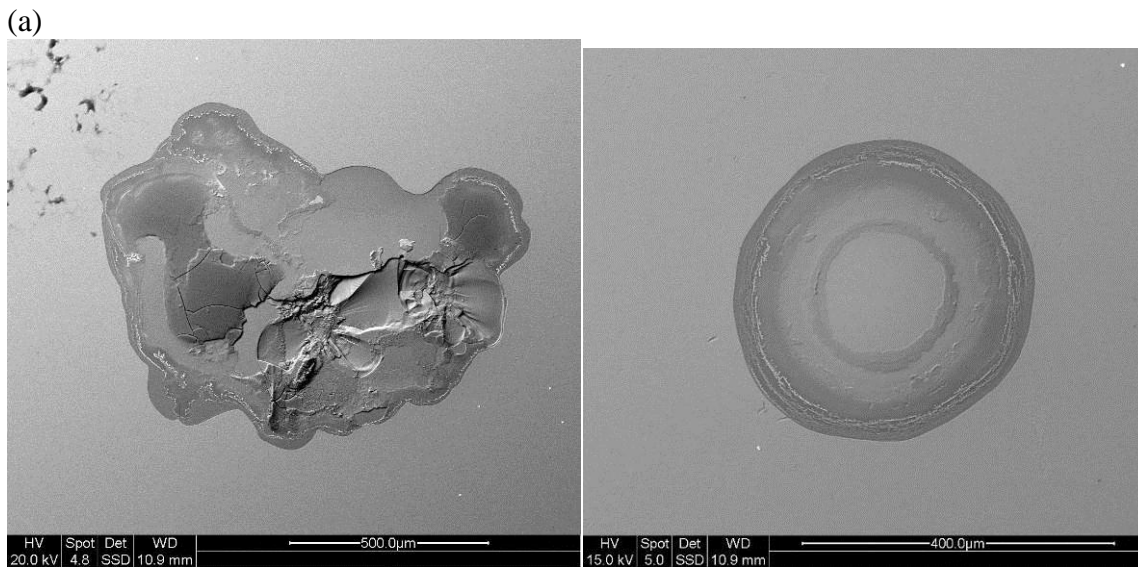
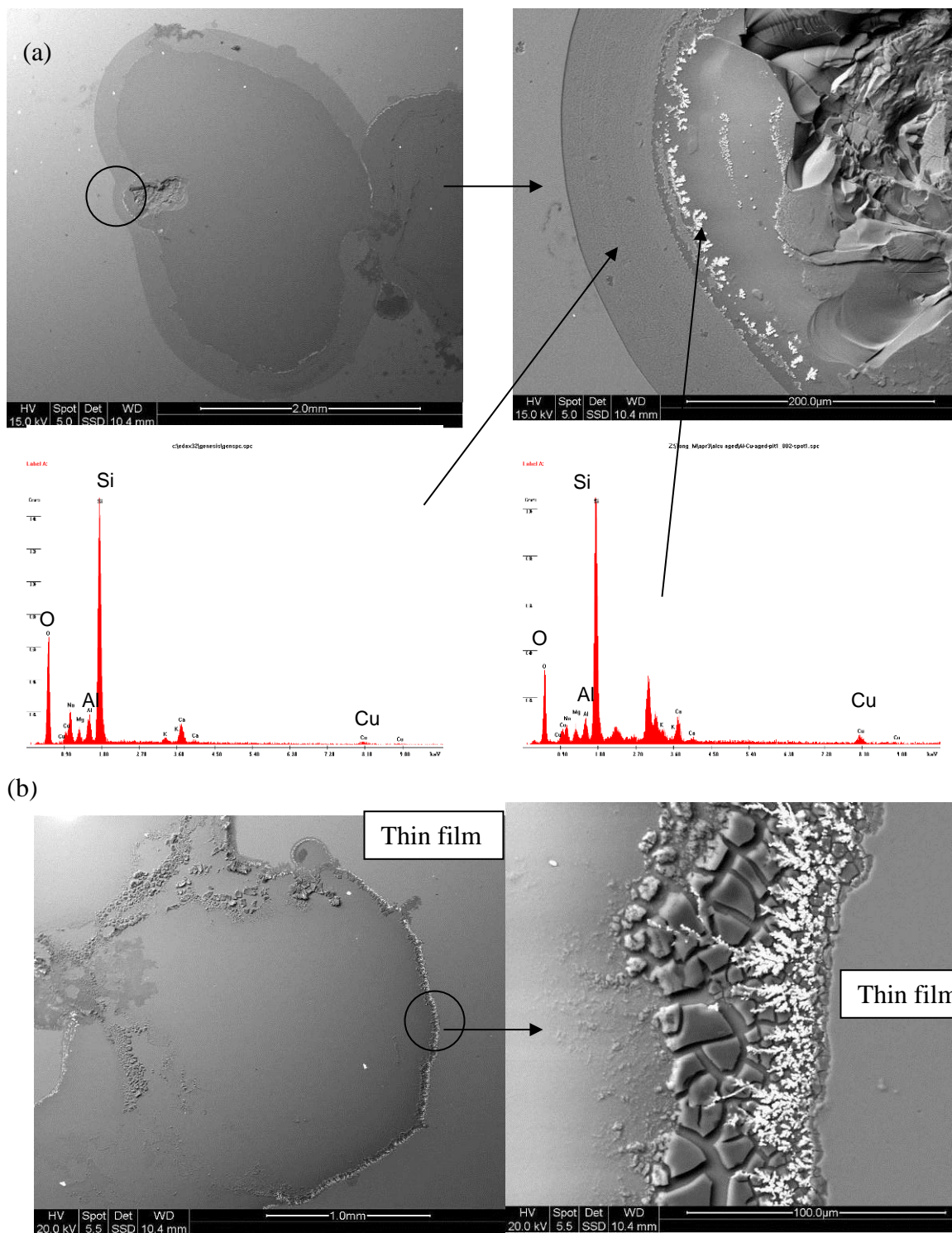Figure 7.9. SEM and EDS results of "As-deposited" Al-Cu thin film.

Figure 7.10. SEM and EDS results of aged Al-Cu thin films.

Pit 1 and pit 2 as shown in Figure 7.8 were calculated according to Equation 7.3 as shown in Figure 7.11c and d.

The analysis shows that the anodic current density itself decays with time. By fitting the anodic current density of pit 1 as a function of time, the equation is shown as follows,

$$i = a \times t^{-0.98}$$ (eq. 7.4).

In the same way, the anodic current density of "pit 2" in Figure 7.8 is given by,

$$i = a \times t^{-0.74}$$ (eq. 7.5)

Figure 7.11 d shows the aged thin film single pit growth current density. The fitting curve is,

$$i = 1.9 - 1.17^{-6} \times t$$ (eq. 7.6)

The current densities estimated from these expressions yield values that range from 2.6 down to 0.2mA/cm^2. However, at the same time as shown in the blue line in Figure 7.11 c and d, the current density of aged thin films is higher than that of as-deposited condition. This is attributed to the inhibiting effect of Cu dissolved in the solid solution of the as-deposited thin film. Nonetheless, multiple pits nucleated at the random sits in as-deposited thin films compared with only single pit nucleated in aged thin films, suggesting that the θ phase particles did not have an effect on the pit initiation.

5.7.3.3 Al-Cu thin films under Deft primers exposed to 0.5M NaCl. Both the as-deposited and aged Al-Cu thin films were coated with a Deft primer (02GN084) and exposed to aerated 0.5M NaCl solutions. The undercoating pit morphologies are shown in Figure 7.12. For the as-deposited thin films, round and irregular pits were observed suggesting that the growth rates were changing at different locations around the pit perimeter with time. However, in the aged thin film, the corrosion propagated primarily and preferentially in one direction. Both for the as-deposited and aged thin films, large numbers of discrete pits nucleated across the whole exposure surface. This suggested that the availability of dissolved oxygen to the substrate was greater than with neat epoxy primer. This is consistent with high pigment loading levels in the Deft primer. In both cases, the pit growth ended with the pit extending under the mask placed on top of the primer.

For the case of as-deposited thin films, multiple pits nucleated at random sites in both the neat epoxy coated samples and Deft primer. At early times the pit morphology was smooth. At later times it became irregular suggesting a decrease in pit growth rate. Both the round pits passivated after a burst of growth leaving an irregular pit active, which grew steadily. However, results show that in as-deposited thin films, the pit initiated after 5 days of immersion in NaCl solution. This was delayed for 7 days for the neat epoxy coated sample immersed to the same solution. This indicates that the Deft primer did not delay the initiation of the pitting corrosion.

For the aged thin films under both the neat epoxy coating and the Deft primer, single pits grew in a preferred direction with an obvious corrosion product ring immediately trailing the corrosion front.

The anodic current density of the pit was also calculated for Deft coated Al-Cu thin films as shown in Figure 7.13. By analyzing pit #1 indicated in Figure 7.12, it was found that the pit current density decreased as $t^{-0.5}$. Pits in aged thin films grew at constant current densities of 1.83mA/cm^2 and 11.58mA/cm^2 showing that pit growth in aged thin films was much faster than that in as-deposited thin films.

(a)

(b)

(c)

d)
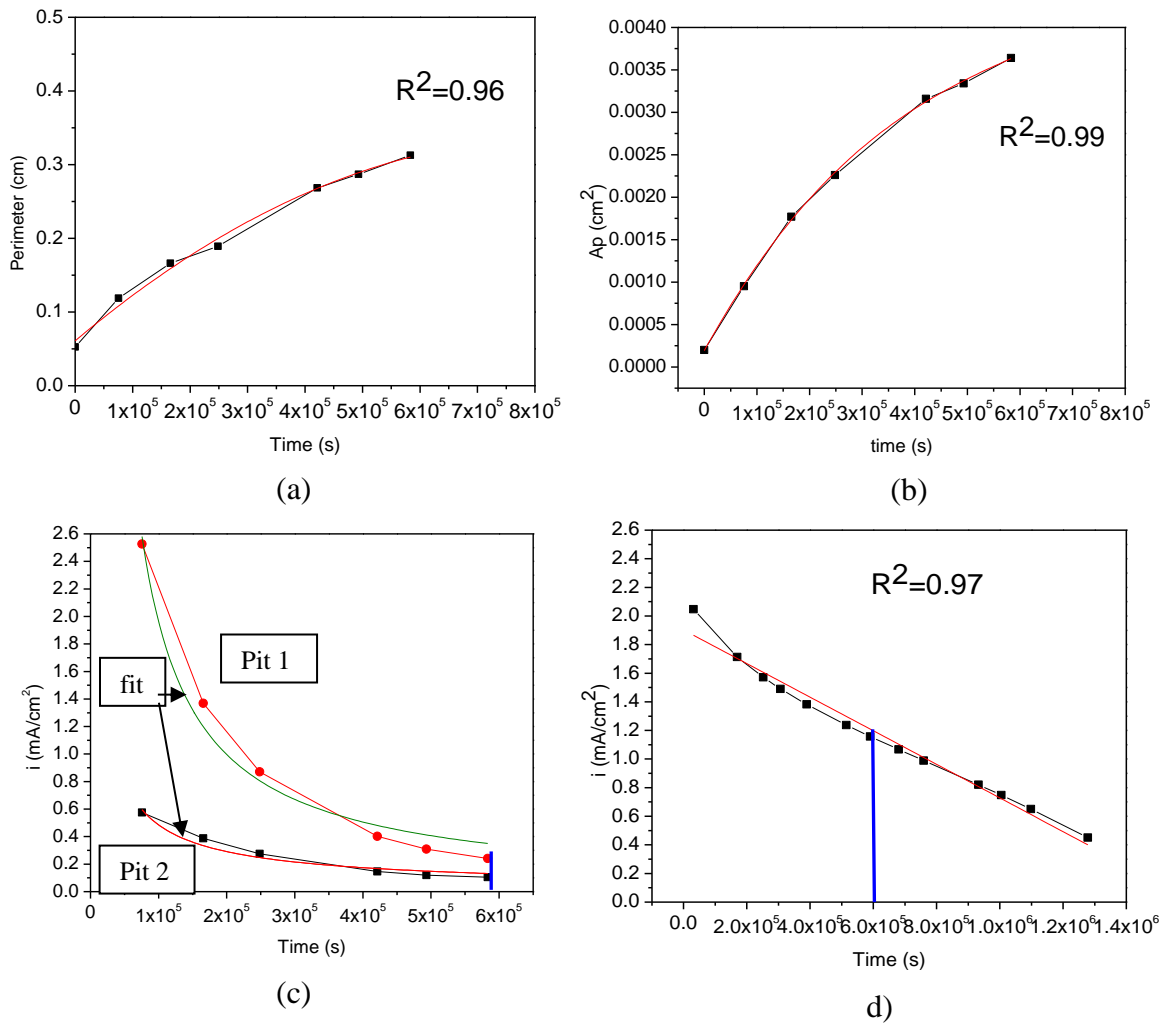
Figure 7.11. Pit geometry measurements and pit current density estimates from Figure **7.**8. a) A plot of the variation of the perimeter length as a function of time for pit #1 in the as-deposited thin film, b) a plot of the pit bottom area as a function of time for pit #1 in the as-deposited thin film, c) pit current densities as a function of time for pits #1 and 2 in the as-deposited thin film, d) pit current density versus time for a pit in the aged thin film.

In these experiments, Deft primers did not significantly inhibit pit growth. For the Deft primer applied to as-deposited thin films, an estimate of the average current density at the time of 60 ks was around $0.2mA/cm^2$ which was identical to that of pits formed under neat epoxy coatings. The average pit current density during an episode of pit growth was found to be as high as $1.83mA/cm^2$ under a Deft primer. The fastest growing active pits under neat epoxy coatings grew at similar rates, which varied from 2.6 to $0.3mA/cm^2$. These comparisons suggest that Deft coatings do not provide significant inhibition in this experimental format.
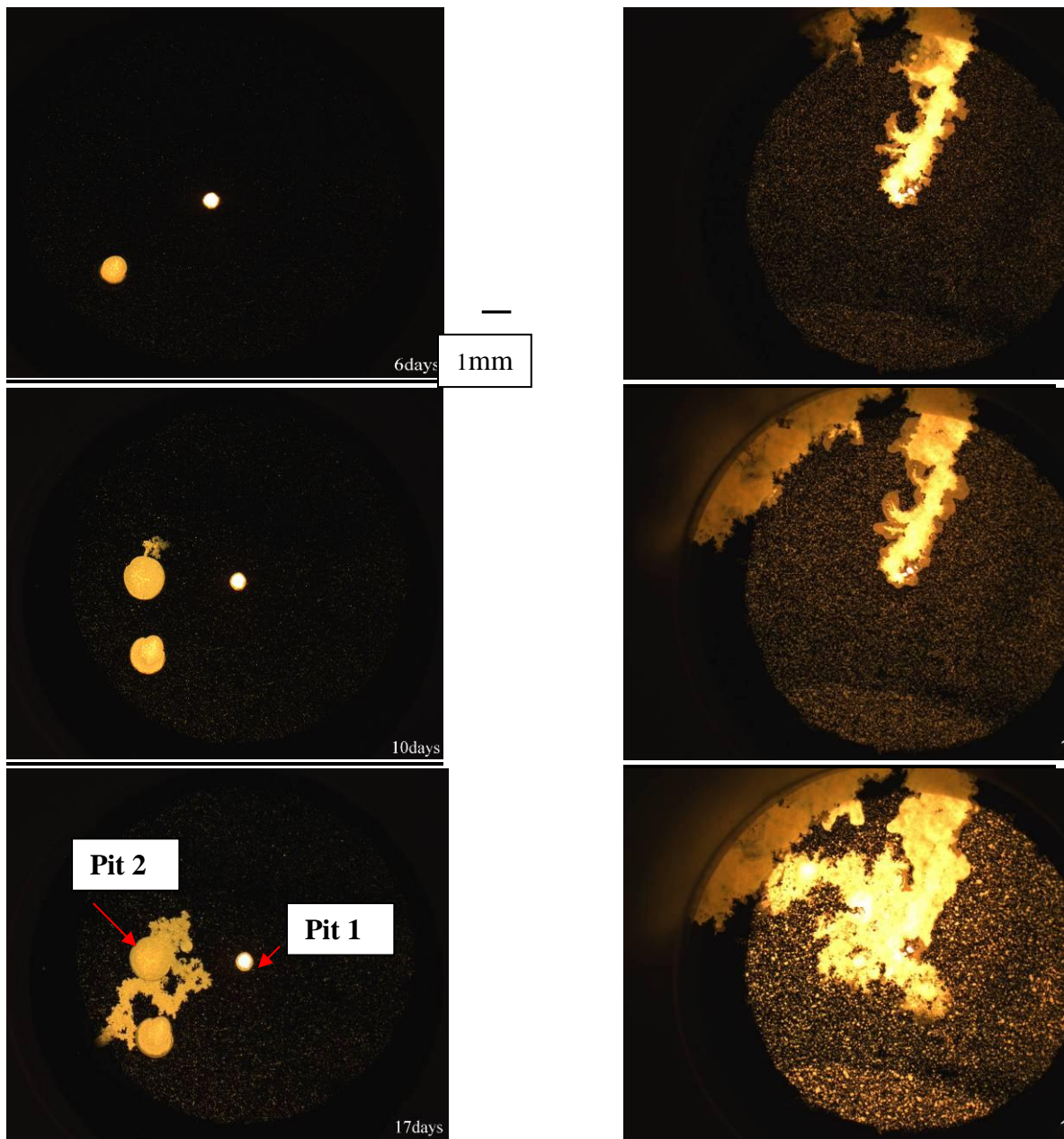
Figure 7.12. Pit morphologies under Deft primers. Left-on as-deposited Al-Cu thin films. Right- on aged Al-Cu thin films. Different exposure times are noted.
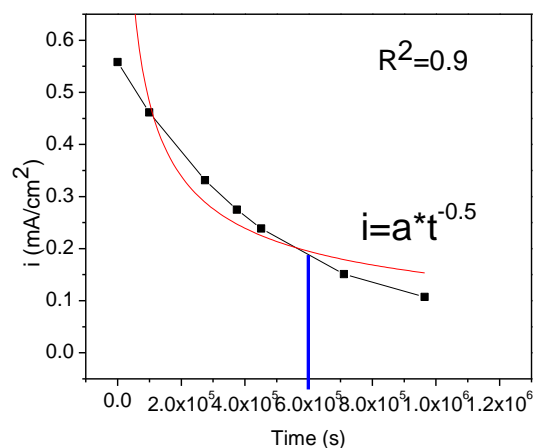
Figure 7.13. Anodic current density as a function of time of pit #1 in as-deposited thin film.

5.7.3.4 Al-Cu thin films under rudimentary SrCrO₄ primers in 0.5M NaCl. There was no indication of pit initiation or growth in as-deposited or aged Al-Cu thin films under SrCrO₄-pigmented epoxy coatings even after an extended exposure times. Chromate inhibitor release was indicated by blanching of the coating in the exposed area after 2 months in aerated 0.5M NaCl (Figure 7.14). This suggested that the SrCrO₄ pigments dissolve into solution releasing powerful chromate inhibitors that reinforce the passivity of the Al alloy substrates.
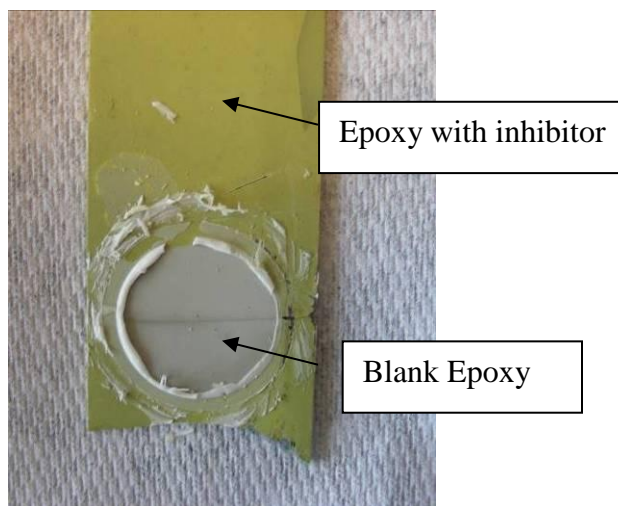
Figure 7.14. Sample after 2 months exposure in aerated 0.5M NaCl.

5.7.3.5 Al-Cu thin films under polyurethane coatings in 0.5M NaCl. Both the as-deposited and aged Al-Cu thin films were coated with a polyurethane topcoat and exposed to aerated 0.5M NaCl solutions. The resulting pit morphologies are shown in Figure 7.15.

356

For the case of as-deposited thin films, pits initiated at the intentionally formed coating defect and then at multiple random sites across the surface. These pits then coalesced until the whole test area was dissolved. In the case of aged thin films, multiple round pits nucleated randomly at the same time and quickly became irregular by extending branches outward from the pit nucleus. This growth pattern occurred because on side of the round pit was passivated by Cu-rich corrosion product while other areas were not. Corrosion proceeded along an irregular front until the whole exposure area was dissolved.

The anodic current densities were also calculated and shown in Figure 7.16. It can be seen that the current density of the as-deposited thin films was somewhat higher than that of the pit analyzed in the aged thin film contrary to earlier findings in which pits grew slower in Al-Cu solid solutions. Compared with the neat epoxy primer and Deft primer, the polyurethane top coat did not show strong corrosion inhibition. This could due to the weak adhesion of polyurethane top coat compared with primer.

5.7.4 Conclusions

The DOI method allows direct visual assessment of undercoating corrosion and enables insightful interpretation of electrochemical measurements collected simultaneously. Under OCP conditions, the corrosion under the coating is very complex and shows strong dependence on the barrier properties of the overlying coating and exposure conditions. In the case of 0.3M HCl solution, the uniform corrosion occurred compared the localized corrosion in the 0.5M NaCl solution. The pit morphology in 0.5 M NaCl solution ranged from round to irregularly shaped pit depending on the corrosion rate. The metallurgical condition of the Al-Cu metallization was also found out to have an influence on the pit propagation. Pit current densities tended to be lower in as-deposited Al-Cu thin films than heat treated ones suggesting and inhibiting effect of Cu retained in solid solution. The DOI method also allows one estimate the localized corrosion growth rates. Kinetic analyses combined with qualitative observations enable understanding of the controlling factors in corrosion damage accumulation.
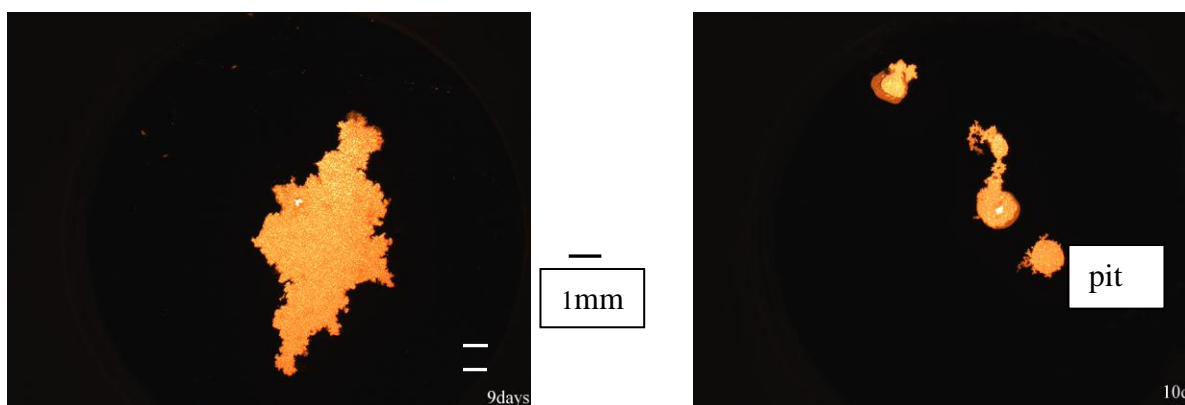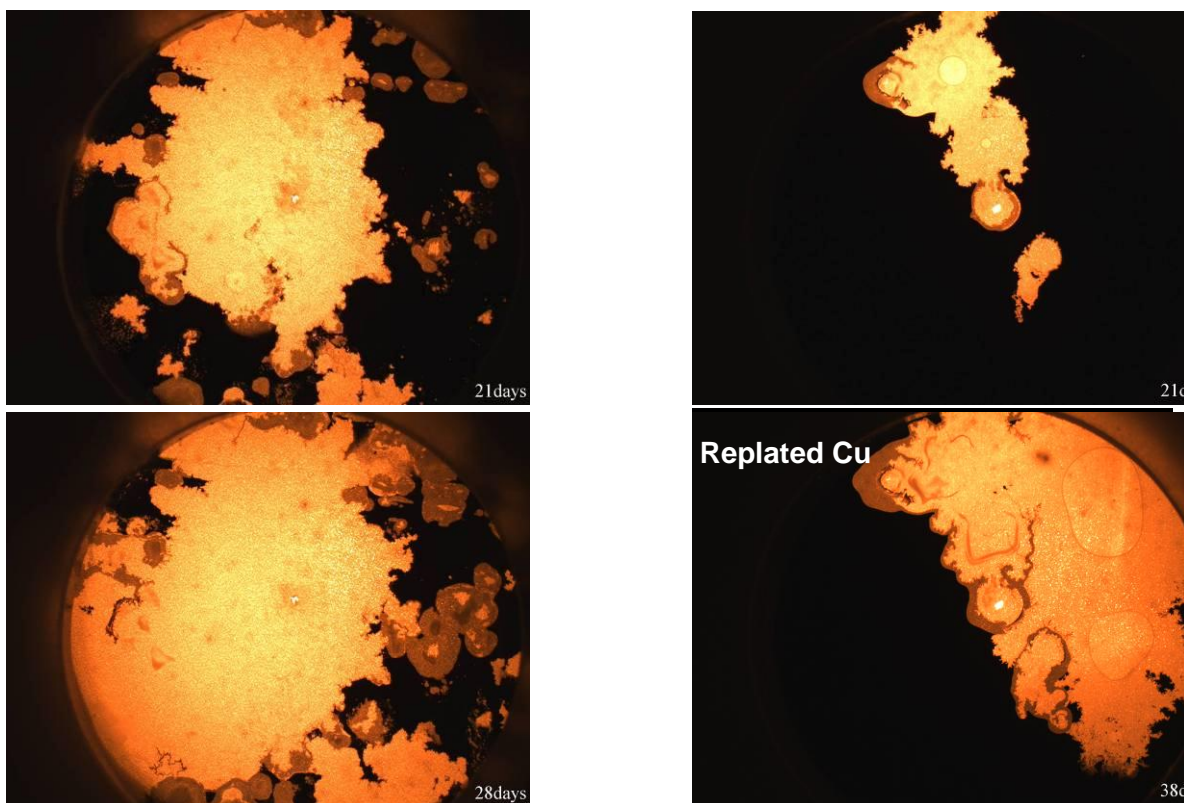
Figure 7.15. Pit morphologies under polyurethane coatings on as-deposited Al-Cu thin films (left) and aged Al-Cu thin films (right) at different exposure times.
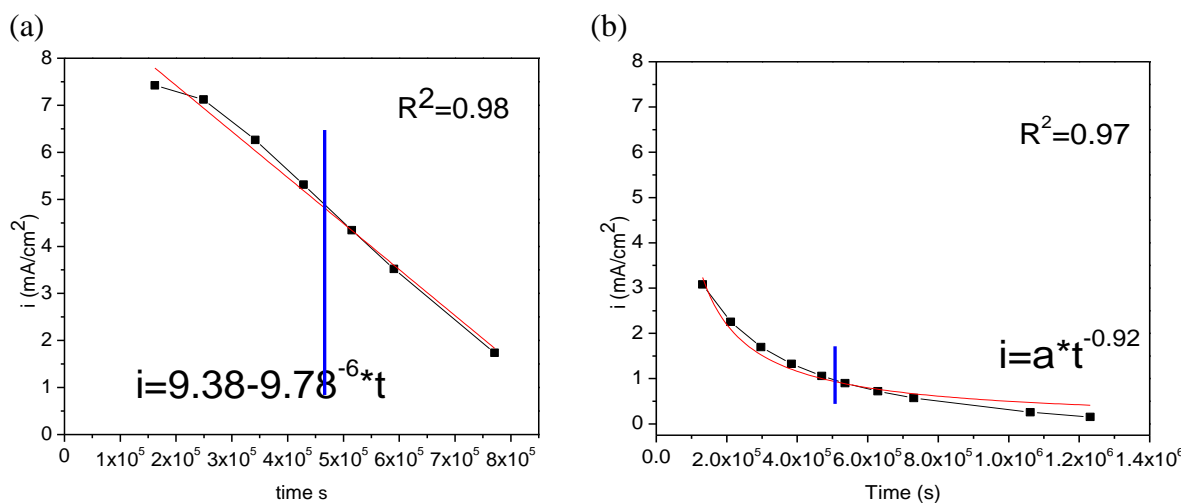

Figure 7.16. Anodic current densities as a function of time. (a) as-deposited thin film (b) aged thin film.

5.7.5 References

1. L. Balazs et al., *Physica A*, **217**, 319 (1995).
2. G. S. Frankel, *Corros. Sci*, **30**, 1203-1218 (1990).

3. L. Balazs, *Physica E,* **54**, 1183-1189 (1996).
4. Y. Hisamatsu et al., *Localized Corrosion NACE-3 (ed. R.W. Staehle, B. F. Brown, J. Kruger and A. Agrawal)*, p.240.
5. D. Lu et al., *Corros. Sci*, 58, 137-143 (2002).
6. A. J. Griffin Jr. et al., in *30th Annual Proceedings-Reliability Physics 1992, p.239*, IEEE/IRPS, New York (1992).
7. S. E. Hernandez et al. *J. Electrochem. Soc*., 142, 1215-1220(1995)
8. D. R. Frear et al., *Metallurgical Transactions*, 21A, 2449-2458 (1990).
9. J. Proost et al., *J Solid State Electrochem*, 2, 150-155 (1998).
10. R. G. Buchheit et al., *CORROSION/2001 Research Topical Symposium—Localized Corrosion, (Houston, TX: NACE International,* 265-292 (2001).
11. G. S. Frankel et al., *J. Electrochem. Soc.* 139, 2196-2201 (1992)

6. Concluding Summary

In this section, conclusions will be drawn for each task in turn.

Task 1. Fundamental Studies of the Trivalent Chrome Process (TCP).

- Trivalent chromium process (TCP) coatings were studied on AA2024, 6061 and 7075 alloys that were first degreased and deoxidized. The TCP coating on all three alloys is approximately 50-100 nm thick. It is primarily hydrated zirconia with coprecipitation of $Cr(OH)_3$. Under the zirconia layer is a K- and F-rich fluoroaluminate interfacial layer (K_xAlF_{3+x}). The Cr-rich regions of the coating are in and around pits.

- The layer forms because of an increase in the interfacial pH caused by both dissolution of the oxide layer and localized oxygen reduction at Cu-rich intermetallic sites.

- TCP coating provides both anodic and cathodic protection by physically blocking Al-rich sites (oxidation) and Cu-rich intermetallics (reduction), resulting in 10x greater polarization resistance and suppressed anodic and cathodic currents around the open circuit potential in potentiodynamic scans.

- TCP coating can release chromium into solution, which can then form a film on the surface of an uncoated alloy surface exposed in close proximity. Artificial scratch experiments showed that the polarization resistance of the uncoated surface near a TCP-coated surface is higher than uncoated controls, which indicates the TCP coating can provide active corrosion inhibition.

- At least in the short-term (4-h in mild and aggressive electrolytes) the structure and chemical composition of the coating are stable as evidenced by unchanging electrochemical properties. Preliminary, evidence indicates that ageing (3-7 day air dry) can have some beneficial effects by increasing the barrier properties of the coating.

- Raman spectroscopy generated evidence for transient formation of Cr(VI) species in the coating after some period of drying and or electrolyte solution exposure. Cr(VI) likely forms due to the oxidation of Cr(III) oxide by locally produced H_2O_2, which is a product of oxygen reduction. This transient Cr(VI) might be the source of the active corrosion inhibition.

Task 2. Mechanisms of selected inhibitors.

- The inhibition performance of common inhibitors found in commercial chromate-free primers. i.e. molybdate, silicate, and praseodymium, was studied. A mechanism for the protection provided by each inhibitor was postulated.

- Molybdate, inhibition is optimal at near-neutral pH at a concentration of 125 mM in 0.1 M NaCl solution. MoO_3 imparts anodic inhibition by ennobling the pitting potential. The inhibition mechanism involves an oxidation-reduction process whereby MoO_2 is formed

and subsequently re-oxidized in two steps to form MoO_3 over the intermetallic particles. At low pH, molybdate is ineffective because of polymerization.

- Silicate is a strong anodic inhibitor in highly alkaline conditions, increasing the pitting potential at the optimum concentration of 25 mM by as much as 1 V. At high pH the dissolution of the aluminum oxide film on the surface promotes the formation of an aluminosilicate thin-film that is physically adsorbed to the negatively charged surface by Na^+ ions. At near-neutral pH, silicate blocks the activation of intermetallic particles on the surface by the formation of silicate- and silica-based particulates. At even lower pH, activation of the aluminum surface promotes the formation of monomeric silicate ions and the deposition of aluminosilicate film across the whole surface, which was shown to provide some corrosion inhibition in comparison to the inhibitor-free case.

- Praseodymium imparts cathodic inhibition at near-neutral pH, lowering the oxygen reduction kinetics by a factor of 10 at the optimum concentration of 0.2 mM. Pr carbonate hydroxide, $Pr_2(CO_3)_2(OH)_2 \cdot H_2O$, forms over the ORR supporting intermetallic particles as the local pH increases. As the cathodes on the surface become blocked by a thick-oxide, new sites are activated resulting in the formation of a thick-film across the whole surface. In low and high solution pH, praseodymium renders poor inhibition. At high pH, a thick Pr oxide film still forms over the intermetallics as a result of ORR but is unable to stop the uniform dissolution of the Al-oxide film.

- *In situ* AFM scratching experiments reveal that at their respective optimum inhibition concentrations, all three inhibitors reduce the removal rate of the S-phase particles in comparison to the inhibitor-free case. In the case of praseodymium, attack in the form of trenching was observed around all IMC particles, but *ex situ* SEM analysis showed the larger particles to be still intact and Mg and Al were still detected over the S-phase particles by EDS.

Task 3. Active inhibition, barrier properties and adhesion.

- Exchange bentonites of Ce, Pr, La and Zn were synthesized and their characterization by XRD showed a shift in their basal d_{001} spacings indicating successful exchange of the sodium cation for the inhibitor cation during synthesis.

- The trend in the d-spacing increase for the bentonites was Pr > Ce = La > Zn. TGA analysis until 250°C showed higher loss in wt% for the exchanged bentonites indicating that the number of water molecules associated with the interlamellar space has increased. This is the cause for the increase in d-spacing. The trend for the d-spacing increase correlated well with the TGA weight loss measurements

- Sodium bentonite exhibited a Cation Exchange Capacity (CEC) of 85 meq/100g. Release measurements confirmed inhibitor cation (Ce^{3+}, Pr^{3+}, Zn^{2+}) release. The fraction of reservoir of the inhibitor in the bentonite was relatively high for Zn bentonite at 0.61 and it was 0.46 and 0.47 for Ce and Pr bentonites. This could be one of the reasons why Ce and Pr bentonites performed inferior to the Zn bentonites in the impedance and salt spray tests.

- La and Zn bentonites showed better performance compared to the other exchange bentonites when incorporated into epoxy coatings with total impedance magnitude in the same order as the $SrCrO_4$ standard.

- The presence of TiO_2 solids increased the permeability of the epoxy resin and impedance suggested strong water uptake by the epoxy coatings, enabling La^{3+} and Zn^{2+} cation release and promoting interfacial passivity.

- EIS measurements showed that PVA behaved like a gel and exhibited very low barrier properties. Bentonites did not passivate the interface suggesting that not enough inhibitor cation was released to completely passivate the surface.

- EIS on the PVB coatings on the other hand suggested no water uptake due to which the inhibitor cation was not released. Bentonites degraded the barrier properties of PVB and provided no inhibition.

- Salt spray exposures showed that Zn bentonite incorporated into PVB performed relatively better compared to the neat PVB and other pigmented bentonites with very few blisters. La bentonite incorporated in epoxy coatings showed no attack around the scribe compared to other pigmented epoxy coatings. However, all the pigmented epoxy coatings showed partial scribe protection.

Task 4. Paint adhesion strength and mechanism.

- The blister test (BT) was developed in this work to study the adhesion of paint to metal surfaces. The BT is a very versatile technique that allows calculation of stress at fracture and adhesion strength. The adhesion strength results from the BT are reproducible and help to discern regarding different surface treatments.

- Roughness degree and surface topography are very important factors for adhesion strength of PVB to AA2024-T3. Adhesion strength increases with roughness and surface area due to a larger interaction in the primer/substrate interface. Randomly abraded samples have higher adhesion strength than random abraded samples.

- Numerous approaches were tested to sample adhesion strength using the BT after adhesion degradation of the interface. However, no adhesion strength degradation was found.

- Galvanic coupling of SS316 fasteners to AA2024-T3 activates the underlying metal due to the high cathodic current on the fastener. The minimum potential along the scribe tends to decrease with increased galvanic coupling owing to activation of the aluminum alloy. This contradicts the typical assumptions of galvanic coupling. The galvanic interaction and coating degradation varies with different fastener materials according to SS316 > Ti 6-4 > AA2024-T3 $\approx$ No fastener.

- Other adhesion test techniques were investigated and found to be inferior to the BT. The pull-off test does not produce adhesive failure across the whole interface so the results do

not represent true adhesion strength. The tape test is very qualitative and does not discern the performance of different coating systems. In contrast, the BT produces adhesive failure of the primer studied, is very reproducible and is able to show adhesion strength difference between different coating systems.

- Conversion coating treatment improves adhesion strength of acetoacetate and epoxy coatings to AA2024-T3. Cleaning and deoxidizing improves adhesion of acetoacetate samples for all conversion coatings except for chromate conversion coating. For epoxy coatings the addition of the cleaning/deoxidizing step improves the adhesion strength of the chromate conversion coating samples, but no effect is noticeable for titania-based conversion coating and TCP.

- Si contamination seems to affect deleteriously the adhesion strength and resistance of coating systems to osmotic blistering.

Task 5. Inhibitor activation and transport in the primer layer.

- Corrosion inhibitive pigments have substantially increased solubilities in strong electrolytes such as salt water. The magnitude of the solubility enhancement increases with increasing charge of the soluble inhibitor complex.

- Exposure to air can increase the solubility of inhibitive pigments both through acidification and carbonation reactions.

- Some existing chromate free inhibitive pigments are formulated with reactive co-pigments or complexing agents to form and stabilize soluble species in response to hydration. In one instance, a praseodymium hydroxide inhibitor was determined to form both anionic and cationic sulfate complexes through reaction with a calcium sulfate additive.

- Corrosion inhibitor complexes can be transported through primer films in response to electric fields. The state of charge on the soluble complex (anionic or cationic) is expected to determine its electromigration to either anodic or cathodic corrosion sites.

- Based on several experiments, the transport and release rates of corrosion inhibitors through and from primer samples are low. Attempts to detect a passivation response by AA2024-T6 immersed in a bulk primer chip slurry were unsuccessful.

- Aerospace primers are relatively permeable to water vapor. A water – reducible primer was found to transmit water vapor at high rates for an extended cure interval compared to solvent base primers. The rate of water vapor transmission is isotropic, with in-plane diffusivity values approximately 3x greater than through-plane values.

- Aerospace primers were found to have a fine structure characterized by a dense layer at the air and substrate interface, encapsulating a central nanoporous layer. This fine structure is believed to account for the isotropic transmission of water vapor and the sluggish transport and release of inhibitors from primer surfaces.

Task 6. Interactions between polymer matrix, pigment, surface treatment, and alloy.

- R_{corr}, determined from EIS testing of coated systems defined as the sum of the pore resistance, the defect resistance together and the solution resistance was a weak predictor of coating performance in exposure testing.

- The metal-coating interface capacitance showed strong correlation with the visual TTF for only those samples that failed during exposure. The percentage of delaminated area showed weak correlation with the visual examination to total corrosion damage accumulation.

- Prediction of the TTF obtained by ANN fed with phase angle information showed strong correlation with the visual TTF for all samples tested. A ranking among coatings was obtained using ANN parameters. The combination of Boegel 8500 conversion coating with Deft02GN084 primer ranked first among the emerging corrosion resistance coatings tested.

- Fuzzy curve analysis was used to discriminate the significance of EIS-based input data in the output variable. From the analysis, discrimination was not only among the type of EIS parameters, i.e. Z_{mod}, Z_{imag}, Z_{real}, or phase angle, but also among the frequencies.

- The most significant variables to influence the TTF extracted from fuzzy analysis were those attributed to the phase angle response at low frequencies. The most significant frequencies were those ranging from the upper breakpoint frequency to about 50 mHz; a range which is related to the evolution of coating defects.

- A pruned ANN was successfully constructed and trained using the most significant variables to predict time to failure of coating exposed to ASTM B117 salt spray. ANN showed proficiency in predicting long-term exposure TTF from short-term exposure EIS results.

- Observations showed a greater concentration of chromate pigment particles in chromate primers than any other pigments particles in compared chromate-free primers. By visual assessment, the volume fraction of praseodymium was smallest within Deft 04GN098. Barium on Sicopoxy had the highest volume fractions inhibitor compound particles and its volume fractions were close to, but not as great as that of chromium within PPG CA7233.

Task 7. Characterization of local environments in coating systems.

- The DOI method allows direct visual assessment of undercoating corrosion and enables insightful interpretation of electrochemical measurements collected simultaneously.

- Under OCP conditions, the corrosion under the coating is very complex and strong dependence on the barrier properties of the overlying coating and exposure conditions.

- The pit morphology in 0.5 M NaCl solution ranged from round to irregularly shaped depending on the corrosion rate.

- In the case of 0.3M HCl solution, uniform corrosion occurred compared the localized corrosion in a 0.5M NaCl solution.

- The metallurgical condition of the Al-Cu metallization was found to have an influence on pit propagation.

- Pit current densities tended to be lower in as-deposited Al-Cu thin films than heat-treated ones suggesting and inhibiting effect of Cu retained in solid solution.

- The DOI method also allows one to estimate the localized corrosion growth rates and kinetic analyses combined with qualitative observations enable understanding of the controlling factors in corrosion damage accumulation.

Appendix 1. Team Members

The Ohio State University
Gerald Frankel, PI
Rudy Buchheit, PI
Yang Guo
Brendy Rincon
Omar Lopez-Garrity
Anusha Chilukuri
Federico Gambina

Michigan State University
Greg Swain, PI
Ben Lee
David Woodbury
Annette Howells
David Skutta
Liangliang Li
Garrett Swain

United Technologies Research Center
Mark Jaworwoski, PI
Weina Li
Weilong Zhang
Xiaomei Yu

Army Research Lab
Brian Placzankis
Tom Braswell
Elisabeth Charleton

NAVAIR
Bill Nickerson

AFRL
Joel Johnson

Boeing Corp.
Joe Osborne
Kristin Brinker

Henkel Corp.
Bill Fristad
Walter Opdycke
Kirk Kramer

Appendix 2. List of Scientific/Technical Publications

Articles in peer-reviewed journals

Y. Guo and G.S. Frankel, Y. Guo and G.S. Frankel, "Characterization of Trivalent Chromium Process Coating on AA2024-T3," *Surf. Coat. Tech.*, 2012, 3895-3902.

Y. Guo and G.S. Frankel, "Active Corrosion Inhibition of AA2024-T3 by Trivalent Chrome Process Treatment," *Corrosion*, **68**, (2012) 045002-1-045002-10.

Liangliang Li, G.P. Swain, A. Howell, D. Woodbury, G.M. Swain, "The Formation, Structure, Electrochemical Properties and Stability of Trivalent Chrome Process (TCP) Coatings on AA2024," *J. Electrochem. Soc.* **158** (2011) C274-C283.

Liangliang Li, D.Y. Kim and G.M. Swain, "Transient Formation of Chromate in Trivalent Chromium Process (TCP) Coatings on AA2024 as Probed by Raman Spectroscopy," *J. Electrochem. Soc.* **159** (2012) C326-C333.

W. Zhang, M. Jaworowski, "In situ Capacitance Measurements for In-Plane Water Vapor Transport in Paint Films," *Progress in Organic Coatings,***74**, July (2012) 534‑539.

S. Dardona, M. Jaworowski, "In Situ Spectroscopic Ellipsometry Studies of Trivalent Chromium Coating on Aluminum," *Appl. Phys. Lett*. **97**, (2010) 181908.

S. Dardona, L. Chen, M. Kryzman, D. Goberman, M. Jaworowski, "Polarization Controlled Kinetics and Composition of Trivalent Chromium Coatings on Aluminum", *Anal. Chem.*, **83** (2011), pp 6127–6131.

B.L. Hurley, S. Qiu, R.G. Buchheit, "Raman Spectroscopy Characterization of Aqueous Vanadate Species Interaction with Aluminum Alloy 2024-T3 Surfaces," *J. Electrochem. Soc.*, **158** , (2011) C125-C131.

Technical reports

Conference or symposium proceedings

Y. Zhai, Y. Guo, G.S. Frankel, J. Zimmerman and W. Fristad, "Chromate-Free and Phosphate-Free Surface Treatments for Al Alloy and Steel Substrates," Proceedings of the 17th ICC, Las Vegas, 2008.

Conference or symposium abstracts

Study of Trivalent Chrome Process Treatment on AA2024-T3," Y. Guo and <u>G.S. Frankel</u>, DoD Corrosion Conference, La Quinta, CA, 8/2/11.

"New Approaches for Measuring Adhesion and Adhesion Degradation," B.C. Rincon Troconis, S. Adhikari, J. Seong, G.S. Frankel, NACE Corrosion 2011, Houston, 3/15/11.

"Cr-Free and Phosphate-Free Surface Treatments for Steel and Al Alloys," B. Rincon Troconis, Y. Guo, K. Unocic, S. Adhikari and G. S. Frankel, ECS Fall Meeting, Vienna, 10/5/09.

"Corrosion Protection of Aluminum Alloys by Trivalent Chrome Process Treatment," Y. Guo and G.S. Frankel, 8th ISE spring Meeting, Columbus, OH, May 2010.

"Corrosion Protection of Al Alloys by Trivalent Chrome Process Coatings," Y. Guo and G.S. Frankel, 212th ECS meeting, Washington, DC, Oct. 2007.

"Corrosion Protection by Trivalent Chromium Process (TCP) Coatings on Aluminum Alloys," L. Li and G.M. Swain, PRiME 2012, Honolulu, Hawaii, 10/10/12.

"Transient Formation of Chromate in Trivalent Chromium Process (TCP) Coatings on AA2024 as Probed by Raman Spectroscopy," L. Li and G.M. Swain, ECS Fall Meeting, Boston, Massachusetts, 10/10/11.

"Physical, Chemical and Electrochemical Investigations of Trivalent Chrome Process (TCP) Coatings Applied to Aluminum Alloys," D. Woodbury, A. Howells, G.P. Swain and G.M. Swain, ECS Fall Meeting, Las Vegas, Nevada, 10/12/10.

"Chromate-free Surface Treatments for Al Alloy and Steel Substrates," Y. Zhai, Y. Guo, G.S. Frankel, J. Zimmerman and W. Fristad, 17th International Corrosion Congress, Las Vegas, 10/08/08

"Nanoscale Cr-free Conversion Coatings for Al Alloy and Steel Substrates," Y. Zhai, Y. Guo and G.S. Frankel, ENMT 2008, Ein Gedi, Israel, 9/18/08.

"Blister Test for Measurements of Coating Adhesion," B.C. Rincon Troconis and G.S. Frankel, MS&T Conference, Columbus, OH, 10/19/2011.

"Blister Test for Measurements of Coating Adhesion and Degradation," B.C. Rincon Troconis and G.S. Frankel, DoD Corrosion Conference, La Quinta, CA, 08/04/2011.

"Effect of Surface Treatments on Adhesion Strength of Polymer/AA 2024-T3 using the Blister Test," B.C. Rincon Troconis and G.S. Frankel, ISE Spring Meeting, Columbus, OH, 05/05/2010.

"El Blister Test, una Herramienta Novedosa en la Evaluación de Recubrimientos (The Blister Test, a Novel Technique for Coating Evaluation)," B. Rincon Troconis and G.S. Frankel. Invited speaker. Universidad del Zulia, Maracaibo, Zulia, Venezuela, 12/07/2011.

"Corrosion Inhibition of AA2024-T3 by Aqueous Silicate, Molybdate, and Praseodymium Species," O. Lopez-Garrity and G.S. Frankel, DoD Corrosion Conference, La Quinta, CA, 8/1/11.

"Corrosion Inhibition of AA2024-T3 by Aqueous Silicate, Molybdate, and Praseodymium Species," O. Lopez-Garrity and G.S. Frankel, MS&T Conference, Columbus, OH, 10/19/11.

"The Secret Life of Chromate Free Primers," M. Jaworowski, SAE AeroTech Congress & Exhibition, November 10 - 13, 2009, Seattle, WA.

"Alternatives to Chromates", M. Jaworowski, Corrosion in the Undersea Navy, Narragansett, RI 9/9/10.

"Succeeding with TCP", M. Jaworowski, Aerospace Chromate Elimination Team, 9/14/10 East Hartford, CT.

"Alternatives to Chromates", M. Jaworowski, 2010 International Workshop on Environment and Energy, 11/3/10 San Diego, CA.

"The Zn^{2+} - vanadate Inhibitor Pair for Corrosion-Resistant Organic Coatings: Inhibitor interaction with complex microstructures and delivery approaches using synthetic ion-exchange compound pigments," R. G. Buchheit, Gordon Research Conference on Aqueous Corrosion, Colby –Sawyer College, New London, New Hampshire, July 11, 2012.

"Corrosion inhibition by vanadates: understanding inhibitor interaction with complex alloy microstructures and demonstration of delivery approaches using synthetic nanostructured ion-exchange compounds," K.D. Ralston, S. Chrisanti, T.L. Young, B. Hurley R.G. Buchheit, Departmental Colloquium Series, Department of Materials Science and Engineering, Iowa State University, Ames, Iowa, April 26, 2012.

"Corrosion inhibition of AA 2024-T3 by the Zn^{2+} cation", A. Chilukuri, R.G. Buchheit, Research in Progress Symposium, NACE conference proceedings, Salt Lake City, USA, March 2012.

"Evaluation of Corrosion Inhibition of 2024-T3 by Zn^{2+}," A. Chilukuri, R.G. Buchheit, 2011 DOD Corrosion Conference, Palm Springs, CA, August 2011.

"Environmentally Conscious Corrosion Protection Based on Cooperative Chemical Inhibition and Inhibitor Delivery by Synthetic Ion Exchange Compounds," R. G. Buchheit, Departmental Colloquium Series, Department of Materials Science and Engineering, University of North Texas, Denton, Texas, November 8, 2011.

"Corrosion inhibition by vanadates: understanding inhibitor interaction with complex alloy microstructures and demonstration of delivery approaches using synthetic nanostructured ion-exchange compounds," R.G. Buchheit, Departmental Colloquium Series, Department of Materials Science and Engineering, Purdue University, West Lafayette, Indiana, April 4, 2011.

"Corrosion inhibition by vanadates: understanding inhibitor interaction with complex alloy microstructures and demonstration of delivery approaches using synthetic nanostructured ion-exchange compounds," R.G. Buchheit, Departmental Colloquium Series, Department of Materials Science and Engineering, University of Michigan, Ann Arbor, Michigan, February 4, 2011.

"Evaluation of the lanthanide cations (Ce^{3+}, Pr^{3+}, La^{3+}) as corrosion inhibitors for the high strength aluminum alloy AA 2024-T3," A. Chilukuri, R.G. Buchheit, International Society of Electrochemistry, Columbus, OH, May, 2010.

"Study of the corrosion inhibition by rare earth metal cations and zinc cation", A. Chilukuri, R.G. Buchheit, "International Society of Electrochemistry, Columbus, OH, USA, May 2010.

"In-situ Monitoring of Undercoating Corrosion Damage Accumulation by Direct Optical Interrogation (DOI)," R. G. Buchheit, Monash University Corrosion Forum, Monash University, Clayton, Victoria, Australia, October 25, 2010.

"Corrosion inhibition of Al-Cu-Mg Alloy 2024-T3 by vanadates: understanding the action of complex aqueous speciation on a complex microstructure," R.G. Buchheit, Deakin University, University Colloquium, Geelong, Victoria, Australia, October 15, 2010.

"Corrosion inhibition of Al alloys by vanadate and cationic zinc, and examples of inhibitor delivery in coating sytems using of ion exchange compounds and the amine functionality in chitosan," R.G. Buchheit, Commonwealth Science and Industry Research Organisation Divisional Seminar, Clayton, Victoria Australia, October 8, 2010.

"Predicting Long-term Coating System Performance Using Neural Network Models and Sensitive Short-term Coating Measurements," R.G. Buchheit, F. Gambina, G. Kumar, Cleveland Coatings Society Sink or Swim Conference, May 18, 2010. (plenary lecture).

"Predicting Long-Term Coating System Performance Using Neural Network Models and Sensitive Short-Term Coating Measurements," F. Gambina, G. Kumar, and R.G. Buchheit, 2010 Research Topical Symposium, Annual NACE meeting, Houston, TX, March 2010.

"Scientific Understanding of Non-Chromate Inhibitors," R.G. Buchheit, ASETS Defense 2009, Sustainable Surface Engineering for Aerospace and Defense, Westminster. CO, September 1, 2009.